UNDERSTANDING
RHEOLOGY AND TECHNOLOGY
OF
POLYMER EXTRUSION

First Edition

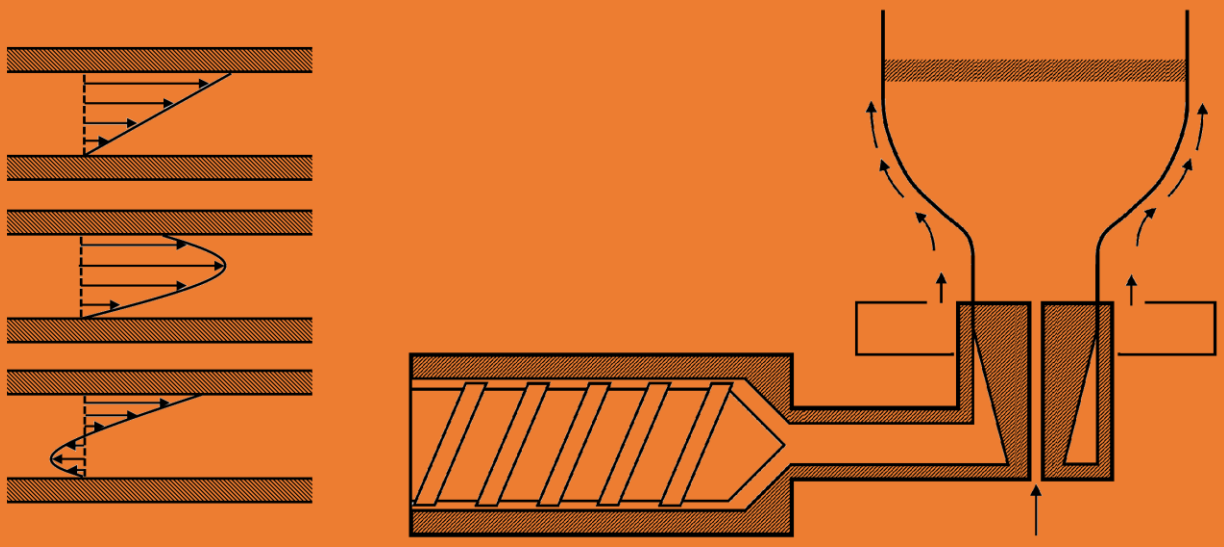

JOHN VLACHOPOULOS

NICKOLAS D. POLYCHRONOPOULOS

www.polydynamics.com

πάντα ῥεῖ

Omne influat

Everything flows

Alles fließt

Tout s’écoule

Todo fluye

Tudo flui

Tutto scorre

Всё течет

HERACLITUS (c.535 BC – c.475 BC)

About the authors

JOHN VLACHOPOULOS was educated at NTUA, Greece and Washington University, St. Louis, USA and he is Professor Emeritus of Chemical Engineering at McMaster University. He served as Department Chair in 1985-1988. He is the author of *Fundamentals of Fluid Mechanics (2016)* (downloadable from www.researchgate.com) and co-editor of *The SPE Guide on Extrusion Technology and Troubleshooting* (SPE,2001) and *Rheological Fundamentals in Polymer Processing* (Kluwer, 1995). He is author/co-author of more than 300 publications in peer reviewed journals, in conference proceedings and in multiauthor books. He was on sabbatical research leave at I.K.T. Stuttgart, Germany (1975) and CEMEF, ParisTech, Sophia Antipolis, France (1981-82, 1988-89). He received from the Society of Plastics Engineers (SPE) the 2001 Education Award at ANTEC in Dallas, TX, and from the Extrusion Division of SPE the 2004 Distinguished Achievement Award at ANTEC in Chicago and the 2014 Bruce Maddock Award at ANTEC in Las Vegas. He is also the recipient of the Stanley G. Mason Award of the Canadian Society of Rheology (2007) and Fellow of the Canadian Academy of Engineering (FCAE). He was President of the Polymer Processing Society (PPS) 2005-2007, and member of several other professional associations. Through his company POLYDYNAMICS INC he has developed and licensed flow simulation software to more than 500 corporations in 30 countries around the world and he is an active consultant in the polymer processing industry.

NICKOLAS D. POLYCHRONOPOULOS was educated at Univ. Patras and Univ. Thessaly, Greece. He has been working for Polydynamics Inc since 2007, at first as Process Simulation Specialist and recently as R&D Engineer. He completed his doctorate at Univ. Thessaly in 2016. He worked for one year (2017-2018) for Rontis Hellas S.A. (Larissa, Greece) as R&D/Production Engineer on endovascular catheters. He has publications in peer-reviewed journals, conference proceedings and multiauthor books. These are in calendering, pultrusion, resin infiltration in porous media, viscoelastic effects in film casting, natural fiber composites, simulation of extrusion, particle sintering and nanofluids. He has presented lectures in Greece, Canada, Germany, Austria, The Netherlands and France.

UNDERSTANDING RHEOLOGY AND TECHNOLOGY OF POLYMER EXTRUSION

First Edition

JOHN VLACHOPOULOS

NICKOLAS D. POLYCHONOPOULOS

John Vlachopoulos

Professor Emeritus

Department of Chemical Engineering

McMaster University

Hamilton, ON, CANADA

Nickolas D. Polychronopoulos

Research & Development Engineer

Polydynamics Inc, Dundas, ON, CANADA

J. Vlachopoulos and Nickolas D. Polychronopoulos
Understanding Rheology and Technology of Polymer Extrusion
First Edition, Polydynamics Inc, Dundas, ON, Canada (2019)

ISBN 978-0-9952407-2-8 (book)

ISBN 978-0-9952407-3-5 (electronic book)

Published by:

POLYDYNAMICS INC
Dundas, ON, CANADA
www.polydynamics.com

PREFACE

This book is based on an introductory university course on polymer processing and a short course for polymer industry professionals. JV presented the course several times at McMaster University, starting in 1993. NDP presented a similar course at U. Thessaly in 2018. The short course to industry has been presented by JV, occasionally with the help of some of his co-workers, 78 times since 1987 in the following countries: Canada, Greece, Sweden, Venezuela, Mexico, USA, Finland, Czechoslovakia, Belgium, Brazil, Australia, Japan, Germany, Italy, Luxembourg, Spain, The Netherlands and New Zealand. The lectures were given in English, a few times in Greek, Spanish, German and once in Italian. Starting in 2003, NDP took part in several of the courses as co-organizer and recently as lecturer. At Polydynamics our experiences in developing and licensing flow simulation software to industry and our consulting activities influenced enormously the evolution of the presentation material.

The feedback from university and industry participants in our courses helped us a lot in deciding what aspects to include, how deeply to delve into the various topics and in shaping the presentation style. Targeting two audiences, university and industry, increased the challenges we faced. For the rheological parts of the book, we assumed that the reader has a basic understanding of fluid mechanics and heat transfer, and we tried to reduce, as much as possible, the number of equations and mathematical manipulations. Of course, we had to go beyond the unidirectional approach and use the double subscript tensor notation in a few spots in our attempt to elucidate certain useful but, to some degree, esoteric concepts. On the practical side, we have included several pages on the melt index test, which is totally omitted in several of the books we cited. For the technological parts, we provided a lot of pictorial explanations and descriptions. Throughout the book we included examples, equipment dimensions and operating conditions that are applicable in real world situations. We tried to convert the vast amounts of fragmented information available in technical books and journals into working knowledge and sound understanding. We believe that this book can be used as a textbook for a university course, or as a reference, or for solving specific and immediate problems.

JV is grateful to his students and coworkers at McMaster University and Polydynamics, especially to those who have directly or indirectly contributed to the topics covered in this book: A. E. Hamielec, A. N. Hrymak, M. R. Thompson, E. Takacs, D. Strutt, T. Nakamura, C. Kiparissides, E. E. Agur, E. Mitsoulis, C. Tzoganakis, H. Mavridis, A. Karagiannis, J. Vlcek, J. Perdikoulias, A. Zahavich, W. Song, R. J. Castillo, Z. Charlton, A. Torres, A. Rincon, C. T. Bellehumeur, M. Kontopoulou, V. Sidiropoulos, H. Larazzabal, V. Hristov, C. Santi, M. Emami, A. Goger, D. Kanev, N. Silvi, M. K. Bisaria, J-J. Tian and S-J. Liu.

NDP wishes to thank his doctoral dissertation supervisor T. D. Papathanasiou for his advice, support and encouragement and his co-workers I. E. Sarris and L. T. Benos for many helpful discussions.

We acknowledge with our deepest appreciation the authors whose work we have used and cited in the chapters of this book.

John Vlachopoulos

Nickolas D. Polychronopoulos

September 2019

CONTENTS

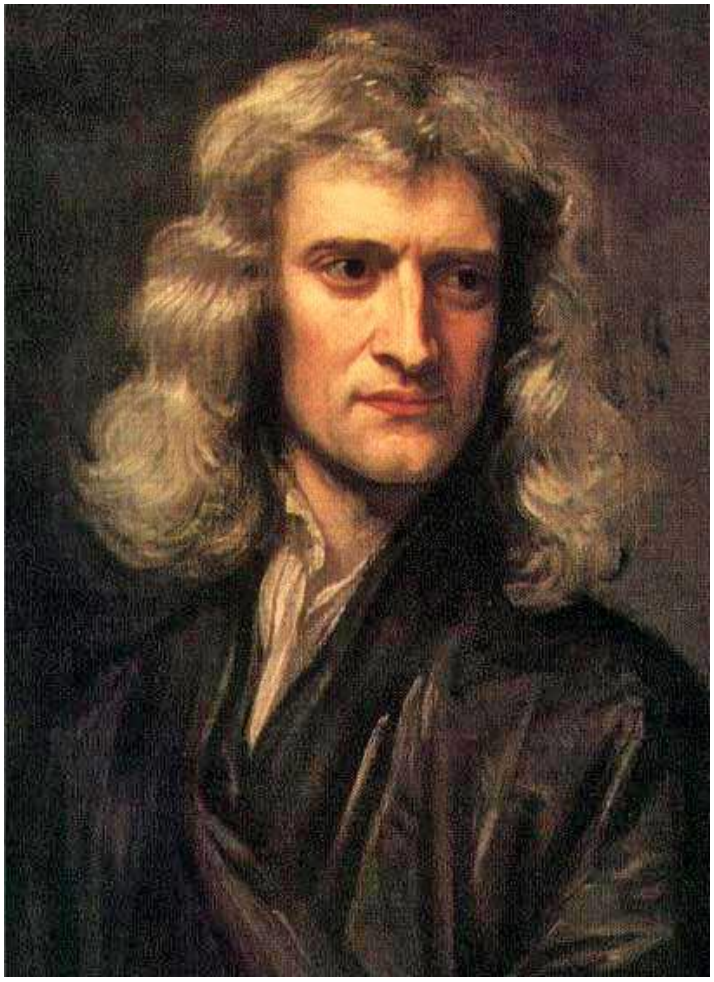

ISAAC NEWTON (1642-1727)

J. Vlachopoulos and N.D. Polychronopoulos "*Understanding Rheology and Technology of Polymer Extrusion*", First Edition, Polydynamics Inc, Dundas, Ontario, Canada (2019)

Chapter 1

POLYMER BASICS

1.1 Introduction

The word ***polymer*** comes from Greek and it means "many parts". Polymers, i.e. plastics and rubber, are substances whose molecules form long chains, made up from smaller parts (repeating units) as shown in Fig. 1.1-1.

Figure 1.1-1. Schematic representation of a polymer chain.

Polymers are characterized through the chemical and physical nature of the repeating unit in the chains. The word **plastics** refers to polymers which have been compounded (mixed) with various additives, before the production of the numerous products used today. Rubbers are polymers with very high degree of deformability. To the general public the word plastics usually implies materials which pose major pollution problems in the oceans and garbage landfills because the vast majority of them are not biodegradable. Plastics are easily recyclable, but collection, separation and recycling efforts vary a lot from one country to another. Plastics are also known (Morton-Jones, 1989) for

- having low strength and stiffness
- having temperature limitations
- deforming continuously (i.e. "creep") under applied force

The above features are definitely drawbacks when compared to more traditional materials like metal, wood or ceramic. But, why are plastics used in vast and continuously

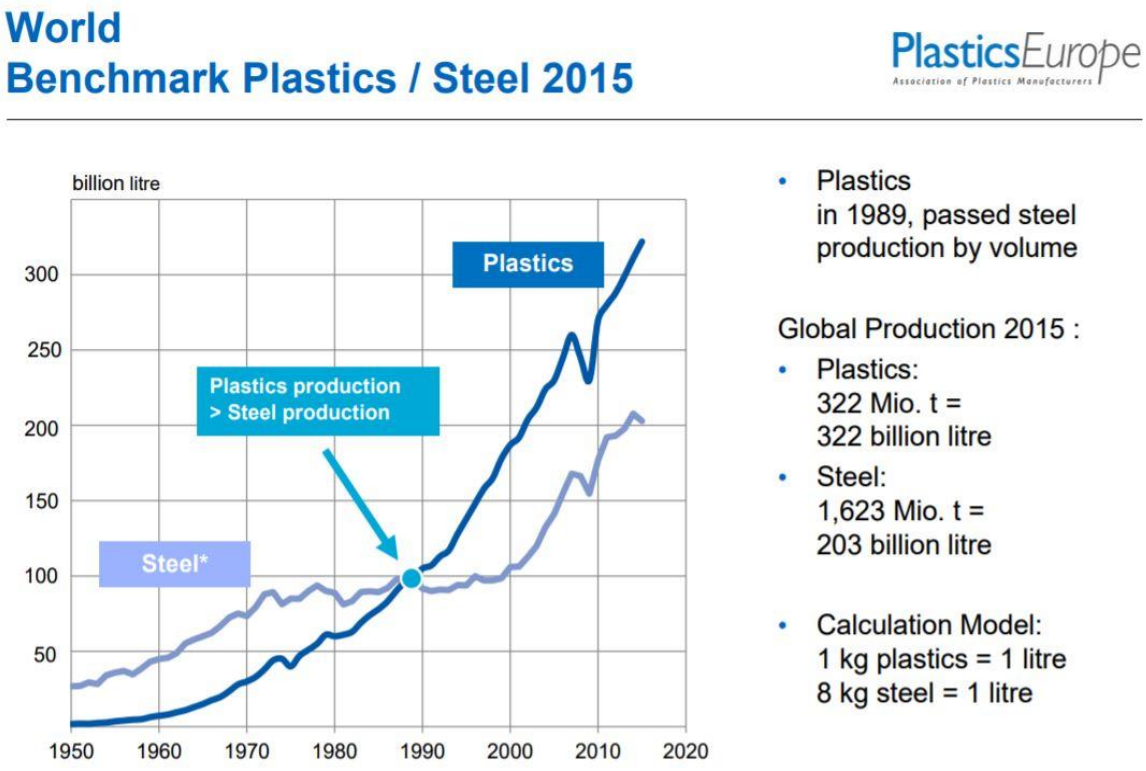

Figure 1.1-2. Volumetric consumption of plastics versus steel (from PLASTICS EUROPE).

increasing quantities? They have surpassed the volumetric production of steel as shown in Fig. 1.1-2 since 1989 and the gap is growing. Here are some advantages of plastics:

- Easily shaped or molded into complex shapes with minimum fabrication and finishing and relatively low cost
- Low densities, i.e. strong low-weight products
- Easy to produce fibers, films, pipe and profiles
- Thermal and electrical insulators
- Other special properties, e.g. often flexible, sometimes transparent, they can last for a long time without significant deterioration, some polymer grades have very low permeability to gases and liquids and they can be used for food and beverage packaging, they can be biocompatible (necessary for medical implants and devices) and are can be used with glass fibers, natural fibers, carbon fibers, carbon nanotubes or graphene for very strong composite structures.

New types of polymers and fiber-reinforced composites exhibit high performance and long service life. They are used extensively in aircraft/aerospace applications not only for military

aircraft (e.g. stealth aircraft are made of polymer matrix composites), but also in commercial aviation. For example, in Boeing 767 (first introduced in 1982) about 3% of the structural weight is due to polymer composites, while in the Boeing 777 (1995) it is about 10% and in the 787 (2011) about 50%. Similarly, Airbus A350 and A380 include significant amounts of polymer composites. Composites are used in aircraft both for reducing the weight and for increasing part performance and overall durability.

- The high performance polymers and composites are, of course, expensive. They make relatively few parts for **aircraft/aerospace, sports equipment** and other applications.
- Currently the biggest market is for lower priced **packaging, automotive, housing, electrical and electronic applications.** In 2014 the average car had 200 kg in plastics and for 2020 it is projected to have 350 kg.
- There is also a growing market for **medical plastics.**
- They are used extensively in **additive manufacturing (3D Printing)** technologies.

The challenge is to produce many parts at high production speeds and low costs, but with high performance and long service life characteristics.

For the production of the most common polymers (e.g. polyethylene, PE), the first step consists on steam cracking of hydrocarbons at very high temperatures for the production of ethylene (monomer, which is a gas). During a second step, ethylene is subjected to polymerization for the generation of long chain molecules and the product is eventually delivered in the form of flakes, powders or pellets.

Prices of monomers and polymers fluctuate in the world market and they are influenced enormously by the price of oil and by political events and we will avoid giving any figures in dollars, euros or any other currency. Roughly, the raw materials cost of commodity plastics (i.e. those produced in large volume) accounts for about 50% of the final plastic product price, but, of course, it all depends on the application, the performance requirements and the capabilities of the fabricator.

1.2 Historical Remarks

Humankind has used polymers since the beginning of recorded history (White, 1990). Leather, wood, wool and cotton are polymeric substances of natural origin. Also

- Important work on rubber was done in the early 1800's.

- The early manufactured **rubber** softened with heat and hardened with cold. In 1839, U.S. inventor Charles Goodyear invented the process of **vulcanization** (heat treatment called curing of a compound of rubber and sulfur) which led to products of considerable durability.
- In 1869, John Wesley Hyatt invented the first **synthetic plastic material** from cellulose nitrate and camphor. Celluloid is a tough material used in combs, film, toys, etc. Further developments led to rayon fibers.
- In 1909, "Bakelite" appeared (black telephones in old movies), named after its inventor Leo Bakeland.
- The polymeric nature of rubber and celluloid was not realized till the 1920's, when the German chemist Hermann Staudinger (Nobel Prize in chemistry 1953) clearly demonstrated the **macromolecular concept of long chains composed of repeating units**. They were confused with colloids before Staudinger.
- Staudinger's book "Die Hochmolekularen Organischen Verbindungen" (High Molecular Weight Compounds) appeared in 1932. Although many other people besides Staudinger made considerable contributions towards the elucidation of the macromolecular nature of polymers, it is reasonable to assume that 1932 marks the dawning of the polymer science age.
- In 1935 LDPE was produced by a small research team at ICI (Imperial Chemical Industries, Great Britain) and Nylon by Wallace Carothers and his team at the DuPont Experimental Station in USA.
- German chemist Karl Ziegler invented the titanium-based catalysts and Italian chemical engineer Giulio Natta used them for the production of polypropylene and other polyolefins. They were awarded jointly the Nobel Prize in chemistry in 1963. **Ziegler-Natta (Z-N) catalysts** have been used for the commercial production of polyolefins since 1956. As of 2019 more than 150 million tons are produced with Z-N and related catalysts annually.
- The discovery of **metallocene catalysts** at the University of Hamburg, Germany, in 1975 by Walter Kaminsky and Hansjoerg Sinn, led to the development of new single site catalysts for the production of polyolefins with a highly defined structure and superior properties.

1.3 Polymer Structure

In the simplest case, a polymer consists of a simple repeating unit

··········A A A A A A A A A A··········

The most important type of linear polymers are **vinyl** polymers

$$-\mathrm{CH_2}-CH- \\ \qquad\quad | \\ \qquad\quad \mathbf{R}$$

If	**R → H**	**POLYETHYLENE (PE)**
	R → CH_3	**POLYPROPYLENE (PP)**
If	**R → C_6H_5**	**POLYSTYRENE (PS)**
	R → Cl	**POLYVINYL CHLORIDE (PVC)**

Polymer chains may be ***linear*** or ***branched***. The branches may be either ***short*** or ***long*** and may themselves have branches as shown in Fig. 1.3-1.

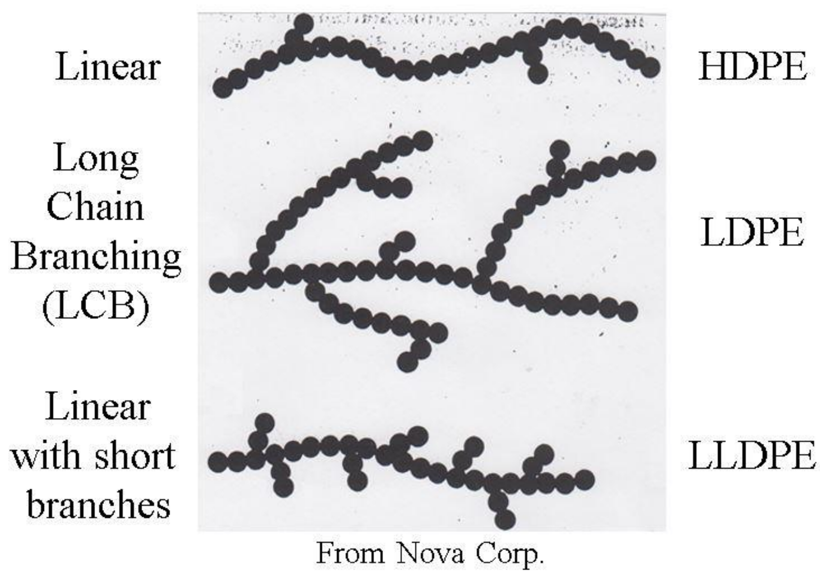

Figure 1.3-1. Sketches of linear and branched chains, from Nova Corporation.

Polymers having **long chain branching (LCB)**, even if less than one branch per ten thousand backbone atoms (called sparsely branched), are of great interest, because of their processing and end-use properties.

HOMOPOLYMERS are made of one type of small molecule (monomer).

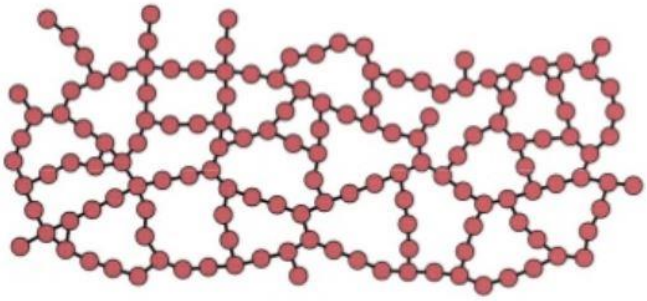

Figure 1.3-2. Sketch of a 3-D network of a typical cross-lined polymer, from the internet.

COPOLYMERS are made of two different types of monomers. COPOLYMERS can be ALTERNATING (if monomers alternate in the chain) or RANDOM (if arranged randomly).

BLOCK COPOLYMERS are those having one type of a monomer grouped together and all monomers of the other also grouped together.

GRAFT COPOLYMERS are those made of monomer B grafted (like branches) to polymer made of monomer A.

CROSS-LINKED polymers like in the sketch of Fig. 1.3-2 are those that form a 3-D network structure, e.g. like vulcanized rubber. They are unable to flow, they are hard solids.

1.4 Polymer Types

Thermoplastics: they can be melted by heating, solidified by cooling and may be re-melted repeatedly (PE, PP, PVC, PS etc.). **Thermosets:** in their fluid state, they are long-chain molecules, but still reactive and harden usually by application of heat and pressure, due to ***crosslinking***. They ***cannot be softened*** again to make them flow (e.g. the Bakelite, phenol formaldehyde, epoxies, most polyurethanes, etc). **Elastomers:** are cross-linked network structures with large deformability and essentially complete recoverability due to high degree of chain flexibility (e.g. natural or synthetic rubber)

Thermoplastics and ***thermosets*** are usually called ***plastics***. Frequently they are referred to loosely as **synthetic resins**, especially in pricing quotations. Pure polymers are seldom used on their own. They are ***compounded***, i.e. combined with other materials, typically by means of mechanical blending of powders or pellets or melt-state mixing to yield a compound which is ready to be used by the processor in the form of pellets, granules, powder or flakes for

production of plastic products by extrusion, injection molding, calendering, compression molding, rotational molding and other processes. The compounds include various types of additives, fillers, reinforcements or other polymers.

Additives:

- colorants
- flame retardants
- stabilizers - to prevent deterioration from light, heat or other environmental factors
- lubricants - to reduce viscosity and improve formability

Fillers:

- inorganic materials either to reduce actual amount of resin or to improve mechanical properties

Reinforcements:

- glass, natural or carbon fibers to increase strength and stiffness

Other polymers:

- to produce **blends** of polymers (for combination of beneficial properties)

1.5 Major Commercial Plastics

High density polyethylene (HDPE): Possesses linear chains due to the polymerization process. Linear chains are easy to compact together. Density=940~970 kg/m^3. Melting temperature ~135^{o}C. Used for containers, bottles, film, tape, wire and cable insulation and household appliances.

Low density polyethylene (LDPE): Has long and short branches. Branching prevents chains from being closely packed. Density=910~920 kg/m^3. Melting temperature~110^{o}C. It is soft and flexible. Used for bottles, film, garment bags, wire coating, and toys.

Linear Low Density Polyethylene (LLDPE): It is a copolymer of ethylene with small amounts of butene or octane-1. Density=910~920 kg/m^3. Melting temperature~124 ^{o}C. Used for thin high-strength film.

Polypropylene (PP): There are three categories of PP depending on tacticity. Tacticity refers to how the methyl groups are oriented with respect to the plane of symmetry of the polymer chain. Commercial PP is usually isotactic, that is all methyl groups are on one side of the chain and it melts at about 165 ^{o}C, but it can be higher. Density=905 kg/m^3. Possesses

many outstanding properties, including chemical resistance and rigidity. Used for automotive parts, appliances, fibers, luggage, etc. Syndiotactic PP has methyl group alternating on either side of the plane of symmetry of the chain and it has lower melting point. Atactic PP has methyl groups randomly aligned, it is amorphous and rubber-like at room temperature and is used as sealant or hot melt adhesive.

Polyvinyl Chloride (PVC): It is soft and processable at temperatures 175-200°C. Rather unstable chemically. It starts degrading at about 205 °C. Rigid PVC (with few additives, density=1400 kg/m^3) is used for pipe and housing applications. Plasticized PVC is used for flexible film sheet, upholstery (density=1300 kg/m^3).

Polystyrene (PS): Amorphous (no crystalline structure) polymer. It is processable above 150 °C. Density=1050 kg/m^3. It is often clear and rigid. Used for packaging, containers and modified with rubber for sporting goods, radio and TV housings, automotive parts, etc.

***Nylon-6 and Nylon-66 (Polyamides, PA)*:** T_{melt}=215°C (NYLON-6), T_{melt}=265°C and density=1140 kg/m^3 (NYLON-66). Used for synthetic fibers (e.g. for Nylon stockings) and other products.

Polyethylene Terephthalate (PET): T_{melt}=260°C, density=1360 kg/m^3, used for film, water and soft drink bottles and fibers.

Polycarbonate (PC): Amorphous polymer, processable above 250°C. Density=1150 kg/m^3. Used for compact disks (CDs), optical fibers, etc.

Polylactic Acid (PLA): Biodegradable polyester produced from corn starch and other renewable resources. Density=1210-1430 kg/m^3 and T_{melt}=150-160 °C used for biodegradable packaging, medical implants and in fused filament fabrication (FFF, 3D printing). PLA has become very popular in recent years due to the fact that it is derived from renewable resources and it is biodgradable.

Other Polymers

- Polymethyl Methacrylate (PMMA)
- Acrylonitrile-Butadiene-Styrene (ABS)
- Polytetrafluoroethylene (PTFE)
- Polyetheretheroketone (PEEK)
- Polyethersulfone (PES)

Table 1.5. **Commercial Classification of Thermoplastics**		
COMMODITY	LDPE, HDPE, PP, PS, PVC, PMMA	Low Performance
ENGINEERING	ABS, PC, PA (Nylon), PET	↕
ADVANCED	Liquid-Crystal Polymers (LCP), PTFE, PEEK, PES, PPS	Very High Performance

1.6 Thermal Properties of Polymers

In molten state, polymers are composed of entangled long molecules as shown in Fig. 1.6-1. "Entangled" does not mean that the molecules are knotted around each other, but that molecular displacements due to Brownian motion are highly restrained laterally. These impediments to motion have a determining role in the high viscosity of polymer melts and their viscoelastic properties. As it can be seen in the sketch of Fig 1.6-1, a polymer molecule is only allowed to move like a snake through the entangled mesh of other chains. That is why de Gennes (1979) coined the term **reptation.**

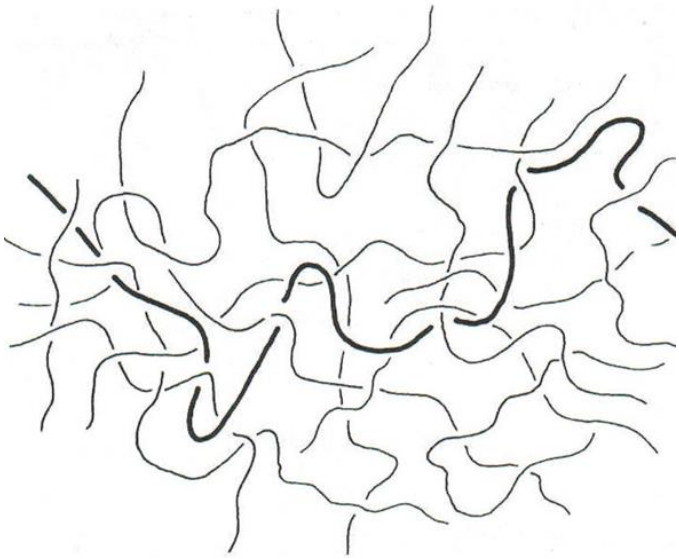

Figure 1.6-1. A long polymer molecule entangled with other long molecules in polymer melt. From Graessley (1982).

Solid polymers exist in crystalline (ordered) or amorphous (random) states. For amorphous polymers there is a certain temperature called the **glass transition temperature**,

T_g, below which the material behaves like glass, i.e. it is hard and rigid. Crystalline polymers also exhibit T_g, but this is masked to some extent by the crystalline structure. It corresponds to low mobility in the backbone of the chain. Crystalline polymers are characterized by the capacity of their molecules to form 3-D ordered arrays. Above their **melting temperature** T_m, they behave as highly viscous liquids. Increased crystallinity in a polymer is associated with increased strength and decreasing transparency. Most crystalline polymers are quite opaque.

- For a truly amorphous polymer like polystyrene, we cannot talk about a melting point.
- Most polymers are semi-crystalline, with crystallinity usually from 20% to 90%.
- Traditionally semi-crystalline polymers were represented in terms of the fringed-micelle model shown in Fig. 1.6-2a. Recently, models involving **folded lamellae** as shown in Fig. 1.6-2b have been proposed, but no completely accepted model exists at present.

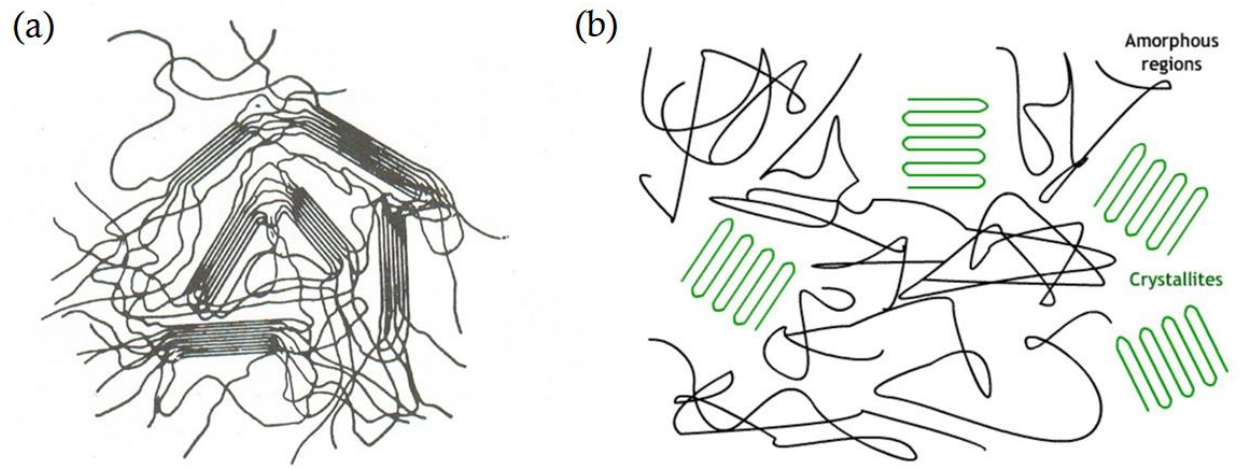

Figure 1.6-2. (a) Fringed-micelle model of solid polymer structure, having ordered (crystalline) and disordered (amorphous) regions and (b) folded lamellae forming crystallites surrounded by amorphous regions (from a Cambridge University online resource).

Specific Heat C_p is the amount of heat required to raise the temperature of a body (per kg) by one degree. **Heat Capacity** is the heat required per mole of a pure substance

Typical values:

- Water (at 20°C, 68°F) = 1 kcal/kg°C = 4182 J/kg°C
- Air (approximately) = 0.239 kcal/kg°C = 1000 J/kg°C
- Polyethylene (approximately) = 0.550 kcal/°C = 2300 J/kg°C
- Steel (approximately) = 0.108 kcal/°C = 450 J/kg°C
- Brick (approximately) = 0.215 kcal/°C = 900 J/kg°

For melting of a solid, heat must be added to shake and demolish the crystal structure present. **Heat of fusion (ΔH_f)** is the amount of heat required to melt a crystalline solid without raising its temperature. It is equal in magnitude (but opposite in sign) to the **heat of crystallization**. For example, for ice

$$\Delta H_f = 333{,}000 \text{ J/kg} = 80 \text{ kcal/kg}$$

This means that to melt 1 kg of water we need the same amount of energy as that required to raise 1 kg of water by 80°C, and yet with the actual melting, there is no increase in temperature. Here are some typical values for polymers:

- HDPE ΔH_f = about 250,000 J/kg
- LDPE ΔH_f = about 200,000 J/kg
- Amorphous polymers like PS, PMMA and PC $\Delta H_f = 0$

Glass transition temperature, melting temperature, crystallization temperature, heat of fusion, heat of crystallization, heat capacity and crystallinity are measured by differential scanning calorimetry (DSC). In this technique, the difference in heat flow between a reference and a sample during controlled heating or cooling is measured. The melting temperature is determined from the valleys and the crystallization temperature from the peaks as shown in Fig. 1.6-3. It should be noted that the difference between melting and crystallization temperatures is small for HDPE and large for PP (homopolymer).

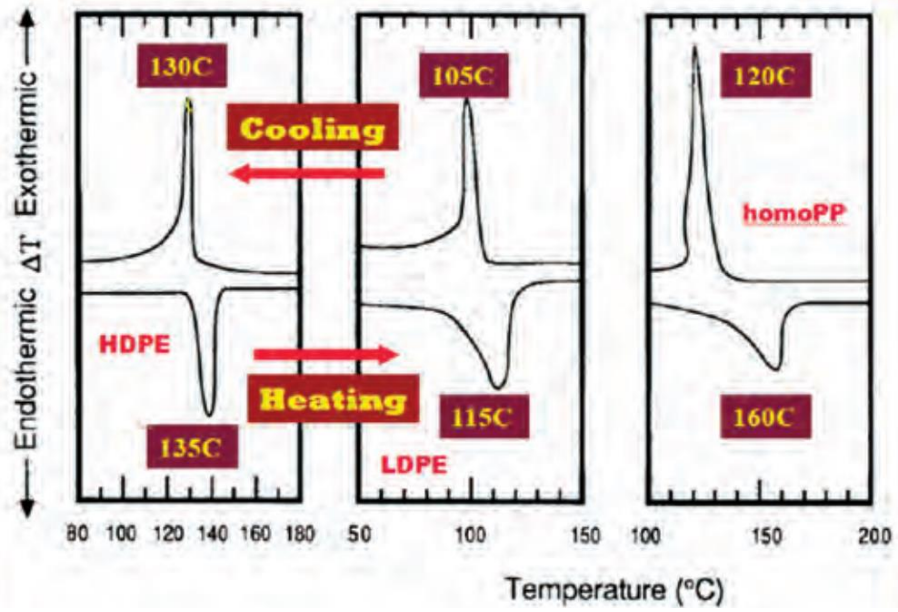

Figure 1.6-3. DSC heating and cooling curves for HDPE, LDPE and PP showing melting and crystallization temperatures. From Throne (2015).

Thermal properties of various common polymers are given in Table 1.6 from Vlachopoulos and Wagner (2001).

Table 1.6. **Typical thermal properties of several common polymers, adapted from Vlachopoulos and Wagner (2001)**

Polymer	Solid Density* ρ (g/cm³)	Glass Transition T_g	Melting Point T_m	Usual Melt Processing Range	Melt Density* ρ (kg/m³)	Thermal Conductivity k(W/m °C) (Btu/h ft °F)	Heat Capacity CP (J/kg °C) Btu/lb_m °F)	Heat of Fusion ΔH (J/kg) (Btu/lb)
HDPE	0.941-0.967	−130°C −202°F	130-137°C 266-278°F	160-240°C 320-464°F	780	0.25 0.145	2200-2400 0.52-0.57	210,000-300,000 90-130
LDPE	0.915-0.935	−130°C −202°F	106-112°C 223-234°F	160-240°C 320-464°F	760	0.20 0.115	2200-2400 0.52-0.57	190,000-240,000 80-100
LLDPE	0.910-0.925	−130°C −202°F	125°C 257°F	160-240°C 320-464°F	760	0.20 0.115	2200-2400 0.52-0.57	190,000-240,000 80-100
PP	0.890-0.910	−20°C −4°F	165°C 329°F	180-240°C 356-464°F	730	0.18 0.10	2000-2200 0.48-0.52	210,000-260,000 90-110
PVC (Rigid)	1.30-1.58	80°C 176°F	175°C 347°F	165-205°C 329-401°F	1250	0.17 0.10	1000-1700 0.24-0.41	170,000-190,000 70-80
PS	1.04-1.10	100°C 212°F	amorphous**	180-240°C 356-464°F	1000	0.15 0.09	1300-2000 0.31-0.48	amorphous**
PMMA	1.17-1.20	105°C 221°F	amorphous**	180-230°C 356-446°F	1050	0.19 0.11	1400-2400 0.33-0.57	amorphous**
PET	1.34-1.39	80°C 176°F	265°C 509°F	275-290°C 527-554°F	1160	0.18 0.10	1800-2000 0.43-0.48	120,000-140,000 50-60
ABS	1.01-1.04	105-115°C 221-239°F	amorphous**	200-290°C 392-554°F	990	0.25 0.145	1300-1700 0.31-0.41	amorphous**
Nylon-66	1.13-1.15	90°C 194°F	265°C 509°F	275-290°C 527-554°F	980	0.20 0.115	2400-2600 0.57-0.62	190,000-205,000 80-88
PC	1.2	140°C 284°F	amorphous**	250-305°C 482-581°F	1050	0.22 0.13	1300-2200 0.31-0.52	amorphous**

***** Melt densities have been estimated for roughly the mid-temperature of the processing range. See Mark (1996) for expressions in the form of $p=A–BT±CT^2$

***** Amorphous resin does not possess crystallinity and consequently no melting point or heat of fusion (i.e. heat to break down crystal structure) can be determined.

1.7 Molecular Weight and Molecular Weight Distribution

Molar Mass (MM) is the term recommended by International Union of Pure and Applied Chemistry (IUPAC), having SI units of (g/mol). However, the term Molecular Weight (**MW** (dimensionless)) is used widely and it is the terminology throughout this book. The Molecular Weight (**MW**) of WATER H_2O is 2×1+16=18. The ethylene **monomer** -(C_2H_4)- has molecular weight (**MW**): 12×2+4×1=28. Polyethylene is composed of many ethylene monomer units

-X-X-X-X-X--(C_2H_4)-(C_2H_4)-(C_2H_4)-(C_2H_4)-(C_2H_4)-X-X-X-X-X-X-

- If $(C_2H_4)_{50}$ it is a wax (**MW**: 50×28=1400)
- If $(C_2H_4)_{5000}$ it is a polymer resin suitable for plastic films (**MW**: 5000×28=140,000)

Commercial polymers generally contain a distribution of molecular weights. The **Molecular Weight Distribution (MWD)** is specified in terms of average molecular weights (Bueche, 1962):

- Number-Average M_n
- Weight-Average M_w
- Z – Average M_z
- Z+1 – Average M_{z+1}

If the number of molecules with molecular weight M_i is given by n_i, the total weight of the sample is $\sum n_i M_i$ and the total number of molecules is $\sum n_i$, the number-average molecular weight is given by

$$M_n = \frac{\sum n_i M_i}{\sum n_i} \tag{1.7-1}$$

If the weight fraction of material having a molecular weight M_i is w_i, we have

$$w_i = \frac{n_i M_i}{\sum n_i M_i} = \frac{n_i M_i}{W} = \frac{weight\ of\ M_i}{total\ weight} \tag{1.7-2}$$

Thus

$$\begin{aligned} n_i M_i &= W w_i \\ n_i &= W \frac{w_i}{M_i} \end{aligned} \tag{1.7-3}$$

and the definition of M_n becomes

$$M_n = \frac{\sum n_i M_i}{\sum n_i} = \frac{\sum w_i}{\sum \left(\frac{w_i}{M_i}\right)} \tag{1.7-4}$$

Other definitions of averages include the weight-average molecular weight

$$M_w = \frac{\sum n_i {M_i}^2}{\sum n_i M_i} = \frac{\sum w_i M_i}{\sum w_i} \tag{1.7-5}$$

the Z–average molecular weight

$$M_z = \frac{\sum n_i {M_i}^3}{\sum n_i {M_i}^2} = \frac{\sum w_i {M_i}^2}{\sum w_i M_i} \tag{1.7-6}$$

and the Z+1–average molecular weight

$$M_{z+1} = \frac{\sum n_i {M_i}^4}{\sum n_i {M_i}^3} = \frac{\sum w_i {M_i}^3}{\sum w_i {M_i}^2} \tag{1.7-7}$$

Example E1.7-1

Consider a polymer for which 99% of the weight is material with M=20,000 and 1% with M=10^9. Determine the M_n, M_w, M_z and M_{z+1}.

Solution

$$M_n = \frac{\sum w_i}{\sum\left(\frac{w_i}{M_i}\right)} = \frac{1}{\frac{0.99}{20{,}000} + \frac{0.01}{10^9}} = 20{,}202$$

$$M_w = \frac{\sum w_i M_i}{\sum w_i} = \frac{0.99 \times 20{,}000 + 0.01 \times 10^9}{1} \cong 10^7$$

$$M_z = \frac{\sum w_i M_i^{\,2}}{\sum w_i M_i} = \frac{0.99 \times 20{,}000^{\,2} + 0.01 \times 10^{18}}{10^7} \cong 10^9$$

$$M_{z+1} = \frac{\sum w_i M_i^{\,3}}{\sum w_i M_i^{\,2}} = \frac{0.99 \times 20{,}000^3 + 0.01 \times 10^{27}}{0.99 \times 20{,}000^2 + 0.01 \times 10^{18}} \cong 10^9$$

We note that the 1% of the very high molecular weight fraction has little effect on the number average molecular weight, but huge effect on the rest (because of the higher powers involved). The **MWD** can be ***narrow*** (***monodisperse*** if all polymer chains have exactly the same molecular weight, which is practically impossible) or ***broad***. The size of the molecular chains and the breadth of the distribution determines several flow and end-use properties. For the "most probable" (Gaussian) distribution

$$w_i = \frac{M}{M_n^{\,2}} exp\left(-\frac{M}{M_n}\right) dM \qquad (1.7\text{-}8)$$

is the weight fraction of polymer with molecular weight $M \pm dM/2$... So, by replacing the summation with an integral, we end up with M_n=$M_w/2$=$M_z/3$=$M_{z+1}/4$

The ratio $\boldsymbol{M_w/M_n}$ is often called the ***polydispersity*** and it is used to denote whether a given polymer grade has narrow or broad *MWD*. For most commercial polymers, M_w~ 10,000 - 500,000. The polydispersity varies according to the polymerization method and conditions

Commercial PS: M_w/M_n ~ 2.5 - 4

Commercial PP: M_w/M_n ~ 2.5 - 10

Commercial PE: M_w/M_n ~ 2.5 - 30

The **viscosity average molecular weight** M_v is obtained from a dilute polymer solution viscosity called the Intrincic Viscosity (IV), usually denoted by $[\eta]$, through the Mark-Houwink equation

$$[\eta] = K M_v^{\ a} \qquad (1.7\text{-}9)$$

where K and α are constants depending on the polymer-solvent system. IV is determined by dissolving less than 1% of polymer in a solvent and measuring the time required for certain volume of the solution to flow through a capillary tube for several different concentrations and extrapolating to 0% concentration. It reflects the capability of the polymer to enhance the viscosity of the solvent. M_v lies between the number and weight average molecular weights. Bottle-grade PET has IV in the range of 0.75 to 1.0 dL/g, which corresponds to average molecular weight between 24,000 and 36,000.

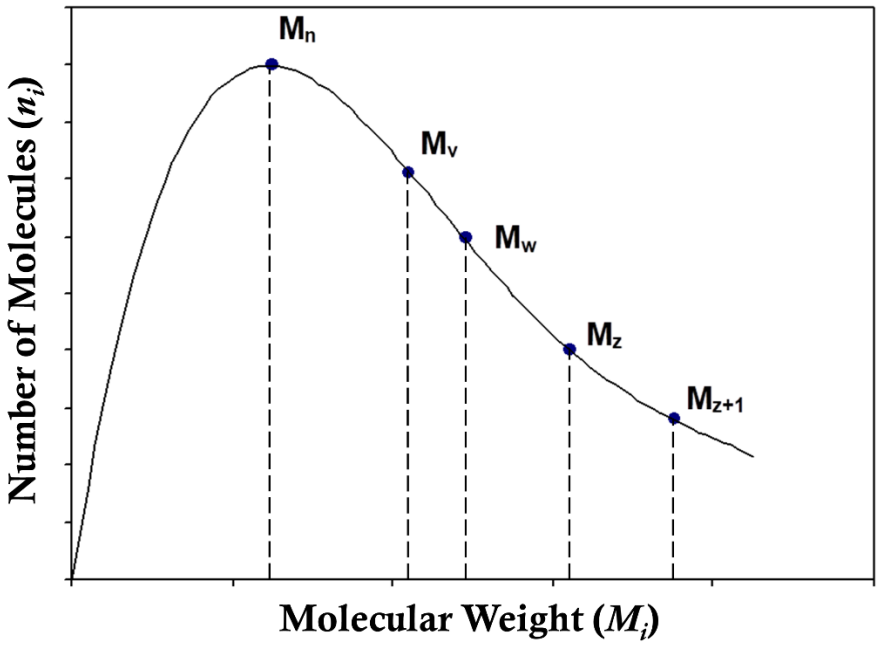

Figure 1.7-1. Schematic representation of a typical molecular weight distribution (MWD).

Measurement of the MWD is usually done by Gel Permeation Chromatography (GPC) (see Grulke, 1994) and the determination of M_n, M_w, M_z and M_{z+1} it is a rather tedious process. A sketch of a typical MWD curve is shown in Fig. 1.7-1 and actually measured MWD curves for two LDPEs are shown in Fig.1.7-2. Fig. 1.7-3 exhibits a bimodal molecular weight distribution of an HDPE copolymer produced in two reactors for the purpose of combining beneficial properties. Values of M_z and M_{z+1} are rarely provided in technical data sheets. Determination of M_v is relatively easy and it is frequently available in technical data

sheets, in lieu of average molecular weight, for polymers like Ultra High Molecular Weight Polyethylene (UHMWPE), PET and Polyamide (PA, Nylon).

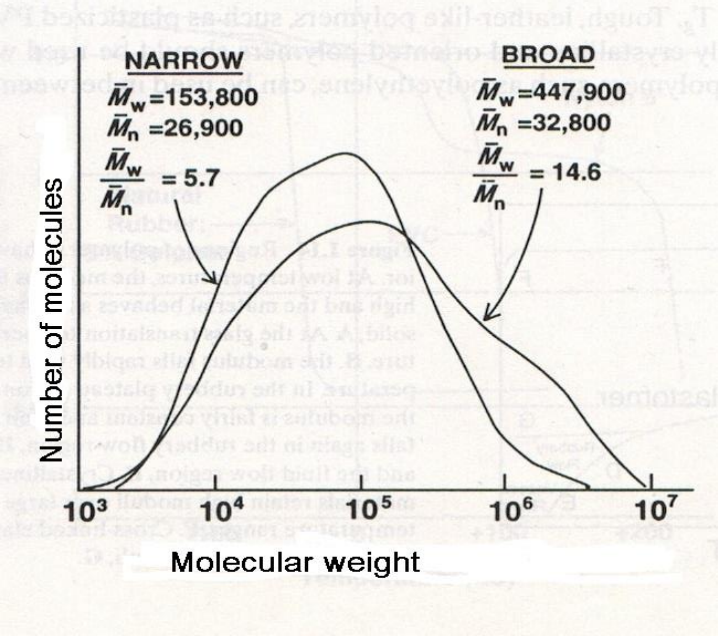

Figure 1.7-2. Molecular weight of two LDPEs determined by GPC. Adapted from Grulke (1994).

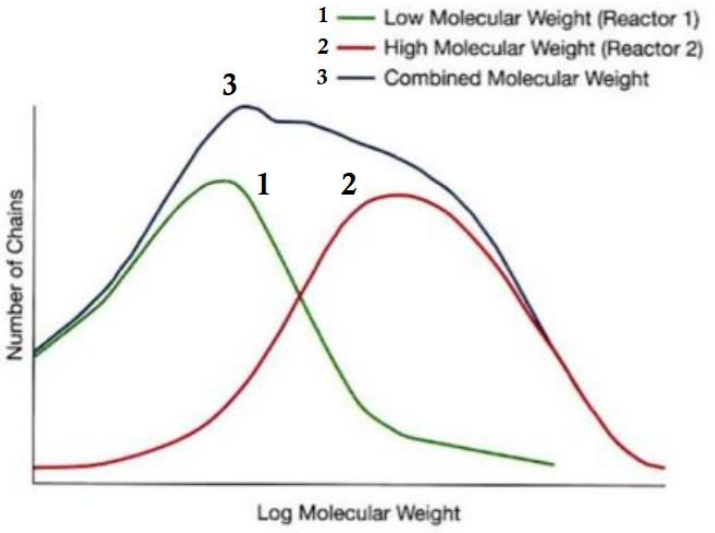

Figure 1.7-3. HDPE bimodal molecular weight distribution. Adapted from Hanik (2018).

Recent developments in metallocene and other single site catalysts (Kaminsky, 2013) have enabled the production of polyolefins of controlled molecular weight and distribution, tacticity (that is spatial molecular arrangements) and long chain branching. It has become possible to produce HDPE, LLDPE, PP and other polyolefins having improved end-use properties.

1.8 Zero-Shear Viscosity and Molecular Weight

At very low shear rates the viscosity of molten polymers approaches a limiting value which is called zero-shear viscosity η_0. As expected, polymer viscosity increases with the molecular weight. In fact, it has been found that for linear polymers of low molecular weight, η_0 is proportional to the molecular weight. However, when the molecular weight exceeds a certain value (M_c) the zero-shear viscosity is proportional to the molecular weight raised to the power of 3.4.

$$\begin{aligned} \eta_0 &= KM & M < M_c \\ \eta_0 &= KM^{3.4} & M > M_c \end{aligned} \qquad (1.8\text{-}1)$$

M_c is the critical molecular weight above which the molecules are long enough that they impede lateral motions, by some sort of an entanglement mechanism. The constant K and the critical molecular weight M_c depend on both the polymer and the temperature (for PE M_c=4,000 and for PS M_c=36,000). However, the exponent shows very little variation for linear

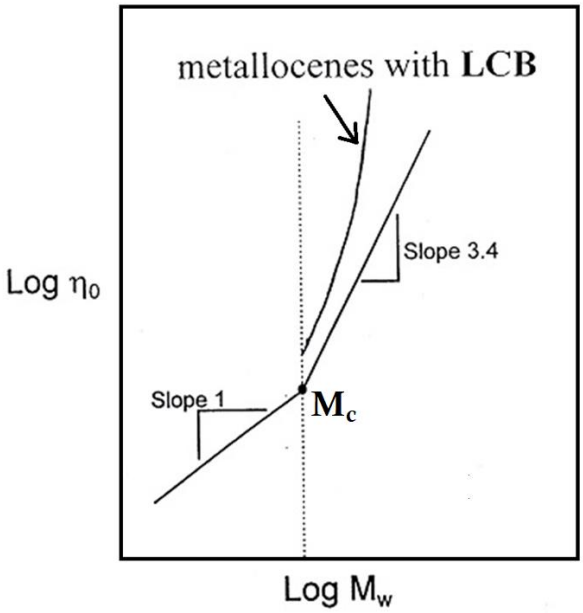

Figure 1.8-1. Zero-shear viscosity versus molecular weight.

polymers (between 3.4 and 3.6). For metallocene polymers with long chain branching (LCB) the exponent can exceed 6.0, as shown in Fig. 1.8-1.

For linear monodisperse polyethylene, Dealy and Larson (2006) give

$$\eta_0(Pa \cdot s) = 3.40 \times 10^{-15} M^{3.60} \quad at \quad 190^o C$$

for example, for a PE having M_w=200,000 (film grade), η_0=41,227 Pa.s.

1.9 Mechanical Properties of Polymers

The most common technique for measuring polymer properties is tensile testing as shown schematically in Fig. 1.9-1. For small deformations of the sample shown in Fig. 1.9-1a, the applied ***stress*** σ is related linearly to the resultant **strain** ε (see Fig. 1.9-1b)

$$\sigma = E\varepsilon \tag{1.9-1}$$

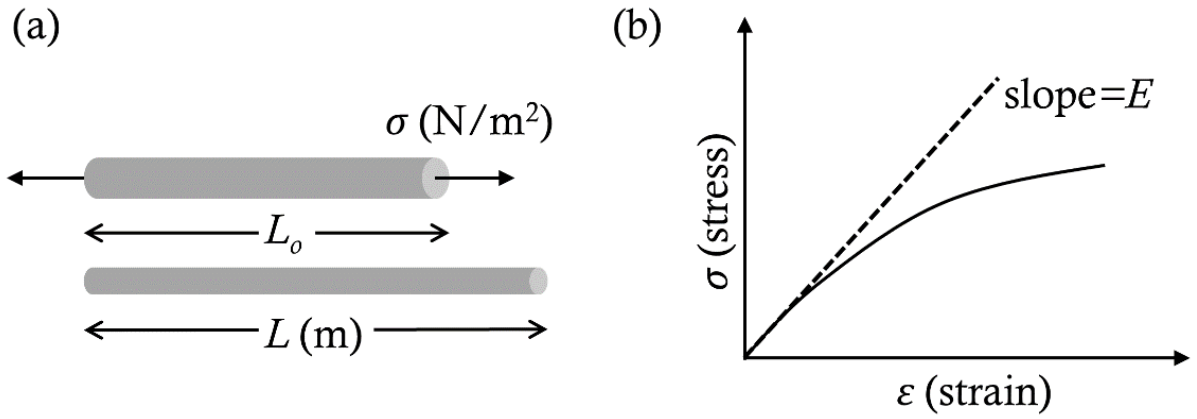

Figure 1.9-1. Schematic representation of tensile testing. The slope in a stress-strain diagram (i.e. small deformations of the sample) is the Young's (tensile) modulus E.

where E is the **Young's modulus of elasticity** with units N/m^2 [=] Pa. In the above equation the strain ε is given by

$$\varepsilon = \frac{L - L_0}{L_0} \tag{1.9-2}$$

and has no units. In technical data sheets it is usually expressed in percentage (%) and denotes how much the sample is elongated during the tensile test.

Typical values of tensile modulus E in GigaPascals, GPa (Giga = 10^9) are shown in Table 1.9.

Table 1.9. **Typical values of tensile modulus *E***	
LDPE	0.2 GPa
HDPE	1.0 GPa
NYLON 66	2.0 GPa
PVC	2.5 GPa
PS	3.4 GPa
STRUCTURAL STEEL	**260 GPa**

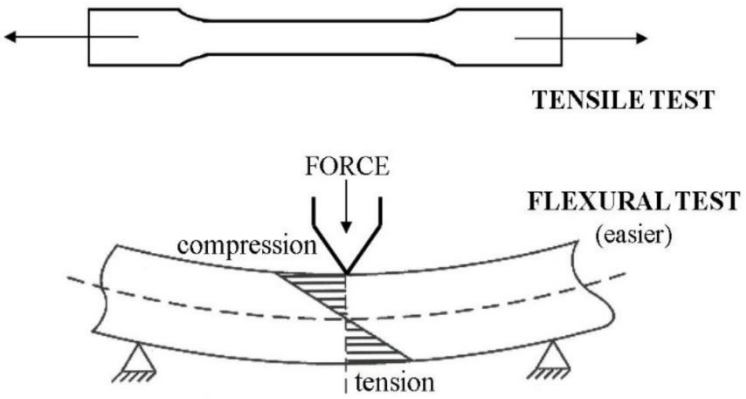

Figure 1.9-2. Schematic representation of Tensile and Flexural Testing.

Frequently, the flexural modulus is given in data sheet of polymer materials, due to different experimental set up. A "dogbone" shaped specimen is stretched for tensile modulus determination. A three-point bending is used for the flexural modulus as shown in Fig. 1.9-2. It is crucial to bear in mind the following (see also Fig. 1.9-3):

- **Flexural Modulus** and **Tensile Modulus** have exactly the same value for ideal elastic materials (although determined by different experimental setups), but for polymers Flexural Modulus is usually a bit higher (up to about 20% or so) than the Tensile Modulus.

"dog-bone" specimen subjected to extension

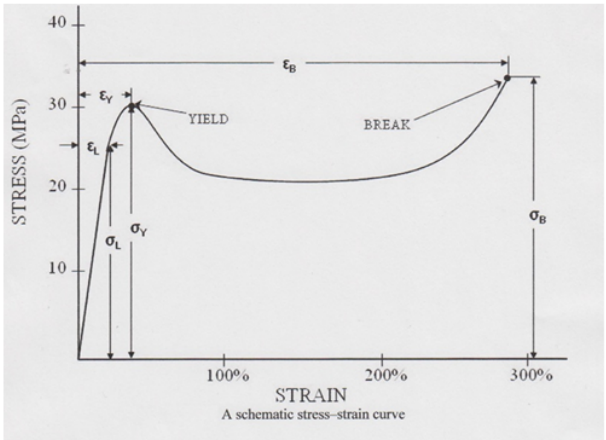

Where:

- STRESS=FORCE/AREA
- STRAIN=$(L-L_o)/L_o$ (specimen change in length)
- TENSILE MODULUS $E=\sigma_L/\varepsilon_L$ (slope of straight line, about 1GPa for HDPE, 2 GPa for PP and 3GPa for PVC, pipe grade)

- ε_Y=STRAIN AT YIELD (about 9% for HDPE, 8% for PP and 4% for PVC)
- ε_B=STRAIN AT BREAK (about 600% for HDPE, 300% for PP and 20% for PVC)
- σ_Y=STRENGTH AT YIELD (about 27 MPa for HDPE, higher for PP and PVC)
- σ_B=STRENGTH AT BREAK (about 32 MPa for HDPE, higher for PP and PVC)

Figure 1.9-3. Schematic of strain-strain behavior of polymers and typical results for three common polymers.

- **Stiffness** is a property of the structure and is proportional to the **modulus** of the material e.g. We talk about the stiffness of PE pipe, but the modulus of PE.
- **Tensile Strength** is the stress required to **break** a specimen measured in **Pa**. Another useful quantity is the stress at yield (**yield strength**)
- **Toughness** is the energy required to break a material. It is determined, from the integral under the stress vs strain curve. A material may be strong and tough if it breaks under high forces at high strains. **Brittle** materials are strong, but they break at low strains (glass is brittle, vulcanized rubber (e.g. tires) is tough). Toughness is measured in J/m^3.

The "strength" of steel is derived from primary (chemical) bonds, while the "weakness" of most plastics is due to relatively weak (about 100 times smaller) cohesive forces (Van der Waals) between the entangled and coiled long chains. To produce super-strong plastics, we must align the polymer chains, because extended chains having carbon-carbon bonds give us a lot of strength. High orientation of polymer chains can be achieved by special processing techniques. Ultra high molecular weight polyethylene (UHMWPE) is processed by **gel spinning** (Nakajima, 1994) for the production of widely available fibers like DYNEEMA having tensile modulus of up to 130 GPa (compare to 260 GPa for steel) and tensile strength of up to 3.9 GPa (compare to 400 MPa for steel). Also, high performance products are possible by **solid phase processing** (Ward *et al.*, 2000). At low temperatures the chains have limited mobility and after stretching they cannot curl up again, so they retain their orientation.

A systematic classification of tensile properties would be on a modulus E versus temperature T diagram as shown in Fig. 1.9-4. This figure shows that it is all a question of chain mobility (none for glass, a lot for melt). Crystallinity inhibits chain mobility and gives hardness to polymers. The modulus vs temperature diagram shows five regions: (1) Glass (the polymer is hard solid), (2) The glass transition region T_g (not sharp), (3) Rubbery plateau, (4) Melting region (sharp drop for semi-crystalline polymers) and (5) Liquid melt.

While T_g is not a sharply defined temperature (Dealy and Wissbrun, 1990), it can be measured within a few degrees by determining the change in heat capacity C_p by Differential Scanning Calorimetry (DSC). We consider T_g as the lowest temperature at which we can consider the material **"flowable like a liquid".** The melting point T_m is meaningful only for semi-crystalline polymers. For Polystyrene (PS) which is amorphous, in practical situations we consider that it "melts", i.e. that flows like a liquid, at 50°C above T_g=100°C. Rule of

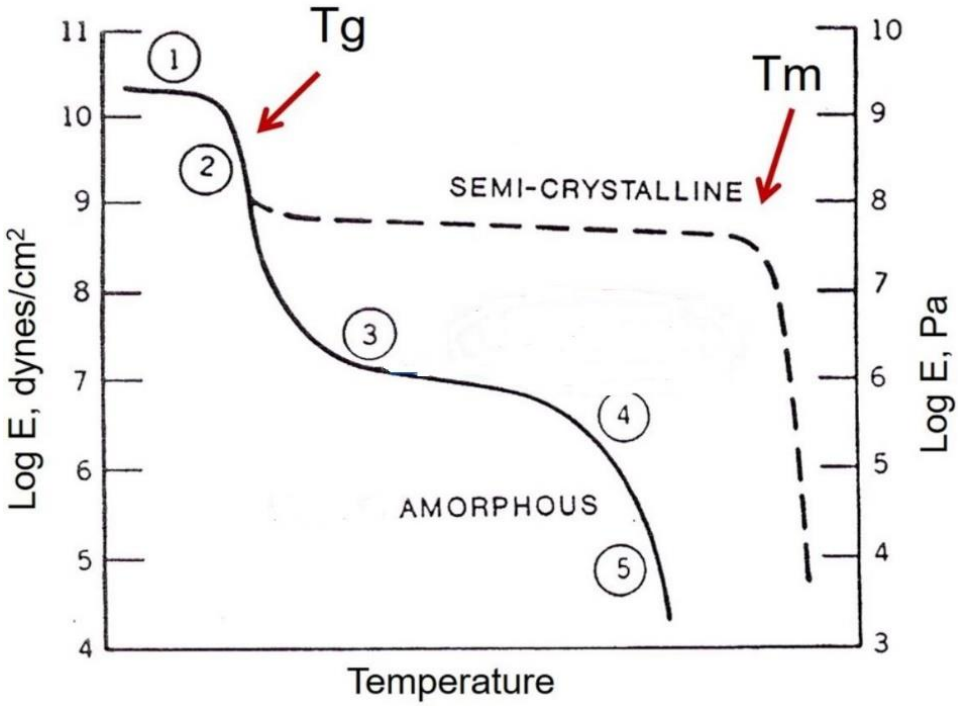

Figure 1.9-4. Modulus versus temperature of semi-crystalline and amorphous polymers.

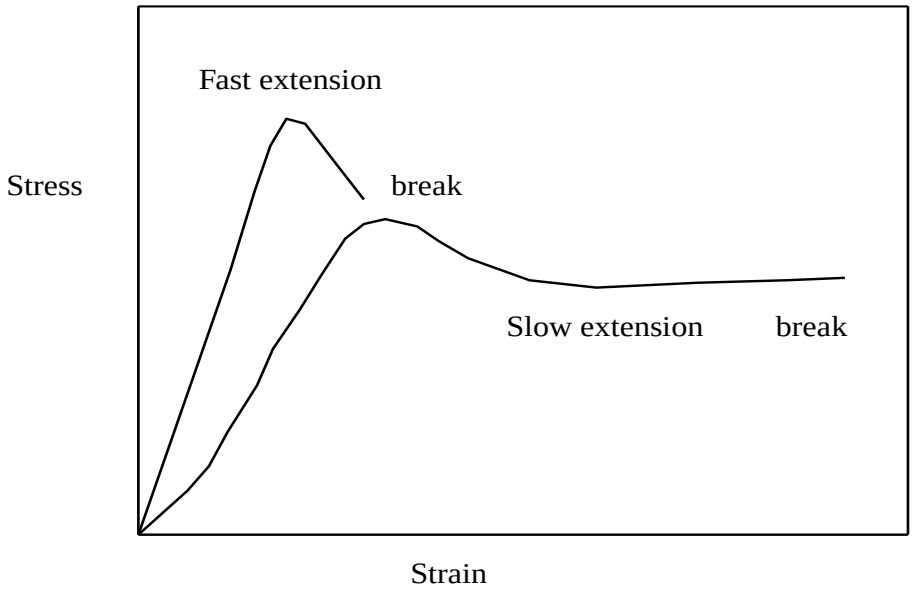

Figure 1.9-5. Schematic representation of slow and fast stress-strain behavior.

thumb: T_g (absolute Kelvin) ~ in the range $0.5\,T_m$ to $0.67\,T_m$. But, small variations in structure can affect chain regularity and the ability to pack, thus can change T_m a lot.

One important characteristic of solid polymers is the time dependence (Crawford, 1987) of their tensile properties. For example, rigid PVC may have a relatively high modulus at high extension rates (> 1 mm/s) while it has lower modulus at low extension rates (< 0.05

mm/s), as shown in Fig. 1.9-5. While the simple tensile test might be adequate for design purposes with steel, plastics must be subjected to additional testing especially for their long-

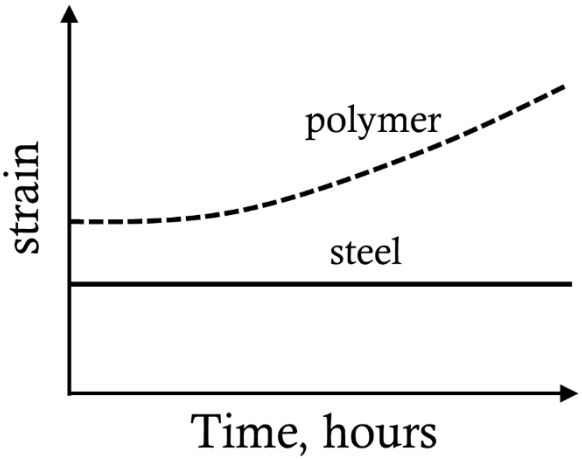

Figure 1.9-6. Schematic representation of creep behavior.

time properties. Under constant stress, polymers tend to "creep", i.e. strain (deformation) increases with time as shown in Fig. 1.9-6. Time-dependence is due to molecular chain rearrangement, i.e. the solid plastics have a tendency "to flow" under the influence of stress.

1.10 Density

Density is defined as the mass per unit volume of a polymer in SI units it is kg/m^3, for polymers it is usually given in g/cm^3. It reflects the ability of the molecules to pack close together. Linear molecules have higher density than similar branched ones, because branching restrains packing. Density values of some common polymers, including medium density polyethylene (MDPE) and metallocene mLLDPE, are shown in Table 1.10. At processing temperatures, the density of the molten polymers is about 10-20% lower than the solid density.

Table 1.10. **Density of solid polymers in gr/cm^3**	
HDPE	0.941 – 0.965
MDPE	0.926 – 0.940
LLDPE	0.910 – 0.925
mLLDPE	0.860 – 0.960
LDPE	0.915 – 0.929
PP	0.890 – 0.910
PVC	1.30 – 1.58

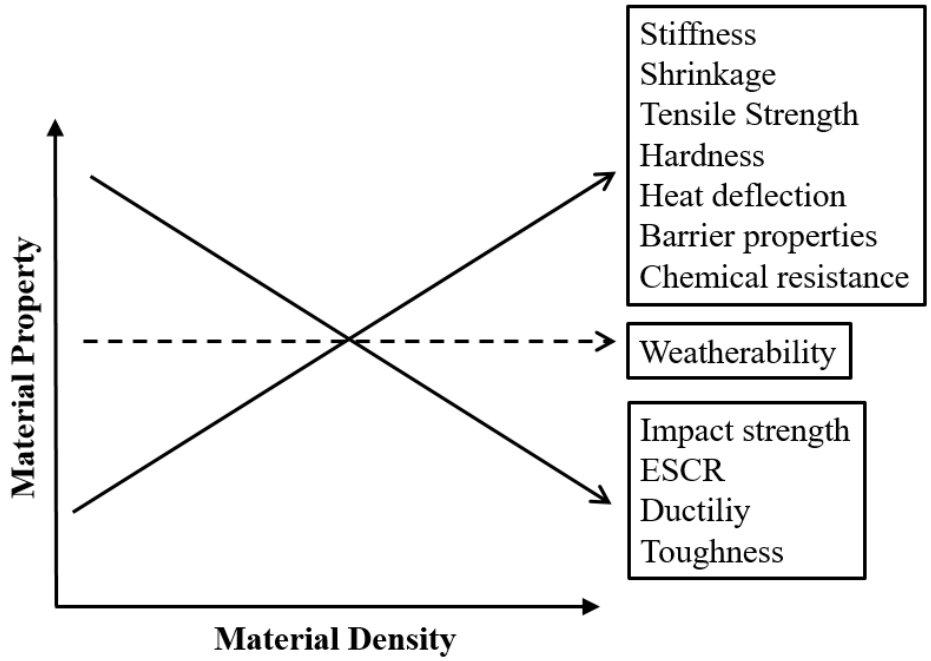

Figure 1.10-1. Density-property relations for polyethylene. Adapted from Nugent (2001).

Density and crystallinity are closely related. For example, HDPE is typically 70-90% crystalline while LDPE has 45-65% crystallinity. Several other properties correlate with density as shown in Fig. 1.10-1 for polyethylene. In this figure shrinkage, refers to the tendency of plastic products to contract after cooling from the processing temperature to room temperature. Hardness is the ability of a solid polymer to resist indentation. Heat deflection temperature is the temperature at which a plastic specimen deforms under a specified load. Barrier properties refer to the resistance to permeation of gases or liquids. Weatherability is the resistance of plastics when exposed to simulated outdoor environments. Impact strength is the energy required to break a test specimen struck by a pendulum weight. ESCR (environmental stress cracking resistance) is the ability of plastics subjected to stresses to resist failure, when exposed to crack initiating substances. Ductility refers to the ability of a material to undergo deformation without fracture.

1.11 Melt Flow Index (or Rate) and Intrinsic Viscosity

ASTM International, formerly known as American Society of Testing and Materials, and the International Organization for Standardization, which uses the abbreviation **ISO**, include numerous standards for testing of polymer materials. One of them, that is usually

included in plastics technical data sheets, is for their "flowability", by the Melt Flow Index (MFI) test (**ASTM D1238, ISO 1133**), which is in **grams per 10 minutes** flowing out of die of standard dimensions under the action of a load of specified weight in kilograms as shown

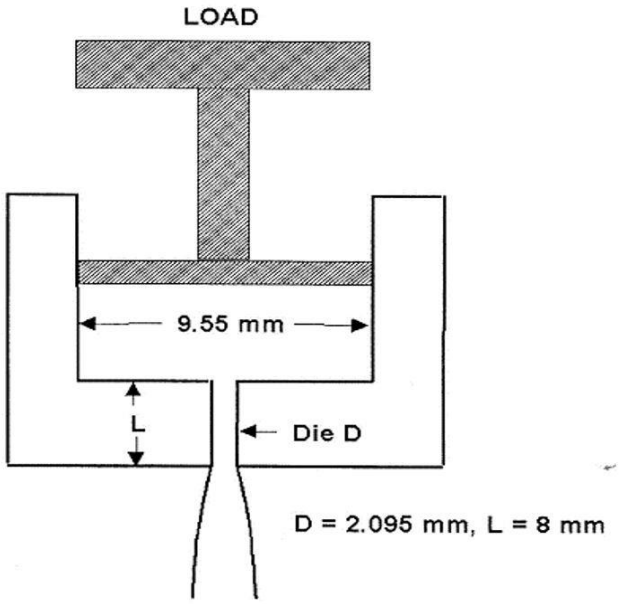

Figure 1.11-1. Schematic of a Melt Indexer.

Table 1.11-1. **Characteristics of TOTAL MDPE HF 513**

Property	Method	Unit	Typical value
Density	ISO 1183	g/cm³	0.934
Melt Flow Rate at 190°C/2.16 kg	ISO 1133	g/10 min	0.15
Melt Flow Rate at 190°C/21.6 kg	ISO 1133	g/10 min	14.5
Melting temperature	ISO 11357	°C	125
Vicat temperature	ISO 306	°C	118
Flexural Modulus (0.25% max)	ISO 178	MPa	620

in Fig. 1.11-1. The test is known also as Melt Index (**MI**) or Melt Flow Rate (**MFR**). Traditionally, the term MFR was used for PP, but it is now used interchangeably with MI or MFI for other polymers. The standard load is 2.16 kg, but also 5 kg, 10 kg and 21.6 kg are used. The temperature of the test is 190°C for PE and 230°C for PP. Other temperatures are specified by the corresponding ASTM and ISO standards, for other polymers. More information about MFI is included in Chapter 5 on rheological measurements. Table 1.11-1

shows part of the technical data sheet of a commercially available polymer from Total Petrochemicals (medium density polyethylene (MDPE)).

It should be noted that under the action of a 2.16 kg load, 0.15 grams of polymer come out of the die in 10 minutes. With a ten times heavier weight (21.6 kg) we obtain 14.5 grams in ten minutes, almost one hundred times more. This high value is due to the *shear-thinning* property of polymer melts. The polymer exhibits less resistance (*lower viscosity*) at high rates of flow. In this table, **Vicat temperature** is the temperature at which a test specimen is penetrated to a depth of 1 mm by a needle of specified dimensions under the action of specified load. It is indicative of the softening point of the polymer. Table 1.11-2 shows the ranges of weight average molecular weights (MW) of PE, standard Melt Index (MI, 2.6kg), high load Melt Index (HLMI, 21.6 kg) and the corresponding products/processes. MI less than 1, is referred to as **fractional Melt Index.** Table 1.11-3 shows characteristics of two very high molecular weight polyethylenes from CELANESE corporation. For GHR 8110, which has average molecular weight of 610,000 it is only possible to measure HLMI (21.6 kg). For GUR413 it is impossible to measure it, due to its extremely high viscosity of this Ultra High

***Table 1.11-2*. Molecular weight and melt index of various PE grades (adapted from J. Kron, Lyondell Basell, TAPPI presentation)**

Terminology	*MW* (Chain Length)	*MI*	*HLMI*	Product
Very Low MW	Below 1000	Above 100	-	Wax, Grease
Low MW	1000–100000	10–100	100–3000	Injection Molding
Medium MW	100000–150000	0.6–10	20–500	Injection Molding Film Extrusion Blow Molding
High MW	250000–750000	0.15–0.6	7–70	Blow Molding Extrusion Film Pipe
Very High MW	750000–2000000	---	2–12	Blow Molding Extrusion Film Pipe
Ultra High MW	Above 2000000	---	---	Forging

Table 1.11-3. **Technical data sheet from CELANESE**

Properties	Unit	Test method	Test specimen	GHR 8110	GUR 4113
Density	g/cm^3	ISO 1183 test method A	sheet	0.95	0.94
Intrinsic viscosity [η] IV	ml/g			510	1785
Average molecular weight	g/mol			$6.1 \cdot 10^5$	$3.9 \cdot 10^6$
Melt Index MFR 190/21.6	g/10 min	ISO 1133	powder	1.4 ± 0.3	–

Molecular Weight Polyethylene (UHMWPE) of 3,900,000. This table also shows the corresponding intrinsic viscosity values (IV).

For some polymer families (polyesters, Nylons etc) MFI is rarely supplied in technical data sheets due to experimental difficulties associated with degradation and moisture absorption. They choose **Intrinsic Viscosity (IV)** (ASTM D2857, D4603 or ISO 1628), where a dilute solution flow rate through a glass capillary tube is compared to pure solvent (as explained earlier). IV American units are 100 cm^3/g (dL/g). IV European units are cm^3/g, usually expressed as (mL/g). IV for bottle grade PET resins is usually between 0.70 and 1.0 dL/g (70 and 100 ml/g). IV is the inverse of concentration and it is directly related to the molecular weight as explained earlier in Section 1.7. Higher IV means higher molecular weight.

PVC polymers are often graded according to their **K-value**, which is a measure of their molecular weight. It is obtained from measurement of intrinsic viscosity in cyclohexanone solution. K-values range usually 35 and 80. Low K-values imply low molecular weight (which is easy to process, but has inferior properties) and high K-values imply high molecular weight (which is difficult to process, but has outstanding properties). Here are some typical K-values: K-57 for injection molding, K-67 (Rigid) for pipe, profiles and K-72 (plasticized) for flexible films, wires and cables.

1.12 Plastics in the Environment and Recycling

Global plastics production is projected to exceed 400 million tons in 2020 and the production growth rate is likely to continue unabated in the foreseeable future, as more people around the world raise their standard of living. If current trends continue, production of plastics will swell to about 2 billion tons per year by 2050. According to a recent study (Geyer *et al.*, 2017), from 1950 till 2015, 8.3 billion tons of plastics have been produced, 6.3 billion

tons of plastics waste has been generated and from this was 9% recycled, was 12% incinerated and 79% ended up in landfills. Plastics in the ocean is frequently in the news. According to some estimates (which are probably not terribly accurate) about 150 million tons circulate in the ocean and about 8 million tons of plastic waste end up in the oceans every year, which is totally unacceptable. Single use plastics like shopping bags, water and soft drink bottles, disposable tableware and most food packaging are the main source of plastics ocean pollution.

While plastics disposal in landfills appears safe in the short term, it will take hundreds of years for the waste to decompose. Actually there is a shortage of landfill space in many countries and the long term environmental impact of the byproducts of decomposition is unknown. Numerous organizations and some governments around the world are planning for zero plastics to landfills in the not too distant future. Plastics disposal in landfills is also wasteful of their value. Plastics are recyclable by one of three methods (Akovali *et al.*, 1998), which are the subjects of major research efforts currently. **Mechanical recycling** involves re-melting and reprocessing into new plastic products. **Chemical recycling** is the conversion back to monomers and chemicals for the production of new polymers and other uses in the chemical and oil industries. **Energy recovery** is accomplished by incineration. The decision on which type of recycling to follow depends on economic, ecological and technical considerations (Rudolph *et al.*, 2017, La Mantia, 2002).

Figure 1.12-1. Plastics identification codes for recycling purposes.

Mechanical recycling is relevant for this book and in the opinion of most experts it is the most promising. It consists of two parts: Reclamation and reprocessing. Reclamation is concerned with the collection and separation of products and/or their constituent materials. Reprocessing may involve production of plastic products from 100% recycled materials or mixing with virgin polymers for upgrading the quality. The identification codes of

Fig. 1.12-1 are very helpful for separating the various polymers at the consumer level. According to Vlachopoulos (2009), mechanical recycling is also beneficial of for reduction of the carbon footprint. For every ton of recycled polyethylene (PE) pellets produced for reprocessing, roughly two tons of CO_2 are saved from the amount required for the production of a ton of virgin PE.

Biodegradable polymers (Chiellini and Solaro, 2003) have received a lot of attention in recent years, with PLA being at the forefront. They offer an excellent solution for single-use or short-term-use applications. These may include food packaging, disposable tableware, water bottles, shopping bags, kitchen-waste bags and agricultural mulch-films. They can be made from renewable resources (like corn and other natural products) or from petroleum and/or natural gas. The demand for biodegradable plastics is rapidly growing, but at present they are less than 1% of the total volume of plastics produced annually. Biodegradable plastics have their own end-of-life problems. Some of them break down at a temperature higher than that of the oceans. PLA, having density in the range 1210-1430 kg/m^3, is not buoyant in water, so it sinks and by not being exposed to UV light it does not break down in ocean water. Biodegradable plastic products can easily contaminate a stream of recyclable plastics and significantly reduce their value. They are no easy solutions for reducing plastics pollution and its impact on the environment. Recycling is likely to play the most important role, while biodegradability will be for niche applications.

Bibliography

Akovali G., Bernardo C., Leidner J., Utracki L.A. and Xanthos M. (eds), *Frontiers in the Science and Technology of Polymer Recycling*, Nato Science Series E, Springer (1998)

Bueche F., *Physical properties of polymers*, Interscience, New York, USA (1962)

Chiellini E. and Solaro R. (eds.), *Biodegradable Polymers and Plastics*, Springer (2003)

Crawford R.J., *Plastics Engineering*, Pergamon Press, (1987)

Dealy J.M. and Wissbrun K.F., *Melt Rheology and its Role in Plastics Processing*, Van Nostrand Reinhold (1990)

Dealy J.M. and Larson, R.G., *Structure and Rheology of Molten Polymers,* Hanser (2006)

De Gennes P-G. *Scaling Concepts in Polymer Physics*, Cornell University Press (1979)

Geyer R., Jambeck J.R. and Lavender Law K., Production, Use, and Fate of All Plastics Ever Made, Sci. Adv., 3 (7), e1700782 (2017)

Graessley W.W., Entangled linear, branched and network polymer systems — Molecular theories in: *Synthesis and Degradation Rheology and Extrusion*, Advances in Polymer Science, vol 47., p. 67-117, Springer (1982)

Grulke E.A., *Polymer Process Engineering*, Prentice-Hall (1994)

Hanik P., Functional Contradictions: Insights into Process Improvement, Chem. Eng. Prog., 114 (12), 30-36 (2018).

Kaminsky W. (ed), *Polyolefins: 50 Years after Ziegler and Natta II. Polyolefins by Metallocenes and Other Single Site Catalysts*, Springer (2013)

La Mantia F. (ed), *Handbook of Plastics Recycling*, Rapra Technology (2002)

Mark J.E., *Physical Properties of Polymers Handbook*, American Institute of Physics, Woodbury (1996)

Morton-Jones D.H., *Polymer Processing*, Chapman and Hall (1989).

Nakajima T. (ed), *Advanced Fiber Spinning Technology*, Woodhead Publishing (1994)

Nugent P., *Rotational Molding: A Practical Guide* , www.paulnugent.com (2001)

Rudolph N., Kiesel R. and Aumnate C., *Understanding Plastics Recycling*, Hanser (2017)

Throne J., Thermoforming Technical Problems I Wish I Could Solve Forming Low-Density Foam, Thermoforming Quarterly of SPE, 34 (3) 18 (2015)

Vlachopoulos J. and Wagner J.R. Jr, *The SPE Guide on Extrusion Technology and Troubleshooting*, Society of Plastics Engineers (2001)

Vlachopoulos J., An Assessment of Energy Savings Derived from Mechanical Recycling of Polyethylene Versus New Feedstock, A report prepared for The World Bank Version 3.2 November 5 (2009)

Ward I.M., Coates P.D. and Dumoulin M.M., *Solid Phase Processing of Polymers*, Hanser Gardner Publishers (2000)

White J.L., *Principles of Polymer Engineering Rheology*, John Wiley and Sons Limited (1990)

HERMANN STAUDINGER (1881-1965)

Nobel Prize in Chemistry (1953)

J. Vlachopoulos and N.D. Polychronopoulos "*Understanding Rheology and Technology of Polymer Extrusion*", First Edition, Polydynamics Inc, Dundas, Ontario, Canada (2019)

Chapter 2

VISCOSITY AND UNIDIRECTIONAL MELT FLOWS

2.1 Introduction

The flow of molten polymers through processing equipment is primarily determined by their viscosity, which is the resistance to flow. Let us consider two long parallel plates placed a small distance h apart, the space between being filled with a fluid. One of the plates is fixed and the other moves parallel to it with a velocity U by the application of a force F, as shown in Fig. 2.1-1. The fluid in contact with each plate "sticks" to it and does not "slip" relative to it. Consequently, the velocity of the fluid touching each plate is the same as that of the plate.

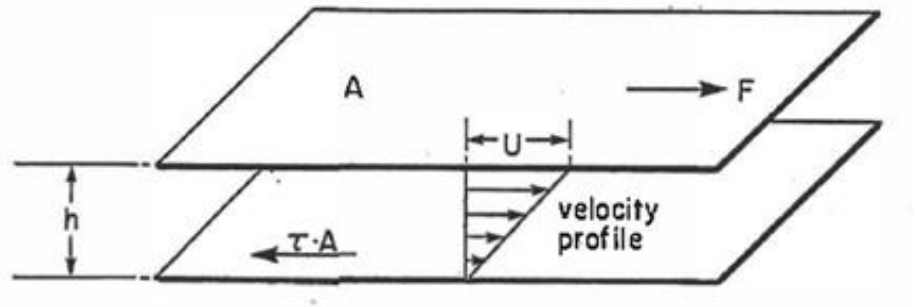

Figure 2.1-1. Schematic of fluid flow between two flat plates. The top plate moves to the right with velocity U.

Experiments have shown that for a large class of fluids (Newtonian) the velocity profile will be a straight line as shown in Fig. 2.1-1 and the force F is proportional to the velocity U, the area in contact with the fluid A and inversely proportional to the gap h

$$F \propto \frac{AU}{h} \tag{2.1-1}$$

The quantity F/A is called shear stress and is denoted by the Greek symbol τ (tau)

$$\tau \propto \frac{U}{h} \tag{2.1-2}$$

In the limit of small deformations, the ratio U/h can be replaced by the velocity gradient du/dy, which is called the shear rate. The proportionality constant between shear stress and shear rate is called **viscosity** and is denoted by the Greek symbol η (eta) in non-Newtonian fluid mechanics (frequently μ for Newtonian). Therefore, we may write

$$\tau = \eta \frac{du}{dy} \tag{2.1-3}$$

Eq. 2.1-3 is referred to as Newton 's law of viscosity with η the viscosity of the fluid. The dimensions of viscosity are force per unit area divided by the velocity gradient. In SI units

$$[\eta] \rightarrow \frac{N/m^2}{\frac{m/s}{m}} = \frac{N}{m^2} \cdot s = Pa \cdot s \quad (pascal \cdot second)$$

Fluids obeying a linear relationship between shear stress and shear rate are called Newtonian. Non–Newtonian fluids are those that exhibit non–linear stress versus shear rate relationships such as **Bingham** plastic, **pseudoplastic (**shear thinning**)** or **dilatant** fluids (shear thickening) as shown in Fig. 2.1-2. With pseudoplastic fluids if we double the applied force we get more

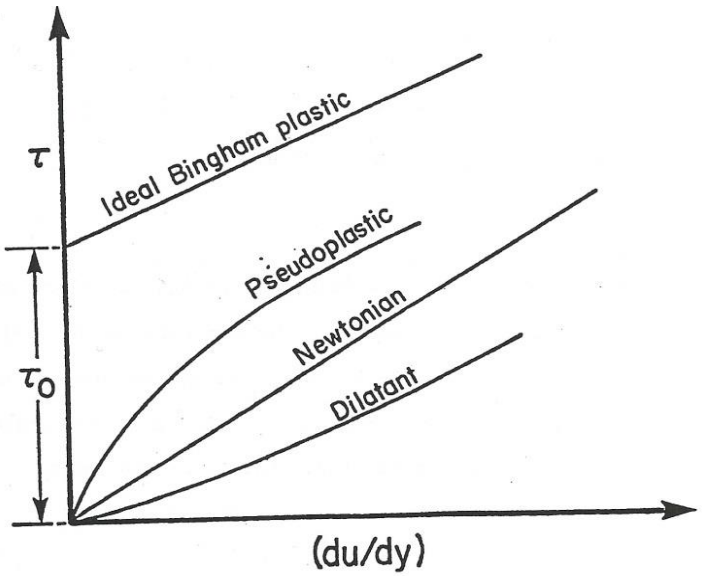

Figure 2.1-2. Shear stress (τ) versus shear rate (du/dy) for Newtonian and non-Newtonian fluids.

than double the flow rate, while with dilatant fluids we get less than double. A Bingham fluid does not flow unless a certain stress (τ_o), called yield stress, is exceeded. For example, ketchup

usually does not flow when you turn a usual size bottle of it upside down, because the stress imposed by the weight is lower than the yield stress. But, when you tap it hard enough, it does (when τ_o is exceeded).

2.2 Viscosity of Suspensions

The non–Newtonian behavior is due to very complex fluid structure. It is important to point out that even the behavior of a dilute suspension of solid spheres is imperfectly understood. Einstein (Batchelor, 1977) formulated and solved the problem for the determination of resistance to shearing caused by the presence of a single sphere of neutral density. By extending the applicability, of the single sphere calculations, to a dilute suspension of spheres, Einstein showed that the response remained Newtonian and the viscosity of the suspension is given by

$$\eta_c = \eta_f(1 + 2.5\varphi) \tag{2.2-1}$$

where η_c is the viscosity of the suspension, η_f the viscosity of the suspending fluid and φ the volume fraction occupied by the spheres. This model is valid for φ up to 1%. For larger values of φ, interactions between spheres (or particles in general) become important and non–linearities appear. For higher concentrations the particle–particle interactions are important and Batchelor's (1977) equation is valid up to perhaps φ=0.1, but it is frequently used for higher fractions

$$\eta_c = \eta_f(1 + 2.5\varphi + 6.2\varphi^2) \tag{2.2-2}$$

The volume fraction is related to the weight fraction by the expression

$$\varphi = \frac{w/\rho_c}{[w/\rho_c + (1-w)/\rho_m]} \tag{2.2-3}$$

where w is the weight fraction of the component, ρ_c is the density of the component added and ρ_m the viscosity of the matrix (suspending fluid). In very dilute solutions, particles will rotate due to the action of the shear field. As the concentration is increased, hydrodynamic interactions between the particles become important. Particles come close to particles on nearby streamlines and the fluid is disturbed in their vicinity. As the concentration is further increased, colloidal interactions (of attraction or repulsion) involve three, four or more particles and the rigorous analyses of Einstein and Batchelor no longer apply.

Since the behavior of dilute suspensions of particles is so complex, it can be easily deduced that the mathematical description of behavior of concentrated suspensions having

different size and shape of particles (e.g. human blood, cement slurries, printing inks) and macromolecular solutions or melts would be a very challenging task.

Example E2.2-1

Assume that Batchelor's equation is valid at any volume ratio and any suspending fluid. Determine the viscosity of a polymer melt (HDPE) if it has been filled with 30 PHR (parts per hundred) calcium carbonate ($CaCO_3$) by weight. The density of the solid polymer is 950 kg/m^3 and the density of the calcium carbonate is 2710 kg/m^3.

Solution

$CaCO_3$	30 PHR
Polymer melt	100 PHR

Therefore, the weight fraction would be

$$w = \frac{30}{(30+100)} \cong 0.23$$

Using the density of the $CaCO_3$ (ρ_c=2710 kg/m^3) and the solid density of HDPE (ρ_m=950 kg/m^3), we can calculate the volume fraction at room temperature

$$\varphi = \frac{0.23/2710}{[0.23/2710 + (1-0.23)/950]} \cong 0.0947$$

At processing temperature, the density of HDPE will be reduced to perhaps 780 kg/m^3 but the density of $CaCO_3$ will pretty much remain unchanged. So, it is better to recalculate the volume fraction for 780 kg/m^3 which gives φ=0.07916. Therefore, from Eq. 2.2-2 we have

$$\eta_c = \eta_f(1 + 2.5 \times 0.07916 + 6.2 \times 0.07916^2) \cong 1.23\eta_f$$

which means that the viscosity of the filled polymer melt will be 1.23 times higher than the viscosity of the suspending fluid (unfilled polymer melt).

Note: For much higher filler loadings the viscosity of a filled polymer can easily be more than 5-10 times the viscosity of the neat polymer melt. When nanoparticles are added, even with loadings less than 5%, the viscosity can increase ten-fold, due to particle-particle interactions.

2.3 Shear-Thinning Behavior of Polymers

In fluid mechanics textbooks**, pseudoplastic** fluids are defined those which exhibit decrease in viscosity as the shear rate increases. This property is frequently called **shear–thinning**. It should not be confused with the term thixotropy, which is the reduction of

viscosity with time, due to structural changes. Dilatant fluids are defined those which exhibit increase in viscosity as the shear rate increases. This shear thickening effect should not be confused with rheopexy, which refers to increase of viscosity with time, due to structural changes. Time-dependent viscosity effects are beyond the scope of this chapter.

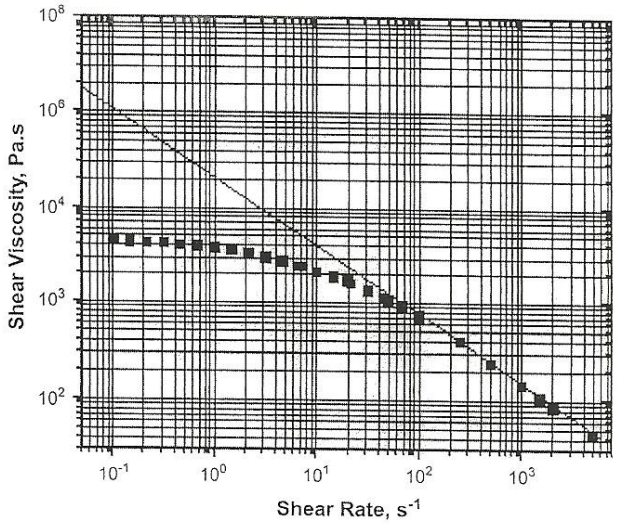

Figure 2.3-1. Viscosity as a function of shear rate of a polymer melt. The straight line represents a power-law fit with $m \approx 20{,}000$ Pa·s^n and $n \approx 0.3$.

Polymer chains tend to align in the direction of flow and disentangle and they exhibit less resistance to flow as the rate of shearing increases (pseudoplastic or shear-thinning behavior). Fig. 2.3-1 shows a typical polymer melt viscosity curve. We note a Newtonian region at very low shear rates and it is possible to have another Newtonian region at very high shear rates in polymer solutions. A significant portion of the curve of Fig. 2.3-1 may be described by the **power–law** expression (also called Ostwald–de Waele model), which is

$$\tau = m\left(\frac{du}{dy}\right)^n \quad \text{or} \quad \eta = \frac{\tau}{(du/dy)} \Rightarrow \eta = m\left(\frac{du}{dy}\right)^{n-1} = m\dot{\gamma}^{n-1} \qquad (2.3\text{-}1)$$

The shear rate is frequently designated with the Greek letter $\dot{\gamma}$, m is a measure of the consistency index of the fluid, the larger the m the more viscous the fluid. The power-law exponent n (always $n<1$ for polymer solutions and melts) indicates the degree of departure from the Newtonian behavior. For $n=1$ the fluid is Newtonian and the viscosity is constant. As n becomes smaller, the shear–thinning behavior is more pronounced. The power–law relation gives

$$\log \eta = \log m + (n-1)\log \dot{\gamma} \qquad (2.3\text{-}2)$$

where $\dot{\gamma}$ is the shear rate. Note that the consistency index m is the viscosity at $\dot{\gamma}$=1 s^{-1} and n-1 is the slope on a log–log graph, as shown in Fig. 2.3-1.

Typical values of the power–law exponent n for some common polymer melts are: polyethylene: 0.3–0.6, polyvinyl chloride: 0.2–0.5 and nylon: 0.6–0.9. The consistency index is usually in the range m=10^3–10^5 Pa·s^n at processing temperatures and it is sensitive to changes in temperature. For the range from 150°C to 250°C, usual in the processing of many polymers, a common representation is

$$m = m_o \, exp[-b(T - T_o)] \tag{2.3-3}$$

where m_o is the consistency index at the reference temperature T_o and b is the temperature sensitivity coefficient. Typically, b is of the order of 0.01–0.04 K^{-1} for most common polymers implying a reduction of viscosity of roughly between 10% and 35% for a 10°C rise in temperature. Some polymer melts have more temperature sensitive viscosity and b can be as high as 0.1 K^{-1}. A more accurate equation of temperature dependence (Arrhenius) is given in Chapter 5, on rheological measurements.

The power–law equation is very useful for many engineering problems involving non–Newtonian fluids. The drawback is that it cannot capture the upper or lower Newtonian regions of viscosity. There are two popular models, which capture both the low and high shear rate viscosity behavior of polymeric liquids:

a) Carreau-Yasuda model

$$\frac{\eta - \eta_\infty}{\eta_o - \eta_\infty} = [1 + (\lambda\dot{\gamma})^a]^{\frac{n-1}{a}} \tag{2.3-4}$$

b) Cross model

$$\frac{\eta - \eta_\infty}{\eta_o - \eta_\infty} = \frac{1}{1 + (\lambda\dot{\gamma})^{1-n}} \tag{2.3-5}$$

where η_0 the viscosity at zero-shear, η_∞ the viscosity at infinite shear and λ, a and n are fitted parameters. For a 5% polystyrene solution in Aroclor (see Bird *et al.*, 1987), the Carreau–Yasuda model is fitted with

η_0=101 Pa·s η_∞=0.059 Pa·s λ=0.84 s n=0.380 α=2

For a polystyrene melt at 180°C

η_0=14800 Pa·s η_∞=0 Pa·s λ=1.04 s n=0.398 α=2

Generally speaking, η_∞=0 for polymer melts and Carreau-Yasuda and Cross models are used in their simpler forms without η_∞. As we will see, there are several practically useful flow

problems for which we can obtain closed-form (analytical) solutions. However, there is no closed-form solution possible for any flow problem with either the Carreau-Yasuda or the Cross models. The meaning of the fitting parameters for the Carreau-Yasuda model is illustrated in Fig. 2.3-2. In the Cross viscosity model the parameter λ is equal to the inverse

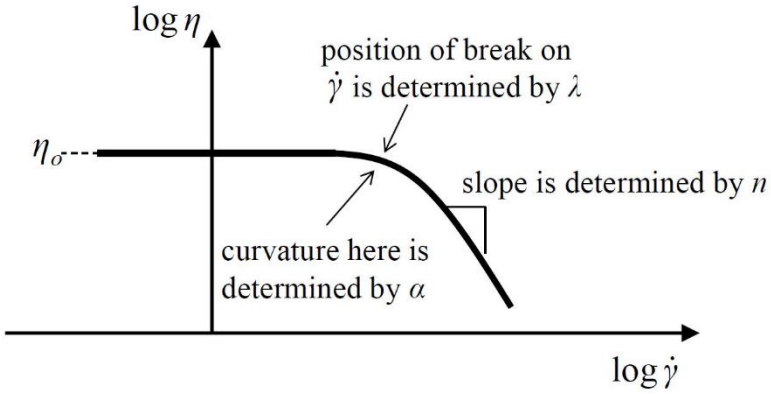

Figure 2.3-2. Meaning of the fitting parameters for the Carreau-Yasuda model. From Morrison (2001).

of the shear rate at $\eta = \eta_0/2$. In the next sections of this chapter, we present analytical solutions to several **unidirectional flow** problems using the power-law model. "Unidirectional" means that the flow is only in one direction, the velocity varies in the perpendicular direction and may also vary the direction of the flow.

Example E2.3-1

A 600 mm long cylinder, 50 mm in diameter, rotates in another cylinder of the same length and 52 mm in diameter. The gap between the two cylinders is filled with molten polymer obeying the power-law model with m=2000 Pa·s^n and n=0.4. The gap is assumed uniform and the inner cylinder rotates at 300 revolutions per minute. Calculate (a) the torque and (b) the power required for the rotation of the inner cylinder.

Solution

L=600 mm=0.6 m

D_i=50 mm=0.05 m

D_o=52 mm=0.052 m

$h=D_o-D_i$=(0.052–0.05)/2=0.001 m

$$U = \pi D_i \frac{revolutions\ per\ minute}{60} = \pi \times 0.05 \times \frac{300}{60} = 0.785\ m/s$$

(a) We start from Eq. 2.3-1

$$\tau = m\left(\frac{du}{dy}\right)^n$$

Approximating the velocity derivative as $du/dy \approx U/h$, where U the velocity of the inner cylinder and h the gap between the cylinders we have

$$\tau = m\left(\frac{U}{h}\right)^n$$

At the surface of the inner cylinder $\tau = F/A$. Therefore, the torque will be

$$T_o = FR_i = \tau AR_i = m\left(\frac{U}{h}\right)^n (\pi D_i L)\frac{D_i}{2} = m\left(\frac{U}{h}\right)^n \frac{\pi {D_i}^2 L}{2}$$

$$T_o = 2000\left[\frac{0.785}{0.001}\right]^{0.4} \frac{\pi \times 0.05^2 \times 0.6}{2} = 67.8\ \mathrm{N \cdot m}$$

(b) The power required for the rotation of the shaft is

$$P_o = FU = \tau AU = m\left(\frac{U}{h}\right)^n (\pi D_i L)U = m\frac{U^{n+1}}{h^n}(\pi D_i L) =$$

$$= 2000\frac{0.785^{0.4+1}}{0.001^{0.4}}(\pi \times 0.05 \times 0.6) = 2128.65\ N \cdot \frac{m}{s} = 2128.65\ W = 2.12kW$$

2.4. Stress and Conservation of Momentum

During fluid flow, stresses are developed either tangentially (shear) or perpendicularly (normal) to surfaces as shown schematically in Fig. 2.4-1. Pressure is a normal stress. Some engineering calculations can be easily carried out for simple shear flow fields. For example, if the viscosity of a fluid is known, the force required to move the plate in the parallel flow arrangement is shown in Fig. 2.4-2.

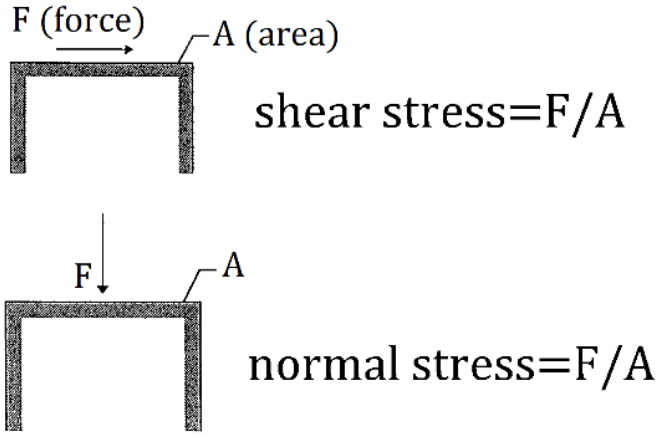

Figure 2.4-1. Schematic representation of shear and normal stresses.

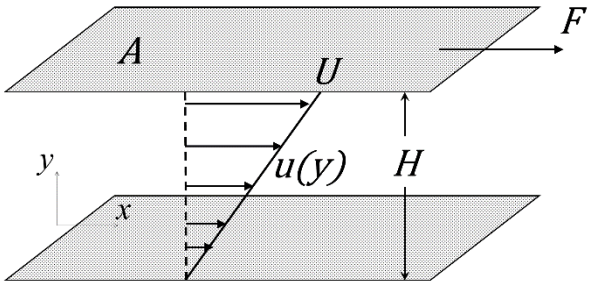

$$F = \tau \cdot A = \eta \frac{\mathrm{U}}{H} A \left(Force = shear\ stress \cdot area = viscosity \frac{velocity}{gap} \cdot Area \right)$$

Figure 2.4-2. Schematic representation of force required to move the top plate in parallel flow arrangement.

A (nearly) parallel flow field can be realized between two concentric cylinders if the gap to radius ratio is small. The torque T_o can easily be calculated by $T_o = FR = \tau AR$ (Torque=Force × Radius = shear stress × Area × Radius) where R the distance from axis of rotation. The power (P_o) required to turn the inner cylinder will be

$$P_o = FU = \tau AU \tag{2.4-1}$$

To solve general flow problems, we must set up a momentum balance (for details see Vlachopoulos, 2016). It turns out that the momentum balance leads to an equation that can be stated verbally as

$$\begin{Bmatrix} inertia \\ forces \end{Bmatrix} = \begin{Bmatrix} pressure \\ forces \end{Bmatrix} + \begin{Bmatrix} stress \\ forces \end{Bmatrix} + \begin{Bmatrix} gravity \\ forces \end{Bmatrix} \tag{2.4-2}$$

Mathematically, this is written in the following form

$$\rho \left(\frac{\partial \bar{V}}{\partial t} + \bar{V} \cdot \nabla \bar{V} \right) = -\nabla p + \nabla \bar{\bar{\tau}} + \rho \bar{g} \tag{2.4-3}$$

The left-hand side term represents the inertia forces, while the terms on the right-hand side are the pressure forces, stress forces and gravity forces respectively. Molten polymers are characterized by **extremely high viscosities** (usually over a million times more viscous than water).

The Reynolds number $Re = \rho UD/\mu$ is very small under usual processing conditions (Re=10^{-1}~10^{-4}). Therefore, the flows are always **laminar** for polymer melts. The following approximations always apply:

- The convective (inertia) forces are insignificant and may be neglected.
- The gravity forces are normally negligible.

- The flow is dominated by the **balance of pressure and stress forces**. It is often referred to as **creeping** or **Stokes flow**.

In Chapter 4, we examine viscoelastic stresses, but in this chapter only viscous forces are considered and polymer elasticity is neglected. Due to the above, Eq. 2.4-3 takes the form

$$0 = -\nabla p + \nabla \bar{\bar{\tau}} \tag{2.4-4}$$

The following should be noted:

- Pressure p is a **scalar**.
- Velocity is a **vector**: $\bar{V} = \bar{V}(V_x, V_y, V_z)$ which means it has components in x, y and z directions (frequently in the literature the velocity components are denoted as (u,v,w) respectively.
- Stress is defined as the ratio Force/Area and can be normal or tangential (shear).
- Stress is a second order **tensor** having nine components

$$\bar{\bar{\tau}} = \begin{Bmatrix} \tau_{xx} & \tau_{xy} & \tau_{xz} \\ \tau_{yx} & \tau_{yy} & \tau_{yz} \\ \tau_{zx} & \tau_{zy} & \tau_{zz} \end{Bmatrix} \tag{2.4-5}$$

where $\bar{\bar{\tau}}$ is the symbolic notation of the stress tensor. τ_{ij} is the so-called index notation of the same tensor. Actually in tensor manipulation it is easier to work with 1,2,3 rather than x,y,z so that the components may be written as

$$\tau_{ij} = \begin{Bmatrix} \tau_{11} & \tau_{12} & \tau_{13} \\ \tau_{21} & \tau_{22} & \tau_{23} \\ \tau_{31} & \tau_{32} & \tau_{33} \end{Bmatrix} \tag{2.4-6}$$

The first subscript is perpendicular to the plane where the stress acts, while the second subscript indicates the direction of the stress (as shown in Fig. 2.4-3)

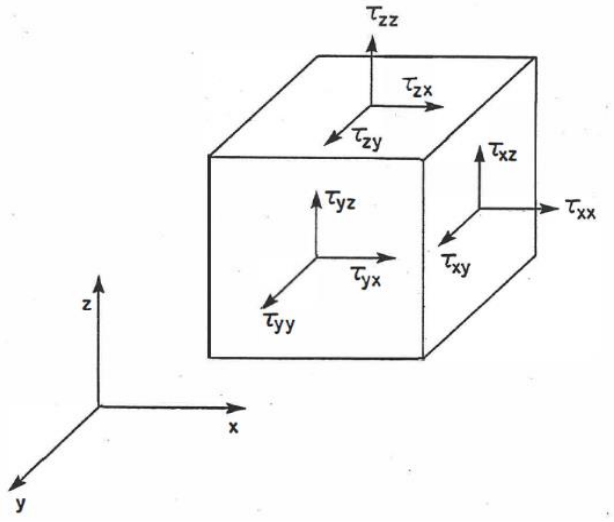

Figure 2.4-3. Stresses exerted on three planes of an elemental volume.

With respect to Eq. 2.4-5, the following should be noted

- Components τ_{xx}, τ_{yy} and τ_{zz} are normal stresses.
- Components τ_{xy}, τ_{yx}, τ_{yz}, τ_{zy}, τ_{zx} and τ_{xz} are shear stresses.
- Stress is a symmetric tensor, which means that $\tau_{xy}=\tau_{yx}$, $\tau_{yz}=\tau_{zy}$ and $\tau_{zx}=\tau_{xz}$

However, it is important to keep the convention that the first index corresponds to the plane of action and the second the direction.

Using the Taylor expansion $f(x+dx)=f(x)+(\partial f/\partial x)\Delta x$ the balance of pressure and stress forces for planar flow between two parallel flat plates, shown in Fig. 2.4-4, can be written as

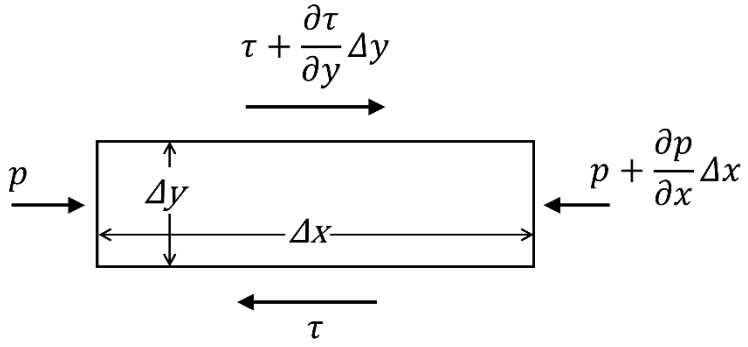

Figure 2.4-4. Force balance for a differential volume element. (Δz length is normal to the page).

$$p\Delta y\Delta z - \left(p + \frac{\partial p}{\partial x}\Delta x\right)\Delta y\Delta z = \left(\tau + \frac{\partial \tau}{\partial y}\Delta y\right)\Delta x\Delta z - \tau\Delta x\Delta z \qquad (2.4\text{-}7)$$

which yields

$$0 = -\frac{\partial p}{\partial x} + \frac{\partial \tau}{\partial y} \qquad (2.4\text{-}8)$$

In **unidirectional flows**, we balance the pressure in the direction of the flow with an opposing shear stress. So, we will only have just two terms in the equation of momentum. In fact, the component in the direction of the flow is the "governing equation" of motion, which we solve in order to obtain the velocity profile and other quantities, as we describe in Section 2.5.

2.5. How to Derive the Governing Equation(s) for a Flow Problem

A crucial step in problem solving is the derivation of appropriate governing equation(s) i.e. equation(s) that contain(s) all the essential information. We have seen that for flow between two flat plates the balance of pressure and stress gives Eq. 2.4-8 and since the stress is given by the viscosity relation $\tau = \eta\frac{\partial v_x}{\partial y}$ the resulting governing equation is

$$-\frac{\partial p}{\partial x}+\frac{\partial}{\partial y}\left(\eta\frac{\partial V_x}{\partial y}\right)=0 \tag{2.5-1}$$

While it was easy to derive this equation from first principles (simple force balance), it can be difficult when the geometry of flow is more complicated. By far, the most common and reliable method is to start from the general conservation equations for mass, momentum (and energy if flow is non-isothermal).

The general equation of conservation of mass (continuity) for incompressible fluids (which is a reasonable assumption for molten polymers) is $\nabla\cdot\bar{V}=0$ or

$$\frac{\partial V_x}{\partial x}+\frac{\partial V_y}{\partial y}+\frac{\partial V_z}{\partial z}=0 \tag{2.5-2}$$

The general equation of conservation of momentum (also known as Navier-Stokes equation) with the low Reynolds number or creeping flow approximation which is valid for virtually all polymer melt flows is

$$0=-\nabla p+\nabla\bar{\bar{\tau}} \tag{2.5-3}$$

or in rectangular coordinates

$$\text{x-direction:}\quad -\frac{\partial p}{\partial x}+\frac{\partial \tau_{xx}}{\partial x}+\frac{\partial \tau_{yx}}{\partial y}+\frac{\partial \tau_{zx}}{\partial z}=0 \tag{2.5-4a}$$

$$\text{y-direction:}\quad -\frac{\partial p}{\partial y}+\frac{\partial \tau_{xy}}{\partial x}+\frac{\partial \tau_{yy}}{\partial y}+\frac{\partial \tau_{zy}}{\partial z}=0 \tag{2.5-4b}$$

$$\text{z-direction:}\quad -\frac{\partial p}{\partial z}+\frac{\partial \tau_{xz}}{\partial x}+\frac{\partial \tau_{yz}}{\partial y}+\frac{\partial \tau_{zz}}{\partial z}=0 \tag{2.5-4c}$$

where

$$\tau_{xx}=2\eta\frac{\partial V_x}{\partial x} \tag{2.5-5a}$$

$$\tau_{xy}=\tau_{yx}=\eta\left(\frac{\partial V_x}{\partial y}+\frac{\partial V_y}{\partial x}\right) \tag{2.5-5b}$$

and similar expressions for the other stress components (Vlachopoulos, 2016).

For flow only in the x-direction, between two flat plates there is pressure variation in the *x*-direction (i.e. the pressure necessary to push the fluid through the channel) as shown in Fig. 2.5-1.

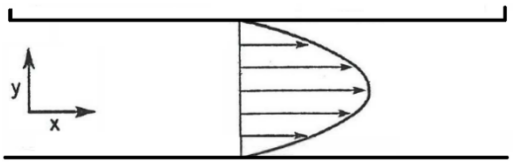

Figure 2.5-1. Schematic representation of a pressure-driven flow between two parallel flat plates.

However, there is no pressure variation in the y or z directions and consequently $\frac{\partial p}{\partial y} = \frac{\partial p}{\partial z} = 0$. Since the fluid is sheared as it is forced to flow through the channel, but without any velocity change along x or z, all the stress components are zero except for the term $\frac{\partial \tau_{yx}}{\partial y}$. Thus, we end up with the governing equation

$$-\frac{\partial p}{\partial x} + \frac{\partial \tau_{yx}}{\partial y} = 0 \tag{2.5-6}$$

where

$$\tau_{yx} = \eta\left(\frac{\partial V_x}{\partial y}\right) \tag{2.5-7}$$

The elimination of terms from the general conservation equations is a relatively easy process and almost failure-proof. The detailed step-by-step methodology is explained in Vlachopoulos (2016).

It is important to remember that for the **unidirectional flow problems**, the governing equation will always be the **equation of momentum in the flow direction with at most two terms**: one term for pressure variation and one term for stress variation. However, it is also possible to have flow in the absence of pressure (called drag or Couette flow) when the fluid is literally dragged by the moving wall.

In Table 2.5-1 we present the governing equations for some basic steady unidirectional flow problems of considerable practical significance. They involve a fluid flowing in one direction only and the velocity varying in the normal direction. Annular Couette flow should be used when the ratio of radius/gap is relatively small e.g. R/H<10, otherwise it can be treated as flow between two flat plates. Several worked out problems in great detail for Newtonian unidirectional flows by Vlachopoulos (2016).

2.6 Pressure Driven Flow of a Power-Law Fluid Between Two Flat Plates

Consider two flat plates of length L and spaced $2b$ apart. We will solve this problem by starting from the general conservation equations. The continuity equation (Eq.2.5-2)) for flow in the x-direction is valid

$$\frac{\partial V_x}{\partial x} = 0 \tag{2.6-1}$$

The x component of the stress form of the equation of conservation of momentum simplifies to the governing equation for this flow problem

Table 2.5-1. **Basic types of steady unidirectional flows**			
Type of flow	**Schematic representation**	**Governing equation**	**Shear stress**
Planar flow	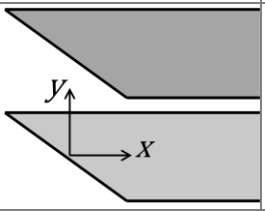	$x-dir: 0 = -\frac{\partial p}{\partial x} + \frac{\partial}{\partial y}(\tau_{yx})$	$\tau_{yx} = \eta\left(\frac{\partial V_x}{\partial y}\right)$
Axisymmetric flow	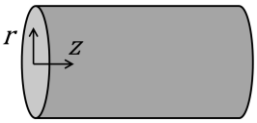	$z-dir: 0 = -\frac{\partial p}{\partial z} + \frac{1}{r}\frac{\partial}{\partial r}(r\tau_{rz})$	$\tau_{rz} = \eta\left(\frac{\partial V_z}{\partial r}\right)$
Radial (squeeze) flow	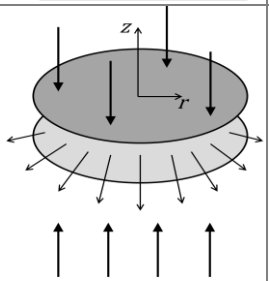	$r-dir: 0 = -\frac{\partial p}{\partial r} + \frac{\partial}{\partial z}(\tau_{rz})$	$\tau_{zr} = \eta\left(\frac{\partial V_r}{\partial z}\right)$
Annular Couette flow	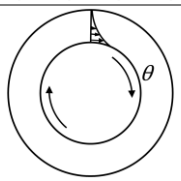	$\theta-dir: 0 = -\frac{1}{r}\frac{\partial p}{\partial \theta} + \frac{1}{r^2}\frac{\partial}{\partial r}(r^2\tau_{r\theta})$	$\tau_{zr} = \eta r\frac{\partial}{\partial r}\left(\frac{V_\theta}{r}\right)$

$$0 = -\frac{\partial p}{\partial x} + \frac{\partial \tau_{yx}}{\partial y} \tag{2.6-2}$$

Although $\tau_{xy}=\tau_{yx}$ (stress is a symmetric tensor) we write τ_{yx} in the above equation because the usual convention is that the second index indicates the direction of the stress component and the first index is the direction perpendicular to the plane where the stress component acts. The *y* component gives again

$$0 = -\frac{\partial p}{\partial y} - \rho g \tag{2.6-3}$$

and the *z* component again

$$0 = -\frac{\partial p}{\partial z} \tag{2.6-4}$$

Eq. 2.6-3 means that pressure variation in the y-direction is hydrostatic, which we can neglect. Eq. 2.6-4 simply states that pressure is constant in the *z*-direction.

The pressure gradient in the x-direction is

$$\frac{\partial p}{\partial x} = -\frac{\Delta p}{L} \tag{2.6-5}$$

thus Eq. 2.6-2 becomes

$$\frac{\partial \tau_{yx}}{\partial y} = -\frac{\Delta p}{L} \tag{2.6-6}$$

Integration gives

$$\tau_{yx} = -\frac{\Delta p}{L} y + C_1 \tag{2.6-7}$$

We now introduce the power–law equation in the form

$$\tau_{yx} = m \left|\frac{\partial V_x}{\partial y}\right|^{n-1} \left(\frac{dV_x}{dy}\right) \tag{2.6-8}$$

The absolute value is necessary for avoiding problems with negative velocity gradient

$$m \left|\frac{\partial V_x}{\partial y}\right|^{n-1} \left(\frac{\partial V_x}{\partial y}\right) = -\frac{\Delta p}{L} y + C_1 \tag{2.6-9}$$

Since $\frac{\partial V_x}{\partial y} = 0$ at y=0 (symmetry) we obtain C_1=0. By replacing the partial differentiation by an ordinary one, we get

$$m \left|\frac{dV_x}{dy}\right|^{n-1} \left(\frac{dV_x}{dy}\right) = -\frac{\Delta p}{L} y \tag{2.6-10}$$

The right hand side is negative and the absolute value of the velocity gradient is raised to the power n-1, therefore dV_x/dy must be negative and may be written as

$$\frac{dV_x}{dy} = -\left(\frac{1}{m}\frac{\Delta p}{L}\right)^{1/n} y^{1/n} \tag{2.6-11}$$

This is integrated to give

$$V_x(y) = -\frac{n}{n+1}\left(\frac{1}{m}\frac{\Delta p}{L}\right)^{1/n} y^{(n+1)/n} + C_2 \tag{2.6-12}$$

The no–slip condition V_x=0 at y =b (the half-gap) gives

$$C_2 = -\frac{n}{n+1}\left[\frac{1}{m}\left(\frac{\Delta p}{L}\right)\right]^{1/n} b^{(n+1)/n} \tag{2.6-13}$$

Hence, the velocity profile is

$$V_x(y) = \left(\frac{n}{n+1}\right)\left[\frac{b^{n+1}}{m}\left(\frac{\Delta p}{L}\right)\right]^{1/n}\left[1-\left(\frac{y}{b}\right)^{\frac{n+1}{n}}\right] \tag{2.6-14}$$

The maximum velocity is at y =0

$$V_{max} = \left(\frac{n}{n+1}\right)\left[\frac{b^{n+1}}{m}\left(\frac{\Delta p}{L}\right)\right]^{1/n} \tag{2.6-15}$$

and the velocity profile can be expressed as

$$V_x(y) = V_{max}\left[1-\left(\frac{y}{b}\right)^{\frac{n+1}{n}}\right] \tag{2.6-16}$$

The average velocity is

$$V_{avg} = \frac{V_x dz dy}{dz dy} \Rightarrow V_{avg} = \frac{\int_{-b}^{b} V_x dy}{\int_{-b}^{b} dy} \Rightarrow V_{avg} = \frac{n+1}{2n+1} V_{max} \tag{2.6-17}$$

The volume rate of flow per unit width is

$$\frac{Q}{W} = V_{avg} 2b \Rightarrow \frac{Q}{W} = \frac{2n}{2n+1}\left[\frac{1}{m}\frac{\Delta p}{L}\right]^{1/n} b^{\frac{1}{n}+2} \tag{2.6-18}$$

and the pressure drop

$$\Delta p = mL\left[\frac{2n+1}{2n}\frac{Q}{W}\right]^{n} b^{-(2n+1)} \tag{2.6-19}$$

where L is the channel length and b the half gap. By setting n=1 we obtain the corresponding results for the Newtonian problem. The velocity profile is exactly parabolic for n=1, more flat for n<1 and more elongated for n>1, as shown in Fig. 2.6-1.

Table 2.6-1. Important expressions for pressure driven flow between two parallel plates	
Shear rate at wall	$\dot{\gamma}_w = \frac{n+1}{n}\frac{V_{max}}{b}, \qquad \dot{\gamma}_w = \frac{2n+1}{n}\frac{V_{avg}}{b}, \qquad \dot{\gamma}_w = \frac{2n+1}{n}\frac{2Q}{4Wb^2}$
Shear stress at wall	$\tau_w = m\left[\frac{2n+1}{n}\frac{2Q}{4Wb^2}\right]^n$ $\tau_w = \frac{\Delta P}{L/b}$
Pressure drop	$\Delta p = mL\left[\frac{2n+1}{2n}\frac{Q}{W}\right]^n b^{-(2n+1)}$
Volume rate of flow (per unit width)	$\frac{Q}{W} = \frac{2n}{2n+1}\left[\frac{1}{m}\frac{\Delta p}{L}\right]^{1/n} b^{\frac{1}{n}+2}$
Maximum velocity	$V_{max} = \left(\frac{n}{n+1}\right)\left[\frac{b^{n+1}}{m}\left(\frac{\Delta p}{L}\right)\right]^{1/n}$
Average velocity	$V_{avg} = \frac{n+1}{2n+1}V_{max}$

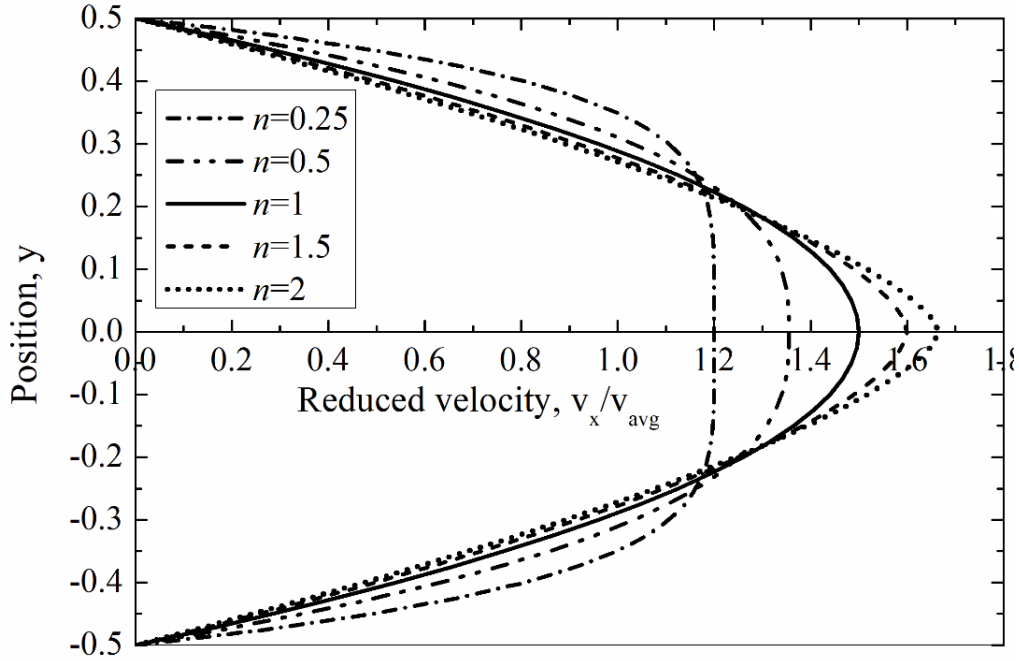

Figure 2.6-1. Velocity profiles for power-law fluids flowing under a pressure gradient between two flat plates with n=0.25 n=0.5 (shear thinning), n=1 (Newtonian) and n=1.5 n=2.0 (shear thickening).

2.7 Pressure Driven Flow of a Power-Law Fluid in a Tube

Again we will solve this problem by starting from the conservation equations which are given by Vlachopoulos (2016).

The continuity equation reduces to

$$\frac{\partial V_z}{\partial z} = 0 \tag{2.7-1}$$

The stress form of the equation of conservation of momentum simplifies to

r component $$0 = -\frac{\partial p}{\partial r} + \rho g_r \tag{2.7-2}$$

θ component $$0 = -\frac{1}{r}\frac{\partial p}{\partial \theta} + \rho g_\theta \tag{2.7-3}$$

z component $$0 = -\frac{\partial p}{\partial z} + \frac{1}{r}\frac{\partial}{\partial z}(r\tau_{rz}) \tag{2.7-4}$$

The r- and θ- components are identical to those for the Newtonian problem and neglected (no flow in r- or θ-). The z- component is the governing equation which contains the shear stress term that will be replaced by the power–law equation

$$\tau_{rz} = m\left|\frac{\partial V_z}{\partial r}\right|^{n-1}\frac{\partial V_z}{\partial r} \tag{2.7-5}$$

We have

$$-\frac{\Delta p}{L} = \frac{1}{r}\frac{\partial}{\partial z}(r\tau_{rz}) \tag{2.7-6}$$

Integration gives

$$r\tau_{rz} = -\frac{\Delta p}{2L}r^2 + C_1 \tag{2.7-7}$$

and dividing by r we have

$$\tau_{rz} = -\frac{\Delta p}{2L}r + \frac{C_1}{r} \tag{2.7-8}$$

C_1 must be zero in order for the shear stress τ_{rz} to remain finite at r=0. Thus

$$\tau_{rz} = -\frac{\Delta p}{2L}r \tag{2.7-9}$$

Introducing the power–law equation (Eq. 2.7-5) we have

$$m\left|\frac{\partial V_z}{\partial r}\right|^{n-1}\frac{\partial V_z}{\partial r} = -\frac{\Delta p}{2L}r \tag{2.7-10}$$

The right hand side is negative and the absolute value of the velocity gradient is raised to the power n-1, therefore $\frac{\partial V_z}{\partial r}$ must be negative and may be written as

$$\frac{dV_z}{dr} = -\left(\frac{\Delta p}{2mL}\right)^{1/n} r^{1/n} \tag{2.7-11}$$

By integrating we have

$$V_z(r) = -\frac{n}{n+1}\left(\frac{\Delta p}{2mL}\right)^{1/n} r^{(n+1)/n} + C_2 \tag{2.7-12}$$

With the help of the no–slip boundary condition V_z=0 at r=R we determine the integration constant

$$C_2 = \frac{n}{n+1}\left(\frac{\Delta p}{2mL}\right)^{1/n} R^{(n+1)/n} \tag{2.7-13}$$

and the velocity profile is

$$V_z(r) = \frac{n}{n+1}\left[\frac{R^{n+1}}{2m}\left(\frac{\Delta p}{L}\right)\right]^{1/n}\left[1-\left(\frac{r}{R}\right)^{(n+1)/n}\right] \tag{2.7-14}$$

The maximum velocity is at r=0

$$V_{max} = \frac{n}{n+1}\left[\frac{R^{n+1}}{2m}\left(\frac{\Delta p}{L}\right)\right]^{1/n} \tag{2.7-15}$$

and the velocity profile can be expressed as

$$V_z(r) = V_{max}\left[1 - \left(\frac{r}{R}\right)^{(n+1)/n}\right] \tag{2.7-16}$$

The average velocity is obtained by integrating over the cross–sectional area and then dividing by the cross–sectional area

$$V_{avg} = \frac{\int_0^{2\pi}\int_0^R V_z r dr d\theta}{\int_0^{2\pi}\int_0^R r dr d\theta} \Rightarrow V_{avg} = \frac{n}{(3n+1)}\left[\frac{R^{n+1}}{2m}\left(\frac{\Delta p}{L}\right)\right]^{1/n} \tag{2.7-17}$$

The volume rate of flow is

$$Q = V_{avg}\pi R^2 = \pi\frac{n}{3n+1}\left[\frac{1}{2m}\left(\frac{\Delta p}{L}\right)\right]^{1/n} R^{\frac{1}{n}+3} \tag{2.7-18}$$

and the pressure drop

$$\Delta p = 2mLR^{-(3n+1)}\left[\frac{Q}{\pi}\left(\frac{1}{n}+3\right)\right]^n \tag{2.7-19}$$

Again, by setting n=1 we obtain the corresponding expressions for Newtonian fluid. The velocity profiles are similar to those of Fig. 2.6-1. For n=1 we get the parabolic (Newtonian) profile, for n<1 the profile is more blunt and for n>1 more pointed.

Example E2.7-1

For the geometry of the melt indexer shown in Fig.1.11-1 (load of 2.16) of Chapter 1, assume that a polymer has melt density 766 kg/m^3 and behaves like a Newtonian fluid (n=1). Determine the shear rate at the wall if we have a polymer with MI=1 another of MI=10 and a third of MI=50.

Solution

The MI value is measured in grams per 10 minutes. Generally, mass per time units, corresponds to flow rate. Therefore, the MI value is simply another form of flow rate. For convenience we convert the MI into to SI units

$$MI = \frac{1gr}{10min} = \frac{10^{-3}\,kg}{10\times 60\,sec} = 1.666\times 10^{-6}\,kg/s$$

and by dividing with the melt density we get the volumetric flow rate

$$Q = \frac{MI}{\rho} = \frac{1.66\times 10^{-6}}{766} = 2.175\times 10^{-9}\frac{m^3}{s}$$

Therefore, the shear rate at the wall of the melt indexer die, can be calculated from (see Table 2.7-1)

Table 2.7-1. Important expressions for pressure driven flow in a tube	
Shear rate at wall	$\dot{\gamma}_w = \frac{n+1}{n}\frac{V_{max}}{R}$ $\dot{\gamma}_w = \frac{3n+1}{n}\frac{V_{avg}}{R}$ $\dot{\gamma}_w = \frac{3n+1}{4n}\frac{4Q}{\pi R^3}$
Shear stress at wall	$\tau_w = m\left[\frac{3n+1}{4n}\frac{4Q}{\pi R^3}\right]^n$ $\tau_w = \frac{\Delta P}{2(L/R)}$
Pressure drop	$\Delta p = 2mLR^{-(3n+1)}\left[\frac{Q}{\pi}\left(\frac{1}{n}+3\right)\right]^n$
Volume rate of flow	$Q = V_{avg}\pi R^2 = \pi\frac{n}{3n+1}\left[\frac{1}{2m}\left(\frac{\Delta p}{L}\right)\right]^{1/n} R^{\frac{1}{n}+3}$
Maximum velocity	$V_{max} = \left(\frac{n}{n+1}\right)\left[\frac{R^{n+1}}{2m}\left(\frac{\Delta p}{L}\right)\right]^{\frac{1}{n}}$
Average velocity	$V_{avg} = \frac{n+1}{3n+1}V_{max}$

$$\dot{\gamma}_w = \frac{3n+1}{4n}\frac{4Q}{\pi R^3} = \frac{4Q}{\pi R^3} = \frac{4 \times 2.167 \times 10^{-9}}{\pi(1.0475 \times 10^{-3})^3} = 2.41 s^{-1}$$

where we have put n=1 since the polymer behaves like a Newtonian fluid. By the same token, we carry out the above for the rest given MI values. All the results are summarized in the following table and we note that $\dot{\gamma}_w$=2.41xMI

MI	***Q* [m³/s]**	$\dot{\gamma}_w$ **[s⁻¹]**
1	2.175×10^{-9}	2.41
10	2.175×10^{-8}	24.10
50	1.088×10^{-7}	120.50

Example 2.7-2

Assume that the Newtonian expression of the wall shear rate is a reasonable approximation for the TOTAL HF 513 of Table 1.11-1 (Chapter 1) having melt density of 766 kg/m³. Determine the power-law parameters m and n ($\tau = m\dot{\gamma}^n$) from the two melt flow rate (melt index MI) values.

Solution

D_R (reservoir) =9.55 mm=0.00955 m
D_d (die) =2.095 mm=0.002095 m
L (die)=8 mm=0.008 m
MI=0.15
HLMI=14.5
M_l (low load) =2.16 kg
M_h (high load) =21.6 kg

Assuming that the pressure drop in the reservoir of the melt indexer of Fig. 1.11-1 is small, the pressure drop in the die is essentially the pressure (force F divided by the load area A) is exerted to the melt in the reservoir. Therefore, we may write for each load

Low load: $$\Delta p_l = \frac{F_l}{A} = \frac{4M_l g}{\pi {D_R}^2}$$

High load: $$\Delta p_h = \frac{F_h}{A} = \frac{4M_h g}{\pi {D_R}^2}$$

The wall shear stress, in the melt indexer die, may then be calculated from Eq. 2.7-9 for $r = R_d$ the radius of the die. Substitution of the above equations in Eq. 2.7-9 and upon rearrangement gives

$$\tau_{w,l} = \frac{2gR_d}{L\pi {D_R}^2} M_l$$

$$\tau_{w,h} = \frac{2gR_d}{L\pi {D_R}^2} M_h$$

Dividing the above equations, we have

$$\frac{\tau_{w,l}}{\tau_{w,h}} = \frac{M_l}{M_h}$$

Since we assume that the Newtonian value of the wall shear rate is a reasonable approximation (i.e. $\dot{\gamma}_w = 4Q/\pi R^3$) we may write for each load

$$\tau_{w,l} = m\left(\frac{4Q_l}{\pi {R_d}^3}\right)^n$$

$$\tau_{w,h} = m\left(\frac{4Q_h}{\pi {R_d}^3}\right)^n$$

where Q_l and Q_h the volumetric flow rate for the low and the high load respectively. Dividing the above equations, we obtain

$$\frac{\tau_{w,l}}{\tau_{w,h}} = \left(\frac{Q_l}{Q_h}\right)^n$$

From the previous problem we saw that, in general, the volumetric flow rate is related to the MI by

$$Q = \frac{MI \times 10^{-3}}{600\rho}$$

Therefore, we may rewrite for the ratio of the shear stresses $\tau_{w,l}/\tau_{w,h}$

$$\frac{\tau_{w,l}}{\tau_{w,h}} = \left(\frac{\frac{MI \times 10^{-13}}{600\rho}}{\frac{HLMI \times 10^{-13}}{600\rho}}\right)^n = \left(\frac{MI}{HLMI}\right)^n$$

Therefore, we obtain

$$\frac{M_l}{M_h} = \left(\frac{MI}{HLMI}\right)^n$$

which can be solved with respect to the power-law index n

$$n = \frac{log(M_l/M_h)}{log(MI/HLMI)} = \frac{log\, M_l - log\, M_l}{log\, M\, I - log\, H\, LMI} = \frac{log\, 2\,.16 - log\, 2\,1.6}{log\, 0\,.15 - log\, 1\,4.5} \approx 0.504$$

The consistency index m, may be calculated by

$$\frac{2gR_d}{L\pi {D_R}^2} M_l = m\left(\frac{4Q_l}{\pi {R_d}^3}\right)^n \Rightarrow \frac{2gR_d}{L\pi {D_R}^2} M_l = m\left(\frac{4 \times MI \times 10^{-3}}{600\pi\rho {R_d}^3}\right)^n$$

from which we may calculate the consistency index m

$$m = \frac{\frac{2gR_d}{L\pi {D_R}^2} M_l}{\left(\frac{4 \times MI \times 10^{-3}}{600\pi\rho {R_d}^3}\right)^n} = \frac{8966.42 \times M_l}{\left(\frac{1846.33}{\rho} \times MI\right)^n}$$

and by substituting the rest of the values we have

$$m = \frac{8966.42 \times 2.16}{\left(\frac{1846.33}{766} \times 0.15\right)^{0.504}} \approx 32343 Pa \cdot s^{0.504}$$

2.8 Capillary Viscometer Analysis and the Rabinowitsch Correction

The most frequently used instrument for the determination of viscosity of polymer melts is the capillary viscometer (schematically shown) in Fig. 2.8-1. The diameter is typically D=1~2 mm and the length to diameter ratio L/D=16~32.

For Newtonian fluids the relation between pressure drop Δp and flow rate Q is used for measurement of viscosity. For non–Newtonian fluids like polymer melts the viscosity is

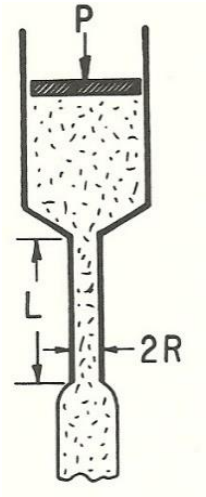

Figure 2.8-1. Schematic of a capillary viscometer of diameter D=2R and length L. The polymer is heated and melted in the reservoir and then pushed by the piston through the capillary die, swelling at the exit. From Nielsen (1987).

not constant but a function of the shear rate. Therefore, in order to use the pressure drop and flow rate measurements, we must be able to express the shear stress and the shear rate in terms of these and then

$$\eta = \frac{\tau}{(du/dy)} \tag{2.8-1}$$

From the previous section we can see that the shear stress at the wall can be obtained from

$$\tau_w = -\frac{\Delta p}{2L} R \tag{2.8-2}$$

This holds for both Newtonian and non–Newtonian fluids. The shear rate at the wall for Newtonian fluids can be obtained from Table 2.7-1 for n=1. We have

$$\dot{\gamma}_w = \frac{4Q}{\pi R^3} \tag{2.8-3}$$

For non–Newtonian fluids we will develop a general expression for the shear rate at the wall by starting from the definition of the volume rate of flow

$$Q = 2\pi \int_0^R r V_z dr \tag{2.8-4}$$

An integration by parts yields

$$Q = \pi r^2 V_z \Big|_0^R - \pi \int_0^R r^2 \left(\frac{dV_z}{dr}\right) dr \tag{2.8-5}$$

Applying the "no–slip" boundary condition at R i.e. V_z=0 at r=R we have

$$Q = -\pi \int_0^R r^2 \left(\frac{dV_z}{dr}\right) dr \tag{2.8-6}$$

Since $r/\mathrm{R} = \tau_{rz}/\tau_w$ (τ_w is the shear stress at the wall), we can eliminate r from the above expression to get

$$\frac{\tau_w{}^3 Q}{\pi R^3} = \int_0^{\tau_w} \tau_{rz}{}^2 \left(\frac{dV_z}{dr}\right) d\tau_{rz} \tag{2.8-7}$$

Differentiating both sides with respect to τ_w and using the Leibnitz rule we obtain

$$\left(\frac{dV_z}{dr}\right)_w = \frac{1}{\pi R^3}\left(\tau_w \frac{dQ}{d\tau_w} + 3Q\right) \tag{2.8-8}$$

or

$$\dot{\gamma}_w = \frac{4Q}{\pi R^3}\left(\frac{3}{4} + \frac{1}{4}\frac{d\, ln\, Q}{d\, ln\, \tau_w}\right) \tag{2.8-9}$$

Eq. 2.8-9 is usually referred to as the Rabinowitsch equation. It gives the shear rate at the wall of a capillary in terms of Q, R and τ_w. The term in brackets may be considered as a "correction"

to Newtonian expression which is simply $4Q/\pi R^3$. To obtain $\dot{\gamma}_w$ we must plot Q versus τ_w, on logarithmic coordinates to evaluate the derivative $d\ln Q/d\ln\tau_w$.

In general, for polymer melts the relation of the measured $\ln Q$ versus the measured $\ln\tau_w$, is non-linear, which means that the derivative $d\ln Q/d\ln\tau_w$ needs to be evaluated at several points of the experimentally obtained $\ln Q$ versus $\ln\tau_w$ curve. It is a time-consuming task. Below, an easier and faster, but less accurate method is presented. For non-Newtonian fluids that obey the power-law equation

$$\tau = m\dot{\gamma}^n \tag{2.8-10}$$

we may write an empirical expression

$$\tau_w = m'\left(\frac{4Q}{\pi R^3}\right)^n \tag{2.8-11}$$

in which n is the slope of the $\log\tau_w$ versus $\log(4Q/\pi R^3)$ plot, that is

$$n = \frac{d\,log\,\tau_w}{d\,log(4Q/\pi R^3)} \tag{2.8-12}$$

So, Eq. 2.8-9 may be written as

$$\dot{\gamma}_w = \frac{4Q}{\pi R^3}\left(\frac{3}{4} + \frac{1}{4n}\right) \tag{2.8-13}$$

Combining Eq. 2.8-11 and Eq. 2.8-13 we obtain

$$m = m'\left(\frac{4n}{3n+1}\right)^n \tag{2.8-14}$$

This means that for a typical polymer melt having n=0.4 the consistency index will be $m = m'\left(\frac{4\times0.4}{3\times0.4+1}\right)^{0.4} = 0.88m'$. In other words, the consistency index will be 88% of its value obtained by plotting the shear stress τ_w against the apparent shear rate ($4Q/\pi R^3$).

Example E2.8-1

(a) What should the load be in kg, in order that a power-law polymer melt with m=7909 Pa·s^n and n=0.46 flow out of a D_T=3 mm diameter tube (see Fig. 2.6) so that the wall shear stress is τ_w=0.14 MPa?

(b) What is the flow rate (kg/h) and the wall shear rate (s^{-1}) under such conditions? The density of the molten polymer is ρ=800 kg/m^3.

Solution

D_R =30 mm=0.03 m

$D_T = 2R_T = 3$ mm$=0.003$ m

$L=25$ mm$=0.025$ m

$\tau_w=0.14$ MPa$=0.14\times10^6$ Pa

$g=9.81$ m/s^2

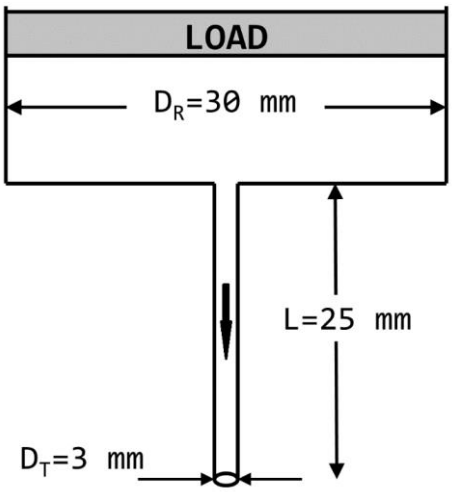

(a) First, we need to calculate the pressure drop in the 3 mm tube, using the following equation (Eq. 2.7-9)

$$\tau_w = -\frac{\Delta p}{2L}R_T = -\frac{\Delta p}{4L}D_T$$

As the sign in the above equation is a matter of convention, we use the positive sign which represents stress exerted from the fluid to the wall. Therefore, solving with respect to Δp and introducing the numerical values

$$\Delta p = \frac{\tau_w 4L}{D_T} = \frac{(0.14\times10^6)\times4\times(0.025)}{3\times10^{-3}} = 4.66\times10^6 Pa$$

For the reasons outlined in Example 2.7-2, the weight m_L of the load can be calculated from

$$\Delta p = \frac{F}{A_R} = \frac{4m_L g}{\pi {D_R}^2} \rightarrow m_L = \Delta p\frac{\pi D_R^2}{4g}$$

where F is the force the load exerts on the fluid, m_L the load weight, g the gravitational acceleration and A_R the load cross-sectional area. Introducing the numerical values in the above equation gives

$$m_L = \frac{(4.66\times10^6)\times\pi\times0.03^2}{4\times9.8} \cong 336\ kg$$

(b) The flow rate can be calculated from Table 2.7.-1

$$\Delta p = 2mLR^{-(3n+1)}\left[\frac{Q}{\pi}\left(\frac{1}{n}+3\right)\right]^n$$

or

$$Q = \frac{\pi R_T^{\frac{1}{n}+3}}{\frac{1}{n}+3}\left(\frac{\Delta p}{2mL}\right)^{\frac{1}{n}}$$

Introducing the numerical values in the above equation gives

$$Q = \left(\frac{3.1414 \times 0.0015^{\frac{1}{0.46}+3}}{1/0.46+3}\right)\left[\frac{4.66 \times 10^6}{2 \times 7909 \times 0.025}\right]^{\frac{1}{0.46}} = 1.06 \times 10^{-6}\frac{m^3}{s}$$

Therefore, the mass flow rate will be

$$\dot{m} = 800\frac{kg}{m^3} \times 1.06 \times 10^{-6}\frac{m^3}{s}3600\frac{s}{h} \cong 3\frac{kg}{h}$$

The wall shear rate can be calculated from Table 2.7-1

$$\dot{\gamma}_w = \frac{4Q}{\pi R^3}\left(\frac{3}{4}+\frac{1}{4n}\right)$$

Substituting the numerical values, we obtain

$$\dot{\gamma}_w = \frac{4 \times 1.06 \times 10^{-6}}{\pi \times 0.0015^3}\left(\frac{3}{4}+\frac{1}{4 \times 0.46}\right) = 519.72 \quad s^{-1}$$

2.9 Pressure Drop for Flow of a Power-Law Fluid Through a Tapered Tube

Truncated conical dies (i.e. tapered tubes like that shown in Fig. 2.9-1) are used very often in processing of molten polymers which, as we have said earlier, are described by the power–law equation satisfactorily. The determination of pressure drop is of primary importance in process equipment design. Here, we will use the results of Section 2.7 to calculate the pressure drop for flow in a slightly tapered tube. We start with Eq. 2.7-19

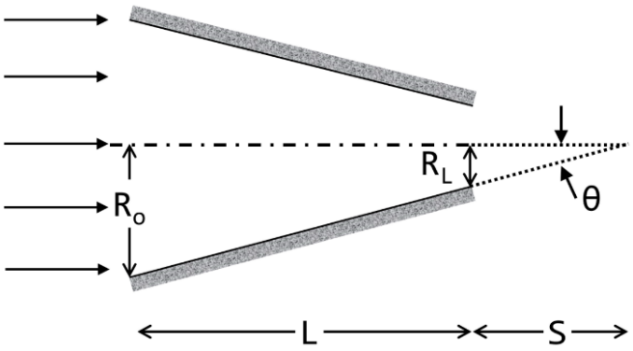

Figure 2.9-1. Geometry of a tapered tube of radius *R* and length *L*.

$$\Delta p = 2mLR^{-(3n+1)}\left[\frac{Q}{\pi}\left(\frac{1}{n}+3\right)\right]^n \tag{2.9-1}$$

Thus, for an infinitesimal tube of length *dz* we may write

$$dp = 2mR^{-(3n+1)}\left[\frac{Q}{\pi}\left(\frac{1}{n}+3\right)\right]^n dz \tag{2.9-2}$$

For a tapered tube we may neglect the velocity in the *r* – direction (small if the taper angle is small) and simply integrate between $z = 0$ and $z = L$, noting that

$$R = R_o - (R_o - R_L)\frac{z}{L} \tag{2.9-3}$$

We get

$$\Delta p = p_o - p_L = \frac{2mL}{3n}\left[\frac{Q}{\pi}\left(\frac{1}{n}+3\right)\right]^n \left(\frac{{R_L}^{-3n} - {R_o}^{-3n}}{R_o - R_L}\right) \tag{2.9-4}$$

Further noting that

$$R_o = \frac{(L+S)}{cot\,\theta} \qquad \text{and} \qquad R_L = \frac{S}{cot\,\theta} \tag{2.9-5}$$

we may write

$$\Delta p = \frac{2m\,cot\,\theta}{3n}\left[\frac{Q}{\pi}\left(\frac{1}{n}+3\right)\right]^n {R_L}^{-3n}\left[1 - \left(\frac{R_L}{R_o}\right)^{3n}\right] \tag{2.9-6}$$

This equation gives good results up to half cone angles of 15° [see Vlachopoulos and Scott 1985)].

It can further be shown that the maximum stretch rate at the narrowest passage is given by

$$\dot{\varepsilon} = \left(\frac{dV_z}{dz}\right)_{max} = \frac{tan\,\theta}{2}\frac{3n+1}{n+1}\frac{2Q}{\pi {R_L}^3} \tag{2.9-7}$$

2.10 Flow Through a Tapered Slit

We start from the pressure drop expression which was derived for flow between two parallel plates

$$\Delta p = mL\left[\frac{2n+1}{2n}\frac{Q}{W}\right]^n b^{-(2n+1)} \tag{2.10-1}$$

For an infinitesimal slit of length *dz*

$$dp = m\left[\frac{2n+1}{2n}\frac{Q}{W}\right]^n b^{-(2n+1)}dz \tag{2.10-2}$$

where

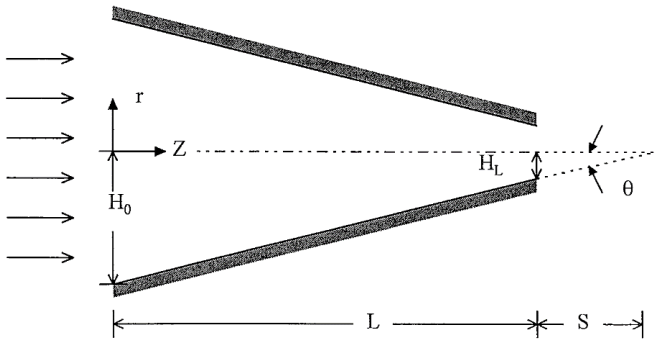

Figure 2.10-1. Schematic representation of a tapered slit of length L and angle θ.

$$b = H_0 - \frac{H_0 - H_L}{L} z \tag{2.10-3}$$

for a tapered slit. Integration between z =0 and z =L yields

$$\Delta P = P_0 - P_L \tag{2.10-4}$$

$$\Delta P = \frac{mL}{2^{n+1} n} \left[\frac{Q}{W} \left(\frac{1}{n} + 2 \right) \right]^n \left(\frac{{H_L}^{-2n} - {H_0}^{-2n}}{H_0 - H_L} \right) \tag{2.10-5}$$

Further noting that

$$H_0 = \frac{L + S}{\cot\theta}, \quad H_L = \frac{L + S}{\cot\theta} \tag{2.10-6}$$

We get

$$\Delta P = \frac{m \cot\theta}{2^{n+1} n} \left[\frac{Q}{W} \left(\frac{1}{n} + 2 \right) \right]^n {H_L}^{-2n} \left[1 - \left(\frac{H_L}{H_0} \right)^{2n} \right] \tag{2.10-7}$$

The derivation of the above expression was based on the implicit assumption of nearly parallel flow. It is a very good approximation for half-angles θ of up to 15°.

It can further be shown that the maximum stretch rate along the plane of symmetry is given by

$$\dot{\varepsilon} = \left(\frac{dV_z}{dz} \right)_{max} = \tan\theta \frac{2n + 1}{n + 1} \frac{2Q}{W H_L} \tag{2.10-8}$$

2.11 Pressure Driven Flow of a Bingham Fluid in a Tube

Although polymers melts do not exhibit yield stress, when mixed with particles or other polymers, they may exhibit both yield stress and shear thinning. The **Herschel-Bulkley** model is suitable

$$\tau_{rz} = \tau_o + \mu_o \left(\frac{dV_z}{dr}\right)^n \quad \text{if } \tau > \tau_o \qquad (2.11\text{-}1)$$

$$\frac{dV_z}{dr} = 0 \quad \text{if } \tau \leq \tau_o \qquad (2.11\text{-}2)$$

We will examine the simplest version where n=1, that is the **Bingham** model. A Bingham plastic (or more precisely ideal Bingham plastic) will not flow unless the shear stress exceeds a certain value τ_o called yield stress. This behavior is mathematically expressed by

$$\tau_{rz} = \tau_o + \mu_o \left(\frac{dV_z}{dr}\right) \quad \text{if } \tau > \tau_o \qquad (2.11\text{-}3a)$$

$$\frac{dV_z}{dr} = 0 \quad \text{if } \tau \leq \tau_o \qquad (2.11\text{-}3b)$$

as shown in Fig. 2.11-1 A Bingham plastic is not a "pure" fluid because it does not flow below the yield stress τ_o.

In pressure driven flow in a tube the shear stress is zero along the axis and increases linearly with r as discussed in the previous sections. Thus the Bingham plastic will behave like a fluid near the tube wall and will move like a solid plug in the center region $r < r_o$ where $\tau \leq \tau_o$ as shown schematically in Fig. 2.11-1.

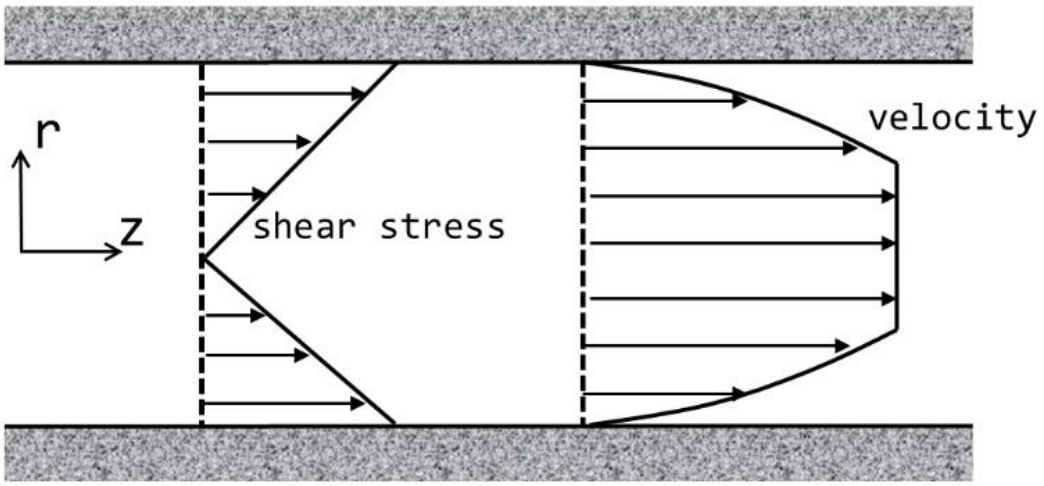

Figure 2.11-1. Shear stress and velocity profile for a Bingham fluid flowing between two flat parallel plates under the influence of a pressure gradient. In the central portion the fluid moves like a solid plug.

The mathematical manipulations of Eq. 2.7-9 up to Eq. 2.7-16 apply here also. We have

$$\tau_{rz} = -\frac{\Delta p}{2L} r \qquad (2.11\text{-}4)$$

Thus, for the wall region $r_o < r < R$

$$\tau_o + \mu_o \frac{dV_z}{dr} = -\frac{\Delta p}{2L} r \tag{2.11-5}$$

This may be integrated with the no–slip condition at the wall (V_z=0 at r=R), to give the velocity distribution

$$V_z = \frac{\Delta p}{4\mu_o L} R^2 \left[1 - \left(\frac{r}{R}\right)^2\right] - \frac{\tau_o R}{\mu_o}\left[1 - \left(\frac{r}{R}\right)\right] \qquad r_o<r<R \tag{2.11-6}$$

At $r = r_o$ this will be equal to the plug velocity

$$V_{plug} = \frac{\Delta p}{4\mu_o L} R^2 \left[1 - \left(\frac{r_o}{R}\right)^2\right] - \frac{\tau_o R}{\mu_o}\left[1 - \left(\frac{r_o}{R}\right)\right] \tag{2.11-7}$$

Also, from Eq. 2.11-4 we have

$$\text{at r=}r_o, \quad \tau_o = -\frac{\Delta p}{2L} r_o \qquad \text{and at } r=R, \quad \tau_w = -\frac{\Delta p}{2L} R \tag{2.11-8}$$

Eliminating r_o and $(\Delta p/2L)R$, we get

$$V_{plug} = \frac{\tau_w}{2\mu_o} R \left[1 - \frac{\tau_o}{\tau_w}\right]^2 \tag{2.11-9}$$

The total volume rate of flow is equal to the sum of the "plug" and the "fluid" regions

$$Q = Q_{plug} + Q_{fluid} = \pi {r_o}^2 V_{plug} + 2\pi \int_{r_o}^{R} V_z r dr \tag{2.11-10}$$

Inserting Eq. 2.11-6 into the integral, integrating and using the expressions for τ_o, τ_w and V_{plug} we have

$$Q = \frac{\pi R^3 \tau_w}{4\mu_o}\left[1 - \frac{4}{3}\left(\frac{\tau_o}{\tau_w}\right) + \frac{1}{3}\left(\frac{\tau_o}{\tau_w}\right)\right]^4 \tag{2.11-11}$$

2.12 Viscous Dissipation (Frictional Heating)

In the previous sections of this chapter, it is assumed that the flow of the polymer is isothermal, that means there are no temperature differences anywhere in the flow field. However, in the real world this is seldom the case. As a polymer is forced to flow through a narrow channel considerable heat is generated due to internal friction (viscous dissipation, frictional heating).

There is an easy way to get an approximate estimate of temperature rise (not the temperature profile, but just an average value). By assuming adiabatic conditions (i.e. no heat transfer to or from the surrounding walls), we can say that the mechanical energy (due to pressure) is converted into heat, so that we may write

$$force \times velocity$$
$$= mass\ flow\ rate\ (Q)\ \times heat\ capacity(C_p) \times temperature\ difference(\Delta T) \quad (2.12\text{-}1)$$

But

$$velocity = \frac{Q}{area},\quad pressure\ change\ (\Delta p) = \frac{force}{area} \quad (2.12\text{-}2)$$

Therefore,

$$(\Delta p)Q = \rho Q C_p \Delta T \quad (2.12\text{-}3)$$

From which we obtain

$$\Delta T = \frac{\Delta p}{\rho C_p} \quad (2.12\text{-}4)$$

It is interesting to note that the melt density of most polymers is close to ρ=1000 kg/m^3 and the heat capacity close to C_p=2000 J/kg . Thus if in Eq. 2.12-4 Δp is given in MPa then ΔT in Celsius is close to MPa pressure divided by 2. But, it should be noted that this is some sort of an average temperate at the exit of the die, while the true temperature profile has maximum near the wall, where the shear rate is highest. This is discussed in Example 2.12-1.

To determine a temperature profile we need the conservation of energy equation. A general derivation in 3D can be found elsewhere (Vlachopoulos, 2016). For unidirectional flow in the *x*-direction between two flat plates the equation of conservation of energy, for a Newtonian fluid, becomes

$$\rho C_p V_x \frac{\partial T}{\partial x} = k\frac{\partial^2 T}{\partial y^2} + \mu\left(\frac{dV_x}{dy}\right)^2 \quad (2.12\text{-}5)$$

For a power-law fluid, the above equation takes the following form

$$\rho C_p V_x \frac{\partial T}{\partial x} = k\frac{\partial^2 T}{\partial y^2} + m\left|\frac{dV_x}{dy}\right|^{n-1}\left(\frac{dV_x}{dy}\right)^2 \quad (2.12\text{-}6)$$

and similarly for tubular (axisymmetric) flow

$$\rho C_p V_z \frac{\partial T}{\partial z} = k\frac{1}{r}\frac{\partial}{\partial r}\left(r\frac{\partial T}{\partial r}\right) + m\left|\frac{dV_z}{dr}\right|^{n-1}\left(\frac{dV_z}{dr}\right)^2 \quad (2.12\text{-}7)$$

In Eqs. 2.12-5 to 2.12-7 the last term in the right-hand side is the **viscous dissipation** term. These equations are P.D.E′s and can easily be solved with numerical methods (e.g. finite differences (FD), finite element (FE) or the finite volume (FV) methods).

However, for fully developed drag flow between two parallel flat plates, we will not have any convection (no change of temperature in the *x*-direction). Assuming that we have a power-law fluid, Eq. 2.12-6 may take the following form

$$0 = k\frac{\partial^2 T}{\partial y^2} + m\left|\frac{dV_x}{dy}\right|^{n-1}\left(\frac{dV_x}{dy}\right)^2 \tag{2.12-8}$$

which may be written as

$$0 = k\frac{\partial^2 T}{\partial y^2} + m\left(\frac{dV_x}{dy}\right)^{n+1} \tag{2.12-9}$$

First we need to calculate the velocity gradient of the above equation. Naturally, we start from Eq. 2.5-6

$$0 = -\frac{\partial p}{\partial x} + \frac{\partial \tau_{yx}}{\partial y} \tag{2.12-10}$$

For drag flow, there is no pressure gradient in the flow direction (i.e. $\partial p/\partial x = 0$). Therefore

$$\frac{\partial \tau_{yx}}{\partial y} = 0 \tag{2.12-11}$$

Substituting Eq. 2.6-8 in Eq. 2.12-11 we have

$$\frac{\partial}{\partial y}\left[m\left|\frac{\partial V_x}{\partial y}\right|^{n-1}\frac{\partial V_x}{\partial y}\right] = 0 \tag{2.12-12}$$

which may be written as

$$\frac{\partial}{\partial y}\left[m\left(\frac{\partial V_x}{\partial y}\right)^n\right] = 0 \tag{2.12-13}$$

It can be easily verified that the solution of the above equation is simply

$$V_x = C_1 y + C_2 \tag{2.12-14}$$

where C_1 and C_2 constants. Notice that the same equation is also derived in the for drag flow of a Newtonian fluid. The boundary conditions of the present problem are the same to the Newtonian drag flow problem. Therefore, the velocity profile is

$$V_x = \frac{V}{H}y \tag{2.12-15}$$

and is shown schematically in Fig. 2.12-1. The velocity gradient is then $dV_x = V/H$, which upon substitution in Eq. 2.12-9 yields

$$0 = k\frac{d^2 T}{dy^2} + m\left(\frac{V}{H}\right)^{n+1} \tag{2.12-16}$$

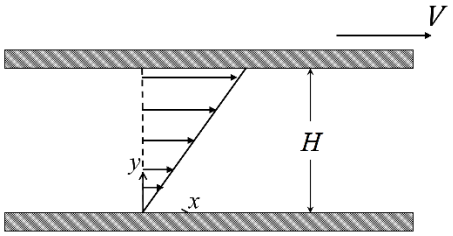

Figure 2.12-1. Schematic representation of the drag flow velocity profile. y=0 is located at the bottom plate.

The above differential equation can be easily solved, to give the following temperature profile

$$T(y) = -\frac{m}{2k}\left(\frac{V}{H}\right)^{n+1} y^2 + C_3 y + C_4 \tag{2.12-17}$$

The constants C_3 and C_4 can be calculated from the boundary conditions. Assuming that the bottom plate has a fixed temperature T_o and the top plate T_H we have

$$At\ y = 0 \ \rightarrow \ T = T_o \tag{2.12-18a}$$

$$At\ y = H \ \rightarrow \ T = T_H \tag{2.12-18b}$$

From Eq. 2.12-18a we obtain C_4=0 and from Eq. 2.12-18b we obtain

$$C_3 = \frac{m}{2k}\frac{V^{n+1}}{H^n} + \frac{T_B - T_o}{B} \tag{2.12-19}$$

Substituting Eq. 2.12-19 in Eq. 2.12-17 and rearranging the terms, we obtain

$$\frac{T(y) - T_o}{T_H - T_o} = \frac{1}{2} Br_n \left(\frac{y}{H}\right)\left[1 - \left(\frac{y}{H}\right)\right] + \left(\frac{y}{H}\right) \tag{2.12-20}$$

where

$$Br_n = \frac{mV^{n+1}}{kH^{n-1}(T_H - T_o)} \tag{2.12-21}$$

may be referred to as a generalized **Brinkman number** for a power-law fluid. Note that for n=1 in Eq. 2.12-20 the well-known Brinkman number is recovered $Br = \frac{mV^2}{k(T_H - T_o)}$, which is a measure of the importance of the viscous dissipation term. High Br number means large temperature rise. For plates with the same temperature, T_H=T_o, Eq. 2.12-20 can be written as

$$T(y) - T_o = \frac{1}{2}\frac{mV^{n+1}}{kH^{n-1}}\left(\frac{y}{H}\right)\left[1 - \left(\frac{y}{H}\right)\right] \tag{2.12-22}$$

It is interesting to note that for the case of T_H=T_o the maximum temperature T_{max} occurs at y=$H/2$

$$T_{max} - T_o = \frac{1}{8}\frac{mV^{n+1}}{kH^{n-1}} \tag{2.12-23}$$

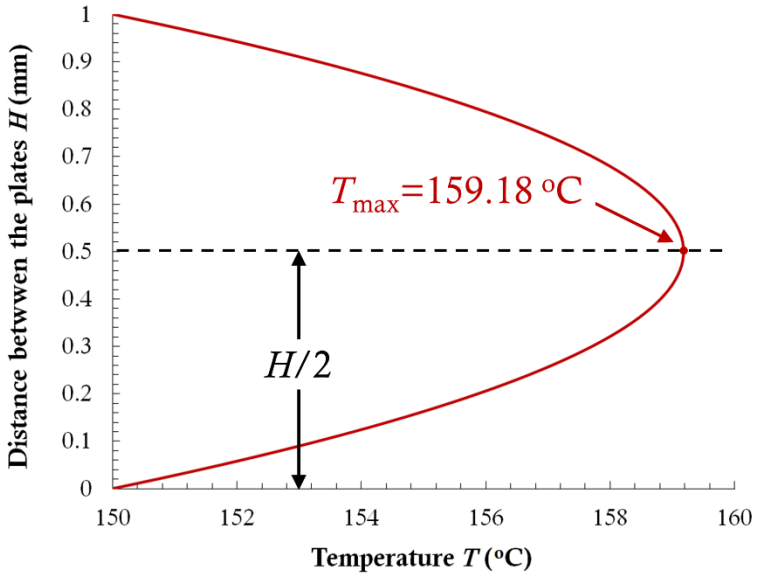

Figure 2.12-2. Temperature profile of a power-law fluid in drag flow between two parallel flat plates of equal temperature, T_o=T_H=150 °C. Power-law parameters: n=0.5 and m=10,000 Pa·s$^{0.5}$.

As an example to the above we plug in Eq. 2.12-23 some typical values encountered in polymer processing: m=10000 Pa·s^n, n=0.5, V=0.15 m/s, k=0.25 W/m·K, H=0.001 m and T_o= T_H=150 °C. The temperature profile is shown in Fig. 2.12-2. The temperature rise would be

$$\Delta T_{max} = T_{max} - T_o = \frac{1}{8}\frac{mV^{n+1}}{kH^{n-1}} = \frac{1}{8}\cdot\frac{10000X0.15^{0.5+1}}{0.25X0.001^{0.5-1}} \cong 9.18 \ ^oC \qquad (2.12\text{-}24)$$

It should be noted that if the temperature rise is, in general, appreciable, the temperature dependence of the viscosity has to be taken into account (m=m(T)), which complicates more accurate calculations.

Example E2.12-1

Consider a polymer melt with the following properties

Property	Value [units]
consistency index (m)	10^5 Pa·s^n
power-law index (n)	0.5
melt density (ρ)	1000 kg/m^3
specific heat (C_p)	2500 J/kg·°C
thermal conductivity (k)	0.2 W/m·°C

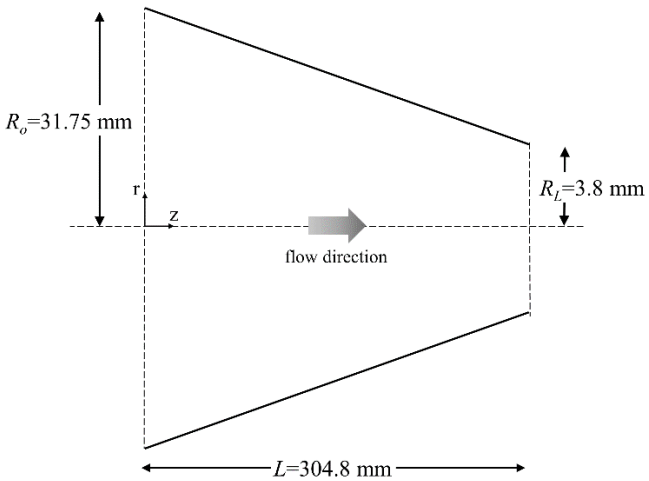

Figure E2.12-1. Schematic representation of the conical extrusion die. Figure not to scale.

The polymer melt with temperature 160 °C, flows inside a conical extrusion die (walls temperature 160 °C) with the relevant dimensions given in Fig. E2.12-1. The flow rate is Q=57 kg/hr. Determine the pressure drop in the die. Determine also the average temperature rise.

Solution

Parameters in S.I. units:

R_o=0.03175 m

R_L=0.0038 m

L=0.3048 m

Q= 57/1000/3600=1.583·10^{-5}=m^3/s

To calculate the pressure drop in the conical extrusion die we use Eq. 2.9-13. Upon substitutions we have

$$\Delta p = \frac{2\times 10^5 \times cot\, 6^o}{3\times 0.5}\left[\frac{1.583\times 10^{-5}}{\pi}\left(\frac{1}{0.5}+3\right)\right]^{0.5} 0.0038^{-3\times 0.5}\left[1-\left(\frac{0.0038}{0.03175}\right)^{3\times 0.5}\right]$$

$$\cong 26\ MPa$$

Therefore, the average temperature rise may be estimated from Eq. 2.12-4. Upon substitution we have

$$\Delta T = \frac{26\times 10^6}{1000\times 2500}\ ^oC = 10.4\ ^oC$$

With this approximation we get only a rough idea on how much the bulk temperature of the melt will rise, near the exit of the die. In reality, however, there is a distribution of

temperatures across the exit gap, with the maximum temperature appearing near the die walls. This, temperature profile, may be determined analytically for simple flows with parallel

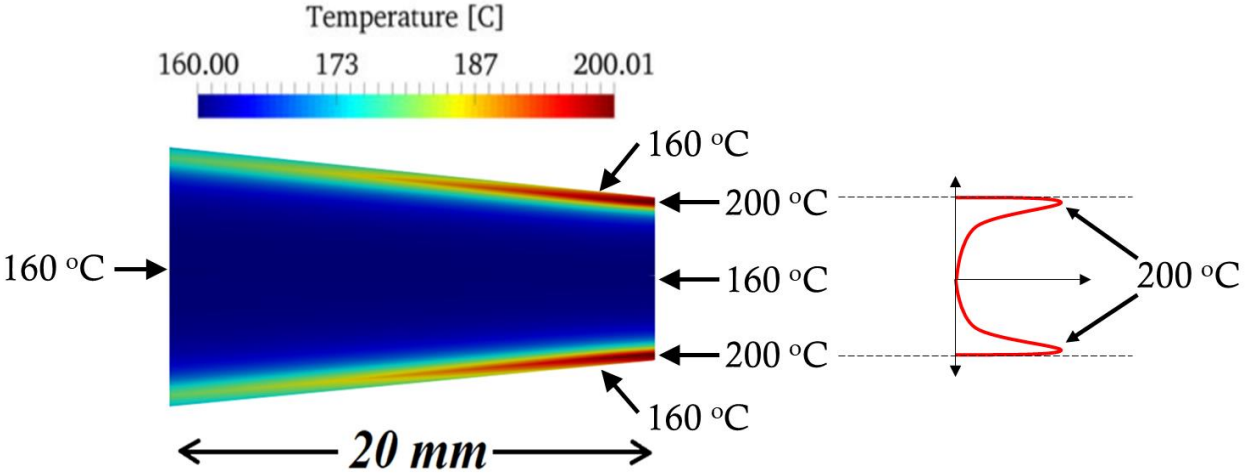

Figure E2.12-2. Temperature distribution field in a conical die via numerical simulation. Note only the final portion of the full length is shown. Far right: temperature profile at the die exit. Adopted from Polychronopoulos *et al.* (2018). (Color available only in electronic version).

gap geometry. Otherwise, numerical simulations are imperative (e.g. 2D or 3D flows). For the case considered here, the 2D numerical simulations exhibit a 40°C temperature rise near the die walls as illustrated in Fig. E2.12-2, which is considerably higher of the roughly 11°C we calculated above. Therefore, such calculations should be carried out with caution.

2.13 Wall Slip

The no-slip condition (i.e. fluid velocity is equal to the velocity of the wall with which it is in contact) has been a cornerstone of fluid mechanics for about 150 years. Historically, the acceptance of the no-slip condition was problematic according to Day (2004). With polymer melts it has been observed that above a certain value of wall shear stress, slippage occurs (usually about 0.09 MPa for PE). The slip velocity V_s is an important quantity but it is difficult to measure. Here is a method developed by Mooney (1931) many years ago. The apparent shear rate is

$$\dot{\gamma}_{app} = \frac{4Q}{\pi R^3} \tag{2.13-1}$$

The flow rate for an average velocity without slip V_{avg}, will be

$$Q = \pi R^2 V_{avg} \tag{2.13-2}$$

In the presence of a slip velocity V_s

$$Q_s = \pi R^2 \left(V_{avg} - V_s\right) \tag{2.13-3}$$

and the apparent shear rate with slip is

$$\dot{\gamma}_{app,s} = \frac{4Q_s}{\pi R^3} = \frac{4\left(V_{avg} - V_s\right)}{R} \tag{2.13-4}$$

which may be written as

$$\dot{\gamma}_{app,s} = \frac{4Q}{\pi R^3} - \frac{4V_s}{R} \tag{2.13-5}$$

or

$$\frac{4Q}{\pi R^3} = \dot{\gamma}_{app,s} + \frac{4V_s}{R} \tag{2.13-6}$$

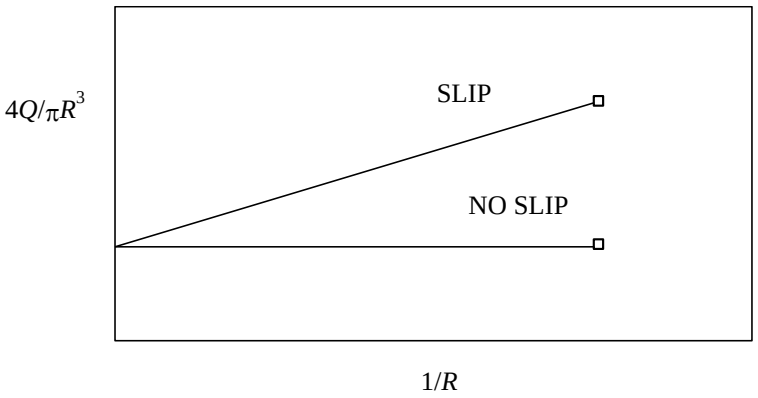

Figure 2.13-1. Wall slip velocity measurement according to Mooney (1931).

This means that a plot of $4Q/\pi R^3$ against $1/R$ should give a horizontal line to the x axis if there is no slip. If slip is present, the slope of the curve should be equal to $4V_s$ as shown in Fig. 2.13-1.

The results of measurements are frequently presented in the form

$$V_s = A\tau_w{}^{\beta} \tag{2.13-7}$$

where β = 2~4 (usually).

For HDPE, slip is believed to occur above a critical value at shear stress of 0.09 MPa, and a representative expression would be (Hatzikiriakos and Dealy, 1992)

$$V_s = 11050\tau_w{}^{3.29} \tag{2.13-8}$$

where τ_w is in MPa and V_s in mm/s (valid approximately in the range 0.1 MPa<τ_w< 0.3 MPa).

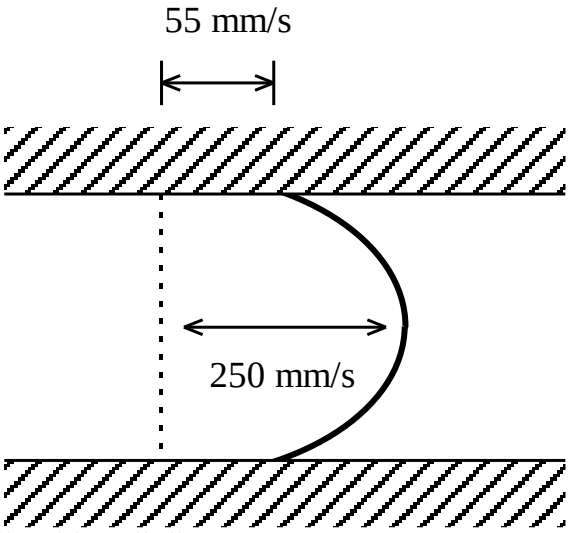

Figure 2.13-2. Velocity profile with wall slip.

To put the above expression in perspective, here are some numbers in a typical extrusion experiment. The wall shear stress might be 0.2 MPa and the maximum velocity at the center of a die might be 250 mm/s. The above equation gives a slip velocity V_s = 55 mm/s. Thus, the velocity profile would look like in Fig. 2.13-2.

Of course, all of the above calculations and estimates should be accepted with some caution. In the majority of cases whenever we measure viscosity at high shear rates and stresses, there is probably going to be some slip involved. So, what we call shear-thinning (reflected in the power-law index *n*) might also involve some slip. Consequently, we may not have good m and n values for flow without slip and this demonstrates some of the difficulties in determining accurate viscosity as a function of the shear rate.

2.14 Viscosity Models for Three-Dimensional Flow Analysis

The power-law model for viscosity of polymers melts and solutions was introduced in connection with simple shear flow between two parallel plates. It was used in solving the various unidirectional flow problems in this chapter. The viscosity was simply a function of the shear rate (velocity gradient) and there was no problem in determining how the shear was defined

$$\eta = m\left(\frac{\partial V_x}{\partial y}\right)^{n-1} \tag{2.14-1}$$

where m and n are constants, V_x the velocity in the flow direction x and y the coordinate normal to the flow direction.

Things were easy in several problems because we made the obvious choice of a coordinate in the direction of the flow and there were no velocity changes in that direction. In the tapered flow analysis there is velocity change in both directions, but we were able to come up with a straightforward solution by assuming a nearly parallel flow field. However, if we had examined a large convergence angle, obviously, we would have strong velocity gradients both in the direction of the flow and in the normal direction. Also, if we had chosen a rectangular coordinate system for pressure driven flow in a tube we would not be able to have a simple definition of the shear rate. Intuitively, we expect that the viscosity, which is a property of the fluid, should be independent of the system of coordinates we choose to solve a problem. So, we must find a measure of the strain rates, which does not depend on the coordinate system chosen. The strain rate for 3-D flow is a tensor (9 components) defined (see Vlachopoulos, 2016) in "short-hand" index notation as

$$D_{ij} = \frac{1}{2}\left(\frac{dV_i}{\partial x_j} + \frac{dV_j}{\partial x_i}\right) \tag{2.14-2}$$

which means

$$\begin{aligned} D &= \frac{1}{2}\left(\frac{dV_x}{\partial x} + \frac{dV_x}{\partial x}\right) = \frac{dV_x}{\partial x} \\ D_{yy} &= \frac{1}{2}\left(\frac{dV_y}{\partial y} + \frac{dV_y}{\partial y}\right) = \frac{dV_y}{\partial y} \\ D_{zz} &= \frac{1}{2}\left(\frac{dV_z}{\partial z} + \frac{dV_z}{\partial z}\right) = \frac{dV_z}{\partial z} \\ D_{xy} &= D_{yx} = \frac{1}{2}\left(\frac{dV_x}{\partial y} + \frac{dV_y}{\partial x}\right) \\ D_{yz} &= D_{zy} = \frac{1}{2}\left(\frac{dV_y}{\partial z} + \frac{dV_z}{\partial y}\right) \\ D_{xz} &= D_{zx} = \frac{1}{2}\left(\frac{dV_x}{\partial z} + \frac{dV_z}{\partial x}\right) \end{aligned} \tag{2.14-3}$$

A tensor has three scalar invariants (quantities that do not change under orthogonal coordinate transformation, see for example Hughes and Gaylord (1964).

The first is the sum of the diagonal components

$$I = D_{xx} + D_{yy} + D_{zz} \tag{2.14-4}$$

The second is

***Table 2.14-1*. The second invariant of the rate strain tensor ($\frac{1}{2}II$) in rectangular, cylindrical and spherical coordinates.**	
Rectangular	$$\frac{1}{2}II = 2\left[\left(\frac{\partial V_x}{\partial x}\right)^2 + \left(\frac{\partial V_y}{\partial y}\right)^2 + \left(\frac{\partial V_z}{\partial z}\right)^2\right] + \left(\frac{\partial V_y}{\partial x} + \frac{\partial V_x}{\partial y}\right)^2 + \left(\frac{\partial V_z}{\partial y} + \frac{\partial V_y}{\partial z}\right)^2 + \left(\frac{\partial V_x}{\partial z} + \frac{\partial V_z}{\partial x}\right)^2$$
Cylindrical	$$\frac{1}{2}II = 2\left[\left(\frac{\partial V_r}{\partial r}\right)^2 + \left(\frac{1}{r}\frac{\partial V_\theta}{\partial \theta} + \frac{V_r}{r}\right)^2 + \left(\frac{\partial V_z}{\partial z}\right)^2\right] + \left[r\frac{\partial}{\partial r}\left(\frac{V_\theta}{r}\right) + \frac{1}{r}\frac{\partial V_r}{\partial \theta}\right]^2 + \left[\frac{1}{r}\frac{\partial V_z}{\partial \theta} + \frac{\partial V_\theta}{\partial z}\right]^2 + \left[\frac{\partial V_r}{\partial z} + \frac{\partial V_z}{\partial r}\right]^2$$
Spherical	$$\frac{1}{2}II = 2\left[\left(\frac{\partial V_r}{\partial r}\right)^2 + \left(\frac{1}{r}\frac{\partial V_\theta}{\partial \theta} + \frac{V_r}{r}\right)^2 + \left(\frac{1}{r\sin\theta}\frac{\partial V_\varphi}{\partial \varphi} + \frac{V_r}{r} + \frac{V_\theta \cot\theta}{r}\right)^2\right] + \left[r\frac{\partial}{\partial r}\left(\frac{V_\theta}{r}\right) + \frac{1}{r}\frac{\partial V_r}{\partial \theta}\right]^2 + \left[\frac{\sin\theta}{r}\frac{\partial}{\partial \theta}\left(\frac{V_\varphi}{\sin\theta}\right) + \frac{1}{r\sin\theta}\frac{\partial V_\theta}{\partial \varphi}\right]^2 + \left[\frac{1}{r\sin\theta}\frac{\partial V_r}{\partial \varphi} + r\frac{\partial}{\partial r}\left(\frac{V_\varphi}{r}\right)\right]^2$$

$$I = \begin{vmatrix} D_{xx} & D_{xy} \\ D_{yx} & D_{yy} \end{vmatrix} + \begin{vmatrix} D_{yy} & D_{yz} \\ D_{zy} & D_{zz} \end{vmatrix} + \begin{vmatrix} D_{xx} & D_{xz} \\ D_{zx} & D_{zz} \end{vmatrix} \tag{2.14-5}$$

And the third is

$$I = \begin{vmatrix} D_{xx} & D_{xy} & D_{xz} \\ D_{yx} & D_{yy} & D_{yz} \\ D_{zx} & D_{zy} & D_{zz} \end{vmatrix} \tag{2.14-6}$$

Form the theory of constitutive equations (Bird *et al.*, 1987, Denn, 1980, 2008) it turns out that the viscosity can be expressed as a function of the second invariant of the strain rate tensor in the following form

$$\eta = m \left| \frac{1}{2} II \right|^{\frac{n-1}{2}} \tag{2.14-7}$$

The function $\frac{1}{2}II$ is given in Table 2.14-1 in rectangular, cylindrical and spherical coordinates. It can easily be shown (by eliminating all the terms equal to zero) that for the case $V_x = V_x(y)$ and $V_y = V_z = 0$ we have $\eta = m\left(\frac{\partial V_x}{\partial y}\right)^{n-1}$.

Also, the shear rate $\dot{\gamma}$ in the Carreau-Yasuda and Cross models must be expressed in terms of the second invariant, just as for the power-law model. In fact, this type of models is referred to as the **Generalized Newtonian Fluid**, as opposed to the **viscoelastic** models, which are briefly discussed in Chapter 4.

Bibliography

Batchelor G.K., The Effect of Brownian Motion on the Bulk stress in a Suspension of Spherical Particles, J. Fluid Mech., 83 (part 1), 97 (1977)

Bird R.B., Armstrong R.C. and Hassager O., *Dynamics of Polymeric Liquids: Volume 1 Fluid Mechanics*, 2nd Ed., Wiley (1987)

Day M.A., The no-slip condition of fluid dynamics, Erkenntnis. 33 (3), 285 (2004)

Denn M.M., *Process Fluid Mechanics*, Prentice-Hall (1980)

Denn M.M., *Polymer Melt Processing: Foundations in Fluid Mechanics and Heat Transfer*, Cambridge University Press (2008)

Hatzikiriakos S.G. and Dealy J.M., Wall slip of molten high density polyethylenes. II. Capillary rheometer studies, J. Rheol. 36, 703 (1992)

Hughes W.F. and Gaylord E.W., *Basic equations of engineering science*, Schaum's Outline Series, McGraw-Hill (1964)

Mooney M., Explicit Formulas for Slip and Fluidity, J. Rheol., 2 (2), 210 (1931)

Morrison F.A., *Understanding Rheology*, Oxford University Press (2001)

Nielsen L.E., *Polymer Rheology*, Marcel Dekker (1977)

Polychronopoulos N.D., Charlton Z., Suwanda D. and Vlachopoulos J., Measurements and Comparison to Predictions of Viscosity of Heavily Filled HDPE with Natural Fibers, Adv. Polym. Tech., 37(4), 1161 (2018)

Vlachopoulos J. and Scott P.S., Pressure Drop for Molten Polymer Flow through Tapered Dies, Adv. Polym. Techn., 5 (2), 81 (1985)

Vlachopoulos J., *Fundamentals of Fluid Mechanics*, Polydynamics, Dundas, ON, Canada, revised internet edition (downloadable from www.researchgate.com), (2016)

J. Vlachopoulos and N.D. Polychronopoulos "*Understanding Rheology and Technology of Polymer Extrusion*", First Edition, Polydynamics Inc, Dundas, Ontario, Canada (2019)

Chapter 3
VISCOELASTICITY

3.1 Unusual Rheological Phenomena

In Chapter 2 we defined Newtonian and Non-Newtonian fluids in terms of the viscosity as a function of shear. We discussed extensively the shear thinning behavior of polymer melts. Actually, the term "non–Newtonian" is broader and the flow phenomena exhibited by non–Newtonian fluids are much more interesting and complex than just the departure from linearity between stress and shear rate. Liquids with complex structure, such as polymer solutions, polymer melts, suspensions of particles, soap solutions, whole human blood, slurries, pastes etc behave in unusual ways. The flow behavior of these liquids is the object of rheology (Bird *et al.* 1987, Tanner, 1985, Macosko, 1994, Münstedt, 2019). Rheology is the science of deformation and flow of materials. The Society of Rheology was founded in 1929 in the USA and adopted the Greek motto (Heraclitus c.535- c.475 BCE) **παντα ρει** (panta rei, all things flow). The philosophical implication is that given enough time all materials will flow. Macromolecular (polymeric) solutions and melts exhibit many unexpected flow phenomena beyond their shear thinning behavior and they are perhaps the most interesting from the rheological point of view. Some of these are explained pictorially in Figs. 3.1-1a to 3.1-1f.

Fig. 3.1-1a shows the rod–climbing or Weissenberg effect (after the Austrian born physicist Karl Weissenberg 1883-1976). While a Newtonian fluid would have a parabolic depressed surface near a rotating rod (Vlachopoulos, 2016), polymeric liquids would climb up the rod. Fig. 3.1-1b shows the phenomenon of extrudate swell exhibited by polymeric liquids. The diameter of the jet emerging from a tube can increase up to 400% while for

Newtonian fluids, like water, it remains approximately the same as the diameter of the tube (actually 13% larger, see Section 3.8). Fig. 3.1-1c shows a siphon experiment. For Newtonian fluids, the siphon works as long as one end of the tube is beneath the surface of the liquid. For polymeric liquids the siphon can work even if the tube end is above the liquid surface!

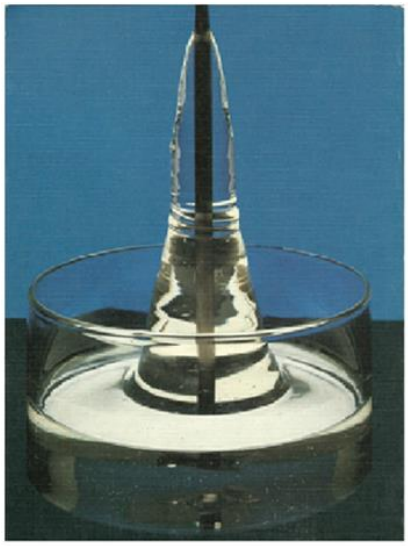

Figure 3.1-1a. Polymeric liquid climbing up a rotating rod (Weissenberg effect). From Thornton Centre of Shell Research Ltd.

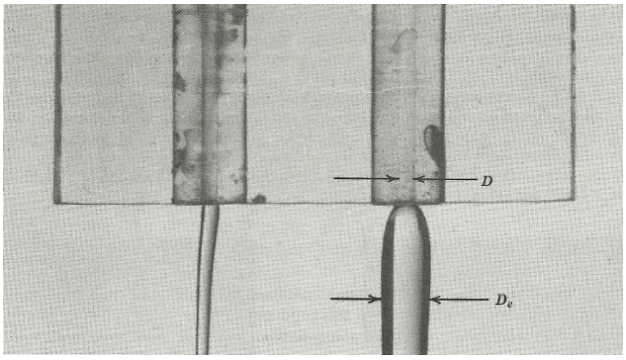

Figure 3.1-1b. Extrudate swell of polymeric liquid emerging from a long tube. From Bird *et al.* (1987).

Fig. 3.1-1d compares the flow pattern for very slow viscous (creeping) flow from a large reservoir into a smaller diameter tube. The polymeric liquid forms a large toroidal vortex. Fluid particles trapped in the vortex will circulate continuously and will not move into the small diameter tube (capillary). Fig. 3.1-1e shows the behavior as the fluids are pumped through tubes. We follow the motion by inserting a streak of dye. Before the motion starts the streak is flat and after starting up the pump, progressively looks like an elongated parabola. When the motion stops (by turning off the pump) the Newtonian fluid comes to rest while the polymeric liquid "recoils". Fig.3.1-1f shows a pressure difference between the inner and the

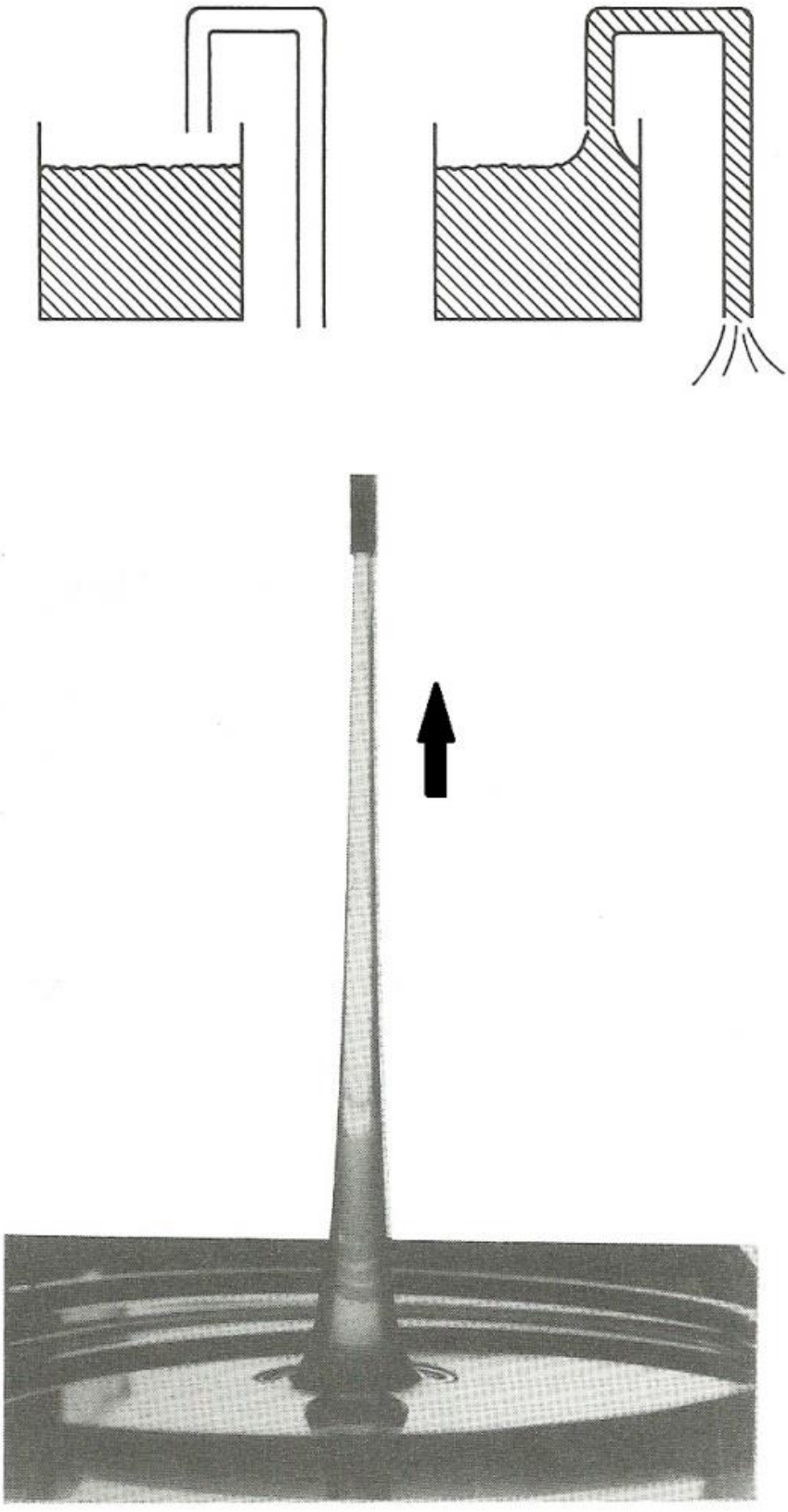

Figure 3.1-1c. Siphon experiment with a polymeric liquid. From Bird et al (1987).

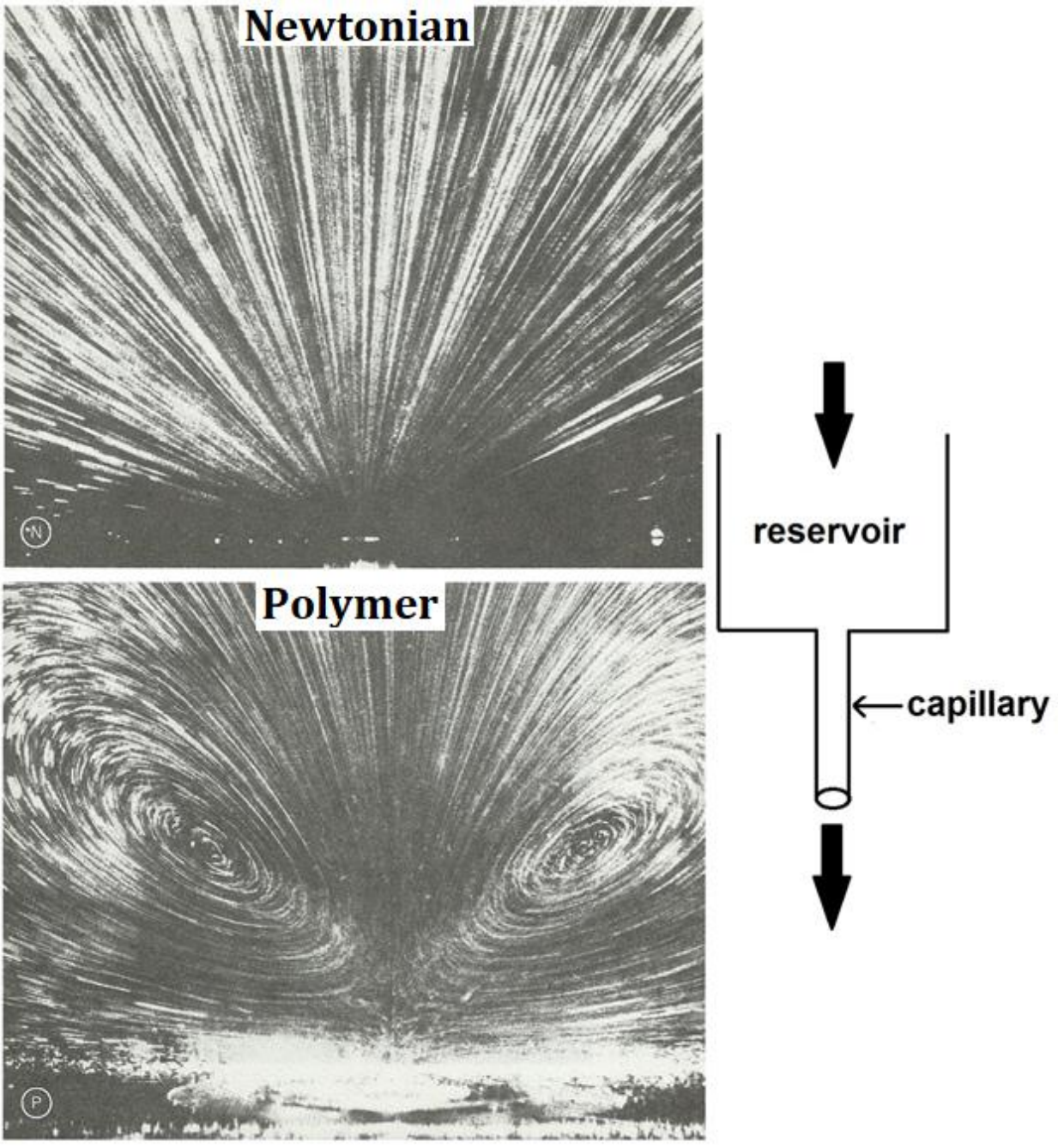

Figure 3.1-1d. Entry from a reservoir into a small diameter (capillary). Top photo: Newtonian. Bottom photo: polymer. From Bird *et al.* (1987).

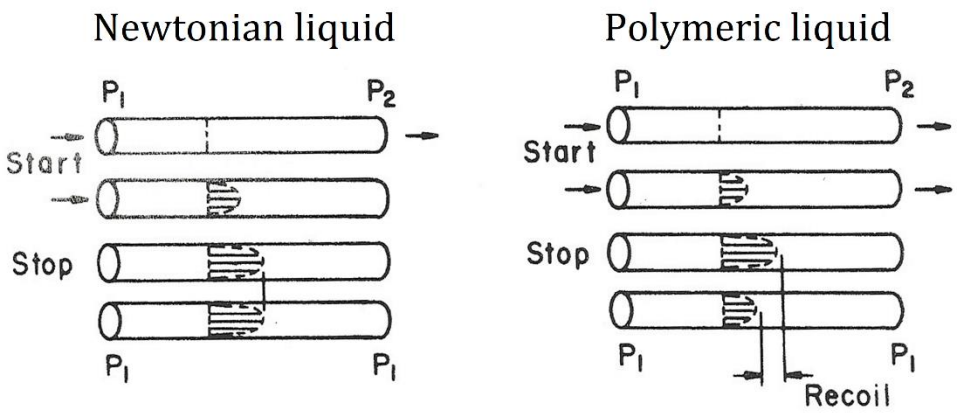

Figure 3.1-1e. Recoil of a polymeric liquid and lack thereof of Newtonian liquid when pumping is stopped. From Bird *et al.* (1987).

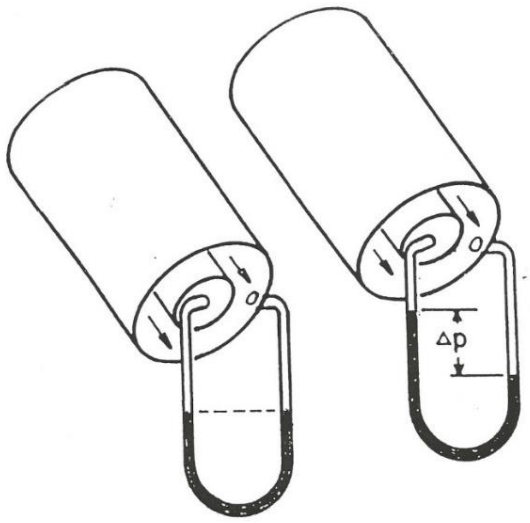

Figure 3.1-1f. Pressure differences during annular flow of Newtonian (left) and polymeric (right) liquids. From Darby (1976).

outer tube for annular flow of a polymeric liquid, while for the same flow field there is no pressure difference for Newtonian flow.

To describe mathematically the various effects, we can start from the equations of mass, momentum (and energy, if temperature differences are present). However, it is necessary to introduce complex constitutive equations that relate stresses to the rates of strain.

3.2 Basic Concepts of Viscoelastic Behavior

The response of polymeric liquids to an imposed stress may, under certain conditions, resemble the behavior of a solid, in addition to the non–linear dependence of stress on shear rate. These liquids are composed of very long molecular chains of molecular weight usually

in the range of 10,000 to 10,000,000 with many commercial products being in the range of 50,000 to 500,000.

When these liquids are at rest, the molecular chains are randomly distributed. When an external stress is applied, the intermolecular bonds are stretched, the chains commence to flow past another, to disentangle and to align in the direction of the flow. However, for these processes to occur certain time is required. On the other hand, the response of small molecular weight liquids, like water, can be instantaneous. From molecular arguments it can be estimated that steady shearing can be established in water in about 10^{-12} seconds and, of course, mechanical instruments would have a much larger response time, so it is impossible to measure directly that constant. With polymeric liquids we can measure characteristic response times usually in the range of 10^{-3} to 10^{3} s (the lower values for solutions and the higher for melts).

It is apparent that time constants are necessary to describe the behavior of polymer melts and solutions. In 1964 Marcus Reiner (Denn, 2011) used the biblical expression that "*mountains flowed in front of the God*" to define a dimensionless group known as the **Deborah Number**, which is the ratio of a characteristic material time (λ) to a characteristic experiment or process time (θ). The biblical name is due to the allusion that in God's (infinite) time solid mountains flow (like liquids)

$$De = \frac{\lambda}{\theta} = \frac{material\ time}{process\ time} \tag{3.2-1}$$

Let us choose a typical polymer melt with a characteristic time λ=1 s. If the process time is very large ($\theta \to \infty$ and $De \to 0$) the material will behave like a fluid. However, when the process time is very short ($\theta \to 0$ and $De \to \infty$) the polymer melt will behave like a solid. Many polymer processing operations require times comparable to the characteristic material times. For example, in polymer shaping and forming operations, the passage through a die or filling of a mold may take place in 0.1 to 10 seconds and *De* might be in the range of 1–10. Consequently, the polymer melt behavior will have both fluid (viscous) and solid (elastic) characteristics and it is said to be viscoelastic.

To study the behavior of viscoelastic materials, we must develop mathematical models (called **constitutive equations**, which are much more complicated than the Newtonian version). The simplest of them involves a simple combination of a Newtonian fluid and an elastic (Hookean) solid.

For the Newtonian fluid we have a linear relation between stress τ and rate of strain $\dot{\gamma}_f$

$$\tau = \eta\dot{\gamma}_f \tag{3.2-2}$$

where η the viscosity.

For the elastic (Hookean) solid we have a linear relation between stress τ and the strain γ_s

$$\tau = G\gamma_s \tag{3.2-3}$$

where G the modulus of elasticity.

We assume that the combined material will have a shear rate equal to the sum of the two shear rates

$$\dot{\gamma} = \dot{\gamma}_f + \dot{\gamma}_s \tag{3.2-4}$$

or

$$\dot{\gamma} = \frac{\tau}{\eta} + \frac{\dot{\tau}}{G} \tag{3.2-5}$$

or

$$\tau + \frac{\eta}{G}\dot{\tau} = \eta\dot{\gamma} \tag{3.2-6}$$

The ratio η/G has dimensions of time and is usually denoted by λ

$$\tau + \lambda\dot{\tau} = \eta\dot{\gamma} \tag{3.2-7}$$

This mathematical model is referred to as a **Maxwell fluid**.

Actually, it is easier to understand the behavior of this mathematical model by referring to the mechanical analogue of Fig. 3.2-1. The spring represents the Hookean solid $\tau = G\gamma_s$ and the dashpot the Newtonian liquid $\tau = \eta\dot{\gamma}_f$.

Let us assume that the mechanical model of Fig. 3.2-1 is suddenly extended to a position and held there. This means that we impose a constant extension (strain γ =const) and therefore $\dot{\gamma} = 0$. Eq. 3.2-7 takes then the following form

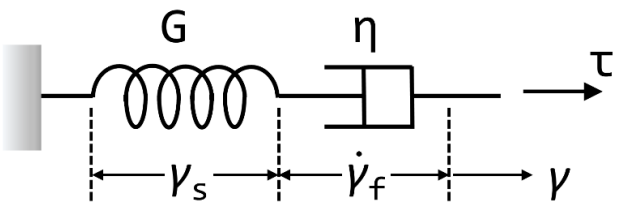

Figure 3.2-1. A mechanical contraption representing the Maxwell fluid model.

$$\tau + \lambda\dot{\tau} = 0 \tag{3.2-8}$$

or

$$\tau + \lambda \frac{d\tau}{dt} = 0 \tag{3.2-9}$$

from which

$$\frac{d\tau}{\tau} = \frac{dt}{\lambda} \tag{3.2-10}$$

that yields

$$\tau = C_1 e^{-t/\lambda} \tag{3.2-11}$$

Let us set $\tau = S$ at $t = 0$

$$\frac{\tau}{S} = e^{-t/\lambda} \tag{3.2-12}$$

We see that for $t = \lambda$

$$\frac{\tau}{S} = e^{-1} = \frac{1}{e} \cong 0.37 \tag{3.2-13}$$

Thus, λ represents the time for the stress to decay by a factor $1/e \cong 0.37$ and is called the **relaxation time**. The physical meaning of this quantity can be better understood by referring to the mechanical analogue of Fig. 3.2-1. If we impose a sudden extension and stop, the spring will respond instantaneously. However, the stress will be relaxed gradually (exponentially) as the dashpot will start moving (viscous flow). Given enough time the stress will become zero.

This model is too crude to represent quantitatively the stress relaxation behavior of polymeric liquids, but it gives a good qualitative picture. The sudden stop of extension and subsequent relaxation of the mechanical model corresponds to the following fluid flow experiment: Assume that a polymeric liquid is sheared in a concentric cylinder viscometer, like that of Fig. 3.2-2a. If the rotation is suddenly stopped i.e. $\dot{\gamma} = 0$, the measured stress will not become instantaneously zero (as for Newtonian fluids) but will decay in an exponential–like manner as shown in Fig. 3.2-2b.

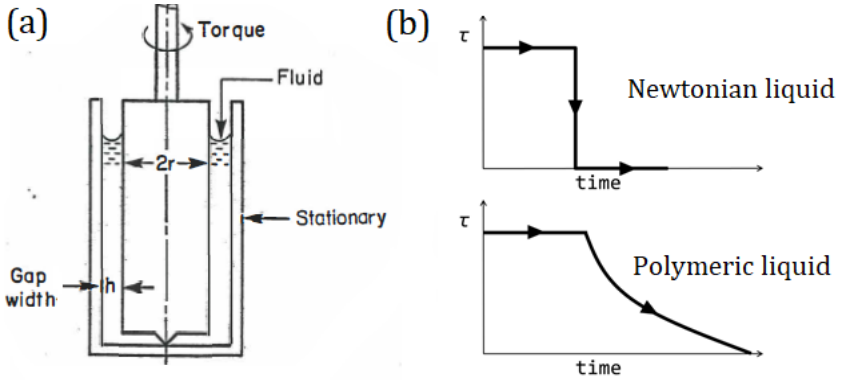

Figure 3.2-2. (a) Coaxial cylinder viscometer and (b) schematic representation of stress relaxation after shear flow cessation for Newtonian (top) and polymeric liquids (bottom).

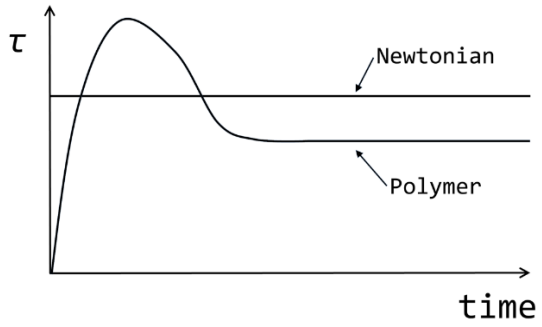

Figure 3.2-3. Stress "overshoot" at flow start-up.

The relaxation behavior is not the only unusual time response for polymeric liquids. If we start suddenly shearing from rest, a Newtonian fluid will respond instantaneously, while a polymer solution or melt will exhibit an overshoot as shown in Fig. 3.2-3.

Under shearing, the long molecular chains can be thought of as acting as springs or rubber bands. By shearing, the springs are stretched around a rotating shaft in Fig. 3.1-1a and exert a contraction force toward the axis of the rotation like a "strangulation" (Darby, 1976) which forces the fluid towards the axis. This results in the rod climbing, or **Weissenberg effect**. Similarly, when a polymeric liquid exits from a tube (Fig. 3.1-1b) the "springs" which are extended inside the tube, contract and this causes the phenomenon of extrudate swell. The contraction of fluid elements which is responsible for the characteristic "puff up", can also be thought of as originating from the relaxation of the viscoelastic forces at the exit.

The pressure difference between the inner and outer cylinder in steady axial flow in an annulus (Fig. 3.1-1f) is due to development of stresses that do not exist in Newtonian fluids. These stresses which are developed in viscoelastic fluids under shear in directions normal to the direction of flow are called **normal stresses**. They increase with shear rate and disappear when the fluid is at rest. The simple molecular picture given earlier, that of stretched springs or rubber bands, is too crude to present reality. There is, of course, some stretching of the macromolecular chains during shear, but also disentaglements and other interactions. There is a great variety of polymer types some of them of equal size chains (monodisperse), other of different size (polydisperse), yet others with branches (short or long) and molecular weights ranging from a few thousand to several million. The development of an accurate description of the various processes at the molecular level during shear or other deformation is an extremely daunting task. We will adopt the continuum mechanics approach and will consider only the stresses developed and the balance of the corresponding forces.

Whenever a polymeric liquid is sheared as shown in Fig. 3.2-4, normal stresses are developed because shearing results also in extension in the *x*-direction and compression in the *y*- and *z*-directions. A measuring device would record the total normal stresses i.e. there will be contributions from both the static pressure in the fluid and the normal stresses developed due to shear. Following the convention adopted that pressure forces are compressive and therefore negative, we may write the total stresses as

$$\sigma_{11} = -p + \tau_{11} \tag{3.2-14}$$

$$\sigma_{22} = -p + \tau_{22} \tag{3.2-15}$$

$$\sigma_{33} = -p + \tau_{33} \tag{3.2-16}$$

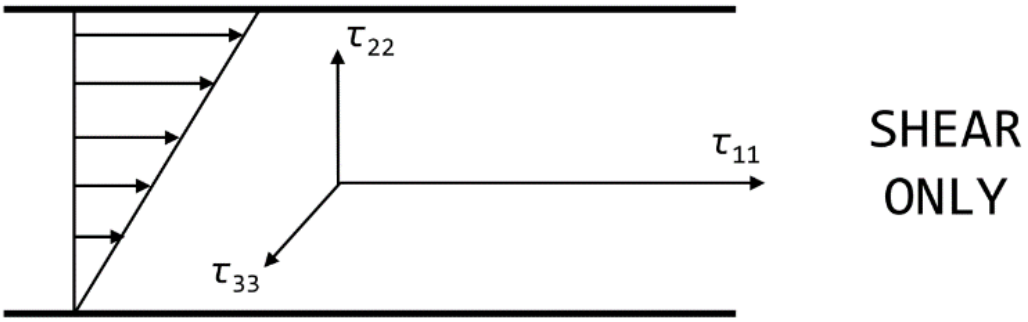

τ_{11}-τ_{22}=N_1 (first NORMAL stress Diff.)

τ_{22}-τ_{33}=N_2 (second NORMAL stress Diff.)

Figure 3.2-4. Simple shear flow of a polymeric liquid between two flat parallel plates.

Measurements of σ_{11}, σ_{22} and σ_{33} will not be useful in assessing the elasticity level of the fluid because the pressure p can be set arbitrarily from an external source (e.g. pump). To eliminate the contribution of pressure we take the differences

$$N_1 = \sigma_{11} - \sigma_{22} = (-p + \tau_{11}) - (-p + \tau_{22}) = \tau_{11} - \tau_{22} \quad \textit{First normal stress difference} \tag{3.2-17}$$

$$N_2 = \sigma_{22} - \sigma_{33} = (-p + \tau_{22}) - (-p + \tau_{33}) = \tau_{22} - \tau_{33} \quad \textit{Second normal stress difference} \tag{3.2-18}$$

The first normal stress difference can be measured directly with a cone–and–plate instrument, which is also known as the Weissenberg rheogoniometer (see sketch in Fig. 3.2-5). As the cone turns the tendency to climb up the rotating shaft is converted in a normal force N_F which can be measured by a suitable mechanical or electronic device.

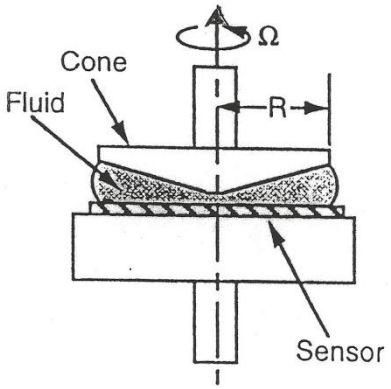

Figure 3.2-5. Cone-and-plate instrument (also known as Weissenberg rheogoniometer).

From flow analysis of the cone-and-plate instrument, it turns out that the first normal stress difference is

$$N_1 = \tau_{11} - \tau_{22} = \frac{2N_F}{\pi R^2} \tag{3.2-19}$$

The second normal stress difference is much more difficult to measure. For different measurement methods the reader is referred to Tanner (2000) and Macosko (1994). Up to the mid 1960's it was thought that N_2=0. More recent measurements showed that N_2 is negative and approximately 10–20% of the magnitude of N_1 (see also Chapter 5).

The normal stress differences are functions of the shear rate and there are sometimes expressed in terms of the so–called **normal stress coefficients** which are defined as follows

$$\Psi_{12}(\dot{\gamma}) = \frac{N_1}{\dot{\gamma}^2} = \frac{\tau_{11} - \tau_{22}}{\dot{\gamma}^2} \tag{3.2-20}$$

$$\Psi_{23}(\dot{\gamma}) = \frac{N_2}{\dot{\gamma}^2} = \frac{\tau_{22} - \tau_{33}}{\dot{\gamma}^2} \tag{3.2-21}$$

The above definitions are analogous to the definition of apparent viscosity coefficient

$$\eta = \frac{\tau_{12}}{\dot{\gamma}} \tag{3.2-22}$$

The square of the shear rate in Eq. 3.2-20 and 3.2-21 is due to experimental evidence that at very low values of $\dot{\gamma}$ the normal stress differences are proportional to $\dot{\gamma}^2$.

For molten polymers the first normal stress difference obeys expressions in the form

$$N_1 = A{\tau_{12}}^b \tag{3.2-23}$$

Usually b is less than 2 (see Section 3.8 on extrudate swell).

Under usual processing conditions, for the fabrication of plastic parts by extruding a molten polymer through a die, the shear stress is likely to be $\tau_{12} = 10^5$ Pa. Using the above

equation, we get approximately $N_1 \approx 7\times10^5$ i.e. under customary processing conditions the first normal stress difference is much larger than the shear stress.

3.3 Extensional (Elongational) Viscosity

We consider the uniaxial stretching of a cylinder of fluid as shown in Fig. 3.3-1. Of course, stretching of a liquid like water is difficult to visualize. However, molten polymers have considerable *melt strength* (see Chapter 5) and can be stretched a lot without breaking. In fact, this property enables the production of synthetic fibers for fabrics, clothing, ropes, and other products.

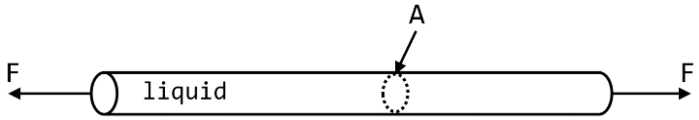

Figure 3.3-1. Stretching of a conceptual liquid cylinder.

As the cylinder is elongated in the *x*–direction it will contract in the *y*– and *z*–directions. If the stretch rate is

$$\frac{\partial V_x}{\partial x} = \dot{\varepsilon} \tag{3.3-1}$$

then the contraction in the other two directions will be

$$\frac{\partial V_y}{\partial y} = \frac{\partial V_z}{\partial z} = -\frac{1}{2}\dot{\varepsilon} \tag{3.3-2}$$

so that the equation of continuity will be satisfied ($\nabla \cdot \mathrm{V} = 0$)

$$\frac{\partial V_x}{\partial x} + \frac{\partial V_y}{\partial y} + \frac{\partial V_z}{\partial z} = 0 \tag{3.3-3}$$

$$\dot{\varepsilon} - \frac{1}{2}\dot{\varepsilon} - \frac{1}{2}\dot{\varepsilon} = 0 \tag{3.3-4}$$

The stretch (or elongation or extension) rate for a rod of length L that is stretched at a velocity V is

$$\dot{\varepsilon} = \frac{\partial V_x}{\partial x} = \frac{V}{L} = \frac{1}{L}\frac{dL}{dt} \tag{3.3-5}$$

In a manner analogous to the definition of shear viscosity we define the extensional (elongational) viscosity as the ratio of the stretching stress to the stretch rate

$$\eta_e = \frac{\sigma_{11}}{\dot{\varepsilon}} = \frac{F/A}{\dot{\varepsilon}} \tag{3.3-6}$$

where F is the force normal to the cross–sectional area A of the cylinder. The (ordinary) shear viscosity η represents the resistance to shearing. The elongational viscosity represents resistance to extension (stretching). Since both quantities represent resistance to flow (shearing in one case and stretching in the other), a question that might be asked is how η and η_e are related.

Starting from the Newtonian constitutive equation (Vlachopoulos, 2016) we have for the total stress tensor

$$\sigma_{ij} = -p\delta_{ij} + \tau_{ij} \tag{3.3-7}$$

where p is the pressure, δ_{ij} the Kronecker delta and τ_{ij} the viscous stress tensor. Alternatively

$$\sigma_{ij} = -p\delta_{ij} + 2\eta e_{ij} \tag{3.3-8}$$

where $e_{ij} = \frac{1}{2}\left(\frac{\partial V_i}{\partial x_j} + \frac{\partial V_j}{\partial x_i}\right)$ which gives

$$\sigma_{11} = -p + 2\eta\frac{\partial V_x}{\partial x} \tag{3.3-9}$$

$$\sigma_{22} = -p + 2\eta\frac{\partial V_y}{\partial y} \tag{3.3-10}$$

$$\sigma_{33} = -p + 2\eta\frac{\partial V_z}{\partial z} \tag{3.3-11}$$

Summing up we get

$$\sigma_{11} + \sigma_{22} + \sigma_{33} = -3p + 2\eta\left(\frac{\partial V_x}{\partial x} + \frac{\partial V_y}{\partial y} + \frac{\partial V_z}{\partial z}\right) \tag{3.3-12}$$

The quantity in the parenthesis is equal to zero (due to the continuity equation ($\nabla \cdot \overline{V}$) for incompressible fluids). Thus

$$p = -\frac{(\sigma_{11} + \sigma_{22} + \sigma_{33})}{3} = -\frac{\sigma_{ii}}{3} \tag{3.3-13}$$

For the uniaxial stretching experiment of Fig. 3.3-1, we have σ_{22}=0, σ_{33}=0 and from Eq. 3.3-6 and Eq. 3.3-13

$$p = -\frac{\sigma_{11}}{3} \tag{3.3-14}$$

$$\frac{2}{3}\sigma_{11} = 2\eta\frac{\partial V_x}{\partial x} = 2\eta\dot{\varepsilon} \tag{3.3-15}$$

Thus

$$\eta_e = \frac{\sigma_{11}}{\dot{\varepsilon}} = 3\eta \tag{3.3-16}$$

Therefore, the elongational viscosity is equal to three times the shear viscosity for Newtonian fluids. This is known as the Trouton relation (see Macosko (1994) historical information).

The (shear) viscosity of polymeric liquids is a function of shear rate and usually obeys, as we have seen in the previous chapter, a power–law relation in the form

$$\eta = m\dot{\gamma}^{n-1} \tag{3.3-17}$$

where usually $0.2<n<0.8$ except for a Newtonian plateau at very low–shear rates. The elongational viscosity for very low stretch rates ($\dot{\varepsilon} < 10^{-3}$) obeys the Trouton relation, exhibits a maximum and drops as a power–law function as shown in Fig. 3.3-2. This may be

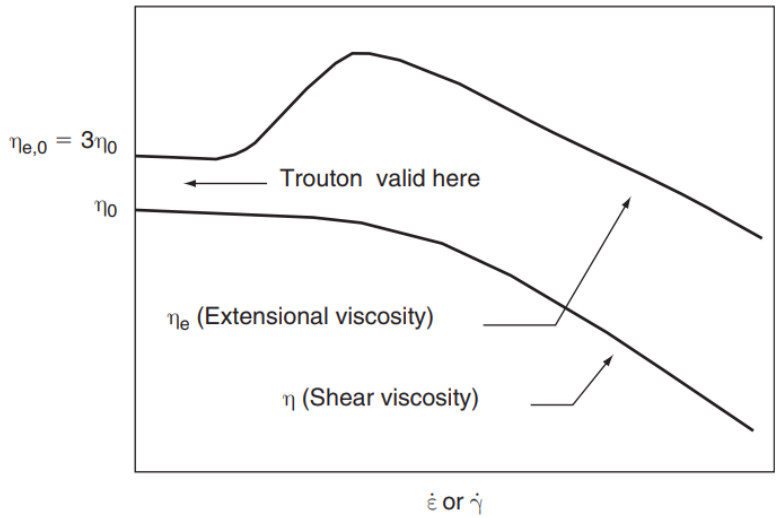

Figure 3.3-2. Extensional (elongational) viscosity η_e as a function of stretch rate and shear viscosity η as a function of shear rate.

expressed mathematically as

$$\eta_e = L\dot{\varepsilon}^q \tag{3.3-18}$$

Usually $n<q<1.0$ which means that stretch "weakening" is less prominent than shear thinning.

The elongational viscosity of polymeric liquids at high stretch rates is many times larger than the corresponding shear viscosity. It is a material property in its own sake and should be measured independently (see Chapter 5).

3.4 Flow in a Sudden Contraction

Flow from a large reservoir into a small diameter tube is encountered in practice very frequently and it is perhaps the most extensively studied problem in rheology. We consider

the axisymmetric sudden contraction problem as shown in Fig. 3.4-1. The Reynolds number is assumed to be very small (creeping flow). Therefore, fluid inertia is negligible and the flow is determined by the balance of viscous and pressure forces. Under these conditions Newtonian fluids exhibit a very small and weak vortex at the corner as shown in Fig. 3.4-1. In fact, the fluid within the vortex is so slow that led some people in the past, to believe that it was a region of stagnant fluid. On the other hand, polymeric liquids for the same low Reynolds number (e.g. $Re = 10^{-3}$–10^{-4}) as shown in Fig. 3.1-1d exhibit very large and strong vortices. The vortex size and strength depends on the elongational viscosity of polymeric liquids.

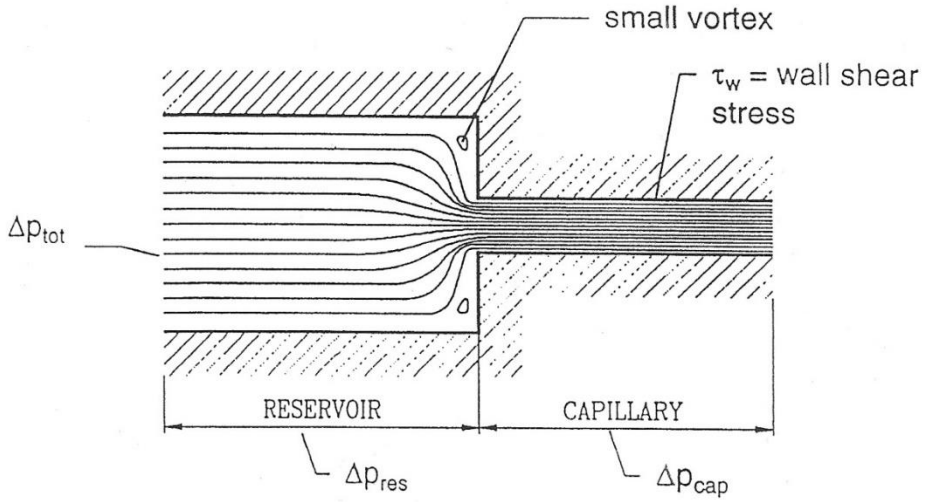

Figure 3.4-1. Newtonian entrance flow into a capillary with sketched streamlines.

Another difference between Newtonian and polymeric fluids is in the pressure drop. Within the reservoir or the small diameter outlet tube of Fig. 3.4-2 the pressure drop is linear. At the tube entry there is an additional pressure drop which is small for Newtonian fluids and large for polymer solutions or melts. The vortex, the entrance and the (relatively small) exit pressure, can be determined (Tanner, 2000, Han, 2007) by solving numerically the creeping flow equations

$$\nabla \cdot \bar{V} = 0 \tag{3.4-1}$$

$$0 = -\nabla p + \nabla \bar{\bar{\tau}} \tag{3.4-2}$$

The calculated excess pressure drop is equal to the total pressure drop minus the (linear) pressure drop in the reservoir for Poiseuille flow minus the same for the small diameter (capillary) tube (neglecting P_{exit})

$$\Delta p_e = \Delta p_{tot.} - \Delta p_{res.} - \Delta p_{cap.} \tag{3.4-3}$$

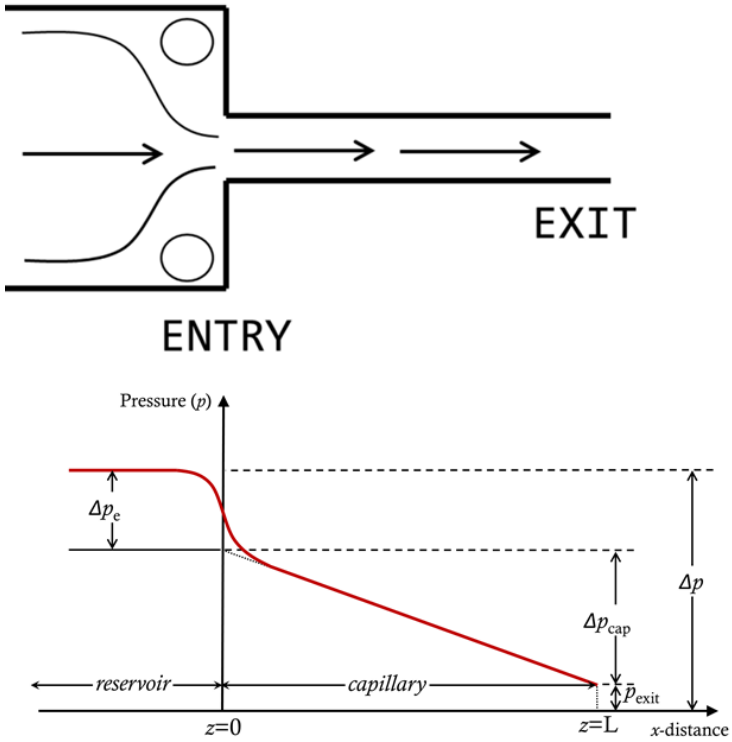

Figure 3.4-2. Polymeric liquid entrance vortex and pressure drops at entry and exit.

where $\Delta p_{tot.}$ is determined from the numerical solution of the conservation Eqs 3.4-1 and 3.4-2. $\Delta p_{res.}$ and $\Delta p_{cap.}$ are determined from the Poiseuille flow equations (see Chapter 2).

The large excess pressure drop at the entrance for polymeric liquids is apparently due to large elongational viscosities exhibited by these substances. Entry flow is mainly elongational in character. Fluid elements are stretched as they enter from a large reservoir into a small diameter tube. Obviously, this stretching is resisted by the fluid elongational viscosity, which is relatively small for Newtonian fluids (3η) and large for polymers (from 3η to more than 100η at very high stretch rates). When the elongational viscosity is very large a portion of the fluid is obstructed from entering to the capillary and a flow recirculation region (vortex), near the corners of the reservoir, is formed.

The excess pressure drop at the entry, which is also called entrance loss, is usually expressed in dimensionless form as

$$n_B = \frac{\Delta p_e}{2\tau_w} \tag{3.4-4}$$

where τ_w is the shear stress at the wall of the outlet tube and is known as the **Bagley correction** in capillary viscometry (Macosko, 1994, Han, 2007).

For Newtonian fluids accurate finite element simulations (Tanner, 2000) gives

$$n_B = \frac{\Delta p_e}{2\tau_w} = 0.587 \tag{3.4-5}$$

For polymer melts measurements usually range from the Newtonian value at low shear rates to about n_B=10. Finite element simulations of polymer melt flow in abrupt contraction is a challenging task and the reader is referred to specialized textbooks (Tanner, 2000, Han, 2007) and publications (Mitsoulis *et al.*, 2003).

3.5 Cogswell's Method for Elongational Viscosity Determination

Cogswell (1972, 1996) proposed a simple method to relate the elongational viscosity η_e to the entrance pressure drop Δp_e. He assumed that the polymer melt flows in a convergent tube (similar to a funnel), with boundaries defined by the broken lines in Fig. 3.5-1. On the boundaries Cogswell assumed that the velocity of the material is zero. Inside the convergent tube it was assumed that the flow field is a combination of simple shear and elongational flow. For each type of flows (simple shear and extensional) the pressure drop was determined separately by applying a force balance on a differential cross-section of the convergent tube

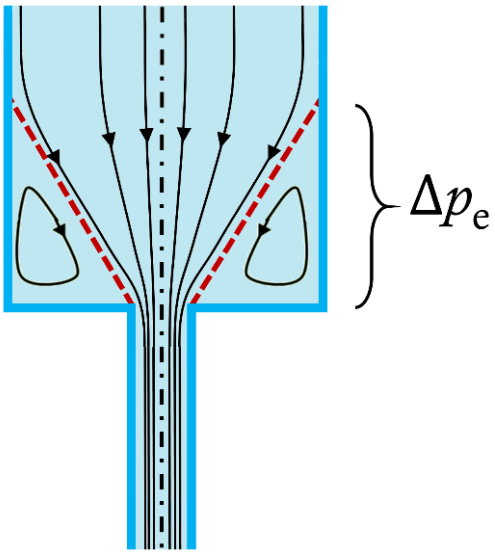

Figure 3.5-1. Schematic representation of Cogswell's idealized convergent tube in a sudden axisymmetric contraction. The excess pressure drop is developed in the convergent section.

followed by an integration over the entire section. Under the above assumptions, Cogswell determined the stretch rate

$$\dot{\varepsilon} = \frac{4\eta\dot{\gamma}_\alpha{}^2}{3(n+1)\Delta p_e} \tag{3.5-1}$$

and the corresponding value of the elongational viscosity

$$\eta_e = \frac{9}{32}\frac{[(n+1)\Delta p_e]^2}{\eta\dot{\gamma}_\alpha{}^2} \tag{3.5-2}$$

where η_e the elongational viscosity, n the power-law index, Δp_e the entrance pressure drop, $\dot{\gamma}_\alpha$ the apparent shear rate and $\eta=m\dot{\gamma}_\alpha{}^{n-1}$ the shear viscosity. Eq. 3.5-2 may be written in a more compact form by using the wall shear stress $\tau = m\dot{\gamma}_\alpha{}^n$ and performing some algebraic manipulations

$$\eta_e = \eta\left[\frac{(n+1)\Delta p_e}{1.89\tau_w}\right]^2 \tag{3.5-3}$$

Let us now examine how good is the Cogswell method for predicting the Trouton ratio η_e/η=3. In Eq. 3.5-3 we introduce n=1 and Δp_e=2×0.587×τ_w and we obtain η_e/η=1.54. Of course, this result is less accurate than we hoped. However, for n=0.5, numerical simulation (Kwag and Vlachopoulos, 1991) for a 6:1 contraction gives Δp_e=2×1.078×τ_w and thus η_e/η=2.9, which is awfully close to Trouton value of 3.0. Due the enormous difficulties for measuring elongational viscosity by stretching a strand for polymer under precisely controlled isothermal conditions, Cogswell's method is frequently used as an approximation.

Example E3.1-1

Assume a polymer with m=10,000 Pa·s^n and n=0.35. The calculated pressure drop through an L=16 mm and D=1 mm die is Δp=6.69 MPa for shear rate 818 s^{-1} and a measured total pressure drop is Δp_{total}=8.69 MPa, thus Δp_e=(Δp_{total}–$\Delta p_{capillary}$) = 2 MPa. Determine the elongational viscosity.

Solution

We start by calculating the wall shear stress

$$\tau_w = m\dot{\gamma}^n = 10000 \times 818^{0.35} = 104584\ Pa$$

Therefore, the shear viscosity will be

$$\eta = m\dot{\gamma}^{n-1} = 10000 \times 818^{0.35-1} = 128\ Pa \cdot s^n$$

The elongational viscosity can be calculated from Cogswell's formula

$$\eta_e = \eta\left[\frac{(n+1)\Delta p_e}{1.89\tau_w}\right]^2 = 128\left[\frac{(0.35+1)\times 2\times 10^6}{1.89\times 104584}\right]^2 = 23883\ Pa \cdot s$$

It is useful to calculate also the stretch rate

$$\dot{\varepsilon} = \frac{4\eta\dot{\gamma}^2}{3(n+1)\Delta p_e} = \frac{4 \times 128 \times 818^2}{3 \times (0.35+1) \times 2 \times 10^6} = 42\ s^{-1}$$

Note also the following:

At shear rate $\dot{\gamma} = 42\ s^{-1}$ the shear viscosity is $\eta = 10000 \times 42^{0.35-1} = 881\ Pa \cdot s^n$ while at stretch rate $\dot{\varepsilon} = 42\ s^{-1}$ the elognational viscosity was calculated above $\eta_e = 23883\ Pa \cdot s$, therefore

$$\frac{\eta_e}{\eta} = 27$$

3.6 The Bagley Correction of Capillary Viscometry

A typical capillary viscometer (see Fig. 2.8-1) consists of a reservoir having a diameter of about 10 mm and a capillary having diameter around 1mm and length over diameter ratio L/D=16–20. When determining the viscosity, the Rabinowitsch correction to the shear rate must be applied (Section 2.8). The shear stress can be obtained from the force exerted on the molten polymer by the piston in the reservoir. As explained, in the previous section, there is also a substantial amount of pressure drop at the entrance to the capillary. This pressure drop Δp_e must be subtracted from the total pressure (Δp_{tot}) imposed by the piston, to determine the pressure due to the capillary of length L and diameter D=2R from

$$\Delta p_{capillary} = \Delta p_{tot.} - \Delta p_e \qquad (3.6\text{-}1)$$

Modern capillary viscometers (two bore) have two pistons and two dies. The long die will be typically of L/D=16–20 and the short die of practically zero length (say L=0.3 mm). The pressure drop caused by the zero length die is simply subtracted from the total pressure, to get the $\Delta p_{capillary}$. Then, the shear stress at the wall is

$$\tau_w = \frac{\Delta p_{capillary}}{2\left(\frac{L}{R}\right)} \qquad (3.6\text{-}2)$$

The true viscosity is then calculated by dividing the above value of wall shear stress by the Rabinowitsch corrected wall shear rate.

Originally, Bagley (1957) perhaps did not believe in the existence of a zero length die (well, there is always a bit of length) and proposed a more elaborate method. He used a single bore viscometer and several dies of same diameter but with different lengths. He plotted the total pressure drop against L/R as shown in Fig. 3.6-1 and obtained the correction by adding

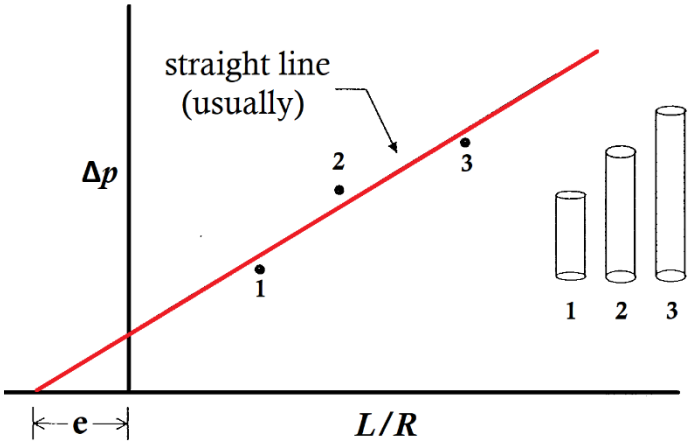

Figure 3.6-1. Schematic representation of the Bagley method to correct the wall shear stress for capillary viscosity measurements.

to the total die length at the intercept (see Fig 3.6-1) of the straight line

$$\tau_w = \frac{\Delta p_{tot.}}{2\left(\frac{L}{R} + e\right)} \tag{3.6-3}$$

The zero length die method and the Bagley method are equivalent as explained pictorially in Fig. 3.6-1. Actually, the Bagley method is a bit more accurate, and it may reveal characteristics not possible with single zero length capillary. In fact, there is at least one manufacturer/vendor of three bore capillary viscometers (Göttfert GmbH). Occasionally, the Bagley method may not produce a straight line and there is also another problem: The pressure at the exit of a long capillary is not zero for polymer melts (Han, 2007, Polychronopoulos and Papathanasiou, 2015) as shown schematically in Fig. 3.4-2. The exit pressure, is related to the first normal stress difference (Vlachopoulos and Mitsoulis, 1985). For most practical applications the Rabinowitsch and Bagley corrections are of sufficient accuracy, for determination of viscosity of polymer melts.

3.7 Constitutive Equations

To describe the flow behavior of polymer solutions and melts it is necessary to develop **constitutive equations** capable of representing not only the departure of viscosity versus shear rate from linearity (e.g. power–law) but also stress relaxation, stress overshoot, normal stresses and elongational viscosity that does not obey the Trouton relation of Newtonian fluids. This is a very challenging task beyond the scope of this book, but we will present a very

brief introduction based on a previous book chapter that we published (Vlachopoulos and Polychronopoulos, 2012).

Constitutive equations are relations between stresses and strains (deformations). In its simplest form, the Newtonian equation is a linear relation between shear stress and shear rate

$$\tau = \eta\dot{\gamma} = \eta\frac{dV_x}{dy} \tag{3.7-1}$$

This is valid for simple shear flow between two flat plates as explained earlier in this chapter and it is directly applicable to unidirectional flows. In polymer processing, however, numerous interesting flow problems require two- or three- dimensional analyses, of creeping (low Reynolds number, *Re*<<1) flows. For incompressible steady flow the mass conservation equation is

$$\nabla \cdot \bar{\nabla} = 0 \tag{3.7-2}$$

or

$$\frac{\partial V_x}{\partial x} + \frac{\partial V_y}{\partial y} + \frac{\partial V_z}{\partial z} = 0 \tag{3.7-3}$$

and the momentum equation

$$0 = -\nabla p + \nabla\bar{\bar{\tau}} \tag{3.7-4}$$

where p is the pressure (which is a scalar) and $\bar{\bar{\tau}}$ the stress, which is a (second order) tensor given by

$$\bar{\bar{\tau}} \rightarrow \begin{bmatrix} \tau_{xx} & \tau_{xy} & \tau_{xz} \\ \tau_{yx} & \tau_{yy} & \tau_{yz} \\ \tau_{zx} & \tau_{zy} & \tau_{zz} \end{bmatrix} \tag{3.7-5}$$

To generalize the Newtonian equation in 3–dimensions we must propose a linear relation between stress components and strain rate components. The strain rate tensor is

$$\bar{\bar{D}} = \frac{1}{2}(\nabla\bar{V} + \nabla\bar{V}^T) = \frac{1}{2}\left(\frac{\partial V_i}{\partial x_j} + \frac{\partial V_j}{\partial x_i}\right) \tag{3.7-6}$$

where

$$\bar{\bar{D}} \rightarrow \begin{bmatrix} D_{xx} & D_{xy} & D_{xz} \\ D_{yx} & D_{yy} & D_{yz} \\ D_{zx} & D_{zy} & D_{zz} \end{bmatrix} \tag{3.7-7}$$

and $D_{xx} = \frac{1}{2}\left(\frac{\partial V_x}{\partial x} + \frac{\partial V_x}{\partial x}\right) = \frac{\partial V_x}{\partial x}$, $D_{xy} = \frac{1}{2}\left(\frac{\partial V_x}{\partial y} + \frac{\partial V_y}{\partial x}\right)$ and similarly the other components can be written out explicitly in terms of the components in the x, y and z directions.

The Newtonian constitutive equation may then be generalized in the form

$$\bar{\bar{\tau}} = \eta\left(2\bar{\bar{D}}\right) \tag{3.7-8}$$

This means that $\tau_{xx} = \eta(2D_{xx}) = 2\eta\frac{\partial V_x}{\partial x}$, $\tau_{xy} = \eta\left(2D_{xy}\right) = \eta\left(\frac{\partial V_x}{\partial y} + \frac{\partial V_y}{\partial x}\right)$ etc.

The models expressing shear thinning behavior of polymer melts (power–law, Carreau–Yasuda and Cross) are generalized by replacing $\dot{\gamma}$ by a function of the second invariant of the strain rate tensor $2\bar{\bar{D}}$. It is called "invariant", because this quantity remains unchanged under rotation of the coordinate axes. It is given in rectangular, cylindrical and spherical coordinates in Table 2.14-1 (Section 2.14). Thus, we have the generalized power–law equation written as

$$\eta = m\left|\frac{1}{2}II\right|^{\frac{n-1}{2}} \tag{3.7-9}$$

Using the expression of the second invariant in rectangular coordinates, it can easily be shown that for simple shear flow (*x*-velocity only, varying in *y*-direction only) we have

$$\eta = m\left(\frac{\partial V_x}{\partial y}\right)^n \tag{3.7-10}$$

The above fluid model which expresses simply the shear thinning behavior is referred to as the **Generalized Newtonian Fluid (GNF)** in the rheological literature. This model cannot explain any of the viscoelastic flow phenomena, such as stress relaxation, normal stresses or extrudate swell.

As explained in Section 3.2 the simplest way to mathematically describe the dual behavior of polymers (viscous like fluids and elastic like solids) is the Maxwell equation

$$\tau + \lambda\dot{\tau} = \eta\dot{\gamma} \tag{3.7-11}$$

For the mechanical contraption of Fig. 3.2-1, the derivative of the stress term is simply with respect to time. However, if we want to use this equation to describe a flowing fluid, the stress term will be function of position and time

$$\tau = \tau(x, y, z, t) \tag{3.7-12}$$

Consequently, the substantial (material) derivative (Vlachopoulos, 2016) will be

$$\frac{D\tau}{Dt} = \frac{\partial\tau}{\partial t} + V_x\frac{\partial\tau}{\partial x} + V_y\frac{\partial\tau}{\partial y} + V_z\frac{\partial\tau}{\partial z} \tag{3.7-13}$$

There is considerable amount of mathematical literature that shows this equation must be further modified in order for the derivative to be independent of the frame of reference

(Astarita and Marrucci, 1974, Bird *et al.*, 1987, Tanner, 2000). With this modification a **Convective Maxwell Model** for 2-D flows takes the form

$$\tau_{xx} + \lambda\left[\frac{\partial \tau_{xx}}{\partial t} + V_x\frac{\partial \tau_{xx}}{\partial x} + V_y\frac{\partial \tau_{xx}}{\partial y} - 2\frac{\partial V_x}{\partial x}\tau_{xx} - 2\frac{\partial V_x}{\partial y}\tau_{yx}\right] = 2\eta\frac{\partial V_x}{\partial x} \tag{3.7-14}$$

$$\tau_{yy} + \lambda\left[\frac{\partial \tau_{yy}}{\partial t} + V_x\frac{\partial \tau_{yy}}{\partial x} + V_y\frac{\partial \tau_{yy}}{\partial y} - 2\frac{\partial V_y}{\partial x}\tau_{xy} - 2\frac{\partial V_y}{\partial y}\tau_{yy}\right] = 2\eta\frac{\partial V_y}{\partial y} \tag{3.7-15}$$

$$\tau_{xy} + \lambda\left[\frac{\partial \tau_{xy}}{\partial t} + V_x\frac{\partial \tau_{xy}}{\partial x} + V_y\frac{\partial \tau_{xy}}{\partial y} - \frac{\partial V_x}{\partial y}\tau_{yy} - \frac{\partial V_y}{\partial x}\tau_{xx}\right] = \eta\left(\frac{\partial V_x}{\partial y} + \frac{\partial V_y}{\partial x}\right) \tag{3.7-16}$$

Note that in Eq. 3.7-14 to 3.7-16, τ_{xy}=τ_{yx} (the stress tensor is symmetric). Let's see how good the above equation is in describing polymer melt flows. Let's examine the simple steady-state shear experiment of Fig. 2.1-1. We see that equations 3.7-14 to 3.7-16 become respectively

$$\tau_{xx} - 2\lambda\frac{dV_x}{dy}\tau_{yx} = 0 \tag{3.7-17}$$

$$\tau_{yy} = 0 \tag{3.7-18}$$

$$\tau_{xy} = \eta\left(\frac{dV_x}{dy}\right) \tag{3.7-19}$$

and then we have the first normal stress difference

$$\tau_{xx} - \tau_{yy} = 2\lambda\eta\left(\frac{dV_x}{dy}\right)^2 \tag{3.7-20}$$

This means that the Maxwell Model predicts a Newtonian viscosity fluid because $\tau_{xy} = \eta(dV/dy)$, which also has normal stress difference in simple shear flow $\tau_{xx} - \tau_{yy} = 2\lambda\eta\left(\frac{dV}{dy}\right)^2$. Actually, the first normal stress difference prediction is not bad, when you compare it to experimental data with polymer melts at low shear rates.

It must be noted that if we solve the 2D Maxwell equations or the corresponding axisymmetric equations for flow through a die we will obtain extrudate swell because the model predicts normal stresses.

If the flow is not steady, then the simplification of Eq. 3.7-16 for the simple shear flow experiment of Fig. 2.1-1 gives

$$\tau_{xy} + \lambda\frac{\partial \tau_{xy}}{\partial t} = \eta\frac{\partial V_x}{\partial y} \tag{3.7-21}$$

If the non-steady shear flow is suddenly brought to rest, then V_x=0 and the above equation becomes

$$\tau_{xy} + \lambda \frac{\partial \tau_{xy}}{\partial t} = 0 \tag{3.7-22}$$

This equation is identical to Eq. 3.2-8 derived for the mechanical contraption of spring and dashpot of Fig. 3.2-1, when extended and then held there. We have already shown that the stresses relax in an exponential manner. So, another good feature of the Maxwell model, is that it predicts stress relaxation.

Next, let's determine the elongational viscosity of the Convective Maxwell Model given by equations 3.7-14, 3.7-15 and 3.7-16, which is defined as

$$\eta_e = \frac{\tau_{xx} - \tau_{yy}}{\frac{dV_x}{dx}} = \frac{\tau_{xx} - \tau_{yy}}{\dot{\varepsilon}} \tag{3.7-23}$$

For steady extension in the *x*-direction and contraction in the *y*- and *z*-directions (see also Section 3.3), Eqs. 3.7-14 and 3.7-15 take respectively the following form

$$\tau_{xx} + \lambda \left[-2 \frac{\partial V_x}{\partial x} \tau_{xx} \right] = 2\eta \frac{\partial V_x}{\partial x} \tag{3.7-24}$$

$$\tau_{yy} + \lambda \left[-2 \frac{\partial V_y}{\partial y} \tau_{yy} \right] = 2\eta \frac{\partial V_y}{\partial y} \tag{3.7-25}$$

Using Eqs. 3.3-1 and 3.3-2 we may write Eqs. 3.7-24 and 3.7-25 as

$$\tau_{xx} - 2\lambda\dot{\varepsilon}\tau_{xx} = 2\eta\dot{\varepsilon} \tag{3.7-26}$$

$$\tau_{yy} + \lambda\dot{\varepsilon}\tau_{yy} = -\eta\dot{\varepsilon} \tag{3.7-27}$$

It can be easily shown that by solving Eqs. 3.7-26 and 3.7-27 with respect to τ_{xx} and τ_{yy} and substituting the results in Eq. 3.7-23, we obtain the elongational viscosity

$$\eta_e = \frac{3\eta}{(1 - 2\lambda\dot{\varepsilon})(1 + \lambda\dot{\varepsilon})} \tag{3.7-28}$$

Note that for $\dot{\varepsilon} = 0$, the model predicts the Trouton ratio η_e=3η. However, for increasing $\dot{\varepsilon}$, η_e grows in an unbounded manner. Specifically, for $\dot{\varepsilon} \to 1/2\lambda$ the elongational viscosity $\eta_e \to \infty$. In reality, η_e increases and then decreases as we have shown schematically in Fig. 3.3-2. Thus, the verdict on this version of Convective Maxwell Model is the following: Reasonable in prediction of first normal stress difference, but very bad for elongational viscosity. This means that it could be used for the study of extrudate swell, but not for entry flow problems.

Actually, the above-described 2-D version is one of the possible generalizations which satisfy mathematical invariance (the model does not depend on the system of coordinates used to describe the motion, stationary or moving with the flow field). In general, the Maxwell model is written as

$$\bar{\bar{\tau}} + \lambda \frac{\Delta \bar{\bar{\tau}}}{\Delta t} = 2\eta \bar{\bar{D}} \tag{3.7-29}$$

where the derivative Δ/Δt is referred to as the **upper convective derivative**, given by

$$\frac{\Delta \bar{\bar{\tau}}}{\Delta t} = \frac{D \bar{\bar{\tau}}}{Dt} - [\bar{\bar{\tau}} \cdot (\nabla \bar{V}) - (\nabla \bar{V})^T \cdot \bar{\bar{\tau}}] \tag{3.7-30}$$

with D/Dt the substantial (material) derivative. There is also the lower convective derivative as well as other forms (e.g. co-rotational) which are the subject of specialized handbooks (Bird et al., 1987, Astarita and Marrucci, 1974, Tanner, 2000) and numerous articles, which have been published in the *J. Rheol.*, *Rheol. Acta, J. Non-Newt. F.M.* and other journals.

There are several possible extensions and generalizations of simple models. For example, the convected Maxwell model can be written in the form

$$\bar{\bar{\tau}} + \lambda(II_D) \frac{\Delta \bar{\bar{\tau}}}{\Delta t} = 2\eta(II_D) \bar{\bar{D}} \tag{3.7-31}$$

where $\lambda(II_D)$ and $\eta(II_D)$ represent the relaxation time and the viscosity respectively, both of them functions of the second invariant of the strain rate tensor. In this form the model is known as White–Metzner. When a generalization is proposed the key criterion is to satisfy the principle of material indifference, which states that the predicted response of a material must be the same for all observers irrespective of their coordinate system of reference. As a consequence of this, in the development of constitutive equations, a coordinate system which moves, rotates and deforms with the material should be used. This requirement results in mathematically complex constitutive equations. Despite their mathematical sophistication, and the requirement of fitting numerous parameters, most viscoelastic constitutive equations fail to predict with any precision most of the unusual rheological phenomena exhibited by polymeric liquids. The most successful constitutive equation is the so–called K–BKZ integral model inspired by the theory of rubber elasticity (Astarita and Marrucci, 1974) and involves more than two dozen experimentally fitted parameters. Current trends involve the development of models based on macromolecular motions. De Gennes proposed the snake–like motion of polymer chains called reptation (Dealy and Larson, 2006, Macosko, 1994] and deduced from scaling relations that the zero shear viscosity must be $\eta_o \approx M^{3.0}$, while experiments give $\eta_o \approx M^{3.4}$ (M is the molecular weight). Based on the reptation concept, Doi and Edwards (Dealy and Larson, 2006, Macosko, 1994) developed a constitutive equation which leaves much to be desired before it can be used for predicting viscoelastic flow phenomena. Several attempts were made to fix the Doi–Edwards theory (Dealy and Larson,

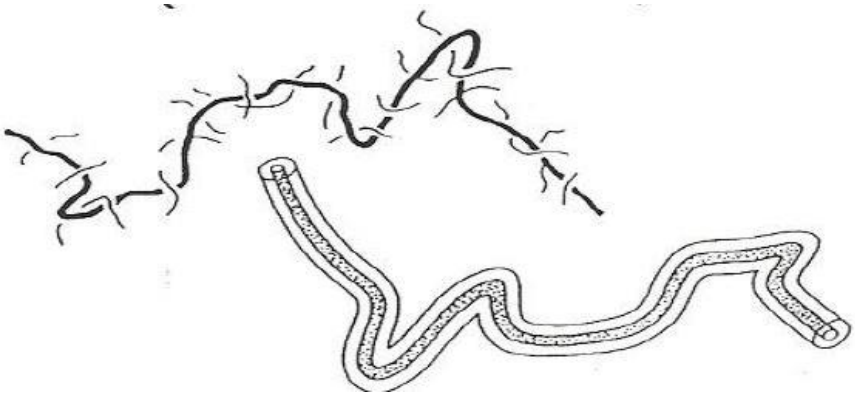

Figure 3.7-1. Schematic representation of De Gennes's conceptual snake–like motion of polymer chains, called reptation.

2006). The most talked about viscoelastic model recently, is the Pom–Pom polymer model, developed by McLeish and Larson [McLeish and Larson (1998), Dealy and Larson (2006)]. The motivation for its development was that the K – BKZ equation fails to predict the observed degree of strain hardening in planar extension when certain functions are adjusted to fit the observed degree of strain softening in shear. The failure to describe the rheology of long – branched polymers suggests that some new molecular insight is needed into the nonlinear relaxation processes, which occur in such melts under flow. The Pom – Pom model uses an H – polymer structure, in which molecules contain just two branch points of chosen functionality and a "backbone" which links the two pom – poms. The Pom – Pom model exhibits rheological behavior remarkably similar to that of branched commercial melts like LDPE. It shows strain hardening in extension and strain softening in shear. It can describe both planar and uniaxial extension. The constitutive equation is integro–differential. For successful application at least 32 parameters must be obtained by fitting experimental rheological data. Of course, fitting 32 or more parameters in a complicated constitutive equation is a mathematical challenge.

Modeling polymer viscoelastic behavior has always been a very controversial subject. While viscoelastic constitutive equations have contributed towards understanding of various deformation mechanisms and flow, they unfortunately have **not** provided us with quantitative predicting power for polymer process and equipment design. Very often the predictions depend on the model used for the computations and are not corroborated with experimental observations. Some viscoelastic problems can be solved with the appropriate viscoelastic constitutive equations, but this is still an area of academic research with very limited practical applications at the moment.

For design of polymer process equipment such as extruders, dies and molds, computer simulations are carried out in 2- or 3- dimensions, using the Generalized Newtonian Fluid (GNF) model. The Carreau–Yasuda and Cross models have a clear advantage over the power–law, because they can capture the viscosity behavior from the Newtonian plateau at low shear rates to high shear regions with substantial shear thinning.

3.8 Extrudate (Die) Swell

Extrudate swell is observed whenever a molten polymer emerges from a die. In polymer extrusion through a round die the diameter of an emerging molten polymer stream is larger than the diameter of the die. This phenomenon is sometimes called the "Barus effect" (Vlachopoulos, 1981), while in industry it is usually referred to as die swell. For the case of a tube with diameter D and the extrudate with diameter d as shown in Fig. 3.8-1, the swelling ratio is simply defined as d/D.

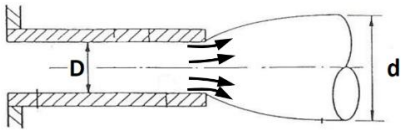

Figure 3.8-1. Schematic representation of an extrudate emerging from a round die.

Even Newtonian fluids exhibit swelling. It is 13% for cylindrical channels and 19% for 2-D slits at a very low Reynolds number. This swell is due to streamline rearrangement at the channel exit. Increasing the Reynolds number, the swelling becomes smaller and eventually a thinning of the emerging Newtonian liquid jet is observed. This is shown in Fig. 3.8-2 where d/D is plotted as a function of the Reynolds number (Re) for a capillary die. For Re=16, $d/D \approx 1$. At higher Re, but still laminar flow, a thinning of the liquid jet (d/D=0.87) is obtained from a momentum and mass balance (inside the tube the profile is parabolic and outside it is flat) as explained by Vlachopoulos (2016).

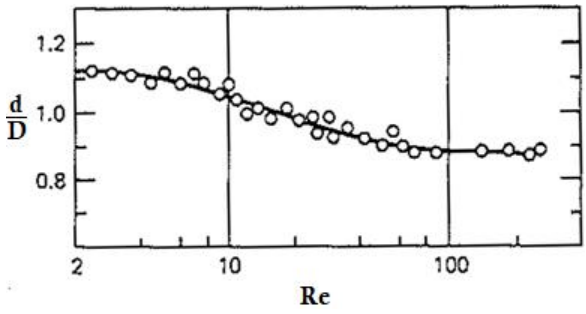

Figure 3.8-2. Experimental data on die swell versus Reynolds number for several Newtonian fluids from a long capillary into air. From Middleman (1977).

Polymers are typically extruded at a very low Reynolds number (Re=10^{-4}~10^{-2}) and they may exhibit extrudate swell ratios of up to 400% or even more, under certain conditions. This is usually attributed to the viscoelastic nature of polymers. As we saw in Section 3.2, when a viscoelastic liquid flows in a channel, shearing results in development of normal stresses. With reference to the round die of Fig. 3.8-3, the stress developed in the flow direction is τ_{zz} and normal to the flow τ_{rr}. As the polymer is sheared inside the tube, the long chains (which can be imagined as behaving like springs) are highly extended in the flow direction z and compressed in the r direction. The **first normal stress difference**, N_1=τ_{zz}-τ_{rr}, is positive and it is released as the polymer emerges from the die. The first normal stress difference release results in a contraction of the polymer chains in the flow z direction and expansion in the normal r direction. This implies a large extrudate swell (just like a release of a bunch of stretched imaginary springs).

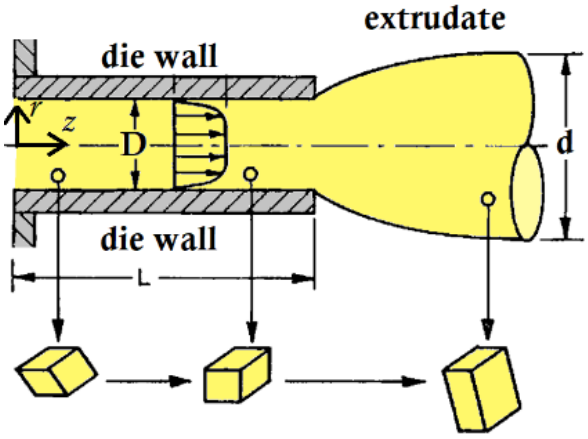

Figure 3.8-3. Schematic representation of a polymer elemental volume deformation as it emerges from a tube.

Extrudate swell is very important in extrusion due to the need to know the exact dimensions of extruded products. Consequently, numerous attempts have been made (Vlachopoulos, 1981) to determine equations for the prediction of the swell ratio from the shear stress and first normal stress difference N_1 developed in capillary (round) and slit (planar) dies. Some of these equations, stem from the theory of rubber elasticity (Treloar, 1975), under the assumption that extruded molten polymers behave as rubber-like solids. The basic idea is an imaginary stretching of the extrudate, so that it will thin back to the diameter of the capillary from which it emerged (Vlachopoulos, 1972, 1981). By replacing the required imaginary tensile force, required to produce the thinning of the extrudate, with N_1, the following equation can be obtained

$$\frac{N_1}{2\tau} = \left[(d/D)^4 + \frac{2}{(d/D)^2} - 3\right]^{1/2} \tag{3.8-1}$$

In the technical literature the left hand side of Eq. 3.8-1 is usually referred to as the recoverable shear (here, is the average), $S_R = N_1/2\tau$ with τ the shear stress. Vlachopoulos *et al.* (1972) modified Eq. 3.8-1 by assuming a parabolic velocity profile inside the capillary to arrive at

$$\frac{N_{1w}}{2\tau_w} = \sqrt{3}\left[(d/D)^4 + \frac{2}{(d/D)^2} - 3\right]^{1/2} \tag{3.8-2}$$

where the subscript "*w*" means that the respective quantities are evaluated on the capillary wall. For the case of planar extrudates, emerging from slit dies, Malkin *et al.* (1976) derived another equation, which after a minor correction becomes

$$\frac{N_{1w}}{2\tau_w} = \sqrt{5}\left[(h/H)^2 + \frac{2}{(h/H)} - 3\right]^{1/2} \tag{3.8-3}$$

where *h* the extrudate thickness and *H* the slit die gap.

Another equation for extrudate swell determination was developed by Tanner (1970) for a Maxwell-type constitutive equation of a viscoelastic fluid. It was assumed that when the material is sheared in a die, normal stresses develop, which are "released" when the die wall instantaneously "disappears" at the die exit, to end up with

$$\frac{d}{D} = 0.13 + \left[1 + \frac{1}{2}\left(\frac{N_{1w}}{2\tau_w}\right)^2\right]^{1/6} \tag{3.8-4}$$

for round extrudates. The value of 0.13 was added by Tanner to account for the Newtonian swell. Tanner's theory for planar extrudates, predicts

$$\frac{d}{D} = 0.19 + \left[1 + \frac{1}{5}\left(\frac{N_{1w}}{2\tau_w}\right)^2\right]^{1/4} \tag{3.8-5}$$

where 0.19 accounts for the Newtonian swell. Several years later, Tanner (2005) revised Eq. 3.8-4 and Eq. 3.8-5 assuming the first normal stress difference obeys

$$N_1 = k\tau^m \tag{3.8-6}$$

(rather than the original assumption $N_1 = const \cdot \tau^2$) and obtained, for round extrudates

$$\frac{d}{D} = 0.13 + \left[1 + \left(\frac{4-m}{m+2}\right)\left(\frac{N_{1w}}{2\tau_w}\right)^2\right]^{1/6} \tag{3.8-7}$$

and for planar extrudates

$$\frac{d}{D} = 0.19 + \left[1 + \left(\frac{3-m}{m+1}\right)\left(\frac{N_{1w}}{2\tau_w}\right)^2\right]^{1/4} \tag{3.8-8}$$

where for m=2 the equations reduce to Eq. 3.8-4 and 3.8-5 respectively. Comparison of Eq. 3.8-2 with Eq. 3.8-3 (or Eq. 3.8-4 with Eq. 3.8-5), shows that for the same $N_{1w}/2\tau_w$, the extrudate of planar dies exceeds that of capillary dies. With planar dies, swelling occurs only in one dimension (y, where x is the flow direction), while in capillaries in two dimensions ($r(x,y)$, with z being the flow direction axis). This is of considerable importance in extrusion of profiles. For example, for a "keyhole" die, like than shown in Fig 3.8-4, it is difficult to determine the exact dimensions of the extruded profile, because one part emerges from a round die and another from a planar one. The swelling at the corners is another challenging problem.

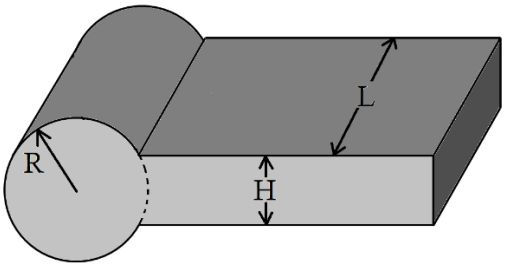

Figure 3.8-4. Schematic representation of a so-called "keyhole" die. *R* the radius of the round part, *H* the thickness of the rectangular one and *L* the length.

In the previous discussion on extrudate swell, it was assumed that the dies are long enough to avoid any influence of the entrance. A question that naturally arises, is, what happens if the length of the channel through which a molten polymer flows is short, as for instance through an orifice die $L/D \approx 0$. Experiments have shown that as $L/D \rightarrow 0$, the swelling increases for same mass flow rate, as shown schematically in Fig. 3.8-5. It is generally

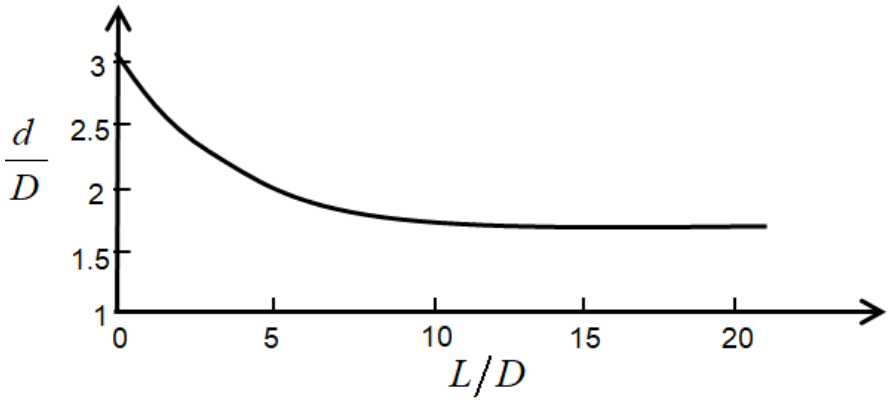

Figure 3.8-5. Schematic representation of swelling as a function of the L/D ratio (die length/die diameter) for same flow rate. Swelling reaches an asymptotic value.

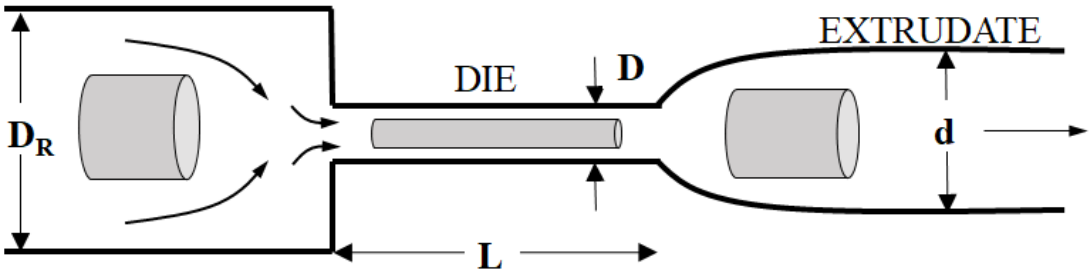

Figure 3.8-6. Schematic representation of the memory of entrance that applies only for short dies. The cylinder corresponds to a conceptual fluid volume.

believed, that this behavior is due to **memory of entrance**. This may be explained in the following simple way: If we assume an imaginary fluid cylinder in the reservoir as shown in Fig. 3.8-6, the cylinder is stretched and thins as it is forced through the die, so when it comes out it swells. For long dies, the memory of entrance fades away (essentially the cylinder "forgets" the state it was in the reservoir) and the swelling is due only to the release of normal stresses at the exit. Further lengthening of the die does not affect the extrudate swell and an asymptotic value is reached as shown in Fig. 3.8-5. Therefore, for short dies, swelling is a combination of two mechanisms: memory of entrance *and* release of normal stresses at the exit. A short die for PS would be roughly $L/D<15$ and for LDPE perhaps $L/D<30$. The reason is that LDPE (branched) is generally more elastic than PS (linear) and it takes longer for the stresses to relax. It should be noted, that the previous simple models (rubber elasticity, Tanner) for determination of extrudate swell, apply only for long dies, that is, only to the asymptotic region of Fig. 3.8-5.

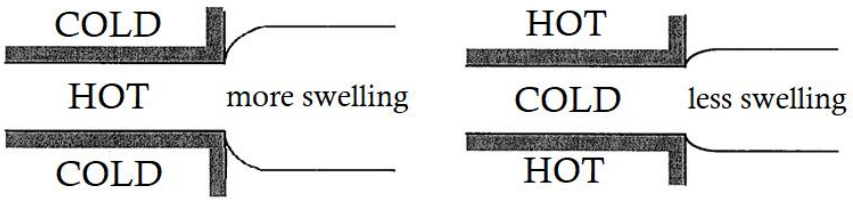

Figure 3.8-7. Schematic representation of thermal swelling.

Thermal effects may also contribute to the extrudate swell. If the walls of a die are colder than the polymer melt flowing through, as shown in Fig. 3.8-7, the viscosity near the wall will be higher than in the center. Therefore, the fluid is "restrained" as it comes out of the die and the swelling is increased. The opposite occurs, if the die is hotter than the polymer melt flowing through. In this case, the viscosity near the wall is lower than the viscosity at the center. This facilitates the flow and the resulting swelling is decreased as shown schematically

in Fig. 3.8-7. Extrudates, in general, may swell up to perhaps 15%, due to thermal effects. It can be easily calculated with numerical analysis methods [(Vlcek and Vlachopoulos (1989)]. Swelling from annular dies is important in pipe extrusion, film blowing and blow molding. In blow molding, a tube, called the parison, is extruded and subsequently, by gas pressure from the inside, the extrudate wall is blown against the mold walls for the formation of bottle-shaped products. As the polymer emerges from the extrusion die, a swelling in thickness and at the same time an increase in the diameter is observed as shown in Fig. 3.8-8, before any gas pressure is applied. The swelling may be followed by sagging or draw-down (due to the extruded material weight), which induces an opposite change in the dimensions: thinning of the thickness and decrease of the diameter. The ratio h/H is referred to as thickness swell and the ratio d/D as the diameter swell. In blow molding technology the term "weight swell" is used to indicate the ratio of the weight of a given length of the extruded parison to

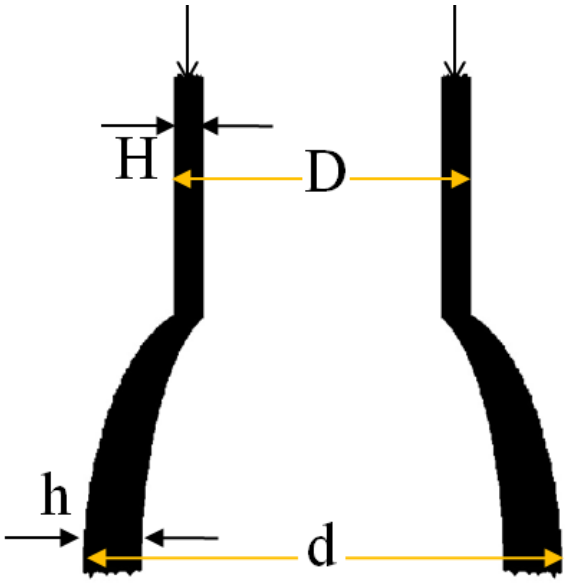

Figure 3.8-8. Schematic representation of swell from an annular die. H is the thickness of the annulus with outer diameter D, and h the thickness of the swelled extrudate with larger outer diameter d.

the weight of the same length of a parison having the same inner and outer diameters as the die. These swell parameters determine the quality and the cost of extrusion blow molded products. Determination of swelling from annular dies used in blow molding, where the thickness is usually relatively small compared to the diameter, is difficult. The shear history imposed by straight, converging or diverging channels is different for each one of the flow geometries shown in Fig 3.8-9. Extrusion blow molded products include small bottles and large fuel tanks, for cars and other vehicles.

Extrudate swell is also encountered in film casting (with flat dies), for the production of thin sheets or tapes and in melt spinning (round dies or dies of various shapes) for fiber production. Upon emergence from the die, the swelled polymer is subsequently drawn by a chilled roll (or a pair of rolls) to form final products with dimensions usually lower than the die dimensions. The process of film casting is shown schematically in Fig. 3.8-10.

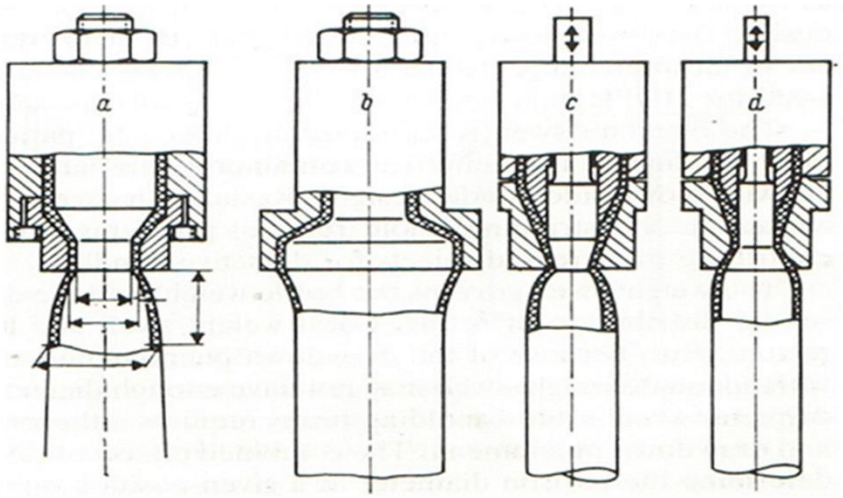

Figure 3.8-9. Various types of extrusion blow molding dies. From a Hoechst technical guide.

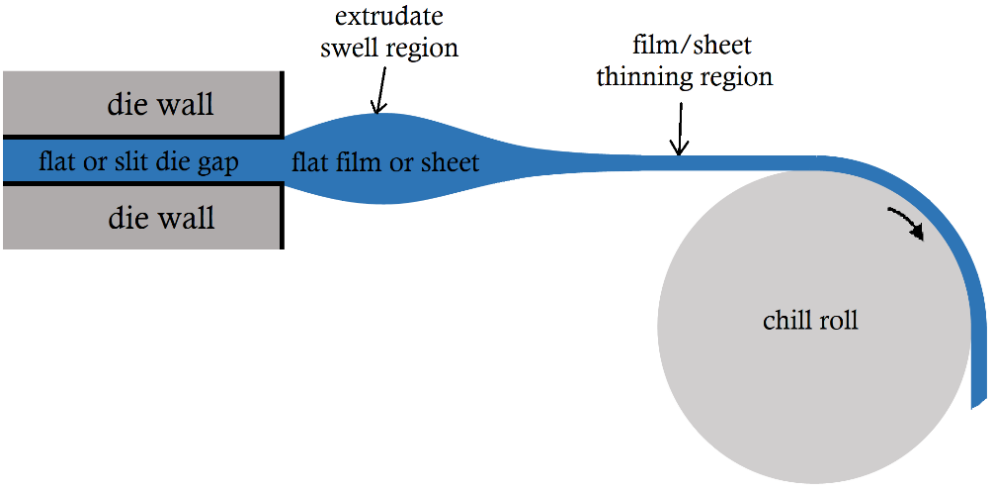

Figure 3.8-10. Schematic representation of the film casting process. The film, after emergence of the die swells and afterwards thins out due to the rolling action of the chilled cylinder. (Figure not to scale).

In film casting, the final sheet is thicker at the lateral sides than at the center. This is called edge beading that will not be discussed here. Clearly, the flow history of the material changes a lot during these processes (similarly to blow molding), especially if the die is relatively short and memory of entrance phenomena come into play. It has been shown experimentally and computationally (mostly 2D numerical simulations with viscoelastic models for long dies),

that small increase of the drawing speed results in a rapid decrease of the swell (Polychronopoulos and Papathanasiou, 2015).

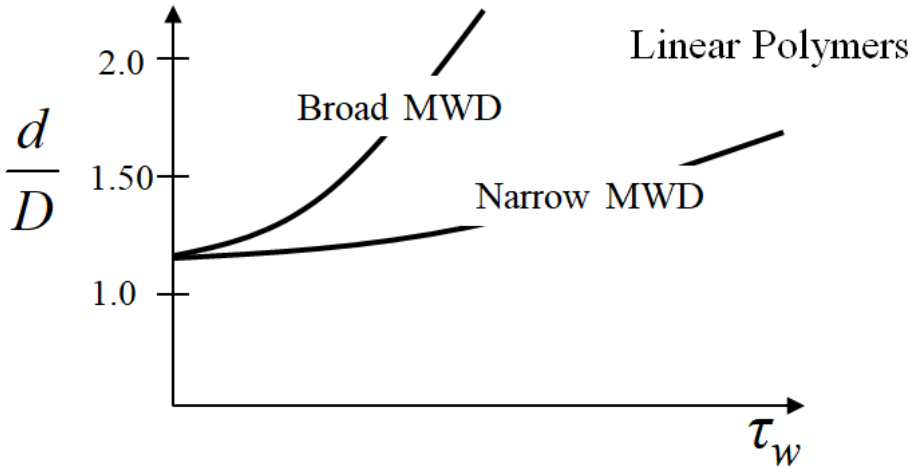

Figure 3.8-11. Effect of MWD on extrudate swell for linear polymers. A broad MWD means that the polymer has a few, but very long chains.

The molecular structure of the polymer has a large effect on extrudate swell. The first normal stress difference (N_1) released at the exit of the die, is very sensitive to the Molecular Weight Distribution (MWD). N_1 depends strongly on the M_z and M_{z+1} molecular weight averages discussed in Chapter 1 of this book. Broad MWD implies that there is a high Molecular Weight (MW) tail (i.e. there are some very long polymer chains) and high values

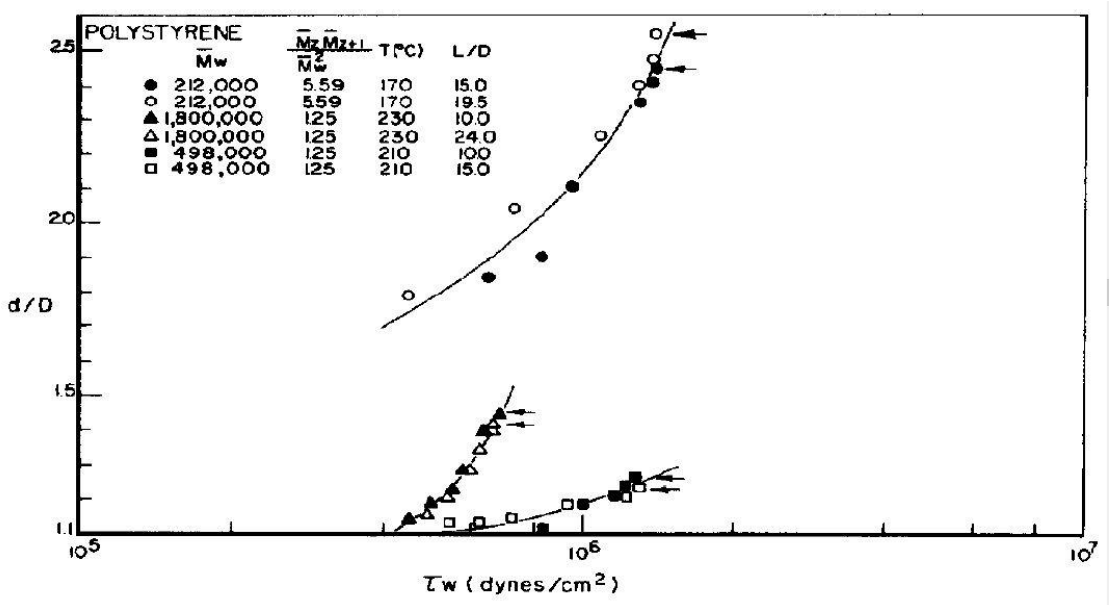

Figure 3.8-12. Extrudate swell of PS for different molecular weight distributions, identified by their different M_w, M_z and M_{z+1} averages. Arrows indicate the flow instability. From Vlachopoulos *et al.*, 1972).

of M_z and M_{z+1}. Such polymers possess large first normal stress difference, which results in large swell. In Fig. 3.8-11, we show schematically the effect of MWD on extrudate swell. Some actual data for PS (Vlachopoulos *et al.*, 1972) are shown in Fig. 3.8-12. For the case of branched polymers, it has been shown that the presence of long branches (Long Chain Branching) increases the extrudate swell (Hamielec and Vlachopoulos, 1983).

In summary, the extrudate swell is the result of the following contributions: (1) Newtonian swell (13% for rod and 19% for sheet), (2) memory of entrance, for short dies (can be very large for orifice dies) (3) normal stress release at the die exit (frequently the largest) and (4) thermal effects (usually about 5~10%). It is debatable whether the individual contributions can be simply added, but we can perhaps write the following expression as a reminder of the various mechanisms, without intention of actually making any calculations

$$\frac{d}{D} \approx \left(\frac{d}{D}\right)_{Newt.} + \left(\frac{d}{D}\right)_{Mem.} + \left(\frac{d}{D}\right)_{N_1} + \left(\frac{d}{D}\right)_{thermal} \tag{3.8-9}$$

Under certain conditions the first normal stress difference can be negative (liquid crystal polymers, polymers filled with carbon nanotubes). In such cases instead of swelling, a thinning of the extrudate is observed at the low *Re* values of polymer processing. This is a rather rare occurrence (Pasquali, 2004).

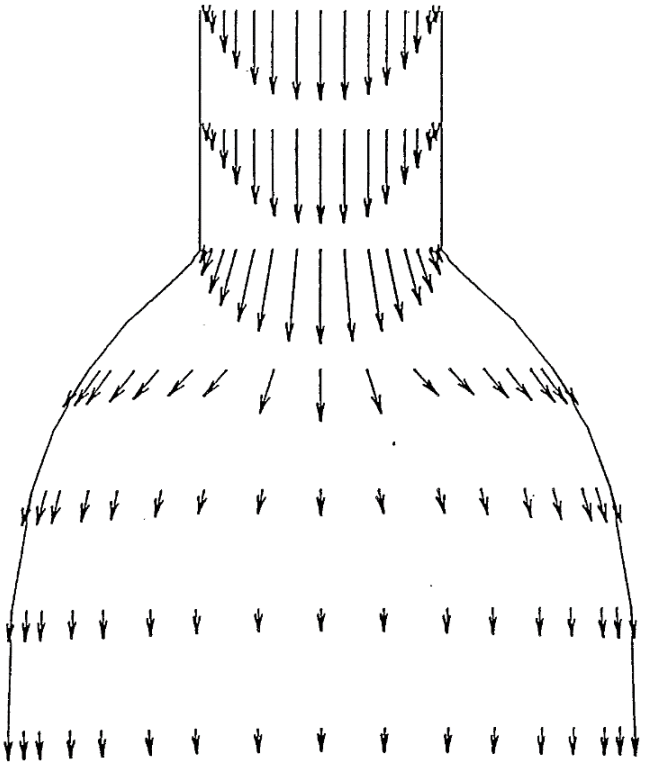

Figure 3.8-13. Numerical prediction of die swell. The arrows correspond to the predicted velocity profiles.

Numerous papers have been published in the literature describing numerical analyses of the extrudate swell problem. Comparisons with experiments have not been very successful to the degree of accuracy required in precision extrusions, but they provided an understanding of this phenomenon. In Fig. 3.8-13 the swelling and the velocity rearrangement at the exit of die is shown from some computer simulations using a commercially available software package (POLYCAD). In this software, rather than using a constitutive equation, the first normal stress difference is introduced in the form $N_1 = A\tau^b$. Despite the oversimplification, the velocity vectors are fully in agreement with theoretical considerations on how a nearly parabolic profile inside the die becomes flat at a certain distance from the exit. For more rigorous approaches see Ganvir *et al.* (2011) and Robertson *et al.* (2017).

Example E3.8-1

Experiments using rotational rheometer, have shown that for polystyrenes the first normal stress difference obeys the following relation

$$N_1 = 3.47 \times 10^{-3} {\tau_w}^{1.66}$$

Using a capillary rheometer, it was found that the swell ratio of this polystyrene is d/D=1.78 for $\dot{\gamma}_w = 166\ s^{-1}$ and $\tau_w = 1.069 \times 10^5\ Pa$. Determine the swell ratio from rubber elasticity and Tanner's theories and compare.

Solution

We start by calculating the first normal stress difference at the wall, from the wall shear stress obtained from the capillary rheometer

$$N_{1,w} = 3.47 \times 10^{-3} {\tau_w}^{1.66} = 3.47 \times 10^{-3} (1.069 \times 10^5\ )^{1.66} = 7.73 \times 10^5\ Pa$$

- From rubber elasticity (Eq. 3.X)

$$\frac{7.73 \times 10^5}{2 \times 1.069 \times 10^5} = \sqrt{3}\left[(d/D)^4 + \frac{2}{(d/D)^2} - 3\right]^{1/2}$$

It turns out, after manipulations, that the above equation is a cubic polynomial if we set $(d/D)^2 = A$

$$A^3 - 7.3573A + 2 = 0$$

which can be easily solved using a symbolic package. Here, we use MuPad (embedded in Matlab) for the algebraic solution. The solution has three values: a negative (non physical) and a value less than unity which suggests that the extrudate thins (non-physical). The third one gives A≅ 2.5646. Therefore

$$\left(\frac{d}{D}\right)_{rub.elas.} = \sqrt{A} \cong 1.6$$

By taking into account, the 13% of Newtonian swell we may write

$$\left(\frac{d}{D}\right)_{rub.elas.} \cong 1.6 + 0.13 = 1.73$$

which is remarkably close to the measured swell ratio (d/D) of 1.78.

- From Tanner's theory (Eq. 3.8-4)

$$\left(\frac{d}{D}\right)_{Tanner} = 0.13 + \left[1 + \frac{1}{2}\left(\frac{7.73 \times 10^5}{2 \times 1.069 \times 10^5}\right)^2\right]^{1/6} \cong 1.53$$

The predicted swell appears to underestimate the measured one.

- From Generalized Tanner's theory (Eq. 3.8-7 with m=1.66)

$$\left(\frac{d}{D}\right)_{Gen.\ Tanner} = 0.13 + \left[1 + \left(\frac{4 - 1.66}{1.66 + 2}\right)\left(\frac{7.73 \times 10^5}{2 \times 1.069 \times 10^5}\right)^2\right]^{1/6} \cong 1.58$$

The predicted swell is still lower than the experimental one. It appears that both versions of Tanner's equation underestimate the swelling, despite their rigorous theoretical basis. In contrast, the rubber elasticity theory predicts a result very close to the measured one. This is probably fortuitous. Measurement of the first normal stress difference is extremely difficult at high shear rates and the equation used above ($N_1 = const \cdot \tau^{1.66}$) based on measurements by Oda *et al.* (1978) is highly suspect, for its validity at the shear rate level where a swelling ratio of 1.78 was measured.

3.9 Melt Elasticity and Stress Relaxation

Polymer melts are composed of entangled macromolecular chains. These long chains require some time to move and rearrange themselves upon imposition of a stress. In short times they behave as elastic solids, but in long times they behave as liquids. This dual nature of solid-like (elastic) and liquid-like (viscous) behavior can easily be demonstrated by the silicone-based polymer toy of Silly Putty: One can easily form a ball of Silly Putty, which can bounce on a table like a rubber ball. However, if this bouncing ball is left undisturbed for a few hours on a table it slowly flows like a very thick syrup and spreads on the table surface. Chapter 2 of this book is entirely devoted to the viscous (inelastic) flow of polymer melts. To understand the processing of polymers, we must also investigate their elastic nature, which is exhibited at short process or experiment times. Firstly, we must determine a characteristic

time λ, such that at times $t>>\lambda$, the entangled polymer chains are able to rearrange themselves and result in liquid-like behavior of the material. In other words, we must determine the time for the stresses to relax. The relaxation time is specific for each material. It is a material property which must be taken into consideration whenever we analyze a process involving molten polymers, design equipment or produce plastic products.

Depending on chain length and macromolecular architecture, relaxation times usually range from 10^{-3}s for dilute polymer solutions to 10^{3}s for polymer melts. They are frequently in the same range as process or experiment times. For example, in blown film extrusion a thin molten polymer film emerges from annular die lips and solidifies at a short distance. The time required to travel from the die lip exit to the freeze-line is of the same order of magnitude as the relaxation time of the extruded polymer. Consequently, blown film bubble stability and film properties will be influenced by polymer elasticity and the time it takes for the stresses to relax. It is one thing to produce a film by extruding a very elastic polymer and entirely another if the extrusion involves a polymer of little elasticity.

In Section 3.2 we have introduced the dimensionless Deborah number, which is the ratio of a characteristic time for the material to a characteristic time of the process

$$De = \frac{\lambda}{\theta} = \frac{characteristic\ material\ time}{characteristic\ process\ time} \tag{3.9-1}$$

A good choice for a characteristic process time would be the residence time. It is not obvious which is the best choice of a characteristic material time, and there are plenty of possible choices.

In Section 3.2 we introduced the Maxwell model and noted that the ratio of viscosity to the modulus of elasticity η/G has dimensions of time, it is usually denoted by λ and expresses the time required for an imposed stress to relax. Let us use this relation to evaluate the relaxation time for water. At room temperature the viscosity of water is about 10^{-3} Pa·s. In the Maxwell fluid model G is the shear modulus. However, a fluid like water cannot sustain shear so we will use the bulk modulus. The bulk elastic modulus of a material determines how much it will compress under a given amount of external pressure. For water this bulk modulus is 2.2. GPa. Thus

$$\lambda = \frac{\eta}{G} = \frac{10^{-3}}{2.2 \times 10^{9}} \approx 0.5 \times 10^{-12}\ s \tag{3.9-2}$$

This means that applied stresses in water would relax instantaneously, as explained pictorially in Fig. 3.2-2b (Newtonian).

From viscosity data available to the authors for a polystyrene melt at 170 °C at shear rate $\dot{\gamma} = 10^{-3}$ s^{-1}, viscosity η=1.03×10^5 Pa·s and shear modulus G=1.03×10^2 Pa, which gives λ=10^3 s^{-1}, while at $\dot{\gamma} = 3 \times 10^2$ s^{-1} we have η=4.71×10^2 Pa·s, modulus G=1.41×10^5 Pa and λ=3.33×10^{-3} s. Since viscosity η and modulus G of polymer melts varies with both temperature and shear rate, we need a spectrum of characteristic times to describe the relaxation behavior. This matter will be dealt with in Chapter 5 of this book on rheological measurements. If we have to choose just one relaxation time we would pick its value at zero shear, which is measurable no lower than $\dot{\gamma} = 10^{-3} \sim 10^{-4}$ s^{-1}, with currently available instruments. Thus this polystyrene polymer would be characterized by two values, its zero shear viscosity η_o=1.03×10^5 Pa·s and the "longest relaxation time" λ_o=10^3 s^{-1}. Another suggestion is made in Chapter 5 on measurements. We would expect that polystyrene product properties to be influenced by both the viscous and the elastic nature of the polymer. Thus, for systematic material selection it would be meaningful to carry out experiments with different polystyrene grades and then develop correlations, like impact strength=$F(\eta_o, \lambda_o, \ldots)$, toughness= $F(\eta_o, \lambda_o, \ldots)$ and other similar ones.

From the analysis of flow of a Convected Maxwell fluid model we have obtained the relation for the first normal stress difference

$$\tau_{xx} - \tau_{yy} = 2\lambda\dot{\gamma}\tau_{xy} \tag{3.9-3}$$

thus the characteristic time related to the elastic normal stress difference is

$$\lambda = \frac{\tau_{xx} - \tau_{yy}}{2\dot{\gamma}\tau_{xy}} \tag{3.9-4}$$

This quantity represents the time for the elastic normal stress to relax. In fact, the ratio (dimensionless number)

$$S_R = \frac{\left(\tau_{xx} - \tau_{yy}\right)_w}{2\left(\tau_{xy}\right)_w} \tag{3.9-5}$$

where w denotes stress values at the channel wall, is known as the **recoverable shear**. The term "recoverable" is used because of the elastic normal stresses that are generated by the application of shear.

Another dimensionless group is the **Weissenberg number**

$$Wi = \lambda\dot{\gamma} \quad or \quad Wi = \lambda \frac{length\ scale}{velocity\ scale} \tag{3.9-6}$$

The Weissenberg number is used mostly in numerical simulations of polymer flows. Again this dimensionless number can be interpreted as the ratio of elastic to viscous forces.

It appears confusing that there are three different definitions for representing the ratio of elastic to viscous forces. We will try to clarify somewhat the situation by examining the flow inside a straight channel of circular cross-section or between two parallel flat plates, which is called **viscometric** (fluid particles on any streamline remain at same distance apart). An obvious choice for a characteristic process time would be the inverse of shear rate at wall $1/\dot{\gamma}_w$ Another obvious choice for the characteristic material time would be Eq. 3.9-4 evaluated at wall. Then the three dimensionless numbers are equal

$$De = S_R = Wi \tag{3.9-7}$$

However, this is **not always** the case. It might be preferable to chose some sort of average process time for the Deborah number and a local characteristic time in the Weissenberg number. In extrusion through a die we may want to use the residence time (can be long) as the characteristic time in the Deborah number, but at die lips the shear rate could be very high. So, we could have a small *De* and large *Wi*. Also the two definitions of *Wi* differ by the factor relating the ratio (length scale/velocity scale) to the shear rate. For flow in a tube $\dot{\gamma}_w$=8×(velocity average/diameter). These differences in definition must be kept in mind when reading the technical literature. The Weissenberg number is the preferred dimensionless parameter in viscoelastic flow simulations.

Another difference is related to the characteristic material time. Frequently, in industry the characteristic time is the parameter λ (e.g. Leal *et al.*, 2006) in the Cross or the Carreau-Yasuda or other such viscosity model (which is a curve fitting parameter of shear thinning, that has dimensions of time). This choice is not the best, because it does not appear to have a direct link to the elasticity of the polymer, but not entirely without merit. Molecular theories show that there is a link between the shear thinning behavior and elasticity (Bird *et al.* 1987). The previously defined λ by Equation 3.9-4 shows a direct link to the elasticity of the polymer, expressed by the normal stresses, and it is a much better choice. When the dimensionless groups *De* and *Wi* were first introduced in the 1960s, it was hoped that they would play a significant role for scale up purposes, similar to that of Reynolds Number (*Re*) in Newtonian fluid mechanics and Nusselt Number in heat transfer. However, due to the difficulties in

defining meaningful characteristic times for the various polymeric materials, the dimensionless groups are of very limited usefulness. In Chapter 5 on rheological measurements we discuss other measures of characteristic times. See also Denn (2008) and Dealy and Wang (2013).

Elasticity is the cause of the various (and to some extent counter-intuitive) phenomena discussed in Section 3.1. The phenomenon of extrudate swell is mainly due to stress relaxation of the first normal stress difference at the die exit, as discussed in Section 3.8 in greater detail. It is of practical importance in extrusion because it determines the final dimensions of extruded products. The second normal stress difference generates some unexpected flow patterns in flow through channels of non-circular cross-section. For polymer melt flows in

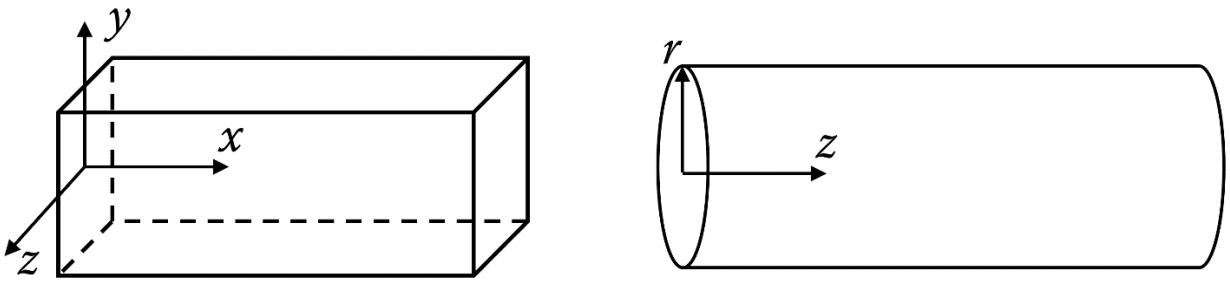

Figure 3.9-1. Coordinates in a rectangular and cylindrical channel.

straight tubes (z-axis, r-radius) we have only first normal stress difference $N_1=\tau_{zz}-\tau_{rr}$). However, for flow in the x-direction in a straight square channel as shown in Fig. 3.9-1 we have two normal stress differences

$$N_1 = \tau_{xx} - \tau_{yy} \tag{3.9-8a}$$

$$N_2 = \tau_{yy} - \tau_{zz} \tag{3.9-8b}$$

The first normal stress difference is positive (it means the fluid is extended in the direction of the flow) and the second normal stress is negative (that is compressive) and about 20% of the value of the first normal stress difference. Since the second normal stress difference is not zero there must be flow in the transverse direction. This transverse flow generates some unexpected flow patterns, as it has been demonstrated by Dooley (2002). He extruded continuous layers of colored and uncolored polystyrene through a square channel having 0.9525 cm sides and 61 cm long. Due to the transverse flow the layers which are circular at entry take the patterns shown in Fig.3.9-2a and Fig.3.9-2b. This means that rectilinear flow (having streamlines parallel to the channel walls) is only possible in the absence of second normal stress difference.

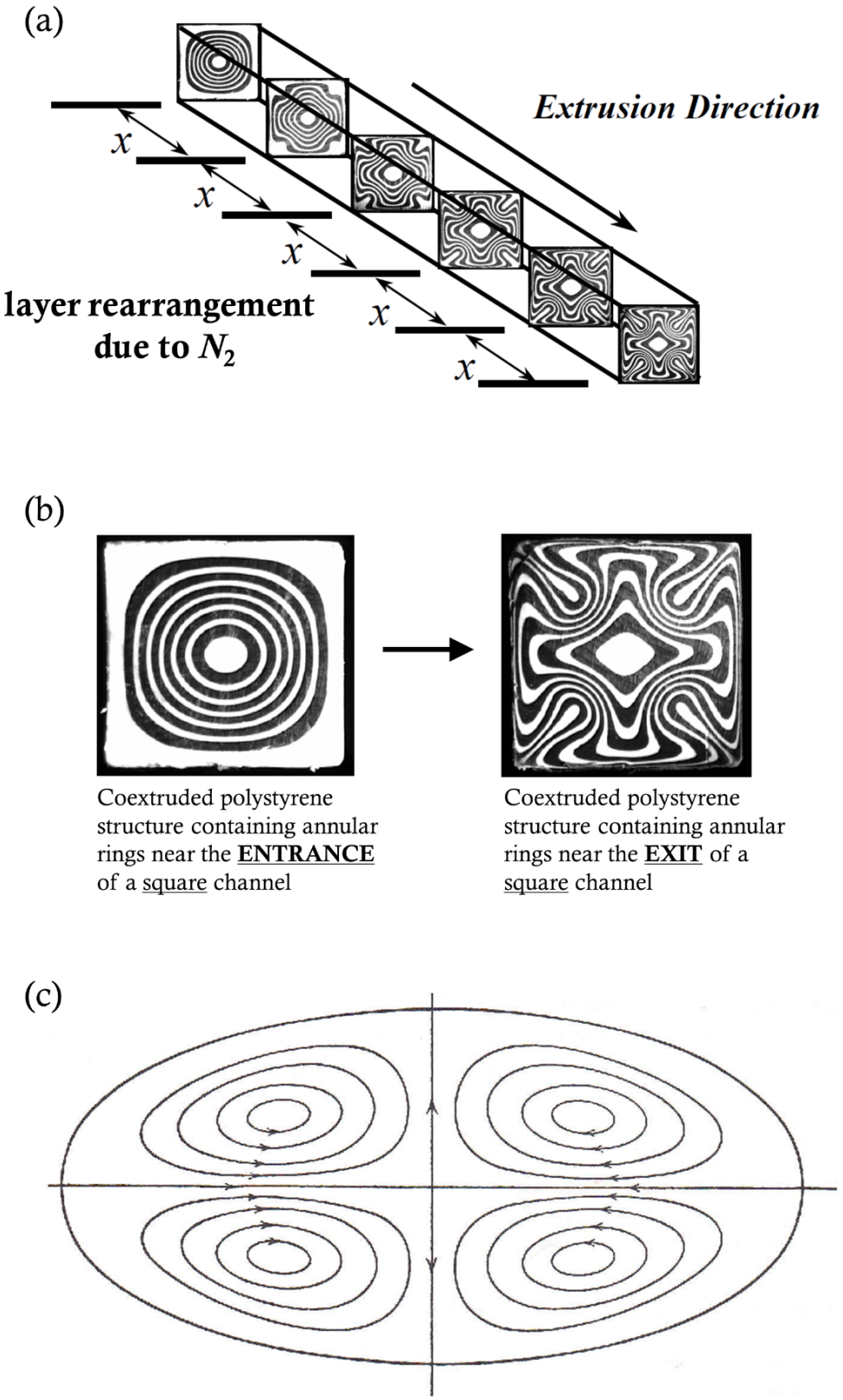

Figure 3.9-2. (a) and (b) flow rearrangement patterns of polystyrene in a square cross-section straight channel as observed by Dooley (2002). (c) secondary flow pattern of a straight channel with elliptical cross-section from Rivlin (1965).

Secondary flow in a straight channel having elliptical cross-section, as shown in Fig. 3.9-2c, has been determined by Rivlin (1965). US patent application 2013/0084355 describes *"…a melt channel wherein at least a portion of the melt channel has a noncircular cross-section for balancing shear in a melt stream of moldable material that flows therethrough. The noncircular cross-section of the melt channel portion may be, for example, capsule-shaped, extended egg-shaped, oval, teardrop-shaped, or peanut-shaped*". In all these, unusually shaped, channels polymer melt flow generates non-zero second normal stress difference, which creates transverse flow and helps in melt homogenization. An internet search at the time of writing of this book resulted in finding two manufacturers advertising the merits of oval shaped melt channels.

Another example that demonstrates the practical importance of melt elasticity is related to stress relaxation, after cessation of shearing in a parallel plate rotational rheometer, as shown in Fig. 3.9-3. Each specimen was subjected to a shear rate of 0.024 s^{-1} for 1 min,

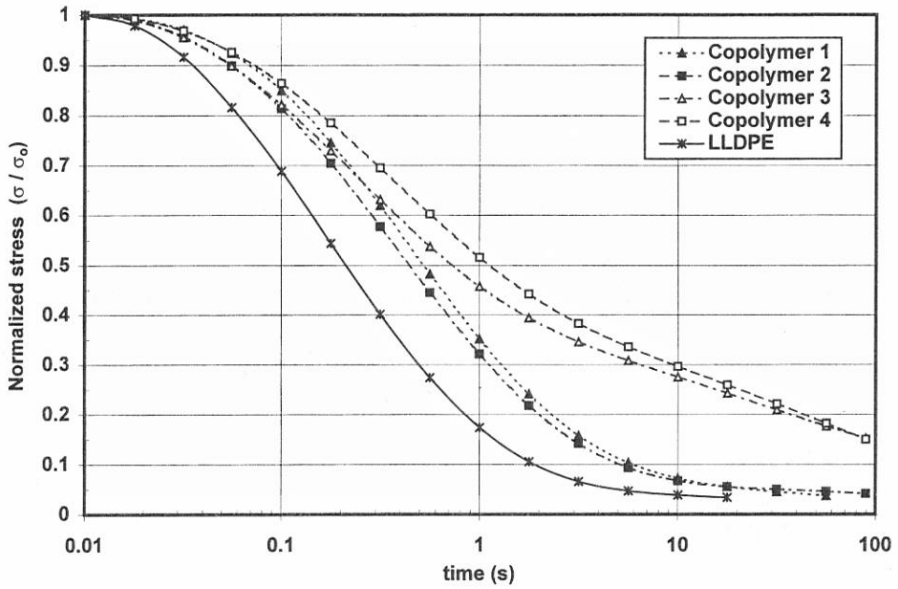

Figure 3.9-3. Stress relaxation results of different polymers at 190 °C in a parallel plate rheometer. From Kontopoulou *et al.* (1997).

then the rotation was stopped and the shear stress was recorded after the cessation of the rotational motion. We can see that for LLDPE, the shear stress relaxes to 5% in less than 10 s while copolymers 3 and 4 require more than 100 s. The differences are due to molecular structure and architecture. If these resins were used for production of plastic products by extrusion or injection molding, stresses would freeze-in during the process of cooling from perhaps 200°C or 250°C to room temperature. The level of frozen-in stresses depends on the rate of cooling. However, much higher stresses would be frozen-in in parts made by

copolymers 3 and 4 than LLDPE. Frozen-in stresses can be released upon reheating, even when plastic parts are left in a hot storage area or during transportation in a vehicle on a hot summer day. The result is warped plastic products.

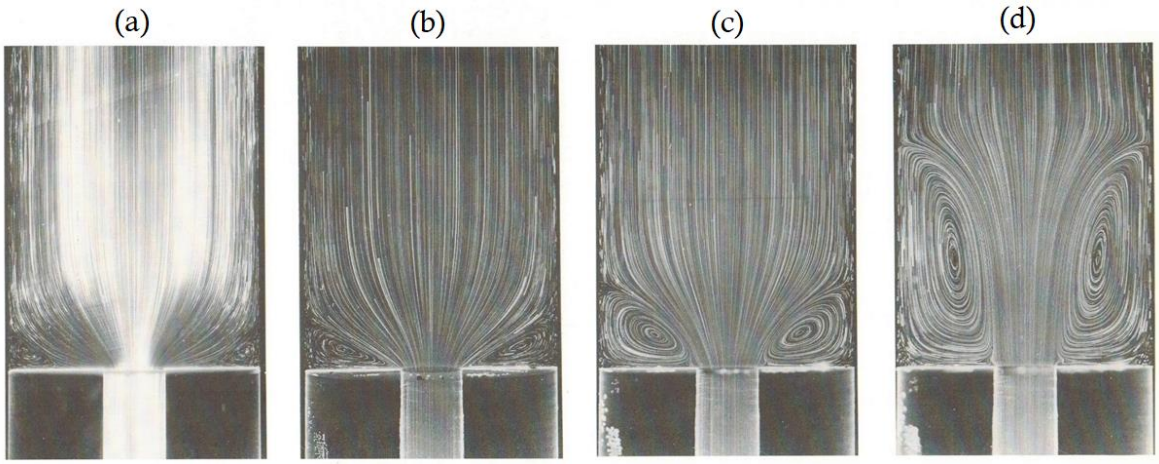

Figure 3.9-4. Streakline photographs illustrating vortex shape and vortex growth at different *Wi* numbers. (a) *Wi*=0.63, (b) *Wi*=0.96, (c) *Wi*=1.43 and (d) *Wi*=1.63. (From Boger et al 1986).

Elastisity is the cause for the growth of the vortex in Fig. 3.9-4 for 0.04% polyacrylamide in water and corn syrup solution. For *Wi*=0.63 the vortex is virtually identical to that for inelastic Newtonian creeping flow. Above *Wi*=1.63 the vortex becomes asymmetric and unstable. Experiments with polymer melts are much more difficult than polyacrylamide in water and corn syrup solutions and some pictures available in the open literature are less dramatic. LDPE melts exhibit corner vortices in entrance flows from a large reservoir to a smaller diameter tube in a 180 entrance angle, which grow with extrusion rate. PS also exhibits vortices which also grow with extrusion rate. In HDPE, PP and PVC melts the flow pattern at the entrance is virtually without vortices, similar to that of inelastic Newtonian fluids. It appears that an increasing elongational viscosity with stretch rate (LDPE, PS) creates significant elongational stresses that lead to the formation of large vortices. White (1990) suggests that both elongational viscosity behavior and normal stresses determine the flow patterns in entrance flows.

Bibliography

Astarita G. and Marrucci G., *Principles of Non-Newtonian Fluid Mechanics*, McGraw-Hill (1974)

Bird R.B., Armstrong R.C. and Hassager O., *Dynamics of Polymeric Liquids. Vol 1, 2nd Ed: Fluid Mechanics*, John Wiley and Sons (1987)

Bagley E.B., End Corrections in the Capillary Flow of Polyethylene, J. Appl. Phys., 28 (5), 624 (1957)

Boger D.V., Hur D.U. and Binnington R.J., Further Observations of Elastic Effects in Tubular Entry Flows, J. non-Newt. Fluid Mech., 20, 31 (1986)

Cogswell F.N., Converging Flow of Polymer Melts in Extrusion Dies, Polym. Eng. Sci., (12) 1, 64 (1092)

Cogswell F.N., *Polymer Melt Rheology*, Woodhead Publishing, Cambridge (1996)

Darby R., *Viscoelastic Fluids: An Introduction to their Properties and Behavior*, Marcel Dekker (1976)

Dealy J.M. and Larson R.G., *Structure and Rheology of Molten Polymers*, Hanser (2006)

Dealy J.M. and Wang J., *Melt Rheology and its Applications in the Plastics Industry*, 2nd Ed., Springer (2013)

Denn M.M., Just What Did Deborah Say, Rheology Bulletin, 80 (1), 12 (2011)

Denn M.M., *Polymer Melt Processing: Foundations in Fluid Mechanics and Heat Transfer*, Cambridge University Press (2008).

Dooley J., Viscoelastic Flow Effects in Multilayer Polymer Coextrusion, Phd Thesis, Eindhoven University of Technology, Eindhoven, The Netherlands (2002)

Ganvir V., Gautham B.P., Pol H., Bhamla M.S., Sclesi L., Thaokar R., Lele A. and Mackley M., Extrudate Swell of Linear and Branched Polyethylenes: ALE Simulations and Comparison with Experiments, J. non-Newt. Fluid. Mech., 166 (1-2), 12 (2011)

Göttfert,https://www.goettfert.com/products/capillary-rheometer/rheograph-25-50-75-120.html

Hamielec L.A. and Vlachopoulos J., Influence of Long Chain Branching on Extrudate Swell of Low-Density Polyethylenes, J. Appl. Polym. Sci., 28 (7), 2389 (1983)

Han C.D., *Rheology and Processing of Polymeric Materials: Volume 1 Polymer Rheology*, Oxford University Press (2007)

Kontopoulou M., Bisaria M. and Vlachopoulos J., An Experimental Study of Rotational Molding of Polypropylene/Polyethylene Copolymers, Int. Polym. Process., 12 (2), 165 (1997)

Kwag C. and Vlachopoulos J., An Assessment of Cogswell's Method for Measurement of Extensional Viscosity, Polym. Eng. Sci., 31 (14), 1015 (1991)

Leal V., Lafuente P., Alicante R., Pérez R. and Santamaria A., New Results on the Correlation Molecular Architecture-Melt Elasticity-Blowing Process-Film Properties for Conventional and Metallocene Catalyzed Polyethylenes, Macromol. Mater. Eng., 291, 670 (2006)

Macosko C.W., *Rheology: Principles, Measurements and Applications*, VCH Publishers (1994)

Malkin A.Ya., Goncharenko, V. V. and Malinovski, V.V. Barus Effects in Polymer Flows through Cylindrical and Flat Dies, Mekhanika Polimerov, 3, 487 (1976)

McLeish T.C.B. and Larson R.G., Molecular Constitutive Equations for a Class of Branched Polymers: The Pom-Pom Polymer, J. Rheol., 42 (1), 81 (1998)

Middleman S., *Fundamentals of Polymer Processing*, McGraw-Hill (1977)

Mitsoulis E. and Vlachopoulos J., A Numerical Study on the Effect of Normal Stresses and Elongational Viscosity on Entry Vortex Growth and Extrudate Swell, Polym. Eng. Sci., 25 (11), 677 (1985)

Mitsoulis E., Schwetz M. and Münstedt H., Entry Flow of LDPE Melts in a Planar Contraction, J. non-Newt. Fluid Mech., 111 (1), 41 (2003)

Münstedt H., *Elastic Behavior of Polymer Melts*, Hanser (2019)

Oda K., White J.L. and Clark E.S., Correlation of Normal Stresses in Polystyrene Melts and its Implications, Polym. Eng. Sci., 18 (1), 25 (1978)

Pasquali M., Swell Properties and Swift Processing, Nature Materials, 3, 509 (2004)

Polychronopoulos N.D. and Papathanasiou T.D., A Study on the Effect of Drawing on Extrudate Swell in Film Casting, Appl. Rheol., 25, 42425 (2015)

POLYCAD Software, Polydynamics inc, Dundas, ON, Canada. Description available in Chapter 4, K.T. O'Brien, *Computer Modeling for Extrusion and Other Continuous Polymer Processes*, Hanser (1992)

Rivlin R.S., Chapter 5 in *Research Frontiers in Fluid Dynamics*, Seeger R.J. and Temple G. (eds), Wiley (1965)

Robertson B., Thompson R.L., McLeish T.C.B. and Ian Robinson, Theoretical Prediction and Experimental Measurement of Isothermal Extrudate Swell of Monodisperse and Bidisperse Polystyrenes, J. Rheol., 61 (5), 931 (2017)

Tanner R.I., *Engineering Rheology*, 2nd Edition, Oxford Engineering Science (2000)

Tanner R.I., A Theory of Die-Swell, J. Polym. Sci. B., 8 (12), 2067 (1970)

Tanner R.I., A Theory of Die-Swell Revisited, J. non-Newt. Fluid Mech. 129 (2), 85 (2005)

Treloar L.R.G., The Physics of Rubber Elasticity, Oxford University Press (1975)

Vlachopoulos J., Horie M. and Lidorikis S., An Evaluation of Expressions Predicting Die Swell, J. Rheol., 16 (4), 669 (1972)

Vlachopoulos J., Extrudate Swell in Polymers, J. Rev. Def. Beh. Mat., 3, 219 (1981)

Vlachopoulos J. and Polychronopoulos N., Basic Concepts in Polymer Melt Rheology and Their Importance in Processing, in*: Applied Polymer Rheology: Polymeric Fluids with Industrial Applications*, Kontopoulou M. (ed.), John Wiley & Sons (2012)

Vlachopoulos J., *Fundamentals of Fluid Mechanics*, revised internet edition, Polydynamics Inc (2016), downloadable from www.researchgate.com

Vlcek J. and Vlachopoulos J., Effect of Die Wall Cooling or Heating on Extrudate Swell, Polym. Eng. Sci., 29 (10), 685 (1989)

White J.L., *Principles of Polymer Engineering Rheology*, Wiley (1990)

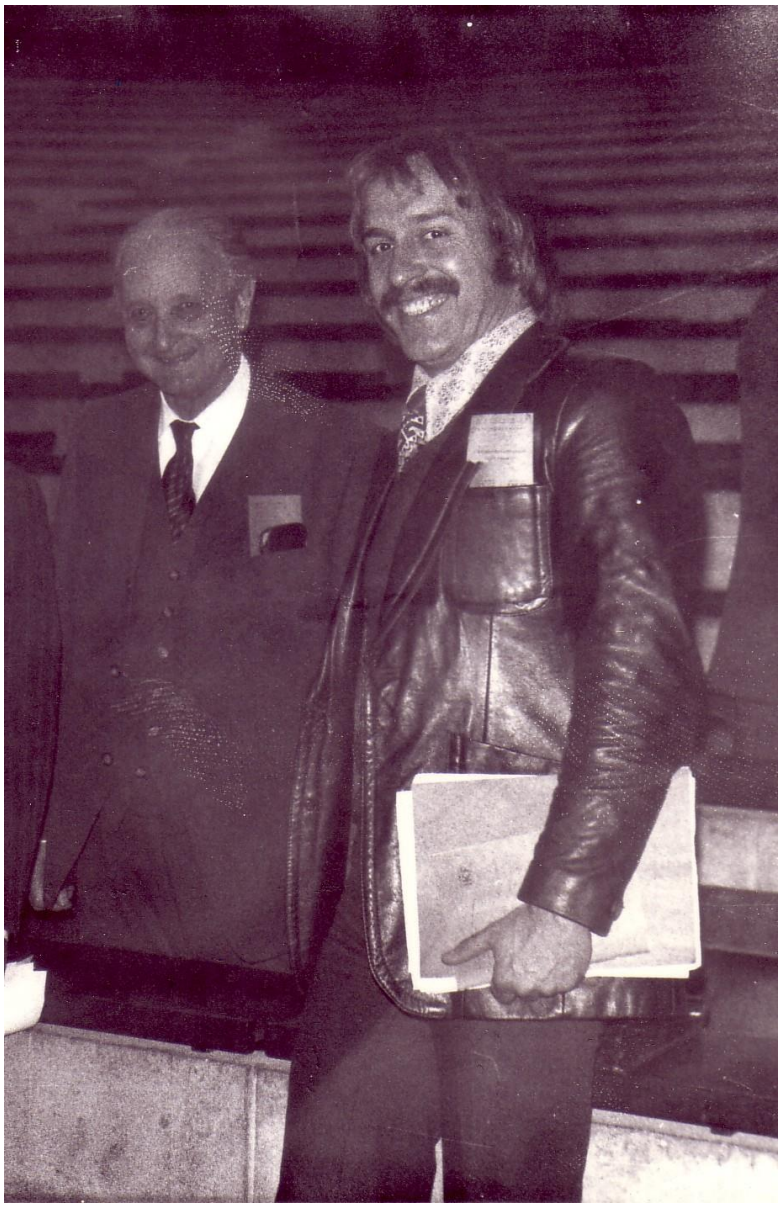

KARL WEISSENBERG (1893-1976)
and
JOHN VLACHOPOULOS
at the University of Stuttgart, Germany
in February 1975

J. Vlachopoulos and N.D. Polychronopoulos "*Understanding Rheology and Technology of Polymer Extrusion*", First Edition, Polydynamics Inc, Dundas, Ontario, Canada (2019)

Chapter 4

SHARKSKIN, MELT FRACTURE, DIE LIP BUILD UP AND SURFACE TEARING

4.1 Flow Instabilities and Extrusion Defects

In Newtonian fluid mechanics the transition from rectilinear flow (laminar) to chaotic flow (turbulent) is the most important and most frequently studied instability. It occurs at a critical Reynolds Number ($Re = density \times velocity \times diameter/viscosity$) frequently quoted as 2300 for flow in tubes. The Reynolds Number is the ratio of inertia to viscous forces. In polymer processing the Reynolds number is usually in the range of 0.01 to 0.0001 and an instability of the turbulent kind is not possible. However, instabilities do occur in polymer extrusion and they appear above a critical wall shear stress in the range of 0.1 to 0.5 MPa, which is actually the range for flow through dies in many industrial extrusion operations. The extrusion instabilities are related to wall slip and viscoelasticity, with manifestations ranging from surface irregularities to gross extrudate distortions

The most common flow instabilities are usually observed with a naked eye on the extrudate emerging from a capillary viscometer, as shown in Fig. 4.1-1. The surface irregularity and the distortions are observed at different shear rates (flow rates). At sufficiently low shear rates, the extrudate is smooth. As the shear rate is increased, a phenomenon that may appear as a loss of surface gloss or some sort of exaggerated haze is observed, commonly referred to as **sharkskin** (occasionally also called mattness). At higher shear rates, the shear stress exhibits oscillations manifested by alternating smooth and irregular sections of extrudate (usually called **s**purt). At even higher shear rates, a gross flow instability with a chaotic pattern of volume distortion occurs, known as gross **melt fracture.**

These extrusion instabilities/defects are usually investigated in conjunction with the corresponding flow curve. A flow curve is simply a plot of shear stress as a function of the apparent shear rate. The shear stress is obtained from the pressure drop and the capillary length to the radius ratio $\tau = \Delta p/2(L/R)$. The apparent shear rate is obtained from the volume rate of flow and the radius, $\dot{\gamma} = 4Q/\pi R^3$. No Rabinowitsch or Bagley corrections are made, because they would interfere with the interpretation of the observations. The onset of extrusion defects is manifested, for some polymers, by mild to steep slope changes of the flow curve as shown in Fig. 4.1-2.

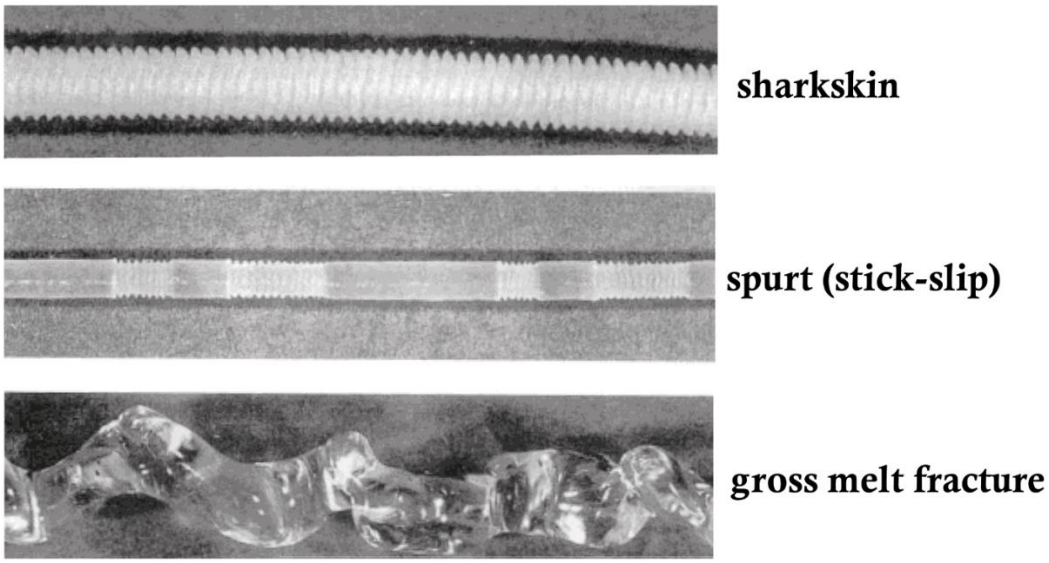

Figure 4.1-1. Different HDPE extrudate irregularities with increasing shear rate (flow rate) from top to bottom.

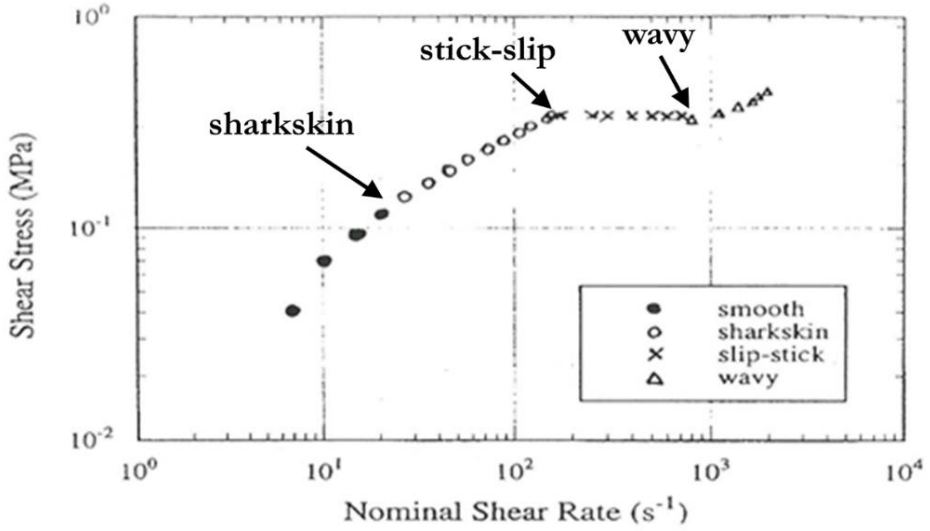

Figure 4.1-2. Flow curve (shear stress as a function of shear rate) for a Unipol LLDPE at 155°C. The flow in the stick-slip region oscillates with the average values shown by symbol "x". Wavy corresponds to gross melt fracture. Adapted from Denn (1994).

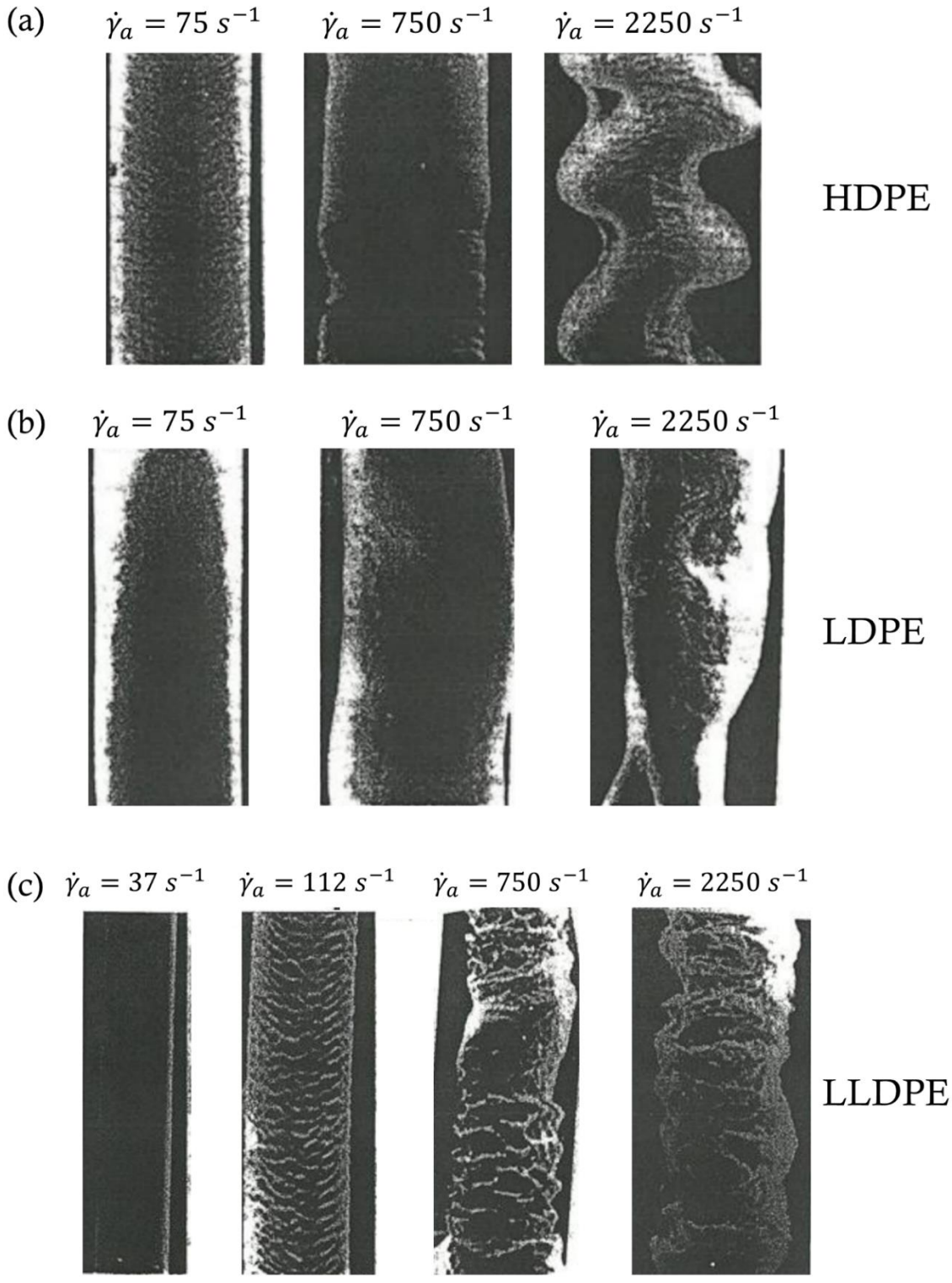

Figure 4.1-3. Extrudates from a capillary die at different apparent shear rates $\dot{\gamma}_a$. (a) HDPE with τ_w values from left to right: 0.20, 0.27 and 0.33 MPa, (b) LDPE with τ_w values from left to right: 0.1, 0.21 and 0.32 MPa and (c) LLDPE. Adapted from Moynihan (1990).

Some pictures of round extrudates and the corresponding apparent shear rates $\dot{\gamma}_a$ are shown in Fig. 4.1-3 for three polymers: HDPE, LDPE and LLDPE. It should be pointed out that LDPE goes from smooth to grossly distorted extrudate without exhibiting any kind of ridged surface that could be called sharkskin. On the other hand, LLDPE exhibits a very pronounced sharkskin. In fact, it was the increased production of LLDPE from the late 1970s, having sharkskin onset at relatively low shear rates, that spurred extensive research in extrusion instabilities. Vergnes (2015) cites 291 papers in his review. Due to the importance of this subject for imposing limitations on output rates, other reviews have been published by Denn (2001), Agassant *et al.* (2006), Malkin (2006) and books by Hatzikiriakos and Migler (2004) and Koopmans *et al.* (2011).

Die lip build up (**drool**), is accumulation of material at the die exit which may damage the surface quality of the extruded product. It requires stopping the extrusion and cleaning of the die. It is not related to sharkskin or melt fracture. It is an extrusion defect, but it is not referred to as instability. Very few studies are available in the open literature on die lip build up. **Surface tearing** is a phenomenon which appears in extrusion of fiber filled polymers, such as wood plastic composites (WPC). It appears like some short of exaggerated sharkskin at very low shear rates and its severity varies with filler loadings.

4.2 Sharkskin

The sharkskin phenomenon is shown with high detail in Fig. 4.2-1 and Fig. 4.2-2. It may be described as the appearance of ridges perpendicular to the flow direction, visible to the naked eye. The onset of sharkskin occurs at a critical wall shear stress usually quoted as $\tau_w \approx 0.14$ MPa for HDPE and it is associated with stick-slip phenomena at the die exit.

Figure 4.2-1. Typical sharkskin on an extrudate of about a 2 mm, exaggerated due to the enlargement. Note the formation of ridges perpendicular to flow direction. Adapted from Dennison (1967).

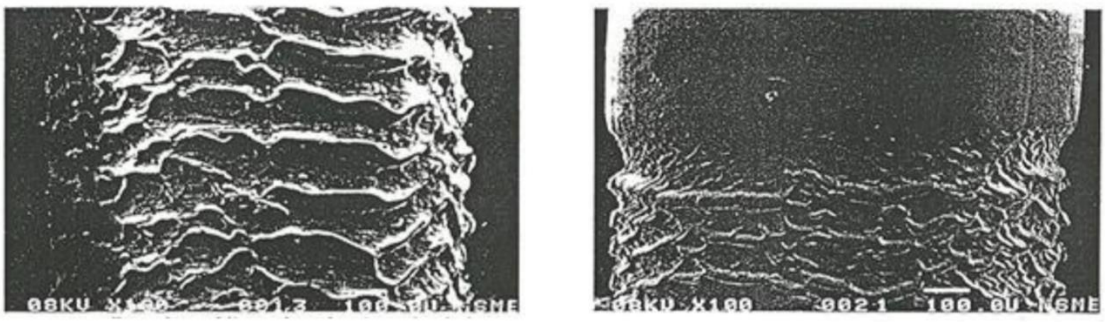

Figure 4.2-2. Extrudates of linear low density polyethylene (LLDPE) exhibiting sharkskin (left picture) and alternating sharkskin and somewhat smooth surface in the stick-slip regime (right picture). Adapted from Pudjijanto and Denn (1994).

Ramamurthy (1988) suggested that loss of adhesion is responsible for sharkskin, i.e. good adhesion prevents sharkskin. He used dies made of different materials (aluminum, copper, bronze, brass) and noticed that the die material has some influence on the loss of extrudate surface gloss and onset of distortions as shown in Table 4.2-1. Recent evidence shows that adhesion may diminish sharkskin, but continuous slip is more beneficial. Stick-slip phenomena have always a detrimental effect. The effects of chemical and morphological conditions of the die wall on critical conditions and the role of adhesion and slip, were investigated by Larazzabal *et al.* (2006a, 2006b).

***Table 4.2-1*. Effect of die material on the critical stresses. From Ramamurthy (1988).**

Measured Critical Apparent Shear Stress Values 1 MI, LLDPE, 220°C; 1 mm × 20 L/D Capillary		
Capillary Die Metal	Critical Stress for Loss of Gloss, MPa	Shear Stress for Gross Distortions, MPa
Aluminum	0.137	0.391
Beryllium Copper	0.104	0.377
Carbon Steel (SAE-4140)	0.144	0.435
Alpha Brass (CDA-360)	0.172	0.413
Bronze (Ampco 45)	0.146	0.434
Copper	0.132	0.415
Stainless Steel	0.151	0.441

The most recent and prevailing point of view suggests that sharkskin is the result of tensile failure (rupture) of the emerging extrudate surface at the die exit (Rutgers and Mackley, 2000, Agassant *et al.*, 2006, Vergnes, 2015). This is due to the abrupt change of the flow inside and outside the die as shown schematically in Fig. 4.2-3a: the skin of the extrudate accelerates

from rest (nearly no-slip at the die wall) to the extrusion velocity outside of the die. This acceleration causes a stretching of the extrudate skin and produces tensile stresses which are generally higher than the stresses the material can withstand, leading to surface rupture (Agassant *et al.*, 2006). If the material slips very close to the die wall, as shown in Fig. 4.2-3b, the velocity change from the die wall to the extrudate skin is small. Therefore, it accelerates less, the stretching is lower and the extrudate comes out of the die smoother. A numerical simulation of the velocity profile inside and outside the die is shown in Fig. 4.2-4 where the

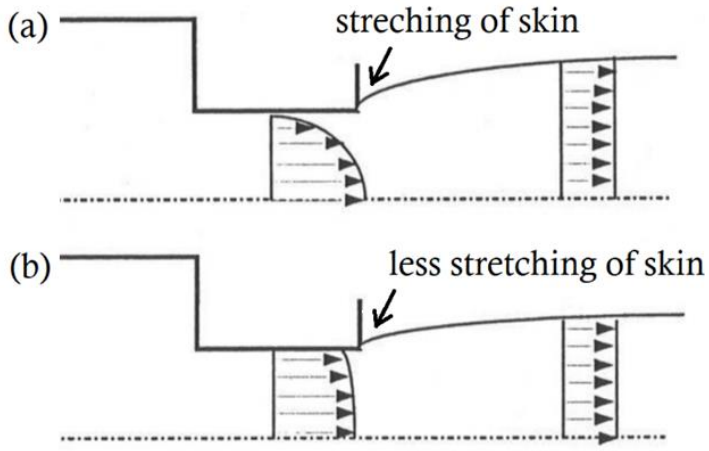

Figure 4.2-3. Schematic representation of the velocity profile rearrangement at the die exit (a) without slip and (b) with slip. Adapted from Agassant *et al.* (2017).

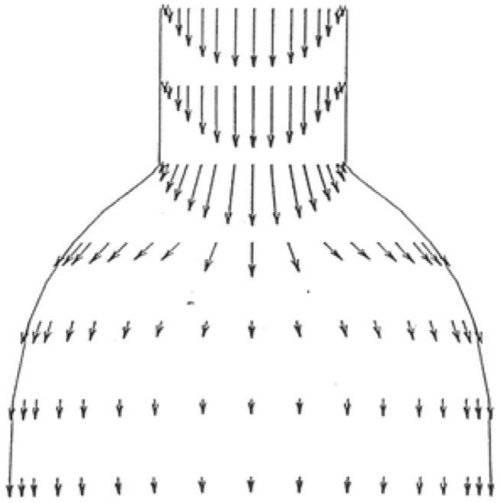

Figure 4.2-4. Extrudate swell with velocity profiles out of a slit die as simulated with POLYCAD®-2D without wall slip.

size of the arrows corresponds to local velocities. With additives, we can postpone sharkskin to a higher apparent shear rate (than that corresponding to a critical wall shear stress of 0.14 MPa). For instance, minute amounts of fluorocarbon polymers are used as polymer

processing aids (PPA) in LLDPE. This is probably because they act on die surface to promote slip, eliminate stick-slip and eventualy delay of the onset of sharkskin to higher flow rates. Commercially available fluorocarbon polymers include: VITON from Dupont, DYNAMAR from 3M and KYNAR from Arkema. Boron nitride is also used as a processing aid (PA) due to its flow enhancement and instability elimination properties (Achilleos *et al.*, 2002). Fluorocarbon processing aids are used extensively in blown film extrusion of LLDPE at weight fractions of less than 1%. It has been observed that at the start of extrusion of a polymer blended with the processing aid no beneficial effect is obtained. However, after a short period of perhaps 20-30 minutes, a hazy extruded film becomes clear and sharkskin-free. Apparently fluorocarbon polymers have affinity with the metal surface and get absorbed (but it requires a certain time) and the extruded polymer slips on a deposited thin layer of the fluorocarbons. The book by Wang (2018) includes considerable amount of details on slip phenomena.

Very pronounced sharkskin is usually observed in linear polymers with a narrow molecular weight distribution (i.e. low polydispersity) and a high molecular weight such as HDPE and LLDPE. These types of polymers tend to have a lower melt strength than polymers with long chain branching (LCB), like LDPE. In branched polyolefins, sharkskin and stick-slip phenomena are almost non-existent. Branched polymers like LDPE possess a high melt strength. Therefore, the skin can stretch and subsequently relax without exceeding a critical tensile stress that may cause rupture. At very high flow rates, they do exhibit extrudate volume distortions, which are at first usually of a regular helical pattern that progressively becomes more and more chaotic, resulting in what we have called gross melt fracture. Sharkskin is also sensitive to the length of the capillary (*L/D).* Generally, longer capillaries delay the onset of sharkskin to significantly higher shear rates. This is perhaps due to the viscous dissipation effect. Longer dies means, increased temperature rise that leads to viscosity decrease and postponement of sharkskin to higher shear rates (Miller and Rothstein, 2004).

Sharkskin may be prevented by offsetting the die lips as shown in Fig. 4.2-5a in multilayer extrusion, because the wall shear stress at the die lip exit of sharkskin-prone LLDPE is significantly reduced. Wall shear stress reduction, and consequently postponement of sharkskin to higher flow rates, can also be achieved by opening the gap at the die lip exit as shown in Fig. 4.2-5b. Sharkskin is a die exit phenomenon and the geometrical, chemical, morphological or thermal conditions at that location are crucial.

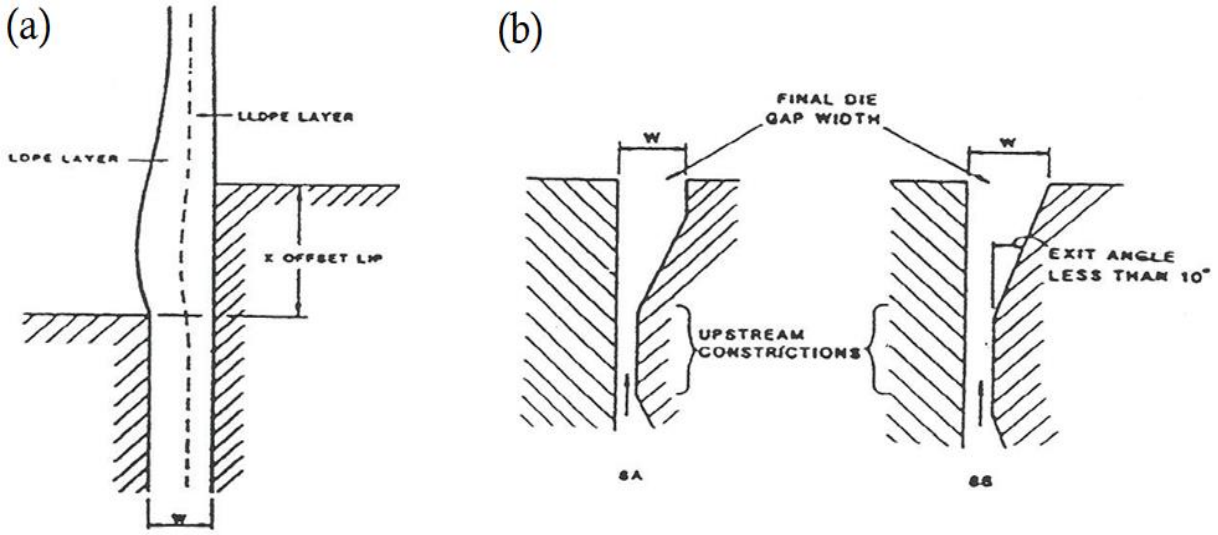

Figure 4.2-5. Different die designs to prevent sharkskin in multilayer film extrusion (a) Offset die design and (b) die lips designs with upstream flow constrictions. Adapted from Kurtz (1984).

4.3 Melt Fracture

While sharkskin (critical $\tau_w \approx 0.14$ MPa) is a surface defect originating at the die exit, melt fracture (with critical wall shear stress being in the range of $\tau_w = 0.25 \sim 0.5$ MPa) is a volumetric gross flow instability that originates at the die entry or in the die land. In addition to the previous pictures, in this chapter, of polyolefin extrudates exhibiting sharkskin and melt fracture instabilities, we show some photographs of biodegradable PLA in Fig. 4.3-1 and the corresponding flow curve in Fig. 4.3-2. At 200 s^{-1} the sample clearly shows sharkskin, which gets progressively worse. At 2500 s^{-1} we observe a volumetric distortion of the extrudate, (gross melt fracture). The term "fracture" is really a misnomer, considering that there is no breaking of anything involved. It came about because researchers in the 1950s were hearing

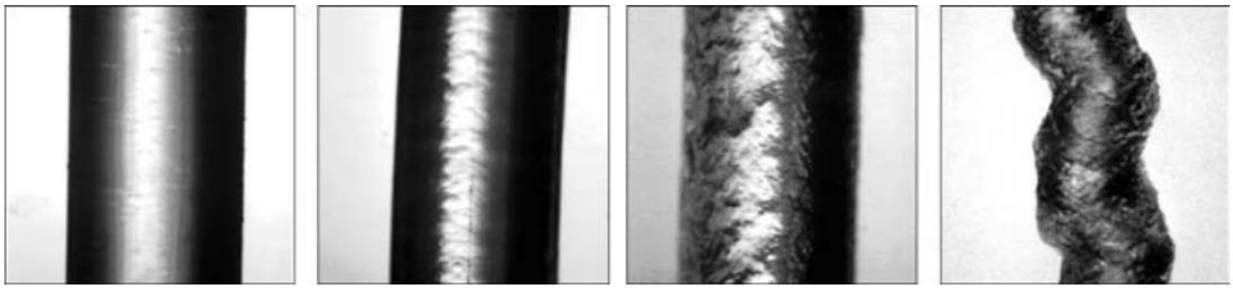

Figure 4.3-1. PLA 4042D extrudates at different shear rates and wall shear stresses. From left to right the values of $\dot{\gamma}_{app}$ are 100, 200, 600 and 2500 s^{-1}, while the corresponding values of τ_w are 0.16, 0.22, 0.33 and 0.45 MPa. From Kanev *et al.* (2007).

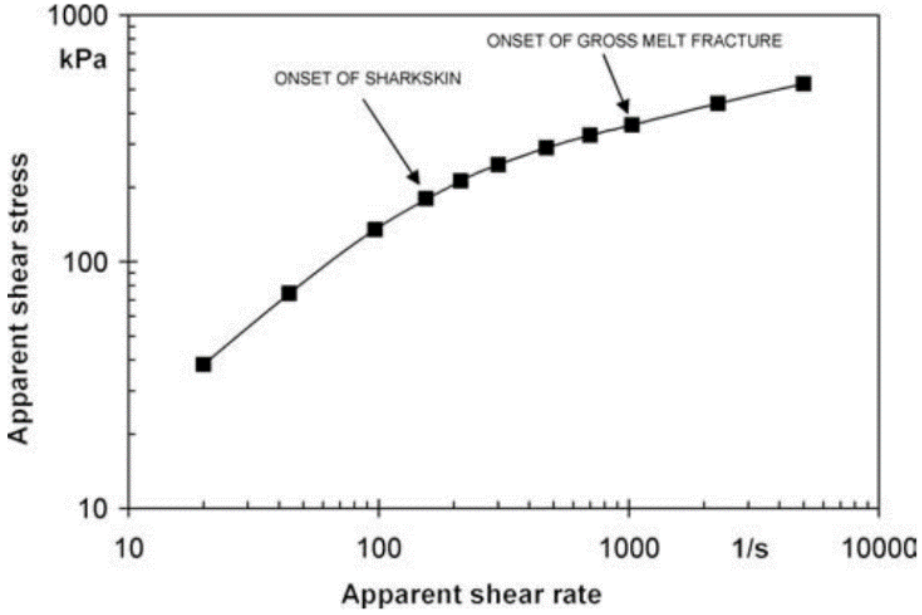

Figure 4.3-2. Flow curve and onset of extrudate instabilities for PLA 4042D at 180°C in a stainless steel die with D=1 mm and L/D=16. From Kanev *et al.* (2007).

some cracking noises. However, it soon became clear that the noises were due to exit of trapped air bubbles, but the term remained and subsequently translated in other languages (rupture d'extrudat (Fr), Schmelzbruch (Ger.) and fractura del fundido (Sp.)). Melt fracture has received less attention than sharkskin by the scientific community, because sharkskin appears at lower shear rates and poses an upper output limit in extrusion of thin film having smooth surface and haze-free optical clarity.

Industrial extrusions usually do not go beyond the shear rate for the onset of sharkskin. However, in the production of pellets (frequently of about 3 mm in diameter) the melt is extruded through numerous holes and extrudates are water cooled and cut by moving knives. At high output rates the critical stress for the onset of melt fracture can easily be exceeded. Cutting of highly distorted polymer strands usually results in production of fine particles, together with the pellets, which are an impediment to subsequent handling operations and feeding of extruders. Thus melt fracture is not only of scientific interest, but also of practical importance.

For some polymers, melt fracture is apparently related to entry flow instabilities. Both experiments and computer simulations have shown that in contraction flows from a large diameter tube into a smaller one, corner vortices form. This is shown in Fig. 4.3-3 for a Newtonian fluid in a 4:1 contraction. The toroidal (doghnut shaped) vortex remains steady even at high laminar flow rates. However, the vortices formed in molten LDPE flow in a planar

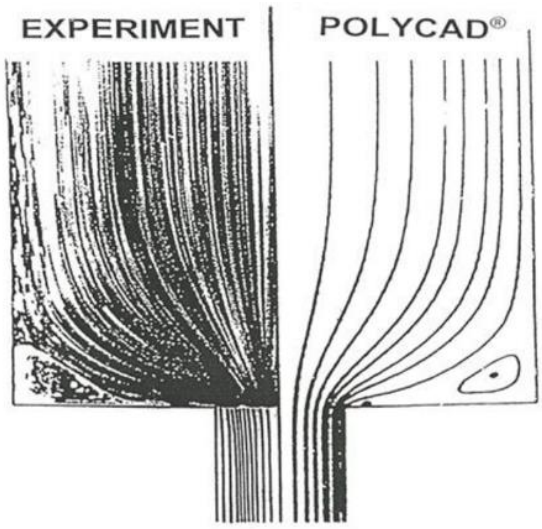

Figure 4.3-3. Newtonian creeping flow in a 4:1 circular contraction. There is a small and weak vortex at the corner (strength 0.00181) as determined by POLYCAD®. The flow pattern is in agreement with experimental one shown on the left half of the figure and taken from Boger *et al.* (1986).

contraction, shown Fig. 4.3-4, would become unstable if the Weissenberg number *Wi* (see Section 3.9) was to increase beyond a certain value. This vortex instability is related to the viscoelastic nature of LDPE. Obviously, unstable vortex in the entry region would result in unstable extrudate coming out of the die. However, HDPE is also viscoelastic but it flows like a Newtonian fluid with a nearly stagnant region at the corner, even at very high flow rates beyond the onset of the volume instability (melt fracture) as shown schematically in Fig.4.3-5b. Both LDPE and HDPE exhibit gross melt fracture, even though they have different entry flow patterns, with onset being at a somewhat lower critical shear stress for LDPE than HDPE, according to Vlachopoulos and Alam (1972). The flow curve for LDPE remains pretty much undisturbed at the onset of melt fracture, while for HDPE a discontinuity appears. The apparent shear rate increases abruptly up to a certain value and then increases along a curve. Decreasing the applied pressure, a hysteresis loop is obtained as shown in Fig. 4.3-5.

The vortex formation in LDPE is apparently related to its high elongational viscosity, as shown in Fig. 4.3-5a. As the LDPE melt approaches the entry to the capillary the stretch rate increases and so does the elongational viscosity, that is the resistance to extension, which results in a large vortex forming, as shown in Fig. 4.3-5b. Large vortex flow patterns have also been observed with PS. The flow curve for PS is similar to that of LDPE as well as the PLA shown in Fig. 4.3-2. LLDPE has a flow curve with a hysteresis loop similar to that of HDPE.

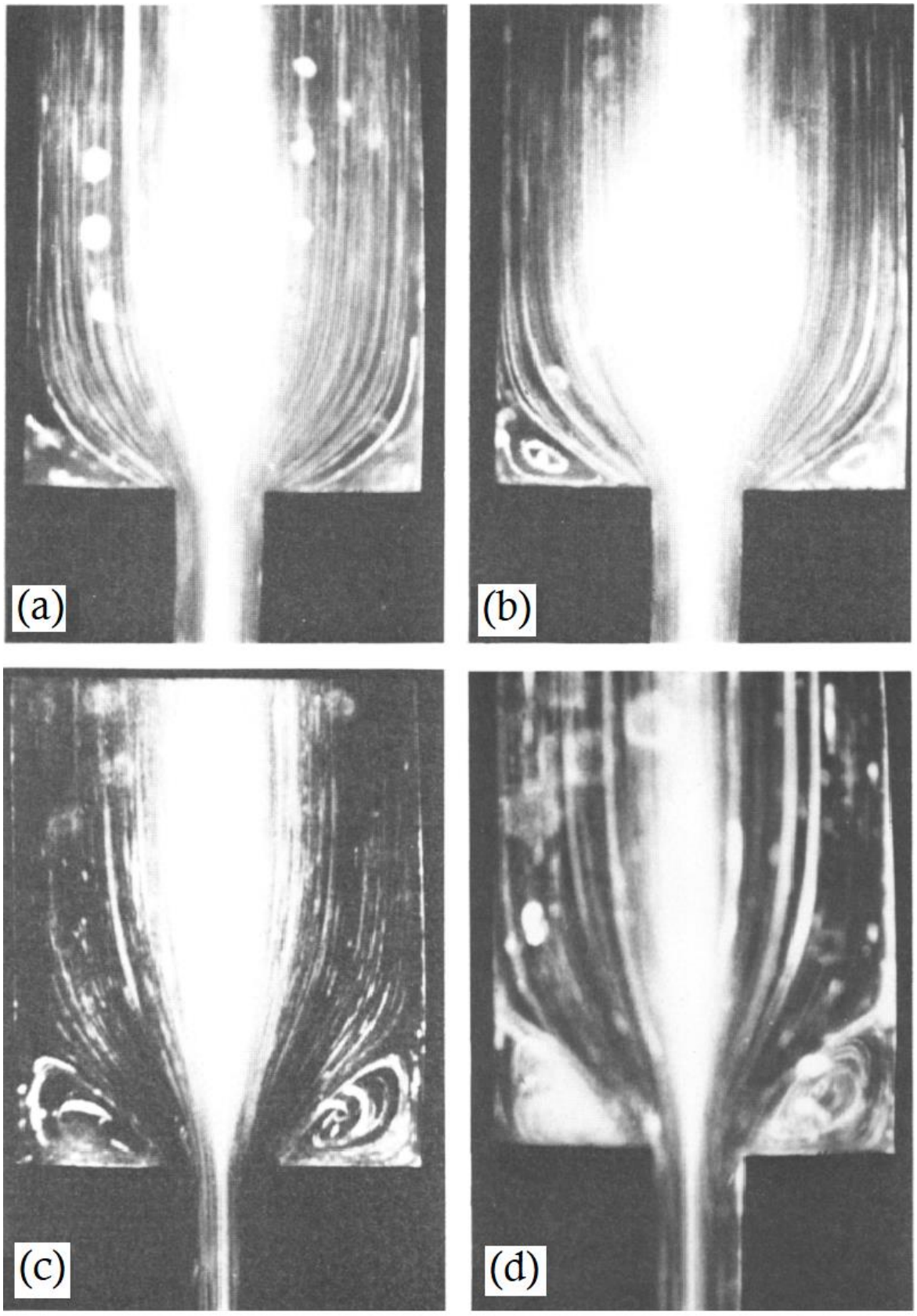

Figure 4.3-4. Streamline patterns obtained by means of streak photography for LDPE at 150°C in a 4:1 planar contraction. (a) $\dot{\gamma}$= 1 s^{-1}, Wi=0.876, (b) $\dot{\gamma}$=2.5 s^{-1}, Wi=1.01, (c) $\dot{\gamma}$=10 s^{-1}, Wi=1.21 and (d) $\dot{\gamma}$=80 s^{-1}, Wi=1.38. From White and Baird (1998).

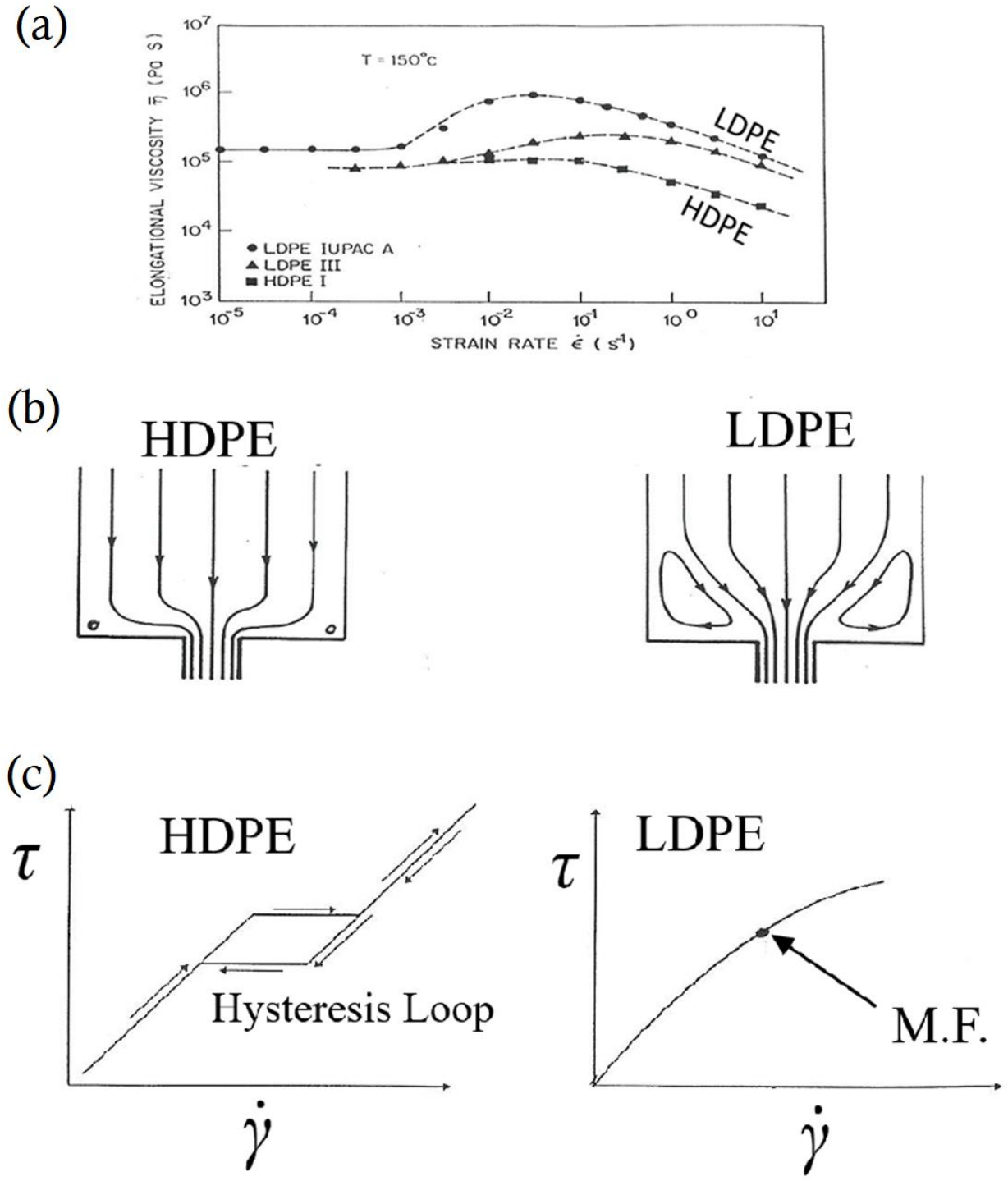

Figure 4.3-5. Comparison of rheological and flow behavior of HDPE and LDPE. (a) elongational viscosity, (b) schematic representation of the flow in a 4:1 sudden contraction and (c) flow curves.

Some researchers suggested that melt fracture occurs when the recoverable shear exceeds a certain value. Recoverable shear is the ratio of the first normal stress to twice the wall shear stress($N_1/2\tau_w$). It can be interpreted as the ratio of elastic forces to viscous forces. Bagley (1961) observed experimentally that when the recoverable shear is about 7 units, melt fracture sets on. This implies that the flow becomes unsteady even in rectilinear flow (parallel streamlines) in the die land (straight, parallel walls). In fact, there have been some mathematical stability analyses confirming such a mechanism.

Vlachopoulos and Alam (1972) determined the critical recoverable shear of PS from extrudate swell measurements (at the onset of melt fracture) using Tanner's equation (Eq. 3.8-4 in Chapter 3). In contrast to Bagley's results, they reported that the onset of melt fracture for PS occurs over a wide range of critical recoverable shear depending on molecular weight distribution (MWD)

$$\left(\frac{N_1}{2\tau_w}\right)_{critical} = 2.65 \times \left(\frac{M_z M_{z+1}}{M_w{}^2}\right) \qquad (4.3\text{-}1)$$

where the MWD term in the parentheses is equal to 1 for monodisperse PS, equal to 3 for PS having Gaussian molecular weight distribution (see Section 1.7) and a much higher value for a sample having a long high molecular weight tail.

This criterion is not useful from the engineering point of view because it is difficult to determine N_1. The criterion of a critical wall shear stress in the range of 0.25 MPa to 0.5 MPa remains the most reliable.

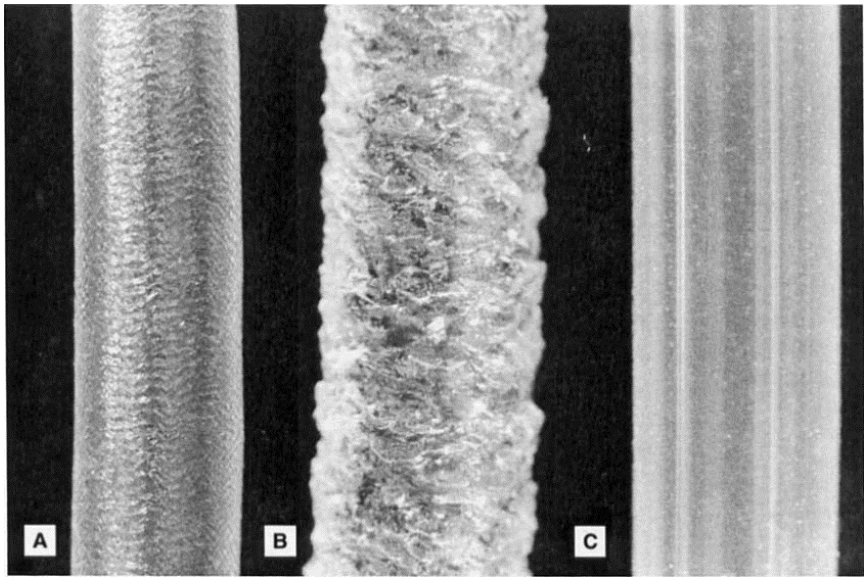

Figure 4.3-6. Extrudate samples of metallocene polyethylene. Sample A exhibits sharkskin at low shear rates and B gross melt fracture at higher shear rates, both with no boron nitride. Sample C is smooth by adding 0.01% boron nitride for the same shear rate as sample B. From Rosenbaum *et al.* (2000).

In slit dies onset of melt fracture to occurs at higher shear stress values (Vlachopoulos and Chang, 1977, Ebrahimi *et al.*, 2018). Addition of boron nitride as a processing aid in a polymer melt may also postpone the onset of melt fracture to considerably higher shear rates, therefore improving processability and increasing production rates. In Fig. 4.3-6, the suppression of gross melt fracture is shown by adding only a small amount (0.01%) of boron nitride in a metallocene polyethylene.

4.4 Die Lip Build-Up (Drool)

Die lip build-up or drool, is not related to sharkskin or melt fracture. It is the undesirable gradual formation of material deposit at the die exit as shown schematically in Fig. 4.4-1. In Fig. 4.4-2 actual photographs of the phenomenon are shown. Frequently, the deposited material may partially or completely break away from the die and adhere to the surface of the extrudate, thus reducing the aesthetic quality and engineering performance of

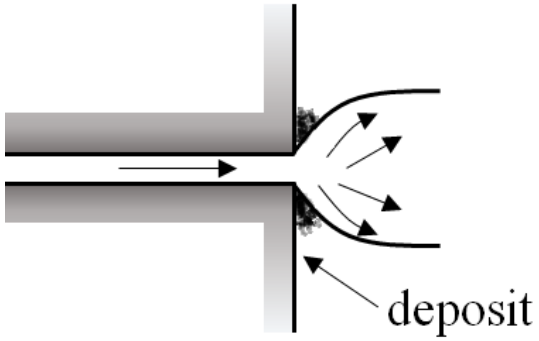

Figure 4.4-1. Schematic representation of the phenomenon die lip build-up.

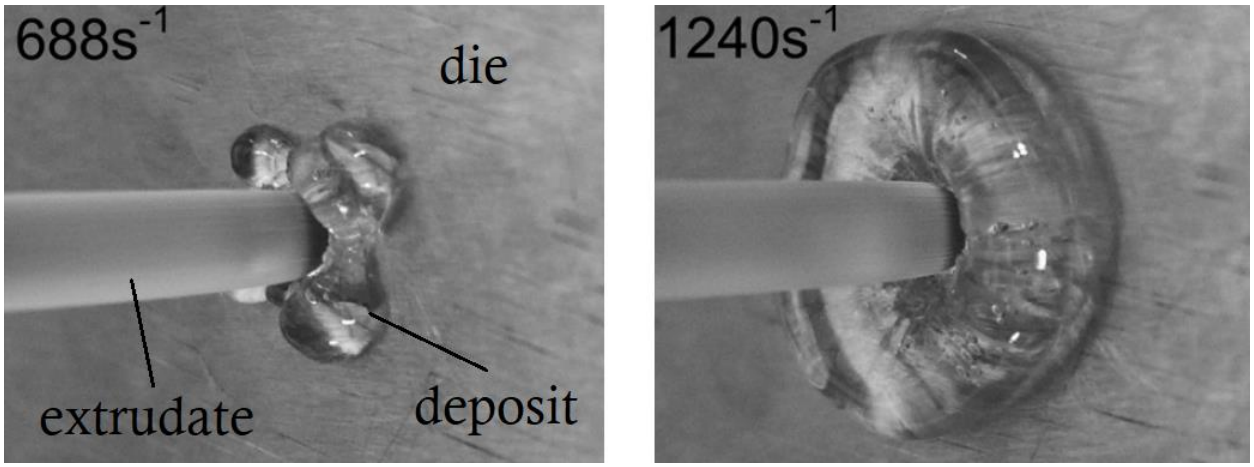

Figure 4.4-2. Die lip build-up at two different shear rates. Adapted from Musil and Zatloukal (2011).

the product. Observations suggest that the formation of die lip build-up is not continuous but intermittent. The deposited material is rich in low molecular weight polymer fractions, pigments, colorants and other low molecular weight additives. Die cleaning is necessary when significant die lip build-up occurs and this is a costly procedure for plastics manufacturers, as it requires periodic shutdowns of the production line.

The onset of drooling is a complex phenomenon with perhaps more than one mechanisms and sources contributing. According to Gander and Giacomin (1997), possible sources include the following: Low molecular weight species, volatiles, fillers, poor dispersion of pigments, draw down, die swell, low die exit angle, short land length, pressure fluctuations in screw, dissimilar viscosities in blends, dirty die start-up, high melt temperature, processing near degradation temperature.

There are some remedies for reduction or elimination of die lip build-up, which include repairing missing plating and removing surface imperfections from die lips. Also, sharp die lips produce more build-up that may be partially relieved using a small angle at the exit (flaring) as shown in Fig. 4.4-3. In an industrial production line of PC optical fiber, a die with sharp die lips required cleaning roughly every 8 hours, while a flared one (6 ^{o} to 12 ^{o}) usually every 6 days. Chaloupková and Zatloukal (2009) reported that for a metallocene LLDPE, build-up was significantly reduced using dies with angle range at the exit 15^{o}-45^{o}. Also, die lip

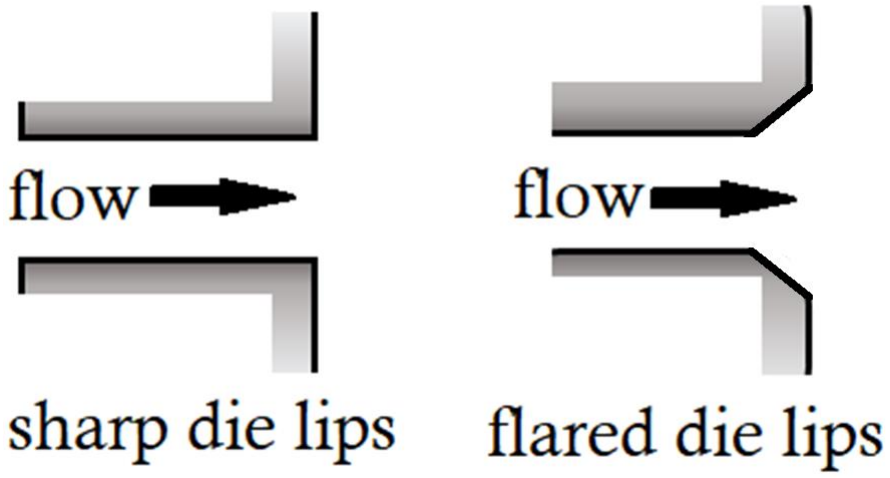

Figure 4.4-3. Schematic presentation of sharp and flared die lips.

build-up may be decreased by removing moisture from the feed material, lowering the extrudate temperature and adding stabilizer to the feedstock resin. As in the case of sharkskin and melt fracture, polymer processing aids (PPA) are sometimes helpful. Regarding the

molecular architecture, polymers with a wide MWD cause more problems, so choosing a more narrow molecular weight distribution may provide some relief.

4.5 Surface Tearing in Extrusion of Fiber Filled Polymers

Natural fibers are used with increasing frequency for the production of composites usually abbreviated as either NFC (natural fiber composites) or WPC (wood plastic composites). These materials are especially popular for decking, fencing and other housing applications due to their advantages in the performance/price equation. Some applications also include injection molded products for automotive applications. The use of recycled polymers for these composites further improves their price performance.

HDPE is the most widely used polymer in WPC, followed by PVC and polypropylene. Other than wood, various types of natural fibers are also used, such as pineapple fibers, rice hulls, jute and hemp fibers (see for example George *et al.*, 1996 and Polychronopoulos *et al.*, 2018). Addition of natural fibers creates miscellaneous processing difficulties including a surface defect.

The surface defect is usually referred to as **surface tearing**, a phenomenon which has been well known since the inception of WPC extrusion in the early 1980s. It appears like some short of exaggerated sharkskin at very low shear rates. Surface tearing is affected by filler loading level. Goettler *et al.* (1982) reported on observations of significant surface irregularities in fiber filled rubber. Hristov *et al.* (2006) carried out detailed observations of the surface quality of HDPE/wood flour composites. A neat HDPE extruded at 20 s^{-1} exhibited a smooth surface, as shown in Fig. 4.5-1a. However, when filled with wood-flour at 25% by weight and extruded again at 20 s^{-1} it exhibited surface tearing, as shown in Fig. 4.5-1b. At 50% loading the surface of the extrudate became even rougher, as shown in Fig. 4.5-1c, but at 60% loading, the roughness was significantly reduced. Increasing the loading to 70% an extrudate of relatively smooth surface was obtained, as shown in Fig. 4.5-1d. The surface tearing phenomenon has also been observed in industrial extrusions, as shown in Fig.4.5-2a. It is apparently due to lowering of melt strength of the polymer as the filler increases, poor addition between matrix and filler and weak shear forces that allow the fibers to move at an angle to the main flow direction. Some patents (Lave, 1996, Muller and Wittenberg, 1998, Nishibori, 1998, Suwanda, 2001) use cooling to freeze a solid skin layer and avoid surface tearing, as

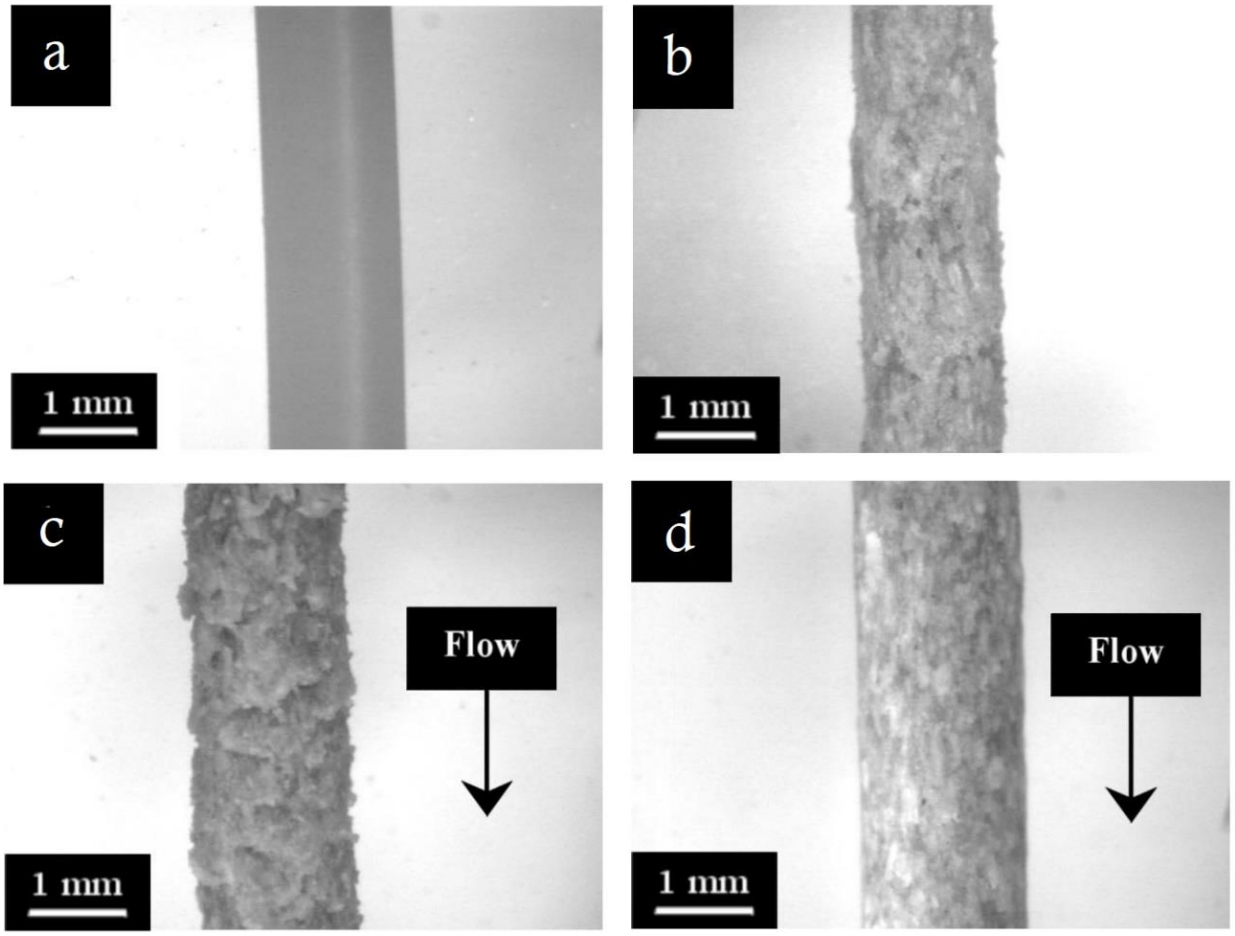

Figure 4.5-1. Optical photographs of HDPE/wood composites at 20 s^{-1} at different wood loadings. (a) neat HDPE, (b) 25%, (c) 50% and (d) 70%. Adapted from Hristov *et al.* (2006).

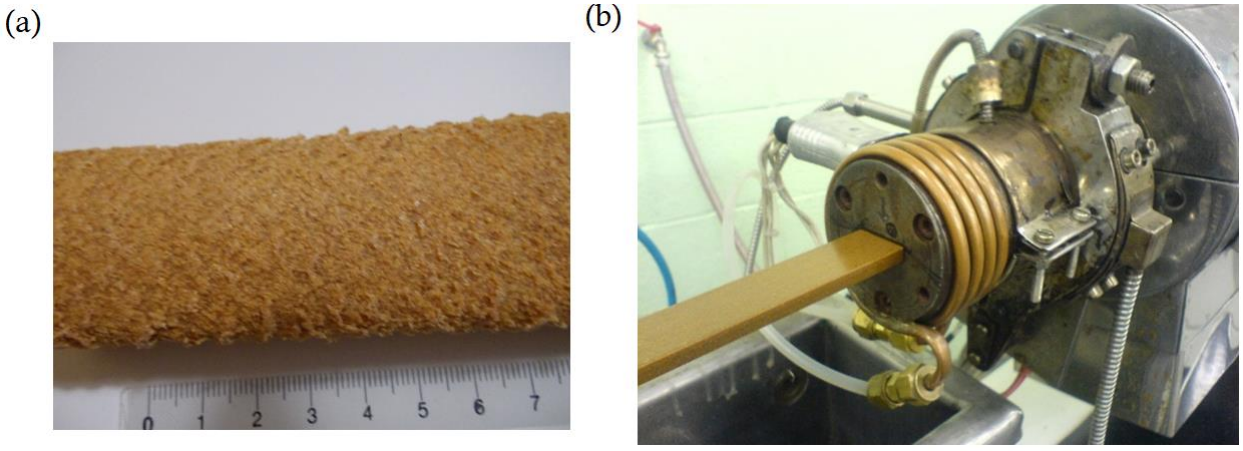

Figure 4.5-2. (a) Surface tearing at the extrusion die exit as observed in an industrial operation (cm scale) and (b) smooth extrudate emerging from a cooled die attached to a laboratory extruder. Adapted from Santi *et al.* (2006).

shown in Fig. 4.5-2b, from Santi *et al.* (2009). Smoothening of the surface at very high loadings is due to enhancement of wall slip. Lubricants are helpful for improving surface quality at any

loading (Hristov and Vlachopoulos, 2006). The presence of sharp edges on a die results in the worst surface tearing phenomena (Charlton, 2001).

Bibliography

Achilleos E.C., Georgiou G., and Hatzikiriakos S.G., Role of processing aids in the extrusion of molten polymers, J. Vinyl Addit. Technol. 8 (1), 7 (2002).

Agassant J.-F., Arda D.R., Combeaud C., Merten A., Münstedt H., Mackley M.R., Robert L. and Vergnes B., Polymer Processing Extrusion Instabilities and Methods for their Elimination or Minimization, Int. Polym. Proc., 21 (3), 239 (2006)

Agassant J.-F., Avenas P., Vincent M., Vergnes B. and Carreau P.J., *Polymer Processing Principles and Modeling*, Hanser (2017)

Bagley E.B., The Separation of Elastic and Viscous Effects in Polymer Flow, J. Rheol., 5, 355 (1961)

Boger D.V., Hur D.U. and Binnington R.J., Further Observations of Elastic Effects in Tubular Entry Flows, J. Non-Newt. Fluid Mech., 20, 31 (1986)

Chaloupková K. and Zatloukal M., Effect of Die Design on Die Drool Phenomenon for Metallocene Based LLDPE: Theoretical and Experimental Investigation, J. Appl. Polym. Sci., 111, 1782 (2009)

Charlton Z., Profile Extrusion of Highly Filled Cellulose-Polyethylene Composites, M.Eng. Thesis, Department of Chemical Engineering, McMaster University (2001)

Delgadillo-Velázquez O., Georgiou G., Sentmanat M., and Hatzikiriakos S. G., Sharkskin and oscillating melt fracture: Why in slit and capillary dies and not in annular dies, Polym. Eng. Sci. 48, 405 (2008).

Denn M.M., Polymer Flow Instabilities, Chem. Eng. Edu., 162 (summer 1994)

Denn M.M., Extrusion Instabilities and Wall Slip, Annu. Rev. Fluid Mech., 33, 265 (2001).

Dennison, M. T. Flow instability in polymer melts: a review. Trans. Plast. Inst. 35, 803–808 (1967).

Ebrahimi M., Tomkovic T., Liu G., Doufas A.A. and Hatzikiriakos S.G., Melt Fracture of Linear Low-Density Polyethylene: Die Geometry and Molecular Weight Characteristics, Phys. Fluids, 30, 053103-1 (2018)

Gander J.D. and Giacomin A.J., Review of Die Lip Buildup in Plastics Extrusion, Polym. Eng. Sci., 37 (7), 1113 (1997)

Goettler L., Sezna J. and DiMauro P.J., Short Fiber Reinforcement of Extruded Rubber Profiles, Rubber World, 187, 33 (1982)

Hatzikiriakos S.G., Wall Slip in Molten Polymers, Prog. Polym. Sci., 37, 624 (2012)

Hatzikiriakos S.G. and Migler K.B. (Eds), *Polymer Processing Instabilities: Control and Understanding,* CRC Press (2004)

Hristov V., Takács E. and Vlachopoulos J., Surface Tearing and Wall Slip Phenomena in Extrusion of Highly Filled HDPE/Wood Flour Composites, Polym. Eng. Sci., 46 (9), 1204 (2006)

Kanev D., Takacs E. and Vlachopoulos J., Rheological Evaluation and Observations of Extrusion Instabilities of Biodegradable Polyesters, Int. Polym. Proc., 22 (5), 395 (2007)

Koopmans, R., Den Doelder, J. and Molenaar, J., *Polymer Melt Fracture*, CRC Press, Boca Raton (2011)

Kurtz, S.J., Proceedings, IX Intern. Congr. Rheol., Acapulco, Mexico (1984)

Larrazabal H., Hrymak A.N. and Vlachopoulos J., Effect of the Chemical and Morphological Conditions of the Die Wall on the Extrusion of Linear Polyolefins, Int. Polym. Proc., 21 (2), 132 (2006a)

Larrazabal H., Hrymak A.N. and Vlachopoulos J., On the Relationship Between the Work of Adhesion and the Critical Shear Stress for the Onset of Flow Instabilities, Rheol. Acta, 45 (5), 705 (2006b)

Laver T., U.S. Patent No 5,516,472 (30 August 1996)

Miller E. and Rothstein J.P., Control of the Sharkskin Instability in the Extrusion of Polymer Melts Using Induced Temperature Gradients, Rheol. Acta 44, 160 (2004)

Muller J. and Wittenberg R., U.S. Patent No 5,851,469 (22 December 1998)

Moynihan R.H., The Flow at Polymer and Metal Interfaces, PhD Thesis, Department of Chemical Engineering, Virginia Tech. Blackburg, VA (1990)

Musil J. and Zatloukal M., Experimental Investigation of Flow Induced Molecular Weight Fractionation During Extrusion of HDPE Polymer Melts, Chem. Eng. Sci., 66, 4814 (2011)

Nishirobi S., U.S. Patent 5,725,939 (10 March 1998)

Polychronopoulos N.D., Charlton Z., Suwanda D. and Vlachopoulos J., Measurements and Comparison to Predictions of Viscosity of Heavily Filled HDPE with Natural Fibers, Adv. Polym. Technol., 37 (4), 1161 (2018)

Pudjijanto S. and Denn M.M., A Stable "Island" in the Slip-Stick region of Linear Low-Density Polyethylene, J. Rheol., 38 (6), 1735 (1994)

Ramamurthy A.V., Extrudate Irregularities and the Polymer-Metal Interface Connection, in: *Proceedings of the Xth International Congress on Rheology*, pp. 85-90, Sydney (1988)

Rosenbaum E.E., Randa S.K., Hatzikiriakos S.G., Stewart C.W., Henry D.L. and Buckmaster M., Boron Nitride as a Processing Aid for the Extrusion of Polyolefins and Fluoropolymers, Polym. Eng. Sci., 40 (1), 179 (2000)

Rutgers R. and Mackley M., The Correlation of Experimental Surface Extrusion Instabilities with Numerically Predicted Exit Surface Stress Concentrations and Melt Strength for Linear Low Density Polyethylene, J. Rheol., 44 (6), 1319 (2000)

Santi C.R., Hage Jr E., Vlachopoulos J. and Correa C.A., Rheology and Processing of HDPE/Wood Flour Composites, Int. Polym. Proc., 24 (4), 346 (2009)

Suwanda D., U.S. Patent No 6,210,616 (3 April 2001)

Vergnes B., Extrusion Defects and Flow Instabilities of Molten Polymers, Int. Polym. Proc., 30 (1), 3 (2015)

Vlachopoulos J. and Alam M., Critical Stress and Recoverable Shear for Polymer Melt Fracture, Polym. Eng. Sci., 12 (3), 184 (1972)

Vlachopoulos J. and Chang T.W., A Comparison of Melt Fracture Initiation Conditions in Capillaries and Slits, J. Appl. Polym. Sci., 21, 1177 (1977)

Wang, S-H., *Nonlinear Polymer Rheology*, Wiley (2018)

White S.A. and Baird D.G., Flow Visualization and Birefringence Studies on Planar Entry Flow Behavior of Polymer Melts, J. non-Newt. Fluid Mech., 29, 245 (1998)

J. Vlachopoulos and N.D. Polychronopoulos "*Understanding Rheology and Technology of Polymer Extrusion*", First Edition, Polydynamics Inc, Dundas, Ontario, Canada (2019)

Chapter 5

RHEOLOGICAL MEASUREMENTS AND THEIR INTERPRETATION

5.1 Introduction

From the four previous chapters it is abundantly evident that good measurements of **shear viscosity**, **elongational viscosity**, **normal stresses differences** and characteristic **relaxation time** are necessary for equipment design and troubleshooting purposes in polymer extrusion and in other polymer processing operations. Of course, shear viscosity is, by far, the most important property for any calculations related to equipment design, output, pressure drop and temperature. The other properties provide intrinsic information about the polymer. There are numerous methods of measurement described in publications and commercial equipment brochures. In this chapter, we present basic information for the most widely used methods. The book by Macosko (1994) is perhaps the most authoritative and comprehensive reference for all kinds of rheological measurements.

For reliable measurements we must have either a simple shear flow (where particle pathlines are parallel and the velocity varies only in one direction) or simple elongational flow (involving stretching, but no shearing). For more rigorous definitions of simple shear, simple shear-free and viscometric flows, we recommend the books of Morrison (2001) and Bird *et al.* (1987). The basic idea is not to have any mixed flow situations, no instabilities, to have good temperature, pressure, force, torque measurements and to minimize potential errors. The person carrying out rheological measurements and the person interpreting the results must be aware of all sources of errors in the measurable quantities. Frequently, corrections may have to be applied.

5.2 Melt Flow Index (Melt Flow Rate)

As explained in the Chapter 1 (Section 1.11), Melt Index (**MI**), Melt Flow Index (**MFI**) or Melt Flow Rate (**MFR**) is the number of **grams per 10 minutes** flowing out of die of standard dimensions under the action of a load of specified weight in kilograms, as shown in Fig. 5.2-1. Traditionally, the term MFR was used for PP, but it is now used interchangeably with MI or MFI for all polymers. Also, the ASTM D1238 and ISO 1133 standards include the melt volume rate (**MVR**) measurement in **cm^3/10 minutes**. MVR can be converted to

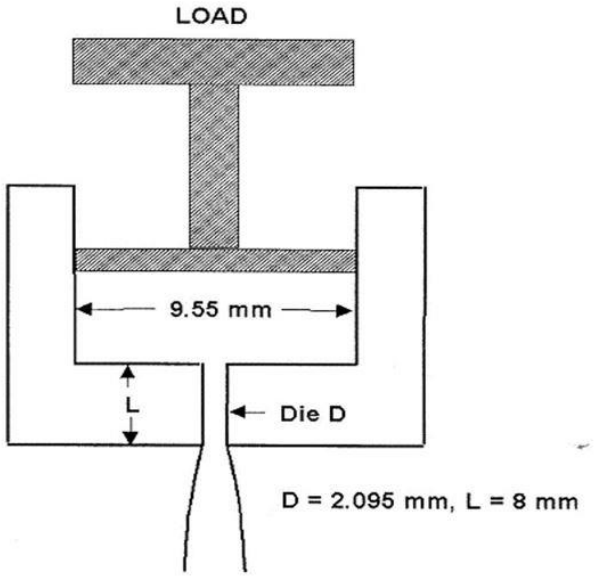

Figure 5.2-1. Schematic of a Melt Indexer (originally called extrusion plastometer).

MFR (MFI) by multiplying it by the melt density of the material. In fact, instruments capable of measuring both MVR and MFI are used for measuring the melt density, which is simply the ratio MFR/MVR. Roughly speaking, the melt density is 90% of solid density for amorphous polymers and 80% of solid density for semi-crystalline polymers. The standard load is 2.16 kg, but also 5 kg, 10 kg and 21.6 kg are used. The temperature of the test is 190°C for PE and 230°C for PP. Other temperatures are specified by the ASTM D1238 and ISO 1133 standards, for other polymers. Depending on the capabilities of melt indexer and procedure followed, measurements can be made in the range of 0.10 to 1500 g/10 minutes. Of course, the usual range is much narrower: For extrusion grades of polyethylene the MFI with the standard load (2.16kg) is usually in the range 0.1 to perhaps 12, while for injection molding grades it may exceed 50.

With the help of equations presented in Chapter 2, it is easy to determine the shear rate, shear stress and the corresponding apparent viscosity from the volume flow rate Q, density ρ and load (kg). The apparent shear rate at the die wall ($4Q/\pi R^3$), is

$$\dot{\gamma}_w = \frac{1846.33}{\rho} MI \quad (\mathrm{s}^{-1}) \tag{5.2-1}$$

and the apparent wall shear stress is

$$\tau_w = 8966.42 \times Load \quad (\mathrm{Pa}) \tag{5.2-2}$$

The corresponding apparent viscosity will then be

$$\eta = \frac{\tau_w}{\dot{\gamma}_w} = \frac{4.86}{MI} \times \rho \times Load \quad (\mathrm{Pa \cdot s}) \tag{5.2-3}$$

To put these quantities into perspective, we calculate the apparent shear rate, shear stress and viscosity (for MFI=1, standard load 2.16 kg and assuming melt density of polyethylene 766 kg/m^3)

$$\dot{\gamma}_w = \frac{1846.33}{766} \times 1 \cong 2.41 \ \mathrm{s}^{-1}$$

$$\tau_w = 8966.42 \times 2.16 \cong 19376 \ \mathrm{Pa}$$

$$\eta = \frac{4.86}{1} \times 766 \times 2.16 \cong 8041 \ \mathrm{Pa \cdot s}$$

We see that the shear rate is very low. However, the measurement with a high load could be more than 100 times higher (depending on how shear-thinning the material might be). Frequently, the ratio of two Melt Flow Index values, obtained with a high and a low load are reported in material data sheets as the **Flow Rate Ratio** (**FRR**). The higher the FRR the more shear thinning the material.

Calculation of Power-Law Parameters

The Melt Indexer is not specifically designed for measurement of viscosity. It is used for material specification and quality control purposes. Low melt index means high viscosity, high molecular weight polymer. High melt index means low viscosity, low molecular weight polymer. Saini and Shenoy (1996) present several correlations between molecular weight and melt index. Having two values of MFI does provide an approximation of the shear viscosity of the polymer. Errors stem from the entrance pressure, due to elongational viscosity (see Section 3.4 in Chapter 3), which is not taken into consideration. For the standard load the entrance pressure loss is relatively small (due to low shear rate), but for the high load the

entrance pressure could perhaps be comparable to that caused by the die (L/D=8/2.095=3.82) for some polymer grades. The entrance pressure loss is high for LDPE (branched, high elongational viscosity) and lower for linear polymers like HDPE, LLDPE and PP, especially those with narrow molecular weight distribution. Thus, LDPE viscosity estimates are likely to have larger errors than estimates for some linear grades of polymers.

Despite the possible errors, we present an approximate calculation of both m and n by using two values of the melt index (*MI*, and *HLMI*), i.e. using a standard melt indexer having a die of 8 mm length and diameter of 2.095 mm (according to ASTM D1238). *MI* refers to standard weight of 2.16 kg and *HLMI* to "High Load" melt index (frequently 10 kg or 21.6 kg). By manipulating the appropriate equations for pressure drop, shear stress and flow rate (Chapter 2), we have

$$power-law\ exponent: n = \frac{\log LL - \log HL}{\log MI - \log HLMI} \tag{5.2-4}$$

$$consistency\ index: m = \frac{8966.42 \times LL}{\left(\frac{1846.33}{\rho} \times MI\right)^n} \tag{5.2-5}$$

where LL is the standard load (usually 2.16 kg) and HL the high load (usually 10 kg or 21.6 kg). The same expressions apply for any two sets of loads and corresponding *MI* values. Of course, the melt indexer is no substitute for a rheometer, but it is the most frequently used instrument in industry. So, whatever rheological information can be obtained, it may be used for problem solving by doing calculations of pressure drop, shear stress and shear rate and eventually for deciding whether more accurate rheological measurements are necessary.

Occasionally, in the extrusion industry another low cost method is used for the determination of the power-exponent n. From the equations presented in Chapter 2 we note that the pressure drop is roughly proportional to the flow rate raised to exponent n, that is

$$\Delta P \sim Q^n \tag{5.2-6}$$

thus we will have

$$\frac{\Delta P_1}{\Delta P_2} = \left(\frac{\rho Q_1}{\rho Q_2}\right)^n \tag{5.2-7}$$

from which

$$n = \frac{\log \Delta P_1 - \log \Delta P_2}{\log(\rho Q_1) - \log(\rho Q_2)} \tag{5.2-8}$$

Thus, from two measurements of pressure drop versus flow rate in an industrial extrusion die, we can obtain the power-law exponent *n*. Best results can be obtained when the flow rates (kg/hr) are far apart and at the same temperature. Obviously, this is a very rough approximation, but it could be useful in the absence of more reliable rheological information (see Example 5.2-2). With heavily filled polymers, especially when particle size is large, it is difficult to make good measurements in rheological instruments having narrow gaps and this approximation might be one of the few options available (Polychronopoulos *et al.*, 2016).

Example E5.2-1

Given that *MI*=1 (for load 2.16 kg), *HLMI*=50 (for 10 kg) and melt density 766 kg/m^3, calculate *m* and *n.*

Solution

Using Eq. 5.2-4 we have

$$n = \frac{\log 2.16 - \log 10}{\log 1 - \log 50} \cong 0.39$$

and from Eq. 5.2-5

$$m' = \frac{8966.42 \times 2.16}{\left(\frac{1846.33}{766} \times 1\right)^{0.39}} = 13{,}742 \text{ Pa} \cdot \text{s}$$

The Rabinowitsch corrected (see Section 2.8, Eq. 2.8-14) consistency index *m* will then be

$$m = m'\left(\frac{4n}{3n+1}\right)^n = 13{,}742 \times \left(\frac{4 \times 0.39}{3 \times 0.39 + 1}\right)^{0.39} = 12082 \text{ Pa} \cdot \text{s}$$

Therefore, the Rabinowitsch (corrected) viscosity is

$$\eta = 12082\dot{\gamma}^{-0.61}$$

Let us now make an estimate of errors due to the entrance pressure loss that was not taken into account. The entrance pressure loss is expressed in terms of the Bagley correction (see section 3.6 in Chapter 3). Eq. 3.6-3 may be rewritten here as

$$\Delta p_{tot.} = 2\tau_w\left(\frac{L}{R} + e\right)$$

From some LDPE data by Laun (1983) *e*=8 approximately, corresponding to *HLMI*=50, thus we have

$$\Delta p_{tot.} = 2\tau_w\left(\frac{8}{2.095/2} + 8\right) = 2\tau_w(7.6 + 8)$$

Which means that the pressure drop due to entrance (elongational viscosity) is **slightly larger** (!) than the pressure drop due to the shear viscosity in the die. **This would result in a large error**. However, for linear polymers like HDPE, LLDPE and PP which are known to have smaller elongational viscosities than LDPE, the Bagley correction, expressed as an equivalent dimensionless capillary length e (White, 1990, Hristov and Vlachopoulos, 2007), is likely to be perhaps less than 2 and the error is acceptable. This example shows the limitations of the melt indexer as a rheological tool and of its usefulness for material specification purposes.

Example E5.2-2

In an extrusion plant the following pressure drop versus flow rate data were obtained

ΔP_1=12.58 MPa for output 80 kg/hr

ΔP_2=15. 92 MPa for output 140 kg/hr

Calculate the power-law exponent.

Solution

From Eq. 5.2-8 we have

$$n = \frac{\log 12.58 - \log 15.92}{\log 80 - \log 140} = 0.42$$

This indirect method can be used in the absence or any other viscosity information. We are missing, of course, the consistency index m. However, if these data were obtained from a die of simple geometry (like tube, slit die or convergent die), we could determine m using an equation from Chapter 2. For this approximate method to provide meaningful results, we must be very careful with temperature control. The assumption has been implicitly made, in the above calculations, that the temperature is the same in both 1 and 2 conditions.

5.3 Capillary Rheometer

It consists of a cylindrical heated reservoir where polymer pellets or powder are melted and subsequently forced to flow through a small diameter tube (capillary), as shown in Fig. 5.3-1. The plunger (piston) moves by means of an imposed pressure (constant stress) or at a fixed speed (constant shear rate). In fact, the melt indexer discussed in the previous section is some sort of a low-tech capillary viscometer, with the pressure imposed by the load. The dimensions of the capillary dies used at McMaster University's polymer processing laborato-

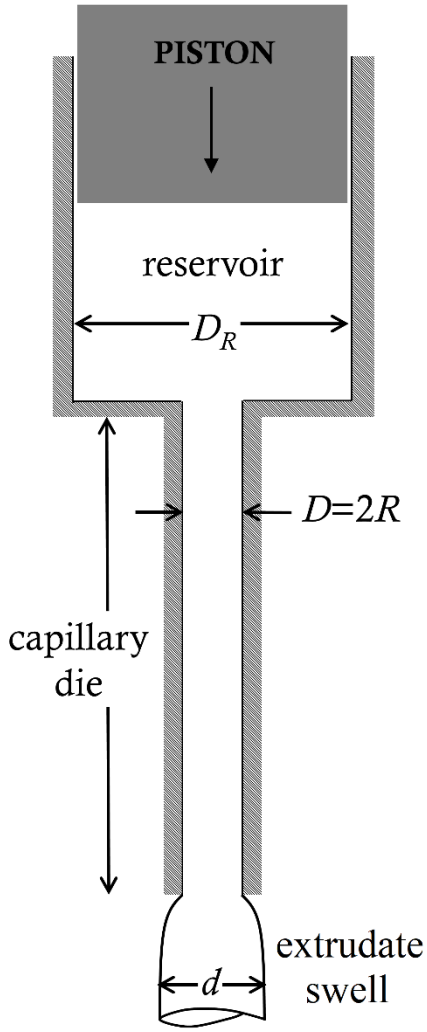

Dimensions of capillary dies at McMaster University		
Length (mm)	**Diameter (mm)**	**L/D**
8	1	8
16	1	16
24	1	24
32	1	32
16	1	16
24	1.5	16
32	2	16

Figure 5.3-1. Schematic representation of a capillary rheometer (figure not to scale). To the right: a table of the available capillary dies at McMaster University.

-ries are also given in Fig. 5.3-1. That is a constant shear rate rheometer. An older instrument had constant pressure imposed by a nitrogen gas cylinder.

Measurements are carried out at different piston speeds and the viscosity is obtained from the measured pressure drop ΔP and the measured volume flow rate Q, determined by the piston speed. In accordance with the equations of Chapter 2, the apparent shear rate (Newtonian) at the capillary wall is

$$\dot{\gamma}_{a,w} = \frac{4Q}{\pi R^3} \qquad \text{(apparent)} \tag{5.3-1}$$

and the corresponding apparent shear stress

$$\tau_w = \frac{\Delta P}{2(L/R)} \qquad \text{(apparent)} \tag{5.3-2}$$

The ratio $\tau_w/\dot{\gamma}_{a,w} = \eta_a$ is the apparent or nominal viscosity. To get the true shear rate for non-Newtonian fluids we must use the Rabinowitch correction equation which was derived in Section 2.8 that reads

$$\dot{\gamma}_{t,w} = \frac{4Q}{\pi R^3}\left(\frac{3}{4} + \frac{1}{4}\frac{d\ ln\ Q}{d\ ln\ \tau_w}\right) \tag{5.3-3}$$

and the **Rabinowitsch corrected viscosity** is

$$\eta = \frac{\tau_w}{\dot{\gamma}_{t,w}} \tag{5.3-4}$$

There is also another correction necessary, which was discussed in Section 3.6, because the measured (total, from the force on the piston) ΔP includes also the entrance pressure loss which is due to the elongational viscosity (Bagley correction). Modern viscometers are of double bore, the second die being of practically zero length (at McMaster's capillary rheometer the "zero" length die is actually 0.25D long). The zero length die measures only the entrance pressure loss which is subtracted from the long die pressure drop, i.e. $\Delta P_{cap.}=\Delta P_{total}-\Delta P_{entrance}$. Thus, the **Bagley corrected shear stress** is

$$\tau_{t,w} = \frac{\Delta P_{cap.}}{2(L/R)} \tag{5.3-5}$$

Thus the **true viscosity** is the ratio of the **Bagley corrected shear stress** to the **Rabinowitch corrected shear rate**

$$\eta_{true} = \frac{\tau_{t,w}}{\dot{\gamma}_{t,w}} \tag{5.3-6}$$

The entrance pressure loss is equivalent to the pressure drop caused by a few capillary diameters (usually from 1 to 5), depending on polymer and shear rate. Thus, if we were to use a very long capillary it would be negligible. However, flow of a highly viscous polymer through a very long capillary would cause a very high pressure drop. Let us assume a polymer having m=10,000 Pa·s, n=0.5 flowing through a capillary twice as long as the longest in Fig. 5.3-1, that is L=64 mm and D=1 mm. With the help of equations of Table 2.7-1 for wall shear rate $\dot{\gamma}_w$=1000 s^{-1}, we get pressure drop through the capillary $\Delta P\cong$80.92 MPa and adiabatic average temperature rise due to viscous dissipation (Eq. 2.12-4) at the exit $\Delta T\cong$40.46 C. Such a temperature rise would result in great uncertainty in temperature at which the viscosity is actually being measured. Problems associated with shear heating in capillary rheometry have been dealt with in the technical literature (Tzoganakis *et al.*, 1987, Laun, 2004).

The entrance correction is used for the estimation of elongational viscosity (Cogswell's method), as explained in Section 3.5

$$\eta_e = \eta \left[\frac{(n+1)\Delta P_{entrance}}{1.89\tau_w} \right]^2 \tag{5.3-7}$$

This method is not very accurate, but it is the only one available for elongational viscosity determination at high stretch rates.

Capillary dies are also used for measurement of wall slip velocity by the Mooney method (Dealy and Wissbrun, 1999) as explained in Section 2.13. This is done by plotting the apparent wall shear rates ($4Q/\pi R^3$) against the inverse of the radius ($1/R$) for capillaries of different R having the same L/R. In fact, three of the dies whose dimensions are given on Fig. 5.3-1 having diameter 1, 1.5 and 2mm are used for such measurements at McMaster University. Using the above dies Hristov and Vlachopoulos (2007) obtained the Mooney plots

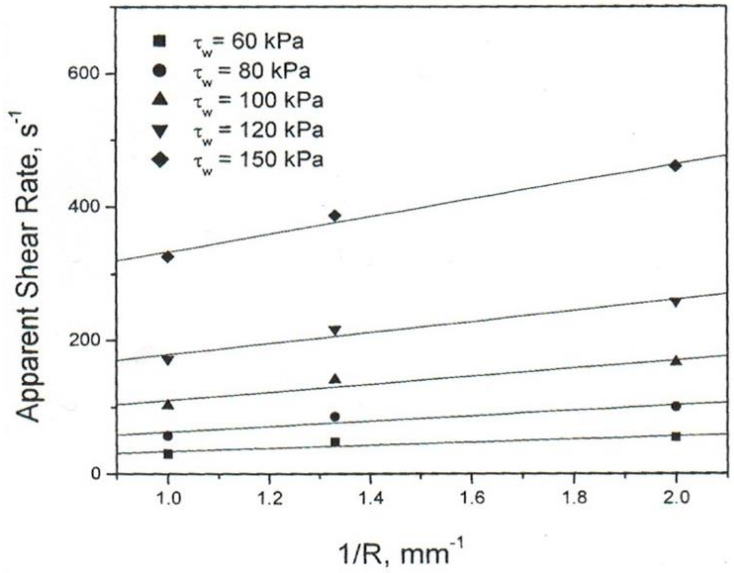

Figure 5.3-2. Mooney plots for a polypropylene with 50% by weight, filled with wood fibers, containing also a lubricant. Adapted from Hristov and Vlachopoulos (2007).

shown in Fig. 5.3-2 for a composite containing also a lubricant for the purpose of enhancing wall slip. To determine the slip velocity, we must use Eq. 2.13-6 which is rewritten here

$$\frac{4Q}{\pi R^3} = \dot{\gamma}_{app,s} + \frac{4V_s}{R} \tag{5.3-8}$$

The shear stress was determined from $\tau_w = \Delta P/(2L/R)$. The slope of each line is equal to $4V_s$ at that stress value. For example, for τ_w=150 kPa, we have (as best as we can read off the numbers): $4V_s$=(450-330)/(2-1)=120 and the slip velocity is V_s=30 mm/s. The same

calculation can be done for the other lines and eventually develop a correlation in the form (see also Section 2.13)

$$V_s = A\tau_w{}^{\beta} \tag{5.3-9}$$

Capillary rheometers are also used for measurement of **extrudate swell.** The diameter of solidified extrudate can easily be measured with the help of a micrometer. However, there are might appreciable errors: As the molten polymer exits from the die it thins under the action of its own weight (**sagging**). To reduce this error, it is advisable to cut the extrudate in short lengths of no more than 3 cm long and measure the diameter at about 1 cm from the leading edge. High crystallinity polymer extrudates exhibit significant differences in diameter when measured before or after **annealing** in a hot liquid bath (Vlachopoulos, 1981). The best way to measure extrudate swell is to extrude into a hot bath of silicone oil and capture images with the help of a laser beam. Buoyancy prevents sagging and with the high temperature in the bath, contraction of extrudate is avoided.

5.4 Rotational Rheometer in Steady Shear

There are two very useful instruments in this category: **cone-and-plate** and **parallel plate**. The coaxial (Couette) viscometer could be included, but it is not suitable for polymer melts due to loading/unloading difficulties and possibility of solidification.

Cone-and-plate instrument

A schematic of the cone-and-plate geometry is shown in Fig. 5.4-1a. The cone rotates with an angular velocity Ω and the torque on the plate M and the total thrust F_z is measured. The cone angle is very small (usually β<6°) so that we can intuitively regard the flow to be locally that between two parallel plates and the shear rate will be constant throughout the cone-plate gap (Bird *et al.*, 1987, Macosko, 1994). It can be shown that for very small angles the shear rate is given by the ratio of the angular velocity Ω (radians/s or degrees/s) to the cone angle

$$\dot{\gamma} = \frac{\Omega}{\beta} \tag{5.4-1}$$

It can further be shown that the shear stress is

$$\tau_{12} = \tau_{\varphi\theta} = \frac{3M}{2\pi R^3} \tag{5.4-2}$$

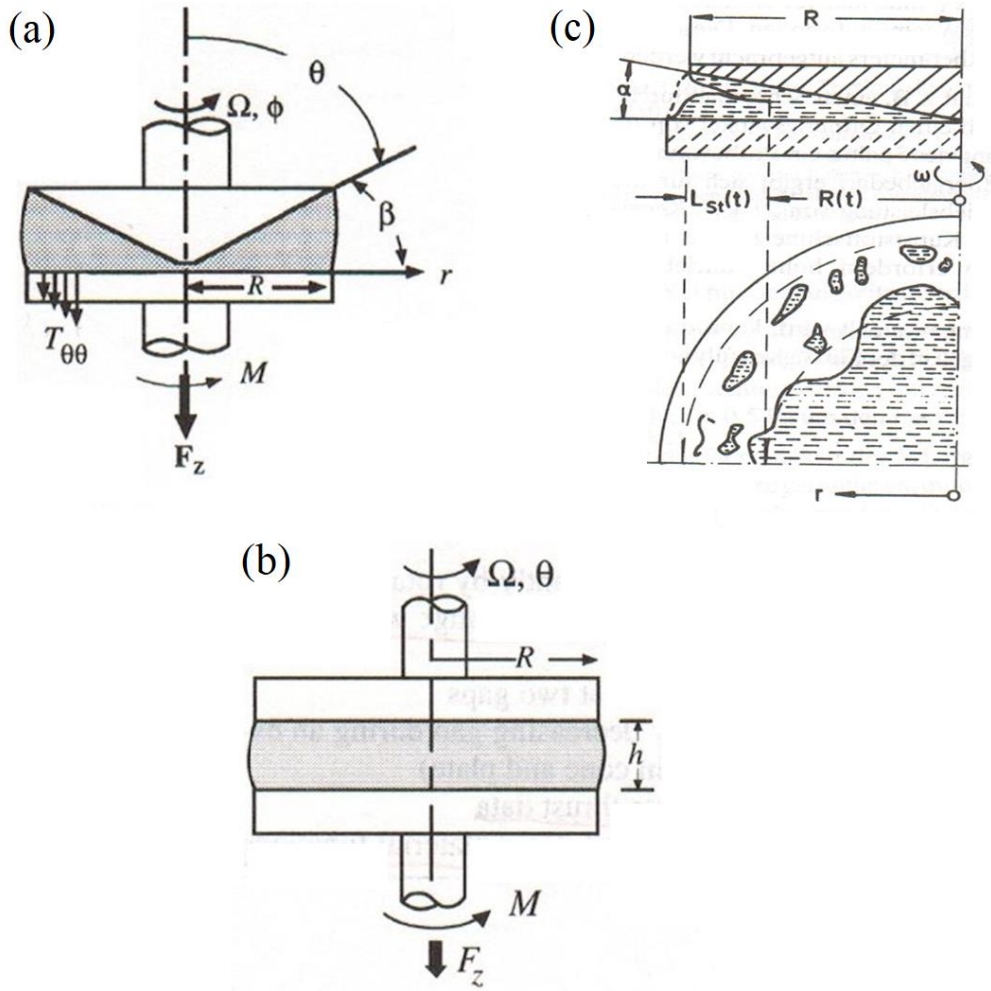

Figure 5.4-1. Schematic representation of (a) cone-and-plate and (b) parallel plate rheometers, adapted from Macosko (1994) and (c) edge instabilities adapted from Pahl *et al.* (1995). Similar edge instabilities also occur in the parallel plate rheometer.

and the viscosity

$$\eta = \frac{\tau_{12}}{\dot{\gamma}} = \frac{3M\beta}{2\pi R^3 \Omega} \tag{5.4-3}$$

and the first normal stress

$$N_1 = \frac{2F_z}{\pi R^2} \tag{5.4-4}$$

On some instruments it is also possible to measure the local pressure distribution from which N_2 can also be obtained.

There are three important assumptions associated with the derivation of the above equations: (i) the inertia forces are neglected, (ii) there are no secondary flows and (iii) the free surface is spherical. For highly viscous polymer melts, there are instabilities at the edges (as shown in Fig. 5.4-1c), which limit the usefulness of this instrument usually to shear rates

of less than 5 s^{-1}. Other problems may relate to eccentricity and misalignment, which can be serious due to the very small angles.

Parallel plate instrument

A schematic of the parallel plate geometry is shown in Fig. 5.4-1b. As with the cone-and-plate, the angular velocity Ω, torque M and total thrust F_z is measured. The difference is that the shear rate in the cone-and-plate is uniform throughout the gap, whereas in the parallel plate it varies linearly as a function of the radius r (zero at axis, maximum at the rim). By simplifying the equations of conservation of momentum in cylindrical coordinates the following expressions can be obtained (Bird *et al.*, 1987, Macosko, 1994)

$$\text{Shear rate:} \quad \dot{\gamma} = \frac{r\Omega}{h} \tag{5.4-5}$$

where h the gap between the plates. Also

$$\text{Shear rate at the edge (at } r = R\text{):} \quad \dot{\gamma}_R = \frac{R\Omega}{h} \tag{5.4-6}$$

The shear stress is calculated from the following equation

$$\tau_{12} = \tau_{\theta z} = \frac{\mathrm{M}}{2\pi R^3}\left[3 + \frac{d\ln M}{d\ln \dot{\gamma}_R}\right] \tag{5.4-7}$$

Thus, the viscosity is

$$\eta = \frac{\tau_{12}}{\dot{\gamma}_R} = \frac{Mh}{2\pi R^4 \Omega}\left[3 + \frac{d\ln M}{d\ln \dot{\gamma}_R}\right] \tag{5.4-8}$$

and the normal stress

$$N_1 - N_2 = \frac{F}{\pi R^2}\left[2 + \frac{d\ln F_z}{d\ln \dot{\gamma}_R}\right] \tag{5.4-9}$$

Instruments are usually capable of both cone-and-plate and parallel plate geometry. Thus after obtaining N_1 from cone-and-plate N_2 can be determined from Eq. 5.4-9.

In the parallel plate rheometer it is easier to load or unload solid polymer samples (disks) than the cone-and-plate, and it is the preferred geometry for measurements with polymer melts. Eccentricities and misalignments are less important, but it suffers with the same instability problems at the edges as the cone-and-plate (Fig. 5.4-1). In the parallel plate it is easily possible to change the shear rate by both changing the angular velocity Ω and the gap h. The range is wider than with the cone-and-plate geometry, but it is difficult to go above 10 s^{-1} with highly viscous polymer melts.

5.5 Oscillatory Shear Rheometry

Instead of applying rotational motion on cone-and-plate or parallel plate rheometers, we can also apply a sinusoidal deformation. The response will be a sinusoidal stress, which might be in phase or out-of-phase as shown in Fig. 5.5-1. We would like to keep the analysis as simple as possible, and we know that materials exhibit **linear** stress-strain behaviour at small deformations (Hooke's Law). So, this analysis is called **Small Amplitude Oscillatory Shear (SAOS)** or **linear viscoelasticity.**

Let us now elucidate the imposition of a sinusoidal strain and the corresponding stress response with the help of some simple mathematical models. The applied strain is a function of time in the following form

$$\gamma(t) = \gamma_o \sin(\omega t) \tag{5.5-1}$$

If the sample between the disks happens to be a Hookean solid (having the mechanical equivalent of a spring), the stress would be

$$\tau(t) = G\gamma(t) = G\gamma_o \sin(\omega t) = \tau_o \sin(\omega t) \tag{5.5-2}$$

where G the elastic modulus, γ_o is the strain amplitude, ω the frequency, t the time and τ_o is the stress amplitude. This means that the strain and stress are in-phase. The maximum of deformation (strain) and maximum of stress occur at the same time. If the sample between the disks happens to be a Newtonian liquid (having the mechanical equivalent of a dashpot), we have

$$\dot{\gamma}(t) = \omega\gamma_o \cos(\omega t) = \dot{\gamma}_o \cos(\omega t) \tag{5.5-3}$$

and the corresponding stress will be

$$\tau(t) = \eta\dot{\gamma}_o \cos(\omega t) = \eta\dot{\gamma}_o \sin(\omega t + \pi/2) = \tau_o \sin(\omega t + \pi/2) \tag{5.5-4}$$

where $\dot{\gamma}_o$ is the strain (shear) rate amplitude and η the viscosity. This means that strain and stress are 90° out-of-phase.

If the sample between the disks is a viscoelastic fluid then we intuitively expect a phase angle δ, between 0° and 90°

$$\tau(t) = \tau_o \sin(\omega t + \delta) \tag{5.5-5}$$

This response is customarily analyzed by decomposing the stress wave into two waves of the same frequency, one in-phase with the strain wave ($\sin(\omega t)$) and one 90° out-of-phase with this wave ($\cos(\omega t)$). Thus, we may write

$$\tau = \tau' + \tau'' = \tau_o' \sin(\omega t) + \tau_o'' \cos(\omega t) \tag{5.5-6}$$

This suggests the following definition of an in-phase modulus (therefore elastic)

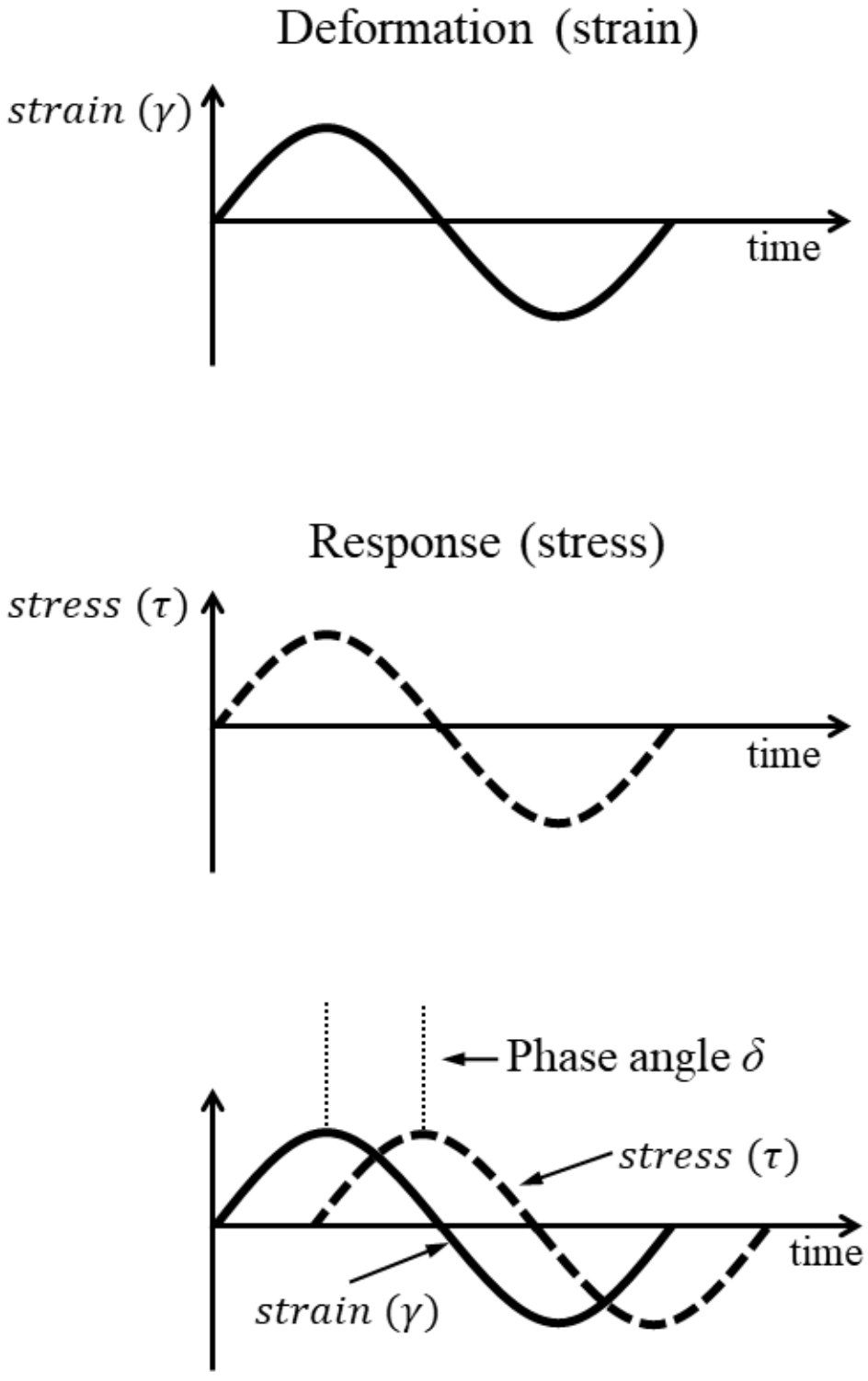

Figure 5.5-1. Schematic representation of oscillatory strain and stress response.

$$G' = \frac{\tau_o{}'}{\gamma_o} \tag{5.5-7}$$

and an out-of-phase modulus (therefore viscous)

$$G'' = \frac{\tau_o{}''}{\gamma_o} \tag{5.5-8}$$

where G' is referred to as **storage modulus** and G'' is referred to as **loss modulus**. With the help of trigonometry we can easily show that

$$\tan\delta = \frac{G''}{G'} \tag{5.5-9}$$

δ is occasionally referred to as the "mechanical loss angle" but more frequent reference is made to simply **tan-delta**, which is the ratio to the lost energy to the stored energy.

The magnitude of the complex modulus is simply

$$|\mathrm{G}^*| = (G'^2 + G''^2)^{1/2} = \frac{\tau_o}{\gamma_o} \tag{5.5-10}$$

We may further define the **dynamic viscosity**

$$\eta' = \frac{\tau_o{}''}{\dot{\gamma}_o} = \frac{G''}{\omega} \tag{5.5-11}$$

and

$$\eta'' = \frac{\tau_o{}'}{\dot{\gamma}_o} = \frac{G'}{\omega} \tag{5.5-12}$$

and the magnitude of the **complex viscosity**

$$|\eta^*| = (\eta'^2 + \eta''^2)^{1/2} = \left[\left(\frac{G'}{\omega}\right)^2 + \left(\frac{G''}{\omega}\right)^2\right] = \frac{1}{\omega}|G^*| \tag{5.5-13}$$

The parameters G', G'', η', η'' and $\tan\delta$ are material functions used for characterizing the behavior of polymeric materials. The question is "how do these relate to the most important property of polymer melts, that is the shear viscosity?".

There is no rigorous proof of any correlation between the dynamic data and the steady shear viscosity. But, there is a very useful empirical relationship, called the **Cox-Merz rule**, which is valid frequently up to high shear rates for most common polymers. This rule states that the steady state viscosity η is equal to the complex viscosity η^*

$$\eta(\dot{\gamma}) = |\eta^*(\omega)| \quad with \quad \dot{\gamma} = \omega \tag{5.5-14}$$

where $\dot{\gamma}$ is in s^{-1} and ω in rad/s. This is of great significance because it extends the range of useful measurements of rotational rheometers from a maximum of no more than 5 s^{-1} (in

steady shear) to over 10^3 s^{-1}. Using a parallel plate rheometer in dynamic (oscillatory) mode is the fastest and most accurate way to obtain viscosity data from perhaps less than 10^{-2} s^{-1} to 10^3 s^{-1}, thus covering the entire range of practically useful measurements. But, there is a caveat: The Cox-Merz rule may not hold for some polymers e.g. polymers with fillers, additives, reinforcements and polymers with unusual molecular architecture.

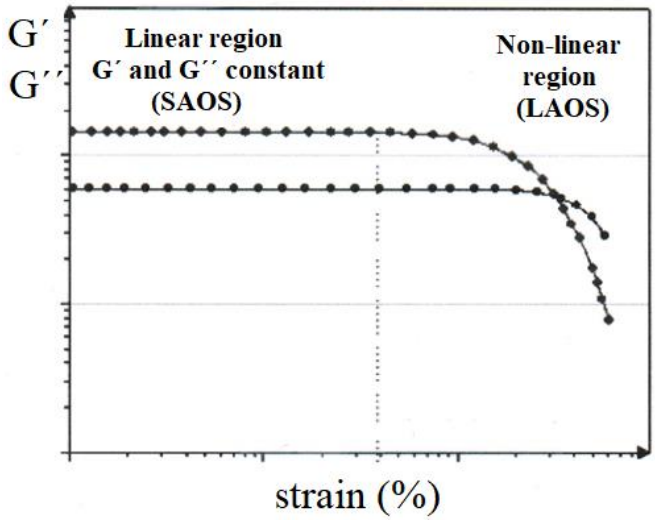

Figure 5.5-2. Strain sweep showing the small amplitude oscillatory shear (SAOS) and the large amplitude oscillatory shear (LAOS) regions.

The cone or the plate of the instrument, instead of rotating, oscillates around the axis and the electronics and software readily provide plots of G', G'', G^*, η' and η'' versus the frequency ω (rad/s). The first thing to do is the **strain (amplitude) sweep** to determine the linear region of viscoelasticity. The amplitude of the deformation (strain) is varied while the frequency is kept constant and G' and G'' are plotted as a function of strain (%) as shown in Fig. 5.5-2. In this figure we see that at low strain amplitude G' and G'' are constant. For polymer melts this usually happens at strain amplitudes γ_o of the order of 1 % to 10 %. G' describes the rigidity of the sample and G'' relates to the viscosity. If $G' > G''$ as shown in the figure, the sample behaves like a viscoelastic solid. If $G' < G''$ in the linear viscoelastic region, the sample behaves like a viscoelastic fluid. The definitions of the moduli are based on the assumption of sinusoidal input of strain and sinusoidal stress response. This happens only in the linear region. In the non-linear region the stress response is not sinusoidal and the analysis presented thus far is not valid. Other, more complex methods are needed for the study of **Large Amplitude Oscillatory Shear (LAOS)**. LAOS could perhaps provide new insights into the behaviour of polymer melts and it is currently of intense research interest (Hyun *et al.*,

2011). However, there have not been any analyses, which could be used for improving the understanding of polymer processing thus far, and consequently LAOS remains outside the scope of this book.

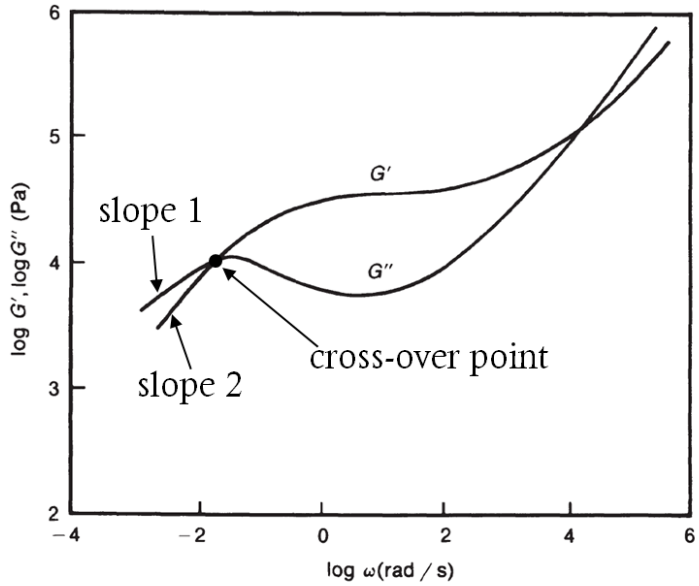

$$G'' \sim \omega \qquad G' \sim \omega^2$$

$$\omega \to 0$$

Figure 5.5-3. Storage and loss moduli as a function of frequency for a monodisperse polymer melt. In broader distribution polymers the minimum in the G'' curve would disappear. Adapted from Dealy and Wissbrun (1999).

During a **frequency sweep**, the frequency is varied while the amplitude of the deformation (strain) is kept constant. The storage and loss moduli against frequency are schematically shown in Fig. 5.5-3 for a polymer melt. At the limit of low frequency, the storage modulus G' is proportional to the frequency ω^2 and the loss modulus G'' is proportional to ω. The cross-over point G_c (where $G'=G''$) has been found to correlate approximately to the polydispersity index (M_w/M_n) of polypropylenes, by Zeichner and Patel (1981) and by Shang (1993)

$$PI = \frac{M_w}{M_n} = \frac{10^5}{G_c} \tag{5.5-15}$$

Caution has been pointed out by Shroff and Mavridis (1995) in using rheological data to infer molecular weight distribution.

The complex viscosity curve coincides with the steady shear viscosity (Cox-Merz rule) as shown in Fig. 5.5-4, for many commercially available polymers. However, for polymers

filled with fibers or particles the Cox-Merz rule is not valid, as shown for a HDPE filled with $CaCO_3$ in Fig. 5.5-5, adapted from Santi et al (2009).

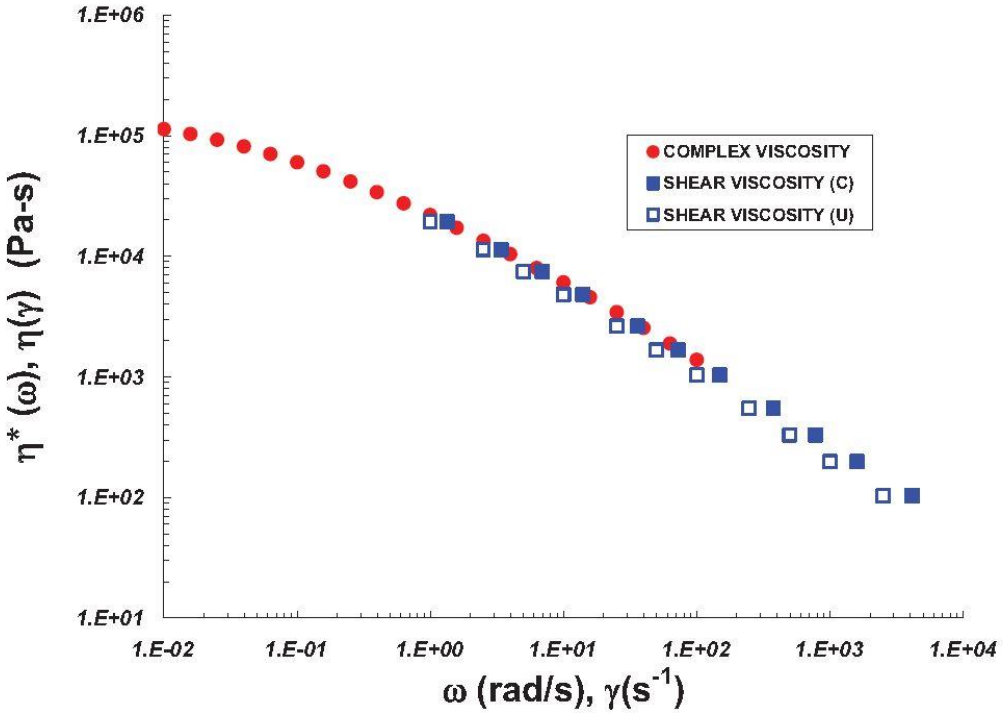

Figure 5.5-4. LDPE viscosity data at 150°C in accordance with Cox-Merz rule. C stands for Rabinowitsch corrected and U uncorrected. Adapted from Garcia-Franco (2013).

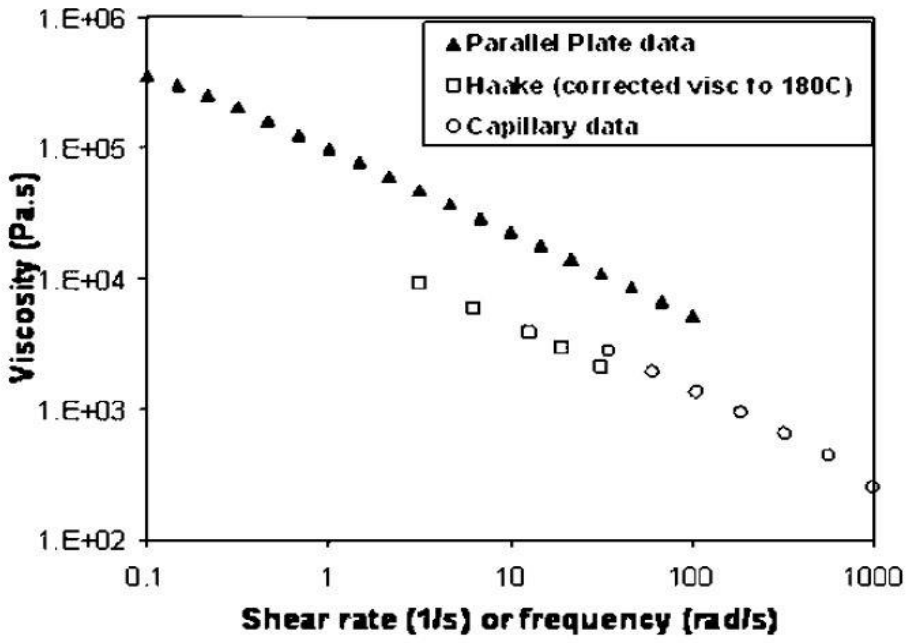

Figure 5.5-5. Complex viscosity (parallel plate) and steady shear viscosity data (capillary rheometer, Haake mixer) not obeying Cox-Merz rule (HDPE 40% filled with $CaCO_3$). Adapted from Santi *et al.* (2009).

There are also correlations between dynamic (G', G'') data and the first normal stress difference N_1. From theory in the limit of small frequencies and shear rates

$$N_1 = 2G' \tag{5.5-16}$$

For higher shear rates and frequencies Laun (1986) proposed an empirical correlation

$$N_1 = 2\frac{G'}{\omega^2}\left[1 + \left(\frac{G'}{G''}\right)^2\right]^{0.7} \tag{5.5-17}$$

This correlation seems to compare very well to with cone-and-plate measurements (Garcia-Franco, 2013) as shown in Fig. 5.5-6.

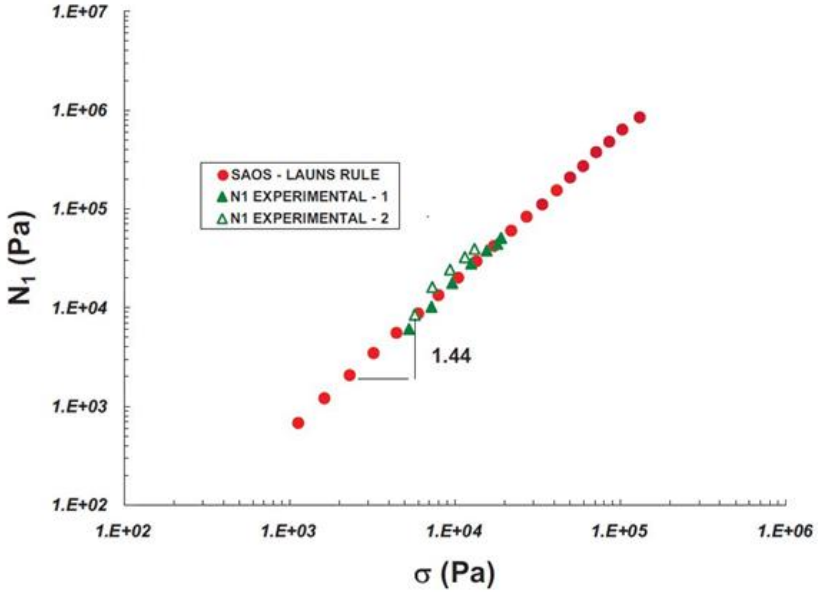

Figure 5.5-6. First normal stress difference versus shear stress obtained from Laun's correlation and cone-and-plate data. Adapted from Garcia-Franco (2013). Approximately N_1=0.034$\tau^{1.44}$.

From the above discussion it is obvious that from SAOS measurements of G' and G'' we further obtain other useful properties, like viscosity and first normal stress difference. Actually, there is much more information contained in G' and G'' plots, because the first parameter is related to the elastic and the second to the viscous nature of the polymer melt. Dealy and Wissbrun (1999) and Dealy and Wang (2013) provide numerous examples and detailed discussion on what information G', G'', tanδ, η' and η'' contain and how it can be examined and evaluated. Even just by visual inspection something can be inferred about the polymer molecular weight distribution. In the caption of Fig. 5.5-3 it is indicated that for broader molecular weight distribution, the minimum in the G' curve would disappear. Fig. 5.5-7 shows the G' and G'' for a HDPE melt filled with wood fibers at different loading levels

from Hristov *et al.* (2006). As the loading level is increased so does the G'. In the low frequency region for the neat HDPE, 25% and 50% loaded, $G'<G''$ which is indicative of liquid-like behavior. At 70% loading G' is close to being horizontal, indicative of solid-like behaviour and $G'>G''$ throughout the frequency range.

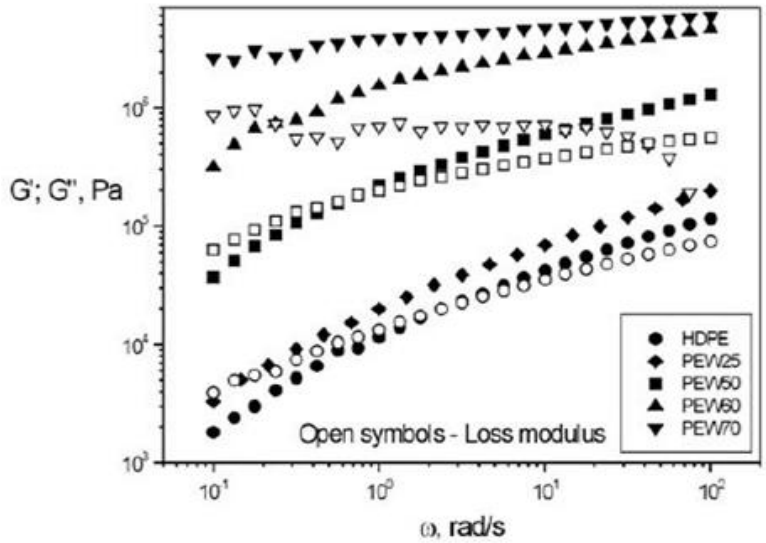

Figure 5.5-7. Storage (G') and loss (G'') moduli as a function of frequency. For clarity G'' for 25% and 60% loadings have been omitted. From Hristov *et al.* (2006).

Actually, just by plotting G' versus G'' some insights might be gained. These are known as **Cole-Cole plots** originally introduced for dielectric relaxations in 1941. Another plot is known as the **Van Gurp-Palmen:** the loss angle δ is plotted as a function of G^*. Dealy and Wang (2013) provide several references on interpretation of Cole-Cole and Van Gurp-Palmen plots. It must be pointed out that the essential information is embedded in the G' and G''. The various ways of plotting simply make it easier to extract some important information related to the material.

Numerous investigations for the analysis of G' and G'' data have resulted in sophisticated mathematical methods. Usually, the analysis starts from the Maxwell Model discussed in Chapter 3

$$\tau + \frac{\eta}{G}\dot{\tau} = \eta\dot{\gamma} \tag{5.5-18}$$

where G is the elastic modulus and η the viscosity. The ratio η/G is the relaxation time λ

$$\tau + \lambda\dot{\tau} = \eta\dot{\gamma} \tag{5.5-19}$$

Introducing a sinusoidal γ and τ, as earlier on this section, and using complex variables mathematics, we end up with

$$G'(\omega) = \frac{G\lambda}{(1+\lambda^2\omega^2)} \tag{5.5-20}$$

$$G''(\omega) = \frac{G\lambda^2\omega}{(1+\lambda^2\omega^2)} \tag{5.5-21}$$

However, if we try to fit any of the G' or G'' curves of this section, we quickly realize that just one pair of parameters G and λ is insufficient. For better fitting we need the so-called Generalized Maxwell Fluid (GNF) which has a mechanical equivalent of several Maxwell elements in parallel as illustrated schematically in Fig. 5.5-8. Then we end up with

$$G'(\omega) = \sum_i \frac{G_i\lambda_i}{\left(1+{\lambda_i}^2\omega^2\right)} \tag{5.5-22}$$

$$G''(\omega) = \sum_i \frac{G_i{\lambda_i}^2\omega}{\left(1+{\lambda_i}^2\omega^2\right)} \tag{5.5-23}$$

About 8-12 pairs of G and λ are sufficient for fitting the G' and G'' curves by some sort of nonlinear regression method (e.g. Least Squares). These parameter pairs comprise the "discrete relaxation spectrum". They are curve fitting parameters which are useful for calculating one rheological property from another.

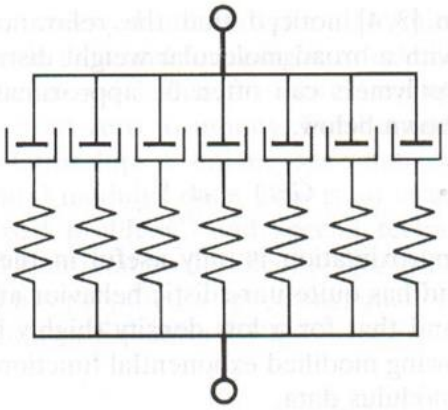

Figure 5.5-8. Schematic illustration of the mechanical analog of Generalized Maxwell model.

Of particular interest in polymer processing is the calculation of zero shear viscosity η_o and the corresponding characteristic (longest relaxation) time $\lambda=\eta_o/G$, from

$$\eta_o = \sum_i G_i\lambda_i \tag{5.5-24}$$

$$\lambda = \sum_i G_i{\lambda_i}^2 \Big/ \sum_i G_i\lambda_\iota \tag{5.5-25}$$

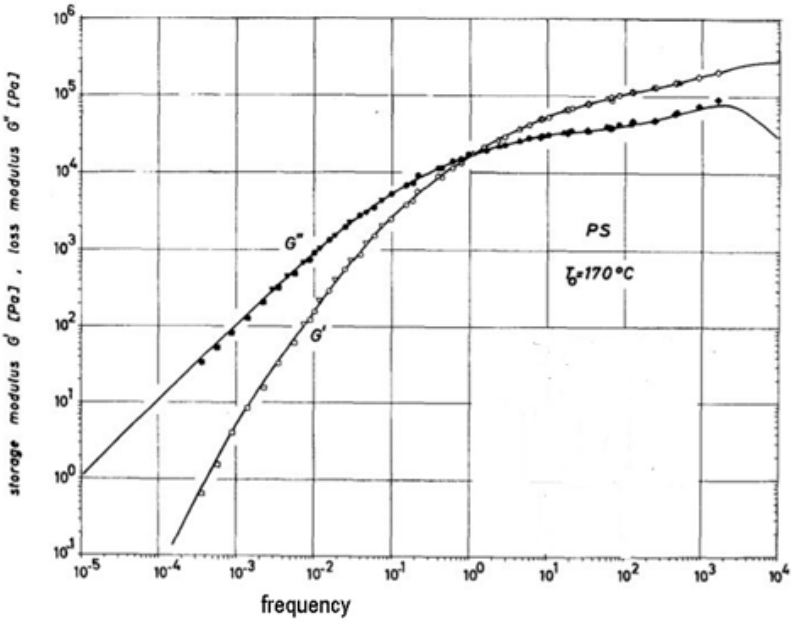

Figure 5.5-9. Polystyrene G' and G'' data at 170°C. Adapted from Laun *et al.* (1979).

Table 5.5-1. **Relaxation times λ_i and moduli G_i for fitting the G' and G'' data of Fig. 5.5-9.**		
i	**λ_i in s**	**G_i in Pa**
1	500	1.44×10^{1}
2	83	1.98×10^{2}
3	15	2.52×10^{3}
4	2.8	9.60×10^{3}
5	0.5	2.46×10^{4}
6	0.083	3.98×10^{4}
7	0.015	3.72×10^{4}
8	0.0028	4.42×10^{4}
9	0.0005	1.36×10^{5}

An example of fitting some polystyrene data at 170°C of Fig. 5.5-9 is shown in Table 5.5-1. From the data of Table 5.5, using equations Eq. 5.5-24 and Eq. 5.5-25 we have

$$\eta_o = \sum_i G_i\lambda_i = 104667.2 \text{ Pa}\cdot\text{s}$$

$$\lambda = \frac{\sum_i G_i{\lambda_i}^2}{\sum_i G_i\lambda_i} = 53.62 \text{ s}$$

There is actually commercially available software (IRIS)) for doing this and much more. From G' and G'' data with the help of such software a lot of information can be obtained including viscosity (with the Carreau-Yasuda parameters), tan-delta, elongational viscosity and even molecular weight distribution. A caveat should be added: determination of molecular weight

distribution from rheological data is a mathematically "ill- posed problem" and the results for various polymers have varying degrees of success, due to short or long chain branching and other aspects of the macromolecular architecture.

5.6 Determination of a Characteristic Relaxation Time

In Chapter 3 we introduced an important parameter of viscoelastic analysis: relaxation time. We first defined a relaxation time in connection with the Maxwell model, as the time required for the stresses to relax after a sudden imposition of strain

$$\lambda = \frac{\eta}{G} \tag{5.6-1}$$

where η the viscosity and G the elastic modulus. Further analysis for simple shear flow resulted in Eq. 3.7-20, which can be rewritten as

$$\lambda = \frac{N_1}{2\eta\dot{\gamma}^2} \tag{5.6-2}$$

In Section 3.9 we were talking about a characteristic relaxation time in the definition of Deborah and Weissenberg numbers, which express the ratio of elastic forces to viscous forces. Then, we presented some results in Fig. 3.9-3 of stress relaxation after cessation of shearing. In the Section 5.5 we concluded that several relaxation times are needed to describe G' and G''. Frequently, in industry, correlations of properties are developed involving the time constant obtained from fitting viscosity data to Carreau-Yasuda or Cross models as shown in Fig. 5.6-1. It is unclear, from all this, which is the most characteristic relaxation time of a polymer melt and how could it be measured.

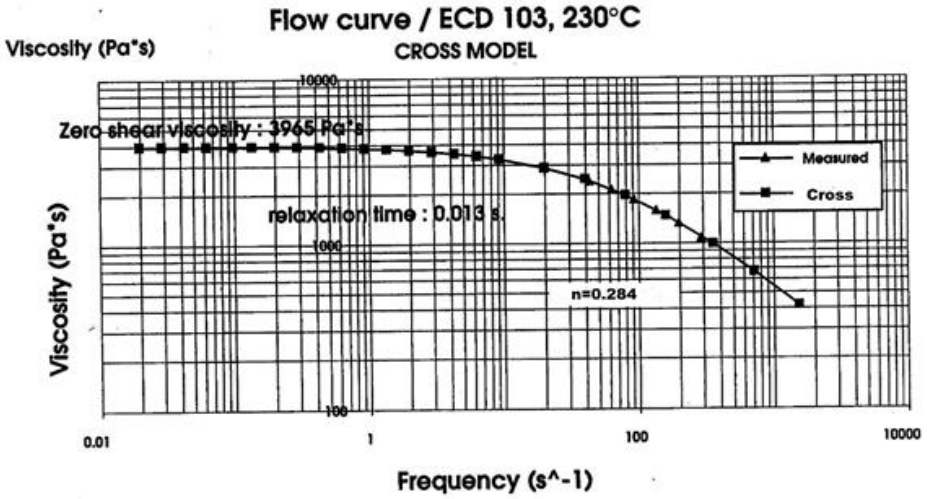

Figure 5.6-1. Relaxation time in the Cross model $\eta = 1/[1 + (\lambda\dot{\gamma})^{1-n}]$ is simply the inverse of the shear rate (which is the same as frequency) at $\eta=\eta_o/2$. Adapted from Ohlsson (1996).

The shear stress relaxation experiment after cessation of shear of Fig. 3.9-3 appears as a good method for differentiation of polymers having different relaxation times. In fact, not only the shear stress but also the first normal stress difference N_1 relaxes, as shown in Fig. 5.6-2. However, sudden cessation of shearing (or sudden imposition) depends a lot on the response of both the instrument (noise) and on the material. It is not a common technique and there are relatively few such experimental data available in the open literature. The most common and most accurate method to study the relaxation behavior of polymer melts is by small amplitude oscillatory shear (SAOS).

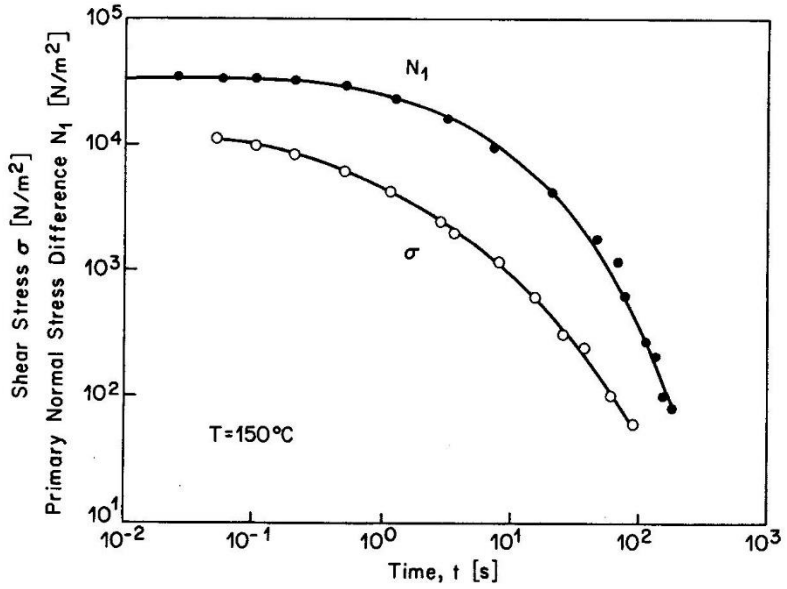

Figure 5.6-2. Shear stress and first (primary) normal stress difference relaxation after cessation of steady-state shearing. Adapted from Laun (1978). The shape of the curves is different from Fig. 3.9-3 because of the logarithmic scale on the vertical axis.

In connection with the measurements of Fig. 5.5-9 we presented relaxation times λ_i and moduli G_i pairs in Table 5.5-1. These are simply curve fitting parameters without any physical meaning. They are useful in obtaining from G' and G'' data other quantities like viscosity, tan-delta etc. Let's take another look at the sketch of G' and G'' as a function of frequency, as shown in Fig. 5.6-3 and at the same time think about the meaning of the Deborah number

$$De = \frac{\text{characteristic material time}}{\text{characteristic process time}} \tag{5.6-3}$$

At very low frequencies the process time is very long and the polymer behaves like a viscous fluid. At very high frequencies the time is very short and the polymer behaves like an elastic

solid. At intermediate frequencies we call the behavior rubbery in Fig. 5.6-3 because the (near) plateau in G' is an indication that there is little relaxation occurring due to the chain entanglements, which act similarly to the cross-links in rubber. For a perfect rubber G' would be constant and G'' would be zero. Thus, from this behavior we can choose two frequencies for determination of physically meaningful characteristic times: in the limit of ω approaching zero (corresponds to zero shear viscosity) and the crossover point where the viscous polymer becomes rubbery.

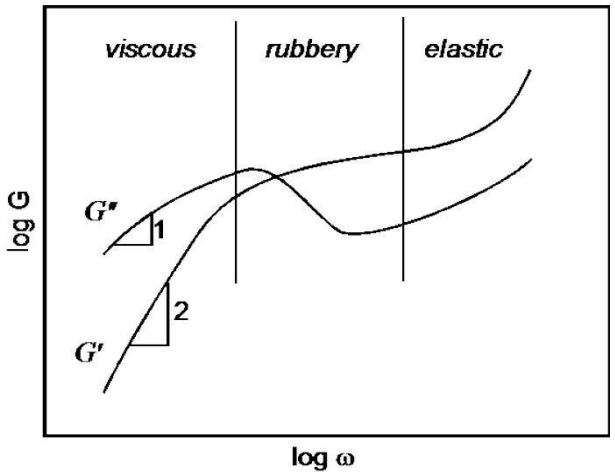

Figure 5.6-3. Typical results of G′ and G′′ as function of frequency.

We have already given an equation (Eq. 5.5-23) for calculating λ_o but let's look at another way of calculating it: In the zero limit of frequency and viscosity, $N_1=2G'$ thus from Eq. 5.6-2 we have

$$\lambda_o = \frac{2G'}{2\eta\omega^2} \tag{5.6-4}$$

We may then replace η with $\eta'=G''/\omega$ and then

$$\lambda_o = \frac{G'}{G''\omega} \tag{5.6-5}$$

Using Table 5.5 associated with Fig. 5.5-9 we calculated λ_o= 53.62 s. Let's see how close we can get by reading, as best as we can, the data of Fig. 5.5-9. Because extrapolation on a logarithmic plot is hazardous, we will use as zero frequency 10^{-3}. We roughly have

$$\lambda_o = \frac{G'}{G''\omega} = \frac{5}{10^2 \times 10^{-3}} = 50 \text{ s}$$

which is close to the previous estimate from the G_i, λ_i summation.

Another characteristic time would be the inverse of frequency at the crossover point which appears roughly to be 1 s. Of course, more accurate values than visual inspection could be obtained from a sophisticated software package like IRIS.

From the two characteristic times (longest and reciprocal of frequency at crossover) which one is better to use? The reciprocal of frequency at the crossover point has significant meaning. It is where $G'=G''$ and the storage modulus appears to approach a plateau, which implies rubber-like behavior. In property correlation the zero shear viscosity does account for

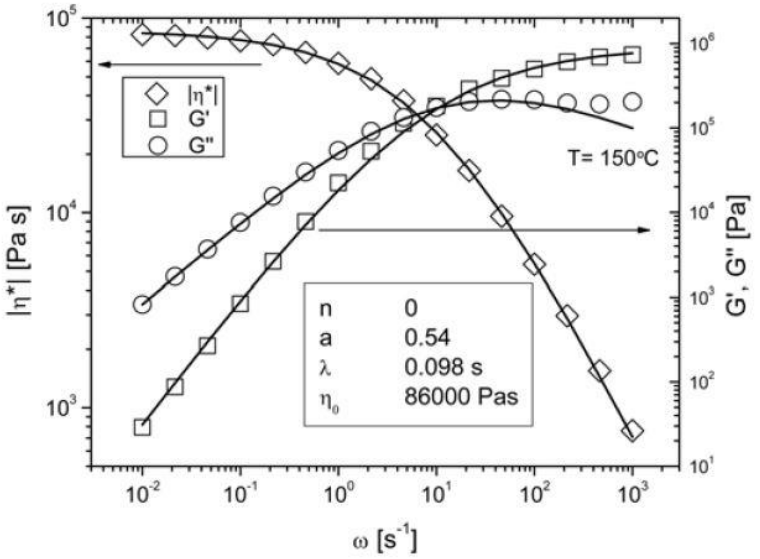

Figure 5.6-4. Viscosity, moduli curves for a LLDPE and Carreau-Yasuda viscosity model parameters. Adapted from Stadler and Mahmoudi (2011).

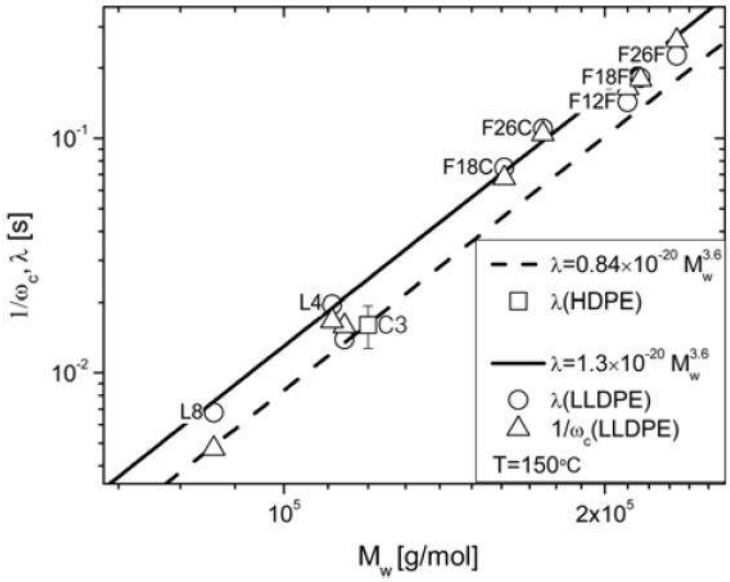

Figure 5.6-5. Relaxation time in the Carreau-Yasuda model and reciprocal of frequency as a function of molecular weight M_w. Adapted from Stadler and Mahmoudi (2011).

the molecular relaxation processes are near zero shear (or frequency), while the crossover point is related to the start of elastic behavior. It has been observed that the crossover relaxation time is close to the relaxation time in the Carreau-Yasuda viscosity model. This is shown in Fig. 5.6-4 and Fig. 5.6-5.

5.7 Melt Strength and Elongational Viscosity

Elongational (or extensional) viscosity is the resistance to stretching of a liquid. For Newtonian fluids Trouton's relation is valid (Section 3.3)

$$\frac{\eta_e}{\eta} = 3 \tag{5.7-1}$$

that is the elongational viscosity is three times the shear viscosity. For polymer melts the Trouton relation is valid at very low stretch and shear rates, but the ratio can exceed 100 and for some polymer solutions it can exceed 1000 at high rates.

In Fig. 5.7-1 it can be seen that the elongational viscosity of LDPE (branched) is higher that that of HDPE (linear) as expected. Due to long chain branching, LDPE is stiffer in stretching than HDPE. Stretching is involved in several polymer processing operations, like fiber spinning, blown film extrusion, flat film extrusion, blow molding, thermoforming and production of foamed plastics.

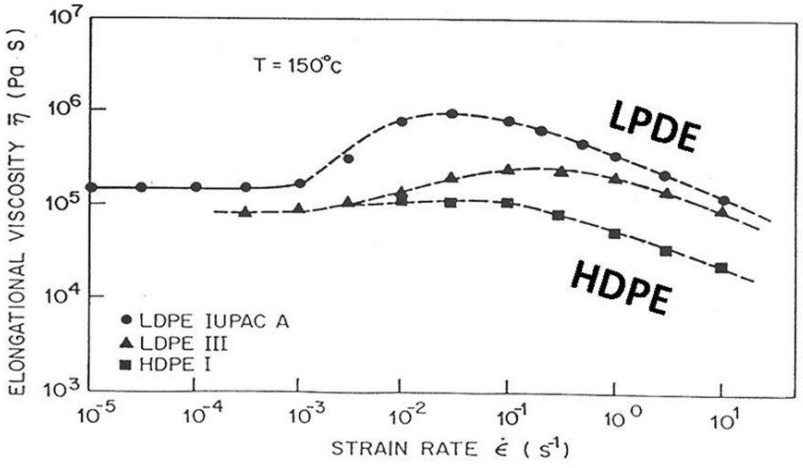

Figure 5.7-1. Steady-state elongational viscosities for three polyethylene melts as a function of extensional strain rate. Adapted from Pahl *et al.* (1995).

Melt strength is the most widely used test in industry for assessing the resistance to stretching of polymer melts. It is the force required to break a polymer extrudate emerging from a capillary rheometer under the influence of two rotating rolls, as shown in Fig. 5.7-2,

according to Laun and Schuch (1989). It can be seen that the melt strength decreases as the temperature increases, while the draw down speed increases. The draw down speed is a measure of **drawability**, which determines the ability of polymer melt to be drawn down to thin gages. Linear polyolefins such as LLDPE, HDPE and PP (especially) have poor melt strength, but they can also produce very thin films under proper processing conditions

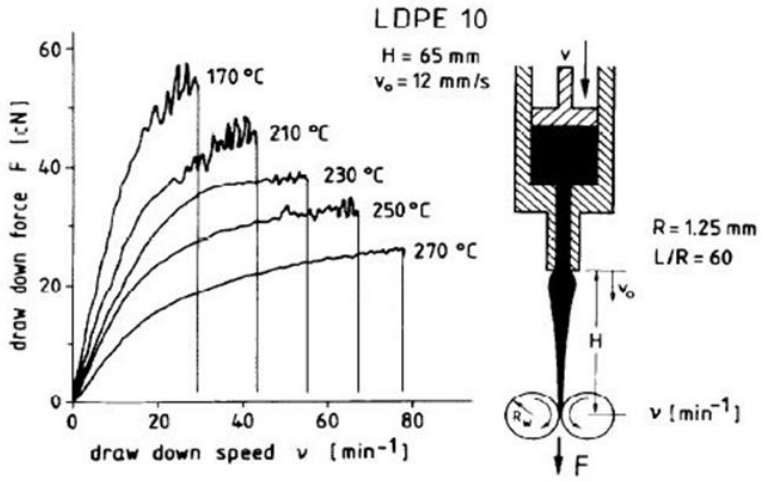

Figure 5.7-2. Melt strength test using the Goettfert Rheotens attached to a capillary rheometer, of a low density polyethylene. From Laun and Schuch (1989).

The melt strength/drawability test is not an accurate rheological measure because the extruded melt is cooled at room temperature and the stretching is also influenced by shearing in the capillary. It is used widely in industry because it resembles the processing conditions for the production of fibers and films. Melt strength is frequently used to assess processability of polymer resins as shown in Fig. 5.7-3.

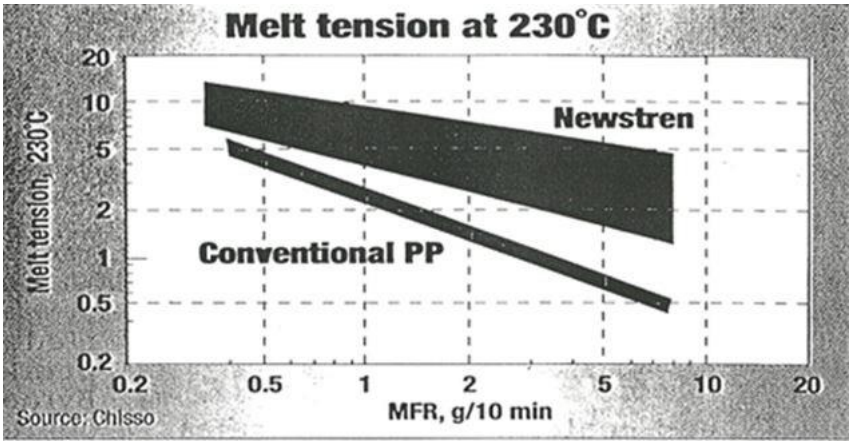

Figure 5.7-3. In was reported (Mod. Plast, Oct.1999, p.22) that CHISSO (Japan) has achieved increased melt tension (melt strength of their Newstren) by introducing long chain branching in the polypropylene chain, which allows the production of large thermoformed and blow molded parts (not possible with conventional (low melt strength) PP).

Elongational viscosity measurements are difficult, due to the requirement of stretching a molten polymer sample, under isothermal conditions of the desired thickness, free of any residual stresses resulting from the preparation of the sample itself. The first such instrument was designed by Meissner (1971) at BASF in Germany. The cylindrical sample is stretched by a pair of gear-like rotors, floating on the surface of an oil bath, as shown schematically in Fig. 5.7-4.

Figure 5.7-4. Schematic of the Meissner (BASF) rheometer.

The Meissner (BASF) extensional rheometer was capable for providing some accurate useful measurements of elongational viscosity, but it was not suitable for routine measurements. Several other instruments were designed, built and marketed, but without much technical or commercial success. After the development of the SER extensional rheometer (Sentmanat, 2004 Xpansion Instruments) elongational viscosity measurements (Sentmanat *et al.*, 2005) are possible for routine laboratory work. SER is a fixture to standard

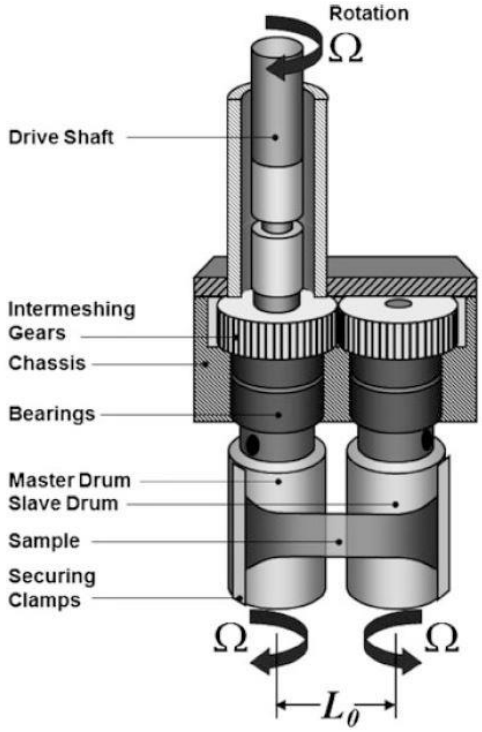

Figure 5.7-5. Sentmanat extensional rheometer (SER), which is a fixture to standard rotational instruments.

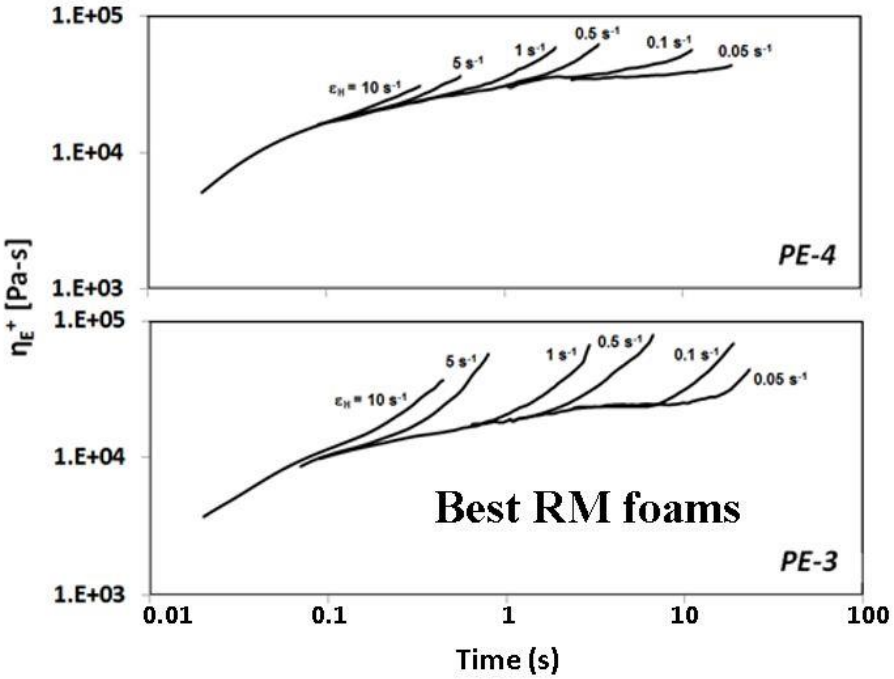

Figure 5.7-6. Extensional stress growth coefficient at various strain rates as a function of time. PE-3 is more strain hardening than PE-4 and some other PE samples not shown. Adapted from Emami *et al.* (2014).

rotational rheometers. Two drums are rotated and the force is calculated from the torque (Fig. 5.7-5). The results are obtained in the form of the stress growth coefficient, which is the ratio of the tensile stress σ_E to the stretch rate $\dot{\varepsilon}$

$$\eta_E{}^+ = \frac{\sigma_E}{\dot{\varepsilon}} \tag{5.7-2}$$

Emami et al (2014) evaluated several grades of PE resins and concluded that resin PE-3 (Fig. 5.7-6) which had the highest strain hardening characteristics was also the most suitable for rotational foam molding. This conclusion was corroborated with actual rotomolding (RM) experiments in the laboratory and pilot scale. High resistance to stretching favors the production of more stable bubbles in foaming, which really involves biaxial stretching.

5.8 Torque Rheometers

They are called rheometers, but they really are batch mixers. They consist of a mixing chamber with two counter-rotating blades similar to those shown in Fig. 5.8-1. They are used mostly for evaluating compounding of polymers with additives and fillers. The torque required for rotating the blades is related to viscosity. Bousmina *et al.* (1999) developed a method for converting torque and speed of rotation into viscosity measurements. They used

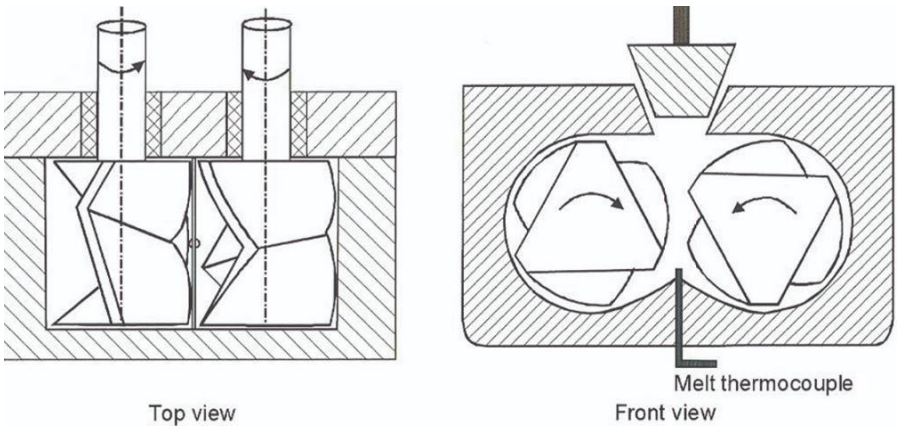

Figure 5.8-1. Sketch of a typical torque rheometer (batch mixer).

a Couette analogy in which each mixing chamber was replaced by a cylinder rotating inside another larger cylinder. An expression for an effective radius of the mixer was obtained for the power-law viscosity model. It was found that the effective internal radius varies only slightly with power-law exponent n, and from this fact a calibration procedure can be performed using a Newtonian fluid or any other well-characterized power-law fluid, for which the consistency m and exponent n are known. This method was used by Santi *et al.* (2009) for the Haake (mixer) data reported in Fig. 5.5-5.

5.9 Temperature and Pressure Dependence of Viscosity

As the temperature supplied to a polymer increases the molecular motions become more rapid and the viscosity of the melt decreases significantly. However, other properties, like the tensile modulus of a solid specimen, are less sensitive. Viscosity dependence on temperature is frequently expressed in a simple exponential form

$$\eta = \eta_{\text{ref}} \exp[-b(T - T_{\text{ref}})] \tag{5.9-1}$$

or, for the power-law model, the consistency coefficient

$$m = m_{\text{ref}} \exp[-b(T - T_{\text{ref}})] \tag{5.9-2}$$

while the exponent n is virtually independent of temperature. η_{ref} is the reference viscosity at T_{ref} and b the temperature sensitivity coefficient with typical values for various polymers given in Table 5.9, together with some typical values of the corresponding power-law exponents. Of course, these values are not meant to be a replacement for good measurements, but rather for rough estimates ("ballpark" in North American parlance). For $T–T_{ref}$ = 10°C (18°F) and b = 0.015 (e.g. for HDPE), the above expression gives a decrease in viscosity (or m) of 14% (for a 10°C temperature increase). Branched polyethylene (LDPE) is more sensitive to

temperature, having b=0.03, which gives a viscosity decrease of 25% for a 10°C temperature rise.

Table 5.9-1. **Typical values of the power-law exponent *n* and the temperature coefficient *b*.**		
Polymer	**Power-law exponent *n***	**Temperature Coefficient *b* (C^{-1})**
HDPE	0.45	0.015
LDPE	0.35	0.03
LLDPE	0.60	0.015
PP	0.35	0.015
PVC (rigid)	0.30	0.10
PS	0.30	0.05
PMMA	0.25	0.10
PET	0.65	0.03
ABS	0.25	0.10
NYLON 6,6	0.75	0.025
PC	0.75	0.04

The simple exponential expression is the preferred model in extrusion flow analysis, but in injection molding and in polymer physics the Arrhenius expression is used

$$\eta = \eta(T_o)\exp\left[\frac{E}{R}\left(\frac{1}{T}-\frac{1}{T_o}\right)\right] \tag{5.9-3}$$

where E activation energy and R=1.987 cal/mol-K =8.314 J/mol-K the gas constant. Typical values for E are 6 kcal/mol linear PE, 12 kcal/mol branched PE, 85kcal/mol for PC and PVC. The Arrhenius expression is valid over a wider range than simple exponential. Good for T_g+100°C and up (T_g is glass transition temperature). Closer to T_g the WLF equation is used

$$log\frac{\eta}{\eta_g} = \frac{-C_1(T-T_g)}{C_2+(T-T_g)} \tag{5.9-4}$$

where reference temperature T_g is the glass transition temperature and the "universal constants" C_1=17.44 and C_2=51.6 K. Actually C_1 and C_2 vary a lot for various polymers (Ferry, 1980). The above expression is based on the free volume theory, according to which polymer chain segments jump into unoccupied sites or holes.

Pressure has similar effect to that of temperature, but opposite in sign. As the pressure increases the molecular mobility decreases and consequently the viscosity increases. The dependence is usually expressed in the form

$$\eta_p = \eta_{ref} \exp\left[\beta\left(P - P_{ref}\right)\right] \tag{5.9-5}$$

The value of β is of the order of 10^{-8} Pa^{-1}. There are limited data available on pressure dependence of viscosity, in the open literature. Cogswell (1996) made a suggestion of a pressure dependence by an equivalent temperature change for a very rough estimate. Some results would indicate that applying 10 MPa is equivalent to decreasing the temperature by about 5°C.

Frequently, it is assumed that the flow is incompressible, and in fact this is almost a universal assumption in analyzing screw extruders and dies. In most extrusion operations it is unlikely to have pressure build-up of more than 50 MPa in the melt conveying zone, and pressure dependence is seldom considered in any calculations. However, in injection molding pressure can reach 200 MPa, and pressure dependence of viscosity is frequently taken into consideration (Volpe and Pantani, 2018).

Bibliography

Bird R.B., Armstrong R.C. and Hassager O., *Dynamics of Polymeric Liquids. Vol 1: Fluid Mechanics*, Wiley (1987)

Bousmina M., Ait-Kadi A. and Faisant J.B., Determination of Shear Rate and Viscosity from Batch Mixer Data, J. Rheol., 43, 415 (1999)

Cogswell F.N., *Polymer Melt Rheology*, Woodhead Publishing Limited (1996)

Dealy J.M. and Wissbrun K.F., *Melt Rheology and its Role in Plastics Processing*, Kluwer (1999)

Dealy J.M. and Wang J., *Melt Rheology and Its Applications in the Plastics Industry*, 2nd Ed., Springer (2013)

Emami M., Thompson M.R. and Vlachopoulos J., Experimental and Numerical Studies on Bubble Dynamics in Nonpressurized Foaming Systems, Polym. Eng. Sci., 54 (8), 1947 (2014)

Ferry J.D., *Viscoelastic Properties of Polymers*, Wiley (1980)

Garcia-Franco C.A., A Note on the Elasticity of Polymer Melts Described by Primary Normal Stress Difference (N1), Macromol. Symp., 325-326 (1), 184 (2013)

Hristov V., Takács E. and Vlachopoulos J., Surface Tearing and Wall Slip Phenomena in Extrusion of Highly Filled HDPE/Wood Flour Composites, Polym. Eng. Sci., 46 (9), 1204 (2006)

Hristov V. and Vlachopoulos J., Thermoplastic Silicone Elastomer Lubricant in Extrusion of Polypropylene Wood Flour Composites, Adv. Polym. Tech., 26, 100 (2007)

Hristov V. and Vlachopoulos J., A Study of Entrance Pressure Loss in Filled Polymer Melts, Appl. Rheol., 17, 57191-1 (2007)

Hyun K., Wilhem M., Klein C.O., Cho K.S., Nam J.G., Ahn K.H., Lee S.J., Eqoldt R.H. and McKinley G.H., A Review of Nonlinear Oscillatory Shear Tests: Analysis and Application of Large Amplitude Oscillatory Shear (LAOS), Progr. Polym. Sci., 36, 1697 (2011)

IRIS DEVELOPMENT (Prof. H. H. Winter, U. Massachusetts, Amherst, MA), 14 Elm Street, Amherst, MA 01002-2007, USA

Laun H.M., Description of the Non—Linear Shear Behavior of a Low Density Polyethylene Melt by means of an Experimentally Determined Strain Dependent Memory Function, Rheol. Acta, 17, 1 (1978)

Laun H.M., Wagner M.H. and Janeschitz-Kriegl H., Model Analysis of Nonlinear Viscoelastic Behavior by Use of a Single Integral Constitutive Equation: Stress and Birefringence of a Polystyrene Melt in Intermittent Shear Flows, Rheol. Acta, 18 (5), 615 (1979)

Laun H.M., Polymer Melt Rheology with a Slit Die, Rheol. Acta, 22 (2), 171 (1983)

Laun H.M., Prediction of Elastic Strains of Polymer Melts in Shear and Elognation, J. Rheol., 30, 459 (1986)

Laun H.M. and Schuch H., Transient Elognational Viscosities and Drawability of Polymer Melts, J. Rheol., 33 (1), 119 (1989)

Laun H.M., Capillary Rheometry for Polymer Melts Revisited, Rheol. Acta, 43, 509 (2004)

Macosko C.W., *Rheology Principles, Measurements, and Applications*, Wiley (1994)

Meissner J., Dehnungsverhalten von Polyaethylen Schmelzen, Rheol. Acta., 10, 230 (1971)

Morrison F.A., *Understanding Rheology*, Oxford University Press (2001)

Ohlsson S., Blown Film Process Modeling, presented at Exxon Chemical Company Film Equipment Machinery Manufacturers Symposium, April (1996)

Pahl M., Gleissle W. and Laun H.M., *Praktische Rheologie der Kunststoffe und Elastomere*, VDI-Verlag GmbH (1995)

Polychronopoulos N.D., Charlton Z., Suwanda D. and Vlachopoulos J., Measurements and Comparison to Predictions of Viscosity of Heavily Filled HDPE with Natural Fibers, Adv. Polym. Technol. 37 (4), 1161 (2018)

Saini D.R. and Shenoy A.V., Melt Rheology of Some Specialty Polymers, J. Elastomers Plast., 17, 189 (1985)

Santi C.R., Hage Jr. E., Correa C.A. and Vlachopoulos J., Torque Viscometry of Molten Polymers and Composites, Appl. Rheol., 19, 13148 (2009)

Sentmanat M. L., Miniature Universal Testing Platform: From Extensional Melt Rheology to Solid State Deformation Behavior, Rheol. Acta, 43 (6), 657 (2004)

Sentmanat M.L., Wang B.N. and McKinley G.H., Measuring the Transient Extensional Rheology of Polyethylene Melts Using the SER Universal Testing Platform, J. Rheol., 49, 585 (2005).

Shang S.W., The Precise Determination of Polydispersity Index (PI) in Rheological Testing of Polypropylene, Adv. Polym. Technol., 12 (4), 389 (1993)

Shroff R. and Mavridis H., New Measures of Polydispersity from Rheological Data on Polymer Melts, J. Appl. Polym. Sci., 57 (13), 1605 (1995)

Stadler F.J. and Mahmoudi T., Understanding the Effects of Short-Chain Branches by Analyzing Viscosity Functions of Linear and Short-Chain Branched Polyethylenes, Korea-Australia Rheol. J. ,23 (4), 185 (2011)

Tzoganakis C., Vlachopoulos J. and Hamielec A.E., Non-Isothermal Polymer Flow from Viscometer Reservoir to Capillary Die, Plast. Rub. Proc. Appl., 7, 155 (1987)

Vlachopoulos J., Extrudate Swell in Polymers, Rev. Deformation Behav. Mater., 3(4), 219 (1981)

Volpe V. and Pantani R., Determination of the Effect of Pressure on Viscosity at High Shear Rates by Using an Injection Molding Machine, J. Appl. Polym. Sci., 135 (24), 45277 (2018)

White J.L., *Principles of Polymer Engineering Rheology*, Wiley (1990)

Zeichner G.R. and Patel P.D., A Comprehensive Evaluation of Polypropylene Melt Rheology, Proceedings 2nd World Congress of Chem. Eng., Montreal (1981)

JAMES CLERK MAXWELL (1831-1879)

J. Vlachopoulos and N.D. Polychronopoulos "*Understanding Rheology and Technology of Polymer Extrusion*", First Edition, Polydynamics Inc, Dundas, Ontario, Canada (2019)

Chapter 6
SINGLE SCREW EXTRUDERS

6.1 Historical Remarks

The word "extrusion" is derived from the Latin words ex and trudere, which mean respectively, "out" and "to push" or "to shove". The earliest extruders were short used mainly for rubber processing during the late 19th and early 20th centuries. Rubber does not require melting per se, but merely softening and pumping through a shaping die, that is why the early extruders were short. The single screw extruder (SSE) is the workhorse of the polymer processing industry. The vast majority of plastics are processed at least once in their lifetime through a SSE. Polymer pellets, flakes or powder are fed into a heated barrel in which an Archimedean screw rotates. The solid polymer particles are compacted as they transported forward, melted and pumped through a die for the purpose of shaping into the desired product. The operating principles of the so-called plasticating screw extruder had started to be understood after the publication of a series of papers in the early 1950's by a Dupont team (Gore, 1953, Carley and Strub 1953a, 1953b, Carley *et al.*, 1953, McKelvey, 1953, Mallouk and McKelvey, 1953, Carley and McKelvey, 1953, Jepson, 1953) and independently, a doctoral thesis by Maillefer (1952). More information on early developments can be found in Bernhardt (1959), McKelvey (1962) and Schenkel (1963). Further research work by Maddock (1959), Tadmor (1966) and Tadmor and Klein (1970) and theoretical and technological developments, as summarized by Torner (1973), Middleman (1977), Tadmor and Gogos (1979, 2006), Chung (2011), Spalding and Campbell (2013) and Rauwendaal (2014) and Agassant *et al.* (2014), laid the foundations for modern extruder technology. The purpose of design developments and innovations is to increase the output rate of stable, high quality melt, free from unmelts and degraded material.

6.2 Designing a Melt Screw Pump

Pump is a device that moves fluids and generates pressure. In classical fluid mechanics the so-called rotodynamic (i.e. centrifugal) pumps generate pressure by transferring the kinetic energy of the rotating impeller to the fluid. These pumps do not work (they cannot even turn) with highly viscous fluids like molten polymers.

The Bernoulli principle, $V^2/2g + p/\rho g = const.$, does not apply for highly viscous fluids, since the inertia (i.e. kinetic energy) is negligible. In molten polymer flow we have a **balance of pressure and stress forces**. So, somehow we must generate pressure from stress (i.e. from the fluid viscosity). Let's see how this can be done. In drag flow between two flat plates, for the open ended channel we have no pressure generation as we saw in Chapter 2. The fluid is just being dragged with the velocity profile being simply a straight line as shown schematically in Fig. 6.2-1.

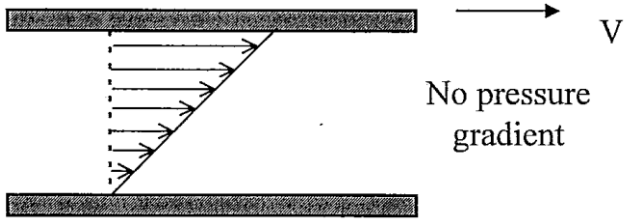

Figure 6.2-1. Drag flow between two flat plates. Top plate moves to the right with velocity V. The fluid sticks to both the moving and stationary plate (no slip condition).

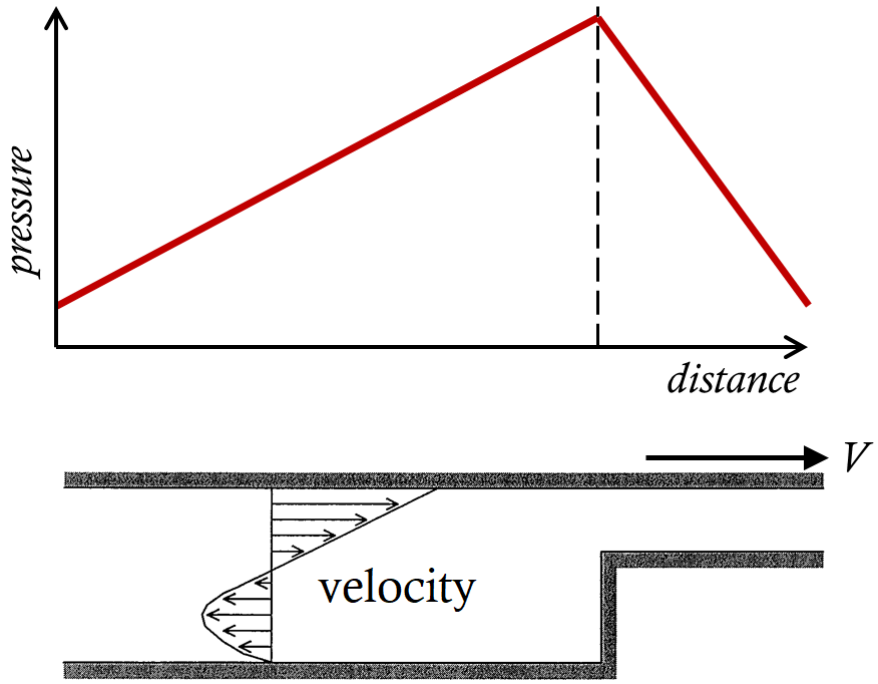

Figure 6.2-2. Drag flow between two flat plates with the one end partially closed causing a pressure build-up. The device is known as the Rayleigh step in the science of tribology.

However, if the end of the channel is partially closed, then a portion of the fluid is still being dragged due to the movement of the plate and at the same time pressure is generated, just as in the case of lubricated bearings (Vlachopoulos, 2016), where two slightly non-parallel surfaces are in relative motion. The anticipated pressure variation and velocity profile in this case are shown schematically in Fig. 6.2.-2.

The simple concept shown in Fig. 6.2-2 is a pump, because it is capable of transporting liquids and generating pressure. Let's see how this simple principle can be put into real practical use. A possible (conceptual) design would be a shallow channel of finite length covered by an infinite moving plate, as shown schematically in Fig. 6.2-3. Another possibility would be to keep the plate stationary and move the shallow channel.

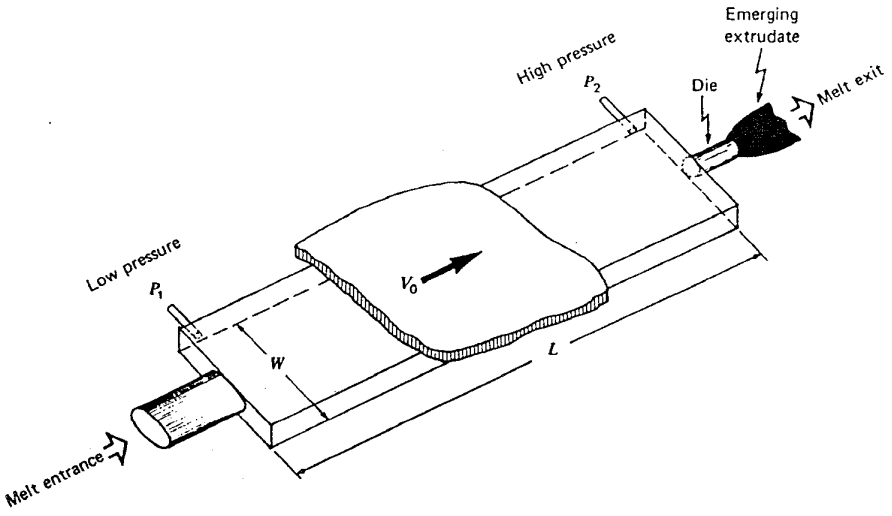

Figure 6.2-3. Conceptual design of a melt screw pump. A plate with velocity V_0 moves over a shallow rectangular channel. From Tadmor and Gogos (1979).

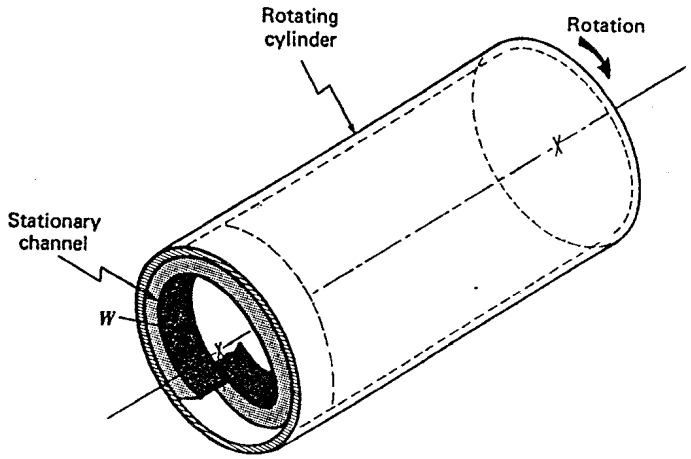

Figure 6.2-4. A "twisted" and "turned", in a helical manner, shallow channel inside a rotating barrel. From Tadmor and Gogos (1979).

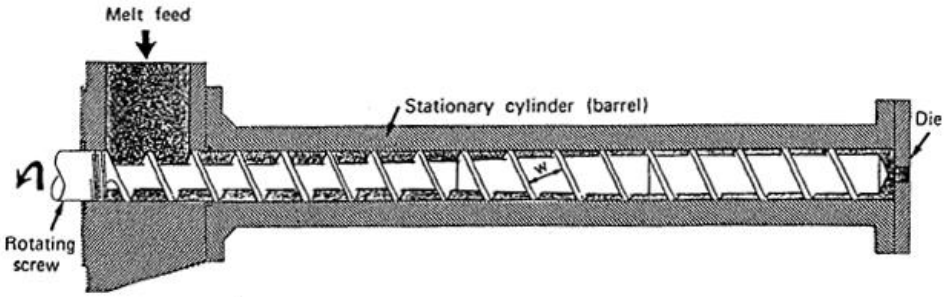

Figure 6.2-5. Schematic representation of a simple single screw extruder. From Tadmor and Gogos (1979).

Of course, a channel filled with a hot melt and an "infinite" moving plate does not represent a practical solution. Let's do a "Gedankenexperiment", as Einstein used to say, (i.e. a thought experiment) for the construction of a practical device. We convert the "infinite" moving plate into a rotating barrel (i.e. a hollow cylinder) and the shallow channel, by twisting and turning, into a helical channel inside the barrel as shown in Fig. 6.2-4. The constructed geometry is reminiscent of a screw inside a hollow cylinder. Therefore, we end up with a melt screw extruder like the one shown in Fig. 6.2-5.

In the above approach we made the assumption that the barrel rotates and the screw is stationary. We made this assumption, to simplify the analysis presented subsequently. Of course, in reality extruders operate in the opposite manner, that is, the screw rotates and the barrel is stationary. The question of whether the simplifying assumption of a stationary screw and a rotating barrel, impacts any further extruder analysis, is to some extend controversial. Some researchers claim significant differences between the rotating barrel and the rotating screw analyses (for screws having deep channels see Campbell and Spalding, 2013).

6.3 Output Determination of a Melt Fed Extruder

We will assume that the flow is isothermal and the melt behaves like a Newtonian fluid. Before presenting any mathematical analysis for the flow of a molten polymer, it is instructive to understand which are the most essential geometrical parameters, used frequently in screw design terminology. These parameters are illustrated schematically in Fig. 6.3-1 for a representative section of a screw. We write below an explanation of each design parameter in Fig. 6.3-1

- D_s: screw diameter (taken at the tip of the flight)
- D_b: barrel diameter = $D_s+2\delta$

- L_s: screw lead or pitch ($L_s = \pi D_s \tan\theta$)
- e: flight width
- W: channel width ($W = L_s\cos\theta - e = \pi D_s \tan\theta\cos\theta$)
- Frequently: $L_s = D_s$ and it is called square pitched screw then $\theta = 17.66^o$ ($\tan\theta = 1/\pi$).

  To simplify the analysis we will neglect the flight clearance δ (which very small), so we will assume $D_s = D_b = D$.

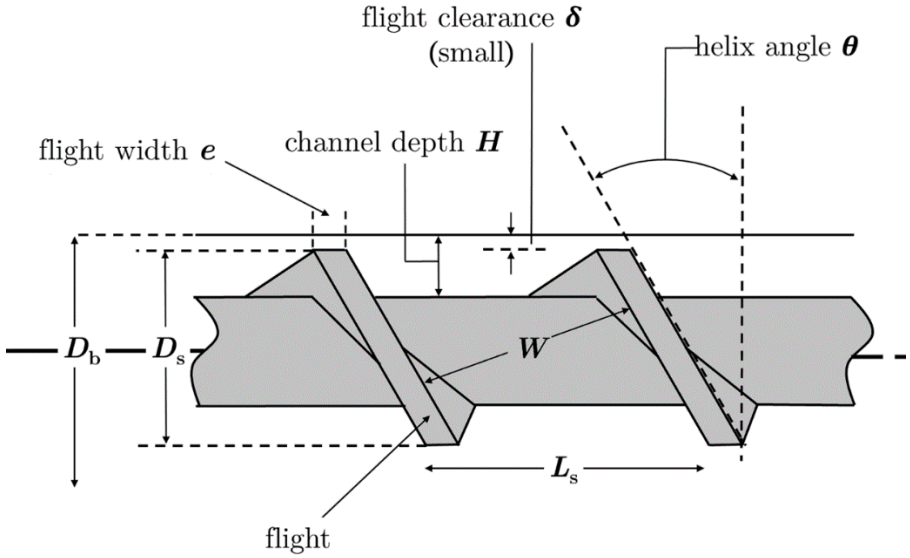

Figure 6.3-1. Screw design terminology in a representative screw section. Polymer melt is transported from left to right. The left flight is frequently referred to as the pushing flight and the right the trailing flight.

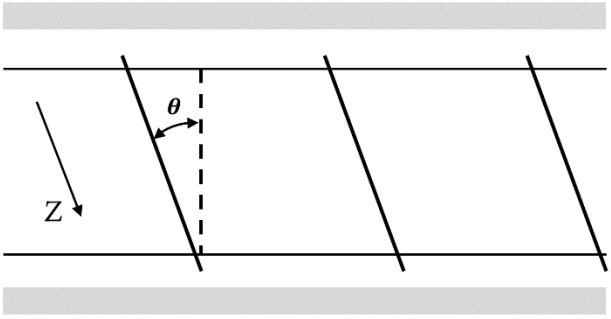

Figure 6.3-2. Notation of the down-channel direction. θ is the helix angle.

To develop a mathematical model let us (conceptually) unwind the channel, and turn it (conceptually) into a channel between two flat plates. We shall use the **assumption that the screw is stationary and the barrel rotates** with $V_b = \pi DN$ where N is the rotational speed in the screw (e.g. rpm). If Z is the down channel direction as shown in the rough schematic of

Fig. 6.3-2, the down channel velocity component will then be $V_{bz} = V_b cos\theta = \pi DNcos\theta$. Also the down channel distance z is related to the axial distance L by $z=L/\sin\theta$.

Let us now use the flat plate equations for **drag flow** with an **opposing pressure flow**. For this case, the flow rate is a drag flow term (half the moving plate velocity multiplied by the flow cross-sectional area) minus a pressure term (which is equation 2.6-18 for a Newtonian fluid (n=1) and $b=H/2$)

$$Q = \frac{1}{2}VHW - \frac{H^3 W}{12\mu}\frac{dP}{dz} \tag{6.3-1}$$

But we must use the helical geometry of the channel i.e. the polymer melt moves in the down channel z-direction. We have

$$W = Lcos\theta = \pi Dtan\theta cos\theta \tag{6.3-2}$$

$$V = V_b cos\theta = \pi DNcos\theta \tag{6.3-3}$$

$$W\frac{dP}{dz} = \frac{dP}{dL}sin\theta = \frac{\Delta P}{L}sin\theta \tag{6.3-4}$$

where N=revolutions per second (rpm/60) of the screw. Substitution in Eq. 6.3-1 we have

$$Q = \frac{1}{2}\pi^2 D^2 HNsin\theta cos\theta - \frac{\pi DH^3}{12\mu}sin^2\theta\frac{\Delta P}{L} \tag{6.3-5}$$

where: $\Delta P = P_{2(\text{exit})} - P_{1(\text{entrance})}$

L: length of the screw (usually L=10~15D *for melt fed extruders*)

θ: helix angle

D: barrel diameter (usually 1~8 inches i.e. 25mm ~ 200 mm)

H: channel depth (usually 2- 10 mm)

N: speed of rotation (usually 50-200 rpm)

μ: Newtonian viscosity

If the clearance δ between the screw flight and the barrel is not negligible, we must subtract the amount of leakage flow rate (i.e. the amount of fluid that escapes over the flight), which can be easily shown (again based on equation 2.6-18) to be given by

$$Q_L = \frac{\pi^2 D^2 \delta^3}{12\mu e}tan\theta\frac{\Delta P}{L} \tag{6.3-6}$$

Therefore, the volume rate of flow equation reads as

$$Q = \frac{1}{2}\pi^2 D^2 HNsin\theta cos\theta - \frac{\pi DH^3}{12\mu}sin^2\theta\frac{\Delta P}{L} - \frac{\pi^2 D^2\delta^3}{12\mu e}tan\theta\frac{\Delta P}{L} \tag{6.3-7}$$

Multiplication with density gives the mass rate of flow, usually reported in kg/hr.

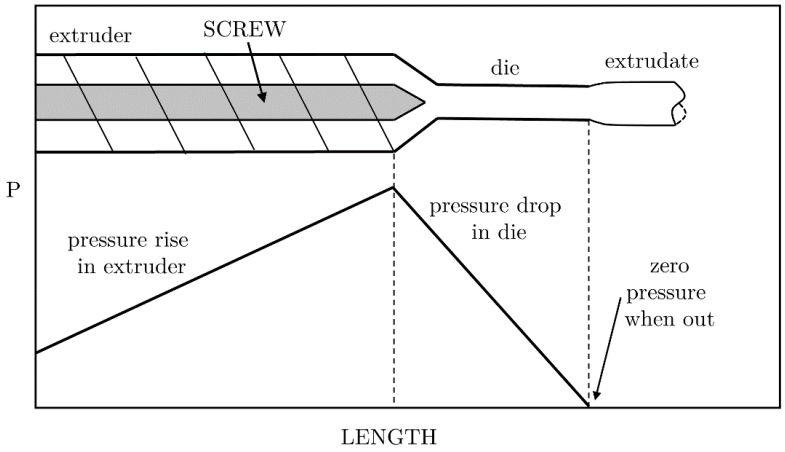

Figure 6.3-3. Schematic representation of the pressure distribution in an extruder followed by a die.

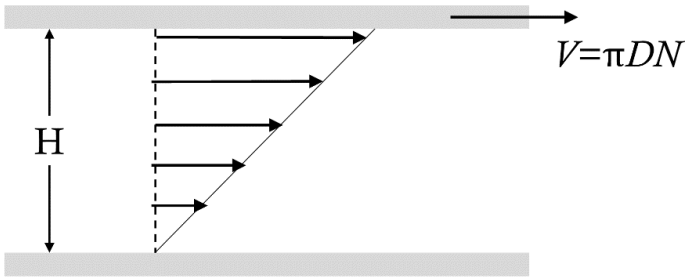

Figure 6.3-4. Schematic representation of a simple drag flow between flat plates.

Of course, polymer melts are shear thinning fluids. Therefore, we need to somehow use an "equivalent" Newtonian viscosity to perform calculations.

For a given extruder L, D, H and θ are fixed so (neglecting the leakage flow) we may write in a general form

$$Q = const \cdot N - const\frac{\Delta P}{\mu} \tag{6.3-8}$$

where N is the screw speed, $\Delta P = P_{exit} - P_{entrance}$ is the pressure rise in the extruder as shown schematically in Fig. 6.3-3 and μ is the melt viscosity (Newtonian). This shows that Q increases linearly with screw rotation and Q versus ΔP is a straight line with negative slope. For drag flow (see Fig. 6.3-4) a characteristic (reference) shear rate would be

$$\dot{\gamma}_{ref} = \frac{\pi DN}{H} \tag{6.3-9}$$

We will calculate the "equivalent" Newtonian viscosity via a simple example. Let $\eta = 10000\dot{\gamma}^{-0.6}$, N=100 rpm, D=90 mm and H=4 mm. We may then define the reference shear rate as

$$\dot{\gamma}_{ref} = \pi \frac{90}{4} \frac{100}{60} \approx 117\ s^{-1}$$

which gives $\eta \approx 571\ Pa \cdot s$. This is the "equivalent" Newtonian viscosity μ in the melt extruder equation for Q (Eq. 6.3-8).

The question may be asked: How good is this simplified (Newtonian) theory? We could say "satisfactory" for prediction of output rate. How could this be improved? Shape factors could be introduced F_d for the drag flow term and F_p for the pressure flow term to account for the reduced flow in the down channel Z-direction, due to the presence of the flights. They depend on the ratio H/W. Both factors are essentially 1 for small aspect ratios. Also the loss of volume due to the flight thickness e could be taken into consideration. A formula including shape factors and flight thickness is given in Section 6.11.

We note that:

1. If there is no pressure build-up in the extruder (i.e. restriction to flow at the end of the extruder), the output would be maximum, i.e. drag flow only

$$Q_{max} = \frac{1}{2}\pi^2 D^2 H N sin\theta cos\theta \tag{6.3-10}$$

2. If the end is closed, Q=0 and we may equate drag and pressure flow

$$\frac{1}{2}\pi^2 D^2 H N sin\theta cos\theta = \frac{\pi D H^3}{12\mu} sin^2\theta \frac{\Delta P}{L} \tag{6.3-11}$$

This gives the maximum possible pressure

$$P_{max} = \frac{6\pi D L N \mu}{H^2 tan\theta} \tag{6.3-12}$$

Since μ is large for polymer melts, extremely large (and very dangerous) pressures can develop.

The above equations enable us to examine the role of channel depth by drawing a straight line between Q_{max} and P_{max} as shown in Fig. 6.3-5. Then by plotting pressure versus flow rate for a die (non-linear for power-law fluids, see Chapter 2, $Q \sim \Delta P^{1/n}$) we can determine the operating point as shown in Fig. 6.3-5. The matching procedure will be more clear in Section 6.12, where we present a numerical example. Well-running extruders if they are also well-matched to their dies are unlikely to have outputs less than 75% of the drag flow output (Eq. 6.3-10).

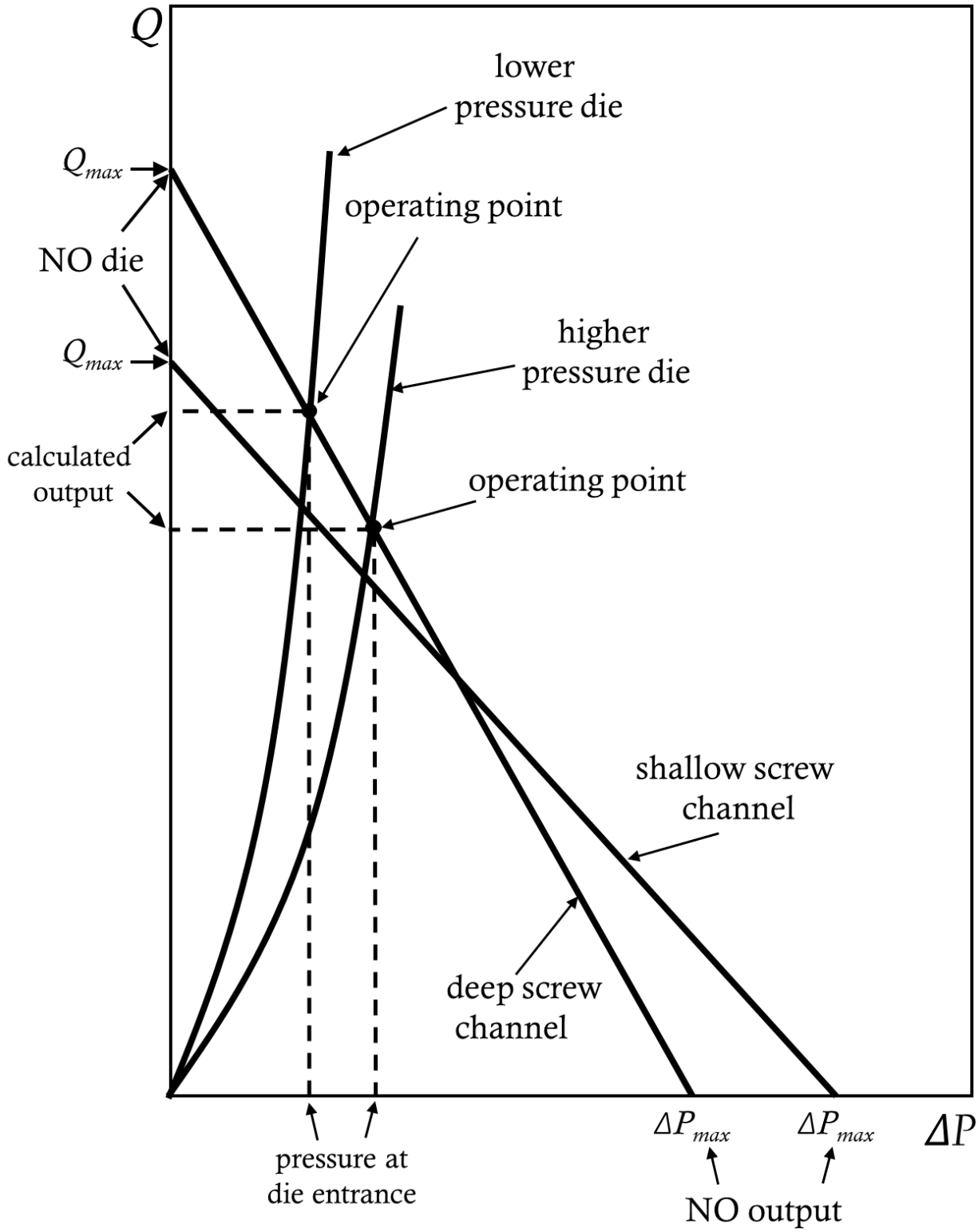

Figure 6.3-5. Operating point determination for a melt fed extruder.

6.4 Solids Conveying in an Extruder

Conventional single screw extruders (also called plasticating) are composed of three different zones as shown schematically in Fig. 6.4-1. After the feed hopper the polymer pellets, powder or flakes get packed into a solid "bed" in the solids conveying zone (also called feed section), which is pushed forward and melted in the melting zone. It can be seen that in the feed zone the channel is deep and progressively becomes shallow to compensate for the reduction of the volume, from solid material and air, into a hopefully air-bubble-free melt Subsequently, the melt is pumped (mainly dragged) through the final flights of the metering zone to the die.

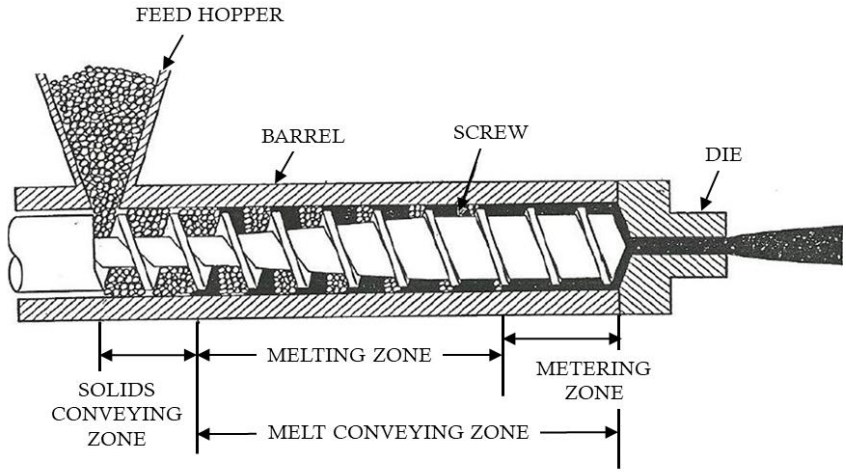

Figure 6.4-1. Schematic representation of a single screw extruder and the various functional zones.

Single screw extrusion is perhaps the most effective way to melt and pump molten polymers through extrusion dies for final continuous shaping into film, sheet, pipe, profiles, fiber and wire coating. From a general perspective, extruder and screw design calls for output maximization, avoidance of material degradation, extrusion stability and melt quality. There are many possible variations of barrel and screw design. The most common are **smooth** or **grooved feed** or **entire grooved barrel**, **conventional single flight** screws with or without **mixing sections** and **barrier screws**. The latter consist of a main flight plus a barrier flight.

To understand how the solid bed is transported in an extruder, we use an analogy of the movement of a nut along a screw shown in Fig. 6.4-2. The nut must be held in place if one wants to move the screw. Thus, for the polymer bed (corresponding to the nut) to move, the friction coefficient on the barrel (corresponding to the fingers) must be larger than the

friction coefficient on the screw. For this reason, the barrel's inner surface is rough and sometimes intentionally grooved to increase the friction coefficient. The screws, on the other hand, have always a smooth (polished) surface to keep the friction coefficient as low as possible.

Figure 6.4-2. A simple nut-screw "experiment" to explain the movement of the packed solid bed in an extruder.

At the start of the screw (under the hopper), the particulate solid bed is loosely compacted. As the solid bed progresses towards the melting section, frictional forces and torques are exerted by the **"rotating" barrel**. These forward forces are opposed by the retarding forces exerted by the root of the screw as well as the flight. This results in pressure build-up in the direction of the flow and the low bulk density solids (previously loosely compressed) are now compressed into a "sturdy" (hopefully) solid bed, which slides down the channel. In fact, Darnell and Mol (1956) developed an isothermal model that relates the mass flow rate of the solid bed to the ratio of outlet to inlet pressure. Their model predicts a downstream pressure rise, which can be simplified in the form

$$P = P_o exp\left\{[C_b f_b cos(\varphi + \theta) - C_s f_s]\frac{kZ_b}{A}\right\} \qquad (6.4\text{-}1)$$

where f_b and f_s are friction coefficients on the barrel and the screw respectively, C_b and C_s are the wetted perimeters, φ is the solids conveying angle, which is different from the helix angle θ, Z_b the down-channel distance and k a constant. The predictions of the model are very sensitive to values of f_b and f_s. The exponential pressure rise is schematically shown in Fig. 6.4-3.

As explained earlier, the friction coefficient of the barrel must be higher than the screw (i.e. $f_b > f_s$). Typical values for the barrel is $f_b \approx 0.4$ and for the screw $f_s \approx 0.25$. The friction coefficients f_b and f_s depend on pressure, temperature, surface condition (new, old, worn out), presence of lubricants or additives in the feeding section, type of feed (i.e. pellets, powders or

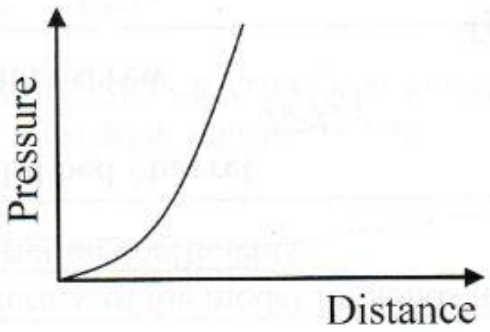

Figure 6.4-3. Exponential pressure rise in the feed (solids conveying) zone.

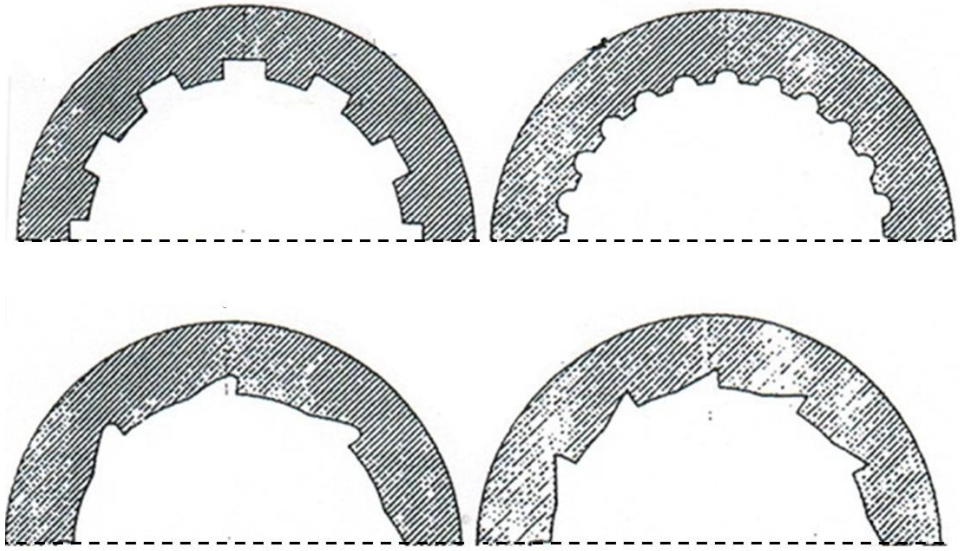

Figure 6.4-4. Shapes of grooves used in the feed section (usually no more than L/D=4 of the extruder). Huge pressures can be developed within a short distance, due to high friction coefficient on the grooved barrel wall.

Figure 6.4-5. Grooved feed barrels. From Extrusion Technical Guide, Qenos, Australia (2015).

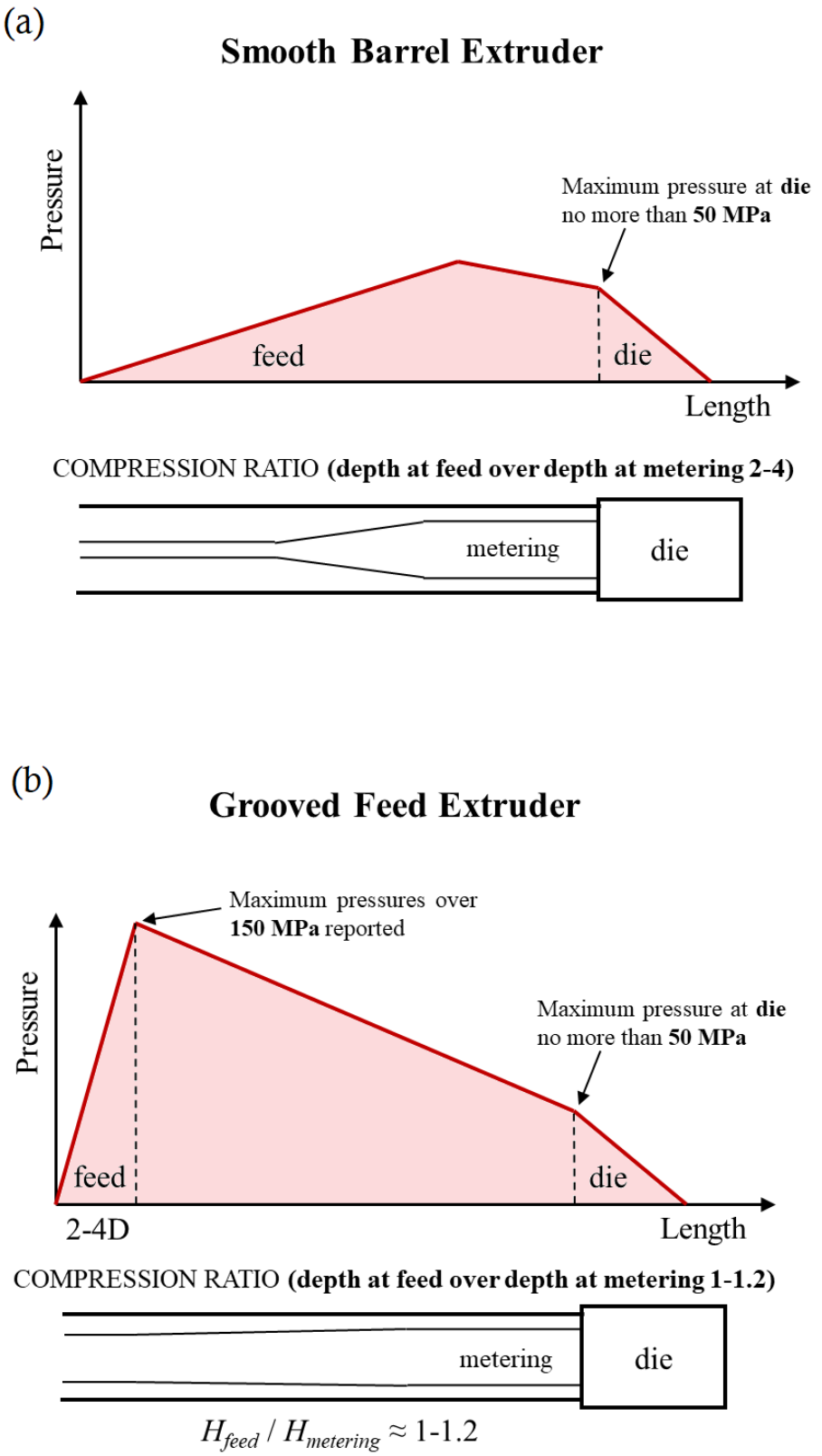

Figure 6.4-6. Schematic representation of the pressure build-up in a (a) conventional smooth barrel and (b) grooved feed barrel extruder. Notice that the screw channel compression for grooved feed barrel extruders, is almost not existent (not needed, the pellets are compressed in the feed section).

flakes), shape of pellets and their size, pellet surface (whether smooth or rough). Thus, it is very difficult to make good, reproducible and meaningful measurements.

Grooved feed extruders feature axial grooves or slots in the part of the barrel immediately following the feed throat (usual range 2D~4D). The grooves can have different shapes are shown in Fig. 6.4-4 and Fig. 6.4-5. Axial rectangular slots seems to be the preferred geometry. Recently, helical slots are also becoming popular.

The grooved barrel can significantly enhance the solid transport rate due to high friction on the barrel and increase the pressure buildup significantly, very close to the feed throat. Maximum pressures usually exceed 100MPa and up to 300MPa have been reported. A typical pressure build-up of a grooved feed extruder is illustrated schematically in Fig. 6.4-6, where the case of a typical smooth barrel extruder is also shown. In grooved feed extruders, the compression ratio (i.e., the channel depth in the feed over the depth in metering section) is roughly 1–1.2, while in smooth barrels, higher compression ratios are met ranging from 2 to 4. Grooved barrel extruders can deliver up to double the output rate given by the drag flow equation above (Eq. 6.3-10). High-speed extruders (with screws rotating above 400 RPM to perhaps 1200 RPM) usually have the entire barrel grooved (Grünschloß, 2007a, 2007b) and can deliver very high output rates.

With grooved feed, the extruder is capable of better flow stability (almost independent of head pressure) and somewhat lower melt temperature due to the increased output. Grooved feed extruders are used extensively in Europe. They perform best, for fractional melt index (MI<1) HDPE and PP, for film, pipe and blow molding. They are not suitable for very hard pellets like PET, or powders like PVC, soft thermoplastic elastomers or regrind. If there is compounding of masterbatches, there is likely to be problems due to insufficient mixing. Other negatives include: high drive power, performance is sensitive to particle characteristics (size and shape of pellets). Grooved feed extruders are not suitable for regrind due to the irregular shape of the particles. Due to these negatives, acceptance has been very slow in North America.

6.5 Melting in an Extruder

In the late 50's, Maddock (1959) observed and analyzed the melting of polymers on the screw using a simple experimental technique. Under steady-state operating conditions, the extruder was abruptly stopped, and both the barrel and screw were left to cool. Afterwards,

the screw was pulled out of the barrel and subsequently the solidified helical polymer was unwound. After that, thin representative sections perpendicular to the flights were cut and observed. It was concluded that melting really occurs in a melt film between the barrel and the solid bed, as shown in the rough schematic of Fig. 6.5-1a. This melt film is subjected to intense shearing in the thin gap and because of the extremely high viscosities of molten polymers, high rates of viscous dissipation (frictional heating) result. Due to the drag flow caused by the barrel movement, the melt film is subsequently collected in a melt pool formed in front of the pushing flight (see Fig. 6.5-1a). Finally, the generated heat melts the packed solid bed completely (see Fig. 6.5-1b). It should be noted that in well-designed extruders, the solid packed bed is melted usually at 2/3 of the screw length from the feed. A real case of HDPE melting is illustrated in Fig. 6.5-1c and 6.5-1d, where the extruder is equipped with a glass-window for visualization purposes. On the basis of Maddock's experiments, Tadmor (1966) developed a model for the melting rate and this model or variations thereof are used for computer simulation of single screw extruders (e.g. NEXTRUCAD).

A basic assumption of Tadmor's model is that the width of the packed solid bed is gradually reducing downstream until it disappears when the pellets are fully melted. However, in reality, there is possibility for solid bed segregation in the channel before complete melting (see for example the last picture in Fig. 6.5-1d). Yet, Tadmor's melting model is a reasonable approximation.

6.6 Melt Pumping in an Extruder (Metering Zone)

After the solid bed is fully melted, the polymer melt is dragged by the "moving" barrel surface in the metering section. Essentially, in the metering section the extruder works as a pump that delivers the molten material into the extrusion die. Therefore, the simple mathematical analysis presented in Section 6.3 can be used to make calculations of the potential (in fact close to the actual) output of the extruder. We stress, once again, that the assumption of a rotating barrel suggests that there exist two velocity components as shown in Fig. 6.6-1. It is actually the down channel component V_{bz} that drags the melt towards the discharge end. The cross channel component V_{bx} induces a cross-channel circulatory-type pattern that results in relatively good mixing.

The flow rate in the metering section is determined by the following equation

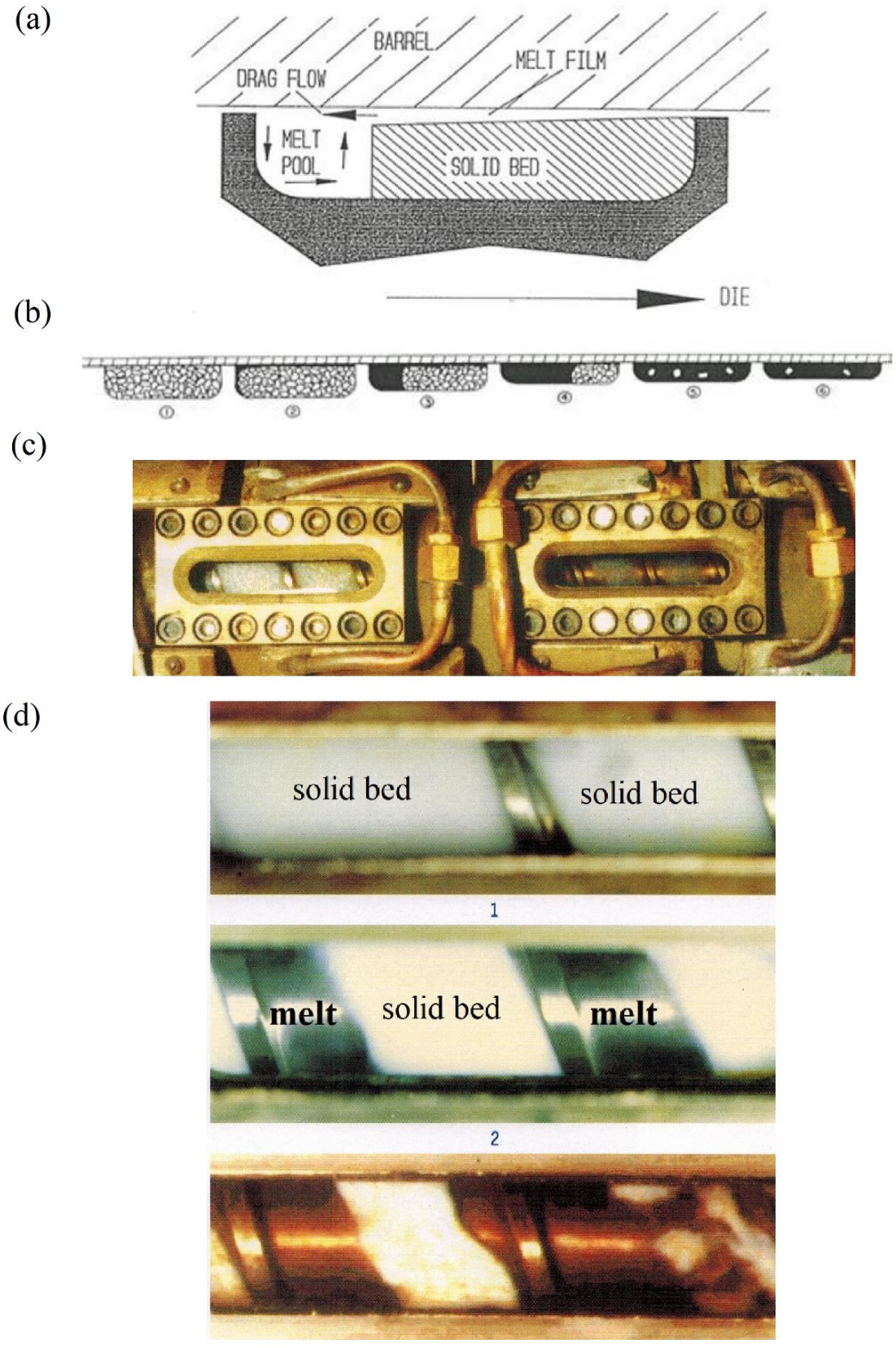

Figure 6.5-1. (a) and (b) schematic representation of Maddock's melting mechanism (Tadmor and Gogos, 1979). (c) and (d) HDPE melting in an extruder equipped with glass window with melt pool formation in front of the pushing flight and solid bed segregation behind the trailing edge (Zhu, 2001).

$$Q_{smooth\ barrel} = Q_{drag} - Q_{pressure(head)} - Q_{leakage\ (over\ flights)} \qquad (6.6\text{-}1)$$

This equation is no different to Eq. 6.3-7 derived in a Section 6.3 and it is written here in a simpler form. It was derived for smooth barrel extruders under the assumption of a Newtonian and isothermal fluid, but it is also a good approximation for Non-Newtonian, non-isothermal conditions.

In conventional smooth barrel extruders, the pressure distribution follows qualitatively the schematic showed in Fig. 6.4-6a. The fact that the pressure is rising downstream, led to the term *back flow*, in that the pressure drives the material opposite to the direction of the net flow. This leads to the erroneous concept that essentially, in some part of the channel, the actual flow is directed towards the feed section. It is imperative to note that **under no condition** does the material flow backward along the melt axis. This is evident from sketches of calculated velocity profiles shown in Fig. 6.6-2 for different values of the ratio Q_p/Q_d where Q_p and Q_d the pressure flow and drag flow respectively. The axial velocity component is always positive. In the most general sense the flow may be described as a helix-within-a-helix (see Fig. 6.6-3a), in that the fluid follows a helical flow pattern inside the helical channel of the screw. From the velocity profiles, one may deduce the path of fluid particles in the channel as shown in Fig. 6.6-3b.

To obtain estimates for the throughput an extruder may deliver, we may identify three categories of simple flow situations in the **down channel direction** depending upon the extruder-die parameters. No matter what happens in the solids or melting zones, the throughput is eventually determined by the metering zone. We may have either:

i. Ideal drag flow (e.g. smooth barrel extruders) as shown in Fig. 6.6-4a, if the die head pressure is too low.

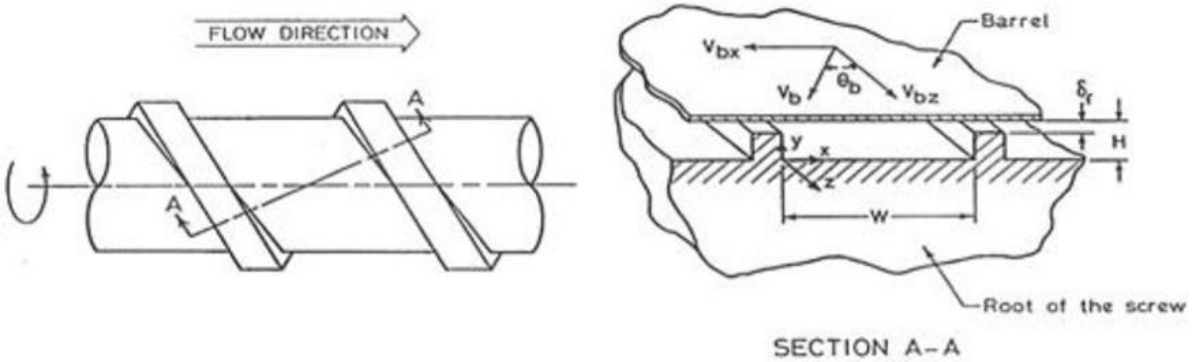

Figure 6.6-1. Schematic representation of the involving velocity components induced by the barrel rotation.

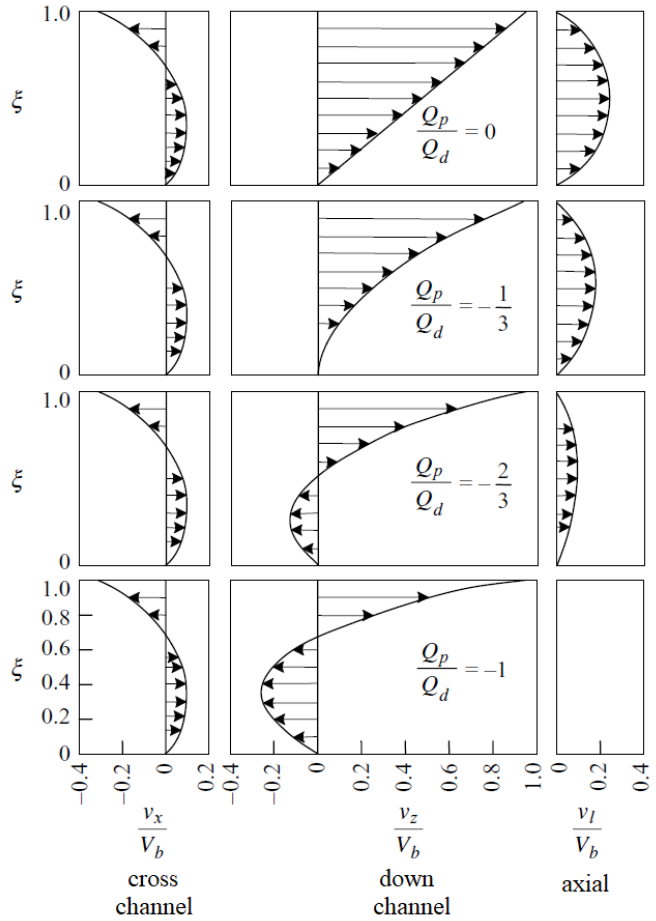

Figure 6.6-2. Cross-channel, down channel and axial velocity profiles for various Q_p/Q_d values (Q_p: pressure flow and Q_d: drag flow) in shallow square-pitched screws (leakage over flights is neglected). From Tadmor and Gogos (2006).

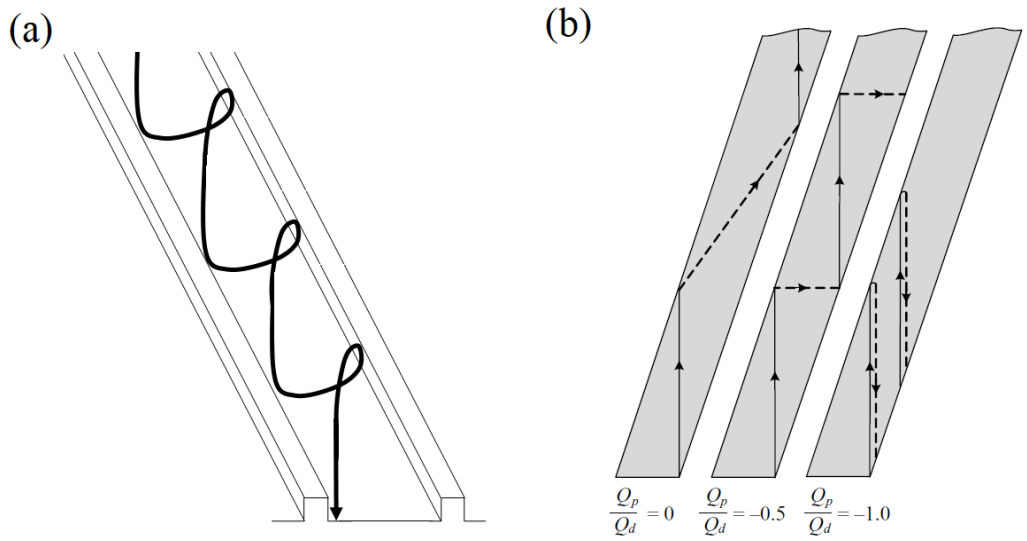

Figure 6.6-3. (a) Schematic representation of the concept flow path helix-within-a-helix in the screw channel. (b) Calculated path of a fluid particle in the screw channel for different values of Q_p/Q_d. Solid lines show the path of the fluid in the upper portion of the channel and the broken lines show the path of the same fluid particle in the lower portion of the channel. From Tadmor and Gogos (2006).

ii. Drag flow **plus** pressure flow (**positive**), as shown in Fig. 6.6-4b, if the extruder tends to "overbite" in the solids zone. This is for the case of grooved barrel extruders.

iii. Drag flow **minus** pressure flow (**negative**), as shown in Fig. 6.6-4c, if the die head pressure is too high.

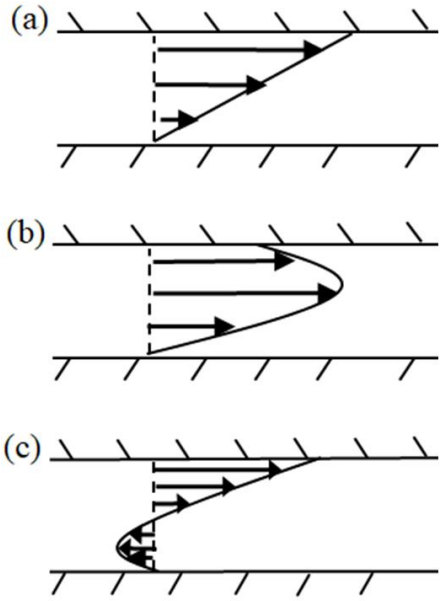

Figure 6.6-4. Different possible flow situations in a single screw extruder. (a) drag flow, (b) drag flow with aiding pressure gradient, caused by a grooved feed and (c) drag flow with adverse pressure gradient, caused by flow restriction in the die.

Industrial experience suggests that for well-running extruders, the throughput should not be less than 75 % of drag flow throughput which we have calculated in the melt screw pump section (Section 6.3). The drag flow throughput is essentially the maximum pumping capacity of the extruder

$$Q_D = \frac{1}{2}\pi^2 D^2 H N sin\theta cos\theta \qquad (6.6\text{-}2)$$

where D is the barrel diameter, H is the channel depth in the metering section, N is the rotational speed (rpm) and θ is the screw helix angle (usually 17.66° i.e. square pitched screw). The above equation may be corrected to account for the screw flight width

$$Q_D = \frac{1}{2}\pi^2 D^2 H N sin\theta cos\theta (1 - e/T) \qquad (6.6\text{-}3)$$

where e is the screw flight width and T the screw pitch. Output less than 75% of drag flow is indication of something wrong. Possibly the die is partially plugged, the screw may be corroded and/or the barrel damaged.

For the case of a grooved barrel, the pressure flow caused by the "overbite" (i.e. grooves) must be added. Grooved feed extruders are able to deliver a higher output than the smooth ones. Usually, the following applies

$$Q_{grooved} \approx 1.5 Q_{smooth} \sim 2 Q_{smooth} \tag{6.6-4}$$

for extruders that have the same diameter at same screw rotational speed.

The curvature of the radius at the screw base, formed between the screw flight and the screw root, is a very important design parameter. Small angles, defined by the ratio R/H as shown in Fig. 6.6-5a, are known to result in polymer resin degradation. This is shown in Fig.

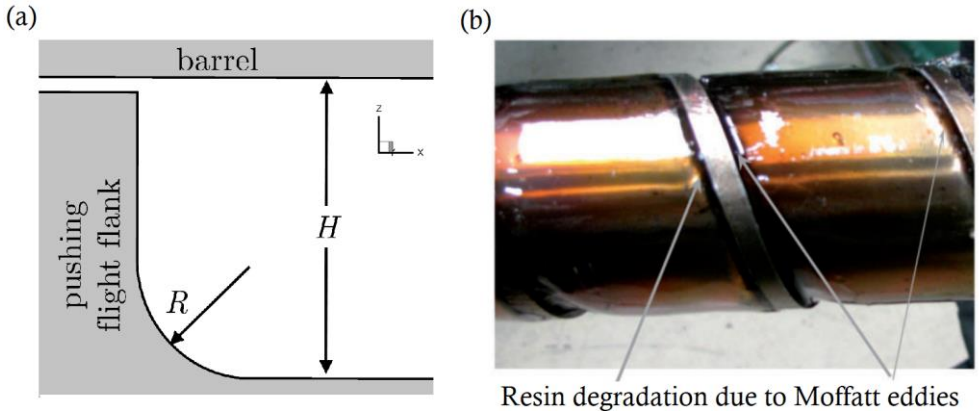

Figure 6.6-5. (a) Screw a flight angle at screw root defined by the ratio R/H and (b) resin degradation due to Moffatt eddies, from Spalding *et al.* (2016).

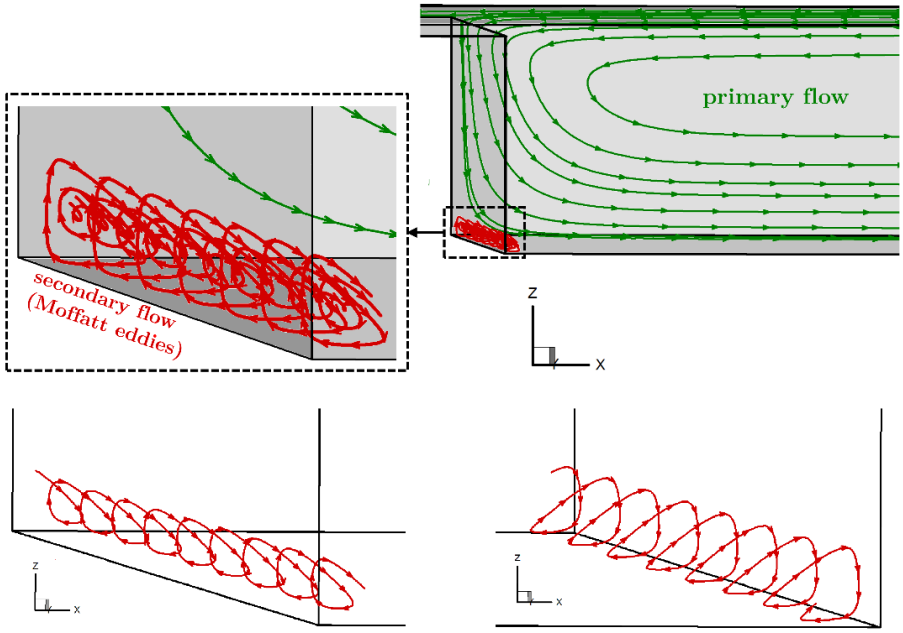

Figure 6.6-6. (a) Numerically computed pathlines for a Newtonian fluid near the pushing flight region showing the primary flow and Moffatt eddies (secondary flow) (b) Moffatt eddies in front of a pushing flight flank (left) and behind a trailing flight flank (right) for a Carreau fluid. From Polychronopoulos and Vlachopoulos (2018).

6.6-5b from Spalding *et al.* (2015), attributed to the so-called Moffatt eddies (Moffatt, 1964). Moffatt eddies appear in the form of spiraling flow, as shown in computer simulations of a screw having sharp corners, by Polychronopoulos and Vlachopoulos (2018) in Fig. 6.6-6. Due to very long residence times the degradation products accumulate, eventually get dislodged and produce defects on the extruded product. Experience based guidelines in industry suggest that the screw flight angle should not be less than 0.5.

6.7 Barrier Screws

Let us recall at first, for conventional single flighted screws, the concept of melt pool existing side by side with a packed solid bed in the channel, shown schematically in Fig. 6.5-1a and 6.5-1b. In all screws at least the first 70% or so of the melting is due to the shear stress in the melt film formed between the barrel and the solid bed surface. However, it is frequently evident that in the metering section, there is still unmelted material in the melt as shown in

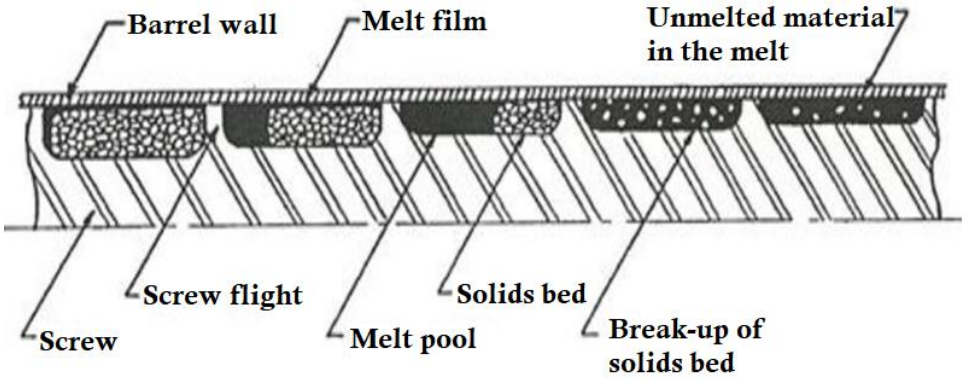

Figure 6.7-1. Schematic representation of a conventional single-flighted screw with unmelted material near the end. From SPIREX (1997).

the schematic of Fig. 6.7-1. Such unmelts may cause severe problems on machine performance and quality of extruded product. For example, unmelts may partially or fully clog the die, leading to excessive (and possibly dangerous) pressures. Surging, which is fluctuation of pressure and output may also occur. Presence of unmelts will affect the properties of the final product, such optical clarity due to presence of visible gels in transparent films, low tensile modulus and poor tensile and impact strength. This occurs, frequently in conventional metering sections, due to the fact that the solid bed can easily break up, especially at the end of the compression section. The remaining solids will receive very little shear as illustrated pictorially in Fig. 6.7-2, thus it will result in unmelted material.

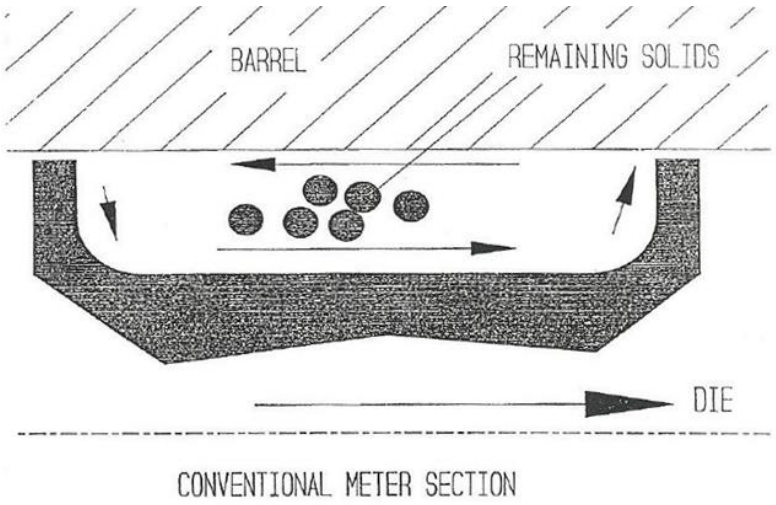

Figure 6.7-2. Schematic representation of unmelted material in a conventional metering section. Arrows inside the channel, indicate the movement of the sheared molten material. From Barr (1993).

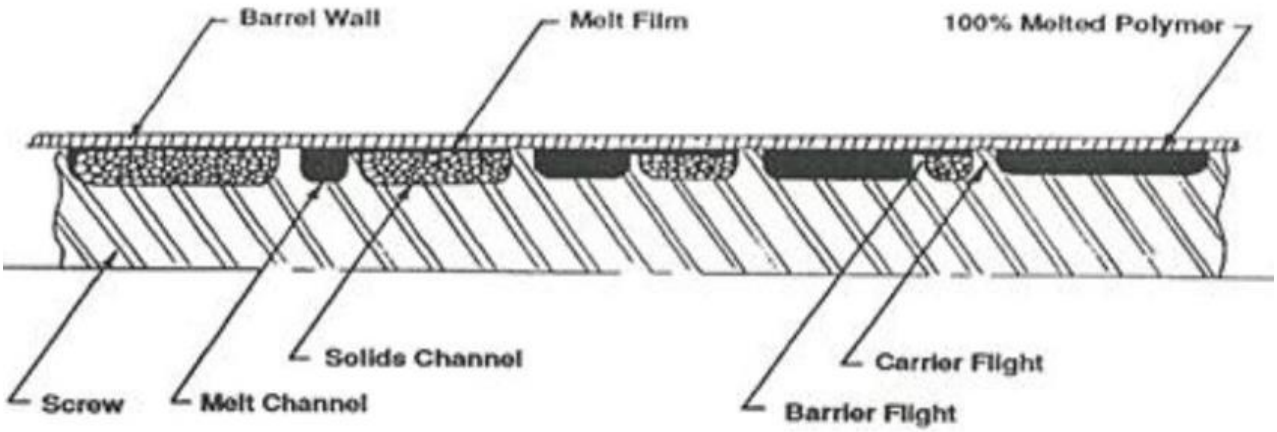

Figure 6.7-3. Schematic representation of the concept of a barrier screw. From SPIREX (1997).

For increased melting efficiency, barrier screws have been invented, starting from the late 1950's and early 1960s. In such screw designs, a secondary flight is added, that usually starts at a "pushing" flight and ends further downstream at a "trailing" flight, separating the solid bed from the molten material. A section of a typical barrier screw is presented in Fig. 6.7-3. It should be noted that the clearance of the secondary flight is generally larger than the one of the primary flight, to allow melt, but not solids to pass. Thus, the solid bed near the trailing flight (solids channel) is separated from the melt pool (melt channel) located at the pushing flight. In such screw-types, the cross sectional area of the solids channel continually decreases as the solid particles are melted downstream. It is possible to melt at least 80% of the material due to shear over the solid bed with very little conductive heating provided by the heaters.

Several barrier-type screw designs have been patented and currently used in the plastics industry. Two of them are the most common. The first type, which is actually the first barrier screw design by Maillefer (1959, 1963), is shown in Fig. 6.7-4a. In this case the width of the solids channel is gradually decreasing while the melt channel is gradually increasing downstream. The second type is referred to as parallel flight barrier screw also known as MC3 or Hartig Barr screw.

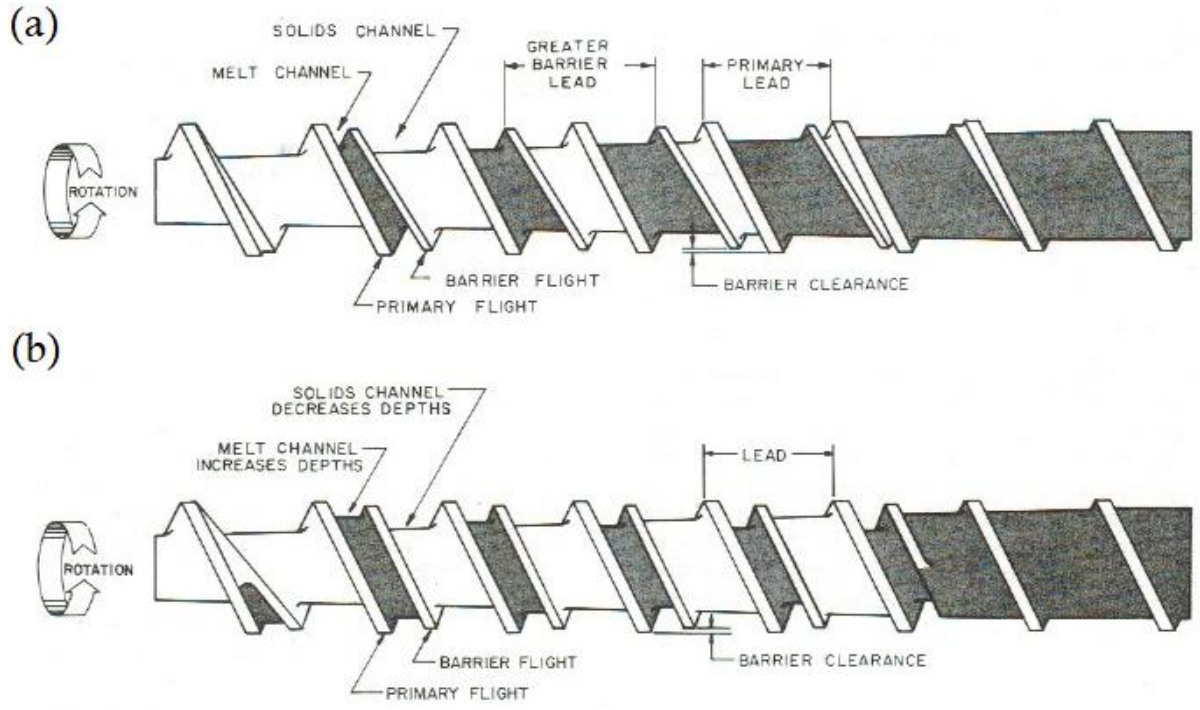

Figure 6.7-4. Schematic representation of the two most common barrier screws. (a) Maillefer screw and (b) parallel flight barrier screw also known as MC3 or Hartig Barr Screw. In both cases, grey color denotes the melt. From Spirex (1997).

In this type, the width of the melt and solids channels is constant throughout the length of the barrier section. However, the depth of the melt channel is increasing downstream (to accommodate the increasing melt flow rate) and the depth of the solids diminishes till both channel converge. The melting capacity of the parallel flight barrier screw is significantly higher than that of the Maillefer screw, since the surface area for melting is larger (by a factor of about 1.3). It may be noted that barrier screws have some negatives. Two are the most important:

i. The continuous reduction of the solids channel width might be a source of instabilities, since the solid bed resists deformation in width (Maillefer barrier screw).

ii. Excessive shear heating results in very high (melt) temperature, especially for LLDPE (which is less shear-thinning than LDPE). Also high temperatures are observed with the new metallocene resins in conventional or barrier screws, because they are not very shear-thinning.

One possible solution, to remedy the above, may be the Barr energy screw, also known as Energy Transfer (ET) screw (Chung and Barr (1983)). In such screws, there is a secondary flight with the clearance (undercut) being much greater than the clearance of the secondary

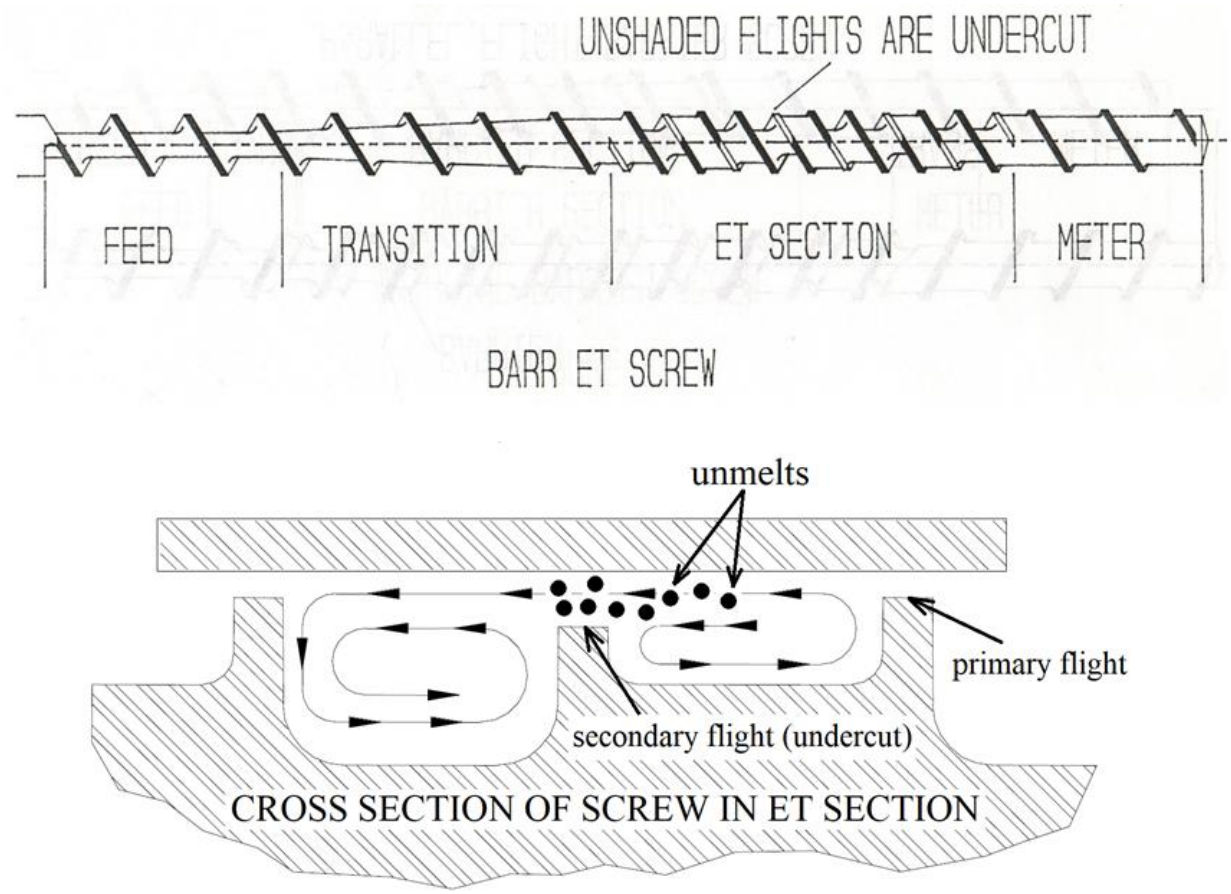

Figure 6.7-5. Top: schematic representation of Energy Transfer (ET) Screw. Notice that the unshaded flights are undercut. Bottom: Schematic of an ET cross-section where the solid circles represent the migration of unmelts (e.g. pellets) over the undercut. Adapted from Barr (1993).

flight of the MC3 barrier screw, as shown in Fig. 6.7-5. This allows for some unmelted pellets to escape from the solid bed and pass through to the melt channel. Because the clearance is large, the shear rates are relatively low. Once in the melt channel, the pellets are mixed with the melt promoting melting by conduction from the melt to the pellets. Therefore, the viscous

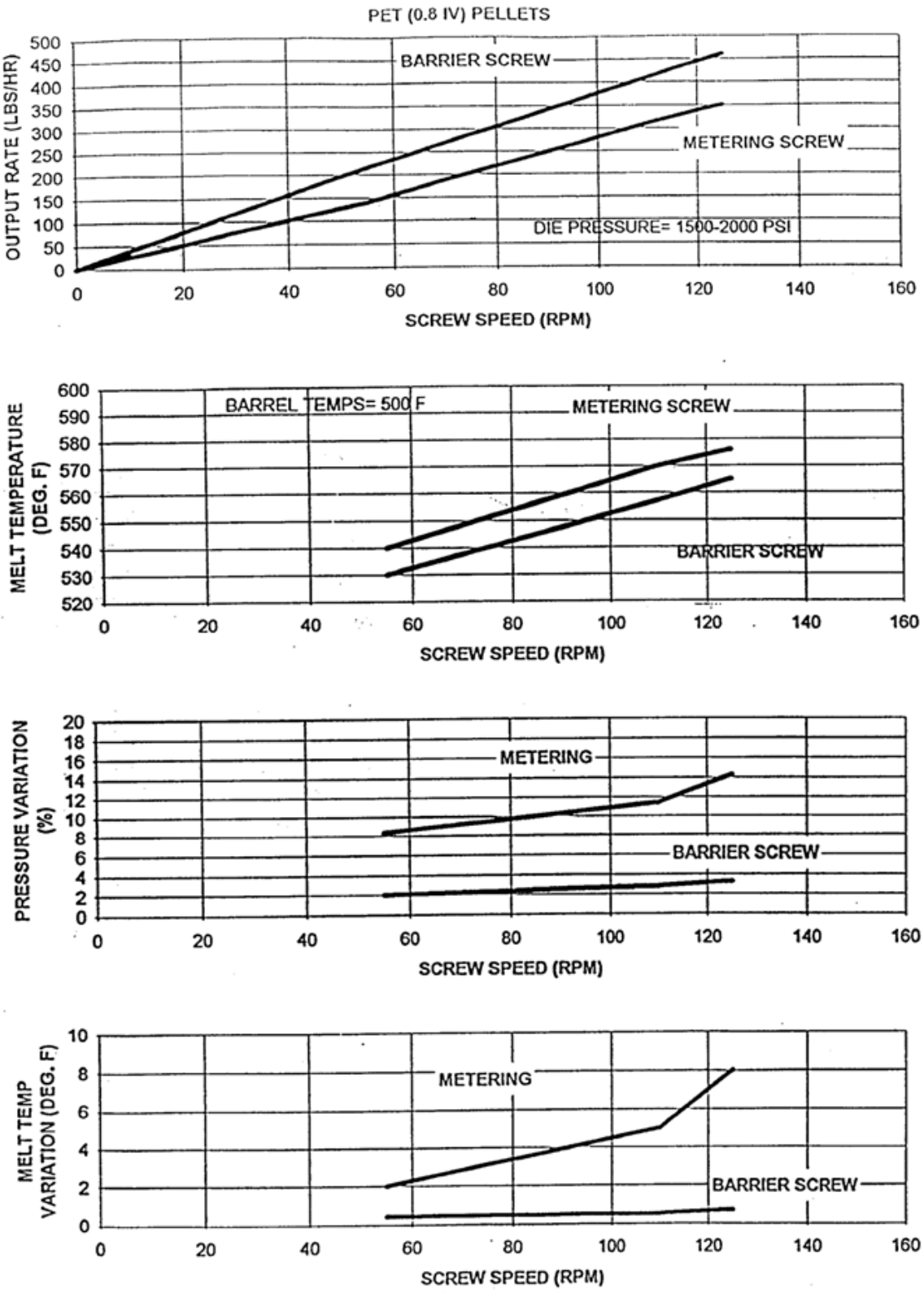

Figure 6.7-6. Comparison of 2.5 inch diameter screws, L/D=24, extruding PET 0.8 IV. Conventional (metering) versus barrier screw. From E. Steward, Davis-Standard Corporation.

dissipation due to shearing is low and the primary conducting mechanism is conduction which results in reduced melt temperature (Myers and Barr, 2002).

Barrier screws generally give higher output rates, lower melt temperature, less pressure and temperature fluctuations, as shown in Fig. 6.7-6. Most screws used today in the extrusion industry are of barrier type and include a mixing section.

6.8 Screws with Mixing Sections

Polymers are often compounded (mixed) with pigments, reinforcing agents, fillers, and other polymers for value-added purposes. Single-screw extruders are primarily melting and pumping machines. They have poor mixing capabilities. To improve the mixing capability, mixing elements are incorporated towards the end of the screw, near the die, as shown in Fig. 6.8-1.

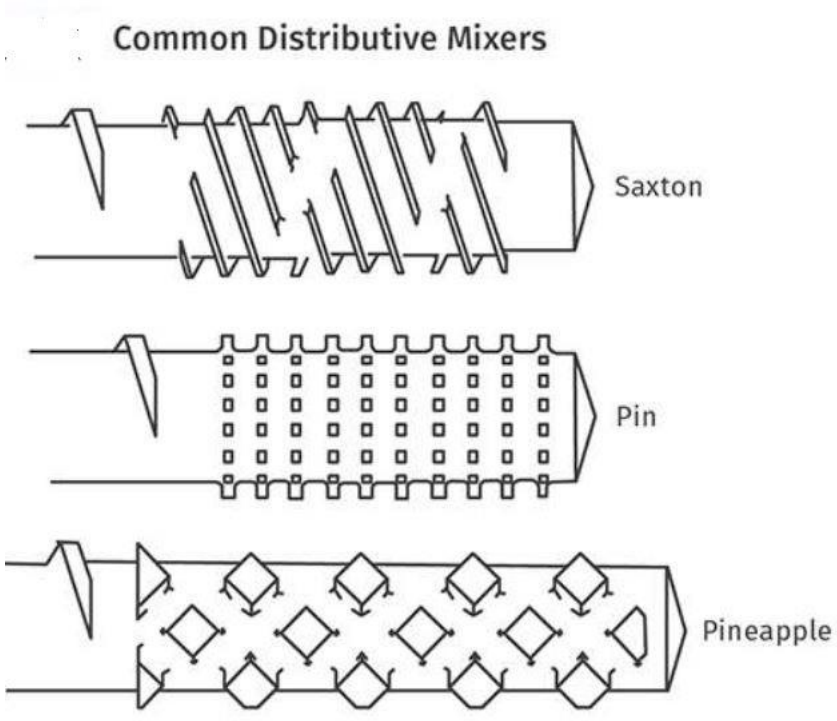

Figure 6.8-1. Mixing elements at the end of an extrusion screw.

In order to understand how good mixing can be achieved, it is necessary to understand the role of shear and elongational flow. Shear can easily be generated. Stirring a cup of liquid, or just shaking it, shear flow occurs. When a surface moves near another stationary surface shear flow is generated in the gap. Fig.6.6-2 shows shear flow profiles in single screw extruders

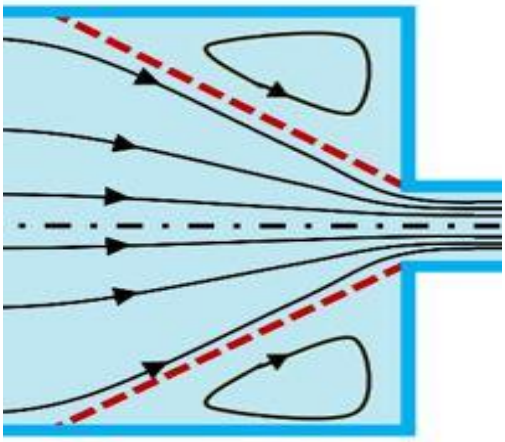

Figure 6.8-2. Elongational flow at the entrance of a small diameter tube.

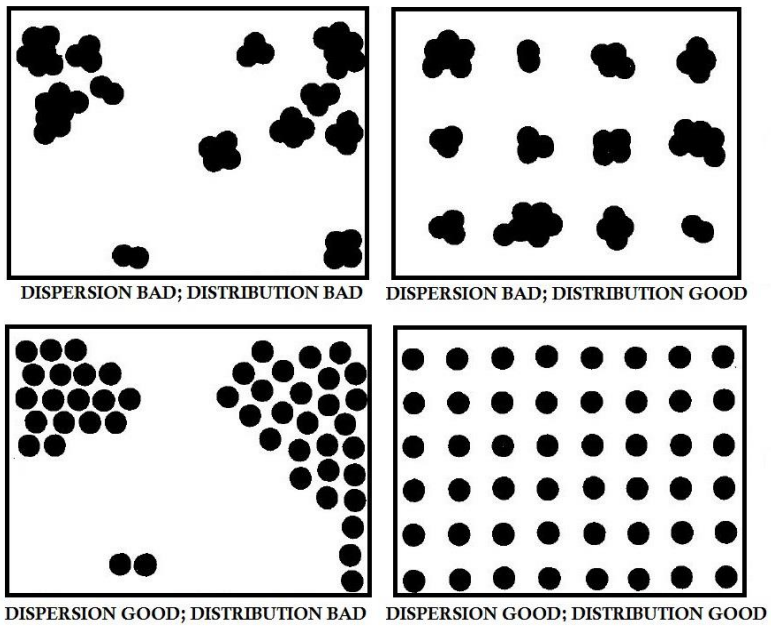

Figure 6.8-3. Schematic of dispersive and distributive mixing as adapted from Gale (1997).

Elongational flow requires stretching of a liquid as we have seen in Chapter 3 when a liquid flows from a large reservoir to a small diameter tube, also shown in Fig. 6.8-2. The flow field has a large diameter in the reservoir and smaller in the tube.

Mixing is a crucial operation in the following sense: the minor component must be **dispersed** (i.e. broken-up, reduced in size) and **distributed** (i.e. spread randomly) throughout the polymer matrix as shown schematically in Fig. 6.8-3.

Dispersion, in general, is determined by the balance of cohesive forces holding solid agglomerates or liquid drops together and the hydrodynamic disruptive forces. Dispersive mixing is dominated by the stress level within the deforming liquid matrix: a critical stress

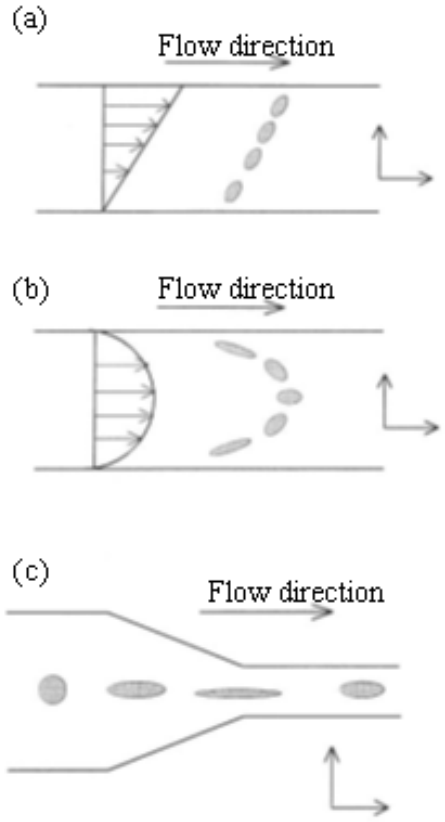

Figure 6.8-4. Drops deforming in shear (a) and (b) and elongational flow (c). Adapted from Han (2007).

level must be exceeded to break up whatever cohesive forces hold a solid or liquid particles together. The stresses exerted by a flowing matrix will deform the liquid drops dispersed in it, may overcome the surface tension forces and eventually break them up. Intuitively, elongational flow appears more effective in deforming and breaking up liquid drops as shown in Fig. 6.8-4.

Taylor (1932, 1934) studied the breakup of a single Newtonian drop in a simple shear field. The drop size was modeled using the capillary number

$$Ca = \frac{\tau R_d}{S} \equiv \frac{viscous\ stress\ \cdot drop\ radius}{interfacial\ tension} \tag{6.8-1}$$

and the viscosity ratio

$$\frac{\eta_d}{\eta_m} \equiv \frac{viscosity\ of\ dispersed\ phase}{viscosity\ of\ matrix\ phase} \tag{6.8-2}$$

Grace (1982) is the author the most frequently cited publication on breakup of Newtonian drops in shear and elongational flows. The results are summarized in Fig. 6.8-5 which are usually referred to as Grace curves. In shear flow, when roughly $\eta_d/\eta_m > 4$, the matrix does

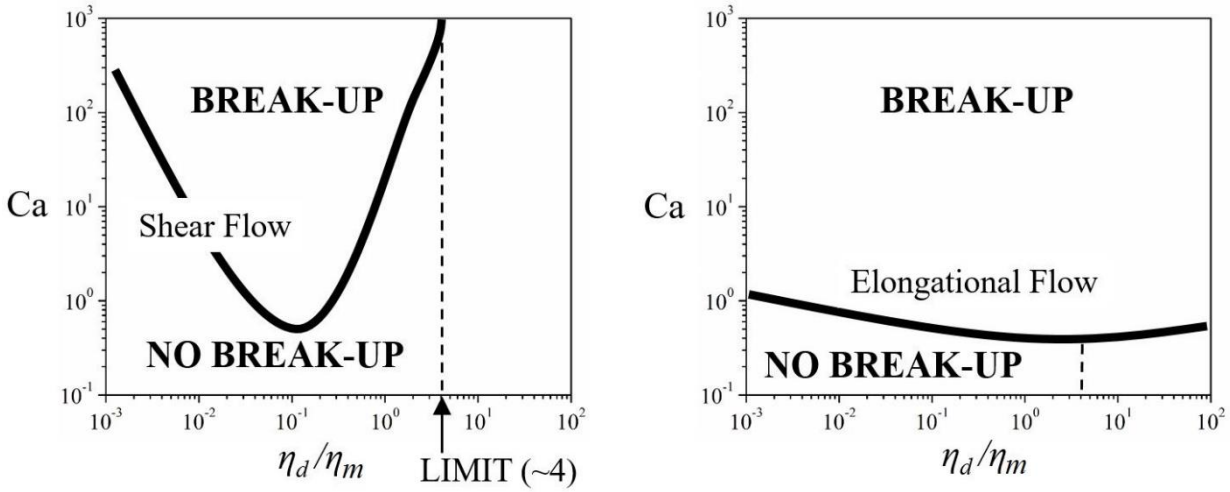

Figure 6.8-5. Grace curves for breakup of droplets in a matrix in shear and elognational flow. Adapted from Grace (1997).

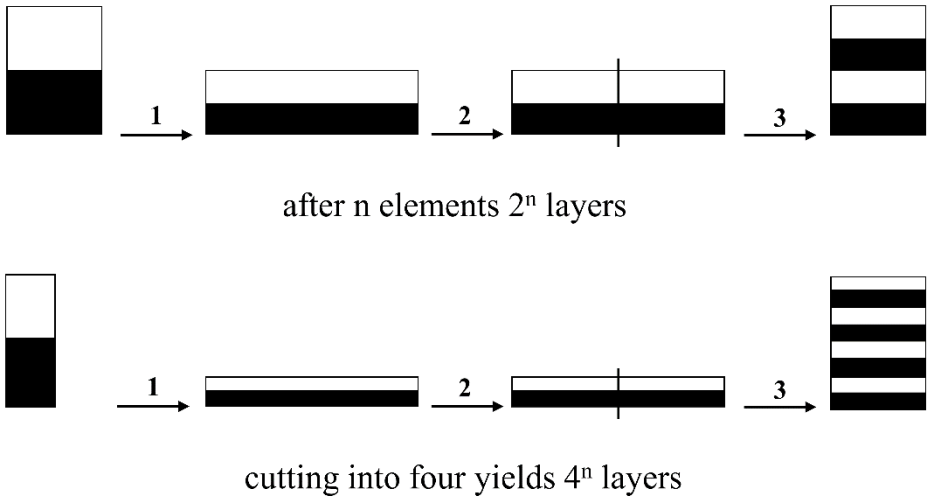

Figure 6.8-6. Schematic representation of baker's transformation. Adapted from Manas-Zloczower (2009).

not exert sufficient stress to cause rupture. However, elongational flow is very effective in causing rupture for virtually all η_d/η_m values. Although Grace curves are for Newtonian fibrils or threads, they correlate qualitatively very well with concentrated blends of polymers.

Distributive (or laminar) mixing is quantified by the growth of the interfacial area between two components. This can best be understood by the so-called baker's transformation, since it resembles to the way dough is mixed by repeatedly rolling and folding (Manas-Zloczower, 2009) as shown in Fig. 6.8-6. For the distributive mixing to be effective, the layers of the material need to undergo a combination of stretching, folding, and re-orientating steps. Elongational flow is more effective than shear for both dispersive and distributive mixing.

In single-screw extrusion of plastics, we need both good dispersion and good distribution as illustrated pictorially on the right bottom corner of Fig. 6.8-3. Mixers must be designed in such a way so as to create both shear and elognational flow regions. Different mixing section designs may be used involving pins or pegs, broken flight sections and other configurations. The mixing elements of Fig. 6.8-1 are referred to as distributive, because they involve shear and flow reorientation, but no elongation. For a mixer to be called dispersive, it must have elongational flow regions. A very common dispersive mixing element is the Union Carbide Maddock mixer which consists of parallel axial flutes. A schematic of the mixer and some details of the flow pattern are shown in Fig. 6.8-7a. The Maddock mixer is categorized as dispersive, because of the narrow flow gaps just over the flights, which generate

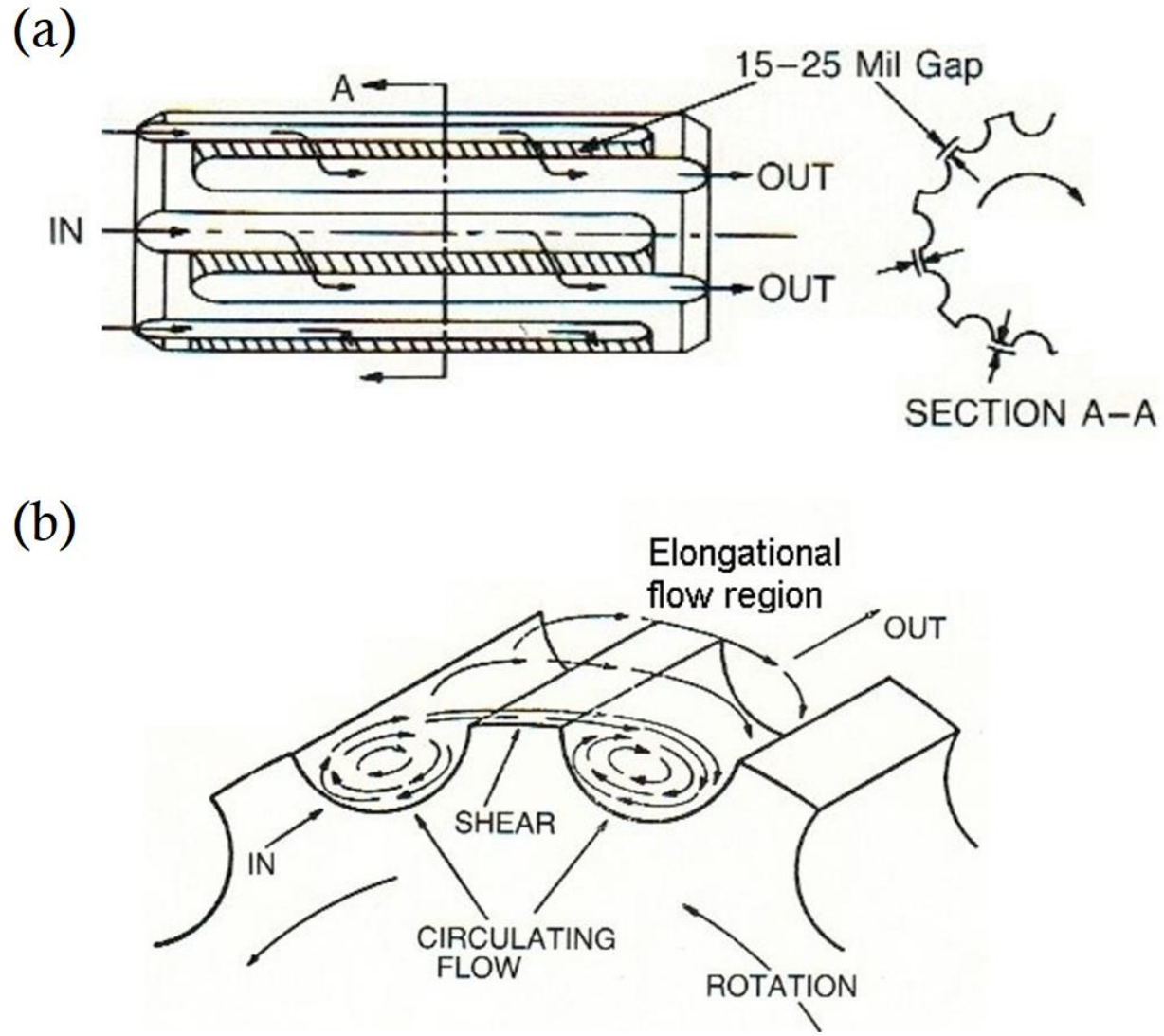

Figure 6.8-7. Schematic representation of a Union Carbide Maddock mixer and flow patterns (15-25mils are equal to 0.381-0.635 mm). Adapted from Maddock (1988).

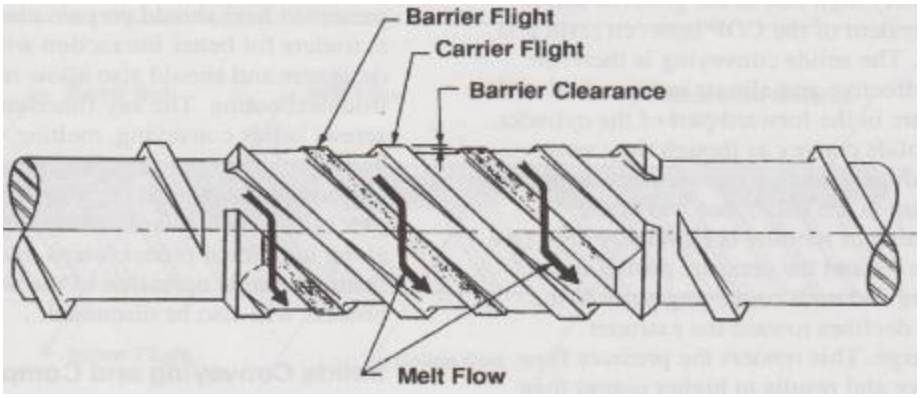

Figure 6.8-8. Schematic representation of an Egan Mixer.

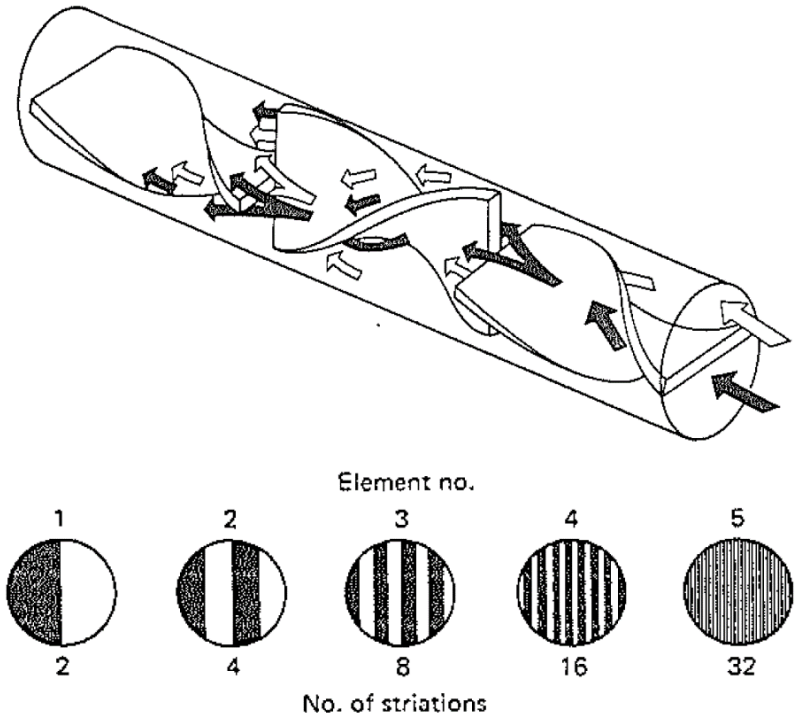

Figure 6.8-9. Schematic of a Kenics static mixer showing also that the stream is halved each time it passes a new mixing element and the interfacial area between the two streams is growing fully in accordance with baker's transformation. From Middleman (1977).

elongational flow as illustrated schematically in Fig. 6.8-7b. Another common type that performs both distributive and dispersive mixing is the Egan mixer shown in Fig. 6.8-8. The geometry of the mixer is reminiscent of a barrier screw.

Actually, after the end of the screw the melt to be supplied to the die might not have the required degree of homogenization. Static mixers are used for as post-extrusion mixing devices. A schematic of a Kenics static mixer is shown in Fig. 6.8-9. It can be seen that it is an excellent application of baker's transformation for distributive mixing. Static mixers also provide temperature homogenization which is frequently required in extrusion.

6.9 Power Requirements

In the hopper, polymer pellets are usually at room temperature (e.g. 20°C). They are packed in the solids conveying zone, melted and subsequently the melt is pumped through the die, coming out at perhaps 200°C, lower or higher, depending on polymer. We will see that most of the energy comes from the rotating screw. Of course, some energy is supplied by the heating bands around the barrel. In well running extruders usually net input of energy occurs in the first section (near the hopper) and net output in the second section (near the die) i.e. the heat generated by frictional heating (viscous dissipation) is really heating the barrel. Power is needed to:

i. Raise the hopper temperature to extrusion temperature at die entry (i.e. mass × specific heat × ΔT, where $\Delta T = T_{out} - T_{in}$ the temperature difference).

ii. Melt the polymer (i.e. mass × heat of fusion).

iii. Pump the molten polymer (ΔP × volume flow rate, ΔP the pressure drop in the die).

Table 6.9-1 **List of symbols and representative values for the parameters of Eq. 6.9-1**

Symbol	Name	Typical Values
C_P	Specific Heat (average)	1500 – 3000 J/kg °C
T_{in}	Usually room temperature	20 °C
T_{out}	Melt temperature in the die	200 °C – 300 °C
ρ	Density (average)	750 kg/ m^3 - 1500 kg/ m^3
Q	Volume flow rate (Note that the mass flow rate is: $\dot{m} = \rho Q$ usually in kg/hr)	Mass rate of flow ($\dot{m} = \rho Q$) from a few kg/hr to over 1 ton/hr depending on diameter and rotational speed
ΔP	Pressure rise	5 MPa – 50 MPa
H_f	Heat of fusion	Most polymers are semi-crystalline and the following are some typical values of the heat of fusion • LDPE: 130,000 J/kg • HDPE: 200,000 – 240,000 J/kg • PP: 230,000 J/kg • PET: 130,000 J/kg • Nylon-6,6: 200,000 J/kg • PS: theoretically zero (amorphous) i.e. non-crystalline For comparison Ice (water): 333,000 J/kg

Thus, the total power required can be expressed as

$$P_o = \rho \cdot Q \cdot C_P \cdot (T_{out} - T_{in}) + \rho \cdot Q \cdot \Delta H_f + \Delta P \cdot Q \qquad (6.9\text{-}1)$$

Let us now make some calculations to find the relative contributions of each term of Eq. 6.9-1. Assume that the molten polymer is LDPE (melt density 760 kg/m^3), output rate of 124.22 kg/hr and pressure rise of 30 MPa. We substitute the above and the material parameters from Table 6.9-1 in Eq. 6.9-1 that gives

$P_o = 124.22 \times 2500 \times (200 - 20)$

$\quad + 124.22 \times 130{,}000$

$\quad + 30 \times 10^6 \times 124.22/760$

$= 55{,}889$ kJ/hr (most important)

$+ 16{,}148$ kJ/hr (somewhat important)

$+ 4{,}903$ kJ/hr (insignificant, the extruder is an inefficient pump)

$= 76{,}950$ kJ/hr (then we multiply with $1/3600$)

$= 21.37$ kJ/s $= 21.37$ kW $\times \left(\frac{1}{0.746}\right) \approx 28.65$ HP

Therefore, we can size the HP (horsepower) of a motor turning the screw. We must take also into account its efficiency. Assume the efficiency is 90%, then the motor power would be

$$Motor\ power = \frac{1}{0.90} \times 21.73 = 24.14 \text{ kW} = 32.36 \text{ HP}$$

Very frequently, the **specific energy consumption (SEC)** is a useful quantity

$$SEC = \frac{P_o}{\dot{m}} = \frac{24.14}{124.22} \frac{\text{kW}}{\text{kg/hr}} = 0.194 \frac{\text{kWhr}}{\text{kg}}$$

since 1kWh=3.6 MJ

SEC=698 J/g

According to Campbell and Spalding (2013) the specific energy consumption in extrusion, usually ranges from 450 J/g for some amorphous polymers to 900 J/g for semicrystalline.

6.10 Generic Screw Design Characteristics

In general, the design of a screw (i.e. compression ratio, channel depths, lengths etc) depend on the polymer type extruded. There is, however, a screw design with generic features which is suitable for a range of different polymers and not necessary tailored to a single polymer. This screw type is usually referred to as a **general-purpose (GP) extrusion screw**. The typical GP screw length is in the range of 24*D*~36*D*. The feed section is usually small

compared to the total length, i.e. 4*D*~*8D,* and the metering section is usually longer 6*D*~10*D*. Note that in injection molding (IM) screws, the length of the feeding section is roughly 50% of the total length, while the transition and metering section take up roughly 25% of the total length respectively. Frequently, screws have helix angle is θ=17.66° and in this case the screw is referred to as square-pitched, because the lead is equal to the barrel diameter. The flight width is usually 0.1*D*. One of the key design parameters is the channel depth in the feed and metering sections. A good first guess for the depth H_f in the feed section would be

$$H_f = 0.11(D + 25) \quad (6.10\text{-}1)$$

in millimeters. The above equation is somewhat different for **injection molding screws**

$$H_f = 0.08(D + 25) \quad (6.10\text{-}2)$$

The compression ratio (i.e. depth at the feed section divided by the depth at the metering section) is usually, H_f/H_m=2~4 and it is highly dependent on the material. The low end value of the range (shallow channel) is used for shear sensitive materials such as PVC and the high end value usually for grades with high melt flow rate (MFR) like PP. Some typical compression ratios for different polymers are shown in Table 6.7.

Table 6.10-1 **Typical compression ratios for different polymers**

Polymer	**Compression Ratio (H_f/H_m)**
HDPE	3.0 ~ 3.5
LDPE	3.5 ~ 4.0
PP	3.0 ~ 4.0
U-PVC	1.75 ~ 2.75
P-PVC	2.5 ~ 3.5
PMMA	1.8 ~ 2.8
PET	2.3 ~ 3.2
PC	~ 2.25
PA66	3.0 ~ 4.0
TPE	~ 3.5

The length *L* of the screw is usually expressed with respect to the screw diameter *D*. In single screw extrusion (SSE) screws are usually L/D=24~36. Shorter screws are used in injection molding (IM) with L/D=18~24. In extrusion, pressure is generated by the rotating screw and longer screws can generate higher pressure. In injection molding pressure is mostly

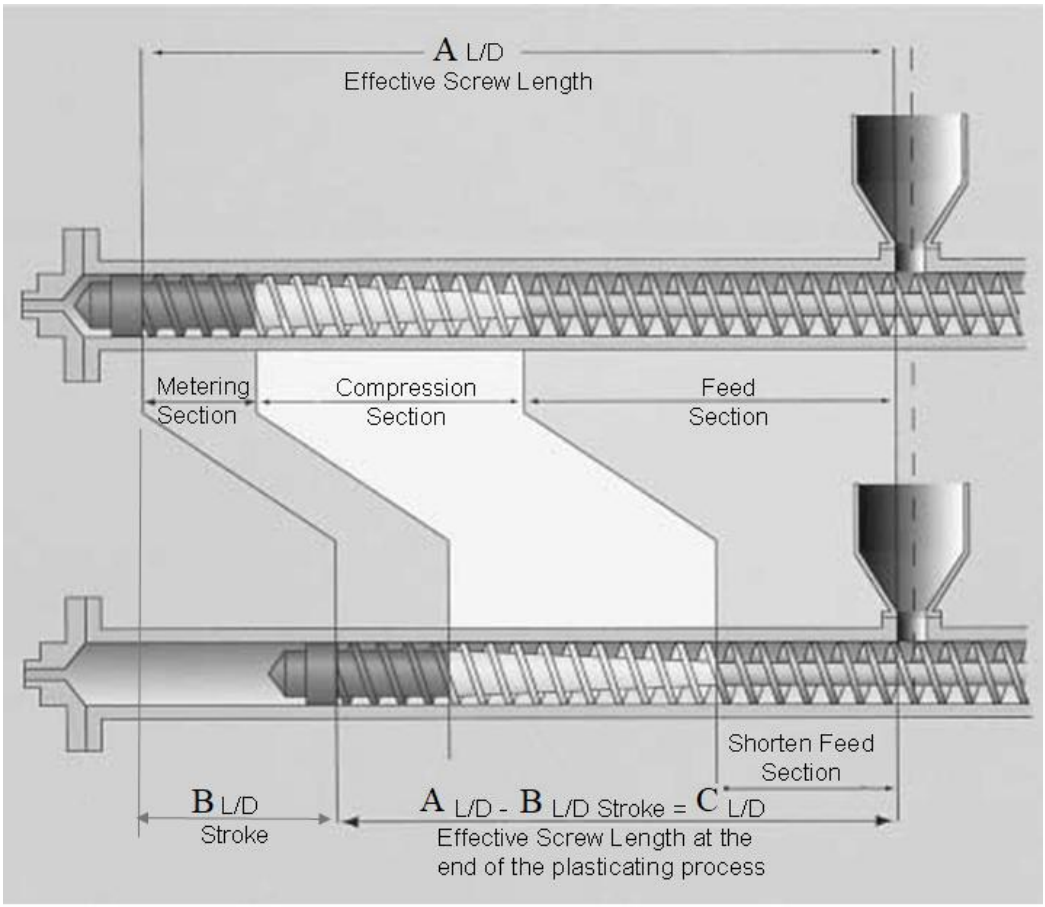

Figure 6.10.-1. Schematic representation of earlier screw designs used in single-screw extrusion (SSE) on top and in injection molding (IM) at the bottom. Notice that earlier IM screws had shorter feed section. Adopted from Womer (2011).

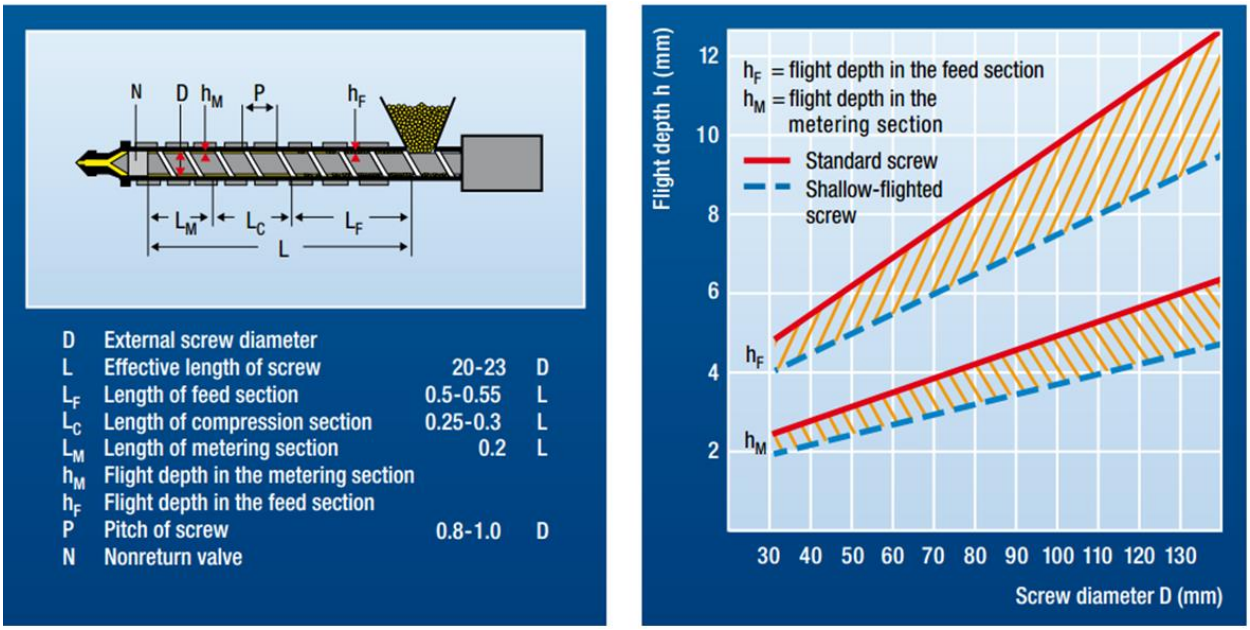

Figure 6.10-2. Recommended channel depth dependence on diameter for injection molding (IM) screws. Adapted from BASF (2007).

generated by the forward action of the screw. Generally, longer screws have higher output (limited by their melting capacity) and better mixing. SSE screws are more sophisticated than IM screws, usually of the barrier type with specially designed mixing sections. IM screws have frequently general-purpose characteristics. Lately, barrier screws are used not only in SSE but also in IM. In early IM screw designs, the feed section was shorter than a typical SSE screw of the same total length as shown in Fig. 6.10-1. The reduction in the length was used to compensate for the reciprocating movement of the screw to fill the mold. Based on better understanding of screw design, more recent IM screw designs involve generally longer screws compared to earlier designs. Helix angle θ=17.66° (square -pitched) is frequently encountered in both SSE and IM. A greater angle means less shear and higher output, whereas a smaller helix angle implies more shear and less output. Geometrical characteristics of some IM screws are given in Fig. 6.10-2.

6.11 Multi-flighted Screws

In barrier screws (Section 6.7) we have a main flight and barrier flight which separates the solids from the melt pool. Here we are talking about two or more identical flights. In Fig. 6.11-1 a conventional single-flighted screw section and a double-flighted one are shown. Something must be said about terminology: lead is the distance the screw moves in one turn. Pitch is the distance between two adjacent screw flights. So, for single flighted screws lead=pitch. For double-flighted screws the lead is twice the screw pitch.

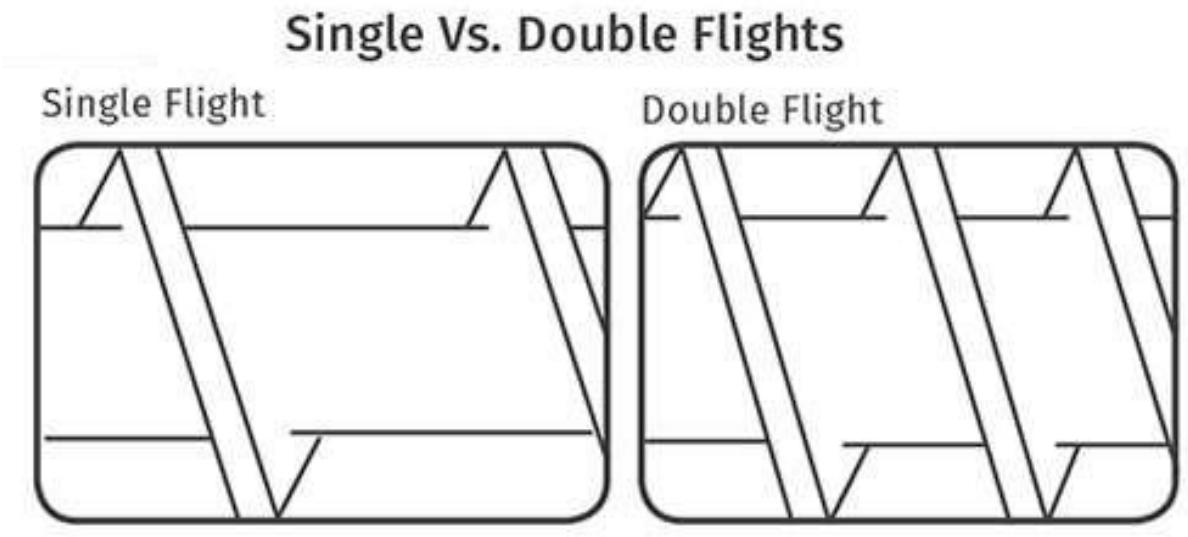

Figure 6.11-1. Schematic of a single-flighted and a double-flighted sections. In single-flighted screws lead=pitch. In double-flighted screws lead=2×pitch. Adapted from Frankland (2014).

Double flights provide more balanced pressure around the circumference than single flights. The double-flights provide more bearing or support area for the screw, thereby preventing screw deflection caused by possibly high pressure loads. Also, double-flighted feed sections work best when teamed with grooved barrels according to Frankland (2014). In terms of the throughput capacity, double flighted screws deliver less output due to the presence of the additional flight that takes up more space in the channel and provides more flow obstruction. For output calculations with multi-flighted screws, the metering zone equation of Section 6.3 is used by including the volume reduction caused of the additional flights (Vlachopoulos and Wagner, 2001). The correction factors (also known as shape factors) F_d for drag and F_p for pressure flow are also included. These account for the flow restriction caused by the flights, while in the derivation of Eq. 6.3-7, we considered only the "rotating" barrel. For shallow channel screws F_d=F_p=1. When the channel depth h approaches the width w, the correction factors approach 0.5 (Campbell and Spalding, 2013)

Table 6.11-1 **Metering flow equation for multi-flighted screws, including correction factors accounting for the effect of flights on drag and pressure flow.**

$$Output = Q_{drag} - Q_{pressure}$$

$$Q_{drag} = \frac{F_d \cdot \pi^2 \cdot D^2 \cdot N \cdot h \left(1 - \frac{n \cdot e}{t}\right) \sin\theta \cdot \cos\theta}{2}$$

$$Q_{pressure} = \frac{F_p \cdot \pi \cdot D \cdot h^3 \left(1 - \frac{n \cdot e}{t}\right) \sin^2\theta \cdot \Delta P}{12 \cdot \mu \cdot L}$$

Q_d	Drag flow pumping term
Q_p	Pressure flow resisting pumping
F_d (channel correction factor)	$0.140\times (h/w)^2 - 0.645\times(h/w) + 1$
F_p (channel correction factor)	$0.162\times (h/w)^2 - 0.742\times(h/w) + 1$
D	Screw diameter
N	Screw speed (RPM)
h	Screw's metering section channel depth
n	Number of flights of the screw
e	Thickness of the flight
t	Flight lead (pitch)
θ	Flight helix angle
μ	Viscosity of the melt calculated at shear rate = $\pi DN/h$
L	Length of the metering section

6.12 Simple Analysis of a Typical Extruder

For understanding the operation and for getting an idea of the magnitude of the parameters involved, we present in this section an example involving a typical single screw extruder and a die. This example is written up as a student homework assignment for the purpose of providing understanding into the various concepts, parameters and quantities involved in extrusion calculations. We assume a typical 4-inch diameter (L/D=26) screw extruder which is a very common machine in the extrusion industry. Nominal diameter is D=2R=100 mm and the length is L=26×0.1=2.6 m. The compression ratio for this screw is 3. This means that the channel depth in the feed zone is 3 times larger than the metering zone. The relative lengths of feed/transition/metering zones: 8D/8D/10D as shown in Fig. 6.12-1.

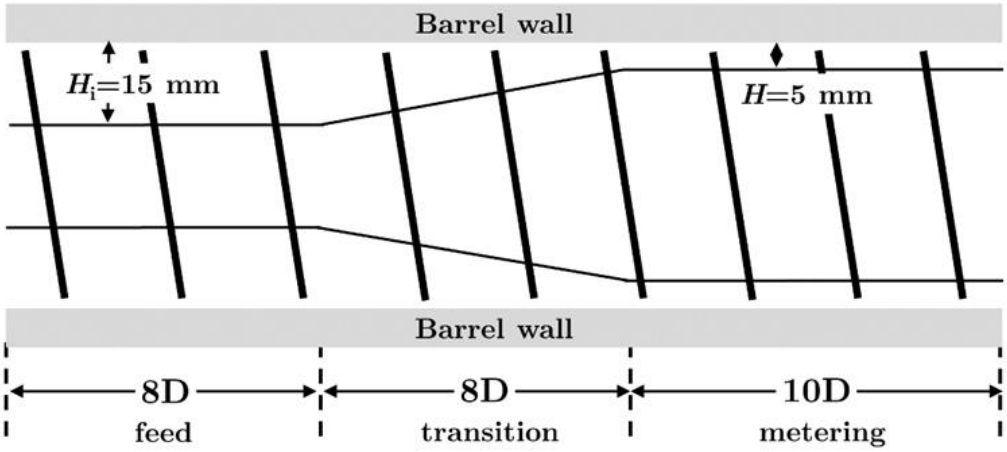

Figure 6.12-1. Schematic representation of the screw geometry.

The channel depth in the metering zone is H=5 mm. The screw is square pitched (helix angle θ=17.66º). The material extruded has melt density ρ=780 kg/m^3, viscosity at T=250 ºC $\eta = 10{,}000 \cdot \dot{\gamma}^{-0.6}$ Pa·s^n (i.e. power–law exponent n=0.4 and m=10,000 Pa·s$^{0.4}$), specific heat C_p=2,300 J/(kg ºC) and heat of fusion ΔH_f= 200,000 J/kg. The polymer pellets enter at T_o=20 ºC and the product exits at T=250 ºC into a round die having radius R_d=4 mm and length L_d=480 mm. The screw rotates at N=60 RPM.

a. Calculate the drag flow output.

b. Calculate the operating point by taking into consideration the head pressure generated by the die.

c. Calculate the power for the motor assuming that it produces 100% of the energy needed to raise the melt temperature from T_o to T, to melt and pump the polymer.

d. Calculate the torque by recalling that

(i) Power: $P_o = F \cdot V$ (force × velocity) from which $F = \frac{P_o}{V}$

(ii) Torque: $T_o = F \cdot R$ (force × radius) from which $T_o = \frac{P_o}{V} R = \frac{P_o}{2\pi RN} R = \frac{P_o}{2\pi N}$

where N is the speed of rotation.

e. Then, after these calculations go "backwards". That is, you are going to start from calculation of torque from $T_o = F \cdot$ *radius*, where $F = \tau_w \cdot A =$ *wall shear stress* × *area* and then calculate the power from $P_o = F \cdot V = \tau_w \cdot A \cdot V$. Although the feed and compression sections have different base screw diameter, assume it is the same from feed to screw exit (i.e. for the length of $L = 26D$). Assume also that the radius for torque equation calculation is the barrel radius minus the gap in the metering zone ($R-H = 50-5 = 5$ mm), therefore $T_o = \tau_w \cdot A \cdot (R-H)$. Based on the above, calculate the power and torque from shear stress calculations.

f. Comment on the differences in calculations between **(c), (d)** and **(e)** and describe what one should have done to minimize the differences.

Solution

We have already derived an equation for output in Section 6.3.

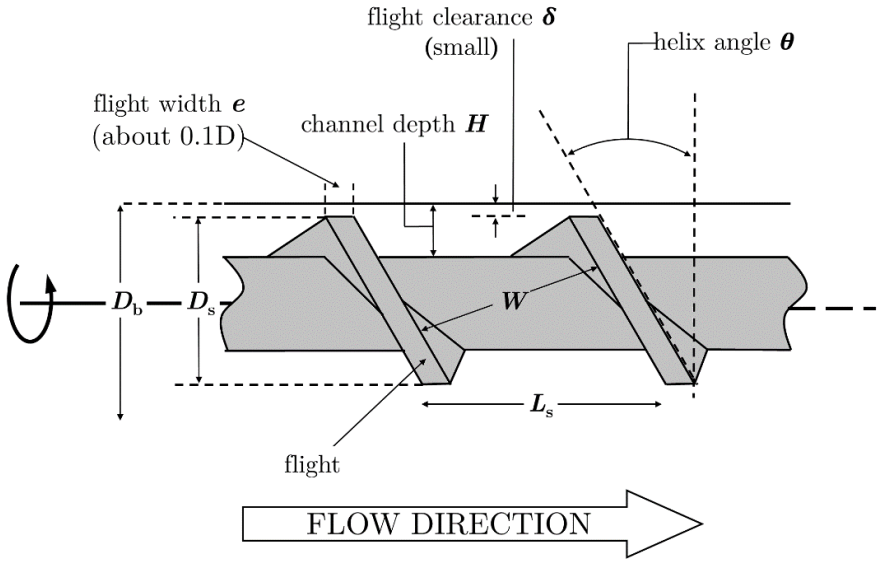

Figure 6.12-2. Schematic representation of a typical single-flighted screw section.

We will repeat a few things by focusing on the screw geometry of Fig. 6.12-2, where

D_s: screw diameter (taken at tip of flight)

D_b: barrel diameter = $D_s+2\delta$

L_s: screw lead or pitch ($L_s=\pi D_s \tan\theta$)

W: channel width ($W=L_s\cos\theta - e)=\pi D_s \tan\theta \cos\theta$ (neglecting flight width e)

and

$$Q = \frac{1}{2}\pi^2 D^2 HN sin\theta cos\theta - \frac{\pi D H^3}{12\mu} sin^2\theta \frac{\Delta P}{L} \tag{6.12-1}$$

where $\Delta P = P_{2(exit)} - P_{1(entrance)}$, L the length of the screw, θ helix angle, D barrel diameter, H channel depth, N speed of rotation and μ an equivalent (Newtonian) viscosity calculated at $\dot{\gamma} = \pi DN/H$. We have $\eta = 10000\dot{\gamma}^{-0.6}$, N=60 rpm, D=100 mm and H=5 mm. Hence, the reference shear rate is

$$\dot{\gamma}_{ref} = \frac{\pi \times 100}{5}\frac{60}{60} \approx 62.8\, s^{-1} \tag{6.12-2}$$

Therefore, $\eta = 10000 \times 62.8^{-0.6} = 834.11$ Pa·s$^{0.4}$. This is the "equivalent" Newtonian viscosity μ in the melt extruder equation for Q (Eq. 6.12-1).

1. If there is no pressure build-up in the extruder (i.e. no constriction of flow at the end of the extruder), the output would be maximum, i.e. drag flow only

$$Q_{max} = \frac{1}{2}\pi^2 D^2 HN sin\theta cos\theta \tag{6.12-3}$$

2. If the end is closed, Q=0 and we may equate drag and pressure flow

$$\frac{1}{2}\pi^2 D^2 HN sin\theta cos\theta = \frac{\pi D H^3}{12\mu} sin^2\theta \frac{\Delta P}{L} \tag{6.12-4}$$

This gives the maximum possible pressure

$$P_{max} = \frac{6\pi DLN\mu}{H^2 tan\theta} \tag{6.12-5}$$

We now proceed with calculations for our problem.

a. To calculate the drag flow output of the extruder (i.e. no die attached at the end) we will use Eq. 6.12-3, which is of course the <u>maximum</u> flow rate the extruder may deliver when there is no die at the end to restrict the flow. Since we have the very common square pitched screw (θ=17.66°), Eq. 6.12-3 may be written in a useful for quick-calculations form

$$Q_{max} = 1.42 D^2 HN \tag{6.12-6}$$

and since the mass flow output is given $\dot{m} = \rho Q$ we may rewrite Eq. 6.12-6 in another useful form

$$\dot{m}_{max} = 1.42 \rho D^2 HN \tag{6.12-7}$$

We then substitute the known values (all in SI units)

$$\dot{m}_{max} \cong 1.42 \times 780 \times 0.1^2 \times 5 \times 10^{-3} \times \frac{60}{60} \times 3600 = 199.37 \text{ kg/hr} \tag{6.12-8}$$

This is the maximum mass flow rate $\dot{m}_{max}$ when there is no die attached to the end of the extruder.

b. To calculate the operating point of the extruder/die we must plot the operating lines for the extruder and the die. The calculation of the operating line of the extruder needs only two set of points in the space of $(\Delta P, \dot{m})$. The first point is for the maximum mass flow rate $\dot{m}_{max}$ (no die at the extruder end), and the second point is for the maximum possible pressure P_{max} when the die is completely closed. The maximum pressure is calculated from

$$P_{max} = \frac{6\pi DLN}{H^2 tan\theta}\mu \tag{6.12-9}$$

and by making the proper substitutions (all in S.I. units) we have

$$P_{max} = \frac{6 \times 3.1415 \times 10^4 \times 0.1 \times 1 \times \frac{60}{60}}{0.005^2 \times tan17.66^o} \times 834.11 \cong 197.53 \text{ MPa} \tag{6.12-10}$$

This is based on the Newtonian constant viscosity assumption for a screw length of L=10D (i.e. the length of the metering (pumping) zone). For the operating line of the extruder we have the two reference points which are (199.37 kg/hr, 0) and (0, 197.53 MPa) and we know that flow rate and pressure have a linear relation (Eq. 6.3-8). To plot the operating line for the die the well-known Hagen–Poiseuille formula for a power–law fluid is used. The equation, in terms of the mass flow rate, is the following (see Table 2.7-1 in Chapter 2)

$$\dot{m}_{die} = \pi\rho\left(\frac{n}{3n+1}\right)\left[\frac{1}{2m}\left(\frac{\Delta P}{L_d}\right)\right]^{\frac{1}{n}} R_d{}^{\frac{1}{n}+3} \tag{6.12-11}$$

We give a typical example of the mass flow rate calculation for the pressure drop of 10 MPa (everything in S.I. units)

$$\dot{m}_{die} = 780 \times 3.1415\left(\frac{0.4}{3 \times 0.4 + 1}\right)\left[\frac{1}{2 \times 10^4}\left(\frac{10^7}{0.480}\right)\right]^{\frac{1}{0.4}} (0.004)^{\frac{1}{0.4}+3} \times 3600 \tag{6.12-12}$$

$$\cong 3.637 \text{ kg/hr}$$

In Table 6.12 we show some results for different mass flow rate through the die and then plot the die operating line in Fig. 6.12-3 together with the extruder. The operating point is determined from the crossing of the extruder line and the die curve. Approximately, by rounding the numbers, $\dot{m}$**≈150 kg/hr** and ΔP **≈ 45 MPa**.

Table 6.12-1	
Pressure drop (ΔP) for the die (MPa)	**Mass flow rate (kg/hr)**
0	0
10	3.6
20	20.5
30	56.6
40	116.4
50	203.1

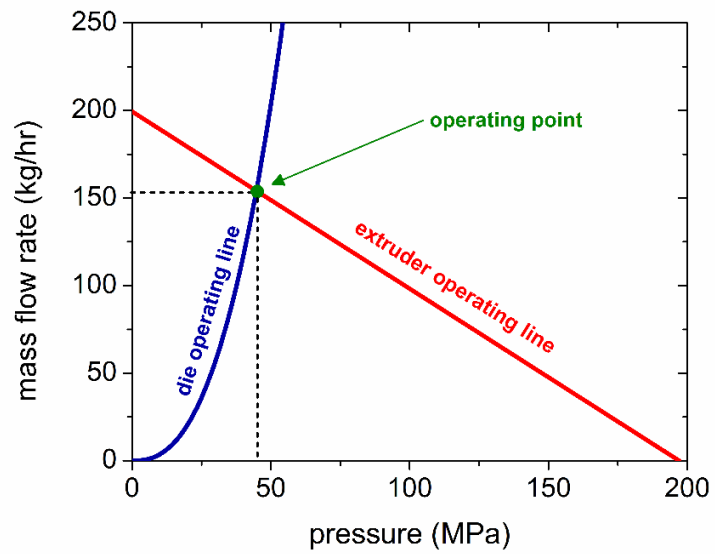

Figure 6.12-3. Calculated operating point by the crossing of extruder with die operating line.

(c) The power supplied by the motor of 100% efficiency is spent for (i) raising the temperature from T_o to T, (ii) melting the polymer and (iii) pumping the polymer. To calculate the amount of the power we shall Eq. 6.5-1, which we write it in terms of the mass flow rate (i.e. $\dot{m} = \rho Q$)

$$P_o = \dot{m}C_P(T_{out} - T_{in}) + \dot{m}\Delta H_f + \Delta P\frac{\dot{m}}{\rho} \tag{6.12-13}$$

Upon substitution (using the $\dot{m}$ and ΔP values corresponding to the operating point) we have

$$P_o = \frac{150}{3600} \times 2300 \times (250 - 20) + \frac{150}{3600} \times 2 \times 10^5 + 45 \times 10^6 \times \frac{150}{3600 \times 780} \tag{6.12-14}$$

$$= 22041.67 + 8333.33 + 2403.85 = 32778.85\ \text{W} = 32.78\ \text{kW} = 43.96\ \text{HP}$$

(d) We calculate the torque from power, as follows

$$T_o = F \cdot R = \frac{P_o}{V}R = \frac{P_o}{2\pi RN}R = \frac{P_o}{2\pi N} = \frac{32778.85}{2\pi \times \frac{60}{60}} = 5217.07\ \text{N} \cdot \text{m} \tag{6.12-15}$$

(e) To calculate the power from shear stress considerations we have

$$P_o = F \cdot V = \tau_w AV = m\dot{\gamma}^n AV = m\left(\frac{V}{H}\right)^n VA = m\frac{(2\pi RN)^{n+1}}{H^n}A \tag{6.12-16}$$

where A is the area on which the wall shear stress acts on. It is given by

$$A = 2\pi(R-H)L_s \tag{6.12-17}$$

where L_s should be the length along the helix (the melt is dragged along the helical channel) which is expressed as $L_s = L/\sin\theta$. Substituting this into Eq. 6.8-25 we arrive at

$$A = \frac{2\pi(R-H)L}{\sin\theta} \tag{6.12-18}$$

Substituting this in Eq. 6.8-24 we have

$$P_o = m\frac{(2\pi RN)^{n+1}}{H^n}\frac{2\pi(R-H)L}{\sin\theta} \tag{6.12-19}$$

and then we substitute the known quantities (everything in S.I. units)

$$P_o = 10^4\frac{\left(2\pi \times 0.05 \times \frac{60}{60}\right)^{0.4+1}}{0.005^{0.4}} \times \frac{2\pi \times (0.05-0.005) \times 2.6}{\sin 17.66} = 39.88\ \text{kW} \tag{6.12-20}$$

Now, to calculate the torque we have

$$T_o = \tau_w A(R-H) = m\dot{\gamma}^n A(R-H) = m\left(\frac{V}{H}\right)^n A(R-H) = m\left(\frac{2\pi RN}{H}\right)^n A(R-H) \tag{6.12-21}$$

Substituting in the above equation the area from Eq. 6.8-26 we have

$$T_o = m\left(\frac{2\pi RN}{H}\right)^n \frac{2\pi(R-H)L}{\sin\theta}(R-H) = m\left(\frac{2\pi RN}{H}\right)^n \frac{2\pi L(R-H)^2}{\sin\theta} \tag{6.12-22}$$

where upon substitution we have

$$T_o = 10^4\left(\frac{2\pi \times 0.05 \times \frac{60}{60}}{0.005}\right)^{0.4} \frac{2\pi \times 2.6 \times (0.05-0.005)^2}{\sin 17.66} = 5712.97\ \text{N} \cdot \text{m} \tag{6.12-23}$$

(f) The present estimates are surprisingly close (fortuitously) to the ones from total energy calculations (power = 32.28 kW and torque = 5217 N·m).

A more accurate calculation would require determination of the frictional heating generated in each of the regions of the screw, the local viscosity and the local shear rate, to determine an accurate wall shear stress. In the metering zone this can be done by integrating the quantity $F \cdot \overline{V}$ over the fluid volume and determination of local temperatures. However, in the transition and feed zones we have a mixture of solids and melt and it is virtually impossible to arrive at good estimates of the stress developed. Thus, the power and torque

calculations based on the energy required to raise the temperature, melt and pump the polymer are easier to do.

In the present calculation, we assumed that the stress generated by the motor is the same throughout the screw and we calculate it at a distance of $H = 0.005$ m from the barrel wall at an assumed temperature of T=250°C throughout, which ended up giving reasonable estimates of power and torque, even though the actual values are different

Comments:

In the present simple calculations, the pressure grows monotonically till the entrance to the die as it is shown schematically in Fig. 6.12-4a. However, the real extruder has a compression section as shown in Fig. 6.12-5. In the compression section there would be some pressure generation and the pressure profile would look like the one shown schematically in Fig. 6.12-4b. However, this cannot be calculated by unidimensional flow equations.

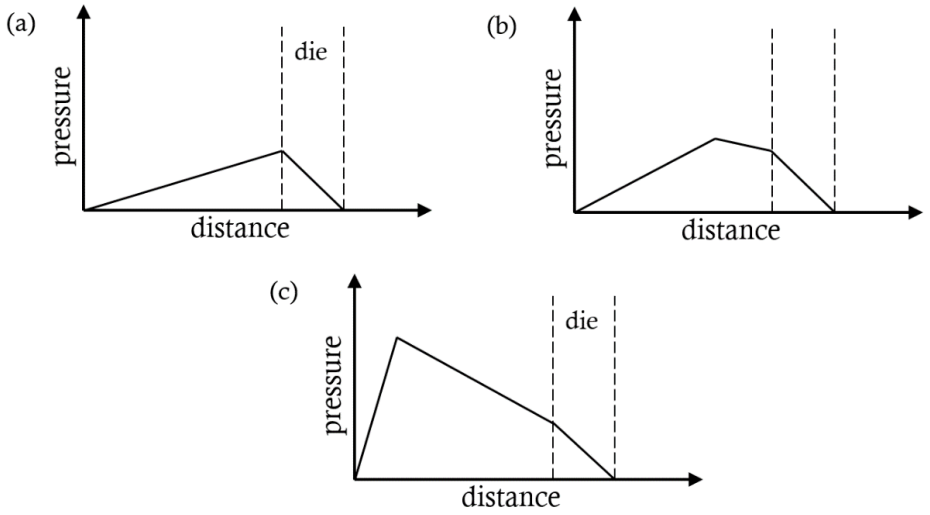

Figure 6.12-4. Schematic representation of typical pressure profiles

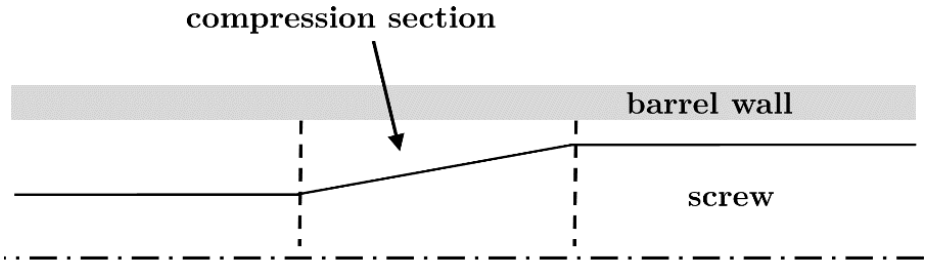

Figure 6.12-5. Schematic representation of a screw compression section. Virtually no compression is needed in grooved feed extruders because of the very high pressure generated in the grooved section.

If a grooved barrel extruder was used there would be significant pressure rise in the solids conveying zone. In grooved feed extruders there is almost no compression like that shown in Fig. 6.12-4c. The compression ratio is about 1.2 to 1.0, i.e. in the feed section the channel has about the same depth (5 mm) as in the metering (pumping) zone. The pressure rise could be 100–200 MPa. The higher pressure would likely result in at least 50% higher output than drag flow. However, this is impossible to determine with simple calculations.

Comparison to computer simulation with NEXTRUCAD

NEXTRUCAD (2013) is a commercially available software package for simulating the operation of single screw extruders. We carried out a simulation and the results are shown in Figs. 6.12-6, 6.12-7 and 6.12-8.

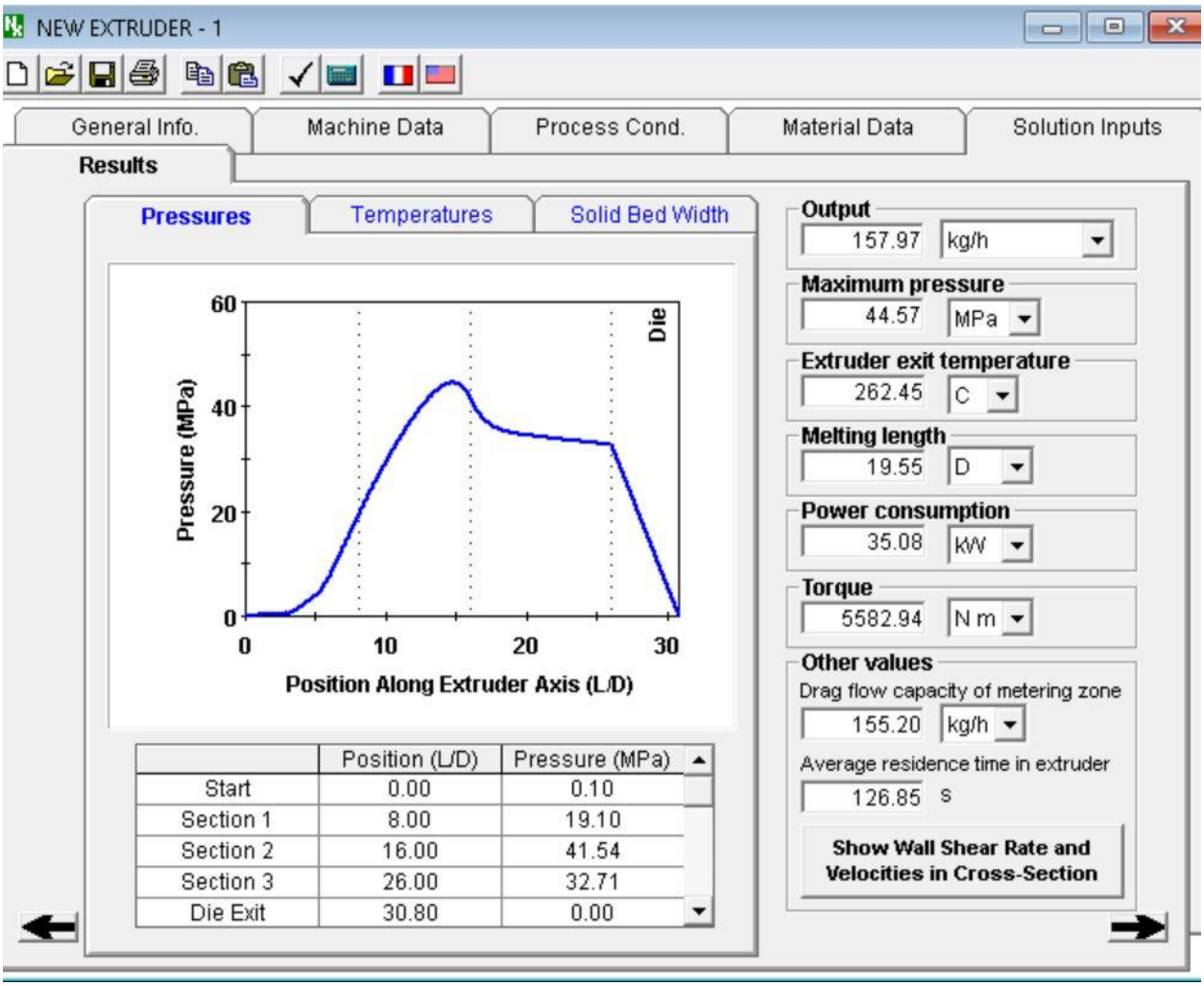

	Position (L/D)	Pressure (MPa)
Start	0.00	0.10
Section 1	8.00	19.10
Section 2	16.00	41.54
Section 3	26.00	32.71
Die Exit	30.80	0.00

Figure 6.12-6. Pressure as a function of position and other quantities.

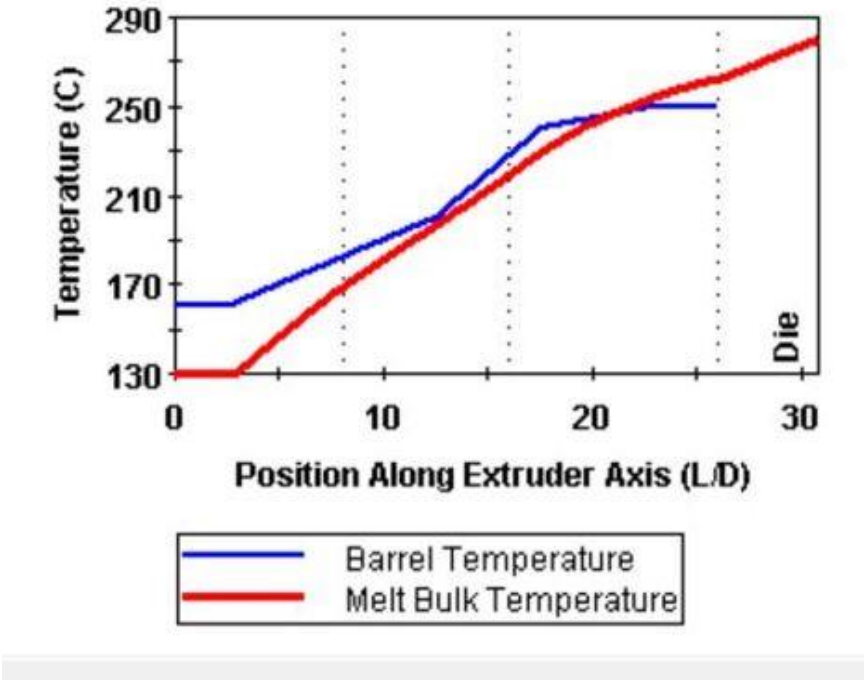

Figure 6.12-7. Set barrel temperature and calculated melt temperature along extruder and die.

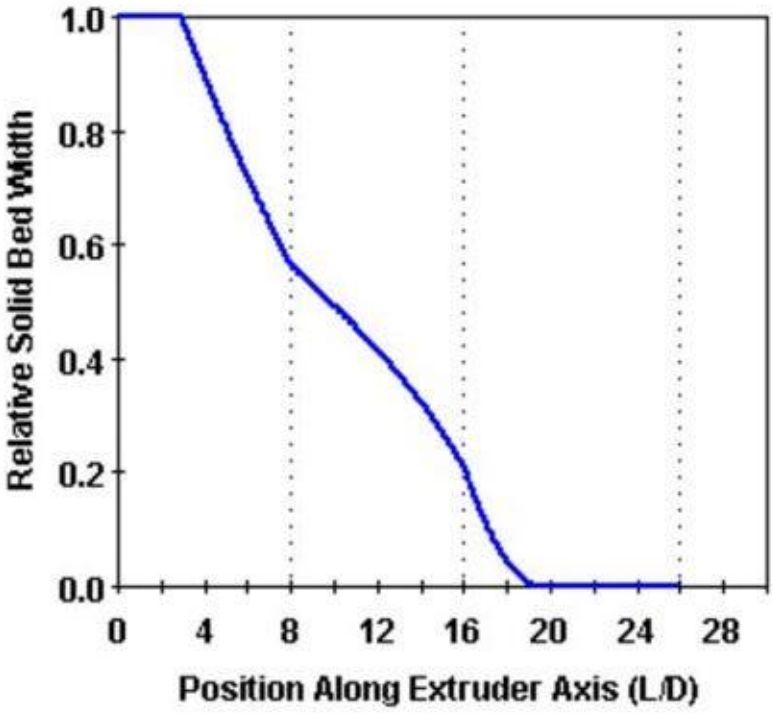

Figure 6.12-8. Relative solid bed width along the extruder length.

NEXTRUCAD also determines the solid bed width. This is very important to know, because no screw would have acceptable performance if the solid bed is not fully melted before the

end of screw. The various quantities by the two methods of calculations are compared in Table 6.12-2.

***Table 6.12-2*. Comparison of calculations**		
	Simple Analysis	NEXTRUCAD
Output (Q) in kg/hr	150	157.97
Power (P) in kW	32.77	35.08
Torque (T_o) in N·m	5217.77	5582.94
Solid bed zero width	N/A	Predicted at L/D=19

It can be seen that the output rate, power consumption and torque can be determined with the simple flow analysis method. The solid bed profile cannot be determined by simple calculations. Of course, calculations with barrier screws (MacGregor *et al.*, 1997 and Castillo *et al.*, 2002), which are the most common types of screws used today, are not possible with simple flow analysis. For screw design purpose computer simulation is necessary. One of the great advantages of computer software is that "what if" scenarios can be easily and quickly examined.

Bibliography

Agassant J.-F., Avenas P., Sergent J.-P., Vergnes B. and Vincent M., *Mise en Forme des Polymères* (4e éd.), Lavoisier, Paris (2014)

Agur E.E. and Vlachopoulos J., Numerical Simulation of a Single-Screw Plasticating Extruder, Polym. Eng. Sci., 22 (17), 1084 (1982)

Barr R.A., A Conductive Melting Screw Design, Presented at SPE Extrusion Division RETEC Toronto (1993)

BASF, Screw Designs in Injection Molding, www.plasticsportalasia.net, Technical Information (2007)

Bernhardt E.C., *Processing of Thermoplastic Materials*, Reinhold, New York (1959)

Campbell G.A. and Spalding M.A., Analyzing and Troubleshooting Single-Screw Extruders, Hanser (2013)

Carley J. F. and Strub S.A., Basic Concepts of Extrusion, Ind. Eng. Chem., 45, 970 (1953a)

Carley J. F. and Strub R. A., Application of Theory to Design of Screw Extruders, Ind. Eng. Chem., 45, 978 (1953b)

Carley J. F., Mallouk R. S. and McKelvey J. M., Simplified Flow Theory for Extruders, Ind. Eng. Chem., 45, 974 (1953)

Carley J. F. and McKelvey J. M., Extruder Scale Up Theory and Experiments, Ind. Eng. Chem., 45, 989 (1953)

Castillo R.J., Strutt D. and Vlachopoulos J., Experiments and Simulations with Barrier Screws, SPE ANTEC Proceedings, 318, San Francisco, CA (2002)

Chung C.I. and Barr R.B., U.S. Patent No 4,405,239 (20 September 1983)

Chung C.I., *Extrusion of Polymers: Theory and Practice* (2nd Ed.), Hanser (2011)

Darnel W.H. and Mol E.A.J, Solids Conveying in Extruders, SPE J., 12, 20 (1956)

Frankland J., EXTRUSION: Double Flights Are Not a Cure-All, www.ptonline.com (2014)

Gale M., Compounding with single-screw extruders, Adv. Polym. Technol., 16 (4), 251 (1997)

Gore W. L., Introduction–Theory of Extrusion, Ind. Eng. Chem., 45, 969 (1953)

Grace H.P., Dispersion phenomena in high viscosity immiscible fluid systems and application of static mixers as dispersion devices in such systems, Chem. Eng. Commun. 14, 225 (1982)

Grünschloß E., A powerful universal plasticating system for single-screw-extruders and injection moulding machines, Int. Polym. Process., 30 (2), 226 (2007a)

Grünschloß E., HELIBAR – A powerful Single Screw Plasticating System, SPE-ANTEC Conference, Cincinnati, 405 (2007b)

Jepson C. H., Future Extrusion Studies, Ind. Eng. Chem., 45, 992 (1953)

MacGregor A., Vlachopoulos J. and Vlcek J., Computer Simulation of Conventional and Barrier Screw Extruders, J. Reinf. Plast. Compos., 16 (14), 1270 (1997)

Maddock B. H., A Visual Analysis of Flow in Mixing in Extruder Screws, SPE J., 15, 383 (1959)

Maddock B.H., The Birth and nature of the plastics Extruder, SPE International Award Presentation, Union Carbide Corporation (1988)

Maillefer C., Etude Theorique et Experimentale sur le Fonctionnement des Boudineuses, Doctoral Thesis, University of Lausanne, Switzerland (1952)

Maillefer Ch., Boudinese à vis, Swiss patent CH363149, Priority Dec. 31 (1959)

Maillefer C., A Two Channel Extruder Screw, Modern Plast., 40, 132 (1963)

Mallouk R. S. and McKelvey J. M., Power Requirements of Melt Exruders, Ind. Eng. Chem., 45, 987 (1953)

Manas-Zloczower I., *Mixing and Compounding of Polymers*, Hanser (2009)

McKelvey J. M., Experimental Studies of Melt Extrusion, Ind. Eng. Chem., 45, 982 (1953)

McKelvey J.M., *Polymer Processing*, Wiley (1962)

Middleman S., *Fundamentals of Polymer Processing*, McGraw-Hill (1977)

Moffatt H.K., Viscous and Resistive Eddies Near a Sharp Corner, J. Fluid Mech., 18 (1), 1 (1964)

Myers J.A. and Barr R.B., Improved Screw Design for Maximum Conductive Melting, Conf. Proc. SPE-ANTEC, 154 (2002)

Polychronopoulos N.D. and Vlachopoulos J., Computer Flow Simulation of Moffatt Eddies in Single Screw Extrusion, Int. Polym. Proc., 33 (5) 662 (2018)

Rauwendaal C., *Polymer Extrusion,* Hanser (2014)

Schenkel G., *Kunststoff-Extrudertechnik*, Hanser (1963)

Spalding M. A., Gou Q. and Sun X., The Incumbent Resin Effect for the Single-Screw Extrusion of Polyethylene Resins, SPE ANTEC Tech. Papers, 789 (2016)

Spirex Corporation, *Plasticating Components Technology*, Youngstown, OH (1997)

Tadmor Z., Fundamentals of Plasticating Extrusion. I. A Theoretical Model for Melting, Polym. Eng. Sci., 6 (3), 185 (1966)

Tadmor Z. and Klein I., *Engineering Principles of Plasticating Extrusion*, Van Nostrand-Reinhold (1970)

Tadmor Z. and Gogos C.G., *Principles of Polymer Processing* (1st Edition), Wiley (1979)

Tadmor Z. and Gogos C.G., *Principles of Polymer Processing* (2nd Edition), Wiley (2006)

Taylor G.I., The viscosity of a fluid containing small drops of another fluid, Proc. R. Soc. Lond. A Math. Phys. Sci., 138 (834), 41 (1932)

Taylor G.I., The formation of emulsions in definable fields of flow, Proc. R. Soc. Lond. A Math. Phys. Sci. 146 (858), 501 (1934)

Torner R.V., *Grundprozesse der Verarbeitung von Polymeren*, VEBDeutscher Verlag fuer Grundstoffindustrie, Leipzig (1973)

Womer T.W., The Evolution of Screw Design Technology for the Injection Molding Process-Part 1, www.plasticstrends.com (2011)

Vlachopoulos J. and Wagner J.R. Jr, *The SPE Guide on Extrusion Technology and Troubleshooting*, SPE (2001)

Vlachopoulos J., *Fundamentals of Fluid Mechanics*, Polydynamics, Dundas, Ontario (2016)

Zhu F., *Extrusion Theory and Application*, China Light Industry press Ltd (2001)

J. Vlachopoulos and N.D. Polychronopoulos "*Understanding Rheology and Technology of Polymer Extrusion*", First Edition, Polydynamics Inc, Dundas, Ontario, Canada (2019)

Chapter 7
FLAT FILM AND SHEET EXTRUSION

7.1 Introduction

The first objective in flat film or sheet production is to spread a continuous polymer melt stream coming from an extruder into a die, which terminates in a rectangular and wide cross–section, having a small gap. After the die, the molten extrudate is cooled on chilled rollers and solidifies. Products of less than 0.25 mm in thickness are usually referred to as films (also cast films) and those over 0.25 mm are referred to as sheets (Ivey, 2001). For this chapter the authors present an abridged version of one of their publications in another book (Vlachopoulos *et al.*, 2012).

The rate at which the extrudate is cooled determines several important properties of the finished product. Longer cooling means there is more time available for crystal growth and thus the crystallites will be larger (Osborn and Jenkins, 1992). Crystallinity affects the density, optical properties, coefficient of friction, impact, barrier and other properties. Compared to blown film (see Chapter 8), the cast film process shows better optical properties, higher output rate per hour and lower gauge variation. Most cast film lines manufactured today are co-extrusion lines. Co-extrusion is defined as the process of simultaneous extrusion of two or more materials through a common die. It is used for the purpose of combining material properties and reducing the cost at the same time. Thickness uniformity in monolayer extrusion and layer uniformity in co-extrusion are the key measures for quality (Vlachopoulos *et al.*, 2012).

Sheet lines, as noted earlier, are lines that produce film with a thickness exceeding 0.25 mm. Typically a sheet line will have a three-roll cooling stack after the die, as shown in Fig.

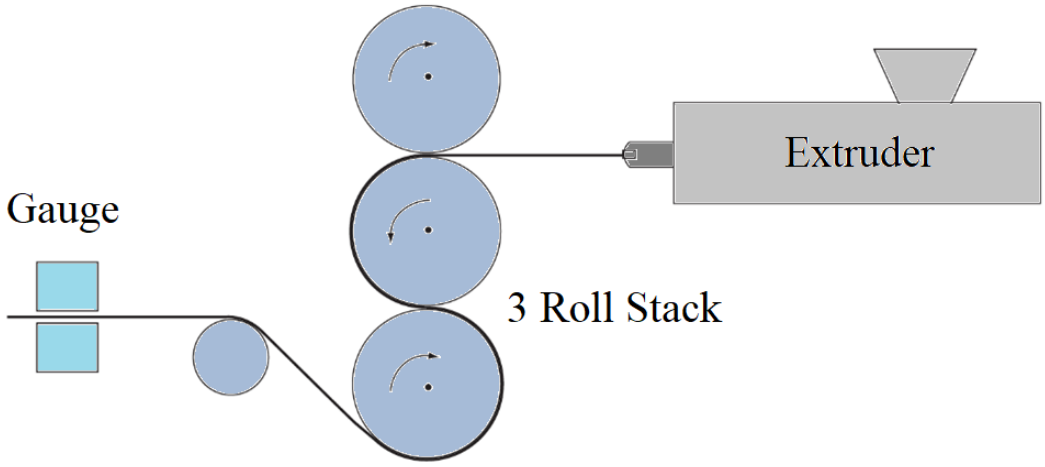

Figure 7.1-1. Schematic of a typical sheet line with a three roll cooling stack after the die.

7.1-1, and again the cooling rate plays a very important role in determining the properties of the finished product. A detailed troubleshooting guide of monolayer and coextruded sheet is available in the open literature (Powers, 1996). Several issues relating to film processing, materials and properties are discussed in a handbook (Butler, 2005).

7.2 Flat Die Design

The molten polymer stream coming from an extruder must be distributed as uniformly as possible into a rectangular shaping area so that a thin wide sheet or film of uniform thickness is continuously produced. Between the melt pipe, coming from the extruder, and the rectangular die lips a distribution channel (usually called a manifold) is needed. The most common dies (Michaeli, 1992, Kanai, 1999) utilize either the simple 'T-slot' or the 'coat-hanger' geometry. T-slot dies are the simplest to manufacture. They have a large manifold of

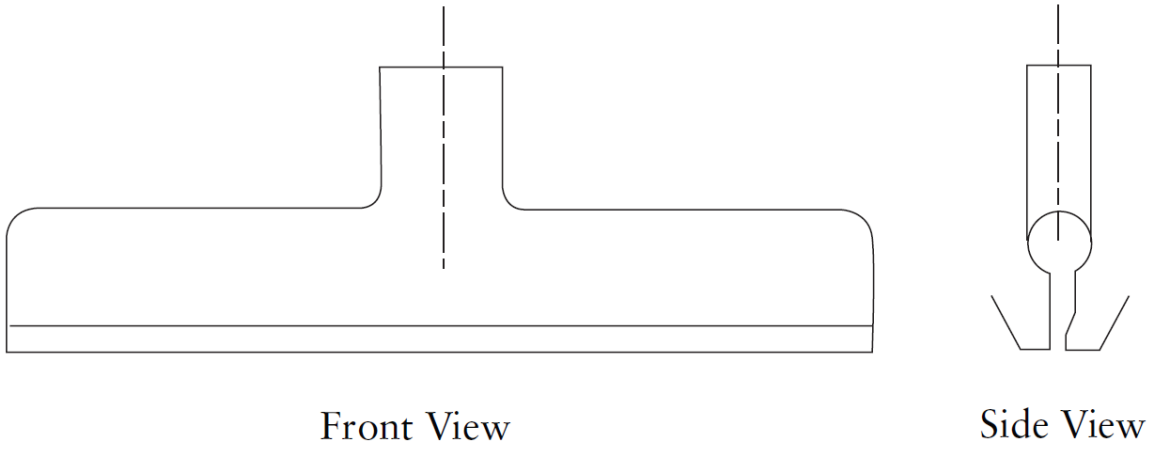

Figure 7.2-1. T-slot die with a constant cross-section circular manifold. From Garton (1992).

usually circular cross-section, which is constant across the entire width of the die, as shown in Fig. 7.2-1. There is very little resistance to flow from the center (feed) to the side ends of the die and even flow distribution is accomplished by the flow controlling action of the die lips. Such dies are used for low viscosity polymers (high melt flow index resins) mainly for extrusion coating applications. A less common type of die, is the 'fish-tail' design, shown schematically in Fig. 7.2-2. Coat-hanger dies usually involve (Garton, 1992) a manifold, a preland, possibly a flow restrictor (also called a 'choker bar'), a secondary manifold and finally the primary land (die lips) as shown schematically in Fig. 7.2-3. A picture of the lower half of a modern flat die is shown in Fig. 7.2-4.

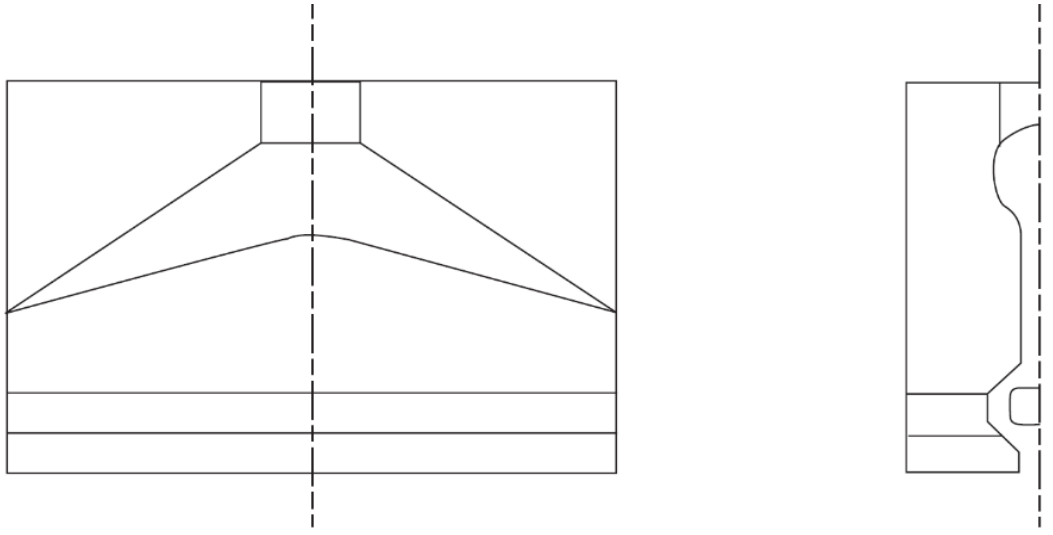

Figure 7.2-2. Schematic of a fish-tail die. From Michaeli (1992).

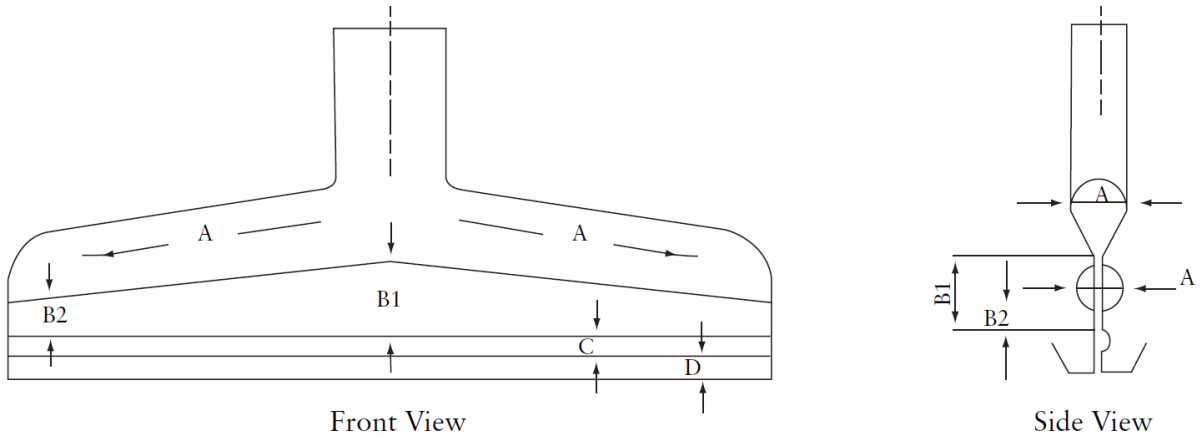

Figure 7.2-3. Schematic of a typical coat-hanger die having a teardrop shaped manifold with a diminishing cross-sectional area from the center to the sides. (A) region is the manifold, (B1) and (B2) are lengths of the preland, (C) corresponds to a secondary manifold and (D) the land (die lips). From Garton (1992).

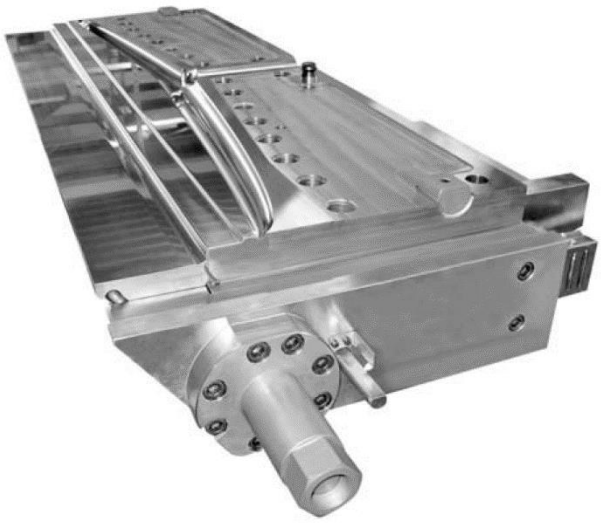

Figure 7.2-4. Picture of the lower half of a modern flat die having a lower sliding lip, which can be adjusted during production. From Vlachopoulos *et al.* (2012).

The manifold cross-sectional area is frequently teardrop shaped (see Fig. 7.2-5) and is gradually reduced from the center (feed) to the side ends. Rectangular manifolds (Fig. 7.2-5) are used in coextrusion and again the cross-sectional area is reduced from the center to the sides. The function of the manifold is to force the polymer to the sides and downstream, at the same time, for the generation of a nearly uniform flow distribution by the end of the preland, so that the necessity for subsequent corrections is minimized. The shape and the dimensions of the manifold are crucial in designing a die capable of producing a film or sheet

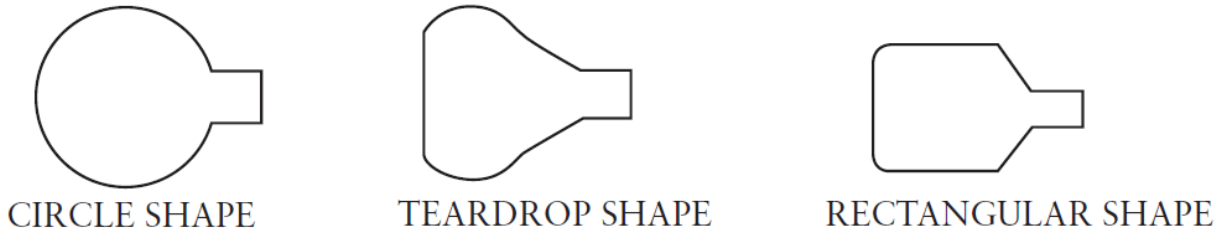

Figure 7.2-5. Schematic of the common types of manifold cross-sections.

of uniform cross-section from the die lips. This design is known to reduce what is usually referred to as the 'M' or 'W' flow output problem of the film or sheet produced, being heavy on each end then having a thin area followed by a thick area in the center (which can be perceived as having the shape of the letter W or an inverted one). The flow distribution in a coat-hanger die is shown schematically in Fig. 7.2-6. A typical coat-hanger die with dimensions is shown in Fig. 7.2-7.

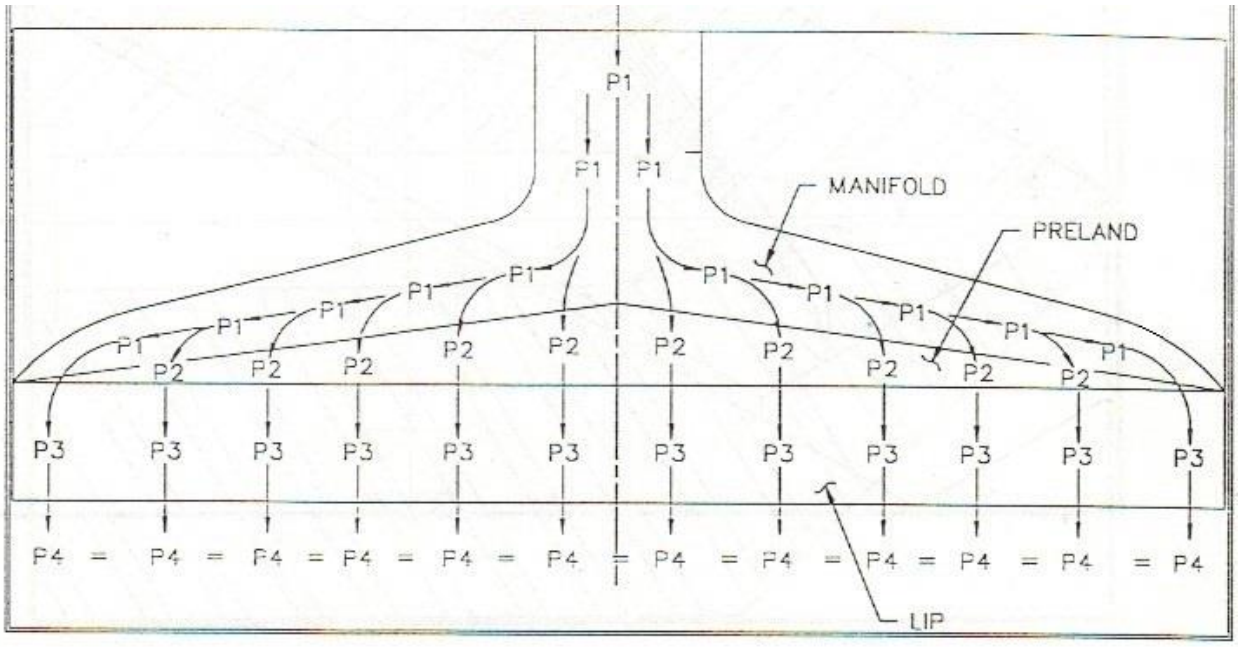

Figure 7.2-6. Flow distribution in a coat-hanger die. From Cloeren (1993).

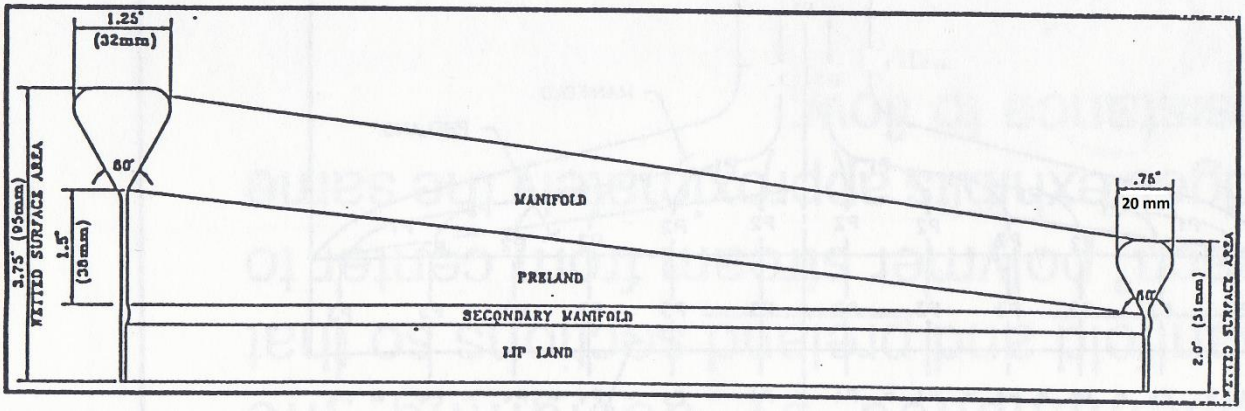

Figure 7.2-7. Typical dimensions of a coat-hanger die. From Cloeren (1993).

Most flat dies include some kind of lip-adjusting systems for fine-tuning of the uniformity. These might be simple adjusting screws or very sophisticated arrangements involving thickness measurement and feedback control. However, these adjusting systems are not capable of correcting large flow non-uniformities which result from poor manifold and preland design. All channel sections must be streamlined, as much as possible, and capable of providing smooth melt flow without any stagnating or recirculating flow regions. A mechanical drawing of a cross-section of a die having a restrictor bar and lip adjustment is given in Fig. 7.2-8.

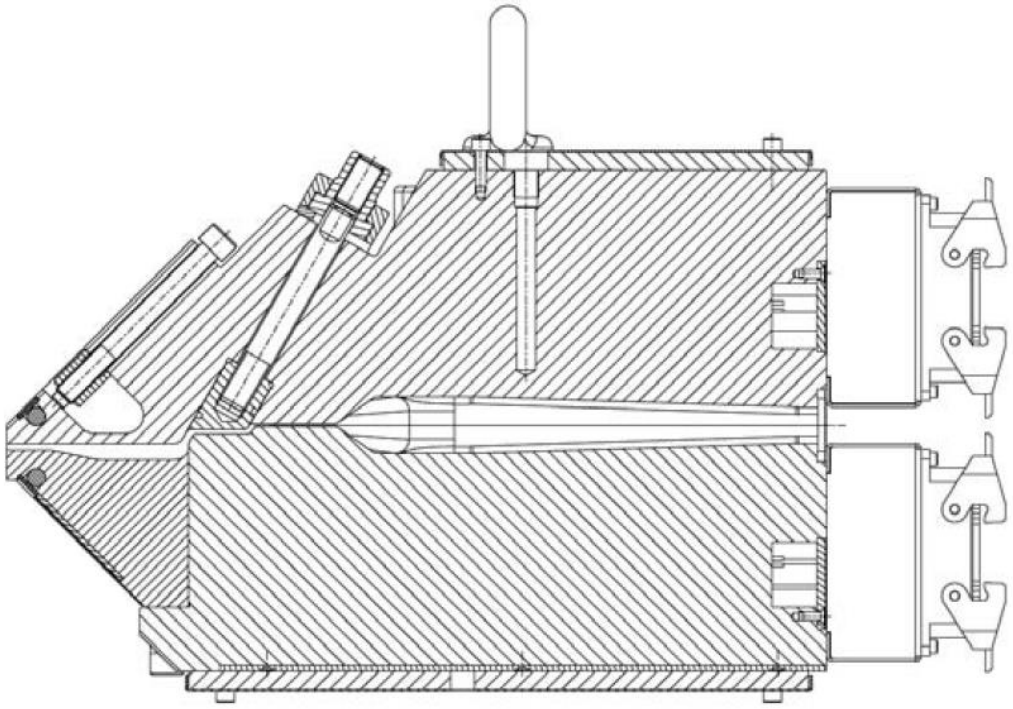

Figure 7.2-8. Mechanical drawing of the cross-sectional area of a die having a restrictor bar and a lip adjustment system. From Vlachopoulos *et al.* (2012).

Flat die design practitioners also recommend that for film production (especially if transparent) the minimum wall shear rate must not be less than 8 s^{-1}. Low wall shear rates are likely to result in visual defects on the film due to polymer degradation, which may look like brown or black spots, haze bands or even a generalized deterioration of the appearance of the sheet or film. Occasionally, such defects might be confused with sharkskin. The origin, however, is totally different. Sharkskin occurs at the die lip exit as discussed in Chapter 4. The low wall shear rate effect originates upstream where the flow channels are deep and consequently the corresponding shear rates may be very low. The previously mentioned

minimum wall shear rate value of 8 s^{-1} has been known and quoted by die designers for several years, even before the extensive use of computer simulation tools, which make possible the accurate determination of the shear rate for a given geometry and given flow rate. Due to long residence times and some sort of sticking of the polymer melt at the die surface, chain scission, cross-linking or other thermal degradations may occur. Some temperature sensitive polymers, notably ethylene-vinyl alcohol (EVOH), polyvinyl chloride (PVC), polyvinylidene chloride (PVDC) and ethylene-vinyl acetate (EVA), are particularly susceptible to this defect. For such materials, the minimum required wall shear rate value to avoid degradation, is probably higher, but there have not been any published studies about this available in the open literature. In co-extrusion, EVOH or the EVA layers may contain defects as a result of this sort of degradation but the other layers could be defect-free, even though low wall shear rates might be encountered in all layers. In such a case, the degradation of the temperature sensitive layer might be confused with interfacial stability (Shroff and Mavridis, 1994, Vlachopoulos and Strutt, 2010). Interfacial instabilities are discussed in Chapter 9.

In addition to good flow channel design, it is important that the die body be free from temperature variations during production. Locally higher temperature is likely to produce a heavy-gauge band, due to higher flow rate, while a locally lower temperature is likely to produce a thin-gauge band. Insulation and temperature control of the die body are essential for achieving film or sheet with low thickness tolerances. Flat dies are usually manufactured in widths ranging from 700 mm to 3,500 mm but may occasionally exceed 5,000 mm. Film or sheet thicknesses usually range from 10 μm to 30 mm. Deckling systems are used to reduce the width of film or sheet produced. As Garton (1992) put it, they are considered a necessary evil in the industry. They compromise the flow distribution because of the restrictions on the two sides of the die. They should definitely be avoided when extruding thermally degradable polymers. Garton (1992) recommends that no more than 25% of the total die width should be deckled. Despite the fact that deckling systems do not produce anything resembling a streamlined flow (which is dictated by rheology), many dies are deckled down to almost 50% of the original slot width.

Due to the large forces that may develop during extrusion and because a flat die is clamped together at the edges, deflection of the die may occur with the largest magnitude at the centre. This is usually referred to as clamshelling. It results in increased flow in the central region, which must be compensated for through lip adjustments.

Early approaches for design methodology of flat dies based on flow analysis, may be found in Tadmor and Gogos (2006). The momentum and continuity equations presented in Chapter 2 can be easily simplified to the generalized Hele-Shaw approximation with the assumption of narrow gap geometry (Dantzig and Tucker, 2001). It applies to geometries in which the gap varies with position (provided there are not abrupt changes). Newtonian and the Generalized Newtonian Fluid (GNF) models of power law, Carreau-Yasuda and Cross models can easily be incorporated. For die design, if we assume that x is the direction of flow from the extruder end to the die lips, y is the lateral direction towards the side ends and z the perpendicular, we can write the Hele-Shaw approximation as:

$$\frac{\partial}{\partial x}\left(S\frac{\partial P}{\partial x}\right)+\frac{\partial}{\partial y}\left(S\frac{\partial P}{\partial y}\right)=0 \tag{7.2-1}$$

The quantity $S(x,y)$, called the flow conductance, is defined as:

$$S(x,y)=\int_0^h \frac{z^2 dz}{\eta(x,y,z)} \tag{7.2-2}$$

where h is the z-direction gap. The primary variable is the pressure and, after finding it, the gap-wise average velocity components are given by

$$\bar{V}_x=-\frac{S}{h}\frac{\partial P}{\partial x} \qquad \bar{V}_y=-\frac{S}{h}\frac{\partial P}{\partial y} \tag{7.2-3}$$

and the full velocity distributions can also be calculated using

$$V_x(z)=-\frac{\partial P}{\partial x}\int_0^h \frac{z'dz'}{\eta(z')} \qquad V_y(z)=-\frac{\partial P}{\partial y}\int_0^h \frac{z'dz'}{\eta(z')} \tag{7.2-4}$$

where z' is a dummy variable of integration. The energy equation can be subsequently used to determine the temperature. This is a very useful approximation because it reduces significantly the complexity required to solve the fully three-dimensional (3D) problem. A version of this approximation was used in a comparative study of computer simulations and experiments with very good results (Vlcek *et al.*, 1991).

7.3 Flat Die Coextrusion

The earliest coextruded sheets and films were produced using multi-manifold dies. In this technology the layers are formed individually in separate dies, which have the usual manifold preland and land sections, and then the layers are joined together before the exit as shown schematically in Fig. 7.3-1a. There is a limitation with such dies due to geometry and

the necessity of having metal walls for each die manifold thick enough for tool integrity and avoidance of non-uniformity arising from clamshelling. While construction is relatively easy for up to three layers, the mechanical complexity and cost increase significantly with each additional layer.

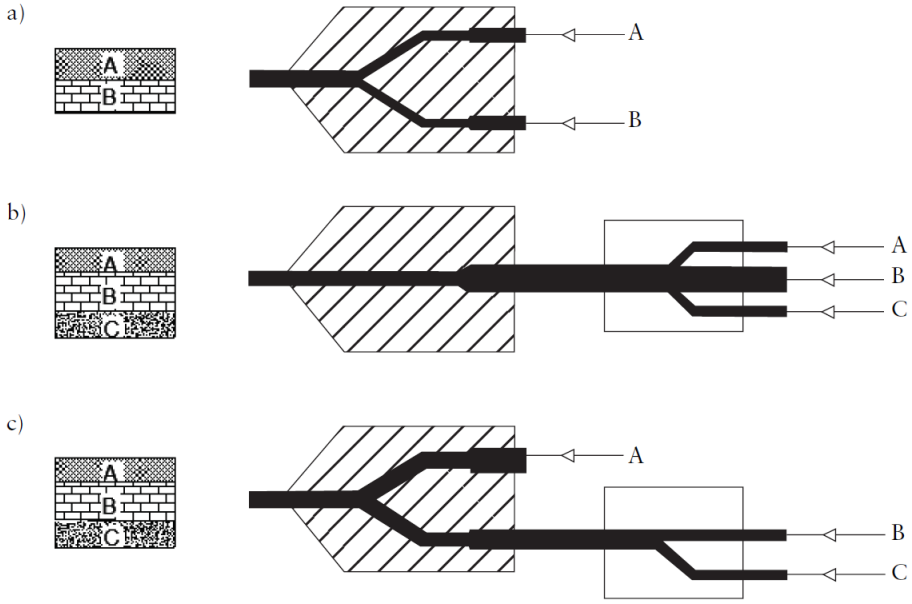

Figure 7.3-1. Schematic representation of multilayer extrusion. (a) multi-manifold, (b) feedblock and (c) combination of feedblock and multi-manifold. From Wirtz (1996).

Chrisholm and Schrenk (1971) and Schrenk *et al.* (1973) developed a new production technology in which, the layers are joined together in a device called a feedblock prior to the die, as shown schematically in Fig. 7.3-1b. Then, the layered structure is extruded through a single manifold. Feedblock systems are a lot simpler and easier to manufacture than multi-manifold dies. They are also easier to assemble, disassemble, clean, operate and are more flexible for implementing whatever changes might be necessary. The main challenge in feedblock die coextrusion is the maintenance of layer uniformity, from the feedblock through the spreading in the manifold, flow in the preland and die lips, to the exit. Despite this challenge, feedblock coextrusion is the dominant technology. In fact, by combining multi-manifold and feedblock dies (see Fig. 7.3-1c) it is possible to produce multilayered films comprising hundreds of layers (Schut, 2006). This is accomplished in a coextrusion feedblock by first splitting the melt flow, then realigning and subsequently stacking a small number of melt streams.

Multi-manifold dies are used for products which are difficult or impossible to fabricate by means of feedblock coextrusion. These include structures which are required to have very

thin skin layers compared to the total thickness and structures with very large viscosity and temperature differences in adjacent layers. The layer nonuniformities in feedblock coextrusion might be due to encapsulation tendencies of the more viscous polymer by the less viscous one (Han, 1981) as it is explained in Chapter 9. Feedblock profiling is used for the

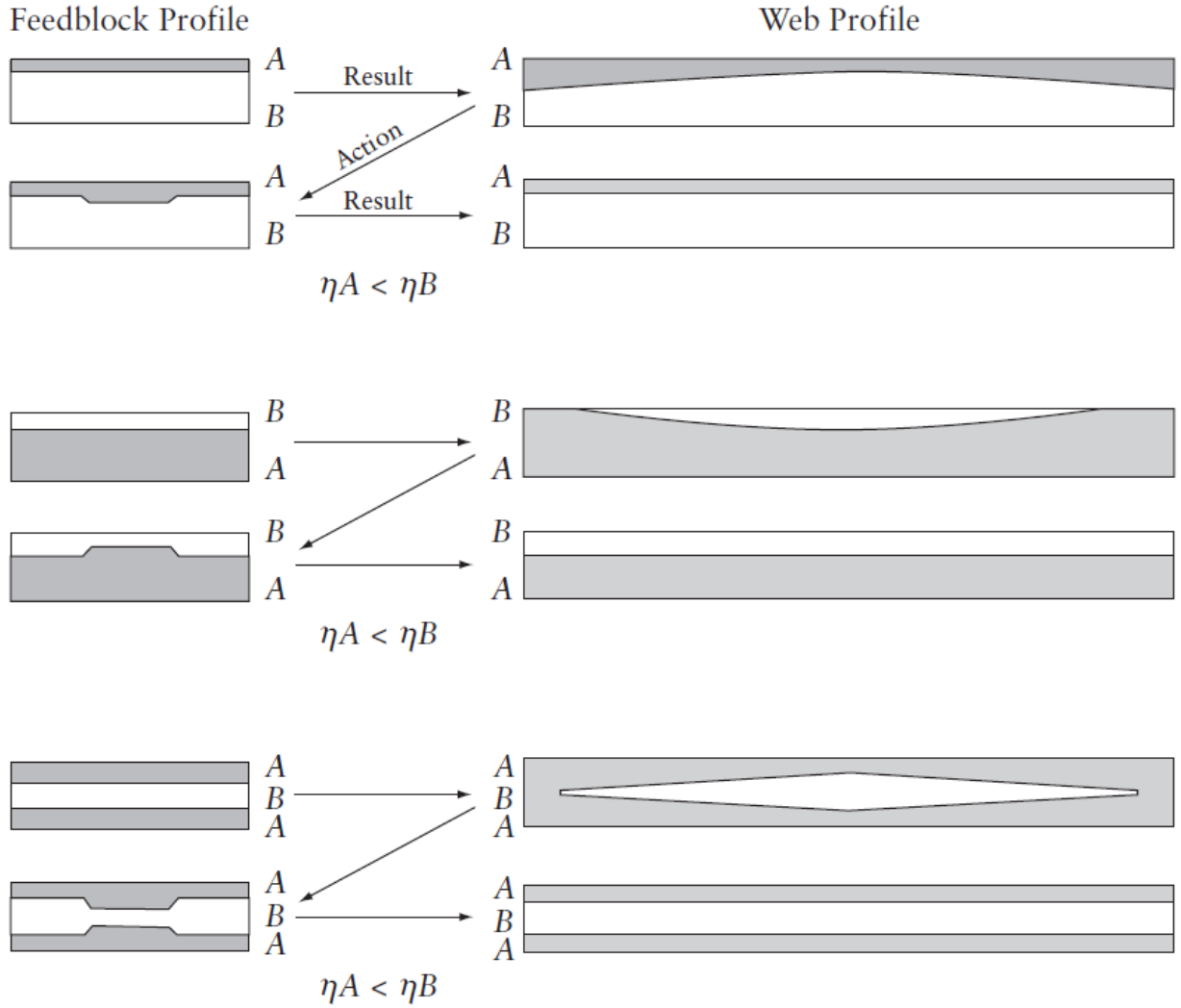

Figure 7.3-2. Feedblock profiling and the resultant effect. From Cloeren (1993).

production of uniform multilayer melt streams by counteracting the encapsulation tendency as shown schematically in Fig. 7.3-2 adapted from Cloeren (1993). Mathematical modelling of coextrusion flows is challenging even for inelastic fluids for two layers only (Torres *et al.*, 1994). Layer spreading in coextruded structures remains "a problem solved more often with art than science" according to Powers *et al.* (2000). This was true at the time of the cited publication in 2000 and it is true today.

7.4 Beyond the Die Exit

As the polymer emerges from the die lips, it swells, it is thinned due to stretching and it is quenched by contacting the cooling rollers. The effect of stretching on extrudate swell of cast film has been studied by Polychronopoulos and Papathanasiou (2015). Three defects occur after the polymer melt leaves the die lips (Sollogoub *et al.*, 2006): draw resonance, neck-in and edge beading. Draw resonance is a periodic fluctuation of film width, thickness and tension. This occurs at a critical draw down ratio (take-up velocity at the chill roll divided by the average velocity at the die exit). Neck-in is the contraction of the lateral width of the extruded film due to the tension imposed by the chill roll as shown schematically in Fig. 7.4-1a. Edge beading (or dog bone effect) is due to the film edges undergoing extension while the neck-in phenomenon is occurring. The thickness of the film on the lateral edges is higher (res-

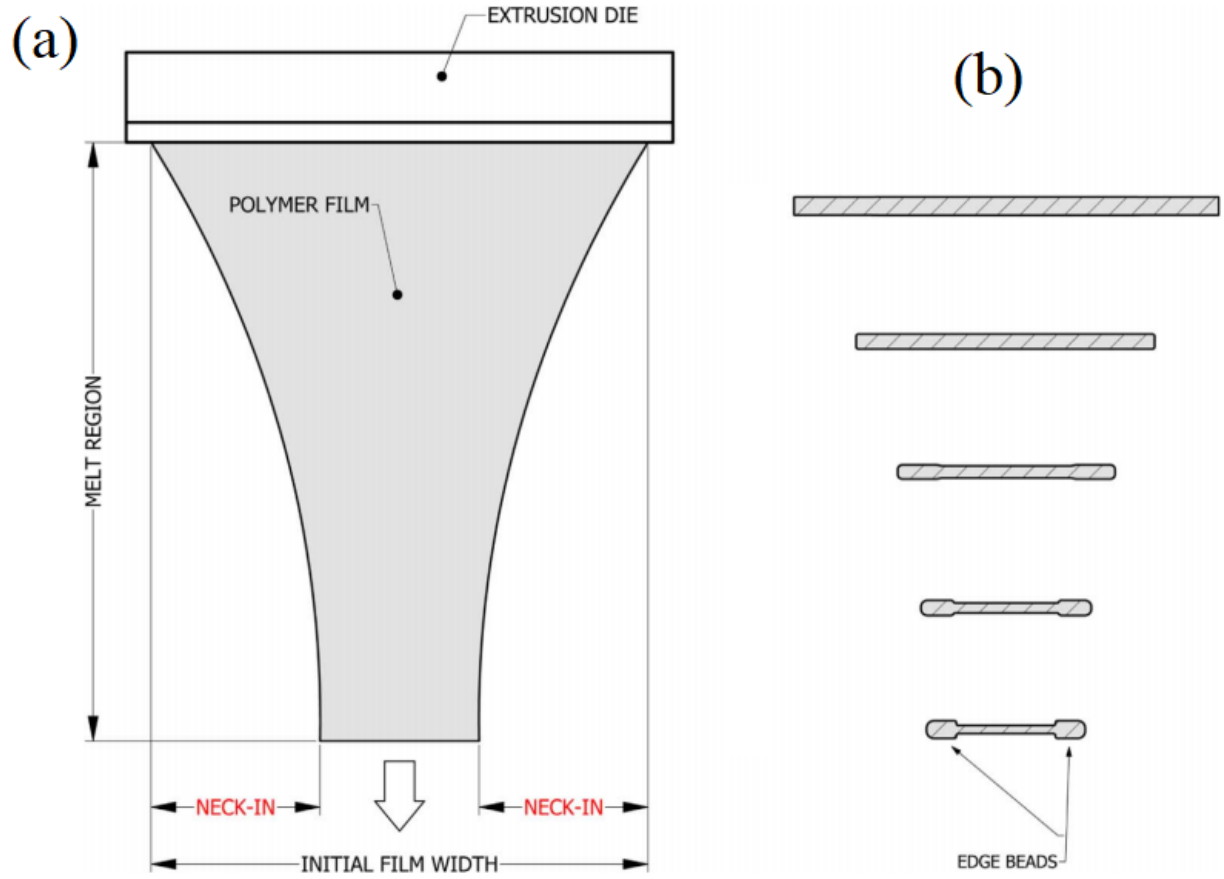

Figure 7.4-1. (a) Neck-in (top view) and (b) edge beading (cross-section view) phenomena during the extrusion film casting process. From Barborik and Zatloukal (2018).

-embling to beads) than the thickness in the central region as demonstrated schematically in Fig. 7.4-1b. Edge beads must be trimmed off before film products are collected in rolls. The

above defects are responsible for reduction in productivity. Apparently, the melt rheological properties play a significant role in their formation and the die designer must be aware of their potential occurrence.

Bibliography

Barborik T. and Zatloukal M., Effect of die exit stress state, Deborah number, uniaxial and planar extensional rheology on the neck-in phenomenon in polymeric flat film production, J. Non-Newt. Fluid Mech., 255, 39 (2018)

Butler T.I., *Film Extrusion Manual*, 2nd Edition, TAPPI (2005)

Chisholm D., and Schrenk W.J., inventors; Dow Chemical, assignee; US 3,557,265 (1971)

Cloeren P., *Proceedings of Advances in Extrusion Technology*, RETEC Extrusion Division and the Ontario Section of the Society of Plastics Engineers, Brookfield, NJ, USA, (1993)

Dantzig J.A. and Tucker III C.L., *Modeling in Materials Processing*, Cambridge University Press (2001)

Garton D.R., "Cast Film Die Design" in: *Film Extrusion Manual*, Butler T.I. and Veazey E.W. (eds.), TAPPI (1992)

C.D. Han, *Multiphase Flow in Polymer Processing*, Academic Press, New York, NY, USA, (1981)

Ivey J., Cast Film and Sheet Extrusion, in: *The SPE Guide on Extrusion Technology and Troubleshooting*, Vlachopoulos J. and Wagner J. (eds), Society of Plastics Engineers, Brookfield, USA (2001)

Kanai T., Flat Die Analysis, in: *Film Processing*, Kanai T. and Campbell A. (eds.), Hanser Publishers (1999)

Mavridis H. and Shroff K.N., Multilayer Extrusion: Experiments and Computer Simulation, Pol. Eng. Sci., 34 (7), 559 (1994)

Michaeli W., *Extrusion Dies for Plastics and Rubber*, 2nd Edition, Hanser Publishers (1992)

Osborn K.R. and Jenkins W.A., *Plastic Films*, Technomic Publishing, Lancaster, PA, USA (1992)

Powers J., Troubleshooting Tips to Cure your Sheet Extrusion Headaches, Plastics Technology, August 1 (1996)

Polychronopoulos N.D. and Papathanasiou T.D., A study on The Effect of Drawing on Extrudate Swell in Film Casting, Appl. Rheol., 25(4), 42425 (2015)

Powers J., Dooley J., Reinhardt C. and Oliver G., Evaluation of Layer Spreading in Coextruded Structures via a Modular Die, *Proceedings of ANTEC 2000*, Orlando, FL, USA (2000)

Schrenk W.J., Chisholm D.S., Cleereman K.J. and Alfrey Jr. T., inventors; Dow Chemical, assignee; US 3,579,647 (1973)

Schut J.H., Microlayer Films: New Uses for Hundreds of Layers, Plastics Technology, 52 (3), 54 (2006)

Sollogoub C., Demay Y. and Agassant J.F, Non-Isothermal Viscoelastic Numerical Model of the Cast-Film Process, J. Non-Newt. Fluid Mech., 138 (2-3), 76 (2006)

Tadmor Z. and Gogos C.G., *Principles of Polymer Processing*, 2nd Edition, Wiley-Interscience (2006)

Torres A., Hrymak A.N., Vlachopoulos J., Dooley J. and Hilton B.T., Boundary Conditions for Contact Lines in Coextrusion Flows, Rheol. Acta, 32 (6), 513 (1993); correction errata in Rheol. Acta, 33 (3), 241 (1994)

Vlachopoulos J. and Strutt D., Rheology of Molten Polymers, in: *Multilayer Flexible Packaging*, Wagner J.R. (ed.), Elsevier (2010)

Vlachopoulos J., Polychronopoulos N.D., Tanifuji S. and Peter Müller J., Flat Film and Sheet Dies, in: *Design of Extrusion Forming Tools*, Carneiro O.S. and Nobrega M. (eds.), Smithers Rapra, London (2012)

Vlcek,J., Mailvaganam G.N., Perdikoulias J. and Vlachopoulos, J. Computer Simulation and Experiments of Flow Distribution in Flat Sheet Dies, Adv. Polym. Tech., 10, 309 (1991)

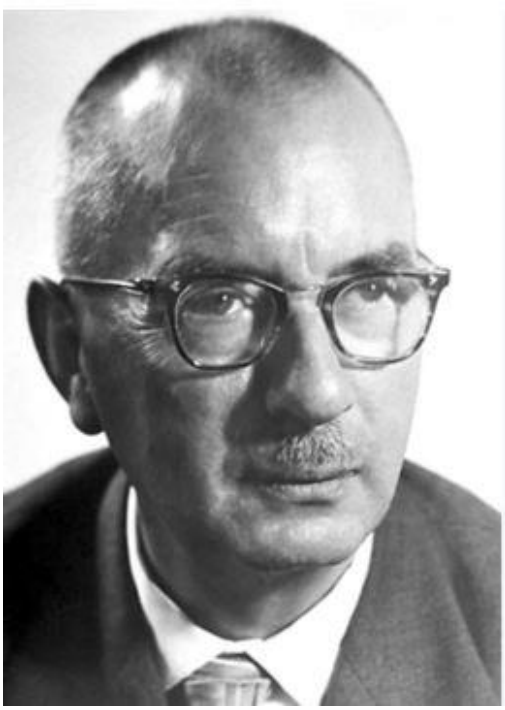

KARL ZIEGLER (1898-1973) and GIULIO NATTA (1903-1979)

Ziegler Natta catalysts are used for the production of more than 100 million tons of polyolefins annually

Nobel Prize Chemistry (1963)

J. Vlachopoulos and N.D. Polychronopoulos "*Understanding Rheology and Technology of Polymer Extrusion*", First Edition, Polydynamics Inc, Dundas, Ontario, Canada (2019)

Chapter 8

BLOWN FILM EXTRUSION

8.1 Introduction

Blown film extrusion is the most important process for the production of plastic films, ranging in thickness from 0.5 mm to as thin as 5 μm according to Butler (2001). The polymer is melted in an extruder and the hot melt is pumped through a die to form a thin-walled tube (usually called bubble), which is simultaneously axially drawn and radially expanded. The inside air pressure required is just few kPa. In most installations the extruder(s) are horizontal and the blown film bubble is formed vertically upward as shown in Fig. 8.3-1. For this chapter, the authors present an abridged version of one of their publications in another book (Vlachopoulos *et al.*, 2012) and some material from Vlachopoulos and Sidiropoulos (2013).

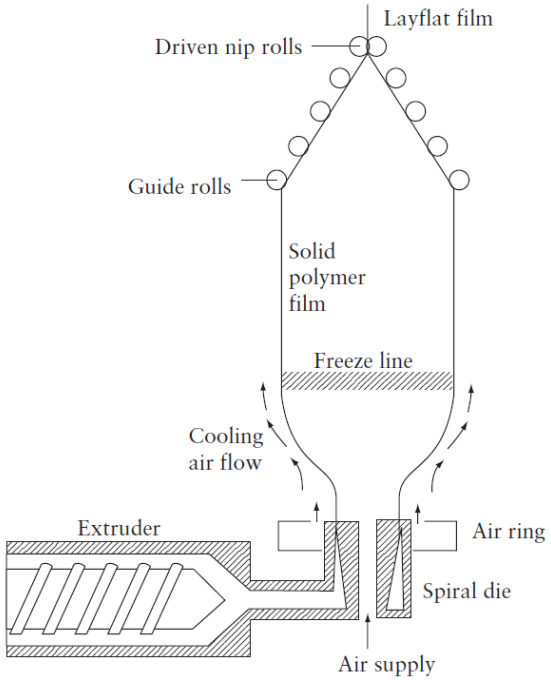

Figure 8.1-1. Schematic of the film blowing process. Adapted from Sidiropoulos (2000).

The amount of radial and axial stretching plays a very important role in the determination of end-use properties. The blow-up ratio (BUR) is defined as the ratio of the final bubble diameter to the die diameter and it is a good indicator of the amount of expansion in the radial or transverse direction (TD). In typical installations, BUR ranges from 1.2 to 4. The amount of stretching in the machine direction (MD) is characterized by a different dimensionless number, the take-up ratio (TUR), which is defined as the ratio of the final film velocity over the velocity at the die lips. In the literature the TUR is often called draw-down ratio (DDR).

Extruder sizes range usually from 25 to 200 mm in diameter with length over diameter (L/D) ratios from 24 to 36:1. Smooth barrel extruders are used in most blown film lines, with grooved feed barrels used increasingly in modern installations for achieving higher output rates (see Chapter 6). The screws are usually of the barrier type. Barrier screw designs have channels machined into their geometry which divide the molten from the solid polymer being processed through the extruder. The purpose of dividing the solid from the molten polymer is to increase melting and hence production rates (see Chapter 6). The goal of any feed screw design is to provide a stable rate of 100% molten homogeneous polymer to the die attached to the extruder. Die lip gaps usually range from 0.76 to 3 mm and the exiting melt stream is typically drawn down to film thicknesses ranging from 0.01 to 0.5 mm. Coextrusion of three to seven layers (sometimes up to 11) is often used for production of film for food packaging. The applications of coextruded films are highly diverse, and cover various industries from industrial to consumer ones.

The main function of the die is to distribute the polymer melt evenly so that the thickness measured around the circumference of the tube being produced is uniform. Due to variations in distribution in the die and uneven cooling after the melt exits the die lips, there is always some film thickness non-uniformity. It is virtually impossible to eliminate film thickness variation, but systems have been developed to reduce it through flow modulation of the melt or the cooling air. If the film thickness variation is left unaddressed, when the film is wound up into a roll, thickness non-uniformity will be evident because the thicker or thinner spots (gauge bands) in the film will cause the roll to be of an uneven diameter. A way to address uneven diameter film rolls is to randomize the bands so that when the film is wound into a roll, the thick spots are spread across the width of the roll. Gauge band randomization (i.e. the distribution of thicker and thinner bands) can be accomplished by employing various

techniques involving rotation or oscillation of the film bubble as it is being produced, by rotating/oscillating the apparatus that collapses the bubble and the nip rolls that pull the film upwards. It is possible that some gauge variation may be caused by the collapsing process itself because the distances from the points where the bubble first touches the collapser to the nip line are not all the same around the bubble circumference, as the cylindrical bubble is flattened (Waller, 2010, Cantor, 2011).

Polymers that are typically used in blown film are low density polyethylene (LDPE), linear low density polyethylene (LLDPE), HDPE and metallocene polyethylene (mPE), although several other polymers are sometimes used including ethylene copolymers, propylene copolymers, polyvinyl chloride, nylon and polypropylene homopolymer (Hensen, 1997). LLDPE gave a big boost to the industry with its excellent drawability and varied end use properties and applications. However, compared to LDPE, LLDPE has weaker melt strength and is prone to bubble instability. To address this issue, blends of LDPE/LLDPE, usually at a ratio of 70/30, are frequently used to combine the best of both polymers (the melt strength of LDPE and the drawability of LLDPE).

8.2 Blown Film Die Design

The purpose of an extrusion die is to impart the desired shape to the polymer melt stream produced continuously by the extruder. In blown film extrusion a thin tubular film is formed as the melt flows through the die lips. The die lip gap usually ranges from 0.76 mm to 3 mm and the die diameter from a few centimeters for laboratory lines to more than one meter for industrial installations producing more than one ton of film per hour. Production rates can easily exceed 1kg/h/mm of diameter for LDPE while for LLDPE it is usually less than 1kg/h/mm of diameter. The annular flow is formed in the gap between the inner mandrel and the outer die body. Several types of die have been proposed and built (Hopmann and Michaeli, 2016) as shown in Fig. 8.2-1, involving mandrels supported by spider legs, screen packs or a breaker plate.

Sometimes, side-fed as opposed to bottom-fed dies are used. The problem with these designs is that they result in the formation of weld lines (Perdikoulias *et al.*, 1999) in the machine direction. These are formed when two polymer streams merge together. Along these merging lines (weld lines), the polymer is poorly bonded due to very low diffusion coefficients of the large polymer molecules within the highly viscous melt. By far the most common die

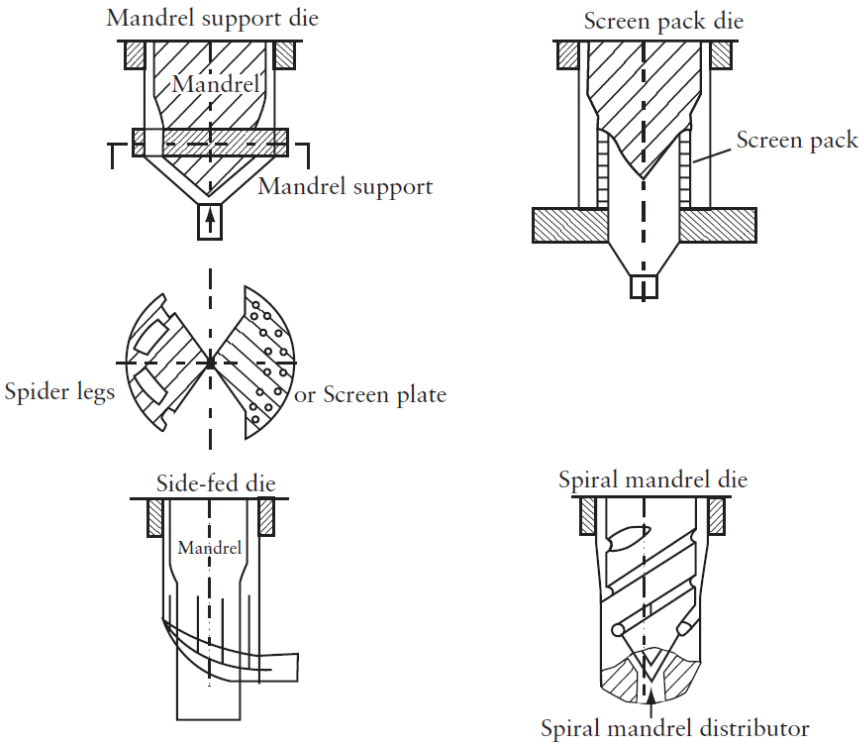

Figure 8.2-1. Different types of dies for blown film extrusion. From Hopmann and Michaeli (2016).

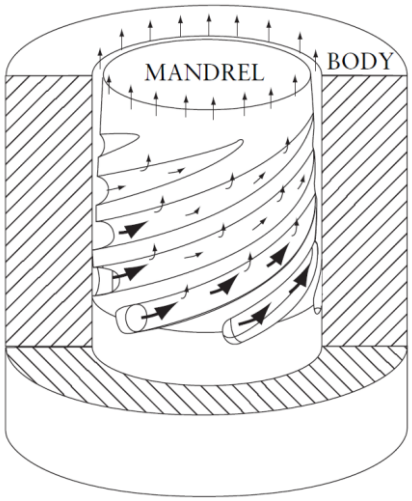

Figure 8.2-2. Schematic of a spiral die. The polymer melt flows from extruder through a melt pipe at the bottom into the runners which guide it to the ports from where the spiral originates. From Perdikoulias (1997).

geometry for blown film production is the spiral mandrel geometry shown schematically in Fig. 8.2-2. The polymer is fed by a number of melt tubes ending with a port at the start of each spiral. The melt flows both along the spirals and in the gap between the mandrel and outer body of the die. The flow rate becomes progressively more uniform around the circumference

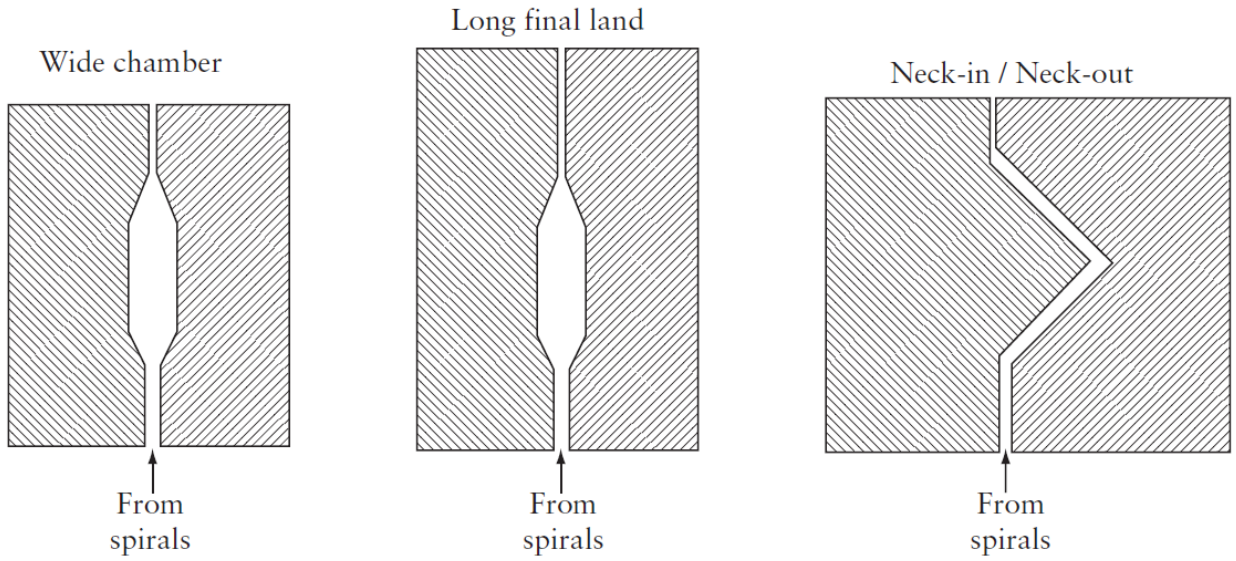

Figure 8.2-3. Relaxation chambers designs. From Vlachopoulos *et al.* (2012).

towards the die exit. After the end of the spirals the melt may pass through a low shear relaxation chamber of the type shown in Fig. 8.2-3, for the purpose of reducing the memory of its complex strain history.

Typically, the number of spirals in a mandrel die should be enough to accomplish uniform distribution of the polymer melt before it exits the die. One generally accepted notion among die designers is that a mandrel die should have one spiral per 25 mm of die diameter. Traditionally, it was believed that the more spirals in a mandrel die, the better the distribution would be. This is not so, since the entire length of each spiral can (and should) be used to distribute the polymer melt. With this in mind, fewer spirals can be used to provide adequate distribution and result in a uniform film thickness distribution at the die exit. Each spiral is machined into the outer diameter of the mandrel and travels a certain distance around the mandrel. Typically, a spiral starts deep and becomes progressively shallower the further down its length. The area which separates the spiral channels is known as the land. The gap over the land formed by the outer body that encloses the mandrel is what determines how much polymer flows over the land and how much travels down the spiral. As the spiral becomes shallower, the gap above the land becomes greater, allowing more polymer to travel over the land as opposed to in the spiral channel. The length of the spiral is another variable that is up for discussion amongst die designers. The length of a spiral is determined by the number of ports it overlaps on the mandrel from start to finish.

It is sometimes believed that a longer spiral, or a spiral with many overlaps, provides better distribution than a spiral with fewer overlaps. This, also, is not so since polymer distribution has a stronger dependence on the gap size between land and outer body. As noted before, if the entire length of the spiral is used for distribution, a shorter spiral that is properly designed will work better than a longer spiral whose length is not being used fully for distribution. Typically, a die with six to eight overlaps is acceptable for blown film die design. The spiral should be long enough for adequate distribution to take place.

As the molten polymer exits the die, the plastic tube being produced should ideally have a uniform thickness. When this molten tube is inflated (into a bubble) and stretched, any excessively uneven thicknesses tend to be exaggerated around the bubble circumference, resulting in film of an unacceptable quality. Mass flow variation and resultant thickness variations of more than 5% above the end of the spirals is usually unacceptable. In a poorly designed die, polymer melts tend to flow preferentially directly above the ports, resulting in periodic thick and thin patterns as shown schematically in Fig. 8.2-4.

Characteristically, the number of thick spots or peaks will correspond to the number of ports in the die. Long die lips and relaxation chambers are sometimes used to reduce the mass flow variation, but they also tend to increase the pressure drop resulting in a reduced production rate. This type of thickness distribution deficiency is a result of an incorrectly designed spiral die which is not distributing the molten polymer properly. The poor flow distribution is caused along the spirals and between mandrel and die body. Fig. 8.2-5 shows schematically the flow rate in the spiral direction as a function of distance. Correspondingly, spiral leakage is the amount of material that flows out of the spiral. If a die has too much

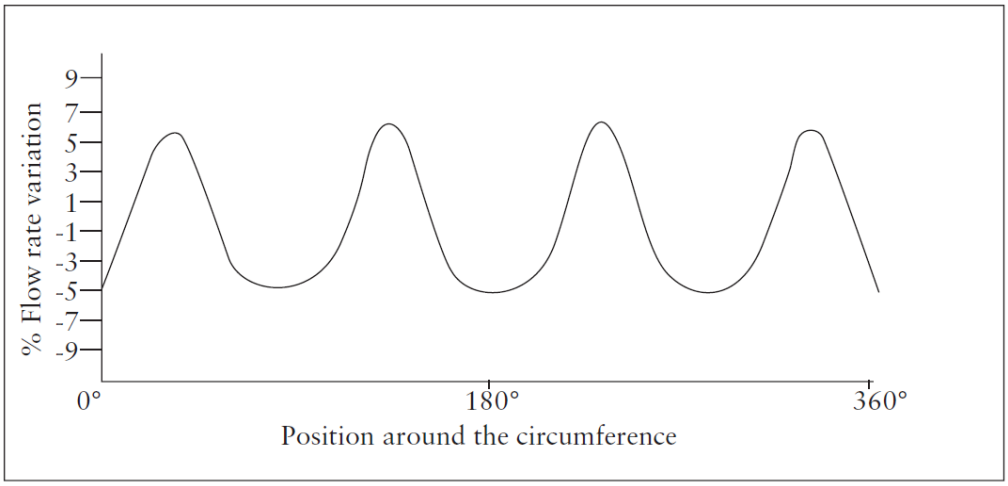

Figure 8.2-4. Schematic representation of circumferential thickness variation as a function of position for a four port die. From Vlachopoulos *et al.* (2012).

spiral leakage, a large portion of the spiral will remain unused for distribution purposes, resulting in a stagnant flow region which may cause polymer degradation and other production problems.

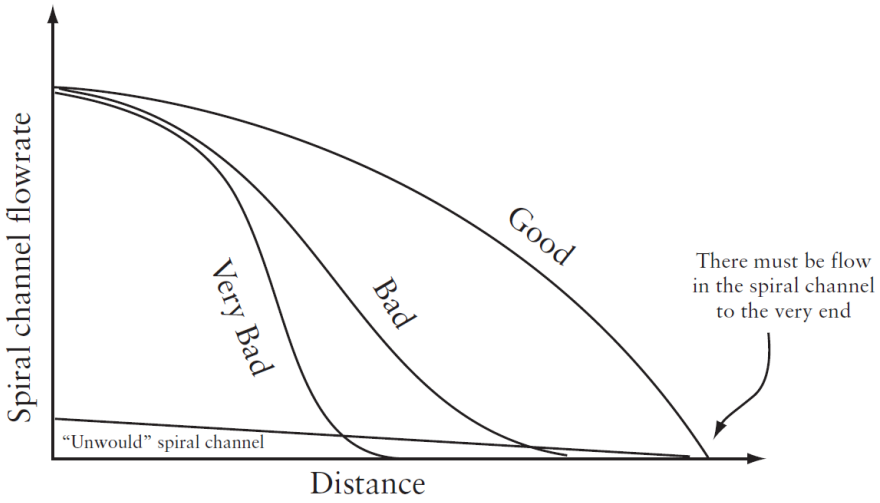

Figure 8.2-5. In a good spiral die design, polymer flow in the channel has to be maintained to the very end. From Vlachopoulos *et al.* (2012).

Several studies have been carried out to model and predict the flow in blow film dies (see Vlachopoulos *et al.*, 2012). The equations of conservation of mass, momentum and energy along with a suitable constitutive equation must be solved simultaneously. The Hele-Shaw approximation described briefly in Chapter 7 is also used for blown film die flow simulation and design. The objective is to design dies with low thickness variation (below 5%) and wall shear rates preferably less than 8 s^{-1} when transparent films are extruded. Low wall shear rate areas are responsible for hazy films or films with black or brown spots, just as in flat film extrusion (Chapter 7).

8.3 Blown Film Co-extrusion

A significant part of blown film being produced is coextruded, that is, it consists of two or more polymer layers. Nowadays, co-extrusion of three to seven layers (sometimes up to 11) is common. Food packaging films are almost exclusively multilayered because they are required to possess barrier and other physical properties. In barrier film co-extrusion, the film structure has thin layers of the expensive barrier polymer, such as ethylene-vinyl alcohol (EVA), while layers of high strength polymers like polyamide (PA) provide the required mechanical properties. Typically, spiral mandrel dies are the standard for producing coextru-

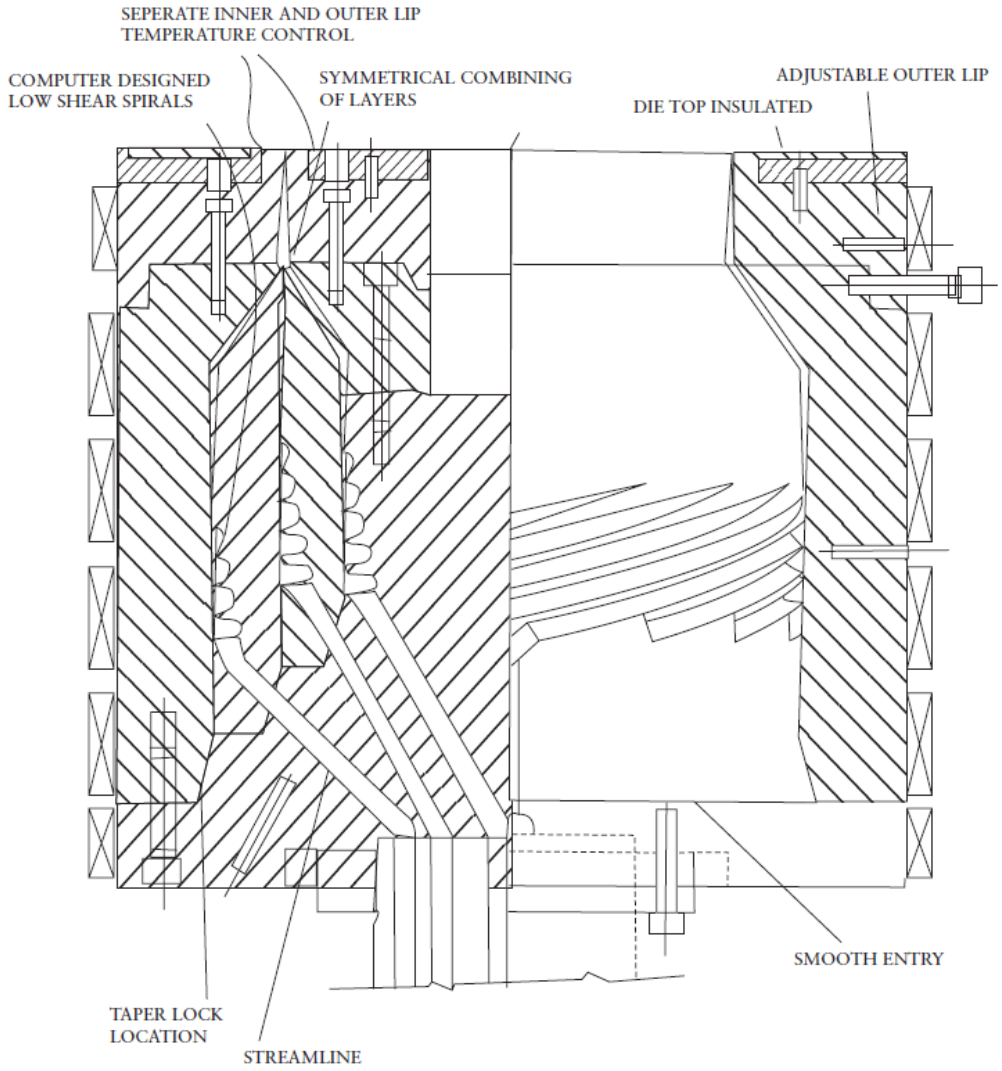

Figure 8.3-1. Mechanical drawing of three-layer co-extrusion die. From Vlachopoulos *et al.* (2012), courtesy of BE, Brampton, ON, Canada.

ded blown film. In co-extrusion spiral mandrel dies, the spirals are nested one inside the other (as shown in Fig. 8.3-1 for a three-layer die) and are fed by different extruders.

Contrary to the traditional spiral dies (where the spiral channels are cut in the surface of a cylinder), in flat plate stackable designs the spirals are cut on plates radially, and stacked one on top of another. A stack of such flat plates, as shown in Fig. 8.3-2 can produce multilayer film structures, while being still easy to disassemble and maintain. The flat plates are interchangeable, so the types of polymers and the order of the layer structure are easily customized. Fig. 8.3-3 shows how the spirals are laid on the surface of each plate. One of the other main differences between cylindrical and stackable dies is the omission of a bottom fed block in the latter. In the stackable die format the polymer melt is fed to the spirals from the

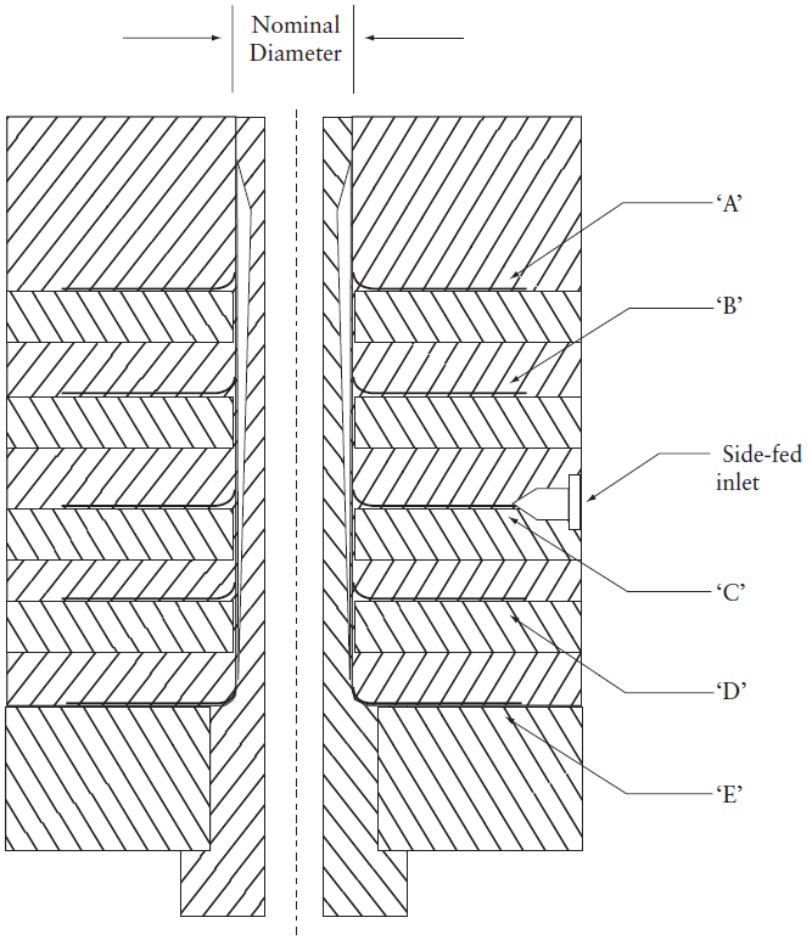

Figure 8.3-2. Schematic of a flat plate (stackable) blown film extrusion die, for five layer coextrusion (A, B, C, D and E). From Vlachopoulos *et al.* (2012), courtesy of BE, Brampton, ON, Canada.

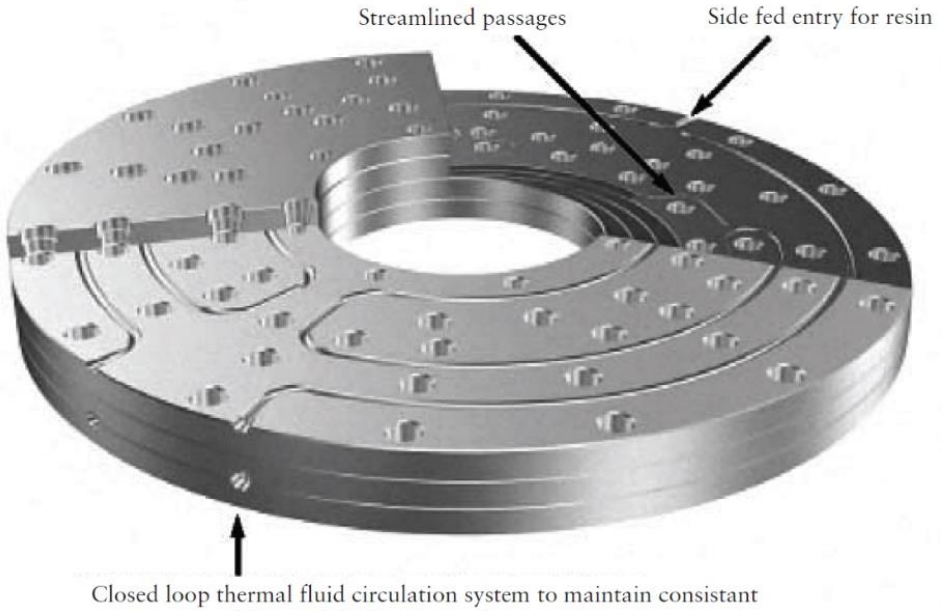

Figure 8.3-3. A side-fed flat spiral modular distributor. From Vlachopoulos et al. (2012), courtesy of BE, Brampton, ON, Canada.

side, directly connected to the extruder, as opposed to being bottom-fed in the cylindrical die design format. This format change has led to a die design that results in the entire melt flow passage from extruder adapter to the exit of the die being highly streamlined with no sharp bends to cause dead spots. Furthermore, all the layers have roughly the same wetted surface area because distribution takes place on the surface of the disc.

8.4 Beyond the Die Exit

Upon emergence from the die, the hot melt is cooled externally (and sometimes internally) by annular streams of high velocity air from film cooling devices called air rings. The external air rings are situated close to the die lips outside and cooling air is blown onto the molten polymer as it is being extruded from the die. Blown film lines may have a single lip air ring or dual lip air rings as shown in Fig. 8.4-1 and occasionally triple lip air rings for better bubble stability. The cooling air helps to cool the hot melt as it exits the die and stabilizes the shape of the molten tubular film. The objective is to cool the extruded melt, so

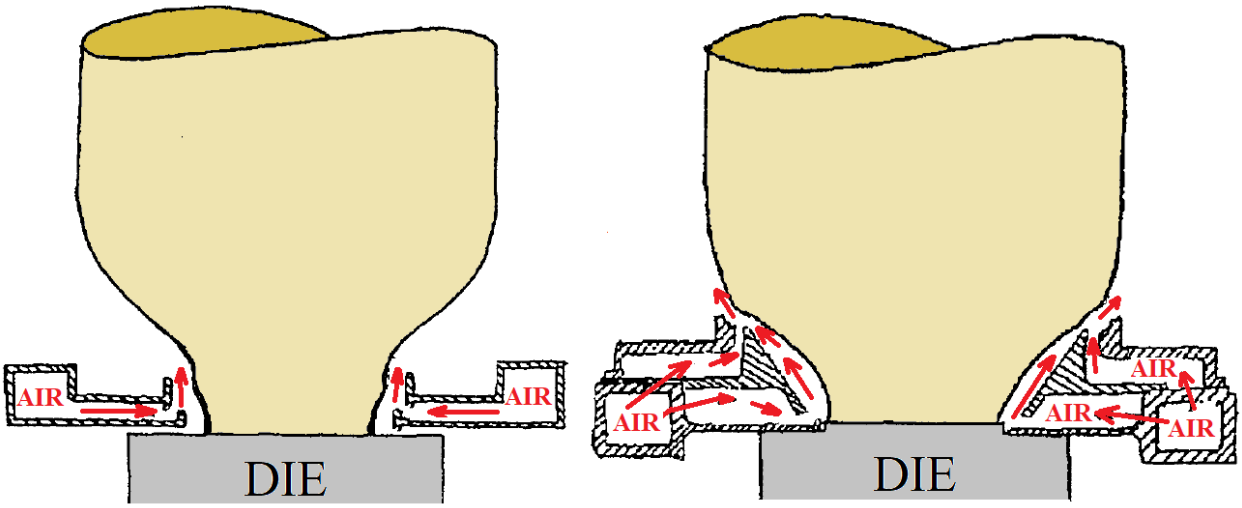

Figure 8.4-1. Schematic representation of air rings for external cooling. To the left, single lip air ring and to the right dual lip air ring. Arrows indicate air flow. Reproduced from Sidiropoulos (2000).

that it solidifies at highest possible rate. The maximum achievable output rate of the production line is often limited by the air cooling capability of the air rings. Specific output rate is a means to determine and compare the production rate of a die irrespective of the die diameter. The specific output rate is determined by dividing the output rate of the die in units of kg/h by the diameter of the die lips in mm. The die specific output rate for lines equipped with dual lip air rings, which cool the bubble from the outside, varies from 0.45 to 1.1

kg/h/mm of die diameter according to Butler (2001). Internal bubble cooling (IBC) increases the cooling capacity of the line by providing cooling from the inside of the bubble. The increased cooling capacity generally produces throughput rates from 0.7 to 2.0 kg/h/ mm of die diameter.

Bubble shapes vary from a conventional bubble shape for LDPE to a high stalk wine-glass like for HMW-HDPE (and some other linear, low melt flow index (MFI) materials). The long and narrow neck usually extends from 5 to 9 die diameters above the die followed by a quick bubble expansion (BUR ranging from 3.5 to 5). The long molecular length of HWM-HDPE (MI less than 0.1) prevents its drawdown below 50 microns when blown in conventional bubbles. The high stalk bubble is achieved simply by reducing the amount of cooling air to allow the freeze line to rise and lengthen the neck. This is illustrated schematically in Fig. 8.4-2 and contrasted with a typical LDPE bubble.

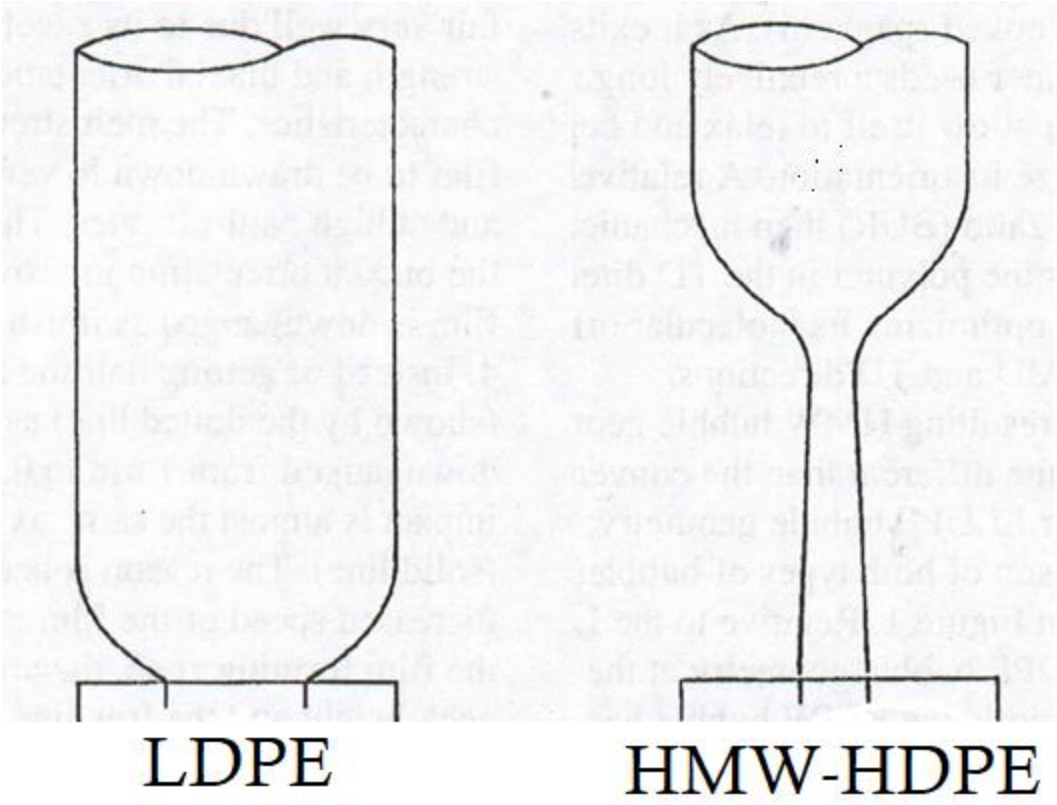

Figure 8.4-2. Schematic representation of a conventional and a high stalk bubble (Bourgeois, 1992).

The general bubble shape may be predicted using the "thin shell" approximation, that describes the balance of forces on the bubble. Details may be found in Sidiropoulos (2000) and Vlachopoulos and Sidiropoulos (2014). Simplification of the thin shell approximation is possible if the bubble is approximated by a quasi-cylindrical geometry (Liu *et al.*, 1995). In

this context, the bubble may be represented by a series of "tubular elements" as shown in Fig. 8.4-3. The simplified equation is

$$\Delta P = \frac{h}{R}\sigma_t \tag{8.3-1}$$

where ΔP the inflation pressure, h the thickness of the tubular element, R the radius of the element and σ_t the stress exerted circumferentially (t direction in Fig. 8.4-4) called the hoop stress. This is the same equation derived for pipes in Section 10.5 (Barlow's formula).

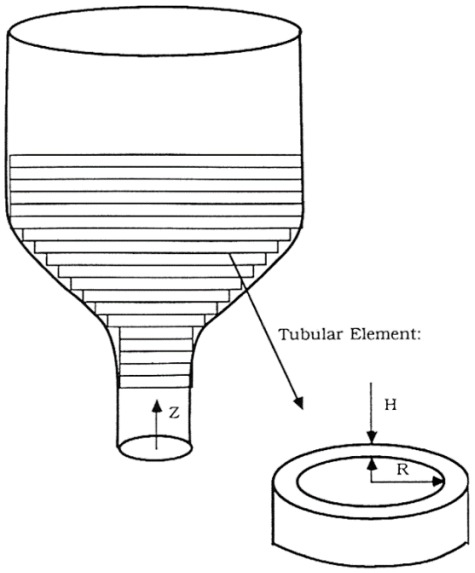

Figure 8.4-3. Diagram showing the "quasi-cylindrical" approximation of a blown film bubble. From Vlachopoulos and Sidiropoulos (2014).

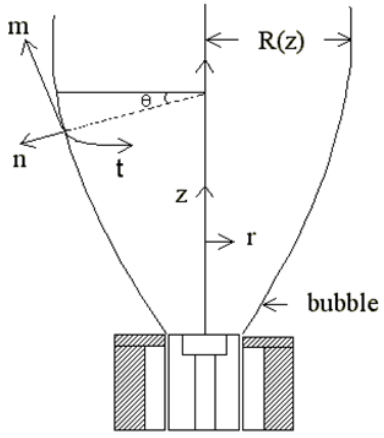

Figure 8.4-4. Blown film bubble and intrinsic coordinate system (n, m, t). From Vlachopoulos and Sidiropoulos (2014).

The rate at which the tubular film is being cooled (mainly by the radial air jet(s) from the air ring(s)) has a great influence on the process because it determines the distance above the die, where solidification is complete (frequently referred to as Freeze Line Height, FLH).

Radiative heating may be responsible for as much as 20% of the heat transfer and must be taken into account. A heat balance (Vlachopoulos and Sidiropoulos, 2014) gives

$$\rho C_p Q cos\theta \frac{dT}{dz} = -2\pi R\left[h_t(T - T_a) + \kappa\varepsilon\left(T - {T_a}^4\right)\right] \quad (8.4\text{-}1)$$

where ρ the density, C_p the heat capacity, Q the polymer flow rate, angle θ is denoted in Fig. 8.4-4, T the temperature, z the axis of symmetry of the bubble, h_t the convective heat transfer coefficient, κ the Stefan-Boltzmann constant and ε the emissivity.

Two important aerodynamic phenomena are associated with the cooling airflow, namely the *Venturi* and *Coanda* effects (Sidiropoulos, 2000, Sidiropoulos and Vlachopoulos, 2000a). The well-known Venturi effect is caused when a fluid flows through a constricted area: its speed increases and the pressure drops. In film blowing, the lower orifice air is flowing through the narrow gap between the bubble surface and the air ring cone. The resulting Venturi effect causes the bubble to be pulled towards the air ring cone, visibly deforming the bubble. The Coanda effect occurs when a free jet emerges close to a surface: the jet tends to bend, "attach" itself and flow along the surface. The surface may be flat or curved and located inclined or offset to the jet. The Coanda effect is more pronounced near curved surfaces. Blown film bubble surfaces with the cooling air impinging on them at an angle, offer the possibility of Coanda type jet attachments and detachments. Fig. 8.4-5 shows a simulation example depicting the calculated airflow streamlines around a typical blown film bubble (Sidiropoulos and Vlachopoulos, 2000a, 2000b). The two simulated airflows (presented on the left and right side of the same figure) correspond to slightly different setups for the adjustable part of the air ring. Although the geometrical differences are minute, the simulation predicts significant differences in the local airflow pattern. The local heat transfer rates are different in the two cases and the onset of the Coanda effect may stabilize or de-stabilize the bubble.

Once solidified, the tubular film must be collapsed to form a lay-flat tube. This particular task is handled by the collapsing system. Some films need sophisticated collapsing systems (for example "tacky" films need low-friction or even non-contact collapsers) while others do fine with simple, roller-equipped collapsing frames. Most collapsing systems induce some form of distortion to the film. Simple triangulation reveals that the distances the film has to travel in the collapsing system are not even across the tube circumference and the film has to stretch in some areas before assuming the final layflat shape. The following equation

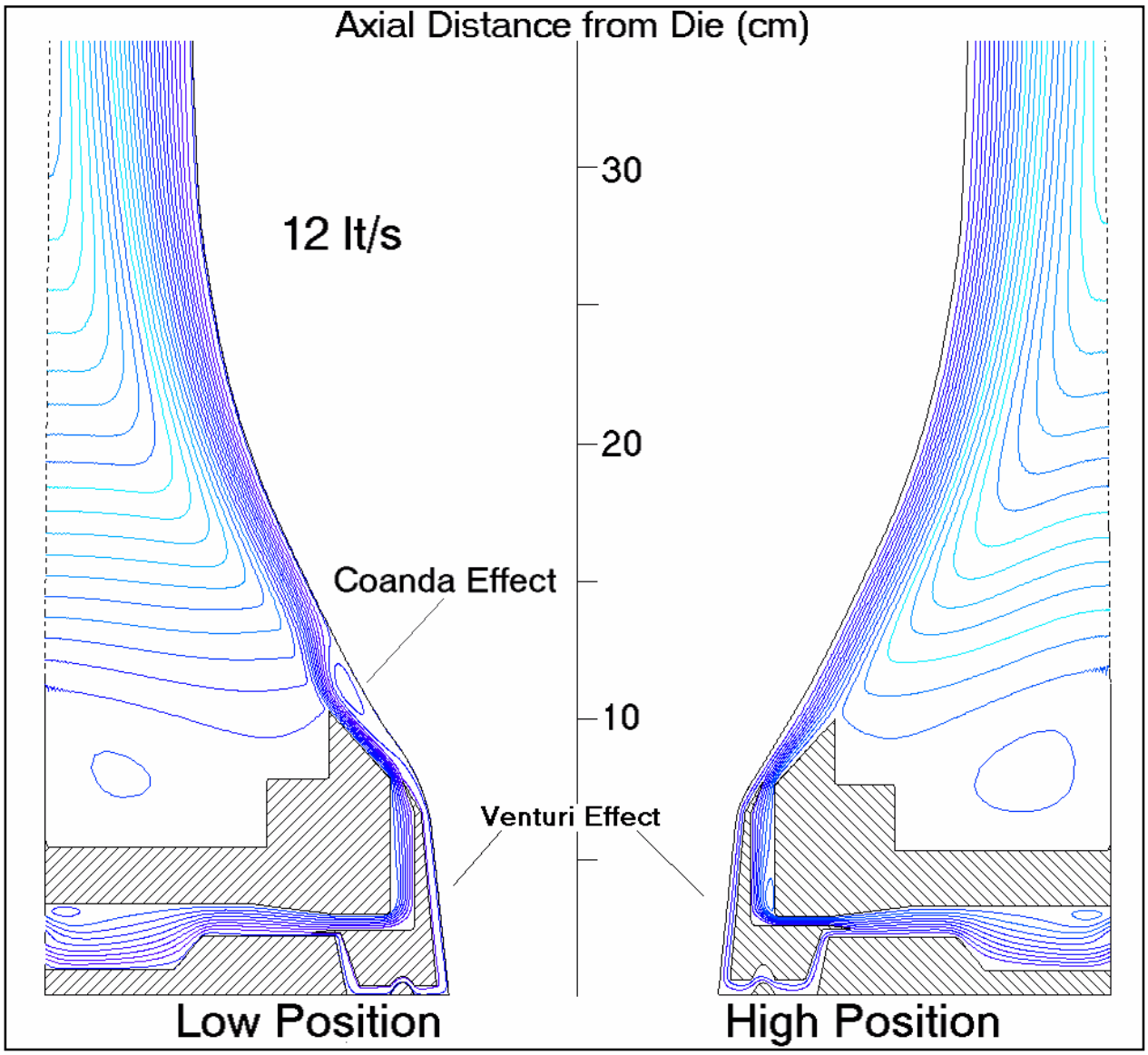

Figure 8.4-5. Cooling air streamlines around an LLDPE blown film bubble for different setups of the adjustable ring (moderate air-flow) left side: low position, right side: high position. From Sidiropoulos and Vlachopoulos (2000b).

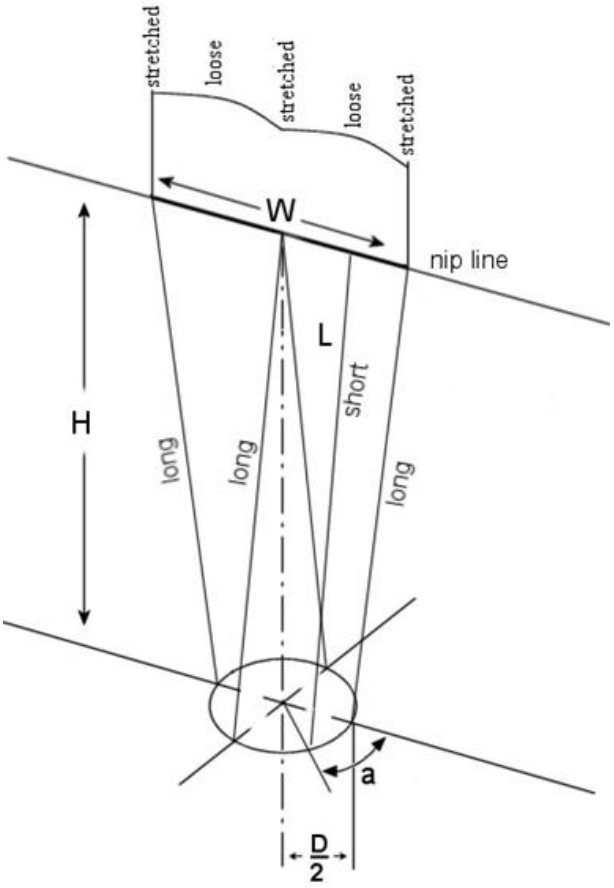

Figure 8.4-6. Film stretching during bubble collapsing process. From Knittel (1992).

can be used to calculate the relative distance (Knittel, 1992) as a function of the position across the tube circumference,

$$L = \sqrt{H^2 + \left[\left(1 + \frac{\pi}{2} - a\right)\pi D + 4 - D\cos a + 2\right]^2 + [D\sin a + 2]^2} \qquad (8.4\text{-}2)$$

Notation of the parameters in Eq. 8.4-3 is shown in Fig. 8.4-6. The uneven stretching creates "stretched" and "loose" regions in the final lay-flat roll. During the collapse, soft, pliable polymers (like LDPE) extend and the film becomes slightly thinner in the "stretched" regions. In higher modulus materials (like HDPE, PET etc.) the strength of the film prevents stretching, resulting in broad wrinkles in the "loose" regions.

Bibliography

Bourgeois, J.R. in: *Film Extrusion Manual*, Butler T.I. and Veazy E.W. (eds), TAPPI Press, Atlanta, GA (1992)

Butler T.I., Blown Film Extrusion, in: *The SPE Guide on Extrusion Technology and Troubleshooting*, Vlachopoulos J. and Wagner J. (eds), Society of Plastics Engineers, Brookfield, USA (2001)

Cantor, K. *Blown Film Extrusion*, 2nd Edition, Hanser (2011)

Butler T.I., *Film Extrusion Manual*, 2nd Edition, TAPPI (2005)

Hensen F., *Plastics Extrusion Technology*, Hanser Publishers (1997)

Knittel R.R., in: *Film Extrusion Manual*, Butler T.I. and Veazy E.W. (eds), TAPPI Press, Atlanta, GA (1992)

Hopmann C. and Michaeli W., *Extrusion Dies for Plastics and Rubber*, 4th Edition, Hanser (2016)

Liu C.-C., Bogue D.C. and Spruiell J.E., Tubular Film Modeling Part 2. Theoretical Modeling, Intern. Polym. Proc., 10 (3), 230 (1995)

Perdikoulias J., Analysis and Design of Annular Dies for Mono- and Multilayer Polymer Flows, PhD Thesis, University of Waterloo, Waterloo, ON, Canada (1997)

Perdikoulias J., Vlachopoulos J. and Vlcek J., Spiral Die Analysis, in: *Film Processing*, Kanai T. and Campbell G.A. (eds.), Hanser Publishers (1999)

Sidiropoulos V., The Effects of Air Cooling on the Film Blowing Process, PhD Thesis, McMaster University, Hamilton, ON, Canada (2000)

Sidiropoulos V. and Vlachopoulos J., An Investigation of Venturi and Coanda Effects in Blown Film Cooling, Intern. Polym. Proc., 15 (1), 40 (2000a)

Sidiropoulos V. and Vlachopoulos J., The Effects of Dual-Orifice Air-Ring Design on Blown Film Cooling, Polym. Eng. Sci., 40 (7), 1611 (2000b)

Vlachopoulos J., Castillo R., Polychronopoulos N. and Tanifuji S., Flat Film and Sheet Dies, in: *Design of Extrusion Forming Tools*, Carneiro O.S. and Nobrega M. (eds), Smithers Rapra (2012)

Vlachopoulos J. and Sidiropoulos V., Die Flow Analysis and Mathematical Modeling of Film Blowing, in: *Film Processing Advances*, Kanai T. and Campbell G.A. (eds), Carl Hanser Verlag (2014)

Waller, P. *A Practical Guide to Blown Film Troubleshooting*, 2nd Edition, Touch Point Group, Thornhill Ontario (2010)

J. Vlachopoulos and N.D. Polychronopoulos "*Understanding Rheology and Technology of Polymer Extrusion*", First Edition, Polydynamics Inc, Dundas, Ontario, Canada (2019)

Chapter 9

CO-EXTRUSION INSTABILITIES

9.1 Introduction

Co-extrusion is the process in which two or more polymers are extruded and joined together to form a single structure with multiple layers. Each layer in the layered structure is chosen to provide a specific end-use characteristic to the product (e.g. barrier properties, heat sealability, strength, chemical resistance etc) resulting in a product that integrates all these properties. Key measures for a good quality final coextruded product are: (i) each layer must have uniform thickness (ii) the layers must adhere perfectly to each other and (iii) free from interfacial instabilities.

The ultimate goal of coextrusion is the production of multilayer films or sheets with good properties, at a lower cost than extruding a single layer as explained schematically in Fig. 9.1-1.

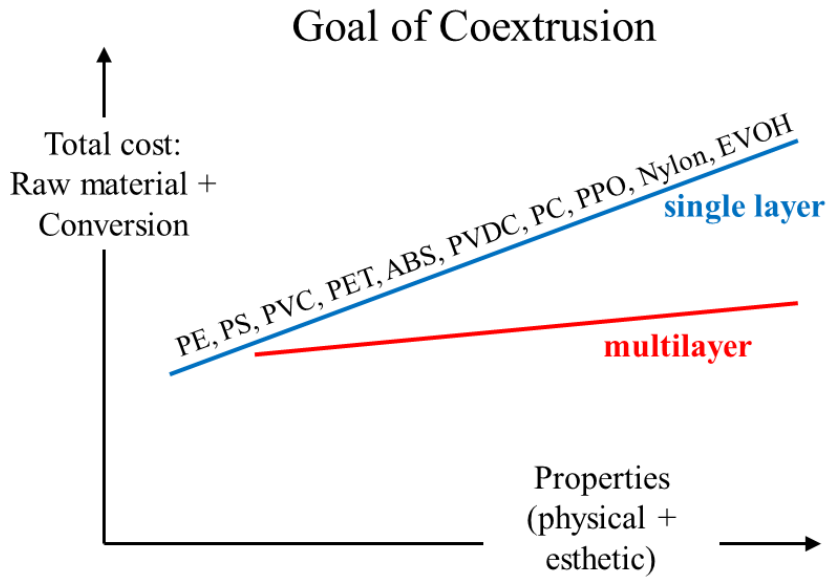

Figure 9.1-1. The goal of coextrusion as suggested by Finch (1990).

Coextruded films are used extensively in food packaging. For example, a three-layer film would have an outside layer suitable for good printing (brand name, company logo, content description and other information) without any ink spreading or other problems. The inside layer would be a barrier material, that is a resin (e.g. Polyvinylidene Chloride (PVDC, commercial name Saran)) which has very low permeability to oxygen, flavors and moisture, so that the shelf-life of the packaged food product is extended. The layer in contact with food should not have any toxicity. Coextrusion is used in blown film, cast film/sheet (flat film thickness less than 0.25mm, flat sheet thickness more than 0.25mm), tube/pipe, profile, extrusion coating and blow molding. For the production of fuel tanks for cars Ethylene Vinyl Alcohol (EVOH), which is a barrier to gasoline vapors, is co-extruded in tubular form with layers of HDPE and subsequently inflated to take the mold shape. Typically, the fuel tank wall is comprised of six layers: a barrier layer, adhesion promoting layers on both sides of it, a layer of regrind (granules made from rejected fuel tanks, to reduce cost) and two layers of virgin HDPE (inside and outside).

Three layer blown film lines are very common, but lines with up to 11 layers are also manufactured and sold. With feed-block technology, for flat film, over 1000 layers can be coextruded. The question may be asked: Why more than three layers in coextrusion for food packaging if just one layer can do what is needed? The reason is that during production the thin polymer layers may have defects at certain points. However, it is highly unlikely that defects from several layers will occur at exactly the same location. So, with more layers there is assurance of defect-free packaging film.

9.2 Layer Encapsulation and Non-uniformities

The main cause of non-uniformities the tendency of the less viscous polymer to go to the region of high shear (wall) to reduce the energy required for the flow, thereby encapsulating the more viscous polymer as illustrated in Fig. 9.2-1 for a round and a flat die. The degree of encapsulation depends primarily on the extent of the viscosity difference and the residence time. Difference in wall adhesion, viscoelastic characteristics of polymers, relative layer thicknesses and length of the flow path are contributing factors (Karagiannis *et al.* 1995). Layer non-uniformities in feed-block flat dies occur when there is a large enough viscosity mismatch. Low-viscosity polymer migrates to the die wall, producing encapsulation as shown in Fig. 9.2-2. This migration can start in the die manifold due to the uneven flow

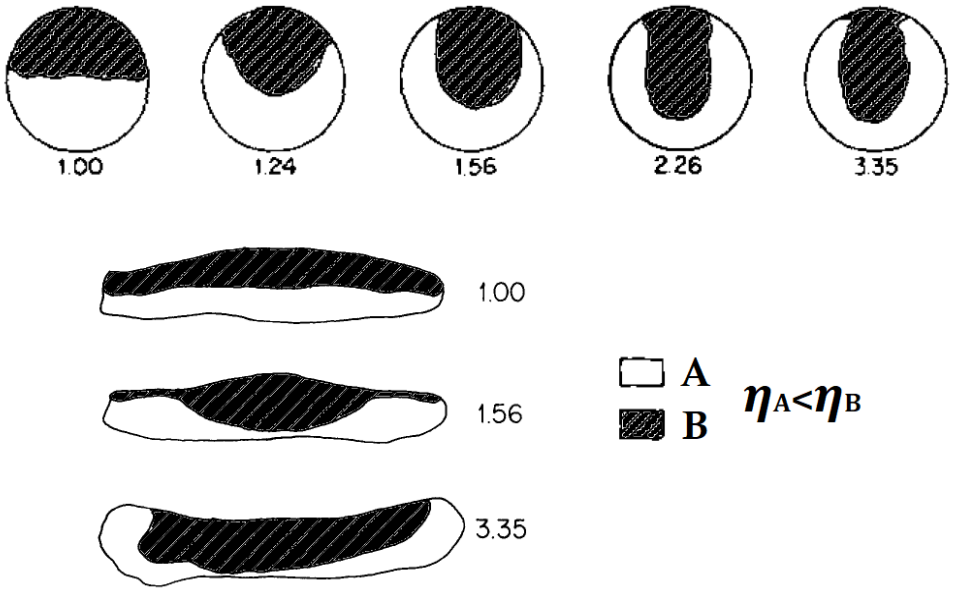

Figure 9.2-1. Cross-sections of a low viscosity polymer encapsulating a more viscous one. Top: at the exit of a capillary die and bottom: at the exit of a flat die. Numbers below or next to the cross-sections correspond to time (in minutes). From Minagawa and White (1975).

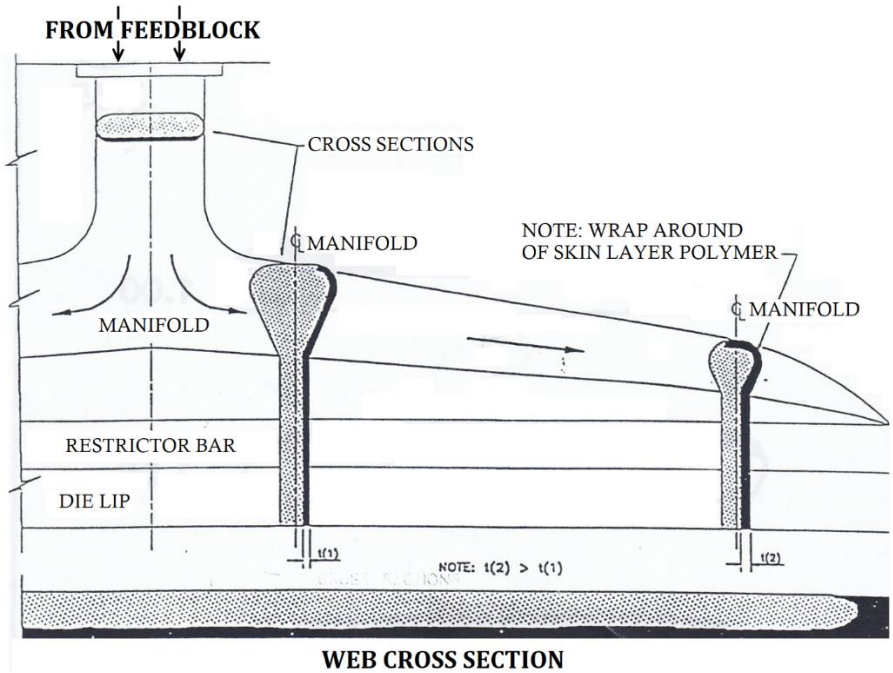

Figure 9.2-2. Layer non-uniformity due to uneven flow leakage in a typical coat-hanger die. From Cloeren (1993).

leakage, resulting in increased layer thickness for low-viscosity polymer at the edges of the film or sheet (Dooley, 2005). A remedy is to profile the feed-block slot so as to compensate for the possible layer migration. The feed-block profiling method has been discussed in Chapter 7 (see also Fig. 7.3-2).

Layer rearrangement may also exist even if the layers are of the same material (same viscosity). In this case, the non-uniform thickness of the two co-extruded melt streams, of the same material, is attributed to flow rearrangement due to high second normal stress difference N_2 (see section 3.9 in Chapter 3). In Fig. 9.2-3 both polycarbonate (PC) and polystyrene (PS)

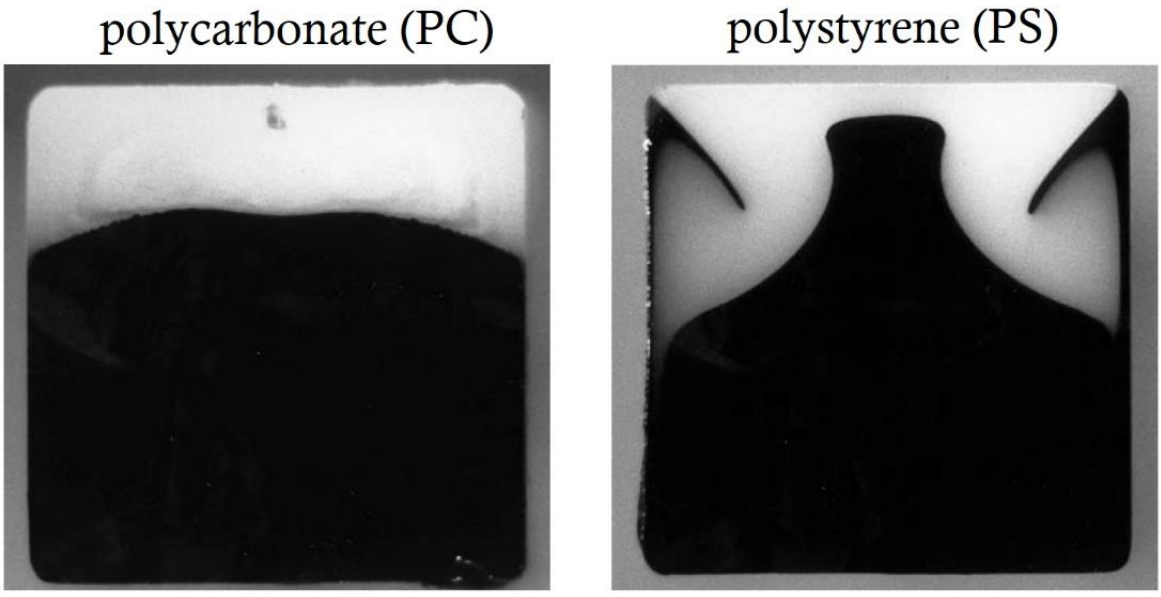

Figure 9.2-3. Co-extrusion of two-layer polymers of the same material in a square channel. To the left, the low elasticity PC exhibits a rather small non-uniformity, which is not the case of the high elasticity PS. From Dooley (2005).

layers were even at the entry to the channel of square cross-section. PC is not very elastic, which means that the normal stress differences are not large, and it shows little rearrangement. On the contrary, PS is very elastic and it shows a significant layer rearrangement, which is counter-intuitive. This means that highly elastic polymers have encapsulation phenomena due to both viscosity mismatch and their large second normal stress difference.

9.3 Interfacial Instabilities

Interfacial instability is an unsteady-state process in which the interface location between layers varies locally in a transient manner. Interface distortion due to flow instability can cause thickness non-uniformities in the individual layers while still maintaining a constant thickness product. These instabilities result in irregular interfaces and even layer intermixing in severe cases (Karagiannis *et al.*, 1995).

There are two types of interfacial instabilities: **zig-zag instability** and **wave pattern instability**. Zig-zag instability appears usually as chevrons pointing in the flow direction as

shown in Fig. 9.3-1, from Zatloukal and De Witte (2006). It is initiated in the die land and it is characterized by a critical interfacial shear stress, in the range of 60-90 kPa (while the critical wall shear stress for the onset of sharkskin is usually quoted as 140 kPa (Vlachopoulos and Strutt, 2010). Optical film clarity is affected significantly by zig-zag instability at the interface. As it can be seen in Fig. 9.3-2a both the "good" and "bad" films have the same contact clarity, as it is evident by the legibility of the text through the film. However, when the film is moved some distance away from the text, Fig. 9.3-2b, the difference in see-through clarity between the two films becomes quite apparent. The text is still legible through the "good" film, but not through the "bad" film. The problems can be remedied by reducing the interfacial shear stress below the critical level.

Wave pattern instability appears as a train of parabolas across the width of the sheet and is oriented in the flow direction as shown in Fig. 9.3-3. It occurs when a fast moving polymer stream merges with a much slower moving stream in a feedblock in flat film coextrusion. When the skin layer is thin relative to the second layer, the wave instability can be more pronounced. Large differences in extensional viscosities between adjacent layers can also make the defect more likely. Dies with large lateral expansion ratios (die lip width divided by manifold entry width) seem to be more susceptible (Ramanathan *et al.*, 1996). Increased melt elasticity appears to promote these types of instability (Martyn *et al.* 2009).

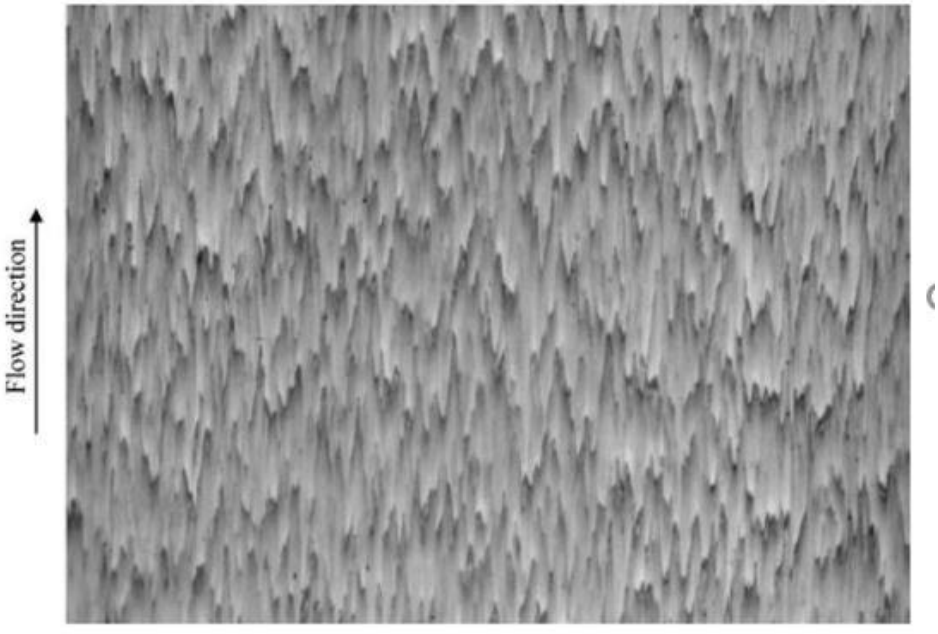

Figure 9.3-1. Zig-zag instability in co-extrusion. From Zatloukal and De Witte (2006).

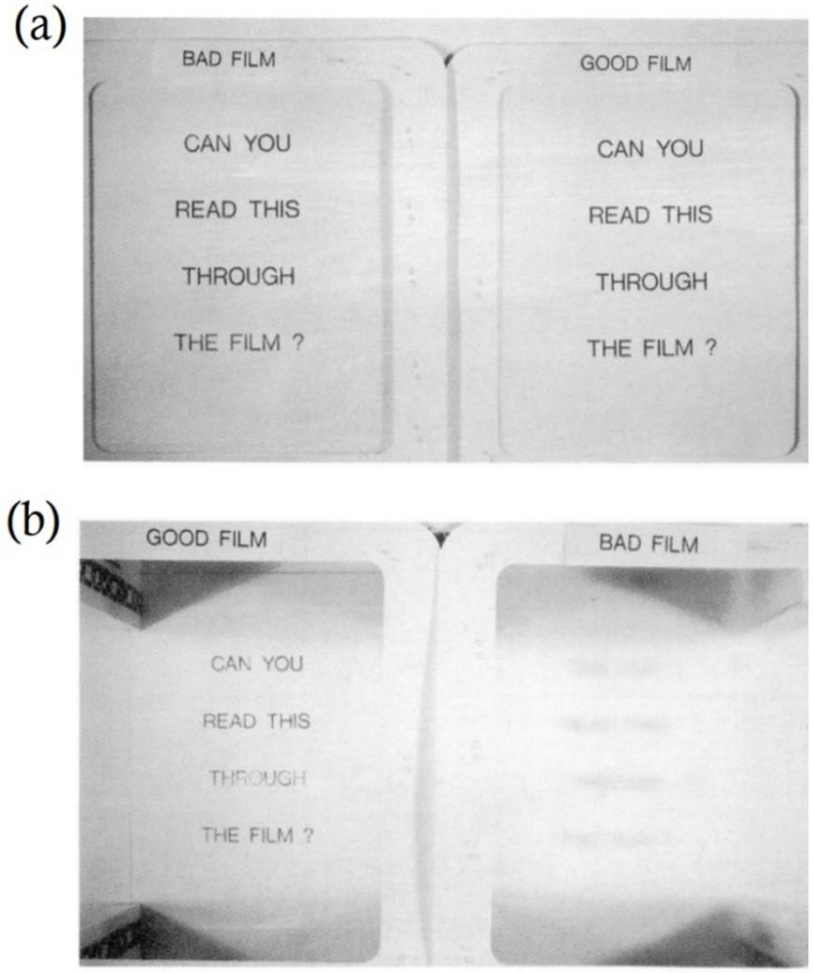

Figure 9.3-2. Film (a) in contact with paper and (b) roughly 2.5 cm above the paper. From Shroff and Mavridis (1991).

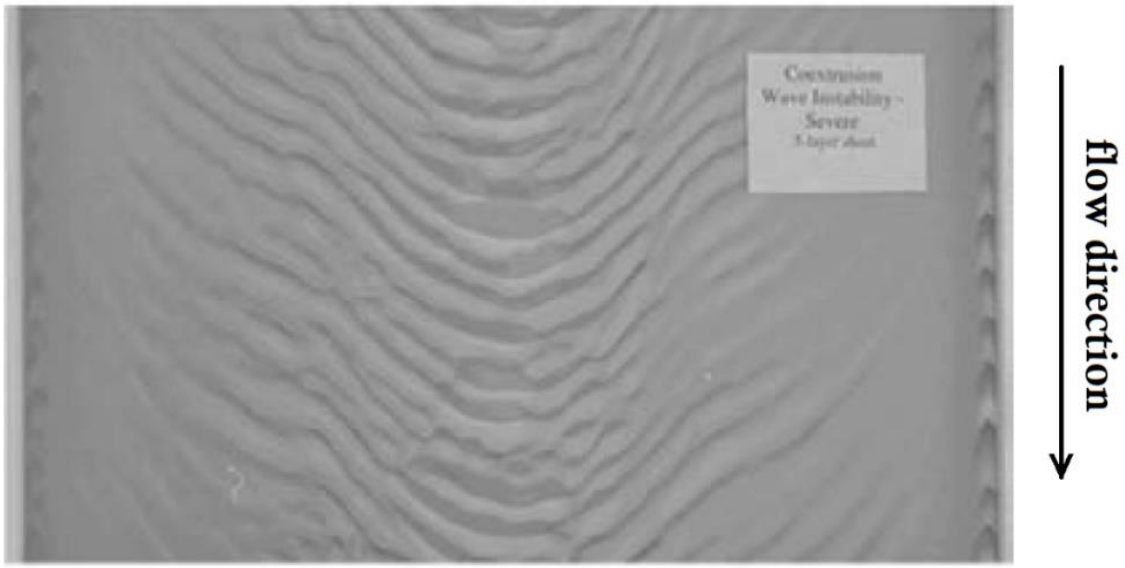

Figure 9.3-3. Wave interfacial instability. From Dooley (2005).

9.4 Co-Extrusion Flow Analysis

A simplified approach for two layers is presented, to provide a basic understanding on how flow description of co-extrusion can be carried out. It should be noted that a complete modeling of the fluid flow would require 2D or 3D numerical solution of the flow equations. Several investigations have been carried out on this basis (see for example the works by Karagiannis *et al.* (1988, 1995), Mavridis *et al.* (1998), Zatloukal *et al.* (2002) and Huang *et al.* (2015)). 3D numerical simulations are a rather challenging task due to the presence of multiple free surfaces inside and outside the die, combined with the swelling of the emerging viscoelastic polymer.

We consider the steady flow of two incompressible Newtonian polymer melt streams between two long parallel plates as shown in Fig. 9.4-1. The fluid motion is from left to right due to an imposed pressure gradient (Vlachopoulos, 2016). The governing equations for each melt stream are the following

$$0 = -\frac{\partial p}{\partial x} + \mu_A \frac{\partial^2 V_x{}^A}{\partial y^2} \quad \text{(for fluid A)} \tag{9.4-1}$$

$$0 = -\frac{\partial p}{\partial x} + \mu_B \frac{\partial^2 V_x{}^B}{\partial y^2} \quad \text{(for fluid B)} \tag{9.4-2}$$

with μ_A the viscosity of the fluid A and μ_B for fluid B. The pressure is a function of the x-direction only and the velocities are functions of the y-direction only. Thus, we may write

$$\frac{dp}{dx} = \mu_A \left(\frac{d^2 V_x{}^A}{dy^2} \right) \tag{9.4-3}$$

$$\frac{dp}{dx} = \mu_B \left(\frac{d^2 V_x{}^B}{dy^2} \right) \tag{9.4-4}$$

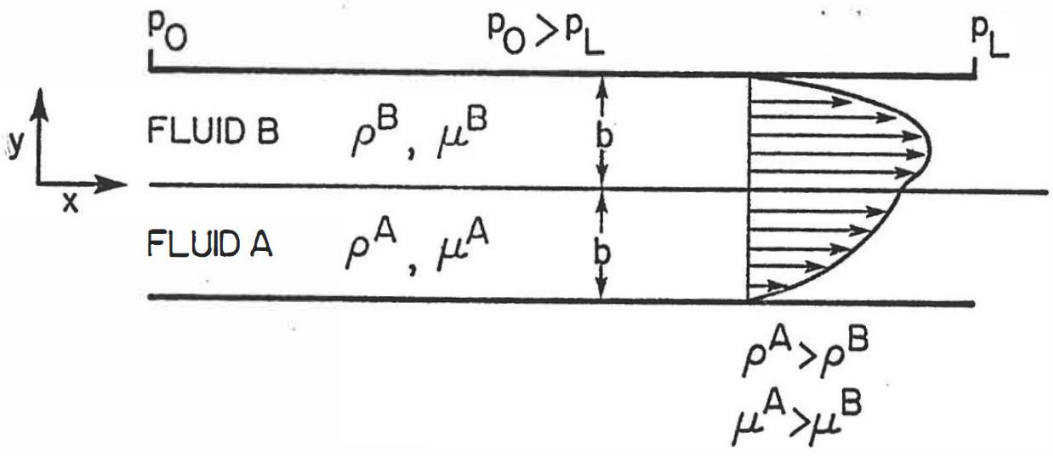

Figure 9.4-1. Pressure-driven flow of two co-extruded melt streams between two parallel plates.

Integrating each equation twice, we obtain

$$V_x{}^A = \frac{y^2}{2\mu_A}\left(\frac{dp}{dx}\right) + C_1 y + C_2 \tag{9.4-5}$$

$$V_x{}^B = \frac{y^2}{2\mu_B}\left(\frac{dp}{dx}\right) + C_3 y + C_4 \tag{9.4-6}$$

In the next step, we must determine the four integration constants by using appropriate boundary conditions. At the upper and lower plates, the velocity is assumed to be zero (no-slip condition). At the interface, the velocities must be equal (i.e. $V_x{}^A = V_x{}^B$) as well as the shear stresses (i.e. $\tau^A = \tau^B$). Thus, the four boundary conditions may be written as

$$\begin{aligned}
&\text{B. C. 1} && V_x{}^A = 0 && y = -b \\
&\text{B. C. 2} && V_x{}^B = 0 && y = b \\
&\text{B. C. 3} && V_x{}^A = V_x{}^B && y = 0 \\
&\text{B. C. 4} && \tau^A = \tau^B && y = 0 \\
&\text{or} && \mu_A\left(\frac{\partial V_x{}^A}{\partial y}\right) = \mu_B\left(\frac{\partial V_x{}^B}{\partial y}\right) && y = 0
\end{aligned} \tag{9.4-7}$$

From B.C.3 we have

$$C_2 = C_4 \tag{9.4-8}$$

and from B.C.4 we have

$$\mu^A C_1 = \mu^B C_3 \tag{9.4-9}$$

Further, using B.C.1 and B.C.2 we obtain

$$C_1 = \left(\frac{dp}{dx}\right)\frac{b}{2}\left(\frac{\mu_A - \mu_B}{\mu_A + \mu_B}\right) \tag{9.4-10}$$

$$C_2 = -\left(\frac{dp}{dx}\right)\frac{b^2}{2\mu_A}\left(\frac{2\mu_A}{\mu_A + \mu_B}\right) \tag{9.4-11}$$

Thus, the velocity profiles are the following

$$V_x{}^A = -\left(\frac{dp}{dx}\right)\frac{b^2}{2\mu_A}\left[\left(\frac{2\mu_A}{\mu_A + \mu_B}\right) + \left(\frac{\mu_A - \mu_B}{\mu_A + \mu_B}\right)\left(\frac{y}{b}\right) - \left(\frac{y}{b}\right)^2\right] \tag{9.4-12}$$

$$V_x{}^B = -\left(\frac{dp}{dx}\right)\frac{b^2}{2\mu_B}\left[\left(\frac{2\mu_B}{\mu_A + \mu_B}\right) + \left(\frac{\mu_A - \mu_B}{\mu_A + \mu_B}\right)\left(\frac{y}{b}\right) - \left(\frac{y}{b}\right)^2\right] \tag{9.4-13}$$

where

$$-\frac{dp}{dx} = \frac{\Delta p}{L} = \frac{p_o - p_L}{L} \tag{9.4-14}$$

The velocity profiles are sketched in Fig. 9.4-1. It should be noted that if $\mu_A=\mu_B$, the velocity profiles for both fluids are identical and Eq. 9.4-13 and Eq. 9.4-14 reduce to the single parabolic expression of Chapter 2.

In a similar fashion, the velocity profiles for power-law fluids can also derived. An example of calculated velocity profiles for power-law fluids is shown in Fig. 9.4-2 for the parameters given in the figure caption.

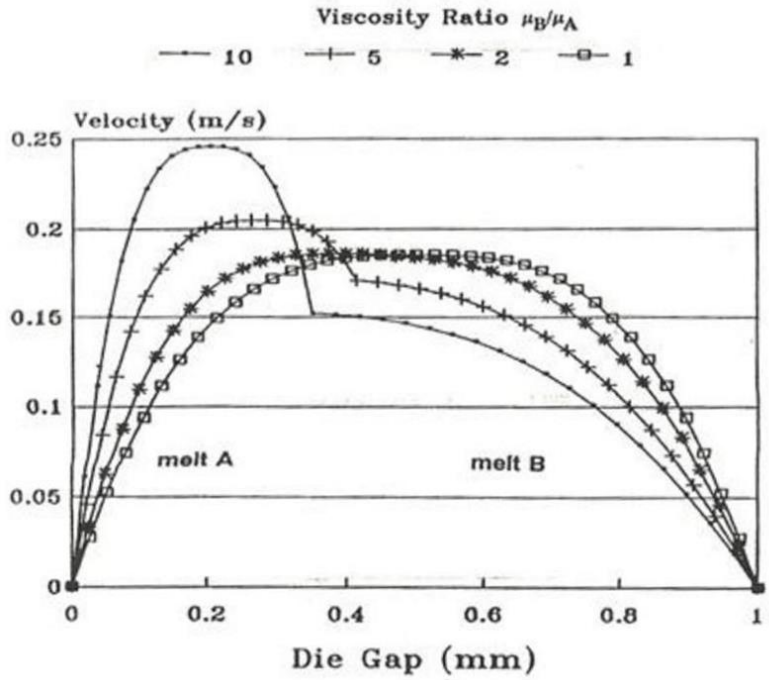

Figure 9.4-2. Velocity profiles for 2-layer co-extrusion of power-law polymer melts. Flow rates for each layer: $Q_A=Q_B=0.5$ m^3/hr, consistency index: $m_A=$ 1000 Pa·s, power-law index: $n_A=n_B=0.5$, plates width: $W=2$ m and gap: $h=1$ mm. Viscosity ratios refer to m_B/m_A ratios. From Karagiannis *et al.* (1995).

It is apparent from Fig. 9.4-2 that as the viscosity ratio increases the velocity profile for the two layers becomes different. The less viscous layer (melt A) exhibits higher velocities than layer B, which leads to a characteristic slope discontinuity at the interface. It is also observed that the viscosity ratio influences the position of the interface. Increase in the viscosity ratio moves the interface from the center of the channel towards the less viscous melt, for this case of flowrate ratio of 1.

As in the flow of a single fluid flowing between two plat plates, the shear stress is zero where the velocity has a maximum and varies linearly from zero to its maximum value at the wall (τ_w) because $\tau=\mu(du/dy)$ throughout the flow area. A velocity and shear stress for three coextruded layers is schematically shown in Fig. 9.4-3.

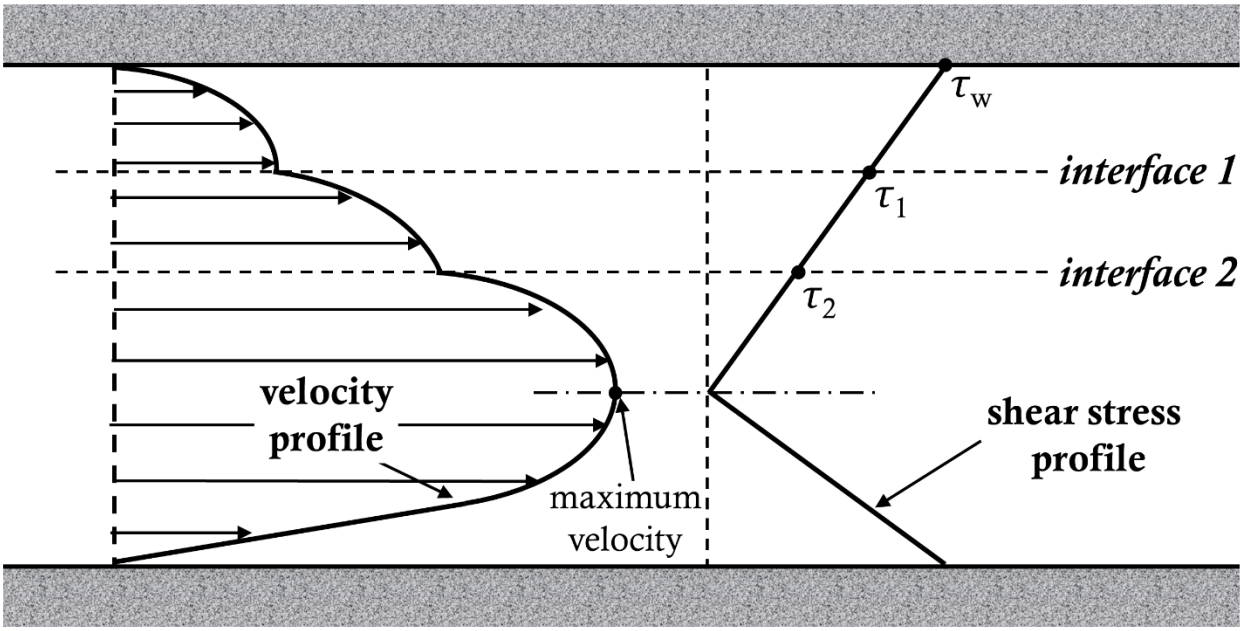

Figure 9.4-3. Schematic representation of the velocity and shear stress profile for a three-layer coextrusion (flat die or tube).

Let us assume that at interface 1 the value of the shear stress (τ_1) exceeds the critical value for the onset of zig-zag instabilities (which is supposed to be 80kPa). The following actions can be taken to reduce the interfacial shear stress and therefore avoid the instability:

a. Reduction of the total extrusion rate. The wall stress on the die is reduced (lower pressure drop)
b. Increase of die gap opening. Similarly, the wall stress level is reduced.
c. Increase of skin layer thickness (by pumping at higher rate the layer near the wall). This will shift the interface away from the wall where the shear stress is maximum.
d. Reduction of skin layer viscosity.

It should be pointed out that viscosity matching is a popular remedy that does not always work. It is often advisable to mismatch the viscosities (add low viscosity skin layer) to reduce the interfacial shear and prevent the onset of zig-zag instability.

Bibliography

Cloeren P., An Overview of the Latest Developments in Flat Die Coextrusion, SPE RETEC Advances in Extrusion Technology, Toronto, Ontario (1993)

Dooley J., Coextrusion Instabilities, in: *Polymer Processing Instabilities Control and Understanding*, Hatzikiriakos S.G. and Migler K.B. (eds), Marcel Dekker (2005)

Huang R., Silva J., Huntington B.A., Patz J., Andrade R., Harris P.J., Yin K., Cox M., Bonnecaze R.T. and Maia J.M., Co-Extrusion Layer Multiplication of Rheologically Mismatched Polymers: A Novel Processing Route, Int. Polym. Proc., 30 (3), 317 (2015)

Karagiannis A., Hrymak A.N., Vlachopoulos J. and Vlcek J., Coextrusion of Polymer Melts, in: *Rheological Fundamentals of Polymer Processing*, Covas J.A., Agassant J.F., Diogo A.C., Vlachopoulos J. and Walters K. (eds), Springer Science and Business Media, B.V. (1995)

Karagiannis A., Mavridis H., Hrymak A.N. and Vlachopoulos J., Interface Determination in Bicomponent Extrusion, Polym. Eng. Sci., 28 (5), 982 (1988)

Martyn M.T., Spares R., Coates P.D. and Zatloukal M., Imaging and Analysis of Wave Type Interfacial Instability in the Coextrusion of Low-Density Polyethylene Melts, J. Non-Newt. Fluid Mech., 156, 150 (2009)

Mavridis, H., Hrymak, A.N. and Vlachopoulos, J. Finite Element Simulation of Stratified Multiphase Flows, AIChE J., 33, 410 (1987).

Minagawa N. and White J.L., Co-Extrusion of Unfilled and TiO2-Filled Polyethylene: Influence of Viscosity and Die Cross-Section on Interface Shape, Polym. Eng. Sci., 15 (12), 825 (1975)

Ramanathan R., Shanker R., Rehg T., Jons S., Headley D.L. and Schrenk W.J. in: *Proceedings of ANTEC*, p.224, Indianapolis, USA, (1996)

Shroff R. and Mavridis H., Computer Flow Analysis: Troubleshoots Film Extrusion, Plastics Technology, 37 (2), 54 (1991)

Zatloukal M., Vlcek J., Tzoganakis C. and Saha P., Viscoelastic Stress Calculation in Multilayer Coextrusion Dies: Die Design and Extensional Viscosity Effects on the Onset of Wave Interfacial Instabilities, Polym. Eng. Sci., 42 (7), 1520 (2002)

Zatloukal M. and De Witte J., Influence of Process Aids on ZigZag Type of Interfacial Instabilities in Multilayer Flows: Theoretical and Experimental Investigation, Plast. Rubber Compos., 35 (4), 149 (2006)

Vlachopoulos J. and Strutt D., Rheology of Molten Polymers, in: *Multilayer Flexible Packaging*, Wagner J.R. (ed.), Elsevier (2010)

JAMES L. WHITE (1938-2009)

Distinguished professor, researcher, author and founder of the Polymer Processing Society

J. Vlachopoulos and N.D. Polychronopoulos "*Understanding Rheology and Technology of Polymer Extrusion*", First Edition, Polydynamics Inc, Dundas, Ontario, Canada (2019)

Chapter 10
PIPE AND TUBING EXTRUSION

10.1 Introduction

Diameters of commercial plastic pipes and tubing range from a couple of millimeters to a couple of meters. Millimeter diameter medical tubing is used in medical devices such as balloon catheters for angioplasty. Large diameter pipes are used for transporting water for drinking or irrigation and other fluids including oil and sewage over large distances. Plastic pipes can be single wall of multiwall and they might be reinforced with external corrugations, embedded fibers or metal inserts. Certain medical tubes are reinforced with metal or fiber braids embedded in the tube wall.

Various grades of polyethylene (PE), polypropylene (PP), polyvinyl chloride (PVC) and other polymers are extruded for water transportation applications. Materials for medical tubing include polyamides (PA, Nylon), PEBAX, PET and polyurethane. The selection of the resins is carried out on the basis of molecular weight (usually expressed by their Melt Flow Index) and mechanical and other properties depending on the intended application. New types of resins and products have been developed for replacement of copper in residential plumbing. C-PVC (C- for chlorinated) pipes can be used for hot water at higher temperatures than PVC. PE-RT (Polyethylene-Raised Temperature) has enhanced mechanical properties at higher temperatures, due to special catalysts used during polymerization. PEX is a cross-linked PE pipe used extensively in home plumbing. Cross-linking takes place either during extrusion (with the help of peroxide) or after the pipe is extruded (with silane or radiation). The cross-linking of molecules provides enhanced mechanical properties.

A typical pipe production line is shown schematically in Fig. 10.1-1. The molten polymer is supplied from an extruder to a die having annular lips. After the die exit, the pipe

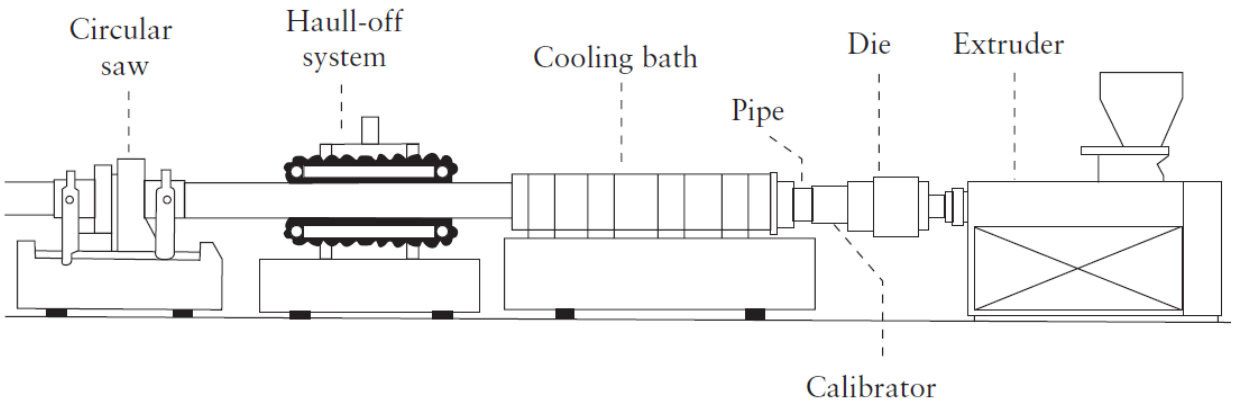

Figure 10.1-1. Schematic representation of a typical pipe production line. From Haudin *et al.* (2012).

travels some distance through the air and subsequently passes through a calibrator (that is a sizing fixture) to a cooling bath. The final stage usually consists of a saw or a rotary knife that cuts the pipe into desired lengths. In medical tubing extrusion, the line is situated inside a clean room with controlled pressure and temperature conditions, so any possible external contamination of the product can be avoided.

10.2 Pipe Dies

Two main types of die designs are used in pipe (and tubing) extrusion. The first one is spiral die design, discussed in detail in Chapter 8. The shape of a spiral die for pipe production is similar to those used for blown film extrusion, but with different considerations for a thicker tubular extrudate. In such dies the mandrel is supported from the back of the die body. There is no flow obstruction in the channel formed between the mandrel and the body. A mechanical drawing of a spiral die is shown in Fig. 10.2-1, from Kainth (2018). The second type is the spider leg design. In this case the central mandrel is supported by rods arranged like legs of a spider. A schematic of a spider leg die is shown in Fig. 10.2-2. The legs are regularly distributed around the mandrel circumference. Some typical spider leg arrangements are illustrated in Fig. 10.2-3. Due to the spider legs the polymer melt flow is split and reattached again downstream to form weldlines, as shown schematically in Fig. 10.2-4. At weldlines, the pipe has reduced mechanical properties due to the slow diffusion of the long polymer chains, essentially poor bonding, which is frequently responsible for failures. General rules may be followed, according to Hopmann and Michaeli (2016), for acceptable spider leg design: the spider lengths should not be longer than 30 to 80 mm, not wider than 9 to 12 mm and the cor-

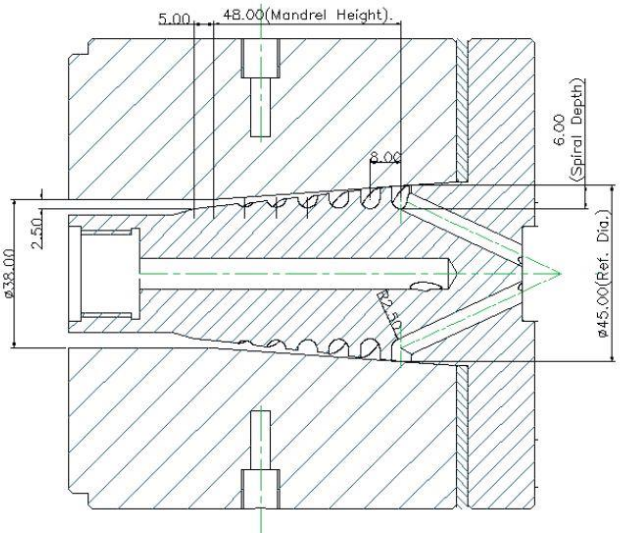

Figure 10.2-1. Spiral die drawing with dimensions in millimeters. From Kainth (2018).

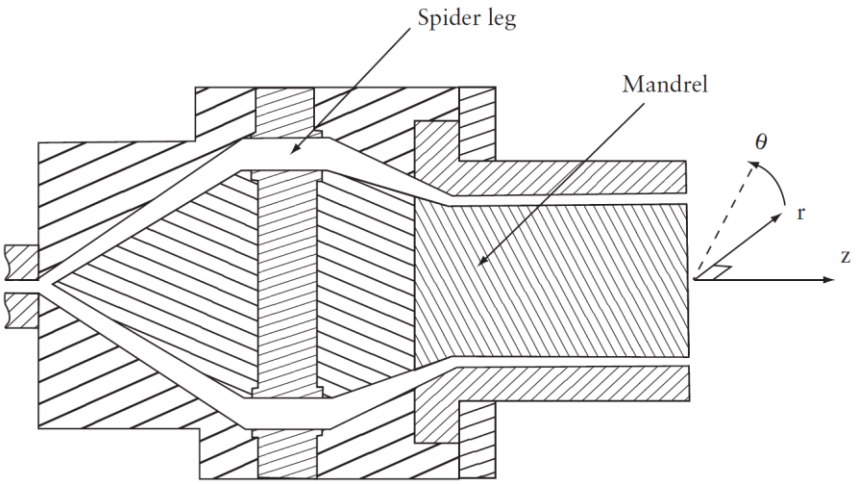

Figure 10.2-2. Schematic representation for a typical geometry of a spider leg die. From Haudin *et al.* (2012).

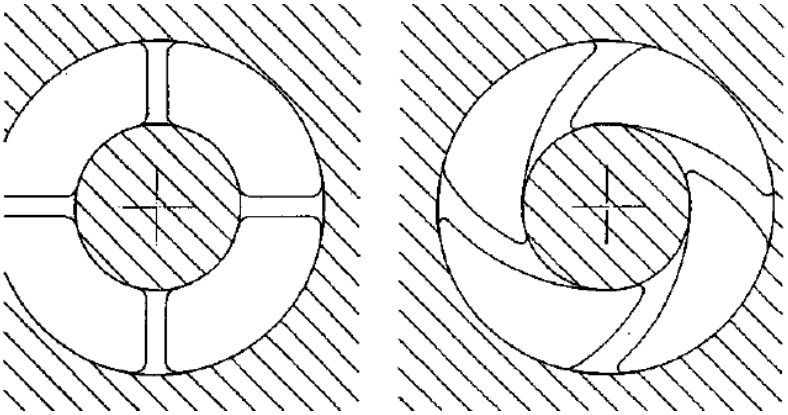

Figure 10.2-3. Some typical spider leg arrangements (cross-section view of the die, the flow is normal to the page). From Hopmann and Michaeli (2016).

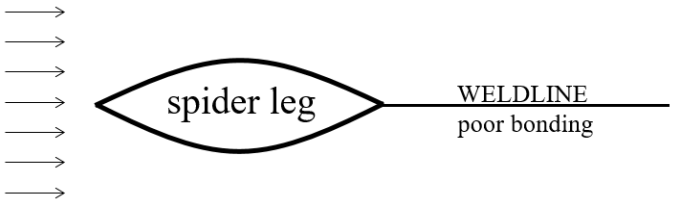

Figure 10.2-4. Schematic representation of a weldline (the flow is from left to right).

ners at the root of the spider legs (see Fig. 10.2-3) should be designed to avoid stagnant melt flow regions. Weldline problems may be reduced with the following (Hendess and Bessemer, 2001, Hopmann and Michaeli, 2016):

1. Melt homogeneity
2. Higher melt temperature (so that the molecules will have more kinetic energy for faster diffusion and better bonding of the two merging melt streams)
3. Higher pressure (may be accomplished with a longer die or constrictions)
4. Special spider leg design. For example, in Fig. 10.2-5 there will be more than one weldline forming, but only for part of the thickness. In Fig.10.2-3 the design on the left side will result in weldlines from inner to outer surface, while the design on the right the weldlines will be bent and less prone to failure under compression.

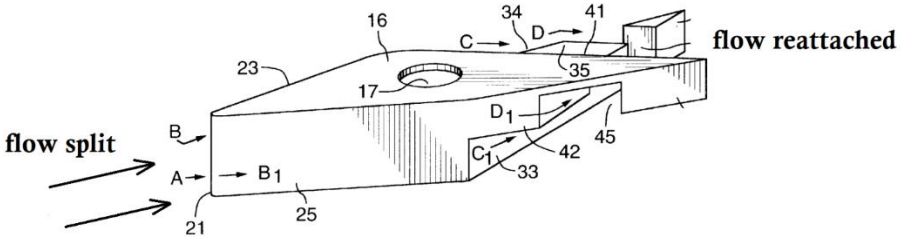

Figure 10.2-5. A special type of spider leg. The molten polymer splits on the left and reattaches to the right at the two tails of the leg. From Lupke and Lupke (2000).

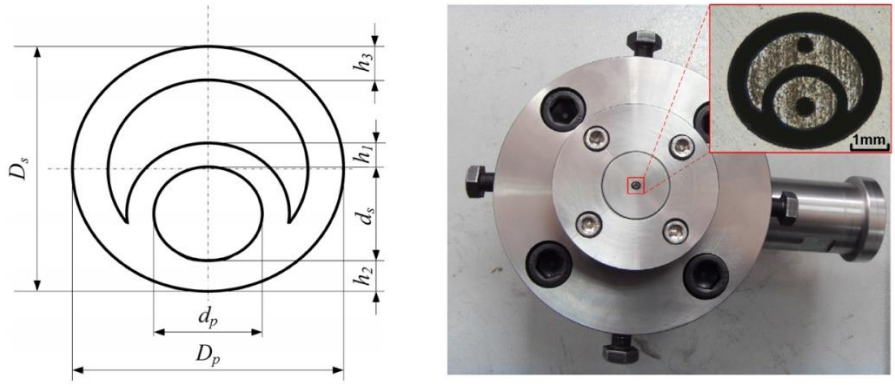

Figure 10.2-6. Schematic representation and assembly of the extrusion die of a typical two-lumen micro-tube. From Tian *et al.* (2015).

At the end of the die there are lips which give the shape to the pipe and determine the dimensions. In customary round pipe extrusion and certain types of medical tubing extrusion, the lips usually have annular geometry of a constant gap. In several medical applications, such as balloon angioplasty, tubes with multiple lumens are widely used. For this case the lips have a more complex geometry. In Fig. 10.2-6, typical double lumen lips are shown. Five-lumen tubes are also possible to fabricate (Jin et al., 2014).

10.3 Pipe Calibration and Cooling

After the polymer exits the forming die, it travels some distance in air before entering the cooling tank. The cooling tank may contain a cold water bath or jets. At the entrance of the cooling tank there is a calibration unit. The purpose of this device is to control the outer diameter of the pipe or tube before final solidification takes place. In the technical literature, it is also referred to as sizing.

Calibration in pipe and tubing extrusion may be performed in two ways. In the first, pressure is applied internally to the extruded pipe so that the external pipe surface contacts the calibrator surface as shown in Fig. 10.3-1a. Water is used to control the cooling rate, but

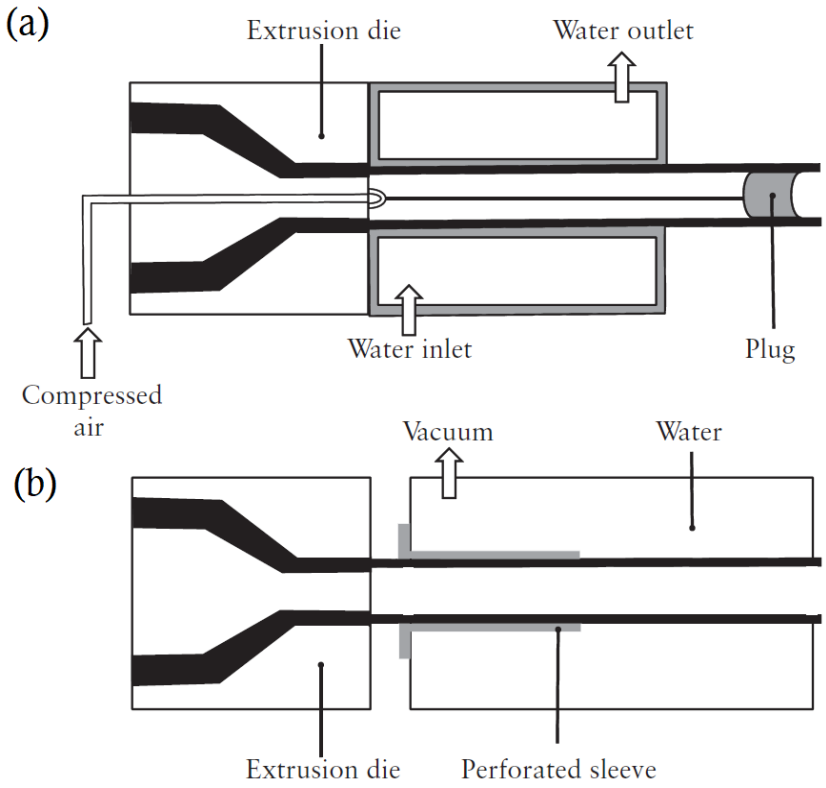

Figure 10.3-1. Pipe extrusion calibration with (a) application of pressure internal to the pipe and (b) vacuum. From Carneiro and Nóbrega (2012).

there is no direct contact between water and pipe. This calibration type is usually called dry cooling (Carneiro and Nóbrega, 2012). In the second way, shown in Fig. 10.3-1b, the external pipe surface is brought into contact with the calibrator surface by the application of vacuum. At least part of the heat is removed with direct contact of water with the pipe external surface and for this reason it is referred to as wet cooling (Hendess and Bessemer 2001; Carneiro and Nóbrega, 2012). The properties of extruded pipe are significantly affected by the rate of cooling. The magnitude of residual stresses is determined to a large extent by the cooling operation. Cooling simulation software is available for optimization purposes (Chillware: www.shs-plus.de/index.php/en/)

10.4 Double-Walled Corrugated Pipes

Corrugations increase significantly the stiffness of metal, paper or plastic sheets. Corrugated pipes are usually double-walled with an inner smooth surface and corrugated external layer, as shown in Fig.10.4-1. Double (or sometimes triple) wall corrugated pipes

Figure 10.4-1. PVC 48 inch (1219 mm) pipe produced on Corma (www.corma.com) equipment.

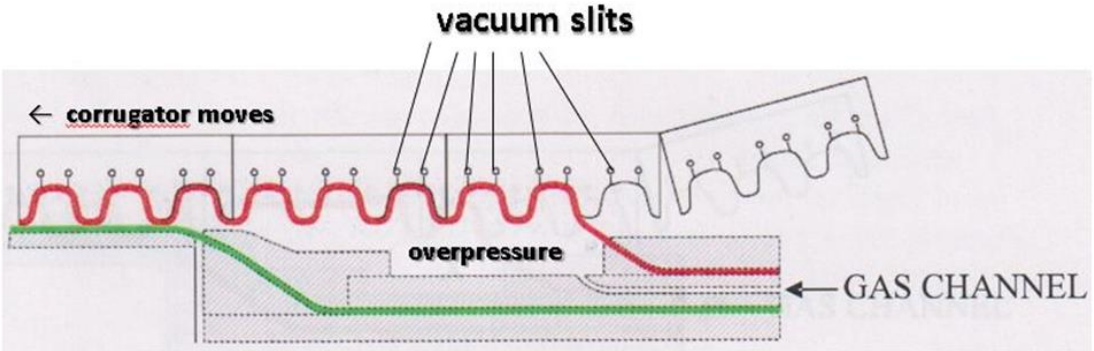

Figure 10.4-2. Sketch of double-wall corrugated pipe extrusion as the corrugator blocks continuously rotate. From Vlachopoulos and Lupke (2018).

made of high density polyethylene (HDPE), polypropylene (PP) or polyvinyl chloride (PVC) are used extensively for sewer and rainwater applications. Dies are either of the spiral or spider variety. Inner and outer layers are extruded simultaneously and the corrugations are formed by the application of internal pressure and external vacuum as a series of mold blocks rotate, usually mounted on two vertical or horizontal chain-like oval tracks, as shown in Fig. 10.4-2. The forming of corrugations is somewhat similar to extrusion blow molding.

10.5 Hoop Stress

Plastic pipes are heavily regulated products and several ASTM and ISO standards apply. For example, polyethylene pipes are classified by the type of material grade used: PE 100 is for very demanding piping applications having a Minimum Required Strength (MRS), according to ISO 4427, of 100 bar (10 MPa) at 50 years and 20°C. PE 80 has MRS of 80 bar (8 MPa) for somewhat less demanding applications and PE 40 has MRS of 40 bar (4 MPa) for low pressure systems. Part of a PE 100 data sheet is shown in Table 10.5-1 We note that the Melt Flow Rate (same as MFI) with 5 kg load is 0.25 g/10 minutes, while MFI with 2.16 kg load is not reported because it is less than 0.1 g/10 minutes and it is not measurable. Also from the same resin producer (www.borouge.com) a PE 80 (for 5 kg load) MFI= 0.3 g/10 minutes (which means a somewhat lower molecular weight).

Table 10.5-1 Polyethylene (PE 100) BorSafe HE3490-LS part of data sheet

Property		Test Method	Unit	Typical Value[1]
Density	(Compound)	ISO 1183-1 Method A	kg/m³	960
Melt Flow Rate	(190°C/5.0 kg)	ISO 1133	g/10 min	0.25
Tensile Modulus	(1mm/min)	ISO 527-2	MPa	1100
Tensile Strain at Break	(50mm/min)	ISO 527-2	%	>600
Tensile Stress at Yield	(50mm/min)	ISO 527-2	MPa	25

A key design parameter in pipes is the circumferential stress which is frequently referred to as hoop stress σ_H, as shown schematically in Fig. 10.5-1a. The hoop stress is a function of the applied pressure and the pipe geometric characteristics. This can be obtained from a simple force balance on the half-cylinder in Fig. 10.5-1b. It is assumed that the cylinder wall is thin (i.e. thickness<<diameter). The applied internal pressure generates a force acting on the pipe, which is given by

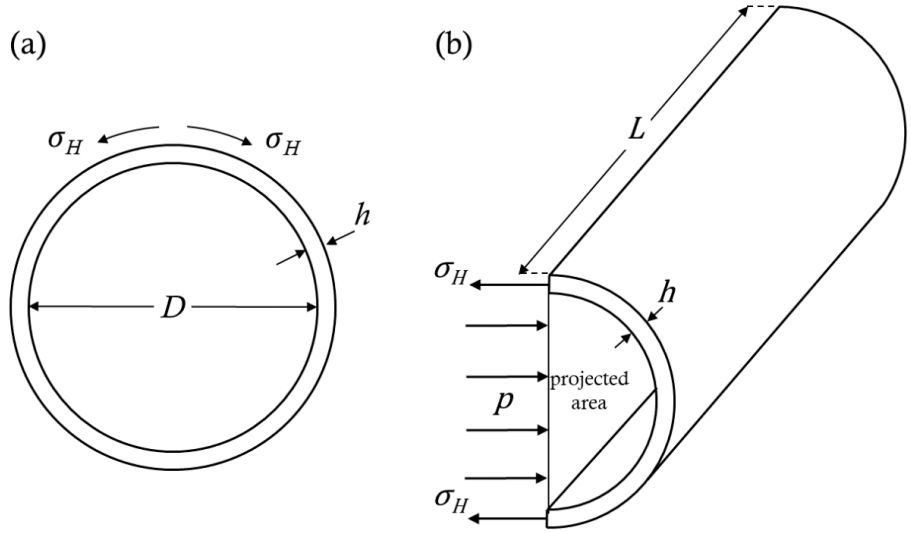

Figure 10.5-1. Schematic representation of the hoop or circumferential stress on a typical cross-section of a pipe with length L normal to the page.

$$F_p = pressure \times projected\ area = pDL \tag{10.5-1}$$

where D the diameter and L the length of the pipe. The force that resists the pressure force is given by

$$F_H = hoop\ stress \times thickness \times length = \sigma_H hL \tag{10.5-2}$$

where h the thickness of the cylinder. The force balance then requires that

$$F_p - 2 \times F_H = 0 \tag{10.5-3}$$

Substituting Eq. 10.5-1 and 10.5-2 in Eq. 10.5-3, we obtain

$$p = \frac{2\sigma_H h}{D} \tag{10.5-4}$$

which is usually referred to as Barlow's formula. This formula can be used for the determination of the maximum allowable pressure to avoid bursting, by using the value of tensile strength of the material for the hoop stress. Depending on diameter and wall thickness PE pipes for water might have bursting pressures perhaps exceeding 10 bar (1 MPa), while some small diameter tubes for angioplasty up to perhaps 40 bar (4 MPa).

Example E10.5-1

Pipe manufacturer FIRAT (www.firat.com) reported the production of 1600 mm PE 100 pipe having wall thickness of 61.2 mm. Determine the pressure rating assuming a safety factor of 1.25.

Solution

PE 100 has Minimum Required Strength of 10 MPa at 50 years and 20 °C. For safety factor of 1.25 the maximum allowable hoop stress will be 10/1.25=8 MPa. The hoop stress analysis presented above is for a very thin tube. However, frequently the diameter of the center of the wall (rather than inner or outer diameter) is used in the calculations. Consequently, the pressure rating for this pipe, using equation Eq. 10.5-4, will be

$$p = \frac{2 \times 8 \times 61.2}{1600 - 61.2} = 0.636\ MPa\ or\ 6.36\ bar$$

This result is fully in agreement with what has been reported (below) at the company's website. SDR stands for Standard Dimension Ratio (outer diameter/thickness).

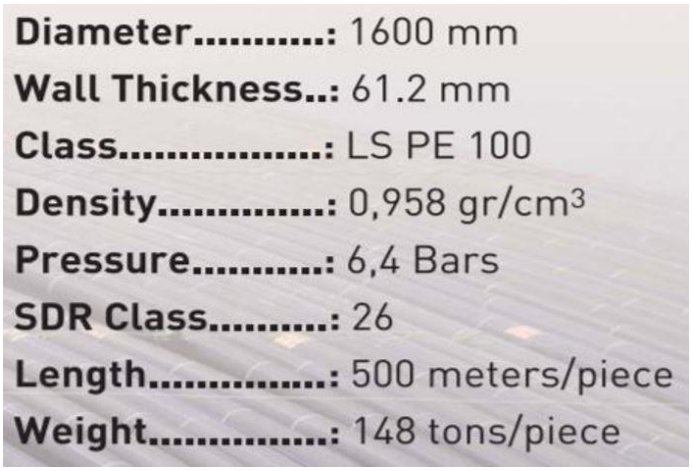

Bibliography

Carneiro O.S. and Nóbrega J.M., Main Issues in the Design of Extrusion Tools, in: *Design of Extrusion Forming Tools*, Carneiro O.S. and Nóbrega J.M. (eds), Smithers Rapra, UK (2012)

Haudin J.-M., Vincent M. and Vergnes B., Pipe Forming Tools, in: *Design of Extrusion Forming Tools*, Carneiro O.S. and Nóbrega J.M. (eds), Smithers Rapra, UK (2012)

Hendess P.M. and Bessemer R.S., Pipe and Tubing Extrusion, in: *The SPE Guide on Extrusion Technology and Troubleshooting*, Vlachopoulos J. and Wagner Jr. J.R. (eds), The Society of Plastics Engineers (2001)

Jin G.-B., Wang M.-J., Zhao D.-Y., Tian H.-Q. and Jin Y.-F., Design and Experiments of Extrusion Die for Polypropylene Five Lumen Micro Tube, J. Mater. Process. Technol., 214, 50 (2014)

Kainth, S. *Die design for Extrusion of Plastic Tubes and Pipes*, Hanser (2018)

Lupke M.A.A. and Lupke S.A., Extruder Head Mandrel Spider, Patent number: U.S. 6,056,528 (2000)

Hopmann C. and Michaeli W., *Extrusion Dies for Plastics and Rubber – Design and Engineering Computations*, 3rd Edition, Hanser (2016)

Tian H., Zhao D., Wang M., Jin G. and Jin Y., Study on Extrudate Swell of Polypropylene in Double-Lumen Micro Profile Extrusion, J. Mater. Process. Technol., 225, 357-368 (2015)

Vlachopoulos, J. and Lupke, M.A. "Innovations in Production of Corrugated Pipes", presented at Plastic Pipes XIX Conference Las Vegas, September 2018

J. Vlachopoulos and N.D. Polychronopoulos "*Understanding Rheology and Technology of Polymer Extrusion*", First Edition, Polydynamics Inc, Dundas, Ontario, Canada (2019)

Chapter 11

PROFILE EXTRUSION

11.1 Introduction

Profile extrusion is the continuous production of plastic or rubber products having generally complex cross-sections. The products may range from simple U-like shapes and corner moldings to refrigerator and vehicle gaskets and window lineals, with very complex cross-sections. Some typical extruded profiles are shown in Fig. 11.1-1.

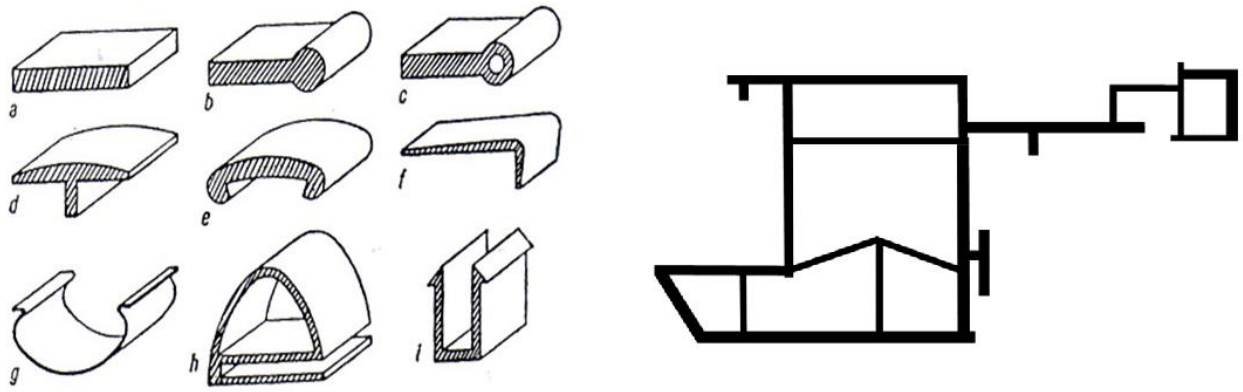

Figure 11.1-1. Schematic representation of some simple extruded profiles, from Schenkel (1966), on the left, and a UPVC profile cross-section like those used for windows, on the right.

In profile die design, the most crucial problem is **flow balancing**, that is to have uniform outflow velocity at the exit, so that a product of multiple local thicknesses is produced continuously. The window profile shown in Fig. 11.1-1, has thick and thick sections, which means that the die lips, would have thick and thin gaps. Since polymer melts have an overwhelming tendency to flow through areas of least resistance, the melt will flow with a higher velocity in the thick gaps. To obtain a quantitative understanding of this, consider the

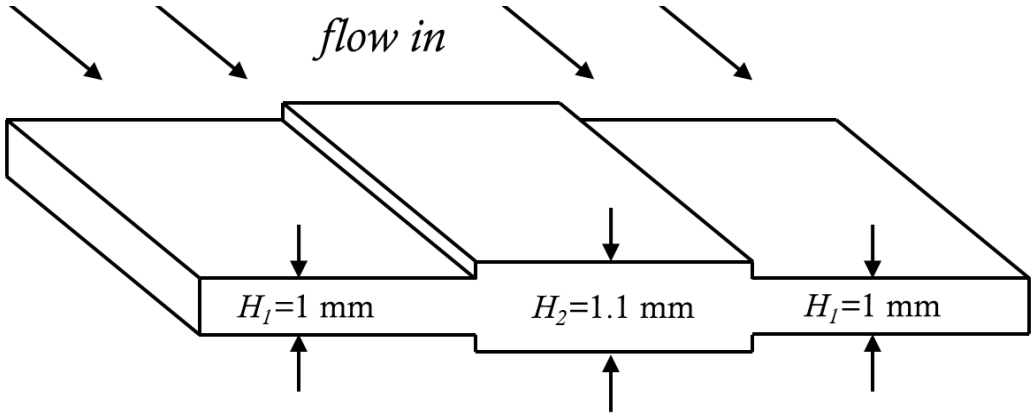

Figure 11.1-2. Schematic representation of a die section with slightly different gaps.

simple schematic in Fig. 11.1-2 showing a die which has a central section with a 10% larger gap. From the flow between two flat plates analysis, presented in Chapter 2, the average velocity will be for each section

$$V_{avg} = \frac{n}{2n+1}\left[\frac{1}{m}\left(\frac{\Delta p}{L}\right)\right]^{1/n}\left(\frac{H}{2}\right)^{\frac{1}{n}+1} \tag{11.1-1}$$

where H is the gap and Δp the pressure drop. The above equation may be written in the following simpler form

$$V_{avg} = A\left(\frac{H}{2}\right)^{\frac{1}{n}+1} \tag{11.1-2}$$

For the two different gaps in Fig. 11.1-2, assuming a Newtonian fluid (n=1), we may calculate the outflow velocity ratio

$$\frac{V_{avg,2}}{V_{avg,1}} \sim \frac{\left(\frac{H_2}{2}\right)^{\frac{1}{n}+1}}{\left(\frac{H_1}{2}\right)^{\frac{1}{n}+1}} = \frac{1.1^2}{1} = 1.21 \tag{11.1-3}$$

which means that the flow through the 10% larger gap H_2 is 21% faster. For a polymer with a power-law value n=0.33 the outflow velocity ratio is given by

$$\frac{V_{avg,1}}{V_{avg,2}} \sim \frac{\left(\frac{H_2}{2}\right)^{\frac{1}{n}+1}}{\left(\frac{H_1}{2}\right)^{\frac{1}{n}+1}} = \frac{1.1^4}{1} = 1.46 \tag{11.1-4}$$

which for this case means that flow through the 10% larger gap is 46% faster. Obviously, if the thickness ratio was larger the ratio of the outflow velocities could be huge. The challenge then is to design the local channel gaps from the end of the extruder to the die lips, so that the

thickness-averaged outflow velocity will be the same in all areas. The last part of the die (lips) is referred to as the die land, where the walls are parallel to the flow path. A long land length is necessary for imparting the desired local thickness and for eliminating or reducing the effects of previous shear history. With a long die land, the effects of any upstream changes in operating conditions will be minimized. The minimum land length to gap ratio is usually 8:1, with values up to 25:1 according to Cykana (2010), for high output rates. However, long land lengths can cause significant pressure drop, when highly viscous materials are extruded, and temperature rise due to viscous dissipation as discussed in Chapter 2.

11.2 Flow Balancing of a Simple Die

In the previous section we discussed differences in the gap thickness and shear-thinning behavior of the material that may lead to large flow imbalance. The smaller the value of the power-law exponent *n* (more shear-thinning) the larger the flow imbalance. A question that naturally arises is how one may design a die to eliminate or at least suppress flow imbalance. The simplest and perhaps the most intuitive technique is to shape the channels from the end of the extruder to the die lips, so as to bring the appropriate amount of polymer melt in each section. By adjusting the channel length behind the die lips the flow resistance in each desired section of the die may be controlled and more material can be brought in where it is needed and less material where it is not needed.

Let us explain the above described methodology with a simple profile die design example. Assume that we want to manufacture a product, the cross-section of which looks like a "keyhole" as shown in Fig. 11.2-1a. The product comprises of two sections, a circular and a rectangular, with prescribed dimensions for radius, gap and width. The lips of the profile die, from where the material is extruded, will have the shape of the product and for simplicity we are going to neglect extrudate swell. Hopmann and Michaeli (2016), recommend that each section of the lips must be designed with a specific length, as shown pictorially in Fig. 11.2-1b, such that in each section the same amount of polymer melt is delivered. In this way, a uniform exit velocity is achieved.

For the flow in the rectangular (slit) section we will use Eq. 11.1-1, which is

$$V_{s,avg} = \frac{n}{2n+1}\left[\frac{1}{m}\left(\frac{\Delta p}{L_s}\right)\right]^{1/n}\left(\frac{H}{2}\right)^{\frac{1}{n}+1} \tag{11.2-1}$$

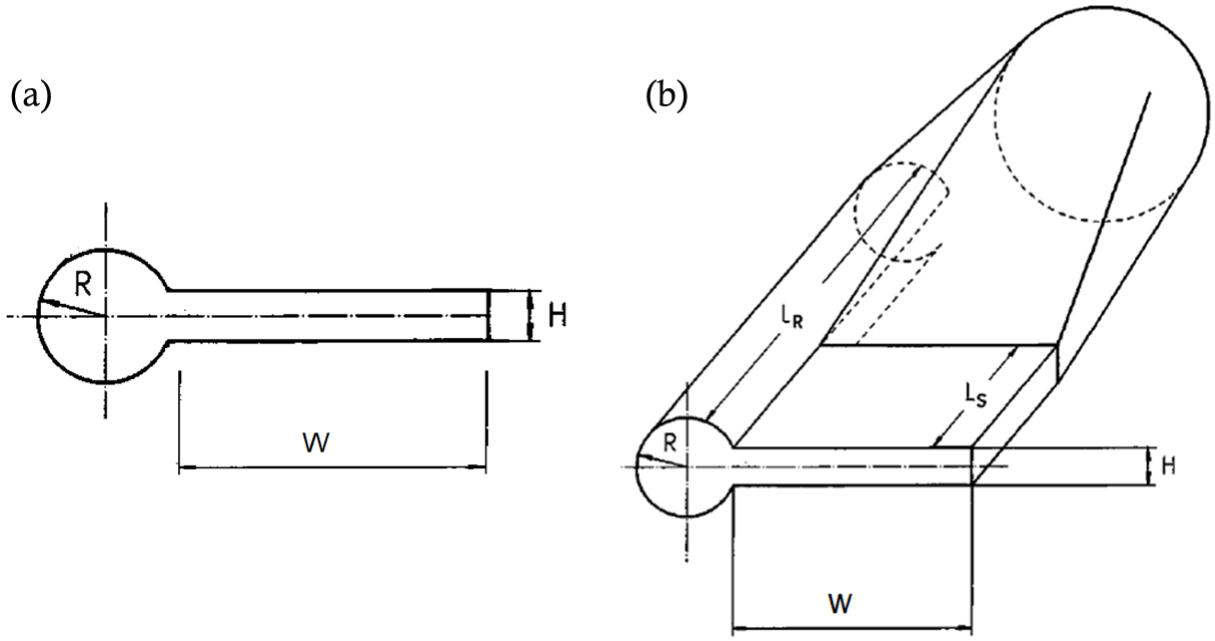

Figure 11.2-1. Schematic representation of an example profile die consisting of a cylindrical and a rectangular section. From Hopmann and Michaeli (2016).

In a similar fashion, for the flow through the circular section we will use the equation of the average velocity for flow in a tube from Chapter 2, that is

$$V_{R,avg} = \frac{n}{3n+1}\left[\left(\frac{1}{2m}\right)\left(\frac{\Delta p}{L_R}\right)\right]^{1/n} R^{\frac{1}{n}+3} \tag{11.2-2}$$

For the requirement of balanced flow, $V_{s,avg}=V_{R,avg}$, we equate Eq. 11.2-1 with Eq. 11.2-2 to arrive at

$$\frac{L_R}{L_s} = \left(\frac{4n+2}{3n+1}\right)^n \left(\frac{R}{H}\right)^{n+1} \tag{11.2-3}$$

Note that the above result shows that the ratio of the lengths for balancing the flow is not a function of the consistency index m. It should be also pointed out that the above analysis does not take into account (Hopmann and Michaeli, 2016) mutual influence of the two melt streams, possibility of cross-flow or the effects of the sidewall of the rectangular section (notice that Eq. 11.2-3 neglects the width W, because the analysis is based on the assumption of infinitely wide flat plates).

Let us now examine what will happen if we attach a die like that shown on the right side of Fig.11.2-1 at the end of an extruder. There will be some overflow of material from the one part to the other, the flow might not be very well balanced and we might not obtain exactly the desired keyhole shaped profile. However, we could use a separator (also called

web). In fact, separators are used in industry for flow balancing purposes. The flow will be balanced, but due to extrudate swell, we will have problems with the final shape. While this flow balancing method is not the sure solution to profile die design it is the first step in that direction, which might be followed by computer assisted design and eventually a trial-and-error on the factory floor. Profile die design is not easy. However, flow balancing either with the help of simple unidirectional flow equations or computer simulations (described in Section 11.4) will help reduce the number of trial-and-error procedures on the factory floor.

Example E11.2-1

Suppose we want to manufacture the profile of Fig. 11.2-1a. Assume that the polymer melt obeys a power law behavior with n=0.4. The rectangular section of the profile must have H=2 mm and W=10 mm. The round section must have a radius R=2.5 mm. What should the lengths behind the profile die lips be so that the flow is balanced?

Solution

For Eq. 11.2-3 to be applied for design calculations, one has to assume a reasonable length behind one of the two sections and then determine the other. We choose to give a length in the rectangular section. A typical value may be L_S=10H=10×2=20 mm. Using Eq. 11.2-3, we have

$$L_R = 20\left(\frac{4\cdot 0.4+2}{3\cdot 0.4+1}\right)^{0.4}\left(\frac{2.5}{2}\right)^{0.4+1} = 33.28 \text{ mm}$$

This is one of many possible solutions to the design problem. Better but more expensive designs would be of the stepped or streamlined variety discussed in Section11.3.

11.3 Types of Profile Dies

Profile die channels must be designed for the purpose of transforming a circular cross-section (just as the polymer melt exits the extruder) into a shape similar to the desired profile product. Depending upon the application, the cost and the ease or difficulty of machining, three types of profile extrusion dies may be distinguished.

(a) *Plate dies (also called "flat back" dies)*

A schematic representation of such a die is shown in Fig. 11.3-1. The polymer melt flows through a channel of initially cylindrical cross-section that is abruptly changed into the desired

profile shape. These dies have low manufacturing cost due to the simplicity in machining. They can be easily cleaned and mounted-dismounted from the production line. A drawback

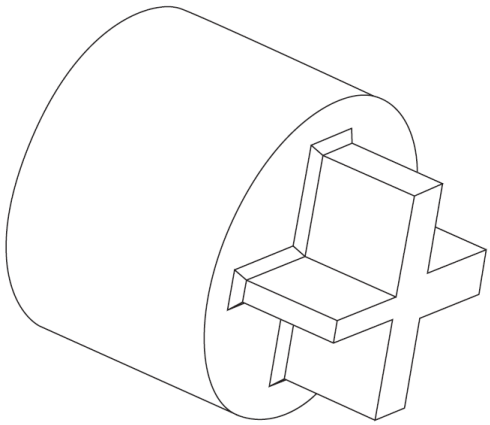

Figure 11.3-1. Schematic representation of a plate die. From Nóbrega and Carneiro (2012).

is that at the region of abrupt cross-section change (flat back), some material may accumulate due to the presence of vortices. As explained in Chapter 3, in such vortices, the material will recirculate and its residence time, will be very large, or theoretically "infinite" in completely stagnant regions (dead spots). Consequently, degradation and burning will occur, which is a very common problem especially with thermally sensitive materials. Plate dies are used for polyolefins, plasticized PVC and rubber. They are mostly used for the production of small profiles (Hopmann and Michaeli, 2016). They are of low cost, easy to develop and easy to modify if needed (Cykana, 2001). Used for short production runs and low outputs.

(b) *Stepped dies*

In stepped dies the circular cross-section channel at the inlet of the die is transformed in a gradual and stepwise manner as shown in Fig. 11.3-2. This is accomplished by connecting several die plates in series. The end of each die plate is connected in a beveled manner with the inlet of the consecutive die plate. According to Hopmann and Michaeli (2016), these transitions are critical for rigid PVC processing. Stepped dies are used only for relatively simple profiles.

(c) *Streamlined dies*

In such dies the initial circular cross-section is smoothly transformed to the desired final shape as shown schematically in Fig. 11.3-3. These dies are required for cases where a high dimensional accuracy in the profile is needed. However, the machining cost is high, as compared to plate and stepped dies (Nóbrega and Carneiro, 2012). According to Cykana

(2010) on a plate die (flat-back) "*the running time can be from one to eight hours with some polymers, a fully streamlined die can run for weeks without stopping to be cleaned out*".

There are four distinctive zones comprising streamlined dies, which are shown schematically in Fig. 11.3-4 (Nóbrega and Carneiro, 2012, Hopmann and Michaeli, 2016)

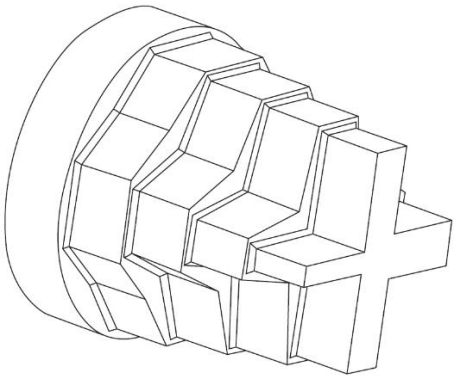

Figure 11.3-2. Schematic representation of a stepped die. From Nóbrega and Carneiro (2012).

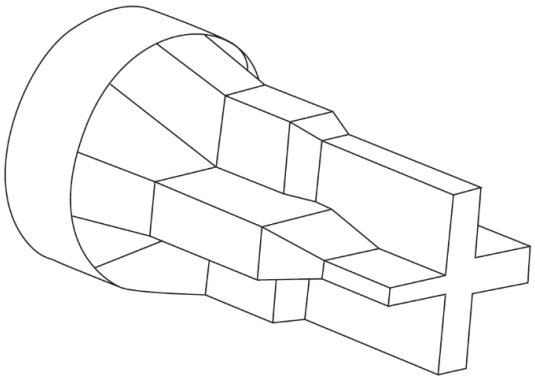

Figure 11.3-3. Schematic representation of a streamlined die. From Nóbrega and Carneiro (2012).

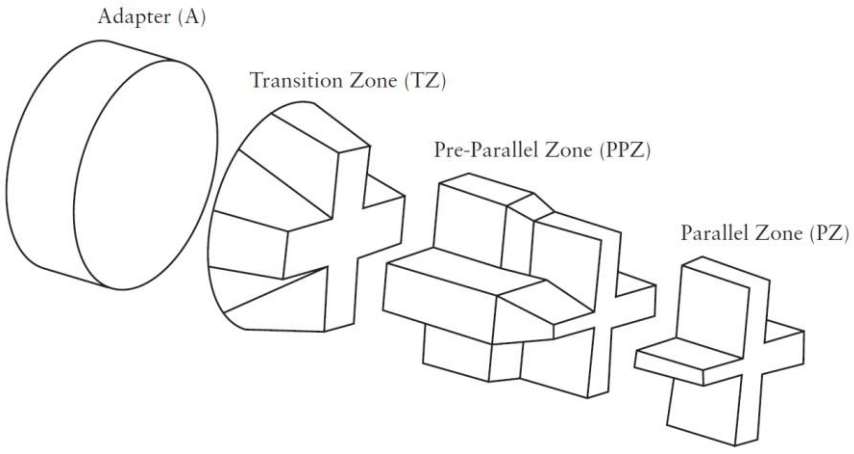

Figure 11.3-4. Schematic representation of the distinctive zones in streamlined dies. From Nóbrega and Carneiro (2012).

- Adapter: A zone of circular cross-section equal in diameter to the extruder barrel, positioned after the breaker plate and the filter.
- Transition zone: This zone serves as a transition section between the adapter and the pre-parallel zone.
- Pre-parallel zone: The pre-parallel zone exhibits downstream a convergent shape where the flow of the molten polymer becomes very restrictive.
- Parallel zone: This is the most important section of a streamlined profile die. It consists of channels with constant cross-section. The presence of this zone allows for a polymer melt to relax the upstream developed stresses. Due to the relatively narrower gaps, as compared to the previous sections, it contributes to a large extent to the total pressure drop. A very long parallel zone may diminish problems related to upstream flow variations and reduce extrudate swell, but it may generate unnecessary large pressures.

11.4 Computer Assisted Profile Die Design

The design guidelines and mathematical formulation presented in Section 11.2 can be used for relatively simple profile dies. That methodology can also be applied for the parallel zone of the streamlined profile die of Fig. 11.3-4. For a full design of a profile die, meaning from the end of the extruder to the very end of the lips, the previously mentioned design principles are rather difficult to be applied.

Trial-and-error procedures on the factory floor involve several hours of machining, running the production line, correcting the die channels and running again and again. As many as ten trials might be necessary for simple profile shapes, and dozens for complicated designs. The manufacturing cost can increase significantly, before a final acceptable design is reached. An alternative is computer assisted die design, which applies to all types of extrusion dies, but it is even more important for profile dies. The main advantage is that the cost is reduced, in the sense that the machining tryouts are carried out on a computer screen. It is tempting to try to use a fully 3D commercially available flow simulation software, especially because of recent availability of significant computer power. Introduction of viscoelasticity though a suitable constitutive equation, is unlikely to produce any useful results for 3D non-isothermal flows. However, the most important information can be obtained from shear thinning, non-isothermal flow simulations, which are demanding, but feasible, even for the

most complicated flow channel geometries. The challenge is to perform numerical shape optimization (Elgeti *et al.*, 2012, Rajkumar *et al.*, 2018) using a 3D non-Newtonian, non-isothermal simulation software. A simplified approach is described below.

Practicing profile die designers (Lee and Stephenson, 1992) know that, as Levy (1981a, 1981b) states, "*the cases where the die orifice geometry can permit flows across the machine direction make die design difficult*". A strategy for the design of profile dies has been suggested, termed as the "Avoid Cross Flow Strategy" (Koziey *et al.*, 1996). In this approach the material flows through a series of cross-sections perpendicular to the machine direction. Each cross-section is subsequently divided into separate segments. The geometry of each cross-section is then adjusted so that the flow rate through each segment is in the same proportion as the area percentage of that segment of the cross-section, relative to the total cross-section area of the final profile. The flow solution on each cross-section is simplified assuming fully developed flow in the machine direction (z) and the equation of conservation of momentum is reduced to

$$\frac{\partial}{\partial x}\left(\eta \frac{\partial V_z}{\partial x}\right) + \frac{\partial}{\partial y}\left(\eta \frac{\partial V_z}{\partial y}\right) = \frac{\partial p}{\partial z} \tag{11.4-1}$$

in the flow z-direction which is perpendicular to the x-y plane of the cross section. In Eq. 11.4-1, η is the viscosity, p the pressure and V_z the velocity in the z-direction. Since there is only one equation involved, the results are obtained rapidly. *Ettinger et al.* (2013) also used equation 11.4-1 in developing their numerical design procedure. The method was applied by Koziey *et al.* (1996) for the L-shaped die shown in Fig. 11.4-1. The final 3D die geometry is shown in Fig. 11.4-2. Several cross-sections at different locations along the length of the die are taken which are also shown individually in Fig. 11.4-3.

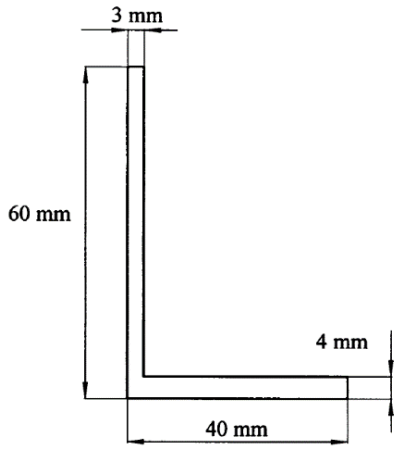

Figure 11.4-1. Schematic representation of a simple L-profile. From Koziey *et al.* (1996).

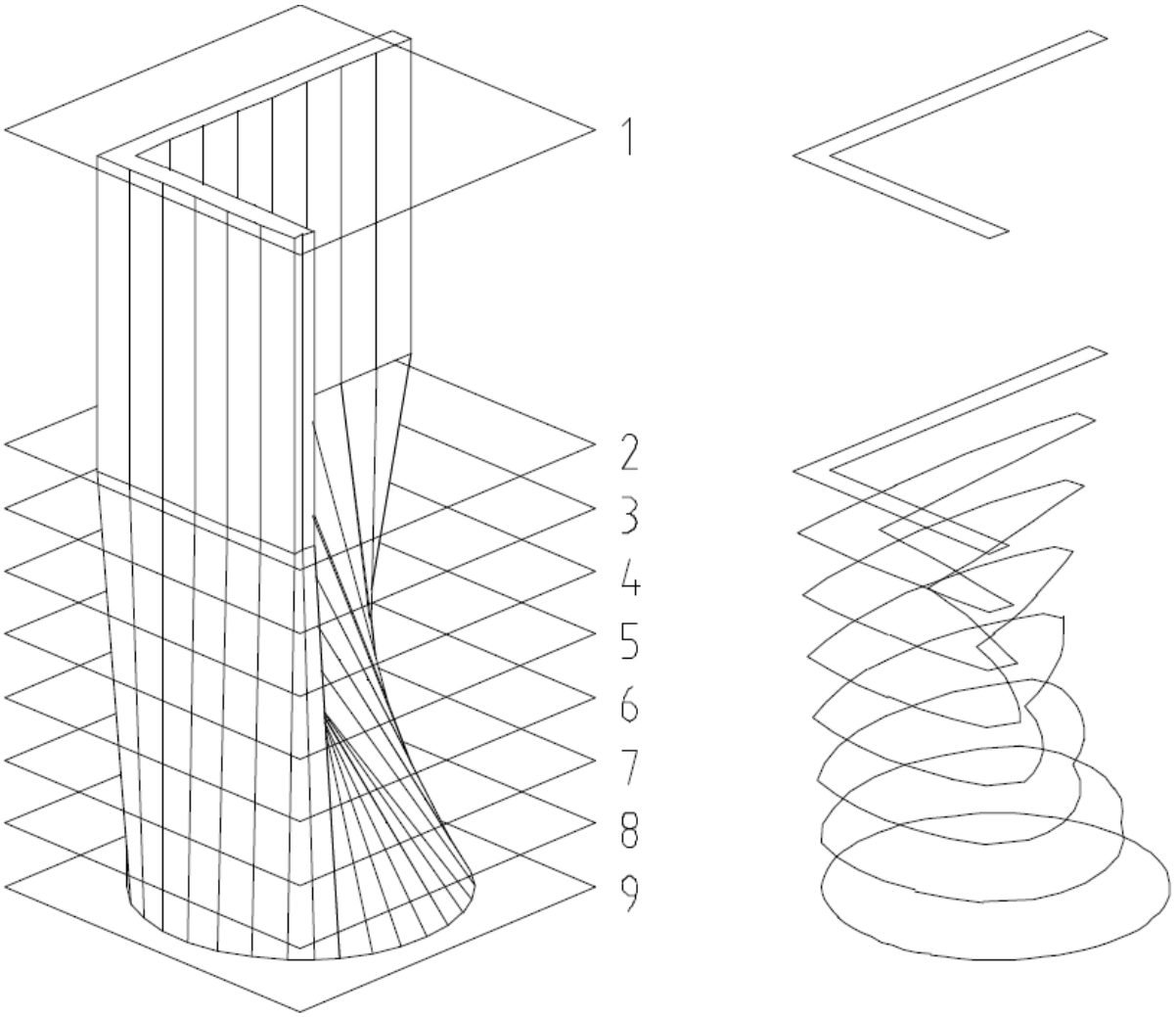

Figure 11.4-2. 3D representation of L-profile die flow channel. From Koziey *et al.* (1996).
Note: This simple profile die could have also been designed with the method of Section 11.2. The corresponding lengths between cross-sections 2 and 1 above, could have been adjusted, just as in the "keyhole" profile die of Fig. 11.2-1. That kind of design would be of less precision than the above streamlined profile die.

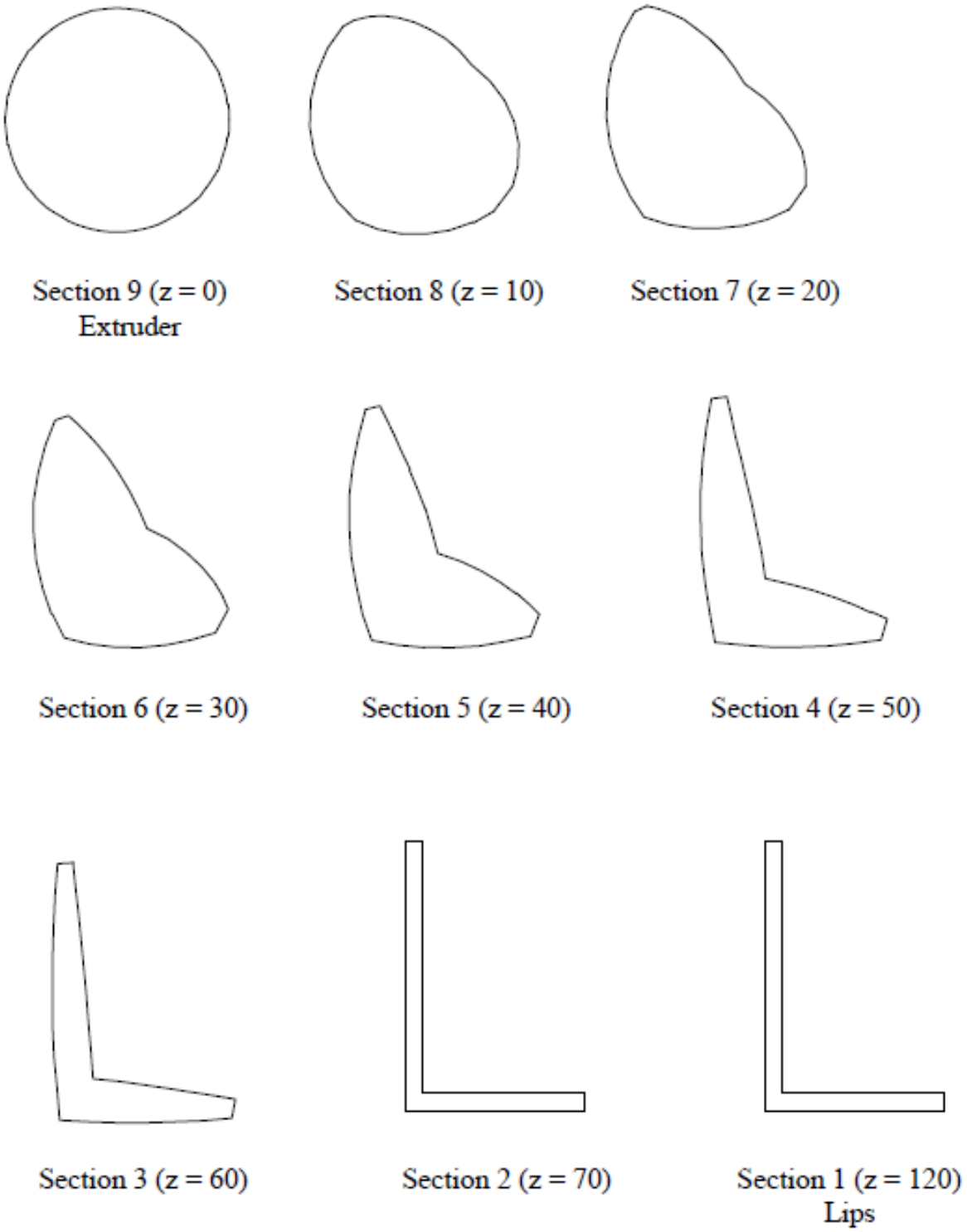

Figure 11.4-3. Sequence of channel cross sections for the L-profile die. From Koziey *et al.* (1996).

It should be pointed out that due to the effect of extrudate swell, the final dimensions of the profile may differ substantially from the dimensions of the die exit, especially for polymer melts exhibiting a high elasticity level. Taking this phenomenon into account is a challenging task and the approach may vary depending on the complexity of the cross-section, from simple cross-type profiles (Gifford, 2003) to complex two-lumen tubular products for cardiovascular angioplasty (Tian *et al.*, 2015). Inverse design methods (Legat and Marchal, 1993, Debbaut and Marchal, 2008), that is finding the die shape which produces an extrudate of prescribed dimensions, have also been developed for profile dies, but without much impact on die design technology.

11.5 Beyond the Profile Die Exit

As the polymer melt exits from the die it swells as a result of viscoelasticity. We have seen in Section 3.8 that even Newtonian fluids swell as they emerge from flow channels (13% for round and 19% for planar). Polyolefins with broad molecular weight distribution swell a lot. PVC does not swell very much. The die designer must take into consideration the anticipated extrudate swell, a task which is not easy. After the exit, the extrudate is drawn down to the desired dimensions of the final product. The percentage of drawdown usually ranges from 3% for certain PVC profiles to perhaps 20% or even 30% for some polyolefin products. As Cykana (2010) put it "*without any drawdown the extrudate would drape and sag*", while with proper amount of drawdown the profile remains aligned and taut.

Due to the difficulties in obtaining the required profile dimensions, calibration (that is sizing) and cooling systems are used for establishing the final dimensions of the product. Calibration/cooling systems for profiles are similar to those for pipes, which are discussed in Chapter 10. More information can be found in Nóbrega and Carneiro (2012).

Bibliography

Cycana D., Tooling know-how; Five Tips on Profile Die Design, www.ptonline.com (2010)

Cycana D., Profile Extrusion, in: *The SPE Guide on Extrusion Technology and Troubleshooting*, Vlachopoulos J. and Wagner Jr. J.R. (eds), The Society of Plastics Engineers (2001)

Debbaut B. and Marchal T., Numerical Simulation of Extrusion Process and Die Design for Industrial Profile, Using Multimode Pom-Pom Model, Plast. Rubber Compos., 37(2-4), 142-150 (2008)

Elgeti S., Probst M., Windeck C., Behr M., Michaeli W. and Hopmann Ch., Numerical Shape Optimization as an Approach to Extrusion Die Design, Finite Elem. Anal. Des., 61, 35-43 (2012)

Ettinger H.J., Pittman J.F.T. and Sienz J., Optimization-Driven Design of Dies for Profile Extrusion: Parametrization, Strategy and Performance, Polym. Eng. Sci., 53 (1), 189-203 (2013)

Gifford W.A., Compensating for Die Swell in the Design of Profile Dies, Polym. Eng. Sci., 43 (10), 1657-1665 (2003)

Hopmann C. and Michaeli W., *Extrusion Dies for Plastics and Rubber – Design and Engineering Computations*, 4rd Edition, Hanser (2016)

Koziey B.L., Vlachopoulos J., Vlcek J. and Svabik J., Profile Die Design by Pressure Balancing and Cross-Flow Minimization, ANTEC Conf. Proceedings, 247-252 (1996)

Lee C. and Stevenson J., Face Relief Strategy for design of profile dies, Intern. Polym. Proc., 7(2), 186-189 (1992)

Legat V. and Marchal J.M., Die Design: An Implicit Formulation for the Inverse Problem, Int. J. Numer. Meth. Fluids, 16, 29-42 (1993)

Levy S., The Technology of Plastics Profile Tooling, Advances in Plastics Technology, 8-53, January (1981)

Levy S., Extrusion Die Design for Thermoplastic Materials Comparison of Extrusion Ease with PVC Materials, Advances in Plastics Technology, 24-31, October (1981)

Nóbrega J.M. and Carneiro O.S., Profile Forming Tools, in: *Design of Extrusion Forming Tools*, Carneiro O.S. and Nóbrega J.M. (eds), Smithers Rapra, UK (2012)

Rajkumar A., Ferrás L.L., Fernandes C., Carneiro O.S., Sacramento A. and Nóbrega J.M., An Open-Source Framework for the Computer-Aided Design of Complex Profile Extrusion Dies, Intern. Polymer Processing, 33 (2), 276-285 (2018)

Schenkel G., *Kunststoff-Extrudertechnik*, Hanser Verlag, Munich (1963), available also in English, *Plastics Extrusion Technology and Theory*, Iliffe Books Ltd., London, (1966)

Tian H., Zhao D., Wang M., Jin G. and Jin Y., Study on Extrudate Swell of Polypropylene in Double-Lumen Micro Profile Extrusion, J. Mater. Process. Technol., 225, 357-368 (2015)

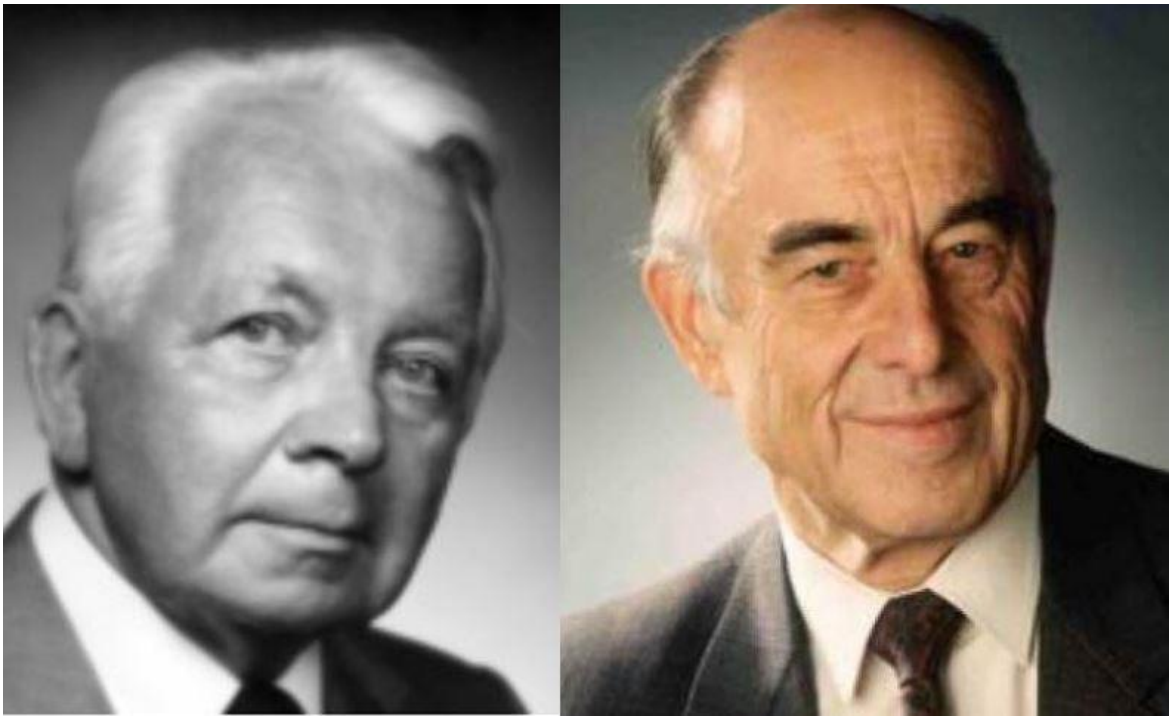

GERHARD SCHENKEL (left) (1923-2001) former Director of IKT, U. Stuttgart

and

GEORG MENGES (right) (1923-2021) former Director of IKV, RWTH Aachen

noted for innovations and publications in polymer processing

J. Vlachopoulos and N.D. Polychronopoulos "*Understanding Rheology and Technology of Polymer Extrusion*", First Edition, Polydynamics Inc, Dundas, Ontario, Canada (2019)

Chapter 12
TWIN-SCREW EXTRUDERS

10.1 Introduction

Two-screw machines were originally developed, not for plastics, but for conveying of ceramic masses to form bricks and for kneading of bread dough (Andersen *et al.*, 2009) in the 1800's. According to Martelli (1983) the first twin screw extruders, for polymers, were developed in the late 1930s by Roberto Colombo of LMP (Lavorazione Materie Plastiche, Torino, Italy) and Carlo Pasquetti, also of Torino. Significant improvements to the technology were made by Erdmenger (Bayer, Germany) in the 1940s, followed by the Werner and Pfleiderer corporation in the 1950's also in Germany. The historical development of the counter-rotating twin-screw extruder is discussed by Schneider (2005).

The screws can rotate in the same direction (co-rotating) or opposite direction (counter-rotating). They can be intermeshing (if the flights of one screw penetrate the channel of the other) or non-intermeshing if the screw flights do not mesh or engage with each other, and classified accordingly in Fig.12.1-1. They can be fully intermeshing or partially intermeshing as shown in Fig. 12.1-2. The screws can be parallel or conical.

The material transport in twin-screw extruders (TSEs) is different from single-screw extruders (SSEs). In SSEs it is drag flow, whereas in TSEs it can be drag flow for non-intermeshing, but positive displacement in intermeshing counter-rotating TSEs. Actually, as Martelli (1983) put it "*Construction differences such as screw placement, shape of the flights, and direction of rotation make TSEs as different from each other as they are, as a group, different from single-screw extruders*". TSEs are usually modular, having removable screw and barrel sections, while SSEs are nearly always one piece. The most common twin-screw extruders are co-rotating

and fully intermeshing TSEs and perhaps the second most common is counter-rotating fully intermeshing. These two types will be discussed in the subsequent sections of this chapter.

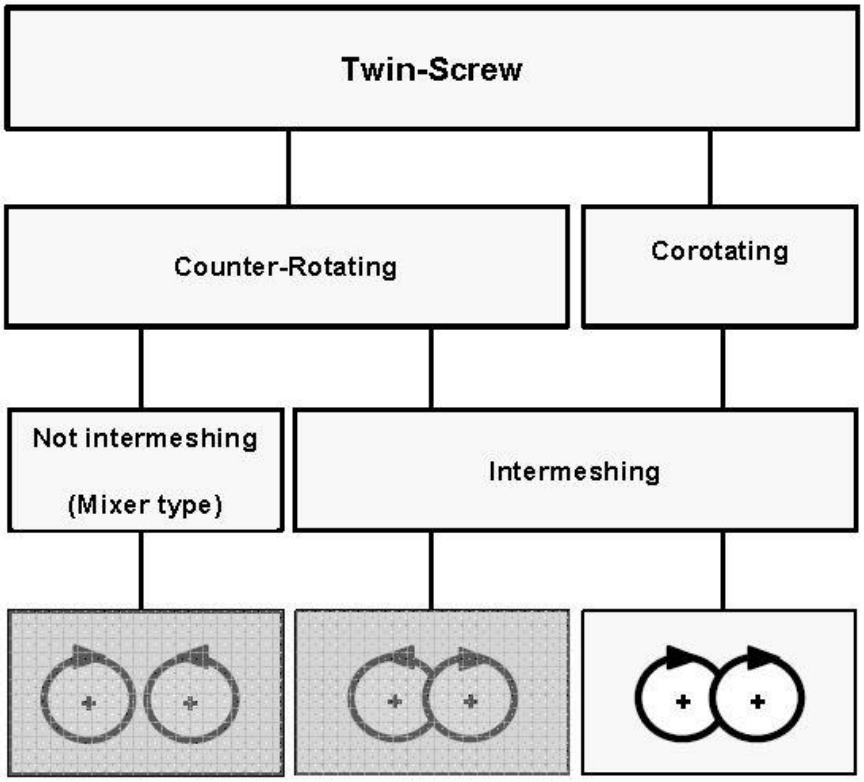

Figure 12.1-1. Twin-screw extruder classification. From Andersen *et al.* (2009).

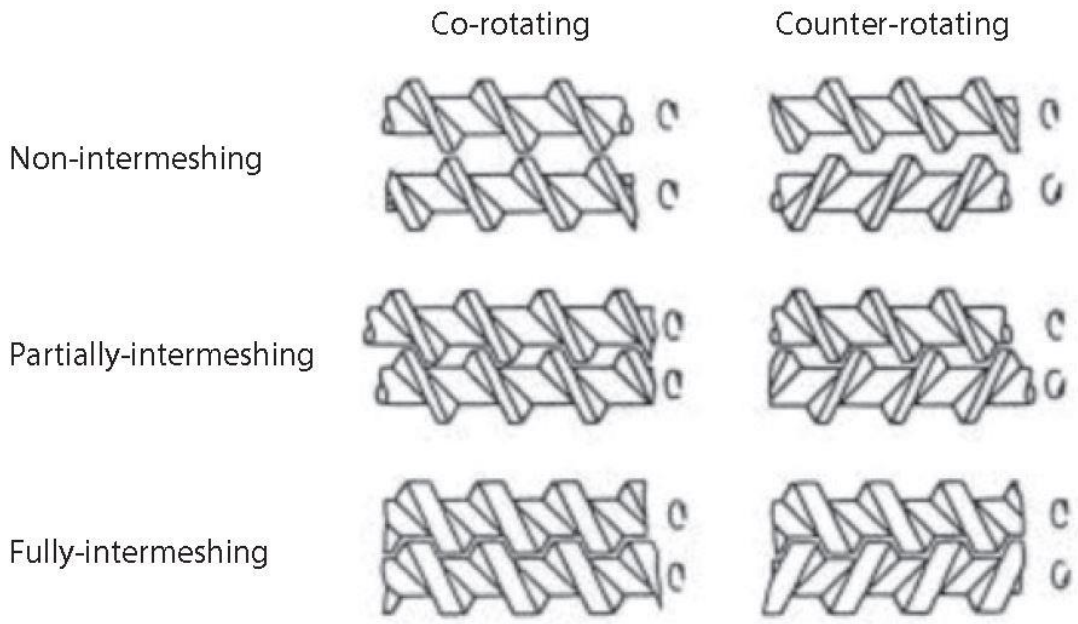

Figure 12.1-2. Different types of twin-screw extruders. From Kimura *et al.* (2018).

12.2 Co-rotating Fully Intermeshing Twin Screw Extruders

Co-rotating TSEs with very closely intermeshing (self-wiping) screws are used extensively for compounding of masterbatches, pelletization, devolatilization, and reactive extrusion. Masterbaches are concentrated blends of pigments, additives, fillers etc, in a base polymer. A masterbatch is added in small amounts to large volume material (the same as or compatible with the base polymer) to achieve desired properties. Frequently, the output of polymer reactors includes high level of solvent, which must be removed (devolatilization) during twin screw extrusion for the production of pellets. Reactive extrusion frequently involves the chemical modification of a resin by addition of other molecules to its backbone chain (grafting). Co-TSEs usually operate at high speeds up to 1400 rpm (sometimes even higher) and production rates of up to 100,000 kg/hr, while single screw extruders seldom exceed 5,000 kg/hr. Twin-screw extruders are usually starve-fed from an external feeder with the degree of fill frequently less than 40%, while single extruders are usually flood fed (degree of fill 100%).

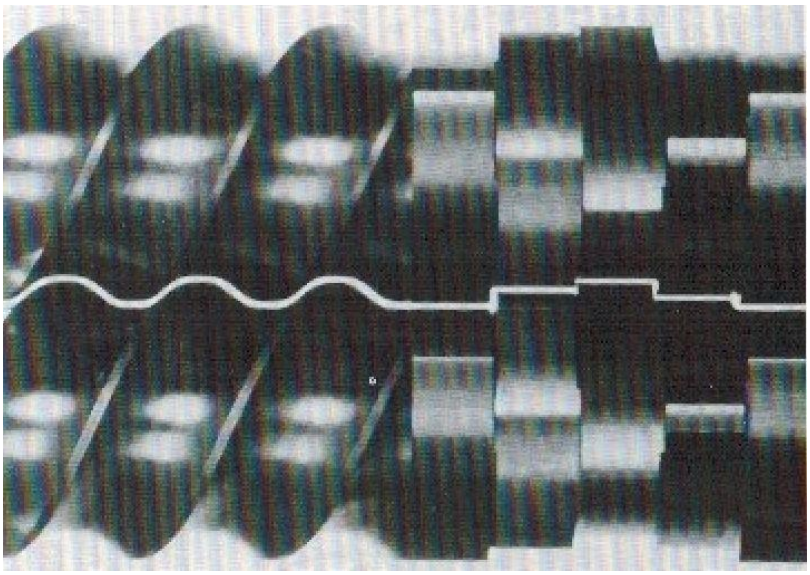

Figure 12.2-1. Werner & Pfleiderer ZSK self-wiping screws. From Todd (1998).

Screws are typically segmented, involving helical flight sections, usually having pitch (distance between the flights) from 0.5*D* to 2*D* and mixing elements. Fig. 12.2-1 shows screws having kneading disks for mixing and Fig. 12.2-2 shows screws having gear elements for mixing. The screw sections and mixing elements are assembled on shafts. There is virtually an unlimited number of screw configurations which can be assembled.

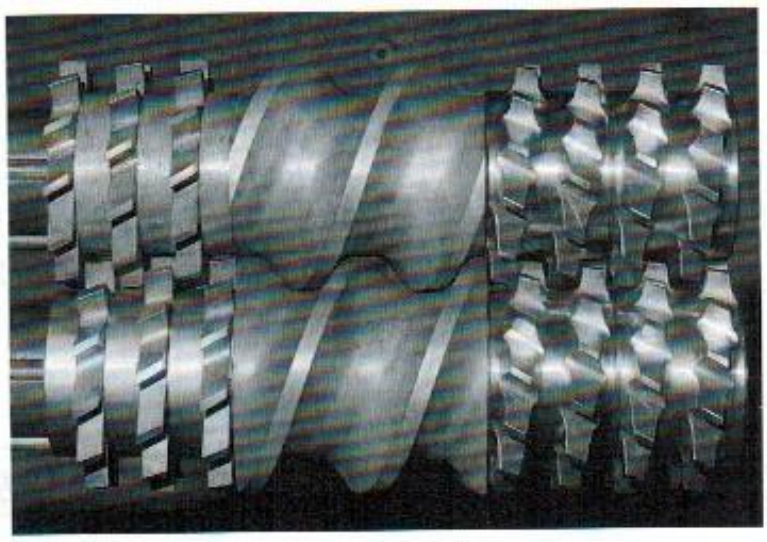

Figure 12.2-2. Mixing elements on a Berstorff ZE90A. Parallel gear rings on the left and gears cut on a helix. From Todd (1998).

The screw sections convey the material forward and mixing elements facilitate the compounding of the resin with the additives, fillers, reinforcements and blending with other resins, as it may be required. Increasing the screw section pitch results in faster conveying rate, but less pressure build-up. The kneading disks are either three-lobal or two-lobal as shown in Fig. 12.2-3. It can be seen that the two-lobal elements have more free volume for material and they have become more common in todays twin-screw extrusion lines. Fig. 12.2-4 shows screw and two-lobal kneading disk profiles. The number of possible configurations is practically infinite, as screw pitch, kneading disk thicknesses and offsets can be chosen. The no-limits flexibility presents also a challenge in choosing the most suitable configuration for the desired tasks associated with local unit operations of conveying, melting, mixing, devolatilization and pumping. Considerable experience is required for optimizing the design and performance.

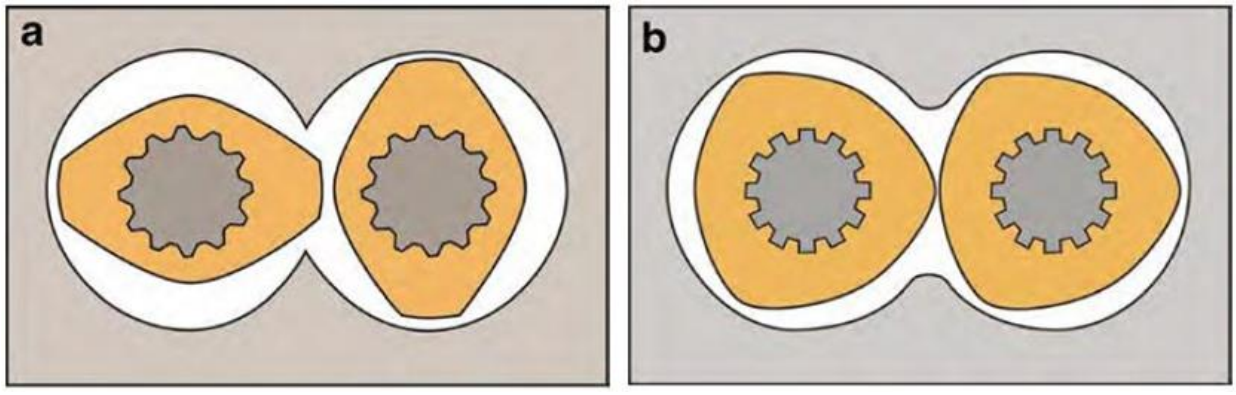

Figure 12.2-3. (a) Two-lobal and (b) three-lobal kneading disks. From Martin (2016).

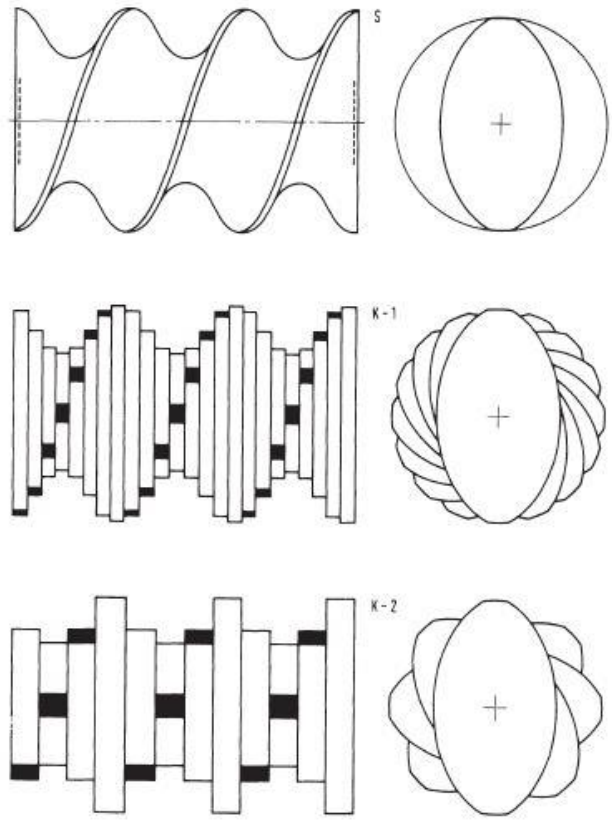

Figure 12.2-4. A double-flighted screw segment and two kneading blocks composed of disks of different thicknesses, but with the same apparent helix angle as the screws. K-1 kneading disks are 0.0062*D* thick and angularly offset 22.5°. K-2 are 0.125*D* thick and angularly offset 45°. From Todd (1991).

12.3 Machine Design and Assembly of Self-Wiping Co-Rotating TSEs

The construction is modular comprising of barrel sections, shaft and screw components. Usually the barrel sections are 4*D* long. The extruder *L*/*D* for standard compounding tasks is between 24 and 48, with up to 60 commercially available. Thus a *L*/*D* =36 machine will have 9 barrel sections of 4 *L*/*D* each. The barrel sections are of rectangular cross-section, as shown in Fig.12.3-1, for providing uniform heat flow around the figure-8 bore.

Screws have evolved from having three-flighted conveying screw sections and three-lobal kneading disks to two-flighted sections and two-lobal disks. A screw conveying section is shown in Fig. 12.3-2.

A very important parameter is the outer diameter to inner diameter ratio (OD/ID). The larger the ratio, the more free-volume is available, as shown in Fig. 12.3-2. Of course, as the ratio increases the available shaft diameter for torque transmission becomes smaller. Cur-

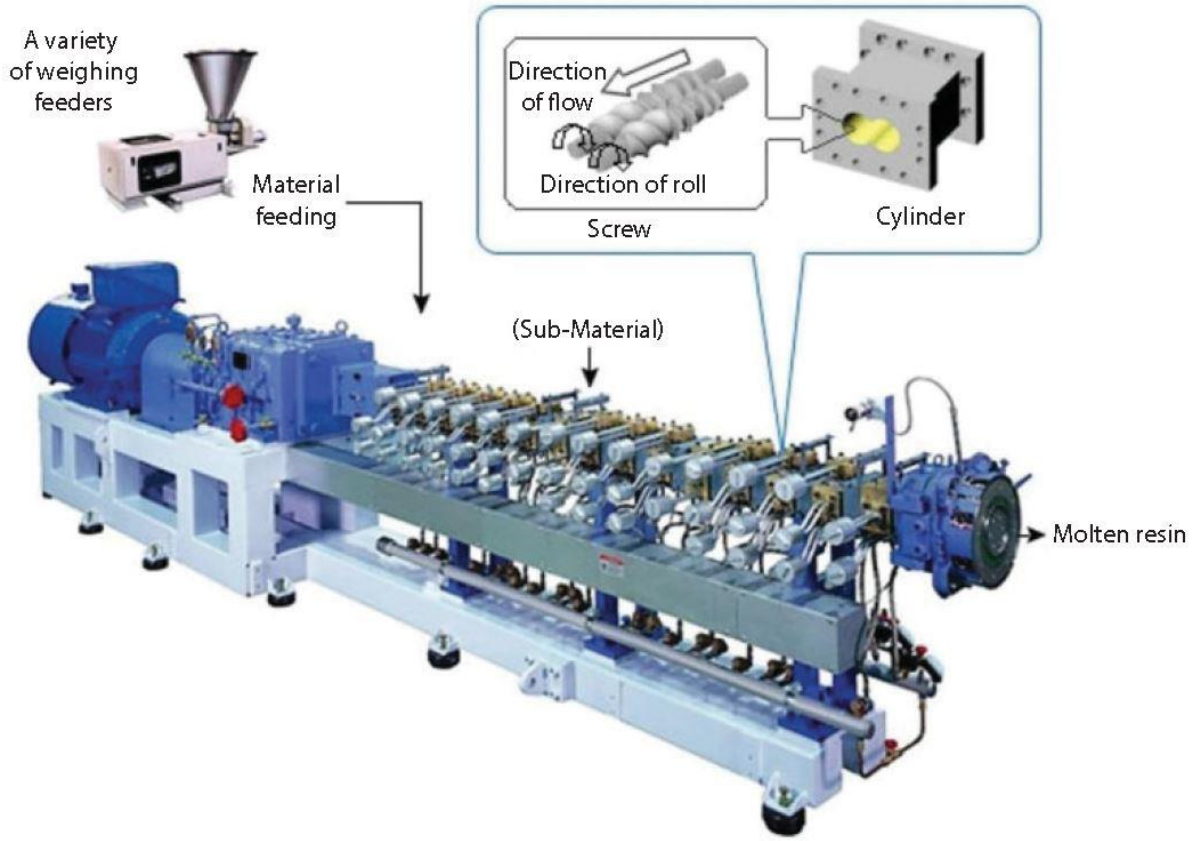

Figure 12.3-1. JSW corporation co-rotating intermeshing TSE. From Kimura *et al.* (2018).

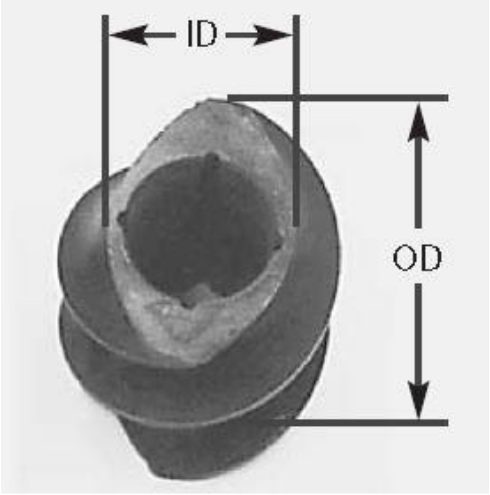

Figure 12.3-2. Conveying screw section showing inner (ID) and outer diameter (OD). From Wagner *et al.* (2014).

rently, many industrial extruders have OD/ID ratio up to 1.80. For high torque transmission, shaft technologies have evolved from a single keyway to hexagonal, octagonal and lately to spline shafts, as shown in Fig.12.3-4.

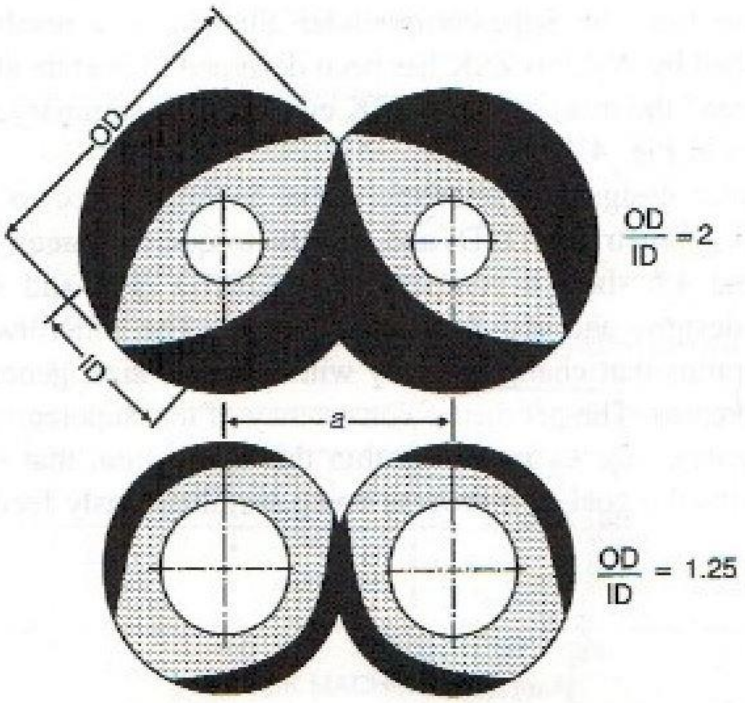

Figure 12.3-3. Extremes of OD/ID ratios for two-lobal TSEs. From Todd (1998).

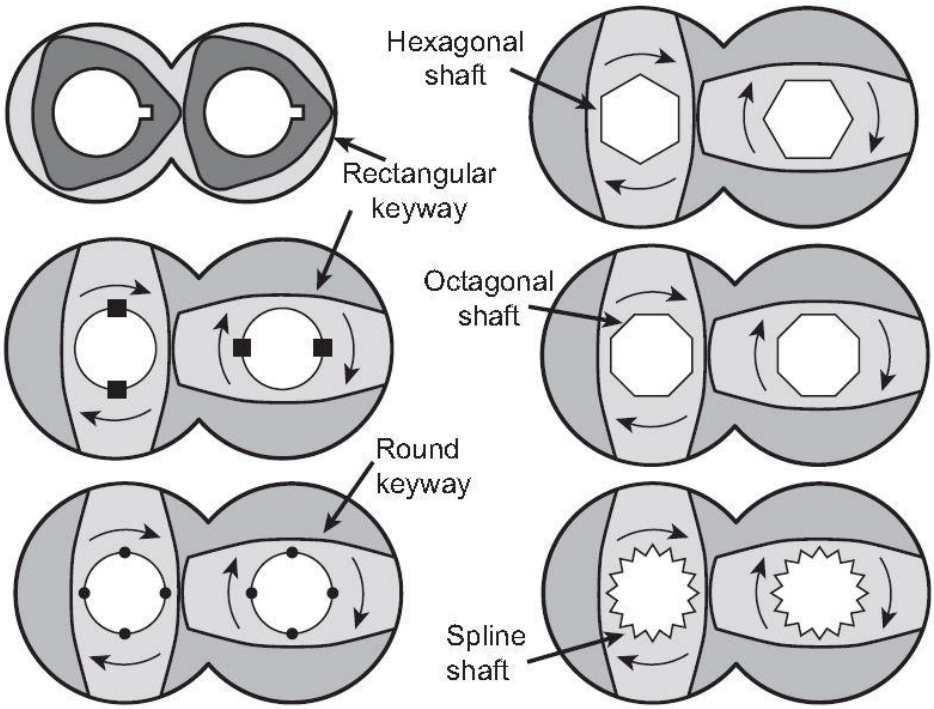

Figure 12.3-4. Shaft technology evolution from keyways to splines. From Wagner et al (2014).

Terminology is important for understanding the various types of commercially available machines. Conveying screw sections are shown in Fig.12.3-5 from Wagner *et al.* (2014). This sections are referred to as 45/45, 60/60 and 30/30, with the first number being screw pitch (length required for one complete revolution of a flight) and the second number is the section length as shown.

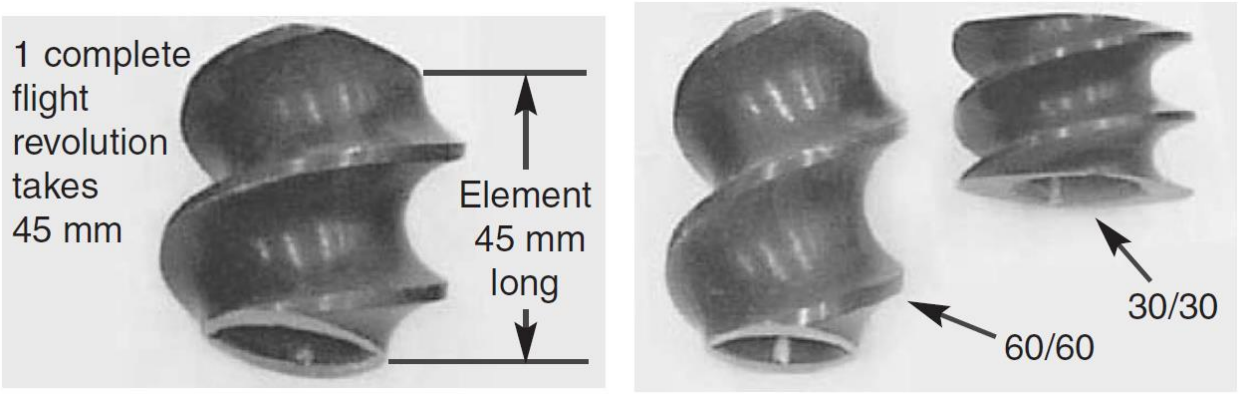

Figure 12.3-5. Theysohn corporation conveying screw sections. From Wagner *et al.* (2014).

Conveying sections can be "right-handed", if they convey the material forward, or "left-handed" if the conveying is rearward. Fig 12.3-6 shows a sequence of a right-handed followed by a left-handed and then another right-handed section. In the right-handed section there is no pressure build up because the material, which is only partially filling the channel, is conveyed forward. In the left-handed section the obstruction results in building up pressure.

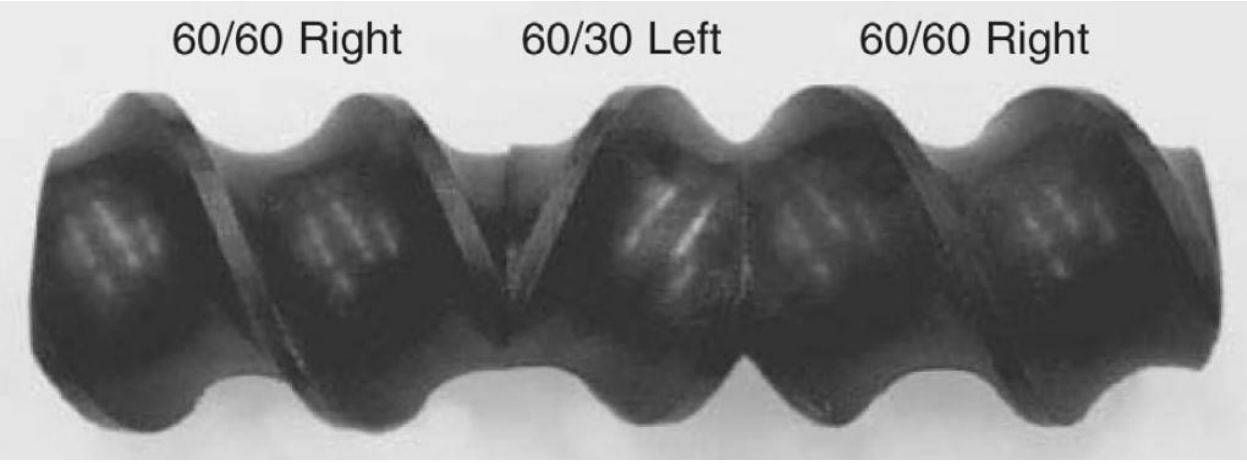

Figure 12.3-6. Sequence of right- and left-handed Theysohn corporation screw sections. From Wagner *et al.* (2014).

Between the conveying screw sections there are kneading blocks as shown in Fig.12.3-7, consisting of disks arranged for forward or rearward conveying or neutral (non-conveying).

The terminology involves three numbers: the first is the rotation angle, the second is the number of disks and the third length in mm. In Fig.12.3-8, the sketch on the top 90/10/40 indicates a kneading block of 40mm in length, having 10 disks rotated at 90°.

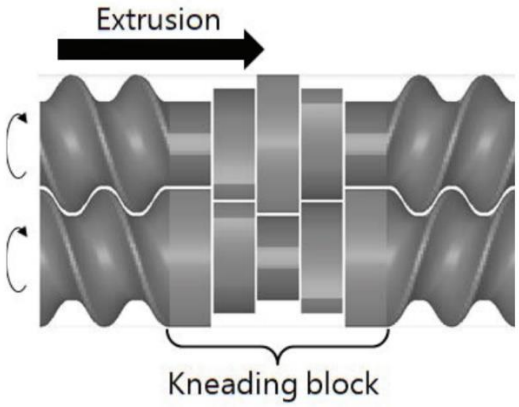

Figure12.3-7. Conveying screw sections and a kneading block. From Nakayama *et al.* (2018).

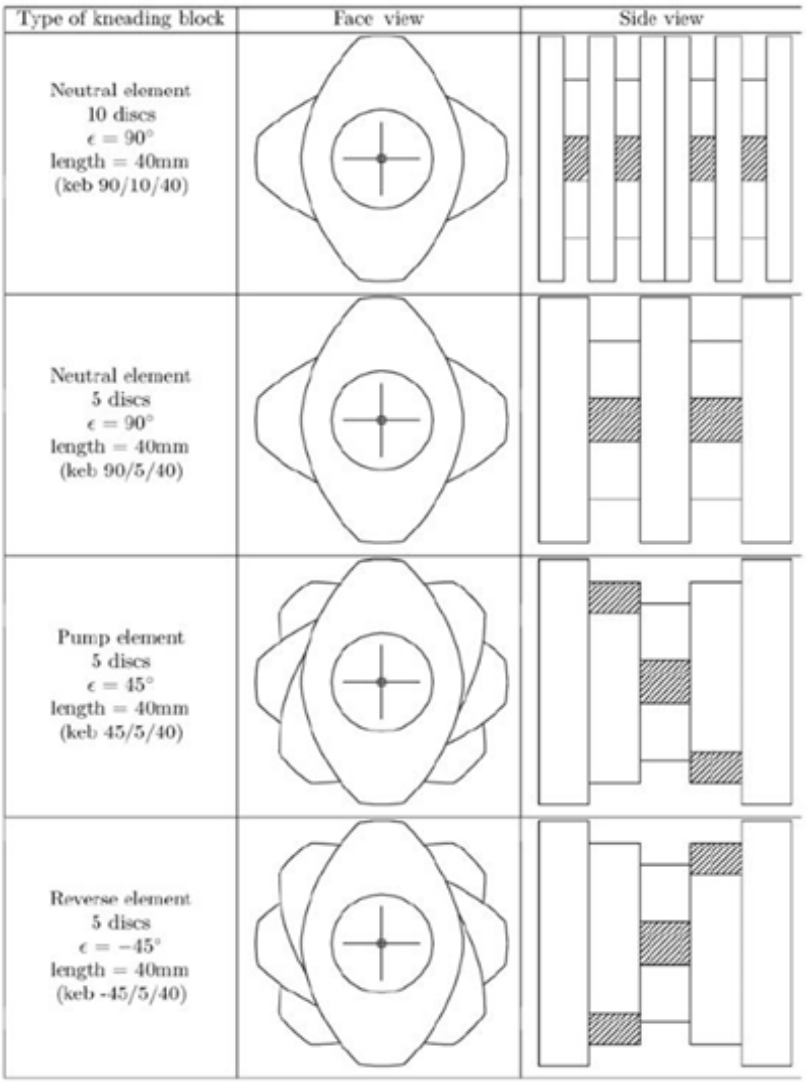

Figure 12.3-8. Kneading block arrangements. From Alsteens et al (2004).

Another important parameter is the specific torque, which relates the available power to the volume of the extruder expressed as the torque divided by the centerline distance cubed T_o/a^3 (Nm/cm^3). Specific torque values have progressed from 13.7 Nm/cm^3 to 18 Nm/cm^3, according to Andersen (2013). Speeds up to 1800 rpm are possible with commercially available machines. High speeds are possible because the deeper channels, having lower shear rates, do not raise the material temperature to undesirable high levels. The (nominal) shear rate is the ratio of the circumferential velocity to the maximum channel depth. As it has been

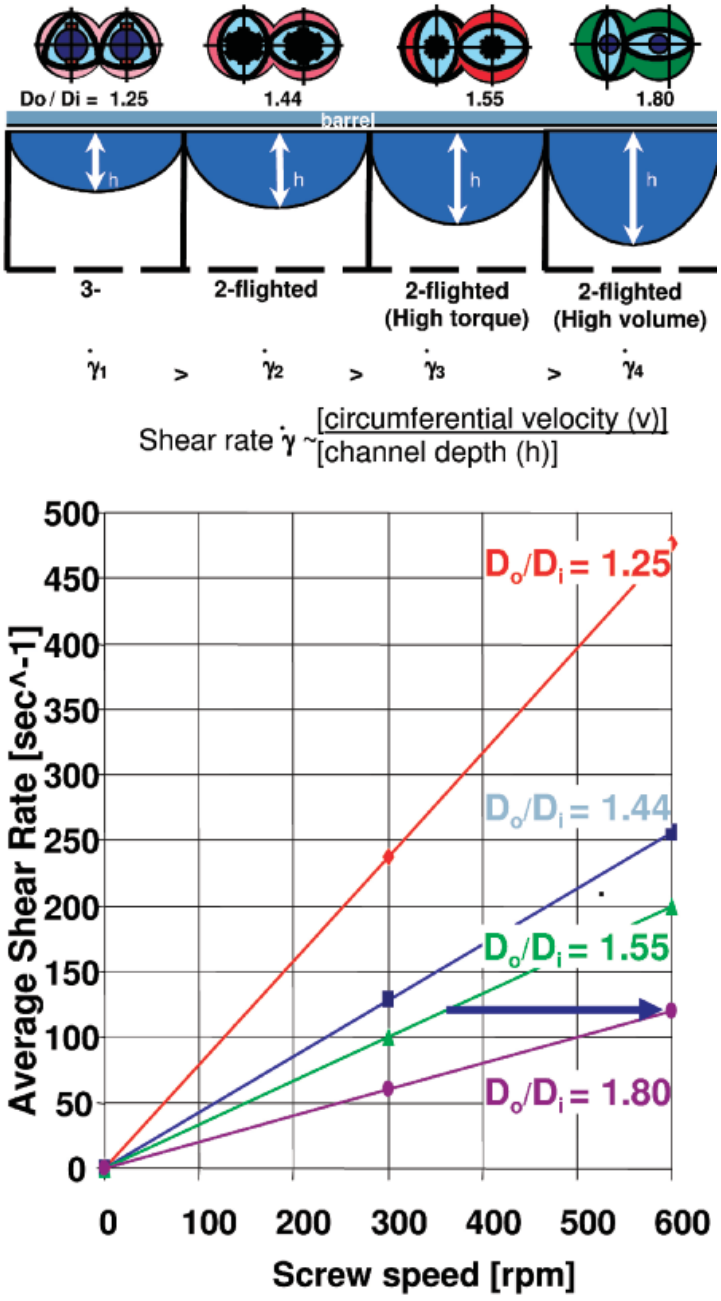

Figure 12.3-9. Schematic representation of shear rate reduction with increasing channel depth. From Andersen and Lechner (2013).

shown in Section 2.12 the temperature rise due to viscous dissipation is proportional to the shear rate raised to the power of (n+1) for power-law fluids having shear-thinning exponent n. The reduction in shear rates with increasing channel depths is shown schematically in Fig.12.3-9, from Andersen and Lechner (2013).

There are numerous types of mixing elements (i.e. gears, slotted vanes, blister rings), however, kneading disks account for 90% of those used in corotating TSEs, according to Martin (2017). The kneading disks must be designed for the type of mixing desired: Wide disks have elongational flow regions, because the lobal pool is squeezed between kneading disk and barrel wall, as shown in Fig. 12.3-10. As discussed in Section 6.8, elongational flow

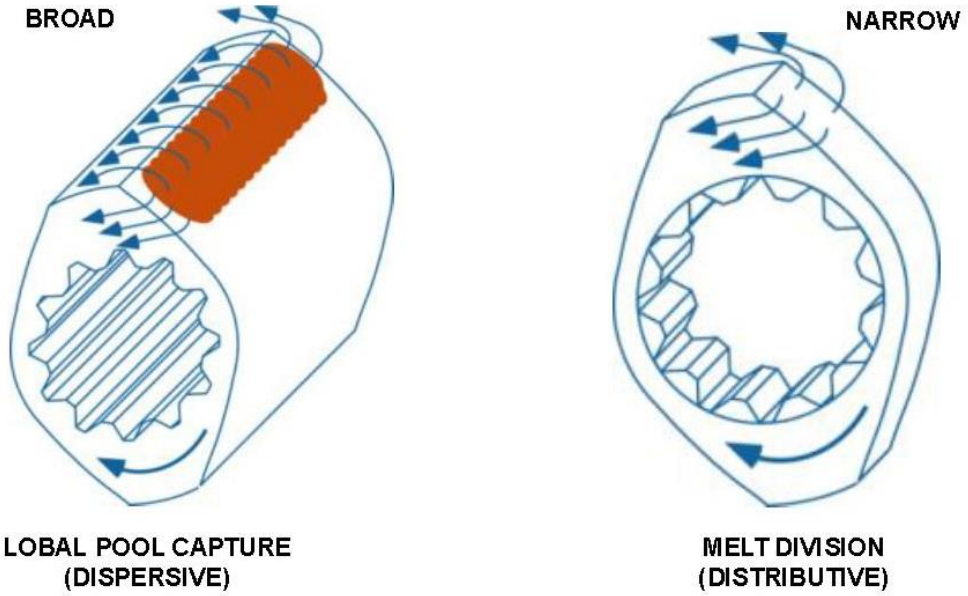

Figure 12.3-10. Mixing by kneading disks. Courtesy of Charlie Martin of Leistritz (2018).

is needed for dispersive mixing, which involves break-up of particles or liquid drops. With narrow disks the molten polymer escapes from the sides generating shear and distributive mixing (spatial rearrangement and spreading). While elongational flow is more effective for both dispersive and distributive mixing, the squeezing of the lobal pool may generate high local temperatures and narrow disks might be more suitable for processing of certain materials.

12.4 Unit Operations in Co-rotating TSEs

***FEEDING*:** Twin-Screw extruders are usually starve fed and the output rate is determined by the rate of feeding. Gravimetric or loss-in-weight feeders provide a

predetermined amount of kg/hr. The degree of fill is usually less than 40% of the available volume. The output is independent of screw speed. The screw rotation speed is used for optimization of compounding, by matching the extruder power to feeding rate. Secondary downstream feeding is possible, because there is no pressure gradient in the partially filled channels. It is frequently used for reinforcing fillers, for various types of solid additives and for liquid additives.

***MELTING*:** Melting takes place in the kneading disks due to repetitive squeezing of the particulate solids. Most of the energy for melting comes from the rotating screws with some energy input also from electrical heaters from the outside. The specific mechanical energy (SME) in Co-TSE usually varies between 0.15 kWh/kg and 0.25 kWh/kg, which includes the energy required for raising the temperature of the polymer particles, melting, mixing and pumping. The exact value depends on several variables relating to screw section design, operating conditions and material extruded. It is interesting to compare these numbers with calculation for a single screw extrusion example in Section 6.9, which gave 0.194 kWh/kg.

MIXING: As explained in the chapter on single screw extrusion (Section 6.8) and is also discussed in the previous section, mixing involves two processes: dispersion (break up of particles or drops) and distribution (spatial rearrangement and spreading). This is mainly accomplished by the kneading blocks and can also be assisted by left-hand screw elements which produce rearward flow. The screw assembly is very crucial for obtaining the desired mixing quality.

DEVOLATILIZATION and ***DEGASSING*:** It is frequently necessary to remove entrained air, residual solvents, water and other undesirable volatile contaminants. This is accomplished in one or more vents either by simple openings to the atmosphere or drawing vacuum. Several techniques have been developed for preventing the melt to escape with the volatiles.

***PUMPING*:** Co-rotating intermeshing self-wiping twin screw extruders are excellent compounders/mixers, but they have poor pressure generation capabilities. Fig. 12.4-1 shows the pressure variation along a typical co-rotating twin screw extruder. 1000 PSI (6.9 MPa) is much lower than pressures encountered in single screw extruders (SSEs), which may be as high as 50 MPa at the die head and in grooved feed SSEs much higher near the hopper.

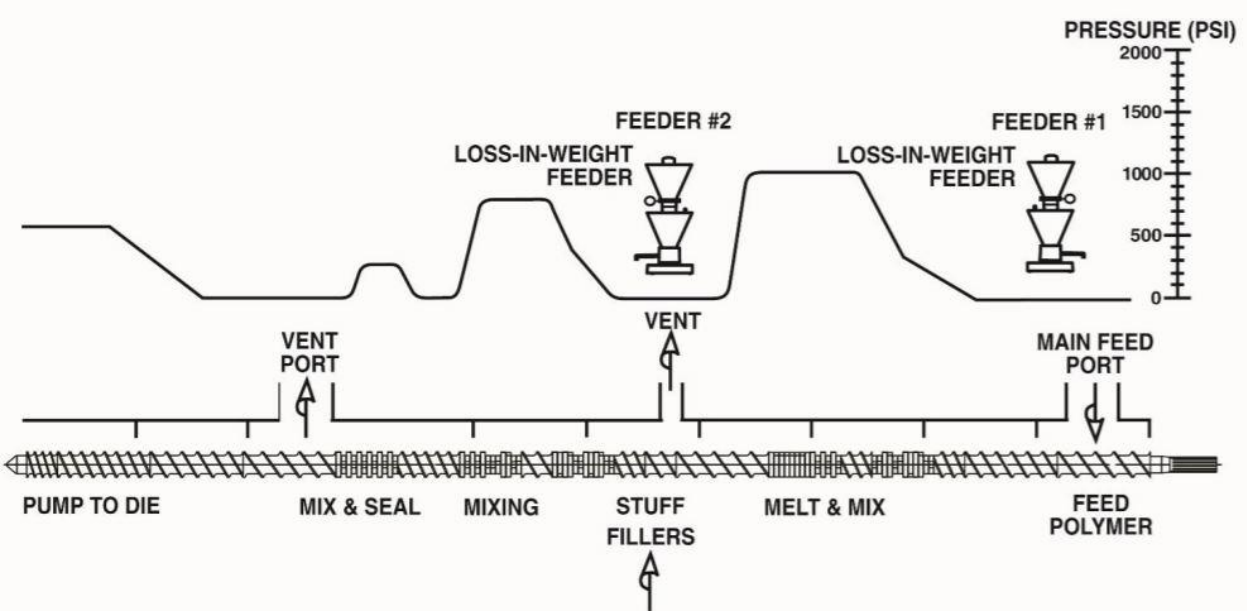

Figure 12.4-1. Typical pressure variation along a co-rotating intermeshing twin screw extruder. From Martin (2017). 1000PSI is 6.9 MPa.

12.5 Flow and Pressurization in Co-rotating TSEs

From the previous sections, it is obvious that mathematical modeling of co-rotating intermeshing twin screw extruders is a formidable task, due to geometrical complexity, which is further complicated by the virtually unlimited possibilities in assembling screw segments. The research findings of several authors are discussed in the books by Todd (1998) and Tadmor and Gogos (2006), White and Kim (2009), Manas-Zloczower (2009) and Agassant *et al.* (2017). Todd (1998) showed that, as a first approximation, the expression derived for single screw extruders, relating flow rate and pressure (see Section 6.3), is also applicable for fully filled conveying screw sections and kneading blocks, in the following form

$$Q = A \cdot N - B\frac{\Delta P}{\mu L} \tag{12.5-1}$$

where N represents the rotation speed, ΔP is the pressure, μ viscosity (Newtonian) and L the length. While the constants A and B were derived from first principles in single screw extrusion, A and B depend on the type of segment (forward or rearward, screw section or kneading block). This equation is the basis of 1D models for co-rotating intermeshing twin screw extruders, which take also into account the degree of fill of the channels and are capable of predicting the pressure and temperature along the extruder and energy consumption. Fig. 12.5-1 shows satisfactory agreement between experimental results and predictions with three

different software packages. Fully 3D simulations have also been carried out by several investigators (e.g. Bravo *et al.,* 2000, Kohlgrüber, 2008 and Nakayama *et al.*, 2018) which provide information on flow and mixing phenomena within the conveying and kneading block channels. Fig. 12.5-2 shows schematically the flow in a starved co-rotating TSE.

Usually, co-rotating TSEs are not capable of providing enough pressure to pump the polymer through the die. Thus at the end of the TSE a pressure generating device like the gear pump shown in Fig. 12.5-3, is attached. Gear pumps can generate and stabilize the pressure because they are positive displacement devices.

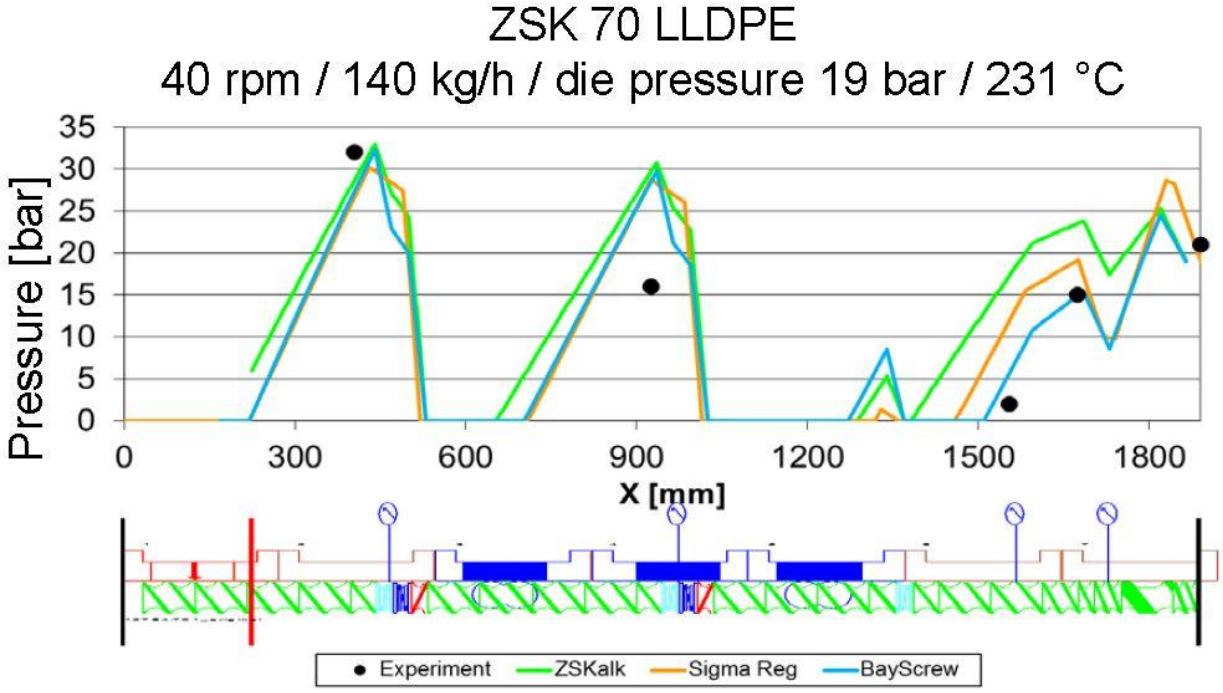

Figure 12.5-1. Experimental results and simulations of a COPERION corotating intermeshing twin screw extruder of 70 mm diameter. From Utracki (2017). Transport is from left to right.

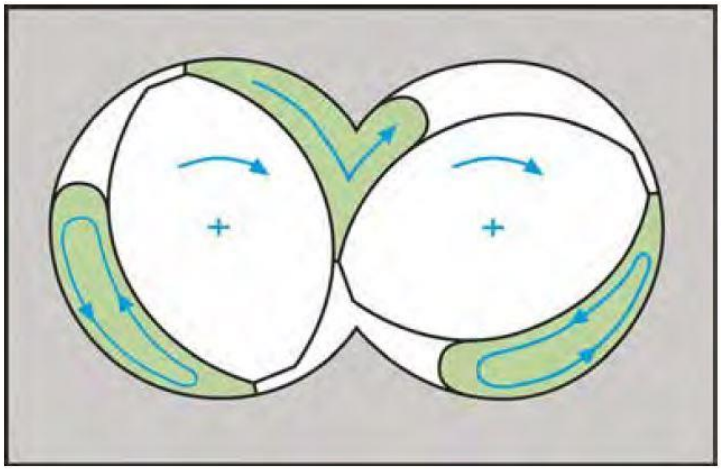

Figure 12.5-2. Schematic diagram of flow in a self-wiping co-rotating TSE. From Martin (2018).

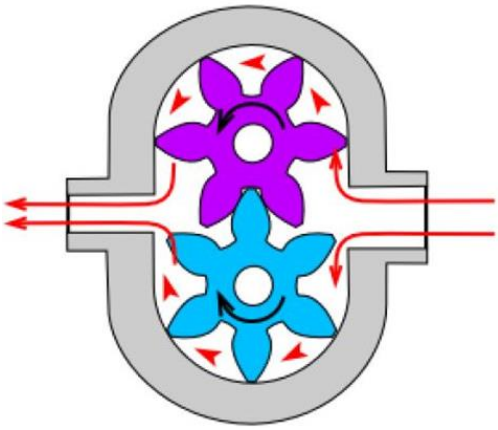

Figure 12.5-3. Schematic of a gear pump. From Martin (2018).

12.6 Counter-rotating Twin-Screw Extruders

Historically, counter-rotating TSEs have received significantly less research and development efforts than co-rotating. There are many more co-rotating TSEs than counter-rotating in operation today. The limitation of counter-rotating devices is mainly due to pressure development in the calendering gap (Speur *et al.,* 1987), which results in a separating force, as shown in Fig.12.6.1. From the flow analysis of the process of calendering (rolling of a viscous polymer melt between two counter-rotating cylinders), it can be shown (Middleman, 1977) that the separating force is given by the following expression (for a Newtonian fluid)

$$F_1 = 1.22\left(\frac{\mu U R}{h_o}\right)L \qquad (12.6\text{-}1)$$

where μ is the viscosity, R the radius, h_o the minimum gap between the cylinders, L the length of the cylinders and U the velocity of rotation.

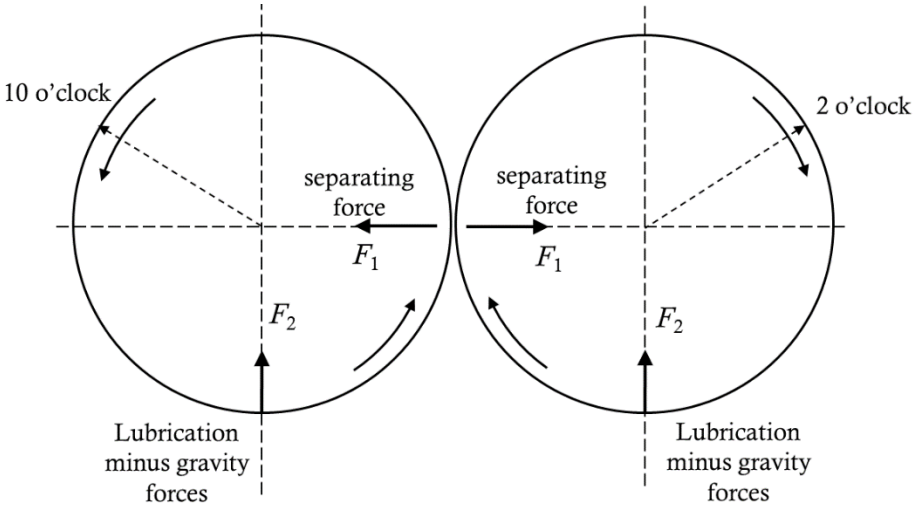

Figure 12.6.1. Separating force in the calendering gap of a counterrotating TSE and upward lubrication force, forcing the screws towards the "10 o'clock and 2 o' clock" position.

This problem has been fully analyzed by A. Demirci et al Polymers 2021, 13, 990, https://doi.org/ 10.3390/polym13070990

It can be seen from Eq. 12.6-1 that the separating force increases as the velocity increases and/or as the gap decreases. There is also gravity and a lubrication force, akin to a slider bearing (Vlachopoulos,2016), acting upwards, which also increases as the speed increases. The result is that the screws are pushed towards the "10 o'clock and 2'oclock" positions, as shown in Fig.12.6-1. Considerable wear and tear can occur at these positions. This is why todays counter-rotating fully intermeshing TSEs run at low speeds. The speed of rotation is usually less than 60 rpm and of course the output rate is lower than co-rotating machines of same diameter running at much higher speeds. The screws are connected to the gear box at the rear end through splines and are free on the front end, so they are deflected away from each other. Higher speeds (200 rpm or more) are achieved for partially intermeshing counter-rotating TSEs, because the gap is larger and the separating force can be tolerated, even at higher rpm.

Low speed closely intermeshing counter-rotating TSEs are primarily used for PVC extrusion of pipe and profiles. The screws are one piece, not modular like the co-rotating TSEs. Higher speed non-intermeshing counter-rotating extruders are used in applications related to blending, devolatilization and reactive extrusion. There are also conical counter-rotating intermeshing TSEs, distinguished by their cone-shaped screws. In the feed the screw diameter might be 100mm and at the discharge perhaps less than 50mm. Due to the converging shape, conical screw designs provide a natural compression over the entire length. Generally, they are shorter than parallel screw designs. Conical TSEs are used in extrusion of wood plastic composites and other products, but, they are less common than parallel designs.

12.7 Low Speed Counter-rotating Intermeshing Twin Screw Extruders

In counter-rotating closely intermeshing extruders, as the screws rotate, they enclose and transport the material in a helically distorted C-shaped chamber, which is sketched in Fig.12.7-1 (top). The C-shape is also shown in a photograph (Fig.12.7-1, bottom) of two intermeshing screws in which the channel segments of one screw were filled with silicon rubber. Two segments have been pulled out and it can be seen that the un-stretched piece retains its C-shape, while the other piece is flattened out by stretching, from Tadmor and Gogos (2006). The material is transported forward, just like in a positive displacement pump. However, there are leakages: Q_f (through the gap between flight and barrel wall, similar to

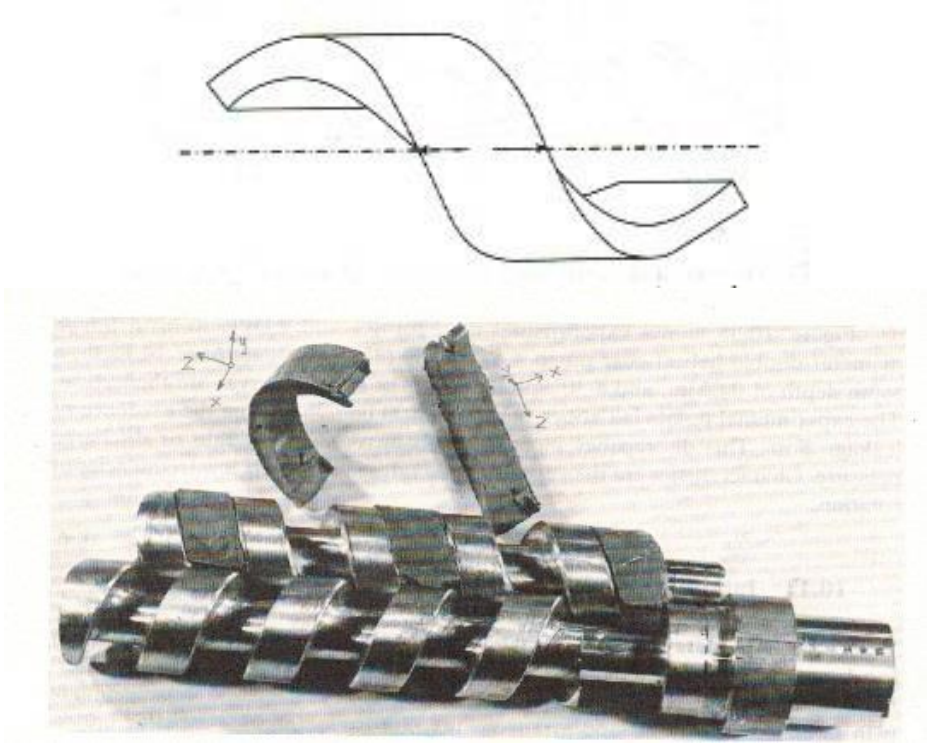

Figure 12.7-1. C-shaped chamber sketched and photographed. From Tadmor and Gogos (2006).

SSEs), Q_c (between the bottom of the channel of one screw and the flight of the other screw), Q_t (between the flanks of the flights) and Q_s (between the flanks of the flights perpendicular to the plane through the screw axis) as shown in Fig.12.7-2. So, the total transport is that of positive displacement minus the leakages. Because of the positive displacement there is small amount of shear involved and consequently little viscous dissipation (frictional heating). For this reason, the low speed counter-rotating twin screw extruders are suitable for extrusion of unplasticized PVC (U-PVC, also called rigid PVC (R-PVC)) and other temperature sensitive materials. U-PVC has a very narrow temperature processing window, melting at about 175°C and starting to degrade at 205 °C, while for HDPE it is roughly 140°C and 250°C respectively.

Schenkel (1963), proposed a simple expression for the determination of the theoretical output by assuming that it is equal to the number of C-shaped chambers becoming free per unit time multiplied by their volume

$$Q_{th} = 2iNV_c \tag{12.7-1}$$

where Q_{th} is the theoretical mass throughput, N is the screw rotation speed, V_c is the C-shaped chamber volume per screw and i the number of flights. Further, Janssen (1978) developed a more detailed analytical model by assuming that the volume of C-shaped chamber can be

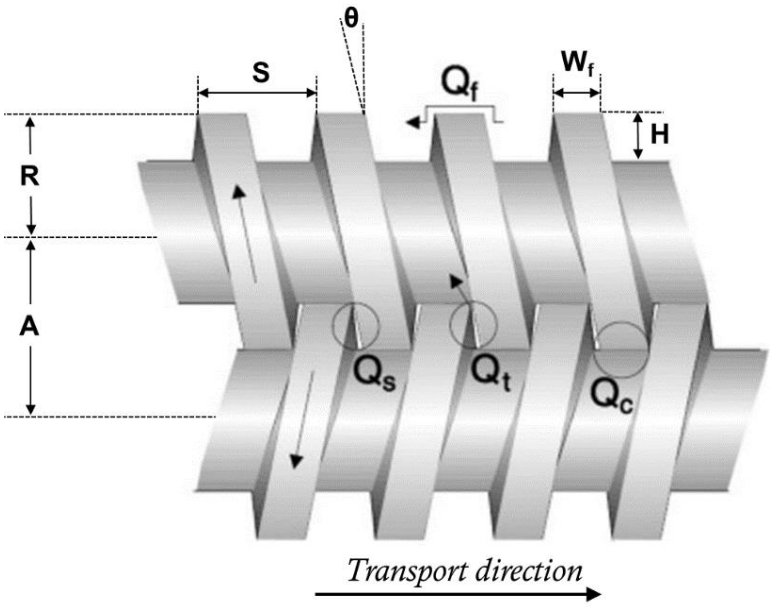

Figure 12.7-2. Computer generated sketch of two counter-rotating screws showing areas of flow leakage From Goger (2013).

calculated by subtracting the volume of a given length of screw from the same length of the empty barrel. The volume, V_1, of one side of the barrel bore over one screw lead was calculated as

$$V_1 = \left[\left(\pi - \frac{a}{2}\right)R^2 + \left(R - \frac{H}{2}\right)\sqrt{RH - \frac{H^2}{4}}\right]S \qquad (12.7\text{-}2)$$

where the variables of R, H and S are shown in Fig. 12.7-2 and α, defined as the overlapping angle in radians (as shown in Fig.12.7-3), is given by the formula

$$a = 2\tan^{-1}\left(\frac{\sqrt{RH - H^2/4}}{R - H/2}\right) \qquad (12.7\text{-}3)$$

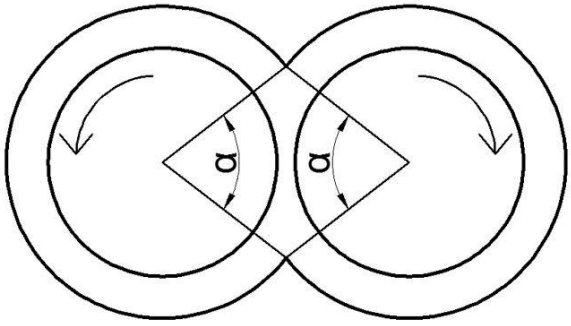

Figure 12.7-3. Definition of the overlapping angle.

The volume, V_2, of the screw root over one lead is:

$$V_2 = \pi(R - H)^2 S \tag{12.7-4}$$

The volume, V_3, of one screw flight is:

$$V_3 = 2\pi \left[\left(RH - \frac{H^2}{2} \right) W_f + \left(RH^2 - \frac{2}{3} H^3 \right) \tan\theta \right] \tag{12.7-5}$$

The total volume of the C-shaped chamber is then

$$V_c = \frac{V_1 - V_2 - iV_3}{i} \tag{12.7-6}$$

Then multiplying Eq. 12.7-1 by the melt density ρ we can obtain the mass rate of flow

$$\dot{m} = 2iN\rho\, V_c \tag{12.7-7}$$

The above simple model provides a rough estimate of the flow rate for flood fed counter-rotating closely intermeshing TSEs. In fact, flood feeding is the usual practice in extrusion of U-PVC. Goger (2013) calculated also the leakages for a given screw design. Detailed mathematical analysis of such machines has been carried out by a number of investigators including Lewandowski *et al.* (2015). Shah and Gupta (2004) compared the flow in co-rotating and counter-rotating TSEs. Generally speaking, there are fewer publications on modeling counter-rotating TSEs than Co-rotating.

Bibliography

Agassant J.-F., Avenas P., Vincent M., Vergnes B. and Carreau P.J., *Polymer Processing Principles and Modeling*, Hanser (2017)

Alsteens B., Legat V. and Avalosse T., Parametric Study of the Mixing Efficiency in a Kneading Block Section of a Twin-screw Extruder, Intern. Pol. Proc., XIX, 207 (2004)

Andersen P., Shih C-K., Spalding M.A., Wetzel M. D. and Womer T.W., Breakthrough Inventions in Polymer Extrusion, SPE ANTEC Proceedings, 668 (2009)

Andersen P.G. and Lechner F., Co-Rotating Fully Intermeshing Twi-Screw Compounding; Advancement for Improved Performance and Productivity, Plast. Engin., 32 (April 2013)

Bravo V.L., Hrymak A.N. and Wright J.D., Numerical Simulation of Pressure and Velocity Profiles in Kneading Elements of a Co-Rotating Twin Screw Extruder, Polym. Eng. Sci., 40, 525 (2000).

Goger A. *Modeling of Counter Rotating Twin Screw Extrusion*, Master's thesis, McMaster University, Hamilton, ON, Canada (2013)

Janssen, L. P. B. M. Twin Screw Extrusion, Elsevier (1978)

Kimura Y., Chaudhary A.K. and Spalding M.A., Twin-Screw Extrusion of Polyethylene, in Spalding, M.A. and Chatterjee (eds), *Handbook of Industrial Polyethylene and Technology*, Scrivener Publishing, 357 (2018).

Kohlgrüber K., *Co-rotating Twin-Screw Extruders*, Hanser (2008)

Manas-Zloczower I. (Ed.) *Mixing and Compounding of Polymers: Theory and Practice*, 2nd Edition, Hanser (2009)

Martelli F.G., *Twin-Screw Extruders: A Basic Understanding*, Van Nostrand Reinhold (1983)

Martin C., Twin-Screw Extruders as Continuous Mixers for Thermal Processing: A Technical and Historical Perspective, AAPS PharmSciTech, published online (16 Feb. 2016)

Martin C., A Typical Twin Screw Extrusion Compounding Systems for Polyolefins, SPE Polyolefins Conference Proceedings (2017)

Martin C., Optimum Twin Screw Extrusion Process Designs for PLA formulations, presented at PPS conference Boston (2018)

Middleman S. *Fundamentals of Polymer Processing*, Mcgraw-Hill (1977)

Nakayama Y., Takemitsu H. and Kajiwara T., Improving Mixing Characteristics with a Pitched Tip in Kneading Elements in Twin-Screw Extrusion, AIChE J., 64 (4), 1424 (2018)

Rauwendaal C., *Polymer Extrusion*, 5th Edition, Hanser (2014)

Schenkel G., *Kunststoff-Extrudertechnik*, Hanser Verlag, Munich (1963), available also in English, *Plastics Extrusion Technology and Theory*, Iliffe Books Ltd., London, (1966)

Schneider H-P., The Historical Development of the Counter-rotating Twin-screw Extruder, Kunststoffe, 5, 44 (2005)

Speur J.A., Mavridis H., Vlachopoulos J. and Janssen L. P. B. M., Flow Patterns in the Calender Gap of a Counterrotating Twin Screw Extruder, Adv. Poly. Tech., 7, 29 (1987)

Tadmor Z. and Gogos C. G. *Principles of Polymer Processing*, 2nd Edition, Wiley (2006)

Todd D.B. *Plastics Compounding*, Hanser (1998)

Todd D.B. Drag and Pressure Flow in Twin Screw Extruders, Intern. Polym. Proc., VI, 143 (1991)

Utracki A. Simulation of Co-Rotating Fully Intermeshing Twin-Screw Compounding Extruders, SPE Polyolefins, Houston Texas (2017)

Vlachopoulos J. and Wagner J.R. Jr (Editors) *The SPE Guide on Extrusion Technology and Troubleshooting*, SPE (2001)

Vlachopoulos, J. *Fundamentals of Fluid Mechanics*, Polydynamics Inc, Canada (2016)

Wagner J.R., Mount E.M. and Giles F. H. *Extrusion: The Definitive Processing Guide and Handbook,* 2nd edition, Elsevier (2014)

White J.L. and Kim E.K. *Twin Screw Extrusion: Technology and Principles,* 2nd Edition, Hanser (2010)

Wiedmann W. and Andersen P., Application of Co-Rotating Twin-Screw Extruders Based on Torque, Volume and RPM, SPE ANTEC Proceedings, 342 (2005)

HERMAN WERNER and PAUL PFLEIDERER

Manufacturers of the first continuous twin-screw device in the 1880's

J. Vlachopoulos and N.D. Polychronopoulos "*Understanding Rheology and Technology of Polymer Extrusion*", First Edition, Polydynamics Inc, Dundas, Ontario, Canada (2019)

SUBJECT INDEX

A

B

C

D

E

F

G

H

I

K

L

M

N

O

P

R

S

T

U

V

W

Y

Z